ISSN 0289-842X

RIKEN Accelerator Progress Report

1985

vol. 19

理化学研究所
the Institute of Physical and Chemical Research

RIKEN Accelerator Progress Report
January-December 1985

理化学研究所
the Institute of Physical and Chemical Research
Wako-shi, Saitama, 351-01 JAPAN

This volume contains recent information of the accelerators at RIKEN (IPCR), informal reports and abstracts of papers which will be published at scientific meetings or in publications by staff members, guests, and visitors.

CONTENTS

I. INTRODUCTION

H. Kamitsubo

Collaborative research work using the 160 cm cyclotron and the variable-frequency heavy-ion linear accelerator (RILAC) has been extensively performed this year. In addition to these two accelerators, a 1 MeV electrostatic accelerator (TANDETRON) and a 250 kV ion implanter were dedicated to the collaborative research works. During the past one year these accelerators have been operated steadily as before.

A variety of studies on nuclear physics have been continued mainly using the 160 cm cyclotron. Collaboration with other institutions has also been continued on nuclear physics.

Well-developed rotational bands were observed experimentally in the excited states of Sn isotopes which are spherical at the ground states, owing to the BGO anticompton spectrometers. Detailed information on the transition properties in rare earth nuclei was obtained from the Coulomb excitation experiments performed at the Japan Atomic Energy Research Institute. Light ion induced reactions were studied at the Research Center for Nuclear Physics, Osaka University, by using polarized protons and deuterons, and an important role of a collective hexadecapole mode in the γ-vibrational band of ^{152}Sm was revealed.

Theoretical studies of nuclear structures were performed by extending the interacting boson model to include s-bosons and a particle alignment. Heavy ion reaction mechanisms were also studied in terms of the transport theory and the time-dependent Hartree-Fock theory.

International collaboration between RIKEN and the IN2P3 (Institut National des Physique Nucleaire et Physique Particulaire, France) was started in this period on the nuclear spectroscopy with BGO anticompton spectrometers and also on the measurements of moments of nuclei far from the stability line.

Experimental work was carried out on the beam foil spectroscopy and on atomic collision processes by measuring the spectra of lights, X-rays and Auger electrons, the impact parameters of scattered projectiles, and the charge distribution of recoiled ions or dissociated target molecules. Various kinds of ions accelerated by the RILAC were also used for these studies. The electron beam ion source, called proto-NICE, developed at Nagoya University was rebuilt and tested for electron ion merging beam experiments at the RILAC.

The theoretical researches on atomic processes have also been performed in various problems such as electron stripping of incident heavy ions by neutral targets, $(\mu^+\mu^-)$ formation by collision of μ^+ with $(\mu^-\mathrm{p})$, charge transfer in low velocity heavy ion impact, some abnormality about generalized oscillator strength, and radiative electron capture. Some are closely related to the experimental research projects at the RILAC and have led to interesting results.

Mössbauer spectroscopy and perturbed angular correlation studies have been continued to investigate the annealing behavior of defect-impurity complexes in metals and the hyperfine fields in magnetic oxides. The distribution of implanted or dissolved impurities in various materials and the lattice location of hydrogen in metals have been investigated by means of the Rutherford back scattering (RBS) method, the elastic recoil detection (ERDA) method, and the channeling method. Regarding the gas atoms introduced into metals by implantation, their diffusion, and the effect on the mechanical properties, *i.e.*, helium embrittlement, were studied. Studies of vacancies in metals have started in cooperation with a research group of Osaka University.

Mössbauer spectroscopy and perturbed angular correlation studies have also been continued to investigate the chemical states of adsorbed metal ions on magnetic oxides and defect structure in surfaces. The after-effects of the EC decay of ^{119}Sb and ^{111}In were compared in oxides. Production of a new probe for surface studies, carrier-free ^{151}Gd, has begun.

A calibration curve for IR absorptiometry of C in Si was obtained with high precision by charged particle activation analysis. ^{15}N and D have been shown to be useful activable tracers in solid state science when $^{15}\mathrm{N}(\alpha, \mathrm{n})^{18}\mathrm{F}$ and $\mathrm{D}(^3\mathrm{He}, \alpha)\mathrm{p}$ reactions are utilized for detection. Determination of heavy elements by RBS and hydrogen by ERDA in semiconductors and metals has been continued. PIXE analysis was applied to medical and geological samples.

Bromospiperone labeled with radiobromine was synthesized; it has made possible PET visualization of dopamine receptor in the brain of monkey. Adsorption of ^{29}Al on soils and uptake of ^{45}Ti and ^{69}Ge by plants were studied.

Construction of the RIKEN Ring Cyclotron is in progress. During the past one year, field distribution measurements have been performed for four sector magnets with and without the injection and extraction elements. Fabrication of the other components such as vacuum chambers and an evacuation system, their RF resonators and power amplifiers and a control system, are under way at factories.

RIKEN Accel. Progr. Rep. 19 (1985)

II. OPERATION OF ACCELERATORS

1. Cyclotron Operation

S. Kohara, K. Ikegami, S. Fujita, K. Ogiwara,
H. Takebe, T. Kageyama, and I. Kohno

The 160 cm cyclotron was operated on the 24 h a day basis during the period from Nov. 8, 1984 to Nov. 7, 1985. Statistics of the machine operation time is shown in Table 1. The total net beam time of 3,507.5 h is 5.4% (654.1 h) less than that (382 days) of the last period.

This decrease in net beam time is due to decrease in scheduled beam time and increase in the time for periodical inspection and repair.

Table 2 shows the beam time allotment to various research activities in this period. The scheduled beam time was decreased by 386.5 h

Table 1. Cyclotron operation in the period XX.

	Oscil-lator	Ion source	Beam
Reading of the time meter on Nov. 07, 1984 (h)	86,420.1	90,909.0	53,950.1
Reading of the time meter on Nov. 07, 1985 (h)	90,854.9	95,638.6	57,457.6
Difference (h)	4,434.8	4,729.6	3,507.5
Percentage of 365 days	50.6%	54.0%	40.0%

Schedule in this period:	
Beam time	224 days
Overhaul and installation	49
Periodical inspection and repair	32
Scheduled shut down	60

Table 3. Distribution of beam time among particles accelerated.

Particle	(h)	(%)
p	458	9.4
d	89	1.8
$^{3}He^{2+}$	446	9.2
$^{4}He^{2+}$	1,117.5	22.9
$^{7}Li^{2+}$	48	1.0
$^{12}C^{4+}$	456	9.4
$^{13}C^{4+}$	120	2.5
$^{14}N^{4+}$	641	13.2
$^{14}N^{5+}$	124	2.5
O^{5+}	1,299	26.7
Ne^{6+}	72	1.5
Total	4,870.5	100

Table 2. Scheduled beam time and research subjects in the period XX.

Subject		Scheduled beam time (h)		
		Heavy ion	Light ion	Total
Nucl. Phys.	Nuclear reaction	2,236	557.5	2,793.5
	RI production	0	185	185
Fields other than Nucl. Phys.	Nuclear chemistry	0	640	640
	Radiation biology	60	66	126
	Radiation chemistry	307	116	423
	Solid state physics	0	22	22
	Radiation damage	0	55	55
	Test of radiation	46	24	70
Outside users	Radiation damage	41	101	142
	RI production	0	21	21
	Test of track detector	0	29	29
	Test of radiation detector	24	60	84
	Radiochemical analysis	46	234	280
Total		2,760	2,110.5	4,870.5
Percent in total		56.7%	43.3%	100%

Maintenance, operation, and engineering:	
Exchange of ion sources	88 h
Machine inspection and repair	768 h
Total	856 h

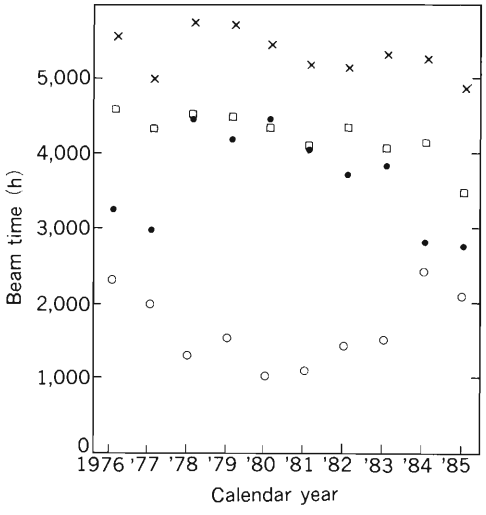

Fig. 1. The cyclotron beam history. ● Heavy ions (Scheduled beam time), ○ Light particles (Scheduled beam time), × Total (Scheduled beam time), □ Net beam time.

compared with that of the last period.

Table 3 shows the distribution of the scheduled beam time among various particles. Figure 1 shows the cyclotron beam history over the past 10 years.

RIKEN Accel. Progr. Rep. 19 (1985)

II-2. RILAC Operation

Y. Miyazawa, M. Hemmi, T. Inoue, T. Kambara, M. Yanokura, M. Kase, T. Kubo, E. Ikezawa, K. Kihara,* T. Aihara,* and Y. Chiba

The RIKEN heavy-ion linear accelerator, RILAC, has been under steady operation and various kinds of ion beams have been used for experiments. Tables 1 and 2 give statistics of operation in the period Sep. 1, 1984-Aug. 31, 1985. The scheduled beam time for 6 days was cancelled owing to trouble in optical fiber cables transmitting control signals to the 500 kV high voltage terminal of the injector and in a coaxial line supplying radio frequency (RF) power from the main amplifier to the feeder.

During the period Aug. 1-Sep. 15, 1985, the 13th drift tube of the 2nd resonator was replaced with a new one because of insulation failure in its quadrupole magnet. At this opportunity, RF measurements were performed concerning possible calibration errors of the tank voltage pick-up in the high frequency region and current distributions at the short end of the resonator. Field distributions along the beam axis in the resonator were also checked by the perturbation method.

Table 3 gives statistics of ions used in this period. Most of users preferred Ar ions as in the last year, and 36% of the total beam time was devoted to this ion. Al and Cu ions were also requested frequently and beam time for those metal ions amounted to about 22% of the total.

The ion source facility installed on the 500 kV high voltage platform was added with some improvements: a static quadrupole lens,[1] which focuses the beam from the ion source at the entrance of the acceleration column, was installed at the beam exit of the chamber; an anode bore of the ion source was modified from 8 to 10 mm.[2] Beams of heavy ions, such as Ar, Kr, and Xe, were intensified by a factor of 5 or more. Five new ion sources adaptable to both gaseous and metalic elements were completed in the machine shop of the institute this summer; parameter studies on their performance are going on.

* Sumijyu Accelerator Service Ltd.

Table 1. Statistics of operation in the period of Sep. 1, 1984-Aug. 31, 1985.

	days	%
Beam time	155	42.5
Frequency change	19	5.2
Overhaul and improvement	46	12.6
Periodic inspection and repair	30	8.2
Machine trouble	5	1.4
Scheduled shut down	110	30.1
	365	

Table 2. Division percentage of beam time by research activities.

	%
Atomic physics	42.5
Solid-state physics	19.4
Nuclear physics	3.2
Radiochemistry and nuclear chemistry	21.3
Radiation chemistry and radiation biology	3.9
Accelerator research	9.7

Table 3. Statistics of ions used in the period of Sep. 1, 1984-Aug. 31, 1985.

Particles	days	%	Particles	days	%
He^{+}	11	6.8	Ne^{4+}	4	2.5
He^{2+}	17	10.5	Al^{3+}	27	16.7
C^{2+}	2	1.2	Al^{4+}	2	1.2
N^{2+}	15	9.3	Ar^{4+}	53	32.7
N^{3+}	4	2.5	Ar^{5+}	4	2.5
$^{15}N^{2+}$	6	3.7	Ar^{6+}	1	0.6
O^{+}	1	0.6	Cu^{4+}	6	3.7
O^{3+}	1	0.6	Kr^{7+}	2	1.2
Ne^{2+}	4	2.5	Kr^{8+}	1	0.6
Ne^{3+}	1	0.6	Xe^{9+}	1	0.6

References

1) M. Hemmi: p. 207 in this report.
2) Y. Miyazawa: p. 212 in this report.

RIKEN Accel. Progr. Rep. **19** (1985)

II-3. TANDETRON-Operation

H. Sakairi, T. Kobayashi, and E. Yagi

The machine was operated for 107 days for one year from November, 1983. About 100 days were alloted to overhaul, repair, and improvement.

The species of accelerated ions were ^{3}He, ^{4}He, ^{11}B, and ^{12}C in the last period. At the end of this period hydrogen acceleration was licenced by the Science and Technology Agency. The test acceleration is now being carried out and a new ion source for hydrogen ion production is in a planning stage.

Subjects of experimental studies carried out during this year were:

(a) Thickness measurements of carbon film coatings (Cyclotron Lab.),

(b) Analysis of silicon ohmic contact systems (Nuclear Chem. Lab. and NEC),

(c) Depth profile of implanted Na ions in high-polymers (Biopolymer Phys. Lab. and Beam Analysis Center),

(d) Composition of TiC films (Beam Analysis Center),

(e) Depth profile and lattice location of Eu in CaF_2 (Semiconductors Lab. and Beam Analysis Center),

(f) Solubility of D in Si (Nuclear Chem. Lab.),

(g) Stress-induced superdiffusion of hydrogen atoms in metals (Metal Phys. Lab. and Beam Analysis Center),

(h) *In situ* observation of heavy ion-induced damage in metals (Metal Phys. Lab. and Beam Analysis Center).

Following improvements are in progress:

(1) Construction of a new beam line connected to an electron microscope is at the final stage of beam alignment. The microscope, used for *in situ* observation of damage process in metals irradiated with heavy ions, has been equipped with an X-ray spectrometer to study precipitation or solution of alloying elements during irradiation.

(2) Automation of time-consuming channeling experiments was planned and a system with a personal computer (PC-9801) is being prepared at the work shop.

(3) A recovery system of ^{3}He gas, a source of ^{3}He ions, is under construction. The ^{3}He ions are used for nuclear reaction analysis, a unique tool for deuterium detection.

Main troubles occurred in the ion sources. The troubled components were a cesium ion gun in the sputtering ion source, a high voltage generator for ion extraction from the sputtering ion source, and a lithium boiler of charge exchanger connected to a duoplasmatron. Electric power sources for an acceleration voltage generator and a beam analyzing magnet also experienced trouble.

RIKEN Accel. Progr. Rep. 19 (1985)

III. RESEARCH ACTIVITIES

1. Nuclear Physics

1. Analyzing Power Measurements of (d, ^{2}He) Reactions on ^{12}C, ^{13}C, ^{14}N, and ^{90}Zr

T. Motobayashi, M. Ishihara, N. Matsuoka,* H. Sakai,* T. Saito,* K. Hosono,* A. Sakaguchi,** S. Shimoura,** and A. Okihana***

[NUCLEAR REACTIONS ^{12,13}C, ^{14}N, ^{90}Zr (polarized d, ^{2}He), E = 70 MeV; measured $\sigma(\theta)$, $A_y(\theta)$. DWBA analysis. Enriched and natural targets.]

The (d, ^{2}He) reaction has a unique property of exciting only spin-flip final nuclear states. This is because of the strong $T = 0$ $S = 1$ final-state interaction of outgoing two protons in small relative energy (around 400 keV). Other light-ion induced charge exchange reactions which excite $T = T_0 + 1$ final states, such as (n, p) and (t, ^{3}He) reactions, always contain the contribution from non spin-flip transitions. Therefore the (d, ^{2}He) reaction has been expected to be a good probe for investigating the isovector spin-flip strength of nucleus, and measurements have been performed on light nuclei.[1)-3)] However, the results obtained up to now are not so promising because the angular distributions are somewhat monotonic irrespective to the transferred angular momentum (l) and there is no significant enhancement for $l=0$ transitions which is expected from the good kinematical matching.

The present experiment was performed with polarized deuterons to investigate the l-dependence of spin-dependent observables. We also measured (d, ^{2}He) energy spectra for a ^{90}Zr target to investigate the spin-flip isovector strength.

Vector polarized deuterons of 70 MeV provided from the RCNP cyclotron were used to bombard targets set inside a small scattering chamber. Outgoing two protons were detected outside the chamber through a thin Mylar window by eight sets of the counter telescopes consisting of SSD ΔE and NaI(Tl) or Si(Li) E detectors. These eight telescopes were set in two 2×2 matrixes. Each counter matrix has 6 combinations of coincidence for ^{2}He detection. The total effective solid angle for ^{2}He detection is about 2 msr in the present setup. A typical energy spectrum of the (d, ^{2}He) reaction on ^{12}C is shown in Fig. 1. Peaks corresponding to the ground-state transition and the 2^--4^- doublet of about 4.5 MeV excitation energy are observed. For the ground-state peak the $l=0$ transition from $p_{3/2}$ to $p_{1/2}$ is the main component. On the other hand, the doublet peak should correspond to the transitions from $p_{3/2}$ to $s_{1/2}$ or $d_{5/2}$ orbits and, therefore,

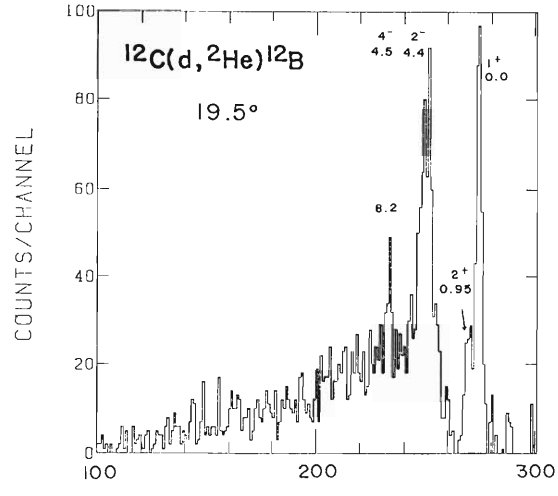

Fig. 1. Energy spectrum of the ^{12}C(d, ^{2}He)^{12}B reaction at 70 MeV.

* Research Center for Nuclear Physics, Osaka University.
** Department of Physics, Kyoto University.
*** Kyoto University of Education.

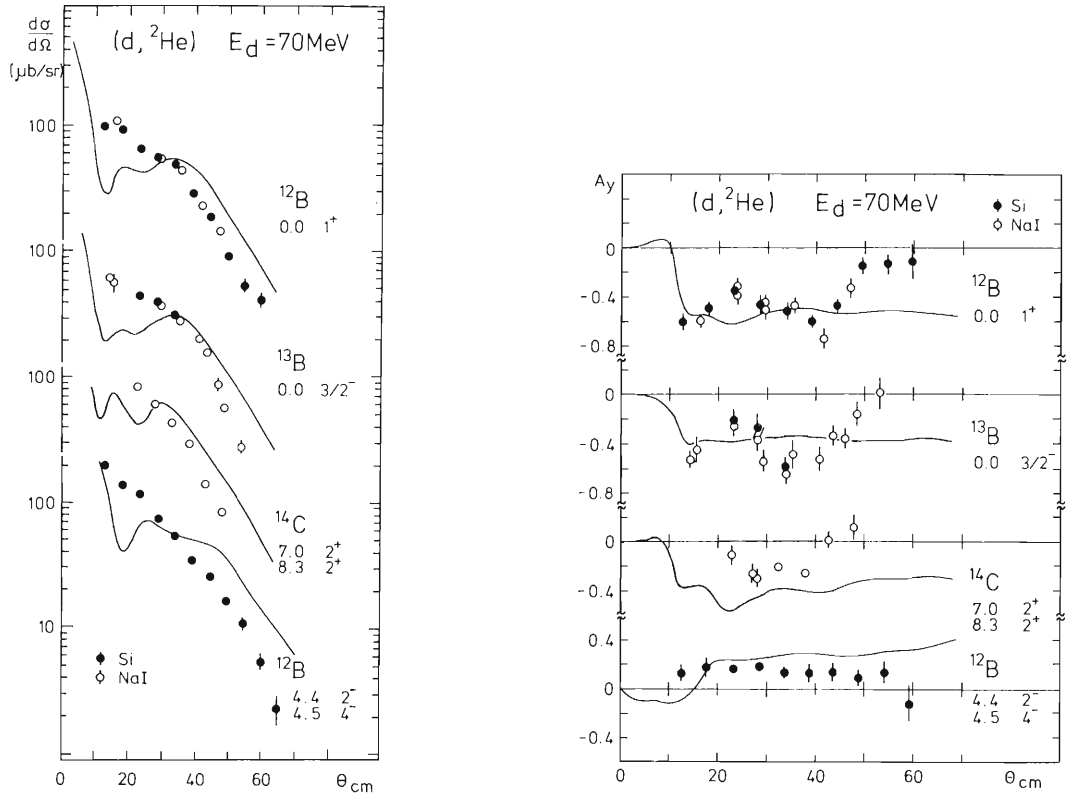

Fig. 2. Differential cross sections (a) and vector analyzing powers (b) of the reactions of ^{12}C(d, ^{2}He)^{12}B, ^{12}C(d, ^{2}He)^{13}B and ^{14}N(d, ^{2}He)^{14}C. Note that for the ^{14}N target yields of two 2^+ states at 7.0 and 8.3 MeV are summed.

transferred angular momentum l is not equal to 0.

Angular distributions of the differential cross section and the vector analyzing power are shown in Fig. 2. Solid lines show the results of DWBA calculations in which one-step charge-exchange spin-flip mechanism was assumed. Cohen-Kurath[4] wave functions were used to calculate the spectroscopic overlap of targets and residual nuclei. It is clearly seen from Fig. 2 that $l=0$ transitions have large negative vector analyzing powers while A_y values for the $l\neq 0$ (according to the DWBA analysis $l=1$ is dominant) transitions are slightly positive. Overall features of these A_y values are well reproduced by the DWBA calculations as shown in Fig. 2. This is a very encouraging result in studying the $l=0$ spin-flip strength in nuclei.

One of the future programs of the study on (d, ^{2}He) reactions is the isovector spin-flip strength in medium heavy nuclei, for example spin-flip dipole and 2 $\hbar\omega$ jump Gamow-Teller resonances. As a first try of this direction we measured the cross sections and A_y of the ^{90}Zr(d, ^{2}He)^{90}Y reaction. As shown in Fig. 3, broad bumps are seen at about 7 and 12 MeV excitation energies. They should correspond to the spin flip dipole resonance ($l=1$, $s=1$) and the spin-flip part of the E2

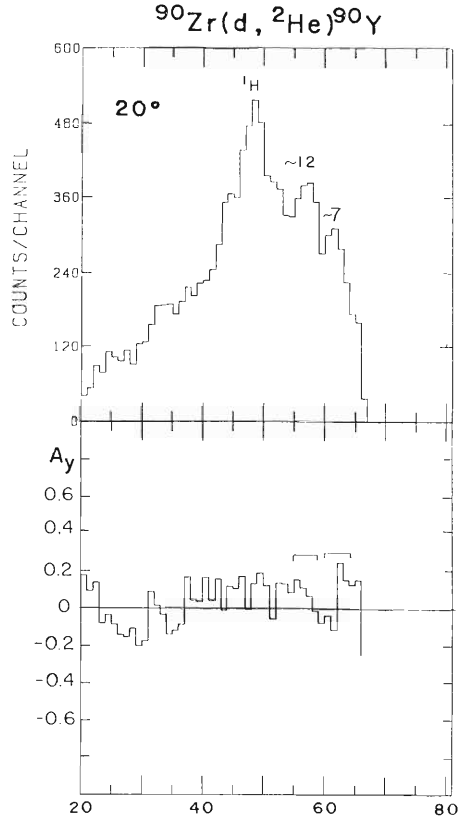

Fig. 3. Energy spectrum and vector analyzing power for the reaction ^{90}Zr(d, ^{2}He)^{90}Y at 20°.

isovector resonance ($l=2$, $s=1$), respectively. Although in the same energy regions non spin-flip resonances are expected (in fact the E1 and E2 isovector resonances have been observed in the energy spectra of the (n, p) reaction[5] on the same target), they are suppressed by the $s=1$ selection rule of the (d, ^{2}He) reaction.

References

1) D. P. Stahael, R. Jahn, G. J. Wozniak, and J. Cerny: *Phys. Rev. C*, **20**, 1680 (1979).
2) K. B. Beard, J. Kasagi, E. Kashy, B. H. Wildenthal, D. L. Freisel, H. Nann, and R. E. Warner: *Phys. Rev. C*, **26**, 720 (1982).
3) S. Kohmoto, M. Ishihara, and T. Kubo: *RIKEN Accel. Progr. Rep.*, **18**, 8 (1984).
4) S. Cohen and D. Kurath: *Nucl. Phys. A*, **101**, 1 (1967).
5) N. S. P. King and J. L. Ullmann: Proc. Conf. The (p, n) Reactions and N-N Forces, Telluride, p. 373 (1979).

RIKEN Accel. Progr. Rep. 19 (1985)

III-1-2. Beta Decay of Polarized Nucleus ^{15}C Produced in Heavy-Ion Reaction

K. Asahi, M. Ishihara, T. Shimoda,* T. Fukuda,** N. Takahashi,* K. Katori,** S. Shimoura,*** N. Ikeda,*** K. Hanakawa,** A. Nakamura,*** T. Itabashi,**** Y. Nojiri,** and T. Minamisono**

[NUCLEAR REACTION ^{232}Th(^{15}N,^{15}C), $E=158$ MeV, β-decay of ^{15}C; measured β-ray asymmetry, NMR; deduced magnetic moment, spin polarization.]

Studies of the β-decay of oriented nucleus have been valuable sources of information on fundamental interactions and nuclear structures. The testing ground for such investigations, however, has been limited to nuclei near the stability line. Recent progress in accelerator and instrumentation has opened a new possibility of access to the region more removed from the stability line. Substantial sizes of polarization observed in projectile-like fragments in heavy-ion reactions[1] suggest a useful application of these reaction products to the β-decay studies.

We report a study of the β-decay of a neutron-rich nucleus ^{15}C ($T_{1/2}=2.449$ s, $Q_\beta=9.772$ MeV) to the ground state of ^{15}N. This $1/2^+\rightarrow 1/2^-$ non-unique first-forbidden transition receives contributions from the rank-zero and the rank-one matrix elements,[2] and is interesting in the study of many-nucleon systems involving virtual mesons, since the rank-zero matrix element is dominated by the time-like component A_0 of the weak axial-vector current in which the mesonic exchange effect is predicted to be enhanced.[3] Experimental discrimination between the rank-zero and the rank-one contributions can be made by observing asymmetry[4] in the angular distribution of β-rays from a polarized nucleus. In the present work we thus measure the β-ray asymmetry in the ^{15}C decay. In addition the asymmetry is utilized to detect the nuclear magnetic resonance (NMR) for determination of the magnetic moment of ^{15}C, which provides additional information on nuclear structure of the parent state.

A 158 MeV ^{15}N beam from the AVF cyclotron at the Research Center for Nuclear Physics, Osaka University, was used. A spectrometer DUMAS[5] provided a means for isotope separation of projectile-like fragments produced in the heavy-ion reaction.[6] Reaction products emitted from the target at $\theta_L=25°$ were transmitted to DUMAS, in which those with $B\rho=0.99$-1.07 Tm passed through the momentum slit in the medium focal plane and then were triple-focussed on a stopper (high-purity graphite) placed at the second focal point. The setup used for the measurement of the β-ray asymmetry is schematically shown in Fig. 1. β-Rays emitted from the products implanted in the stopper were detected by using counter telescopes placed above and below the stopper. Observed time and energy spectra of β-rays revealed that the background contribu-

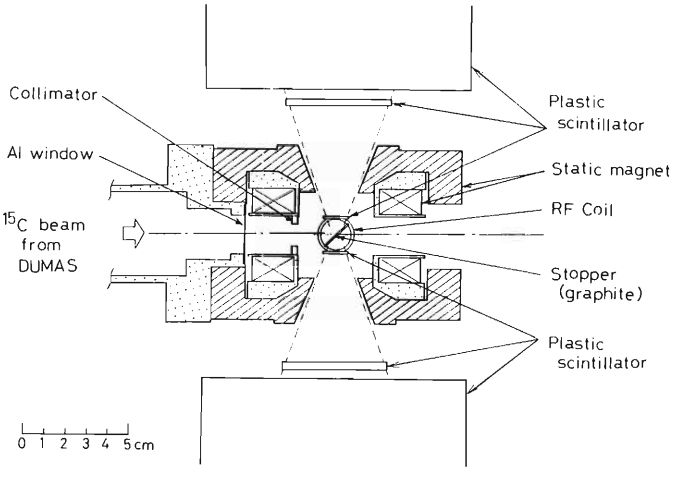

Fig. 1. Experimental setup used for the measurement of β-ray asymmetry.

* College of General Education, Osaka University.
** Faculty of Science, Osaka University.
*** Faculty of Science, Kyoto University.
**** Research Center for Nuclear Physics, Osaka University.

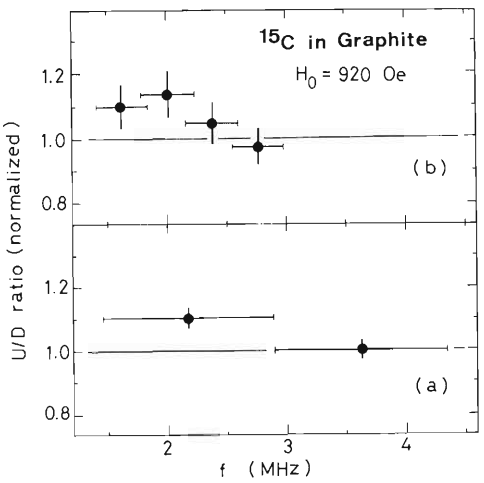

Fig. 2. Up/down ratio of β-ray yield, measuerd after the application of an rf field with its frequency swept over the ranges (a) $\Delta f = 1.3$ MHz and (b) $\Delta f = 0.43$ MHz.

tion due to activities other than ^{15}C was indeed small. Spin inversion technique using NMR was utilized in the asymmetry measurement: An up/down ratio of the β-ray yield was measured both with spins inverted by applying an rf field for NMR, and with spins unaltered. The result for the β-transition to ^{15}N($1/2^+$) (Gamow-Teller transition) is shown in Fig. 2, from which the value for the ^{15}C magnetic moment was found to lie in the region between 1.0 and 2.0 nm. Figure 3 shows spin polarization of ^{15}C in the ^{232}Th(^{15}N, ^{15}C) reaction deduced from the observed asymmetry on the basis of the known asymmetry factor $A = -2/3$ for this allowed transition.

Development of a setup for more refined measurements of magnetic moment and β-ray asymmetry for forbidden transition is in progress.

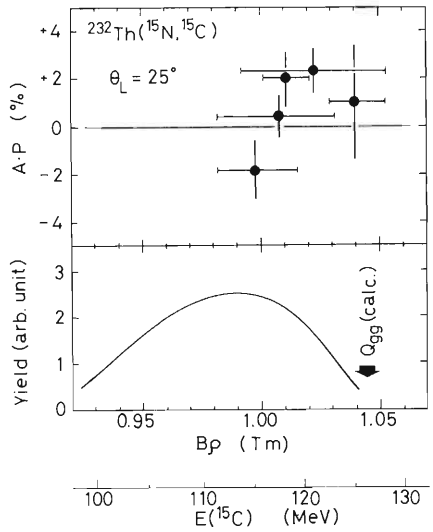

Fig. 3. Energy dependence of the obtained polarization P multiplied by the asymmetry factor $A = -2/3$, for ^{15}C products in ^{232}Th(^{15}N,^{15}C) reaction at $E_L = 158$ MeV.

References

1) K. Tanaka, M. Ishihara, H. Kamitsubo, N. Takahashi, A. Mizobuchi, Y. Nojiri, T. Minamisono, and K. Sugimoto: *J. Phys. Soc. Jpn.*, **44**, Suppl., 825 (1978).
2) E. K. Warburton, D. E. Alburger, and D. J. Millener: *Phys. Rev. C*, **29**, 2281 (1984).
3) K. Kubodera, J. Delorme, and M. Rho: *Phys. Rev. Lett.*, **40**, 755 (1978).
4) M. Morita: Beta Decay and Muon Capture, W. A. Benjamin Inc., Reading, p. 173 (1973).
5) T. Noro, M. Nakamura, H. Sakaguchi, H. Sakamoto, H. Ogawa, M. Yosoi, T. Ichihara, N. Isshiki, M. Ieiri, S. Kobayashi, and H. Ikegami: *RCNP Ann. Rep.*, **1982**, p. 189 (1982).
6) K. Asahi, M. Ishihara, T. Shimoda, T. Fukuda, N. Ikeda, C. Konno, S. Shimoura, K. Katori, Y. Nojiri, and T. Minamisono: *RIKEN Accel. Progr. Rep.*, **18**, 41 (1984).

RIKEN Accel. Progr. Rep. 19 (1985)

III-1-3. Nuclear Polarization Produced by a Tilted-Foil Method in 35.5 MeV Al Ions

M. Ishihara, H. Ohsumi, S. Kohmoto, K. Asahi, K. Sugimoto,*
T. Tanabe,* T. Hattori,** H. Hamagaki,* and K. Haga***

[NUCLEAR POLARIZATION *via* Beam-tilted foil reaction with 35.5 MeV Al ions; observed resultant nuclear polarization using analyzing power of Coulomb-excitation scattering.]

The present report is concerned with investigation on a spin-polarization phenomenon observed for beam ions transmitted through tilted foils. In such beam-foil reactions atomic spins of ions can be oriented appreciably.[1] The process may be easily used for production of nuclear polarization by further letting the ions fly in vacuum.[2] In the free flight, initial atomic polarization will be transferred to nuclear polarization through exertion of hyperfine interaction. So far the phenomenon has been studied and used mainly at low energies below few 100 keV/nucleon.[1),2)] In this work induced nuclear polarization has been observed for the first time in an energy domain of ~ MeV/nucleon. Such information on higher-energy ions is particularly useful in application to nuclear spectroscopy, since unstable nuclei of primary interest are often produced with high velocities.

The experiment was performed with Al ions accelerated at the RIKEN Heavy-Ion Linear Accelerator (RILAC). The beam energy was chosen to be 35.5 MeV. A schematic view of the experimental setup is shown in Fig. 1. The ions were transmitted through thin carbon foils. The atomic polarization was supposed to be generated at the exit surface of the foil and the nuclear polarization to be induced during subsequent free flight of ions. A stuck of 2 or 5 foils was used to enhance the polarization by exploiting an accumulative effect of multiple foils. The normal of the foils was tilted with respect to the beam direction by a fairly large angle ($\alpha=60°$), since the polarization is expected to be proportional to sin (α). In practice the angle α (hence the polarization axis) was reversed periodically at a short time interval.

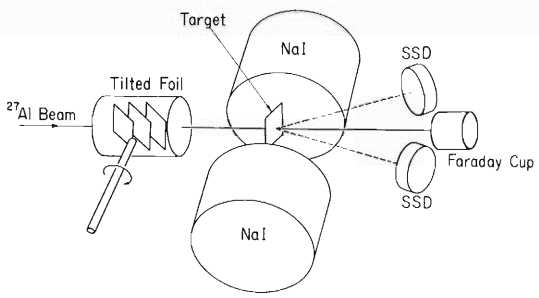

Fig. 1. Schematic view of the experimental setup.

Observation of the nuclear spin orientation was made by introducing a new method based on asymmetry of the Coulomb-excitation scattering process. The second carbon foil placed about 10 cm downstream from the tilted foils served as a target for the scattering. The scattered particles were detected with two Si detectors placed in the plane normal to the polarization axis and at symmetric angles $\pm40°(\pm5°)$ with respect to the beam. The angles were chosen to optimize the balance among cross section, analyzing power, and s/n ratio. The kinematical condition for this geometry afforded another advantage that only carbon recoils hit the detector eliminating a need for a complicated particle identification procedure. Two NaI detectors of $6''\phi\times6''$were employed to detect γ-rays in the deexcitation of the Coulomb-excited states, and the scattered particles were registered in coincidence with these γ-rays. This procedure eliminated the contribution from the strong elastic (Rutherford) scattering and served to distinguish different branches of the Coulomb-excitation. Figure 2 shows a coincidence γ-ray spectrum. Two peaks at 0.84 and 1.01 MeV are due to deexcitation of the 1st

* Institute for Nuclear Study, The University of Tokyo.
** Tokyo Institute of Technology.
*** Faculty of Engineering, The University of Tokyo.

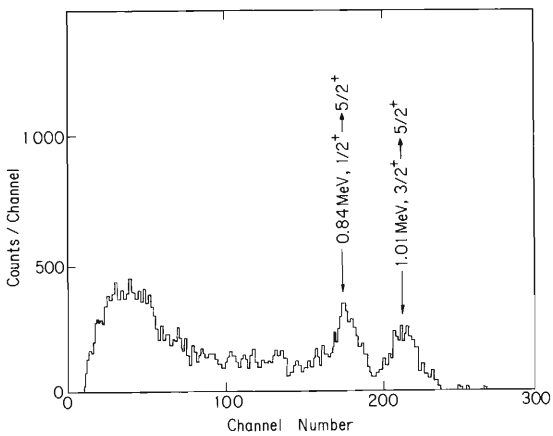

Fig. 2. γ-Ray spectrum observed in coincidence with Coulomb-scattered particles.

$(1/2^+)$ and the 2nd $(3/2^+)$ excited states to the ground state $(5/2^+)$, respectively, and the intensities of the peaks represent the strengths of the Coulomb-excitation processes leading to these excited states.

Using coincidence rates $N_{+(-)}{}^{L(R)}$, the left-right asymmetry A of the scattering was defined by,

$$A=(1-\rho)/(1+\rho) \tag{1}$$

with

$$\rho=(N_+{}^{L}N_-{}^{R}/N_-{}^{L}N_+{}^{R})^{1/2} \tag{2}$$

where subscripts indicate tilt angle directions ($\pm$ for $\alpha=\pm 60^\circ$) and particle detectors (left (L) and right (R)). This asymmetry is a function of nuclear spin orientation parameters of the Al beam and is written as

$$\begin{aligned} A&=(\sum_{\text{odd}} P_k q_k)/(\sum_{\text{even}} P_k q_k) \\ &=(P_1 q_1+P_3 q_3)/(q_0+P_2 q_2+P_4 q_4) \end{aligned} \tag{3}$$

where P_k are polarization tensors of rank k for ^{27}Al nuclei and q_k are constant factors determined by kinematical variables and the initial and final spins in the Coulomb-excitation. The experimental results of A are summarized in Table 1. The system asymmetry was determined by observing chance coincidence events. The

Table 1. Summary of the left-right asymmetry (A) in the present measurement.

Number of foils	$5/2^+\rightarrow 1/2^+$	$5/2^+\rightarrow 3/2^+$	System asymmetry
2	$+1.3\pm 1.0\%$	$+1.6\pm 1.1\%$	$-0.3\pm 0.5\%$
5	$+1.5\pm 0.7\%$	$+2.5\pm 0.8\%$	$-0.07\pm 0.20\%$

polarization P_1 and a higher rank tensor P_3 may be determined by applying Eqn. (3) to a pair of the A values for the $5/2^+\rightarrow 1/2^+$ and $5/2^+\rightarrow 3/2^+$ transitions. In the calculation one may ignore the second and the third terms in the denominator which are considerably smaller than the first term. The P_1 values thus obtained are $1.5\pm 0.9\%$ and $2.3\pm 0.6\%$ for two and five tilted foils, respectively.

In conclusion a new method based on Coulomb-excitation analyzing power has been used successfully and has proven its high efficiency for the measurement of nuclear polarization of high velocity ions. An appreciable polarization has been found even at 35.5 MeV, indicating that the polarization phenomenon prevails over a fairly wide energy range. It is to be noted that Al projectiles at this energy are deeply ionized ($\bar{q}=9.2$) after passing through foils. This result is encouraging for the application of the tilted-foil method to high energy nuclear experiments. The present method can determine not only the polarization but also higher rank tensors. A non-vanishing value observed for P_3 reveals that orbital angular momenta of $l\geqq 2$ are significantly involved when the atomic states are excited at the surface of the foil. This is in contrast to the usual belief that the contributions from s and p waves are dominant.

References

1) H. G. Berry and M. Hass: *Ann. Rev. Nucl. Sci.*, **32**, 1 (1982) and references therein.
2) G. Goldring and Y. Niv: *Hyperfine Interaction*, **21**, 209 (1985); Y. Nojiri and B. I. Deutch: *Phys. Rev. Lett.*, **51**, 180 (1983).

RIKEN Accel. Progr. Rep. **19** (1985)

III-1-4. Deuteron D-State Effects on the Vector Analyzing Power and Polarization in (d,p) Reactions

T. Kubo and H. Ohnuma*

NUCLEAR REACTIONS ^{116}Sn(d,p)^{117}Sn(0.159 MeV, 3/2$^+$) at $E=55.4$ MeV and ^{118}Sn(p,d)^{117}Sn(0.159 MeV, 3/2$^+$) at $E=60.8$ MeV, measured A_y, DWBA analysis, deuteron D-state effects.

Since the early work of Johnson and Santos[1] and Delic and Robson,[2] the deuteron D-state effects in direct (d,p) reactions have been the subject of many experimental and theoretical studies. At low incident energies (less then several tens of MeV), it is well established that the D-state effects are small on the vector analyzing power (A_y) and the proton polarization (P_y). Recently, however, it was shown by Cadmus and Haeberli at $E_d=8.22$ MeV[3] and by our group at $E_d=22$ and 55.4 MeV[4),5] that the D-state effects can be observed clearly for the linear combinations of A_y and P_y. They measured both A_y and P_y for the $l_n=0$ transitions in (d,p) reactions: ^{116}Sn(d,p) ^{117}Sn(g.s., 1/2$^+$) and ^{117}Sn(d,p)^{118}Sn (g.s., 0$^+$), and obtained the quantities[6] $S_p=2(P_y-A_y)$ and $S_d=3A_y-2P_y$. Their DWBA analyses clearly show the importance of the D-state effects on S_p and S_d, in contrast to A_y and P_y. The D-state effects are magnified markedly by transforming A_y and P_y into S_p and S_d.

We point out in the present report that similar magnification of the D-state effects should be observable in more general cases, *i.e.*, $l_n\neq0$ transitions.

According to the expressions given from the DWBA theory for the observables, the D-state effects arise from two terms involving the D-state contribution: the SD term which linearly depends on the S- and D-state amplitude and the DD term which depends quadratically on the D-state amplitude.[6] The analyses in Refs. 3 and 5 showed that the D-state effects observed clearly for S_p and S_d arise primarily from the DD terms. We have made a further analysis, and found that (1) the DD term of A_y (A(DD)) and that of P_y (P(DD)) are almost equal in magnitude and opposite in sign, *i.e.*, $A(\mathrm{DD})\simeq -P(\mathrm{DD})$, and (2) this relation gives rise to the magnification of the D-state effects. The DD terms of A_y and P_y are constructively added by transforming them into S_p and S_d. Consequently the contributions of the DD terms in S_p and S_d become large compared with those in A_y and P_y, so that the magnification of the D-state effects is observed.

We have found that the relation $A(\mathrm{DD})\simeq -P(\mathrm{DD})$ holds regardless of l_n. Figure 1 shows the exact-finite-range (EFR) DWBA calculations only with the D-state for A_y and P_y in the reaction ^{116}Sn(d, p)^{117}Sn at $E_d=55.4$ MeV leading to 1/2$^+$, 3/2$^+$, 5/2$^+$, 7/2$^+$, and 11/2$^-$ states: these correspond to the DD terms. The distorting potential parameters used are given in Table 1. It is clearly seen that the relation $A(\mathrm{DD})\simeq -P(\mathrm{DD})$ holds for all the transitions. Furthermore we have found that this relation exactly holds, *i.e.*, $A(\mathrm{DD})=-P(\mathrm{DD})$, in the absence of the spin-orbit distortions. The reason why this relation is not much affected by the spin-orbit distortions is that

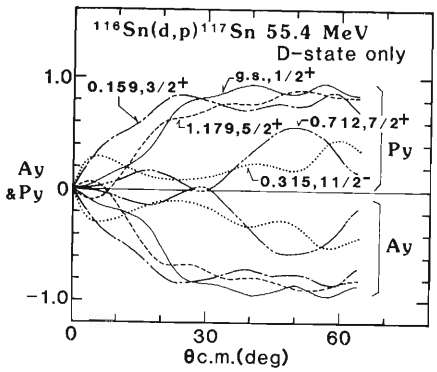

Fig. 1. EFR DWBA calculations only with the D-state for A_y and P_y in the reaction ^{116}Sn(d,p)^{117}Sn at 55.4 MeV leading to the states shown in the figure.

* Department of Physics, Tokyo Institute of Technology.

Table 1. Distorting potential parameters used in the EFR DWBA calculations. The deuteron parameters are those of an adiabatic potential and the proton parameters are those which reproduce the elastic scattering.

	V_0	r_0	a_0	W	W_D	r_I	a_I	V_{so}	r_{so}	a_{so}	r_c	Ref.
d	96.67	1.17	0.79	7.93	10.26	1.29	0.633	6.20	1.01	0.75	1.25	5, 7
p	41.93	1.197	0.687	3.80	5.10	1.24	0.808	6.11	1.057	0.80	1.25	8

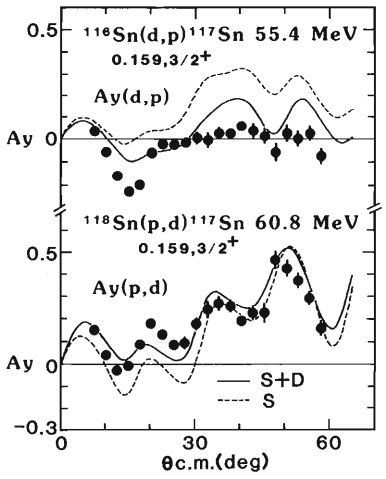

Fig. 2. Angular distributions of A_y in the reactions ^{116}Sn(d,p)^{117}Sn(0.159 MeV, $3/2^+$) at 55.4 MeV and ^{118}Sn(p,d)^{117}Sn(0.159 MeV, $3/2^+$) at 60.8 MeV compared with EFR DWBA calculations with (solid lines) and without (dashed lines) the D-state.

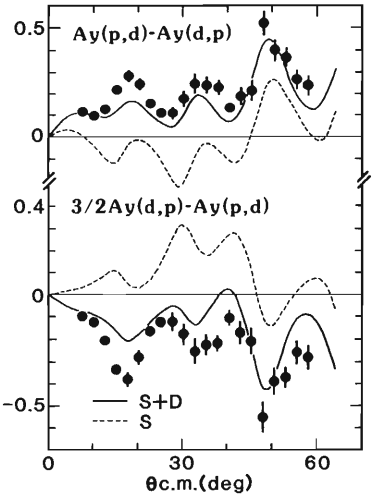

Fig. 3. Linear combinations of the A_y of (d,p) reaction and that of (p,d) reaction shown in Fig. 2 (see text).

the DD terms are determined primarily by the central-potential distortions.

The results shown in Fig. 1 suggest that the magnification of the D-state effects can be observed for suitable linear combinations of A_y and P_y also in $l_n \neq 0$ transitions.

The magnification of the D-state effects should also be possible in linear combinations of A_y of a (d,p) reaction and that of a (p,d) reaction, as long as the latter corresponds to an approximate inverse reaction of the former. The angular distributions of A_y for the reactions ^{116}Sn(d,p)-^{117}Sn(0.159 MeV, $3/2^+$) at $E_d = 55.4$ MeV (A_y(d,p)) and ^{118}Sn(p,d)^{117}Sn(0.159 MeV, $3/2^+$) at $E_p = 60.8$ MeV (A_y(p,d)) are shown in Fig. 2 along with the EFR DWBA calculations with and without the D-state. Figure 3 shows the linear combinations A_y(p,d)-A_y(d,p) and $3/2A_y$(d,p)-A_y(p,d) defined similarly to S_p and S_d. The distorting potential parameters used are listed in Table 1. It can be seen from Fig. 3 that the D-state effects are markedly magnified and the data can not be fitted by the S-state alone. This result confirms the suggestion mentioned above.

It should be noted that the relation $A(\mathrm{DD}) \simeq -P(\mathrm{DD})$ is the general nature of the D-state effects on A_y and P_y in (d,p) reactions. In addition, the present results predict that the relation $A_y \simeq -P_y$ holds at incident energies of several hundreds of MeV, where the contributions from the DD terms become dominant.

References

1) R. C. Johnson and F. D. Santos: *Phys. Rev. Lett.*, **19**, 364 (1967).
2) G. Delic and B. A. Robson: *Nucl. Phys. A*, **156**, 97 (1970).
3) R. R. Cadmus and W. Haeberli: *Nucl. Phys. A*, **349**, 103 (1980).
4) H. Ohnuma, T. Kubo, N. Kishida, T. Hasegawa, N. Ueda, T. Fujisawa, T. Wada, K. Iwatani, and T. Suehiro: *Phys. Lett. B*, **97**, 192 (1980).
5) T. Kubo, H. Ohnuma, T. Kishimoto, M. A. Brennan, Y. Yoshida, M. Sugitani, and T. Suehiro: *Phys. Lett. B*, **127**, 403 (1983).
6) R. C. Johnson: *Nucl. Phys. A*, **90**, 289 (1967).
7) J. D. Harvey and R. C. Johnson: *Phys. Rev. C*, **3**, 636 (1971).
8) G. B. Fulmer, J. B. Ball, A. Scott, and M. L. Whiten: *Phys. Rev.*, **181**, 1565 (1969).

RIKEN Accel. Progr. Rep. 19 (1985)

III-1-5. Self-Consistent Transport Coefficients for Damped Large Scale Collective Motion

S. Yamaji, H. Hofmann,* and R. Samhammer*

[FISSION transport equation, linear response theory, two-center shell model.]

The microscopic expressions for the transport coefficients are derived by exploiting locally generalized RPA-type dispersion relation.[1] These expressions are evaluated for the dynamics of fission around and behind the barrier by applying the two-center shell model[2] at finite temperature and a finite coupling of one particle-one hole excitations to more complicated configurations.[3]

The actual microscopic computations were performed for the symmetric fission of a ^{212}Po nucleus. From the parametrization of mean field introduced in Ref. 2, the center-separation z_0 is taken as a macroscopic variable. The other variables such as neck-parameter ε and deformation δ are fixed to be 0.35 and 0.0, respectively. We calculated the potential energy $V(z_0)$ as the sum of Coulomb energy and nuclear macroscopic energy.[4]

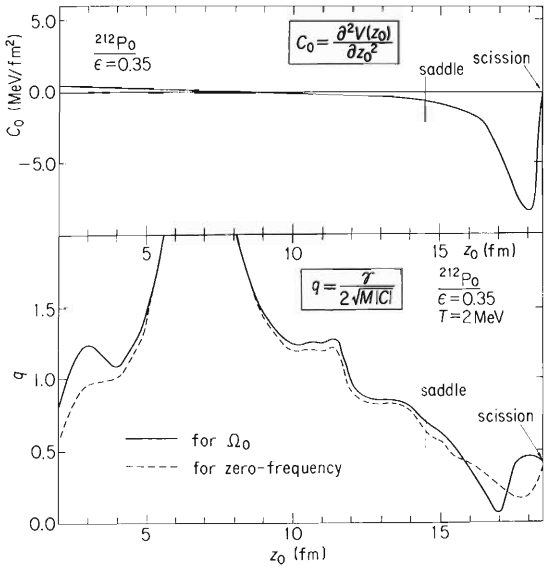

Fig. 1. The stiffness coefficient C and dimensionless parameter q *vs.* the center-separation z_0 for the symmetric fission of ^{212}Po.

The stiffness coefficient C, which is equal to $\partial^2 V(z_0)/\partial z_0^2$ is shown in the upper part of Fig. 1. In the lower part, the dimensionless quantity $q=\gamma/2\sqrt{M|C|}$ is shown as a function of z_0, where M, γ, and C are coefficients for inertia, friction, and stiffness. This parameter q governs the solution of transport equation and is often used as a phenomenological parameter.[5] The analysis of the mean saddle-to-scission time, mean kinetic energy at scission, and variance in kinetic energy for 120 MeV $\alpha+^{209}\mathrm{Bi}\rightarrow^{213}\mathrm{At}\rightarrow$fission yields the empirical value of order of 1 for the parameter q.[5] The solid and dashed lines correspond to the local frequency Ω_0 determind by the RPA-dispersion relation and the Markoff-limit $\Omega_0\rightarrow 0$,[6] respectively.

From the present microscopic calculation of transport coefficients, we have found that the effect of the local phonon on the parameter q is large, especially for large value of stiffness C in the region between barrier and scission, although the parameter q for zero-frequency reproduces the order of magnitude of the empirical value of q. This indicates that we have to solve the transport equation improved by taking into account the effect of the local phonon on the coefficients in order to study the collective motion of fission.

* Physik-Department der Technischen Universität München.

References

1) H. Hofmann and A. S. Jensen: *Nucl. Phys. A*, **428**, 1c (1984).
2) A. Iwamoto, S. Yamaji, S. Suekane, and K. Harada: *Prog. Theor. Phys.*, **55**, 115 (1976).
3) P. J. Siemens, A. S. Jensen, and H. Hofmann: *Nucl. Phys. A*, **441**, 410 (1985).
4) H. J. Krappe, J. R. Nix, and A. J. Sierk: *Phys. Rev. C*, **20**, 992 (1979).
5) J. R. Nix, A. J. Sierk, H. Hofmann, F. Scheuter, and D. Vautherin: *Nucl. Phys. A*, **424**, 239 (1984).
6) H. Hofmann and P. J. Siemens: *Nucl. Phys. A*, **275**, 464 (1977).

RIKEN Accel. Progr. Rep. **19** (1985)

III-1-6. Application of Time-Dependent Mean-Field Theory to Heavy-Ion Collisions

K. Ikeda, S. Yoshida, and S. Yamaji

〔NUCLEAR REACTIONS time-dependent mean-field theory.〕

We have studied the numerical application of Reinhardt's time-dependent mean-field (TDMF) S-matrix theory[1] to a one-dimensional elastic scattering problem, in which a 4-nucleon and an 8-nucleon system interpenetrate with no energy loss. The details will be published elsewhere.[2]

The mean-field which is a self-consistent solution of the TDMF equation is iteratively obtained. This iteration procedure works fairly well except at lower energies where the ordinary TDHF evolution of the densities results in high excitation of the fragments or fusion.

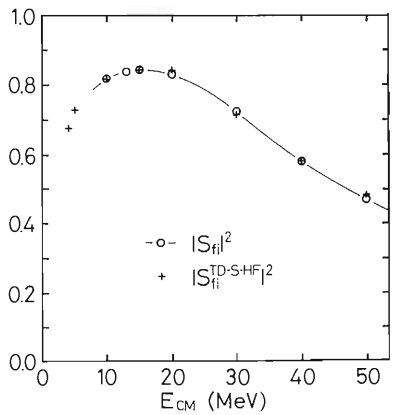

Fig. 1. Comparison between $|S_{fi}|^2$ (denoted by open circles) and $|S_{fi}^{TD\text{-}S\text{-}HF}|^2$ (denoted by crosses) that were made maximum by choosing the starting time according to the matching condition.

Table 1. Comparison of the time advance for different definitions.

E_{CM}(MeV)	10	20	30	40	50
$-\frac{2q_i}{v_{rel}}\left(\frac{fm}{c}\right)$	76.1	41.9	28.4	21.3	16.8
$-\frac{d(\arg(S_{fi}))}{dE_{CM}}\left(\frac{fm}{c}\right)$	74.3	41.4	29.6	22.5	19.7

In Fig. 1, the resultant S-matrix elements are compared with the corresponding values calculated by using the TD-S-HF theory.[3] They agree quite well if we seek the starting time that makes $|S_{fi}^{TD\text{-}S\text{-}HF}|$ maximum, fixing the initial positions of the fragments in the TD-S-HF calculation. This matching condition is reasonable since the TDHF wave packet has a classical character in the translational motion.[3]

As for the phase, the difference between the TDMF result and TD-S-HF one is a few tens percent of 2π.

Rather than showing the phase $\arg(S_{fi})$ of the S-matrix element, it may be interesting to compare $d(\arg(S_{fi}))/dE_{CM}$ with $2q_i/v_{rel}$, where E_{CM},q_i, and v_{rel} are the center-of-mass energy, relative distance, and relative velocity for the initial preparation stage, respectively. Both of them are interpreted as the time delay of the scattering process. The former is the quantum mechanical case while the latter is classical. In Table 1 the time advances which are obtained by changing the signs of the time delays are tabulated and show a good agreement between the two quantities. This indicates that they are consistently interpreted as a time advance of the elastic interpenetration.

The good agreement between the TDMF calculation and TD-S-HF one in this work can motivate application of the TD-S-HF theory to more realistic systems for which the TDMF calculation is very time consuming.

References

1) H. Reinhardt: *Nucl. Phys. A*, **390**, 70 (1982).
2) K. Ikeda, S. Yoshida, and S. Yamaji: *Z. Phys. A*, **323**, 285 (1986).
3) J. J. Griffin, P. C. Lichtner, and M. Dworzecka: *Phys. Rev. C*, **21**, 1351 (1980).

RIKEN Accel. Progr. Rep. 19 (1985)

III-1-7. High-Spin States in ^{110}Sn

H. Harada, T. Murakami, H. Tachibanaki, K. Yoshida,
J. Kasagi, T. Kubo, and T. Inamura

[NUCLEAR REACTION ^{98}Mo(^{16}O,4n)^{110}Sn, $E=76$ MeV measured γ-γ coincidence, deduced levels.]

In the course of the systematic study of the nuclear structure of Sn isotopes, we have investigated high-spin states in ^{110}Sn. Last year, we reported a sequence of 809, 741, 809, and 448 keV γ-rays and proposed a tentative level scheme of ^{110}Sn.[1] However, the level scheme has been found to have difficulty in interpreting the intensities of the γ-rays obtained in γ-γ coincidence measurements. Thus a γ-γ coincidence study with much better statistics has been required to correct the level scheme of ^{110}Sn.

We have performed the γ-γ coincidence measurement with five BGO anti-Compton spectrometers (BGOACS) reported in Ref. 2. Reduction of Compton scattered events by about 1/3 for a Ge(Li) detector has provided superior γ-ray spectra of the γ-γ coincidence.

High spin states of ^{110}Sn were excited by the ^{98}Mo(^{16}O,4n)^{110}Sn reaction with beam energy of 76 MeV. The target used was a 98% enriched ^{98}Mo foil, 0.95 mg/cm^2 in thickness, and backed with a thin lead layer. Five sets of BGOACS were placed at 35, 45, 90, 135, and 145 degrees to the beam direction, and the distance between the target and Ge detector was set to be 15 cm. A collimator of 4 cm thick heavy metal was set in front of each BGOACS. Event-by-event data were recorded on a magnetic tape by using a CAMAC data taking system.[3] About 3×10^7 coincidence events were obtained in the present experiment, more than four times as good statistics as the previous one.

We have found new γ-rays which correct the previous level scheme. They are 846, 1,092, and

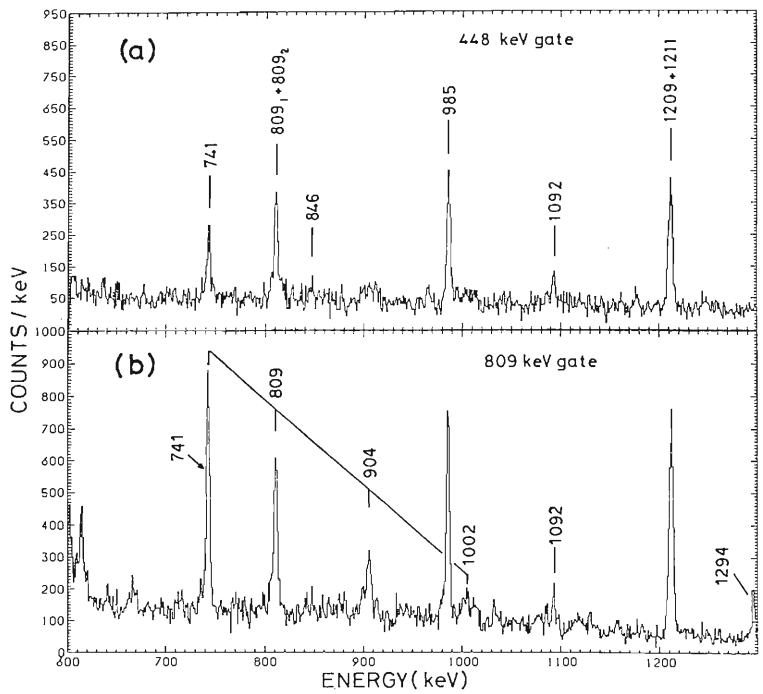

Fig. 1. γ-γ coincidence spectra gated by 448 keV (a) and 809 keV (b) transitions from the ^{98}Mo(^{16}O,4nγ)^{110}Sn reaction at 76 MeV.

1,294 keV γ-rays. In Fig. 1 are shown γ-ray spectra gated by the 448 keV (a) and the 809 keV (b) γ-rays. As can be seen from Fig. 1, the 846 and 1,092 keV γ-rays are seen in both spectra, while the 1,294 keV γ-ray is seen only in spectrum (a). This observation requires the new level at 5,225 keV as shown in Fig. 2.

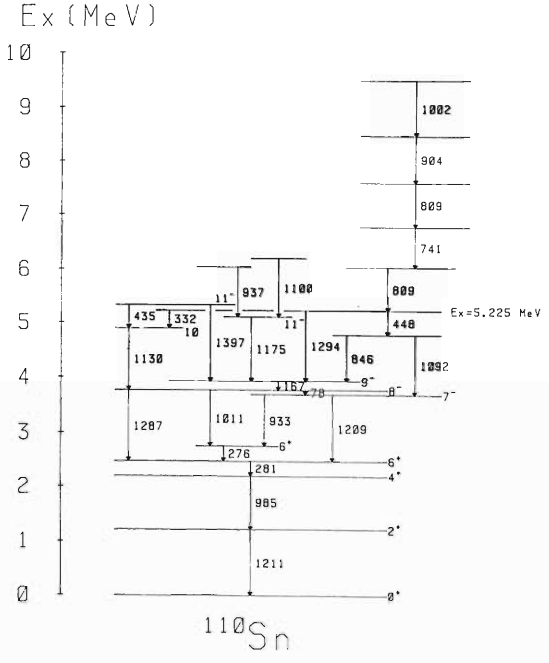

Fig. 2. Proposed level scheme of ^{110}Sn. Numerical figures indicate γ-ray energy in keV.

In addition to these new γ-rays, we have also found the 904 keV and 1,002 keV transitions as shown in Fig. 1 (b). They are also observed in the spectrum gated by the 741 keV γ-ray. Thus, there exist band-like transitions consisting of 741, 809, 904, and 1,002 keV γ-rays as shown in Fig. 1 (b). These γ-rays are placed on the 5,225 keV level together with the 8,091 keV γ-ray. The proposed level scheme shown in Fig. 2 suggests that the deformed states become the yrast states of ^{110}Sn above 6 MeV excitation. Angular distribution of γ-rays and the lifetime measurements with BGOACS are being planned to establish the band structure in ^{110}Sn.

References

1) H. Harada, T. Murakami, H. Tachibanaki, K. Yoshida, J. Kasagi, and T. Inamura: *RIKEN Accel. Progr. Rep.*, **18**, 22 (1984).
2) M. Fukuda, Y. Gono, Y. Ishikawa, M. Sugawara, T. Inamura, M. Ishihara, T. Nomura, I. Kohno, H. Kamitsubo, J. Kasagi, and T. Murakami: *RIKEN Accel. Progr. Rep.*, **18**, 152 (1984).
3) T. Inamura, T. Murakami, J. Kasagi, H. Kumagai, and Y. Gono: *RIKEN Accel. Progr. Rep.*, **17**, 124 (1983).

RIKEN Accel. Progr. Rep. **19** (1985)

III-1-8. High-Spin States in ^{112}Sn

H. Harada, T. Murakami, H. Tachibanaki, K. Yoshida,
J. Kasagi, T. Kubo, and T. Inamura

[NUCLEAR REACTION ^{100}Mo(^{16}O,4n)^{112}Sn, $E=72$, 76 MeV, measured γ-γ coincidence, deduced levels.]

The low-lying levels in ^{112}Sn have been investigated extensively and the yrast levels up to 9^- state are interpreted as neutron two-quasiparticle states.[1),2)] The effect of the generalized seniority mixing predicted by Bonsignori *et al.*[3)] has been found in the enhanced B(E2) values of the $9^-\rightarrow 8^-$ transitions in ^{110}Sn and ^{112}Sn.[4)] The spherical nature of the yrast levels are then well established below 4.5 MeV excitation. On the other hand, a feature of the deformed nucleus is also seen in ^{112}Sn. The deformed rotation-like band whose members are connected with 468 keV ($6^+\rightarrow 4^+$), 663 keV ($8^+\rightarrow 6^+$), 741 keV ($10^+\rightarrow 8^+$), and 864 keV ($12^+\rightarrow 10^+$) transitions has been reported by Bron *et al.*[5)] Therefore, it is very interesting to investigate the higher-spin region of

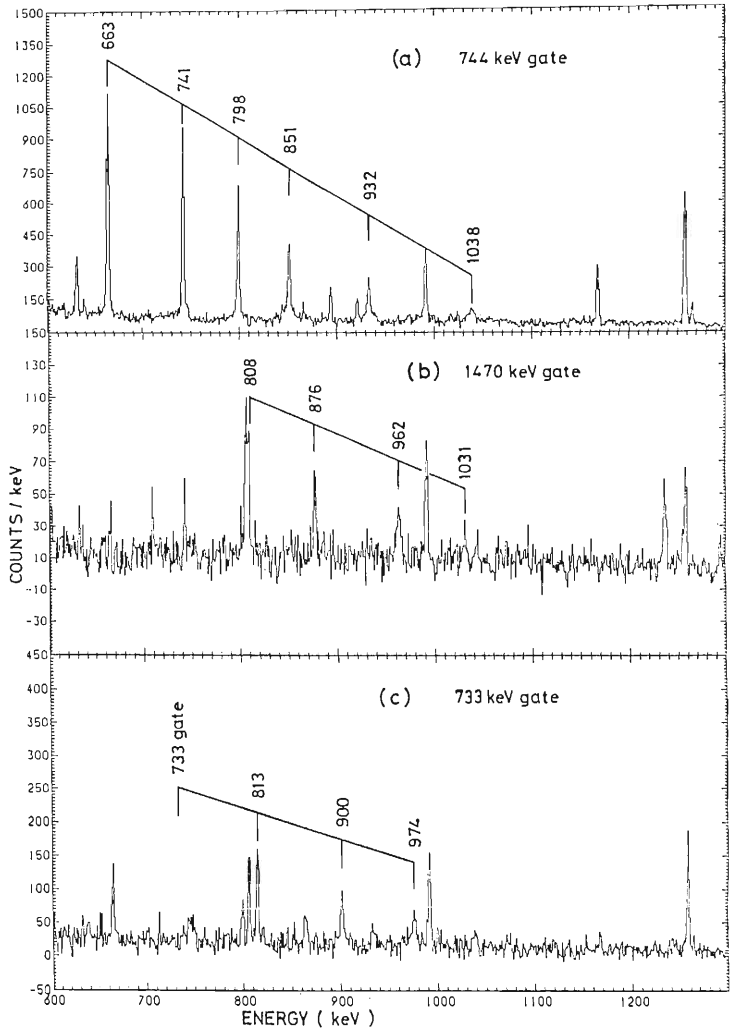

Fig. 1. γ-γ Coincidence spectra gated by 744 keV (a), 1,470 keV (b), and 733 keV (c) transitions from the ^{100}Mo(^{16}O,4nγ)^{112}Sn reaction.

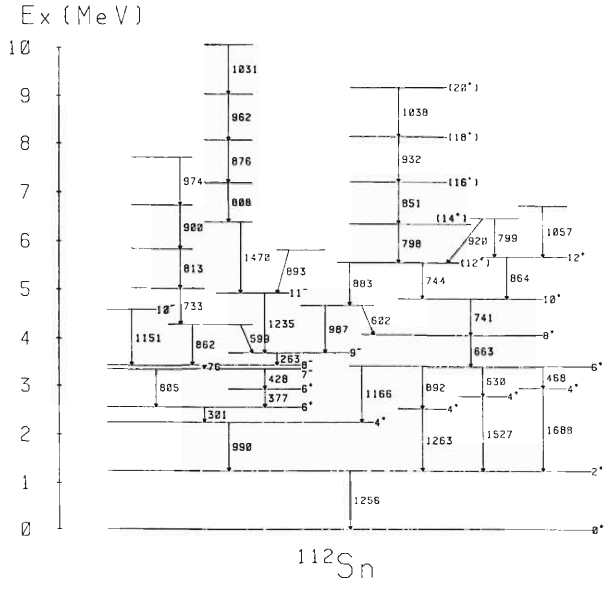

Fig. 2. Proposed level scheme of ^{112}Sn. Numerical figures indicate γ-ray energy in keV.

^{112}Sn and to see whether the shape coexisting picture is still effective or not.

γ-γ Coincidence measurements were carried out with the BGOACS[6] for the ^{100}Mo(^{16}O, 4n)^{112}Sn reaction at $E(160)=72$ and 76 MeV. The target used was a self-supporting foil, backed with lead, 2 mg/cm^2 in thickness, and enriched to 95% in ^{100}Mo. The same experimental sutup was used as reported in Ref. 7.

In addition to the previously known band, we have found other band like transitions in the present experiment. In Fig. 1, shown are γ-ray spectra gated with the 744 keV (a) and 1,470 keV (b) γ-rays. The γ-ray peaks indicated by the transition energies are considered as rotational-like intra-band transitions. The band shown in Fig. 1 (a) is connected with the previously known band by the 744 keV ($(12^+)\rightarrow 10^+$) transition and is considered to form the yrast levels. The other band shown in Fig. 1 (b), is connected with the spherical negative parity states. The proposed level scheme of ^{112}Sn is shown in Fig. 2. Tentative spin assignments of the band members up to 20^+ are based on the stretched quadrupole character of the angular distribution of the γ-rays. Spin parity assignments and lifetime measurements are highly desirable to confirm the band structure in ^{112}Sn. Such experiments are now in progress.

References

1) T. Yamazaki and G. T. Evan: *Nucl. Phys. A*, **134**, 81 (1969).
2) A. van Poelgeest, J. Bron, W. H. A. Hesselink, K. Allart, J. J. A. Zalmstra, M. J. Uitzinger, and H. Verheul: *Nucl. Phys. A*, **346**, 70 (1980).
3) G. Bonsignori, M. Savoia, K. Allart, A. van Egmond, and G. Te Velde: *Nucl. Phys. A*, **432**, 389 (1985).
4) J. Kasagi, H. Harada, T. Murakami, H. Tachibanaki, K. Yoshida, and T. Inamura: p. 22 in this report.
5) J. Bron, W. H. A. Hesselink, A. van Poelgeest, J. J. A. Zalmstra, M. J. Uitzinger, H. Verheul, K. Heyde, M. Waroquier, H . Vincx, and P. van Isacker: *Nucl. Phys. A*, **318**, 335 (1979).
6) M. Fukuda, Y. Gono, Y. Ishikawa, M. Sugawara, T. Inamura, M. Ishihara, T. Nomura, I. Khono, H. Kamitsubo, J. Kasagi, and T. Murakami: *RIKEN Accel. Progr. Rep.*, **18**, 152 (1984).
7) H. Harada, T. Murakami, H. Tachibanaki, K. Yoshida, J. Kasagi, T. Kubo, and T. Inamura: p. 18 in this report.

RIKEN Accel. Progr. Rep. 19 (1985)

III-1-9. Enhanced E2 Transitions between 9^- and 8^- States in ^{110}Sn and ^{112}Sn

J. Kasagi, H. Harada, T. Murakami, K. Yoshida,
H. Tachibanaki, and T. Inamura

[NUCLEAR REACTION ^{98,100}Mo(^{16}O,4n)^{110,112}Sn, $E=72$, 76 MeV, measured recoil distance, deduced mean lifetimes.]

The low-lying states of Sn isotopes with a closed $Z=50$ proton shell have provided the opportunity to investigate the validity of the neutron quasiparticle or generalized seniority (v_g) concept. Recently, the influence of the generalized seniority mixing has been investigated in the low-lying states of Sn nuclei by Bonsignori *et al.*[1] They showed that most of the low-lying states have 10-30% of $v_g=4$ admixtures in predominant $v_g=2$ configurations. Of particular interest is the main source of the generalized seniority mixing which they claimed to be a kind of particle-phonon coupling mechanism, and hence the effect of $v_g=4$ admixtures results in enhanced E2 transition probabilities. This enhancement is predicted to be seen for the transitions between high-spin states with the simplest $v_g=2$ configurations.

Within the $v_g=2$ configurations, the 9^- states can consist only of the $(h_{11/2}g_{7/2})$ configuration, and the 8^- state is predicted to consist mainly of the same configuration.[1),2)] In ^{110,112}Sn, the 9^- and 8^- states are well established and values of E2/M1 mixing ratio for the transition between them are also known.[2)] Therefore, we have measured the lifetimes of the 9^- and 8^- states in ^{110}Sn and ^{112}Sn to see whether the E2 transitions are really enhanced or not. The predicted B(E2) values with $v_g \leqq 4$ configurations for the $9^- - 8^-$ transitions are about 200 e^2fm^4 [1)] more than 7 times larger than those of the calculation with $v_g=2$ configurations.

Levels in ^{110}Sn and ^{112}Sn were populated in the ^{98,100}Mo(^{16}O,4n)^{110,112}Sn reactions with 72-76 MeV ^{16}O beams from the RIKEN 160 cm cyclotron. In addition to n-γ-γ coincidence and n-γ angular correlation measurements with a neutron multiplicity filter,[3)] recoil-distance measurements were carried out. Stretched foils of ^{98}Mo (98.3% enriched and 950 μg/cm^2 in thickness) and ^{100}Mo (94.5% enriched and 677 μg/cm^2 in thickness) supported with thin gold foil were used as target

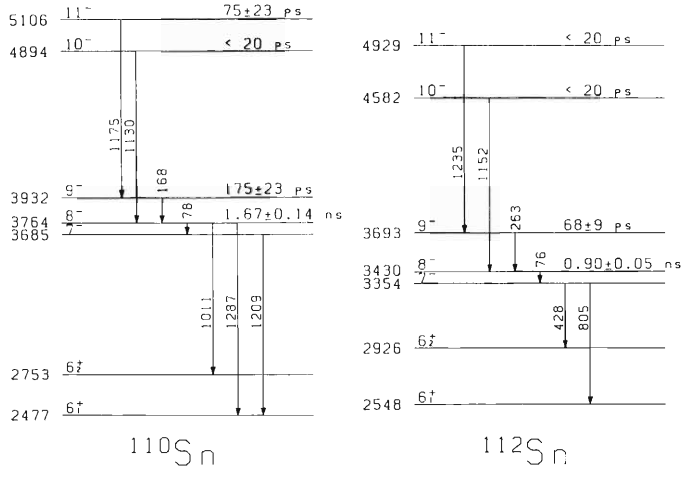

Fig. 1. Decay scheme of negative parity levels in ^{110}Sn and ^{112}Sn observed with the ^{98,100}Mo(^{16}O,4nγ)^{110,112}Sn reactions.

and thick Ta foil served as recoil stopper. γ-Rays were detected with a Ge(Li) detector placed at 140° to the beam direction in coincidence with the neutron multiplicity filter. The usefulness of the neutron multiplicity filter to reduce unwanted events is fully described in Ref. 3.

Decay schemes of the negative-parity states in ^{110}Sn and ^{112}Sn presented in Fig. 1 are based on the n-γ-γ coincidence data. They agree well with the previous investigation[2] except for the existence of the $8^- - 6_1^+$ transition in ^{110}Sn. Spin and parity assignments given in Ref. 2 are consistent with the results of the angular distribution measurements in the present work.

The results of the recoil-distance measurements for the 9^- and 8^- states in ^{110}Sn and ^{112}Sn are shown in Fig. 2. Relative yields of non-shifted γ-ray peaks are plotted against the target-stopper distance. The electromagnetic properties of the negative-parity states obtained in the present work are shown in Table 1. As can be seen from the table, the B(E2) values of the $9^- - 8^-$ transitions are very large, about five times the single-particle value.

In Table 2 are shown the transition probabil-

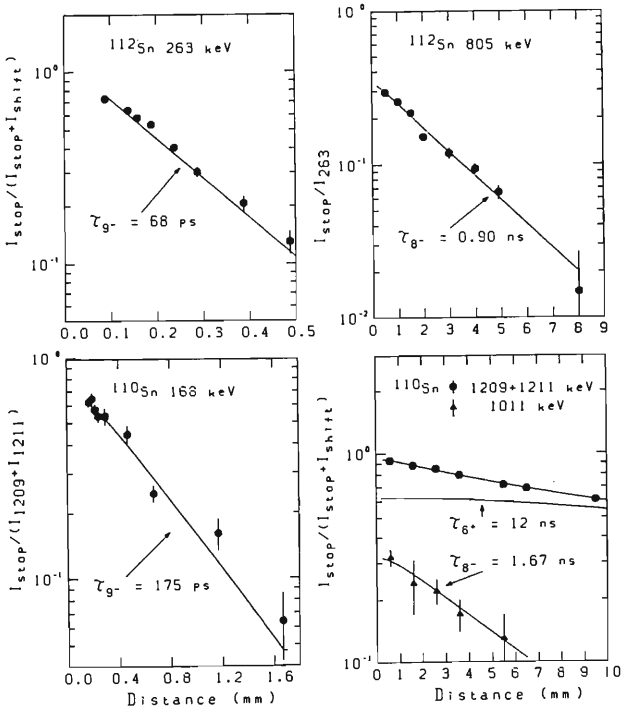

Fig. 2. Plots of relative yields of the stopped peaks against the target-stopper distance for 168, 1,011, and 1,209 keV γ-rays from ^{110}Sn, and 263, and 805 keV γ-rays from ^{112}Sn.

Table 1. Electromagnetic properties of negative parity levels in ^{110}Sn and ^{112}Sn.

Nucleid	E_x (keV)	τ (ps)	E_γ (keV)	J_i^π	J_f^π	δ	B(M1)($0.01\mu_n^2$)	B(E2) (e^2fm^4)
^{110}Sn	5,106	75±23	1,175	11^-	9^-			4.8±1.5
	4,894	3< <20	1,130	10^-	8^-			
	3,932	175±27	168	9^-	8^-	0.08±0.03	6.8±1.1	200^{+180}_{-120}
	3,764	1.67±0.14[a]	78	8^-	7^-	0.05±0.03[b]	2.7±0.3	160^{+240}_{-100}
			1,011	8^-	6^+			6.5±0.8[c]
			1,287	8^-	6^+			0.6±0.1[c]
^{112}Sn	4,929	3< <20	1,235	11^-	9^-			
	4,582	3< <20	1,152	10^-	8^-			
	3,693	68±9	263	9^-	8^-	0.13±0.01	4.6±0.6	150±30
	3,430	0.90±0.05	76	8^-	7^-	0.04±0.03[b]	6.5±0.4	260^{+530}_{-250}

[a] ns. [b] Ref. 2. [c] B(M2) value in μ_n^2fm^2.

Table 2. B(M1) and B(E2) values of the $9^- - 8^-$ transitions compared with the calculations.

Nucleid	Configuration of 8^- state	B(M1) ($0.01\mu_n^2$)	B(E2) (e^2fm^4)
^{110}Sn	Experiment	6.8±1.1	200^{+180}_{-120}
	$(h_{11/2}g_{7/2})$	13.1	55
	$0.72(h_{11/2}g_{7/2})+0.69(h_{11/2}d_{5/2})$	6.8	33
	Calculation with $v_g \leqq 4$[a]	9.6	169
^{112}Sn	Experiment	4.6±0.6	150±30
	$(h_{11/2}g_{7/2})$	13.1	74
	$0.59(h_{11/2}g_{7/2})+0.81(h_{11/2}d_{5/2})$	4.6	35
	Calculation with $v_g \leqq 4$[a]	9.8	206

[a] Ref. 3.

ities between the 9^- and 8^- states compared with calculations. With the simplest two quasiparticle configuration of $(h_{11/2}g_{7/2})$ for the 8^- states, the calculated B(M1) values are about two times larger than the experimental ones, whereas the calculated B(E2) values are less than half of the experimental ones, as indicated at the second rows in Table 2. The configurations given at the third rows are obtained so as to reproduce the experimental B(M1) values. However, the B(E2) values calculated with these configurations are smaller than those of the simplest configuration.

The results of the generalized seniority mixing calculation[1] with the effective interaction of the finite range force are also listed in Table 2. The experimental B(E2) values are in good agreement with them, although the B(M1) values are slightly smaller than those of the calculation. Therefore, it can be concluded that the observed enhanced E2 transitions between the 9^- and 8^- states are due to the small admixtures predicted in Ref. 1. It should be stressed that the enhancement is observed only for the transitions between the states with rather simple $v_g=2$ configurations such as the 9^--8^- transition.

References

1) G. Bonsignori, M. Savoia, K. Allaart, A. van Egmond, and G. Te Velde: *Nucl. Phys. A*, **432**, 389 (1985).
2) A. van Poelgeest, J. Bron, W. H. A. Hesselink, K. Allaart, J. J. A. Zalmstra, M. J. Vitzinger, and H. Verheul: *Nucl. Phys. A*, **346**, 70 (1980).
3) T. Murakami, J. Kasagi, H. Harada, and T. Inamura: *Nucl. Instrum. Methods A*, **241**, 172 (1985).

RIKEN Accel. Progr. Rep. 19 (1985)

III-1-10. Aligned Bands in Ge Isotopes in the Interacting Boson Model

N. Yoshida and A. Arima*

[NUCLEAR STRUCTURE ^{66,68,70,72}Ge; interacting boson model, high-spin states.]

In a previous report,[1] we reported a result of calculations of energy levels and B(E2) values of the Ge isotopes in the interacting boson model coupled with a fermion pair in the $g_{9/2}$ orbital. The present report describes a result of further calculations for these isotopes.

Since the model is almost the same as that used in Refs. 1 and 2, we here give only an outline of the model. The Hamiltonian is given by

$$H = H^{B} + H^{F} + V^{BF}$$

The boson Hamiltonian H^{B} is the one fitted to low-lying levels. The fermion Hamiltonian H^{F} consists of single-particle energy and the surface delta interaction. The single-fermion energies are taken as being close to the quasiparticle energies. As the interaction between bosons and fermions V^{BF}, we assume the quadrupole-quadrupole interaction. The quadrupole operator includes the terms which allow a boson to change into a pair of fermions. We determine the parameters in V^{BF} for ^{68}Ge so that the locations and B(E2) values of the three 8^{+} states are reproduced. The variation of these parameters with mass number is estimated considering the microscopic theory of the IBM by Scholten who took into account the mass number dependence by using the u and v factors of the BCS theory.[3] For calculation of B(E2) values, we assume the same effective charges for proton and neutron bosons and determine them from experimental B(E2; $2_1^+ \rightarrow 0_g^+$) values for each isotope. We assume fermion effective charges to be 1.5 e for protons

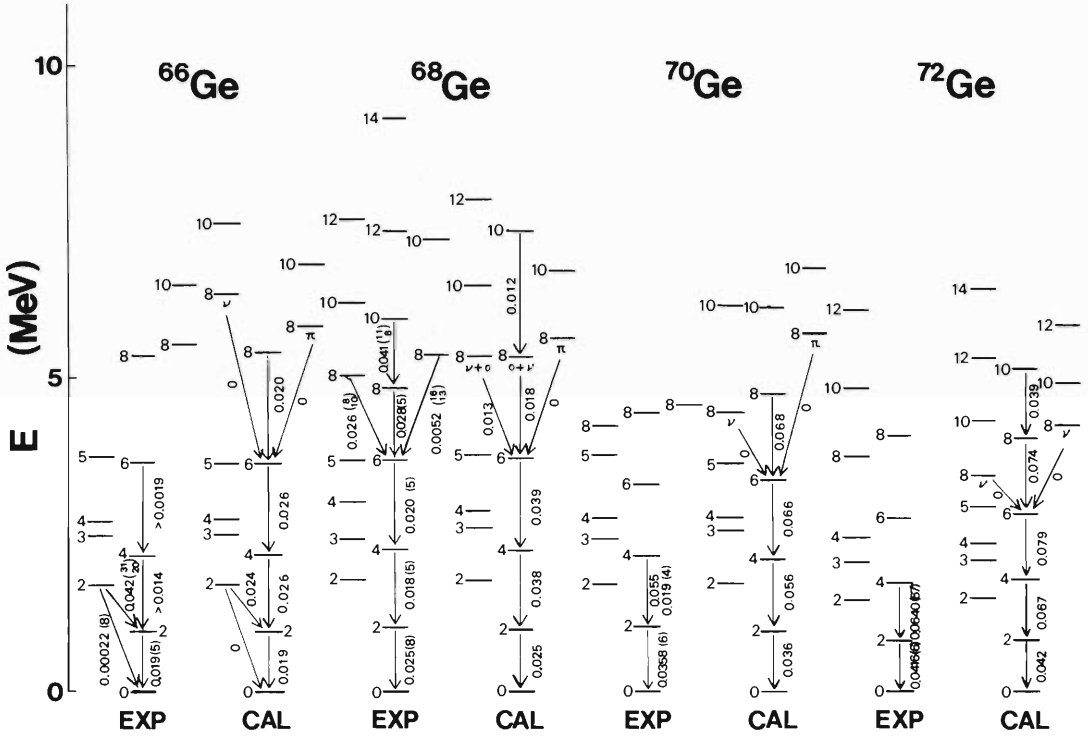

Fig. 1. Energy levels and B(E2) values in ^{66,68,70,72}Ge. Bands with π and ν in the figure are proton- and neutron-aligned bands, respectively. B(E2) values are given in units of e^2b^2.

* Department of Physics, The University of Tokyo.

and 0.5 e for neutrons. In the M1 operator, we assume 1 μ_N and 0 for the g-factors of proton bosons and neutron bosons, respectively. As for the g-factors of the fermions in the $g_{9/2}$ orbital, we assume 1.16 μ_N and -0.21 μ_N for protons and neutrons, respectively, which are determined from g-factors of $9/2^+$ levels of neighboring nuclei.

The calculated and observed energy levels and B(E2) values are compared in Fig. 1, which shows good overall agreement. The energy level of the first 8^+ state is lowered as the mass number increases. This trend is reproduced by the calculation. In ^{66}Ge, the IBM calculation reproduces the odd-even staggering like 2, (3, 4), (5, 6),$\cdots$ observed in the γ-band. In ^{68}Ge, the calculation suggests that the first and the second 8^+ states are both mixed ones of the zero- and the two-neutron-mixed states. By this mixing, we are able to reproduce appreciable amount of E2 transitions to the first 6^+ state from both of the first and the second 8^+ states, although they are still smaller than the observed values. In ^{70}Ge, the lowest 8^+state is found from calculation to be of neutron nature, and the second a boson state. In ^{72}Ge, the first 8^+ state seems to be a neutron state, while the second a boson state. The above arguments about the nature of these bands, however, are all dependent largely on the choice of parameters, so we can not draw a reliable conclusion. As is well known, one of the experimental methods to determine the character of bands is the measurement of g-factors. Figure 2 shows the calculated g-factors. The calculation reproduces the g-factor of 2_1^+ of ^{72}Ge, but it gives only a half of the g-factor of 2_1^+ of ^{70}Ge. Among the high-spin states, the states with an aligned $g_{9/2}$ proton pair are expected to have positive g-factors, and the states with an aligned $g_{9/2}$ neutron pair to have negative g-factors.

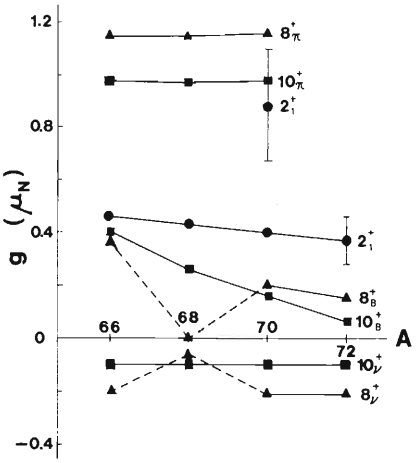

Fig. 2. Calculated g-factors of 2_1^+, boson 8_B^+, proton-aligned 8_π^+, neutron-aligned 8_ν^+, boson 10_B^+, proton-aligned 10_π^+, and neutron-aligned 10_ν^+ levels in ^{66,68,70,72}Ge.

References

1) N. Yoshida and A. Arima: *RIKEN Accel. Progr. Rep.*, **18**, 26 (1984).
2) N. Yoshida, A. Arima, and T. Otsuka: *Phys. Lett., B*, **114**, 86 (1982).
3) O. Scholten: Ph. D. Thesis, Univ. of Groningen (1980).

RIKEN Accel. Progr. Rep. 19 (1985)

III-1-11. The sdg Interacting Boson Model Applied to ^{168}Er

N. Yoshinaga, Y. Akiyama,* and A. Arima**

〔NUCLEAR STRUCTURE ^{168}Er; sdg interacting boson model.〕

Applying the sdg interacting boson model (the sdg IBM) to ^{168}Er where the number of active bosons is 16, we are forced to truncate the model space because the full space is too large for computer analysis. Since ^{168}Er is a well deformed nucleus, we take U(15)⊃SU(3) scheme[1] and take as many as possible SU(3) basis states, which have large eigenvalues of the Casimir operator of SU(3). The basis states taken into account are those belonging to the SU(3) representations: (64, 0), (60,2), (58,3), $(56,4)^2$, (54,5), $(52,6)^3$, $(50,7)^2$, $(48,6)^4$, (55,3), (53,4), $(51,5)^2$, $(49,6)^2$, $(47,7)^3$, (58,0), (56,1), (54, $2)^3$, $(52,3)^3$, $(50,4)^6$, $(48,5)^6$, and $(46,6)^{10}$. Here the superscript indicates the multiplicity of the irreducible representation.

We take two-body interactions with SU(3) tensor character (00), (22) and (06)+(60) only. Other interactions such as (44), (66), (82)+(28), (10,4)+(4,10), (12,0)+(0,12), and (88) tensors are not included in this analysis. We construct four two-body interactions V_1, V_2, V_3, and V_4 besides the Casimir operator of SU(3) and L^2 operators. In terms of them our Hamiltonian reads

$$H = a_1V_1 + a_2V_2 + a_3V_3 + a_4V_4 + a_5C_{SU(3)} + a_6L^2$$

where a's are parameters to be determined. The four interactions through V_1 to V_4 are the linear combinations of six (22) and four (06)+(60) tensors. Among four interactions three interactions (V_1, V_2, V_3) are used for adjusting the positions of the β, $K=0_3^+$ and $K=4_1^+$ bandheads. The V_1 produces the anharmonic effect. With the interaction V_1 only the $K=2_1^+$ and $K=4_1^+$ bands are too low in energy compared with other bands. The interaction V_2 is used to lower the $K=0_2^+$ band. The $K=0_3^+$ band is adjusted by V_3. The interaction V_4 is used to make the eigenstates close to the SU(3) states (actually the strength of V_4 is related to the position of $K=1^+$ bands).

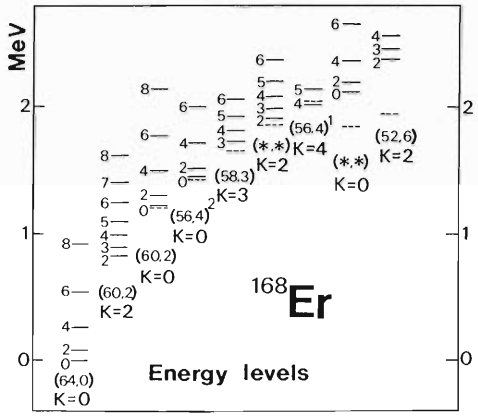

Fig. 1. Energy levels of all positive parity bands below 2.4 MeV. Solid lines show the theoretical ones and dashed lines show the experimental bandhead energies. The label below each bandhead represents an SU(3) representation (λ,μ) of its main component and K quantum number. States with asterisks cannot be assigned to definite SU(3) representations because the probability of their main components is less than 50%. The SU(3) label $(56,4)^1$ and $(56,4)^2$ indicates $(56,4)^{w=0}$ and $(56,4)^{w=1}$, respectively.

Figure 1 shows the energy levels obtained by diagonalizing the Hamiltonian with an appropriate set of parameters. The solid lines show the theoretical energy levels and the dashed lines show the bandhead energies of experiment. We see overall agreement with the experiment[2),3)] is much more improved compared to that of Ref. 4. The most remarkable is the reproduction of the anharmonicity,[5),6)] that is, $E(K=4_1^+)/E(K=2_1^+)=2.5$, which is mainly due to the effect of configuration mixing. By first-order perturbation we cannot reproduce this strong anharmonicity.[4)] This $K=4_1^+$ band belongs mainly to $(56,4)^{w=0}$ representation where w is the SU(3)-seniority quantum number.[1)] Another $K=4^+$ band arising from $(56,4)^{w=1}$ is pushed up at 3.8 MeV. This band would be degenerate in energy with the $K=4^+$ band from $(56,4)^{w=0}$ in case of a Hamiltonian consisting of only the Casimir operator of SU(3) and L^2 operator. The predicted $K=0_3^+$ band has

* Department of Physics, College of Humanities and Sciences, Nihon University.
** Department of Physics, Faculty of Science, The University of Tokyo.

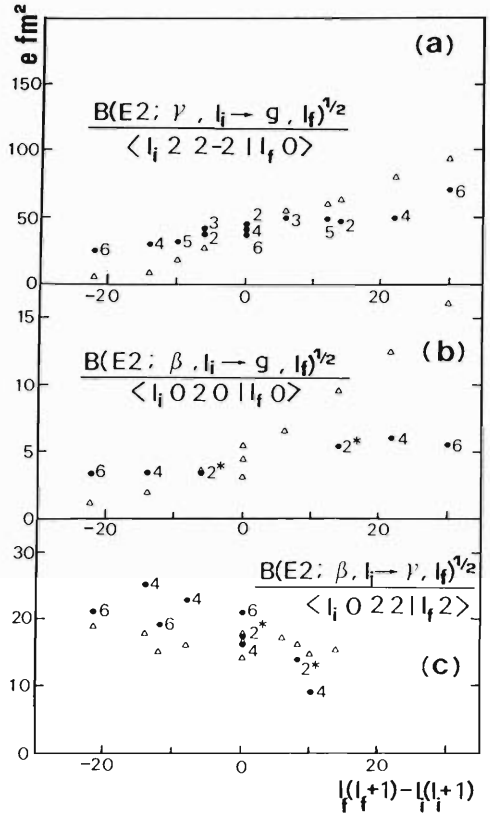

Fig. 2. (a) Analysis of E2 matrix elements for the γ to g transitions. Experimental values are shown by filled circles while theoretical ones are shown by open triangles. Points are labeled by I_f only for experiment. For more details see Ref. 5. (b) Analysis of E2 matrix elements for the β to g transitions. Asterisks indicate that for the $I=2_\beta$ states only relative intensities have been determined. (c) Analysis of E2 matrix elements for the β to γ transitions.

the nature of one-phonon state theoretically,[7] which is consistent with recent ^{167}Er(d,p) and ^{167}Er(t,d) reactions.[8] The lowest $K=3^+$ band is predicted at a reasonable position, which cannot be described in terms of the sd IBM-1. Below 4 MeV we have two $K=1^+$ bands which are not shown in Fig. 1. One starts at 2.7 MeV and the other at 3.8 MeV.

The one-body E2 operator is given by four independent parameters in this model:

$$Q_\mu = e_1(s^\dagger \tilde{d}_\mu + h.c.) + e_2(d^\dagger \tilde{d})_\mu^{(2)} + e_3((d^\dagger \tilde{g})_\mu^{(2)} + h.c.) + e_4(g^\dagger \tilde{g})_\mu^{(2)}$$

This differs from the sd case where only two independent parameters exist. With three M_0 values tabulated at Table III of Ref. 5 and the absolute B(E2) of $L=2_1^+ \to L=0_1^+$, the determined four parameters are ($e_1=-0.327$, $e_2=0.406$, $e_3=-0.420$, $e_4=0.519$) whose ratio is close to $(-2\sqrt{7/5} : 11/\sqrt{14} : -18/\sqrt{35} : 3\sqrt{11/7})$ that is given by a generator of SU(3). Figure 2 shows the Mikhailov plot analyses (MPA) for $\gamma \to g$, $\beta \to g$, and $\beta \to \gamma$. The general experimental trend of the E2 transitions is well reproduced, that is, the theoretical slope of the $\gamma \to g$, $\beta \to g$, and $\beta \to \gamma$ MPA's is positive, positive, and negative, respectively. It should be noticed in Fig. 2 that the theoretical MPA's are not like straight lines because of the effect of band mixing. The theoretical B(E2) prediction gives B(E2; $K=4_1^+ \to K=2_1^+$)/B(E2; $K=2_1^+ \to K=0_1^+$)$\fallingdotseq$1.4. This indicates that the $K=4_1^+$ band has the nature of 2γ band theoretically. The E2 transitions for $K=0_3^+ \to g$ are predicted to be as weak as for $\beta \to g$, which is also consistent with the experiment.

In summary we have calculated energy levels and E2 transitions of ^{168}Er in terms of the sdg IBM. This model is shown to solve the problem of anharmonicity regarding the excitation energy of the first $K=4^+$ band relative to that of the first $K=2^+$ one. The level scheme including the $K=3^+$ band is well reproduced and the calculated B(E2)'s are consistent with the experimental data.

References

1) Y. Akiyama: *Nucl. Phys. A*, **433**, 369 (1985).
2) W. F. Davidson, D. D. Warner, R. F. Casten, K. Schreckenbach, H. G. Borner, J. Simic, M. Stojanovic, M. Bogdanovic, S. Koicki, W. Gelletly, G. B. Orr, and M. L. Stelts: *J. Phys. G*, **7**, 455(1981).
3) D. D. Warner, R. F. Casten, and W. F. Davidson: *Phys. Rev. Lett.*, **45**, 1761(1980); D. D. Warner, R. F. Casten, and W. F. Davidson: *Phys. Rev. C*, **24**, 1713(1981).
4) H. C. Wu and X. Q. Zhou: *Nucl. Phys. A*, **417**, 67(1984).
5) A. Bohr and B. R. Mottelson: *Phys. Scr.*, **25**, 28(1982).
6) T. S. Dumitrescu and I. Hamamoto: *Nucl. Phys. A*, **383**, 205(1982).
7) N. Yoshinaga: Ph. D. thesis, University of Tokyo (1985).
8) D. G. Burke, B. L. W. Maddock, and W. F. Davidson: *Nucl. Phys. A*, **442**, 424(1985).

RIKEN Accel. Progr. Rep. 19 (1985)

III-1-12. Inelastic Scattering of Polarized Protons Exciting the γ- and Octupole-Vibrational Band in ^{152}Sm at 65 MeV

T. Ichihara, H. Sakaguchi,* M. Nakamura,* M. Yosoi,* M. Ieiri,* Y. Takeuchi,* H. Togawa,* T. Tsutsumi,* and S. Kobayashi*

NUCLEAR REACTIONS ^{152}Sm(p,p')E_p=65 MeV, polarized beam, measured differential cross sections and analyzing powers, ground state rotational band, γ-vibrational band, octupole-vibrational band; coupled-channel calculation, rotation-vibration model, asymmetric rotor model, hexadecapole ($Y_{42}+Y_{4-2}$) term.

The collective vibrational states in deformed nuclei are of considerable interest in investigating the nuclear structure.[1] In particular, the understanding of the γ-vibrational band is a long-standing problem.

Recent experiments and the analysis of the inelastic scattering of polarized protons exciting the γ-vibrational band in ^{166}Er and ^{168}Er have shown that the large hexadecapole term ($Y_{42}+Y_{4-2}$) together with the usual quadrupole term (Y_{22}) is necessary in order to reproduce the experiment data.[2),3)]

In order to investigate the systematic trend in the hexadecapole component of the γ-vibrational band, we have measured the inelastic scattering of the polarized protons from ^{152}Sm.

The experiment has been performed with 65 MeV polarized protons from the cyclotron at the Research Center for Nuclear Physics, Osaka University. The data have been obtained using a high resolution spectrograph RAIDEN. The overall energy resolution was 20-26 keV (FWHM). The beam current on the target was 30-60 nA and the beam polarization was 78-82 %.[4] Figure 1 shows a typical momentum spectrum on the focal plane counter for ^{152}Sm(p,p') scattering at θ_{lab}=48°. The ground state rotational band, the γ-vibrational band, the β-

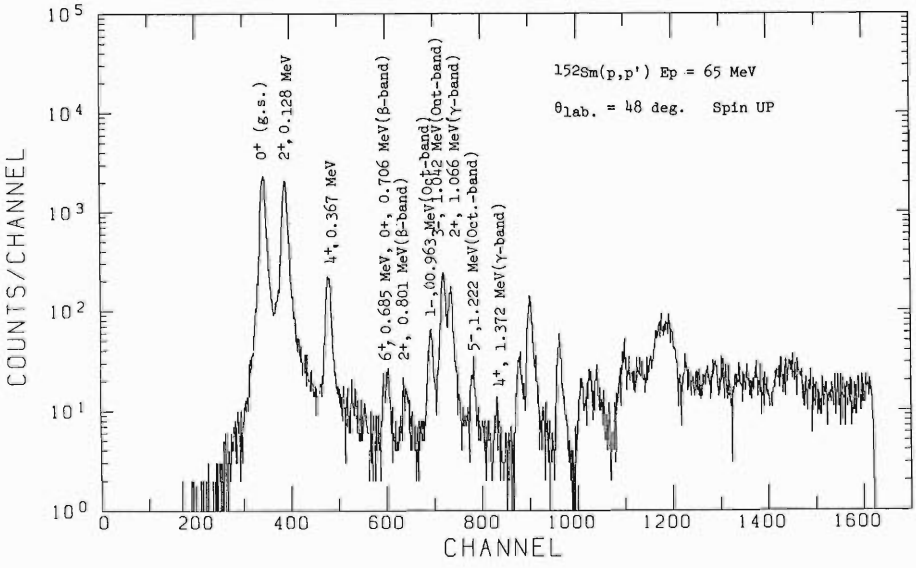

Fig. 1. Typical momentum spectrum on the focal plane counter for ^{152}Sm(p,p') scattering at 65 MeV.

* Department of Physics, Faculty of Science, Kyoto University.

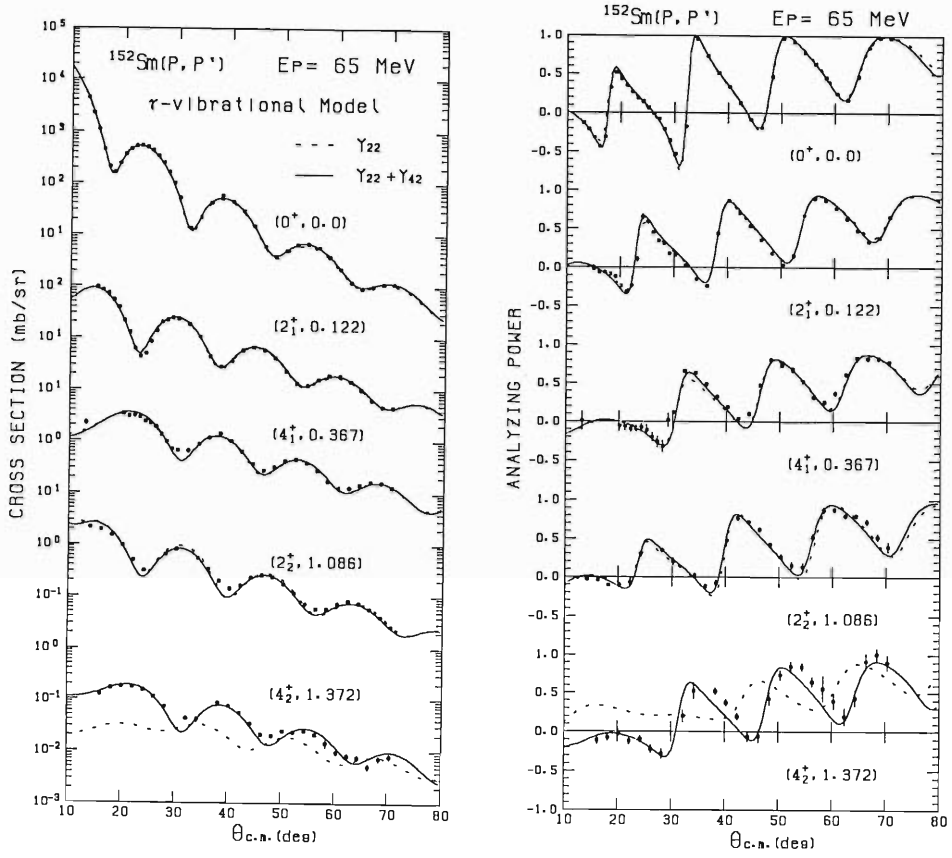

Fig. 2. Measured angular distributions of ^{152}Sm(p,p') scattering at 65 MeV for the ground-state rotational band and γ-vibrational band. Solid (dashed) curves show the coupled-channel calculation assuming the $Y_{22}+Y_{42}$(Y_{22} only) mode γ-vibrational model.

vibrational band, and the octupole vibrational band are strongly excited as shown in the spectrum.

Coupled-channel calculation assuming the γ-vibrational model has been performed using a modified version of the code ECIS79,[5] which includes the form factors of the surface vibration in deformed nuclei in order to calculate the β-,γ-, and octupole-vibration in deformed nuclei. Figure 2 shows the results of the calculation. Excellent fits have been obtained if we introduce the hexadecapole term ($Y_{42}+Y_{4-2}$) in the γ-vibrational band.

It has been found that the hexadecapole ($Y_{42}+Y_{4-2}$) transition strength in the γ-vibrational band is linear as a function of neutron number in the $152<A<168$ region. It would, therefore, be concluded that the hexadecapole component in the γ-vibrational band is tightly related to the (N,n3)=(5,2) neutron sub-major shell.

Figure 3 shows the result of the coupled-channel calculation for 0^+, 2^+, 4^+, 1^-, 3^-, and 5^- states in ^{152}Sm assuming the octupole-vibrational band. For the octupole vibration, the additional Y_{10} term is necessary in order to remove the spurious center-of-mass motion.[6] The importance of the correction term is clearly understood from Fig. 3. These results indicate the applicability of the rotation-vibration model of Bohr and Mottelson.[1]

References

1) A. Bohr and B. R. Mottelson: Nuclear Structure, W. A. Benjamin, Inc., Reading, Vol. II (1975).
2) N. K. Glendenning and R. S. Mackintosh: *Phys. Lett. B*, **29**, 626 (1969).
3) T. Ichihara, H. Sakaguchi, M. Nakamura, T. Noro, F. Ohtani, H. Sakamoto, H. Ogawa, M. Yosoi, M. Ieiri, M. Isshiki, Y. Takeuchi, and S. Kobayashi: *Phys. Lett. B*, **149**, 55 (1984).
4) T. Ichihara, H. Sakaguchi, M. Nakamura, T. Noro, F. Ohtani, H. Sakamoto, H. Ogawa, M. Yosoi, M. Ieiri, M. Isshiki, and S. Kobayashi: *Phys. Rev. C*, **29**, 1228 (1984).
5) J. Raynal: code ECIS79, unpublished; *Phys. Rev. C*, **20**, 31 (1979).
6) M. N. Harakeh: Lecture Notes of 1983 RCNP Kikuchi Summer School, p. 133 (1983).

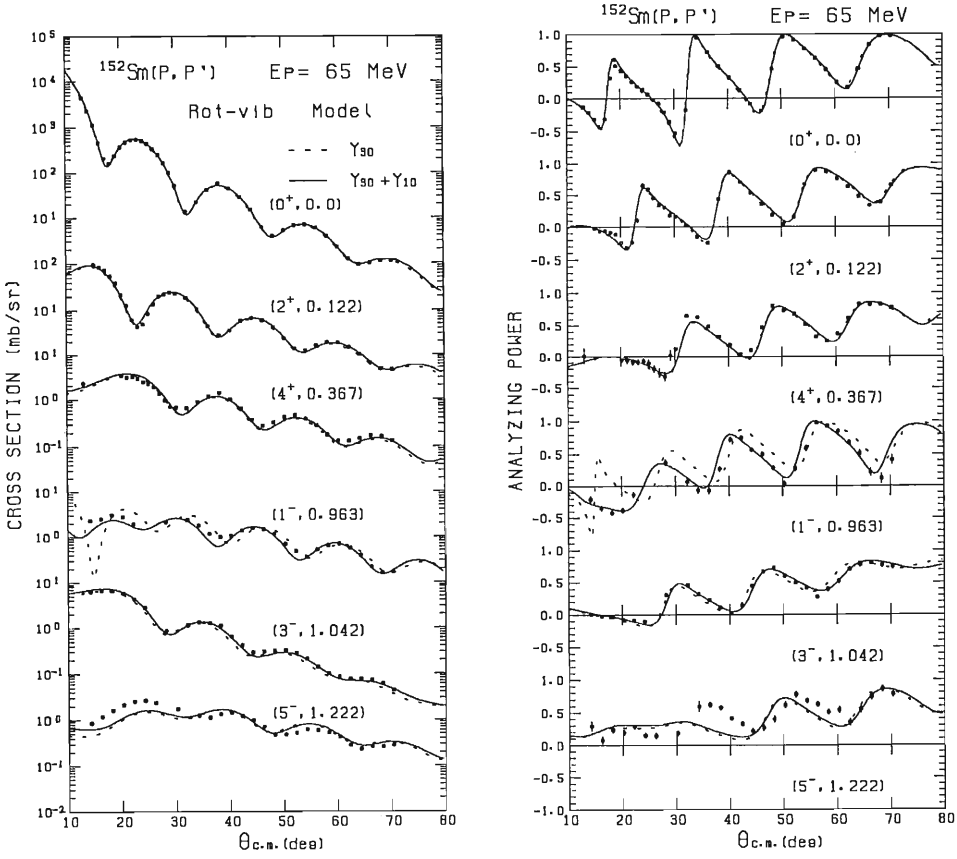

Fig. 3. Measured angular distributions of ^{152}Sm(p,p′) scattering at 65 MeV for ground-state rotational band and octupole-vibrational band. Solid (dashed) curves show the coupled-channel calculations assuming the octupole vibrational model with (without) center-of-mass motion correction.

RIKEN Accel. Progr. Rep. 19 (1985)

III-1-13. Multiple Coulomb Excitation of ^{161}Dy

T. Inamura, A. Hashizume, M. Ohshima,* T. Ishii,*
S. Kikuchi,* T. Aruga,* and S. Ichikawa*

[NUCLEAR REACTIONS ^{161}Dy(^{81}Br,^{81}Br′γ), $E=305$ MeV; measured E_γ nuclear lifetimes; recoil distance method.]

It is well known that high-j orbitals such as $i_{13/2}$ give rise to a large perturbation of the rotational levels of deformed nuclei. Recently, we have demonstrated such a rotational perturbation effect on M1 and E2 transitions in ^{167}Er as well as on level energies.[1] This perturbation effect is clearly dependent on signature r, a quantum number classifying rotational spectra; r is defined as $r=\exp(-i\pi\alpha)$, where $I=\alpha$ mode 2, I being the spin value of the rotational state.[2]

The nucleus ^{161}Dy is the one whose groundstate rotational band is built on the $i_{13/2}$ neutron orbital as in ^{167}Er. Therefore, it would be interesting to study whether there is the same signature dependence in ^{161}Dy as was observed for ^{167}Er. The ground-state rotational band of ^{161}Dy has been well established up to $33/2^+$,[3] and an energy plot such that $[E(I)-E(I-1)]/2I$ *vs.* I^2 shows marked signature dependence as observed in ^{167}Er. However, nuclear lifetimes are not available for highly excited states with spins larger than 9/2. In order to measure nuclear lifetimes of higher spin states, we are making a multiple Coulomb excitation experiment on ^{161}Dy. Here we present our preliminary results.

The nucleus ^{161}Dy was multiply Coulomb-excited with a ^{81}Br beam of 305 MeV from the JAERI tandem accelerator. The ^{161}Dy target was a self-supporting metallic foil of 2.5 mg/cm^2 in thickness. Deexcitation γ-rays were measured with a Ge(Li) detector placed at 45° to the beam in coincidence with backward scattered projectiles which were detected at $\theta=100°$-$150°$ to the beam with a plastic scintillator ($\Omega=0.5$ sr). Nuclear lifetimes were measured by the recoil distance method,[4] *i.e.*, lifetimes were deduced from the ratio of the yield I_u of the unshifted γ-ray peak to the total (I_u+I_s) that was plotted as a function of the recoil distance. The quantity I_s is the yield of the Doppler-shifted peak. Figure 1 shows the observed ratios against the distance. Correction for the kinematical effect on the recoil velocity has been made in the analysis. It should be stated that the Doppler-shift attenuation method[1),4)] is inadequate for ^{161}Dy because γ-rays are too narrowly separated to make a lineshape analysis.

As is seen from Fig. 1, we have for the first time measured lifetimes of $11/2^+$, $15/2^+$, $17/2^+$, and $19/2^+$ states. (For $13/2^+$ there are intruder γ-rays which make it hard to deduce the true lifetime.) Preliminary lifetimes and B(E2) values for cross-over transitions are summarized in Table 1. Values of B(M1) and B(E2) for stop-over transitions are to be estimated after completing a mixing ratio analysis. Branching ratios and conversion coefficients, which are needed to deduce the cross-over B(E2; $I\rightarrow I-2$), were obtained from Ref. 3. Lifetimes measured for $15/2^+$ and $19/2^+$ seem unreasonably short. They should be remeasured in coming experiments. Much higher spin states could also be studied through multiple Coulomb excitation with beams of ^{58}Ni or ^{81}Br.

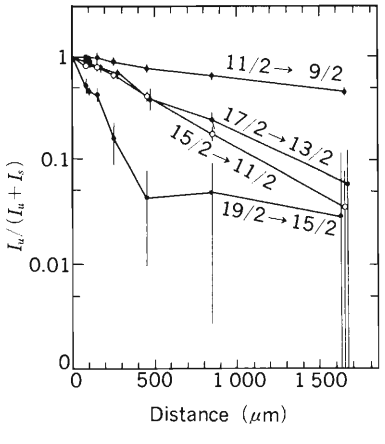

Fig. 1. Ratios of the unshifted component I_u to the total (I_u+I_s) as a function of target-stopper distance. Solid lines are drawn to guide the eye.

* Japan Atomic Research Institute, Tokai.

Table 1. Lifetimes of the ground-state rotational band members in ^{161}Dy and B(E2) values for cross-over transitions (preliminary).

Level	Mean life τ(ps)	Transition	E_γ (keV)	B(E2) (e^2b^2)
$9/2^+$	303.0*	$9/2^+ \rightarrow 5/2^+$(GND)	100.5	0.79±0.04*
$11/2^+$	192±20	$11/2^+ \rightarrow 9/2^+$	140.4	0.69±0.08
$13/2^+$				
$15/2^+$	(43±4)	$15/2^+ \rightarrow 11/2^+$	222.8	(—)
$17/2^+$	50±6	$17/2^+ \rightarrow 13/2^+$	240.7	1.2±0.1
$19/2^+$	(1.3±0.4)	$19/2^+ \rightarrow 15/2^+$	311.6	(—)

* Ref. 3.

References

1) M. Ohshima, E. Minehara, M. Ishii, T. Inamura, and A. Hashizume: *Nucl. Phys. A,* **436**, 518 (1985).
2) M. J. A. de Voigt, J. Dudek, and Z. Szymanski: *Rev. Mod. Phys.*, **55**, 949 (1983).
3) *Nuclear Data Sheets,* **43**, 134 (1984).
4) For example, D. B. Fossan, and E. K. Warburton: Nuclear Spectroscopy and Reactions, (ed. by J. Cerny), Academic Press, New York and London, Part C, p. 307 (1974).

RIKEN Accel. Progr. Rep. 19 (1985)

III-1-14. The Life-Time of the Levels in the Ground-State Band in ^{173}Yb

A. Hashizume, T. Inamura, M. Ohshima,* E. Minehara,*
S. Kikuchi,* and H. Kumahora**

[NUCLEAR REACTIONS ^{173}Yb(^{58}Ni,^{58}Ni'γ), $E=200$ MeV; measured E_γ, I_γ, Doppler shift, deduced life-times.]

By using multiple Coulomb excitation with a 200 MeV ^{58}Ni beam from the JAERI UR tandem accelerator, the ground-state rotational band up to spin $27/2^-$ in ^{173}Yb have been excited.[1] The excited states are shown in Fig. 1. It is known that high-j orbitals give rise to a perturbation on level energies and transition moments of ground-state rotational band. We have found the perturbation on transitions in ^{167}Er[2] built on $i_{11/2}$, $7/2^+[633]$ and also studied the band in ^{167}Dy[3] built on $f_{7/2}$, $5/2^-[523]$. As the ground-state rotational band in ^{173}Yb is built on the neutron orbital $h_{7/2}$, $5/2^-[512]$, these three nuclei would show some systematic trend about the perturbation effect.

The Doppler broadened γ-ray line shapes were observed at 0 degree by using a Compton-suppressed γ-ray detector. The line shapes of the cross over γ-rays emitted from the states of the

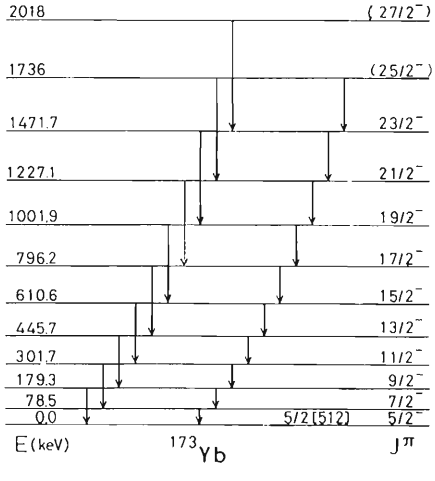

Fig. 1. The ground-state band in ^{173}Yb excited by 200 MeV ^{58}Ni.

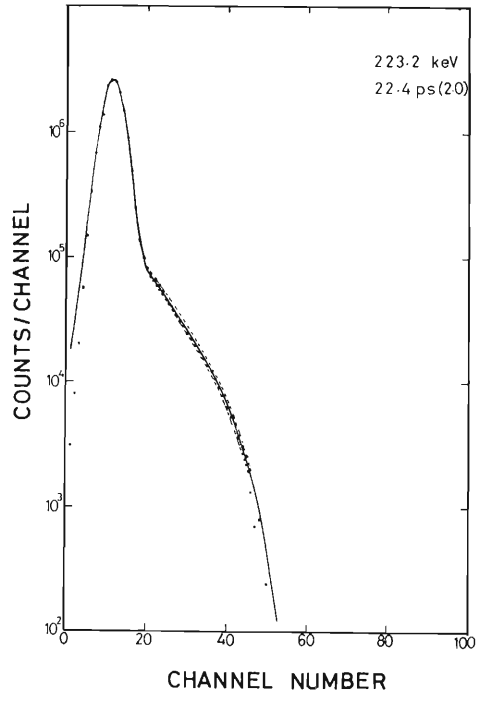

Fig. 2. Results of lineshape analysis of the 223.2 keV γ-ray. Solid curve represents the best fit and dashed ones show the range of uncertainties.

spin from $11/2^-$ to $21/2^-$ were analyzed. The experimental line shapes were fitted with a code which included the effects on the line shape of angular distribution of recoiling nuclei, feeding from higher levels, and the finite size of the germanium detector. The typical results of analysis were shown in Figs. 2 and 3. The life-times obtained in the present study were listed in Table 1.

Combining these life-times and γ-ray intensities, it is possible to learn the transition probabilities. Detailed analysis are in progress.

* Japan Atomic Energy Research Institute, Tokai.
** Department of Physics, Hiroshima University.

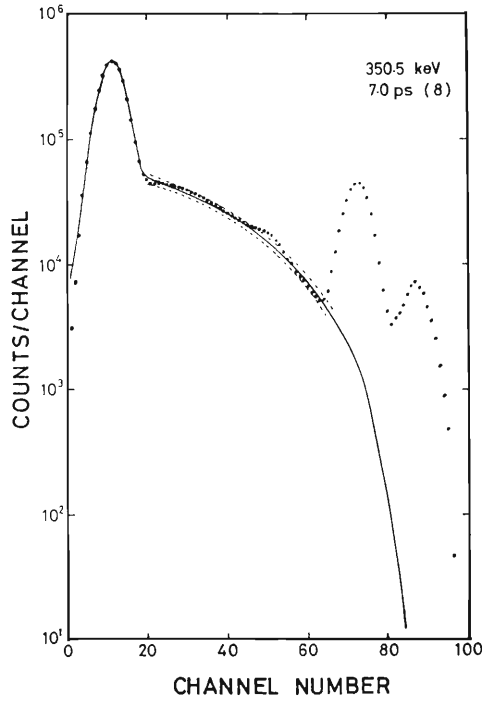

Fig. 3. Results of lineshape analysis of the 350.5 keV γ-ray. Solid curve represents the best fit and dashed ones show the range of uncertainties.

Table 1. Newly obtained life-times of levels in ^{173}Yb.

E (levels) (keV)	Spin	E_γ (cross over) (keV)	life-time (ps)
301.7	$11/2^-$	223.19	22.4±2.0
445.7	$13/2^-$	226.39	17.4±2.5
610.6	$15/2^-$	308.87	10.5±1.0
796.2	$17/2^-$	350.50	7.0±0.8
1001.9	$19/2^-$	391.26	4.4±0.6
1227.1	21/2	430.92	2.7±0.5

References

1) A. Hashizume, T. Inamura, M. Ohshima, E. Mine-hara, S. Kikuchi, and H. Kumahara: *RIKEN Accel. Progr. Rep.*, **18**, 28 (1984).
2) M. Ohshima, E. Mine-hara, M. Ishii, T. Inamura, and A. Hashizume: *Nucl. Phys. A*, **436**, 518 (1985).
3) T. Inamura, A. Hashizume, M. Ohshima, E. Mine-hara, S. Kikuchi, and H. Kumabara: *RIKEN Accel. Progr. Rep.*, **17**, 26 (1983).

RIKEN Accel. Progr. Rep. 19 (1985)

III-1-15. High-Energy Single-Proton States Studied by γ-Triton Coincidence Measurement in the ^{208}Pb(α,t)^{209}Bi Reaction

M. Ishihara, H. Ohsumi, T. Motobayashi, and Y. Nagai*

[NUCLEAR REACTION ^{208}Pb(α,t)^{209}Bi at $E=60$ MeV; coincidence energy spectra of tritons and γ-rays.]

We have been continuing investigation on highly excited single-particle states in ^{209}Bi using a proton stripping (α,t) reaction on ^{208}Pb. Of primary interest is observation of strength distributions of proton single-particle states in the excitation region of $6\hbar\omega$ such $1j_{15/2}$, $1i_{11/2}$, $2g_{9/2,7/2}$ states. In ^{209}Bi, single-particle states of $5\hbar\omega$ excitation are well explored and known to constitute a main portion of the level scheme in the lower excitation region below 4.0 MeV. On the other hand, the distributions of $6\hbar\omega$ states are rarely known since they range toward the high-energy continuum region.

A standard method to locate single-particle strengths is to observe differential cross sections in a single-particle transfer reaction. Such measurements have been carried out recently *via* the ^{208}Pb(α, t)^{209}Bi reaction[1),2)] and indicated significant strengths of high-spin single-particle states in the continuum spectral region. It is found, however, that the information of the cross sections is not sufficient to identify different single-particle states and to deduce spectroscopic factors quantitatively. This is because of similarity in angular distribution among different l-states and also due to the presence of a continuum background whose behavior is ambiguous.

This note reports a coincidence measurement between γ-rays and triton ejectiles in the ^{208}Pb(α, t)^{209}Bi reaction at 60 MeV to solve above problems. We have previously found[3)] that the highly excited states between the proton separation energy S_p (3.8 MeV) and the neutron separation energy S_n (7.8 MeV) primarily decay by γ transitions, which feed directly to low-lying $5\hbar\omega$ single-particle states. These γ-rays of $1\hbar\omega$ transition are most probably due to E1 decays with spin sequences such as $1j_{15/2}\rightarrow 1i_{13/2}$, $1i_{11/2}\rightarrow 1h_{9/2}$, and $2g_{9/2}\rightarrow 2f_{7/2}$. If this is the case, the strengths of the different $6\hbar\omega$ states can be identified and deduced from observed intensities of these high-energy transitions whose final states can be distinguished from missing energies.

In the present experiment, two telescopes of Si solid-state detectors were set at fixed angles of $\theta=16°$ with Al absorbers placed in front to protect the detectors from strong elastically-scattered particles. Five NaI detectors of $6''\phi\times 6''$ were used to obtain γ-ray spectra at different angles. In addition, γ-rays were detected with a setup called HERMES consisting of a central NaI detector of $6''\phi\times 10''$ and four sectors of NaI detector surrounding it. By using the surrounding detectors in an anti-coincidence mode, only peaks with full γ-ray energies were registered. Figure 1 shows a triton spectrum obtained in coincidence with whole γ-rays. The region of interest is the continuum part between 4.0 and ~8.0 MeV, while the spectrum in the lower excitation is well understood to consist of well separated $5\hbar\omega$ states. Figure 2 shows a γ-ray spectrum obtained with HERMES in coincidence with tritons whose energies correspond to excitation of states between $E_x=7.0$–7.4 MeV. While the statistics is rather poor, implication of the data is clear and promising. The peak of the highest energy is centered at 7.2 MeV corresponding to the transition to the ground state ($1h_{9/2}$). The second highest peak around 5.6 MeV corresponds to the transition to the second excited state ($E_x=1.6$ MeV, $1i_{11/2}$). The 3rd bump around 4.6 MeV may be a partner of a bump around 2.6 MeV which corresponds to multiplets of $h_{9/2}\otimes 3^-$ configuration. The peaks at 0.9 and 1.6 MeV are partly due to the second-chance decays in sequence with the high energy transitions of 4.6 and 5.6 MeV, respectively. The spectrum clearly shows the branching ratios of deexcitation of the initial continuum states to the $1h_{9/2}$ and $1j_{13/2}$ states. Thus the strengths of the $1j_{11/2}$ and $1i_{15/2}$ states may be unambiguously determined. In a similar manner the branching ratios were

* Faculty of Science, Osaka University.

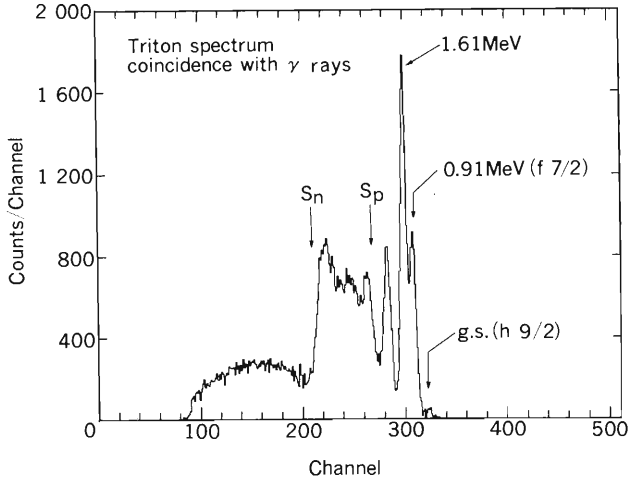

Fig. 1. The triton spectrum obtained in the ^{208}Pb (α, t)^{209}Bi reaction at 60 MeV and $\theta=16^{\circ}$ in coincidence with γ-rays.

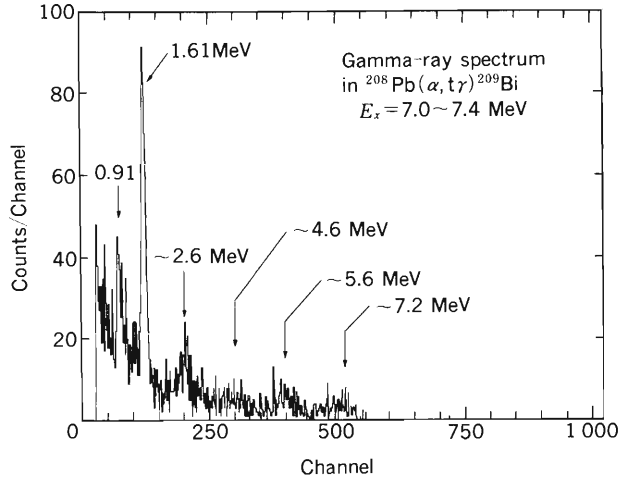

Fig. 2. The γ-ray spectrum obtained with HERMES in coincidence with tritons feeding excited states of ^{209}Bi at E_x=7.0-7.4 MeV.

obtained for the continuum states as a function of E_x over the whole region between S_p and S_n. A final quantitative analysis is now under progress.

References

1) S. Gales, C. P. Massole, S . Fortier, E. Gerlic, J. Guillot, E. Hourani, J. M. Maison, J. P. Schapira, B. Zweiglinski, P. Martin, and V. Comparat: *Phys. Rev. Lett.*, **48**, 1593 (1982).
2) E. Takada, M. Ishihara, Y. W. Hui, Y. Mihara, T. Murakami, Y. Toba, and R. E. Tribble: *RIKEN Accel. Progr. Rep.*, **17**, 21 (1983).
3) M. Ishihara, H. Ohsumi, T. Motobayashi, Y. Nagai, and T. Shimada: *RIKEN Accel. Progr. Rep.*, **18**, 39 (1984).

RIKEN Accel. Progr. Rep. 19 (1985)

III-1-16. Search for New Isotopes of Neptunium

H. Kudo, T. Nomura, K. Sueki, Y. Hatsukawa,
Y. Horikoshi,* and M. Magara**

[NUCLEAR REACTION ^{209}Bi+^{20}Ne, E=95-115 MeV; α-decay, fast-pulsed technique, slow-pulsed technique, He-jet transport.]

There are a number of undiscovered isotopes in the transuranium region. We paid attention to a neutron deficient side, and tried to identify new isotopes of neptunium using ^{20}Ne on ^{209}Bi reaction by detecting α-particles. Irradiations were performed at the cyclotron in the lab-energy of 95-115 MeV, which corresponds to the excitation energy of a compound nucleus of 28-46 MeV. In this excitation energy region, large cross sections for ^{209}Bi(^{20}Ne, 3n)^{226}Np and ^{209}Bi(^{20}Ne, 4n)-^{225}Np reactions are expected. As ^{226}Np is an odd-odd nucleus, it is probable that this nucleus disintegrates by EC decay. If this is the case, we could measure α-particles from ^{226}U which has a half-life of 0.5 s and from the successive daughter nuclides by using a He-jet transport system. The Q-value for the ground-state α-decay of ^{225}Np which seems to have the most favorable production condition in the present reaction system is evaluated as 8.605 MeV from the empirical mass formula.[1] From the systematics by Taagepera and Nurmia,[2] the half-life of ^{225}Np by α-decay is estimated as around a few hundreds of microseconds.

The nuclides whose half-lives lie in the range of a few tens to a few hundreds of nanoseconds were identified by means of a fast pulsed-beam technique developed by Nomura *et al.*[3] In this technique, the sharp phase bunching of the cyclotron beam and the fast timing property of a Si detector make it possible to distinguish delayed α-particles from promptly emitted charged particles in a nanosecond timing. Time distributions of α-decays were taken between natural beam bunches of the cyclotron by use of a time-to-amplitude converter, for which beam bursts from the cyclotron generate the zero-time signals, that is, start and stop pulses for the time-to-amplitude converter were provided from a fast signal of a Si detector and the rf-oscillator of the cyclotron. The nuclides of half-lives of sub-millisecond to a few tens of milliseconds were measured by a slow-pulsed beam technique. A slow-pulsed beam was obtained by operating the ion source with a pulsing mode. In the in-beam experiments, Bi target of about 500 μg/cm^2 in thickness was inclined 30° to the beam direction and normal to the detector surface in order to minimize escape of recoil products from the target and to obtain

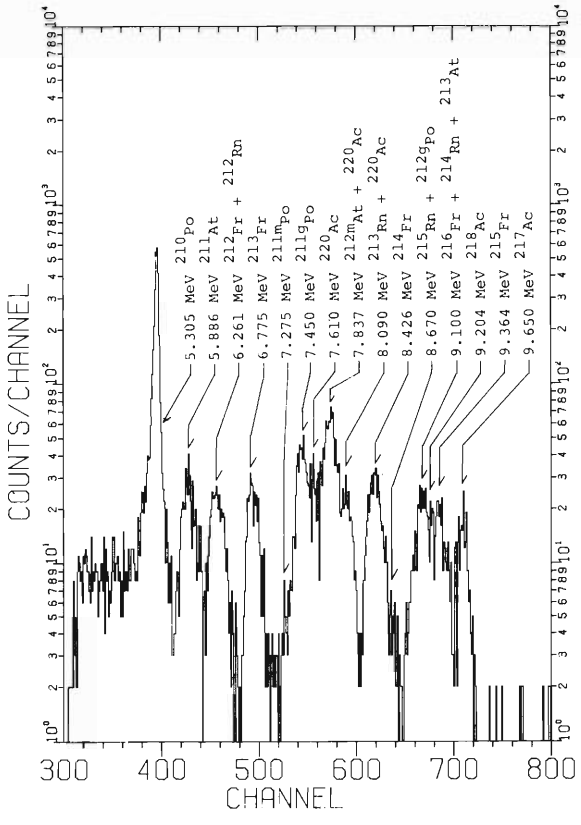

Fig. 1. An example of α-spectra obtained in the reaction of 110 MeV ^{16}O on ^{209}Bi by a fast pulsed-beam technique.

* Faculty of Science, Niigata University.
** Faculty of Science, Tokyo Metropolitan University.

good resolution of the α-spectrum. To check the electronic circuit of nanosecond timing, the reaction of ^{16}O on ^{209}Bi was employed. An example of α-spectrum is shown in Fig. 1. Measured half-lives ranged from 90 ns (^{215}Fr) to 7.22 h (^{211}At), and the FWHM of α-spectrum was about 90 keV.

For the measurement of the nuclides of half-lives longer than a few hundreds of milliseconds, a He-jet transport system[4] was used. In this measurement, two Si detectors were mounted for detection of α-particle emitters. One was placed just at the exit of gas jet, where accumulation and saturation of radioactivity were observed depending on the half-life of the nuclide. The other detector was placed 3–60 cm apart from the collecting position, and the products deposited on the collecting tape were moved to the front of the detector by means of a micro-computer-controlled stepping motor. In order to estimate the transport efficiency of the He-jet transport system, a recoil catcher foil method was employed. The shortest half-life observed was 119 ms of ^{212m}At by the He-jet transport system in the reaction of ^{20}Ne on ^{209}Bi.

Data analysis is still in progress; however, a preliminary analysis has given no indication of new isotopes of neptunium so far. Only a few α-particles were observed above 8 MeV except for ^{213}Rn, ^{211m}Po, and ^{212m}Po both in the He-jet and nanosecond timing experiments (see Fig. 2); this means that neither protactinium isotopes nor actinium isotopes which are daughter and granddaughter nuclides of neptunium isotopes of interest were measured. Judging from the detection efficiencies, the production cross sections for (^{20}Ne, xn) products are less than a few μb.

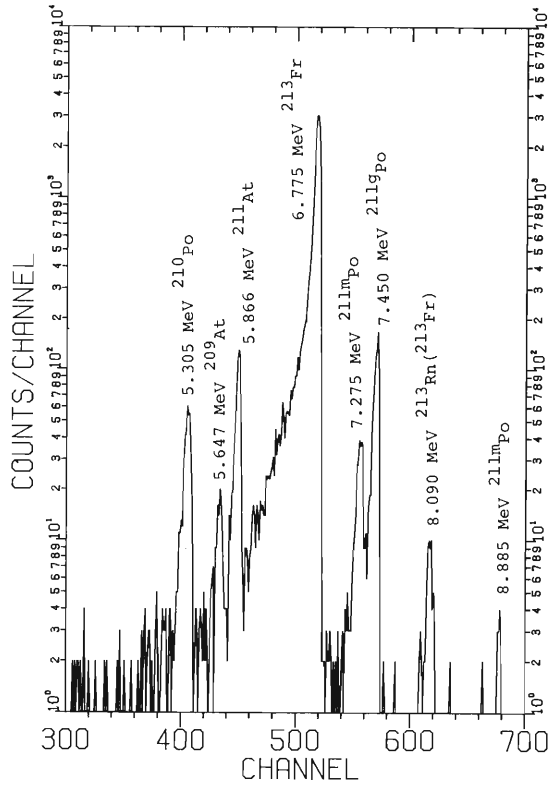

Fig. 2. A part of the α-spectrum obtained in the reaction of 115 MeV ^{20}Ne on ^{209}Bi by a He-jet transport system.

References

1) A. H. Wapstra and K. Bos: *At. Data Nucl. Data Tables*, **17**, 474 (1976).
2) T. Taagepera and M. Nurmia: *Ann. Acad. Sci. Fenn. A*, **78** (VI), 1 (1961).
3) T. Nomura and K. Hiruta: *Nucl. Instrum. Methods*, **108**, 61 (1973).
4) H. Kudo, T. Nomura, and J. Fujita: *RIKEN Accel. Progr. Rep.*, **18**, 127 (1984).

RIKEN Accel. Progr. Rep. 19 (1985)

III-1-17. Low Energy Nuclear Fission of ^{237}Np

T. Ohtsuki,* Y. Hatsukawa, T. Miura, H. Nakahara,
K. Sueki, and I. Kohno

[NUCLEAR REACTIONS proton induced fission of ^{237}Np; E_p=9.0-16.0 MeV, measured γ-rays and α-rays, mass yield curves, excitation functions, statistical analysis.]

Since discovery of nuclear fission in 1939, many experiments have been performed on nuclear fissions of actinoid elements. No appropriate theory for understanding of these data, however, has been proposed yet, especially for characteristics of mass-yield curves in fissions. In the deformation process of the fissioning nucleus toward fission, three possibilities have been discussed on the critical point for mass division: (1) saddle point, (2) scission point, and (3) somewhere during the dynamical descent from saddle to scission. Kudo *et al.*[1),2)] reported that their data on fragment angular distributions and excitaion functions observed in the proton-induced fission of ^{232}Th could be consistently explained by assuming two kinds of saddles, one leading to asymmetric mass divisions and the other leading to the symmetric.

In the present study, we have tried a detailed investigation of excitation functions in the proton-induced fission of ^{237}Np[3)] in the energy range of 9-16 MeV. We will report preliminary results of the mass yield curves, total fission cross sections, and ^{237}Np(p,2n)^{236}Pu reaction cross sections. We have attempted to reproduce the peak-to-valley (P/V) ratios of these mass yield curves by statistical calculation using an ALICE code by assuming two kinds of barriers of different height.

Neptunium targets were prepared by electrodeposition on a 4.8 mg/cm^2 thick Al foil from an ethanol solution at 150 V. The amount of Neptunium deposited was determined by α-ray spectrometry. These targets were wrapped with an Al catcher foil of 4.8 mg/cm^2, and stacked into 9 layers. As a proton energy monitor, 10 mg/cm^2 Cu foils were inserted into the target stack at an appropriate interval. The bombardment was performed at RIKEN Ring cyclotron for 30 min and 5 h, at an incident proton energy of 16 MeV with about 2 μA beam current. After bombardment the resulting activities were measured directly with a Ge(Li) detector. The produced nuclides were identified from their characteristic γ-ray energies, and their formation cross sections were evaluated from the observed photopeak areas, photo abundances, genetic relationships, the degree of saturation during the bombardment, and the target thickness. The ^{237}Np(p,2n)^{236}Pu reaction cross sections were obtained by α-spectrometry.

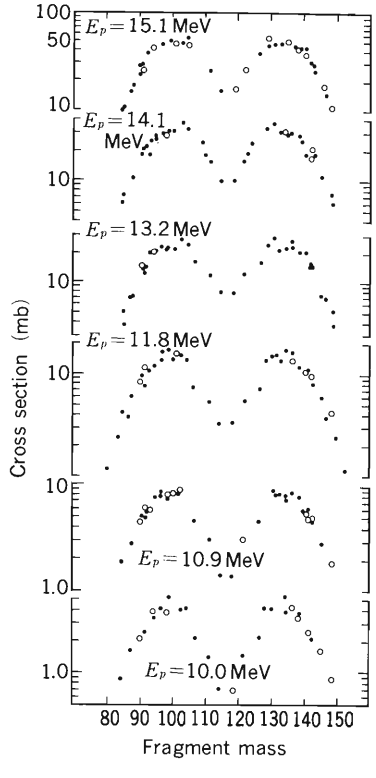

Fig. 1. Mass yield curves from 10 MeV to 15 MeV at an interval of about 1 MeV. ●, experimenntal data; ○, mirror points.

* Faculty of Science, Tokyo Metropolitan University.

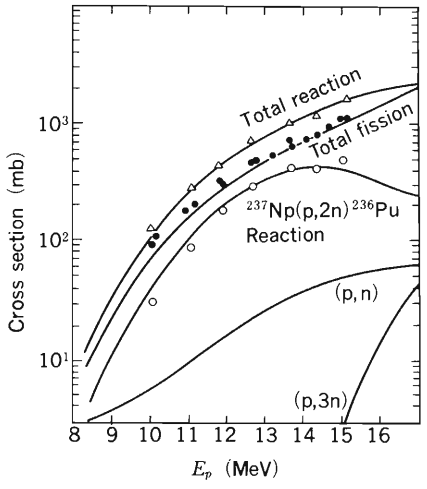

Fig. 2. Fission cross sections of proton-induced fission of ^{237}Np. ●, total fission cross section; ○, ^{236}Pu formation cross section; △, total reaction cross section. Solid lines represent the results of statistical calculation.

The observed mass-yield curves from 10 MeV to 15 MeV at an interval of about 1 MeV are shown in Fig. 1. The total fission cross section, total reaction cross section, and ^{237}Np(p,2n)^{236}Pu cross section are given in Fig. 2. The solid lines show the best fit obtained by the ALICE code for the competition of neutron evaporation and fission in which two kinds of threshold energies are assumed. The parameters used are listed in Table 1. Cross-section ratios for several fission products are shown in Fig. 3. The cross-section ratio of the asymmetric to the symmetric product (^{99}Mo/^{115}Cd) is found to vary with incident proton energy; but the ratios among the symmetric product (^{112}Pd/^{115}Cd) and the asymmetric (^{99}Mo/^{91}Sr, ^{97}Zr/^{143}Ce) are found to be insensitive to incident energies. The experimental P/V ratios are reproduced well by using the parameter sets given in Table 1, as depicted in Fig. 4.

Table 1. Parameters used in the statistical calculation (ALICE code).

Mode of fission	Multiple chance fission	E_f (MeV)	a_n (MeV^{-1})	a_f/a_n	$\hbar\omega$ (MeV)
Asymmetric fission	(p,f)	5.90	$A/8$	1.05	1.0
	(p,nf)	5.59			
	(p,2nf)	5.76			
Symmetric fission	(p,f)	7.92	$A/8$	1.15	1.0
	(p,nf)	6.88			
	(p,2nf)	7.32			

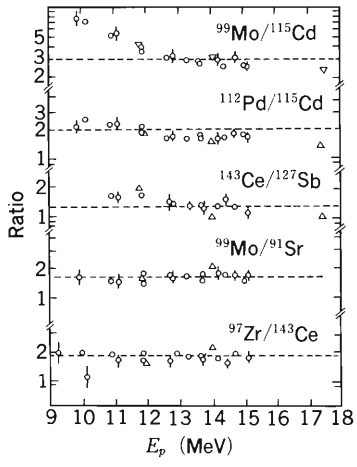

Fig. 3. Cross section ratios as a function of incident proton energy. ○, this work; △, for comparison (the results in Ref. 3).

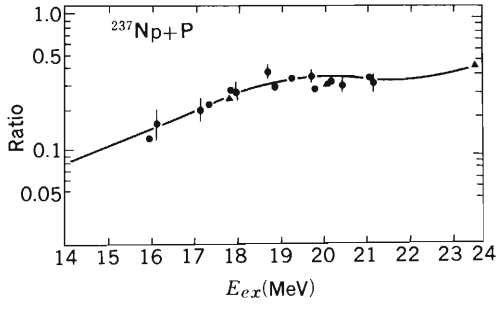

Fig. 4. Cross section ratio of ^{115}Cd to ^{99}Mo. Solid line represents the result of statistical calculation using the modified ALICE code. ●, this work; ▲, for comparison (the results in Ref. 3).

In conclusion, from the incident-energy independence of cross section ratios observed among the symmetric or asymmetric products, the existence of two kinds of threshold energies is suggested, and the cross section data obtained in the present study are well reproduced by the statistical analysis of the neutron evaporation-to-fission competition on an assumption of two fission barriers, one for the asymmetric and the other for the symmetric mass division.

References

1) H. Kudo, H. Muramatsu, H. Nakahara, K. Miyano, and I. Kohno: *Phys. Rev. C*, **25**, 3011 (1982).
2) H. Kudo, Y. Nagame, H. Nakahara, K. Miyano, and I. Kohno: *Phys. Rev. C*, **25**, 909 (1982).
3) P. Polak and A. H. W. Aten, Jr.: *J. Inorg. Nucl. Chem.*, **42**, 641 (1979).

RIKEN Accel. Progr. Rep. 19 (1985)

III-1-18. Low Energy Nuclear Fission of ^{238}U: Correlation between Angular Anisotropy of Fission Fragment and Fragment Mass

Y. Hamajima,* K. Sueki, M. Magara,** H. Nakahara, and I. Kohno

[NUCLEAR REACTION ^{238}U(p,f), E_p=14.5, 16 MeV; FISSION angular distribution, Bohr's channel theory, two kinds of configurations for transition state, mass division, statistical calculation.]

Kudo *et al.*[1] have found using a radiochemical technique that there exists clear dependence of angular anisotropy on fragment mass in the 15 MeV proton-induced fission of ^{232}Th, and similar dependence was confirmed later by Hamajima *et al.* with a counter technique.[2] Hamajima *et al.*, however, observed no clear dependence when the proton energy was changed to 13 MeV.[3] These data were explained successfully by Bohr's channel theory[4] which had been considered to be well established in low energy nuclear fission, if it was assumed that the final mass division modes could be closely related to two kinds of configurations at the outer barrier, one leading to symmetric mass division and another to asymmetric division, as suggested by Möller and Nilsson.[5]

In the present work an experimental study on the correlation between the angular distribution of the fission fragment and the fragment mass was extend to the system of 14.5 and 16 MeV proton-induced fission of ^{238}U.

The uranium target (about 0.1 mg/cm^2 in thickness) prepared by vacuum evaporation of UF_4 onto a carbon film (30 μg/cm^2) was bombarded with 14.5 and 16 MeV protons from the cyclotron. Details of the experimental set-up, counting and data analysis have been reported previously.[2]

The examples of the observed angular anisotropies ($W(\theta)/W(90)$) for mass ratios (M_H/M_L) of 1.0 (circles) and 1.5 (squares) at 16 MeV are shown in Fig. 1 (a). The solid curves represent the results of least-squares fitting of a functional form of ($a+b\cos^2\theta$). The angular anisotropies ($W(0)/W(90)=1+b/a$) obtained from the fitting for respective mass ratios for 14.5 (circles) and 16 MeV (squares) are plotted in Fig. 1 (b). The difference in the anisotropies between

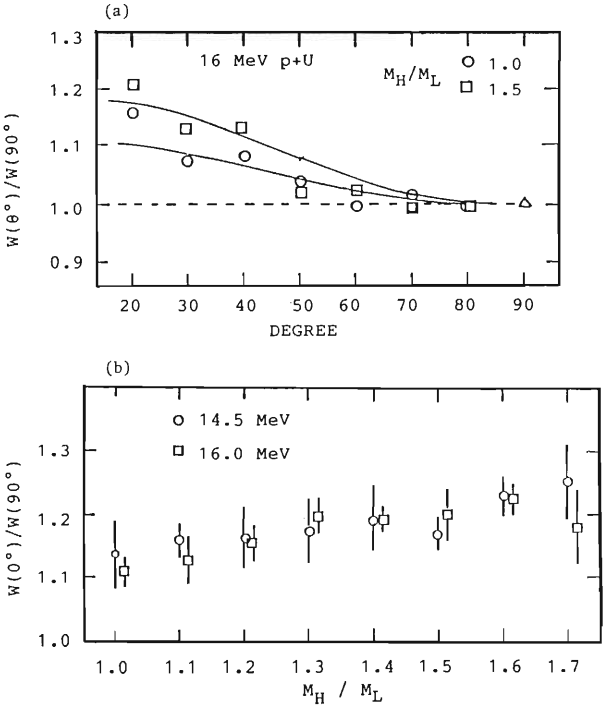

Fig. 1. Angular anisotropies $W(\theta)/W(90)$, (a) as a function of θ with mass ratios (M_H/M_L) of 1.0 (circles) and 1.5 (squares) for 16 MeV proton-induced fission of ^{238}U and (b) as a function of mass ratios for 14.5 MeV (circles) and 16 MeV (squares). Curves in (a) are the results of least-squares fitting of a form ($a+b\cos^2\theta$). Error bars attached to the data points in (b) are due to counting statistics and fitting.

14.5 MeV and for 16 MeV is not significant within the associated errors derived from counting statistics and fitting. The anisotropies of asymmetric mass divisions seem to be slightly higher than those of symmetric divisions at these proton energies. Calculated results of the contributions of multiple-chance fission (R), and theoretically expected angular anisotropies (W), and apparent anisotropies (W_{app}) for 14.5 MeV (a) and 16 MeV

* Faculty of Science, Kanazawa University.
** Japan Atomic Energy Research Institute.

Table 1. Theoretically predicted angular anisotropies on 14.5 MeV (a) and 16 MeV (b) proton-induced fission of ^{238}U.

(a) 14.5 MeV

		B_f (MeV)	t (MeV)	K_0^2	R(%)	W	W_{app}
	p,f	5.03	0.68	77.2	60	1.06	
Asym.	p,nf	5.98	0.49	56.2	2	1.08	1.10
	p,2nf	4.91	0.31	26.0	38	1.16	
Sym.	p,f	7.37	0.60	67.8	100	1.06	1.06

(b) 16 MeV

		B_f (MeV)	t (MeV)	K_0^2	R(%)	W	W_{app}
	p,f	5.30	0.72	81.0	46	1.06	
Asym.	p,nf	5.98	0.53	61.0	2	1.08	1.08
	p,2nf	4.91	0.38	44.5	52	1.10	
Sym.	p,f	7.37	0.63	71.8	100	1.07	1.07

B_f, fission barrier height (MeV); t, nuclear temperature (MeV); R, contribution to each mode fission (%); W, angular anisotropy ($W(0)/W(90)$); W_{app}, apparent anisotropy ($W(0)/W(90)$).

(b) are listed in Table 1. The calculation was based on extended Bohr's theory[6] and the statistical theory,[7] on an assumption of two kinds of configurations, symmetric and asymmetric, for the transition state where both the fission probability and angular distributions are determined. Fission barrier heights for asymmetric mass division used in the calculation were by about 0.5 MeV higher than the reported values[8),9)] (see Table 1). The theoretical anisotropies W_{app} of 1.06 and 1.10 for symmetrically divided fission fragments and asymmetrical ones for the 14.5 MeV are shown to be lower than those corresponding to the observed values of 1.13 and 1.20. The predicted W_{app} of 1.07 and 1.08 for the 16 MeV are also low in comparison with observed ones of 1.11 and 1.19 for the respective modes of the mass divisions. However, the theoretical prediction that there would not be significant fragment-mass dependence for both 14.5 and 16 MeV proton induced fissions is consistent with the present observations. Therefore, present results also support the conclusion of Refs. 2 and 4 that the symmetric mass divisions require extra energy of about 2 MeV compared to the asymmetric divisions at the transition state where fission probabilities and angular distributions are determined.

References

1) H. Kudo, Y. Nagame, H. Nakahara, K. Miyano, and I. Kohno: *Phys. Rev. C,* **25**, 909 (1982).
2) Y. Hamajima, K. Sueki, M. Magara, H. Nakahara, and I. Kohno: *RIKEN Accel. Prog. Rep.,* **17**, 29 (1983).
3) Y. Hamajima, K. Sueki, M. Magara, H. Nakahara, and I. Kohno: *RIKEN Accel. Prog. Rep.,* **18**, 143 (1984).
4) A. Bohr: Proc. 1st UN Conf. on the Peaceful Uses of Atomic Energy (II), pp. 151, 911 (1955).
5) P. Möller and S. G. Nilsson: *Phys. Lett. B,* **31**, 283 (1970).
6) R. Vandenbosch and J. R. Huizenga: Nuclear Fission, Academic Press, New York (1973).
7) H. Kudo, H. Muramatsu, H. Nakahara, K. Miyano, and I. Kohno: *Phys. Rev. C,* **25**, 3011 (1982).
8) R. Vandenbosch and G. T. Seaborg: *Phys. Rev.*, **110,** 507 (1958).
9) B. B. Back, H. C. Britt, O. Hansen, B. Leoux, and D. J. Garrett: *Phys. Rev. C,* **10**, 1948 (1974).

RIKEN Accel. Progr. Rep. 19 (1985)

III-1-19. Decay Properties of Light Einsteinium Isotopes

Y. Hatsukawa, M. Magara,* T. Otsuki,* M. Nakata,*
K. Sueki, H. Nakahara, and I. Kohno

[NUCLEAR REACTIONS $^{238}U(^{14}N, xn)^{252-x}Es$, $x=5$-7, $E_{lab}=$ 80-103 MeV, $^{237}Np(^{12}C, xn)^{249-x}Es$, $x=4.5$, $E_{lab}=67$-81 MeV; He-jet transport, measured α-spectrum and half-life.]

In a previous progress report,[1] the decay properties and excitation functions of neutron-deficient Es isotopes ($A \geq 274$) produced by the reaction $^{14}N+^{238}U$ were reported. In the present work, four isotopes of Es with masses 244 through 247 were investigated further by means of α-ray spectroscopy. We produced neutron-deficient isotopes of Es by bombarding a ^{238}U target with ^{14}N ions and a ^{237}Np with ^{12}C ions at the cyclotron. Beam energies were $E_{lab}(^{14}N)=80$-103 MeV, $E_{lab}(^{12}C)=67$-81 MeV. The reaction products recoiled out of the targets were stopped in a fast flowing He gas (a He-jet system[2]), and transferred onto the collecting tape heated at 195°C in order to get rid of oil that would deteriorate the resolution of α-spectra. After an appropriate collection period (generally 8 or 3 min), the deposited recoil atoms were moved to face Si(Au) surface barrier detectors for α-ray measurements. α-Decay events were recorded together with external clock pulses and stored in a magnetic tape in the list mode for data analysis.

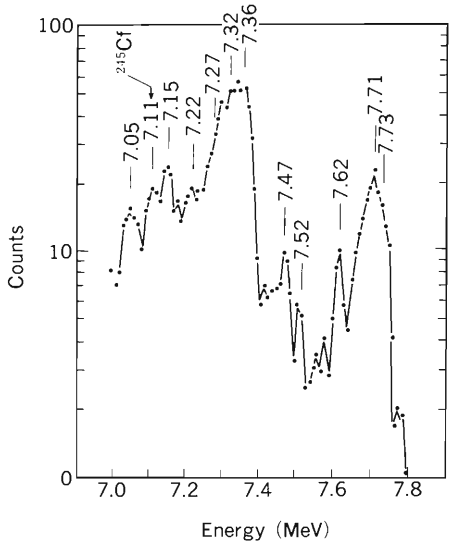

Fig. 1. A part of α-particle spectra combined from five bombardments of ^{238}U with 80-94 MeV ^{14}N ions.

The α-particle spectra displayed in Fig. 1 are the sum of the results obtained by several bombardments of the ^{238}U with 80-103 MeV ^{14}N ions. The single peak shape and channel energies were determined by using α-rays of ^{211m}Po,^{213}Fr, and ^{214}Ra produced by separate bombardment of a ^{209}Bi target with ^{14}N. The α-peaks at 7.73, 7.36, and 7.32 MeV have been assigned to ^{245}Es, ^{246}Es, and ^{247}Es, respectively. In addition, some other α-peaks were also observed, which, from their energies and half-lives, could not be assigned to any of the nuclei produced by ^{14}N on Bi or Pb, possibly included in the ^{238}U target as impurities, or those produced by transfer reactions of ^{238}U. Further, from the excitation functions referring to the known α-rays, it is concluded that all the

Table 1. Summary of results.

Nuclide	Energy (MeV)	Half-life (min)	Branching ratio
^{247}Es	7.32	$5.24^{+0.52}_{-0.43}$	
^{246}Es	7.05	$4.70^{+0.72}_{-0.55}$	
	7.22	$3.15^{+0.33}_{-0.27}$	0.15
	7.36	$3.20^{+0.80}_{-0.50}$	1.00
^{246}Es	7.15	$7.43^{+1.90}_{-1.26}$	0.99
	7.27	$7.73^{+0.92}_{-0.75}$	1.00
^{245}Es	7.62	$1.18^{+0.27}_{-0.18}$	$\simeq$0.34
	7.71	$1.37^{+0.34}_{-0.23}$	1.00
	7.73	$1.22^{+0.14}_{-0.11}$	0.82

* Faculty of Science, Tokyo Metropolitan University.

peaks but 7.11, 7.47, and 7.52 MeV α-rays belong to the Es isotopes produced by $^{238}U(^{14}N, xn)$ reactions. (The 7.11 MeV α-peak is assigned to the decay of ^{245}Cf.) They could be grouped according to their half-lives and the projectile energy dependency as presented in Table 1. The errors attached to relative intensities merely reflect statistical uncertainties in counting and those given for α-particle energies are mostly caused from energy calibration. The preliminary results suggest that ^{245}Es emitts three different α-rays, and that ^{246}Es has two isomer states, one of which emitts four and the other two α-rays. More complete and quantitative discussions of level schemes may, however, become possible only after measurements of γ-rays in coincidence with α-particles.

In order to confirm the above results, bombardments of a ^{237}Np target with 67–81 MeV ^{12}C ions were performed. The obtained spectra are shown in Fig. 2. α-Rays belonging to ^{245}Es were mainly observed. Rough estimates of their half-lives are in good agreement with those obtained in the $^{238}U+^{14}N$ reaction. More detailed analysis of the data is in progress.

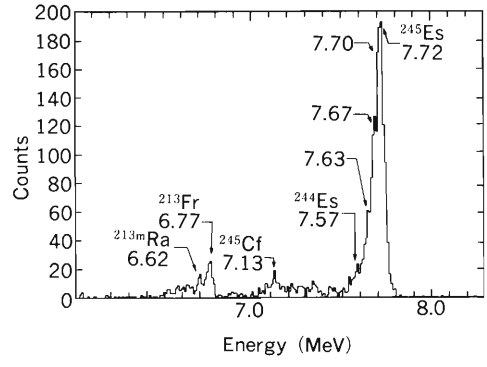

Fig. 2. A part of α-particle spectra combined from three bombardments of ^{237}Np with 67–71 MeV ^{12}C ions.

References

1) M. Magara, K. Sueki, H. Nakahara, H. Kudo, Y. Hamajima, and I. Kohno: *RIKEN Accel. Progr. Rep.*, **18**, 37 (1984).
2) H. Kodo, T. Nomura, and J. Fujita: *RIKEN Accel. Progr. Rep.*, **17**, 127 (1983).

RIKEN Accel. Progr. Rep. 19 (1985)

III-2. Atomic and Solid-State Physics

1. Electron Stripping Cross Sections from Multi-Charged Ions by Neutral Atoms Using Born Approximation Calculation†

S. Karashima, X. Zhang,* Q. Ma,* Y. Liu,* and T. Watanabe

In a previous paper[1] we have calculated the electron stripping cross section from energetic multi-charged ions by collision with a neutral target, such as

$$A^{q+} + B \rightarrow A^{(q+1)+} + e + B(\Sigma) \qquad (1)$$

where Σ denotes all electronic states including ionized states. In this study we applied the binary encounter approximation (BEA) with the electron velocity distribution obtained from Thomas-Fermi statistics. In the calculation we made an assumption that the cross section for electron stripping from the incident ion by collision with the target nucleus is much larger than that by collision with electrons in the target. Under this assumption the process can be considered to be equivalent to the electron ionization process by the target nucleus. This assumption is considered to be valid if $3q \geqq Z_2$ (q: charge of an incident particle in units of electronic charge, Z_2: the atomic number of the target). With this consideration we have made calculation only for H and He targets.

In order to extend our research to the targets other than H and He, we should take into account the consideration of electron-electron collisions in the process. In this case, owing to the opposite sign of interaction potentials of electron-nucleus terms compared with that of electron-electron terms, the cross section may be much influenced by the interference terms between the above two interactions. Therefore, we can not make use of classical approximations such as BEA which includes no interference effects.

Here we use the Born approximation for the processes. In the heavy particle collisions such as the present ion-atom systems, the Born approximation gives a reasonable results[2] in the velocity region above 0.3 times of the orbital electron velocity to be ionized.

Because of the large reduced mass of the colliding system, the trajectory of an incident particle can hardly be changed by collisions in the velocity region.

Let us consider the reaction in which atom B is excited or ionized from an initial state (n', l') to a final state (n'', l''), and at the same time ion A is ionized from an initial state (n, l) to a continuum state κ ejecting one electron (n, n', n'': principal quantum numbers and l, l', l'': azimuthal quantum numbers).

The cross section based on the Born approximation can be written as[3]

$$\sigma(nl \rightarrow \kappa\ ;\ n'l' \rightarrow n''l'') = \frac{M^2}{2\pi\hbar^4 K_i^2} \int_{K_{min}}^{K_{max}} |N(nl \rightarrow \kappa\ ;\ n'l' \rightarrow n''l'')|^2 K dK \qquad (2)$$

where M is the reduced mass, $M = M_A M_B / (M_A + M_B)$; M_A and M_B are the mass of ion A and target atom B, respectively, the momentum transfer is $\boldsymbol{K} = \boldsymbol{K}_f - \boldsymbol{K}_i$, $\boldsymbol{K}_i = M\boldsymbol{v}_i/\hbar$, $\boldsymbol{K}_f = M\boldsymbol{v}_f/\hbar$; $\boldsymbol{v}_i$ and $\boldsymbol{v}_f$ are the initial and final velocities of relative motion, respectively and

$$N = \int\int\int \Psi^*(\boldsymbol{r}_A|\, nl)\Psi^*(\boldsymbol{r}_B|\, n'l')\, V(\boldsymbol{R}, \boldsymbol{r}_A, \boldsymbol{r}_B) \times e^{i\boldsymbol{R}\cdot\boldsymbol{K}} \Psi(\boldsymbol{r}_A|\, \kappa)\Psi(\boldsymbol{r}_B|\, n''l'')\, d\boldsymbol{r}_A d\boldsymbol{r}_B d\boldsymbol{R} \qquad (3)$$

$\Psi(\boldsymbol{r}_A|\, nl)$ and $\Psi(\boldsymbol{r}_A|\, \kappa)$ are wave functions of an electron bound to nucleus A, whereas $\Psi(\boldsymbol{r}_B|\, n'l')$ and $\Psi(\boldsymbol{r}_B|\, n''l'')$ are wave functions of an electron bound to nucleus B.

The interaction potential with the relative position vector $\boldsymbol{R}$ between the particles is given by

† Collaborated work of Atomic Processes Laboratory, The Institute of Physical and Chemical Research (RIKEN) with Theoretical Physics Group in Department of Modern Physics, University of Science and Technology of China.

* Department of Modern Physics, University of Science and Technology of China.

$$V(\boldsymbol{R}, \boldsymbol{r}_A, \boldsymbol{r}_B)=e^2\left[\frac{Z_A Z_B}{R^2}-\frac{Z_A}{|\boldsymbol{R}+\boldsymbol{r}_B|}-\frac{Z_B}{|\boldsymbol{R}-\boldsymbol{r}_A|}+\frac{1}{|\boldsymbol{R}+\boldsymbol{r}_B-\boldsymbol{r}_A|}\right] \quad (4)$$

Substitution of Eqn. (4) into Eqn. (3) gives

$$N(nl\to\kappa\ ;\ n'l'\to n''l'')=\frac{4\pi e^2 a_0^2}{t^2}Z_B \times\left[-\delta_{n'l',\,n''l''}+T(n'l'\to n''l'')\right]T(nl\to\kappa) \quad (5)$$

where

$$T(p\to q)=\int e^{it\cdot r}\Psi^*(\boldsymbol{r}|p)\Psi(\boldsymbol{r}|q)d\boldsymbol{r} \quad (6)$$

where $\boldsymbol{r}$ in atomic units and $t=\boldsymbol{K}a_0$ (a_0: Bohr radius).

Therefore, Eqn. (2) has the form

$$\sigma(nl\to\kappa\ ;\ n'l'\to n''l'')=\left[\frac{8Z_B^2}{s^2}\int_{t_{min}}^{t_{max}}|-\delta_{n'l',\,n''l''}+T(n'l'\to n''l'')|^2\,|T(nl\to\kappa)|^2\times t^{-3}dt\right]\pi a_0^2 \quad (7)$$

where $s^2=(1/2)mv_i^2/I_H$, $I_H=(1/2)me^4/\hbar^2$ is the ionization potential of hydrogen and m the electron mass.

Using the energy transfer $\Delta E=(\hbar^2K_i^2/2M-\hbar^2K_f^2/2M)/I_H$, we can obtain

$$t_{min}=K_{min}a_0=(K_i-K_f)a_0 \simeq\frac{\Delta E}{2s}\left(1+\frac{m\Delta E}{4Ms^2}\right) \quad (8)$$

and

$$t_{max}=K_{max}a_0=(K_i+K_f)a_0 \simeq\frac{2Ms}{m}\left[1-\frac{m}{4Ms^2}\Delta E\left\{1+\frac{m\Delta E}{4Ms^2}\right\}\right] \quad (9)$$

The initial wave functions for A and B having the number of electrons ρ_A for A and ρ_B for B in their electron orbits can be written as follows:[4]

$$\Psi_i^A=\Psi_i^A(l^{\rho_A}SL)=\sum_{S''L''}(l^{\rho_A}SL\{|l^{\rho_A-1}(S''L'')lSL) \quad (10)$$

and

$$\Psi_i^B=\Psi_i^B(l^{\rho_B}SL)=\sum_{S''L''}(l^{\rho_B}SL\{|l^{\rho_B-1}(S''L'')lSL) \quad (11)$$

where L and S are the total orbital angular momentum of electrons and the total spin angular momentum, respectively, and $(l^\rho SL\{|l^{\rho-1}\times(S''L'')lSL)$ denotes a fractional parentage coefficient. In Eqns. (10) and (11), $S''L''$ corresponds to the quantum numbers for the final possible configurations.

For the final state of the system $(A^{(q+1)+}+e)$ we use an antisymmetric wave function as[4]

$$\Psi_f^A(\boldsymbol{x}_1,\boldsymbol{x}_2,\cdots,\boldsymbol{x}_N)=N^{-\frac{1}{2}}\sum_{i=1}^{N}(-1)^{N-i}\Psi_f^A(\boldsymbol{x}_1,\boldsymbol{x}_2,\cdots,\boldsymbol{x}_{i-1},\boldsymbol{x}_{i+1},\cdots,\boldsymbol{x}_N)\Psi(\boldsymbol{k},\boldsymbol{x}_i) \quad (12)$$

The wave function $\Psi(\boldsymbol{k},\boldsymbol{x})$ describes an ejected electron:

$$\Psi(\boldsymbol{k},\boldsymbol{x})=\Psi(\boldsymbol{k},\boldsymbol{r})\delta(\sigma|m_s) \quad (13)$$

where $\delta(\sigma|m_s)$ is a normalized spin function. The ejected one-electron wave function $\Psi(\boldsymbol{k},\boldsymbol{r})$is a Coulomb wave function which describes the free electron moving in the field of ion $A^{(q+1)+}$:

$$\Psi(\boldsymbol{k},\boldsymbol{r})=e^{-\frac{1}{2}\pi\eta}\Gamma(1+i\eta)e^{i\boldsymbol{k}\cdot\boldsymbol{r}}\times{}_1F_1\{-i\eta,\ 1\ ;\ i(kr-\boldsymbol{k}\cdot\boldsymbol{r})\} \quad (14)$$

where

$$\eta=\frac{mZ_AZ_Be^2}{\hbar^2k} \quad (15)$$

Calculations are in progress for excited-state wave functions and continuum wave functions aiming at obtaining the electron stripping cross sections for the various kinds of projectile ions and traget atoms.

References

1) S. Karashima, T. Watanabe, Y. Awaya, and Y. Liu: *Nucl. Instrum. Methods A*, **240**, 505 (1985).
2) T. Watanabe: *J. Phys. B*, **18**, L111 (1985).
3) D. R. Bates and G. Griffing: *Proc. Phys. Soc. A*, **66**, 961 (1953); *A*, **67**, 663 (1954); *A*, **68**, 90 (1955).
4) G. Peach: *J. Phys. B*, **1**, 1088 (1968); *B*, **3**, 328 (1970).

RIKEN Accel. Progr. Rep. 19 (1985)

III-2-2. $(\mu^+\mu^-)$ Formation Cross Section for Collision of μ^+ with (μ^-p) : Total and Differential Cross Sections†

Q. Ma,* X. Zhang,* Y. Liu,* and T. Watanabe

Under the collaboration research projects with the theoretical group in University of Science and Technology of China, the calculation for $\mu^+ + (\mu^- p) \rightarrow (\mu^+\mu^-) + p$ was extended. We have already made calculations for the process only for the ground initial state $(\mu^- p)$ and ground final state $(\mu^-\mu^+)$ by the Classical Trajectory Monte Carlo (CTMC) approximation as well as by the quantum-mechanical first Born approximation (FBA) and the distorted-wave Born approximation (DWBA).[1)-4)] The calculation using CTMC for the ground to the states n (principal quantum number)$=2$ was also made. As a continuation of this serial research, the total cross section and the differential cross section for the process including excited states before and after collision were obtained by using FBA. The differential cross section for the process from the ground to the ground state was also made.

The method used in the present study was essentially the same as in previous ones.[3),4)] Introducing the coordinate system shown in Fig. 1, we can write the total Hamiltonian in the initial coordinate system $\boldsymbol{R}$ and $\boldsymbol{r}$ or in the final coordinate system $\boldsymbol{R}'$ and $\boldsymbol{r}'$. Here $\boldsymbol{R}$ and $\boldsymbol{R}'$ mean the coordinates of relative motion and $\boldsymbol{r}$ and $\boldsymbol{r}'$ mean the coordinates of inner motion. The large amount of change in the reduced masses of the bound systems before and after collision is one of the characteristic features of the present problem. The reduced masses of the system in the initial state frame, ν, for the inner motion and μ for the relative motion are given by

$$\nu = \frac{m_\mu m_p}{m_\mu + m_p}, \quad \mu = \frac{m_\mu (m_p + m_\mu)}{m_p + 2m_\mu} \tag{1}$$

and those in the final state frame are given by

$$\nu' = \frac{m_\mu}{2}, \quad \mu' = \frac{2m_p m_\mu}{m_p + 2m_\mu} \tag{2}$$

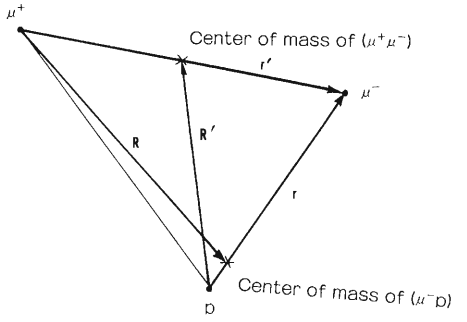

Fig. 1. Coordinate system of colliding particles. $\boldsymbol{R}$ and $\boldsymbol{r}$ are the position vectors of the relative motion and inner motion before collision and $\boldsymbol{R}'$ and $\boldsymbol{r}'$ are those after collision.

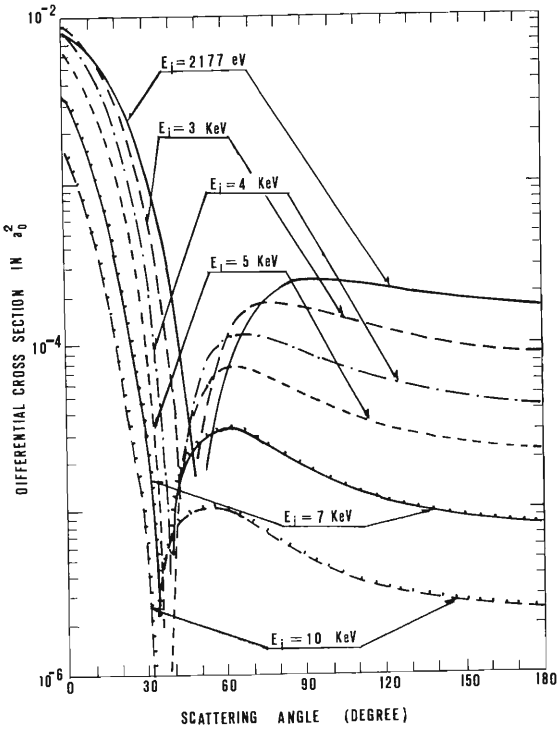

Fig. 2. Differential cross section for $\mu^+ + (\mu^- p)_{1s} \rightarrow (\mu^-\mu^+)_{1s} + p$ for impact energies from 2,176.81 eV to 10^4 eV in the center-of-mass system.

where m_p and m_μ are the masses of p and μ, respectively.

The first Born scattering amplitude in the

† Collaborated work with Theoretical Physics Group in Department of Modern Physics, University of Science and Technology of China.

* Department of Modern Physics, University of Science and Technology of China.

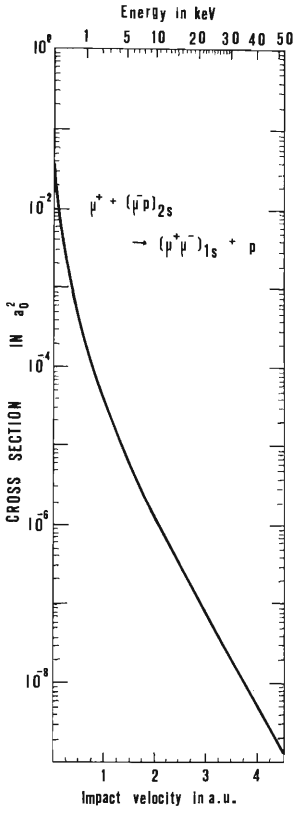

Fig. 3. Total cross section for $\mu^+ + (\mu^- p)_{2s} \rightarrow (\mu^-\mu^+)_{1s} + p$ as a function of relative velocity v.

prior form is written as

$$f^{\mathrm{FBA}}(\theta) = -\frac{\mu'}{2\pi\hbar^2}\int d\boldsymbol{R}' \int d\boldsymbol{r}' \exp(-i\boldsymbol{k}_f\cdot\boldsymbol{R}') \Psi_f(\boldsymbol{r}')H'_i \exp(i\boldsymbol{k}_i\cdot\boldsymbol{R})\Psi_i(\boldsymbol{r}) \quad (3)$$

where H'_i is the (inter-atomic) interaction Hamiltonian in the initial form, *i.e.*,

$$H'_i = \frac{-1}{r_{+-}} + \frac{1}{r_{p+}} \quad (4)$$

where r_{+-} and r_{p+} and the distance between μ^+ and μ^- and that between μ^+ and p, respectively, and $\boldsymbol{k}_i$ and $\boldsymbol{k}_f$ are the wave vectors of relative motion in the initial and the final states. The differential cross sections in FBA are given by

$$\frac{d\sigma}{d\Omega} = \frac{k_f}{2\eta k_i}|f^{\mathrm{FBA}}(\theta)|^2, \quad \eta = \frac{m_p}{m_p + m_\mu}. \quad (5)$$

The total cross section is given by

$$\sigma = \frac{k_f}{2\eta k_i}\int |f^{\mathrm{FBA}}(\theta)|^2 d\Omega \quad (6)$$

The only difference in the formula from that in the previous one[3),4)] appears in the wave function of the initial and final states, Ψ_i and Ψ_f in Eqn. (3).

The present study concerned with the processes from 1s to 1s for the differential cross section (DCS), from 1s to 2s, 2p for the DCS and the total cross section (TCS), and from 2s to 1s for DCS and TCS. Detailed description of the reduction of the practical formulas of scattering amplitude and the discussion of the physical meaning of the calculated results will be given elsewhere.

References

1) A. Ohsaki, T. Watanabe, K. Nakanishi, and K. Iguchi: *RIKEN Accel. Progr. Rep.*, **18**, 41 (1985).
2) A. Ohsaki, T. Watanabe, K. Nakanishi, and K. Iguchi: *Phys. Rev. A*, **32**, 2640 (1985).
3) Q. Ma, X. Zhang, Z. Liu, Y. Liu, and T. Watanabe: *RIKEN Accel. Progr. Rep.*, **18**, 45 (1985).
4) Q. Ma, X. Zhang, Z. Liu, Y. Liu, and T. Watanabe: *Phys. Rev. A*, **32**, 2645 (1985).

RIKEN Accel. Progr. Rep. 19 (1985)

III-2-3. Continuous Energy State Model for Charge Transfer in Collisions of Fully Stripped Ions with Hydrogen Atoms

F. Koike

An investigation has been made for the charge transfer processes in collisions of fully stripped ions with hydrogen atoms:

$$A^{Z+}+H(1s) \rightarrow A^{(Z-1)+}(q)+H^{+} \qquad (1)$$

where A represents an atom, Z represents its atomic number, and q represents a set of atomic quantum numbers. If Z is high, the initial H 1s state couples with a number of the states of $A^{(Z-1)+}$, and in many cases, the transferred electron is actually distributed into the various q-states. Consequently, we must solve an exceedingly large set of coupled-channel equations if we represent the electronic state in terms of the channel-wavefunctions.

In the present report, a decoupling technique is proposed employing a continuous energy state model for the final electronic states. The coupled-channel equations are reduced to a number of smaller sets of inhomogeneous coupled-channel equations that can be solved independently of each other. As for the approach that could fall in the same category as the present one, we can point out a work of Presnyakov *et al.*[1] In the present work, a number of the restrictions imposed on the application of their theory has been removed, and the rotational coupling between the final electronic states has been taken into account, which they have neglected completely. The outline of the present formalism is as follows. The probability amplitude for finding the system in the initial hydrogenic state a_0 is given by the overlap of the initial state wavefunction ψ_0 with the total wavefunction Ψ, *i.e.*, $a_0 = <\psi_0 \mid \Psi>$. If Ψ is expanded in terms of the final state wavefunctions ψ_q as $\Psi \sum_q \hat{a}_q \psi_q$ and also if Ψ satisfies the semiclassical time-dependent Schrödinger equation, *i.e.*, $H\Psi = i(\partial/\partial t)\Psi$, we can derive the following coupled equation by differentiating the present overlap integral with respect to the time t. We have

$$\dot{a}_0 = -i \sum_q <\psi_q| H - i\partial/\partial t| \psi_0> {}^{*}a_q' \qquad (2)$$

It can be shown[2] that we can solve Eqn. (2) with respect to a_0 to the lowest order without any knowledge about a_q' if we employ the continuous energy state model for the final states. We obtain

$$a_0(t) = \exp\left[-i\int_{-\infty}^{t} E_* \, dt'\right] \qquad (3)$$

where E_* is the resonance energy that may be a complex number, and it is given by the pole of the Green's function of the space spanned by the initial H 1s state.

The final state component is given by $\Psi - a_0\psi_0$, and this may be expanded in terms of ψ_q as

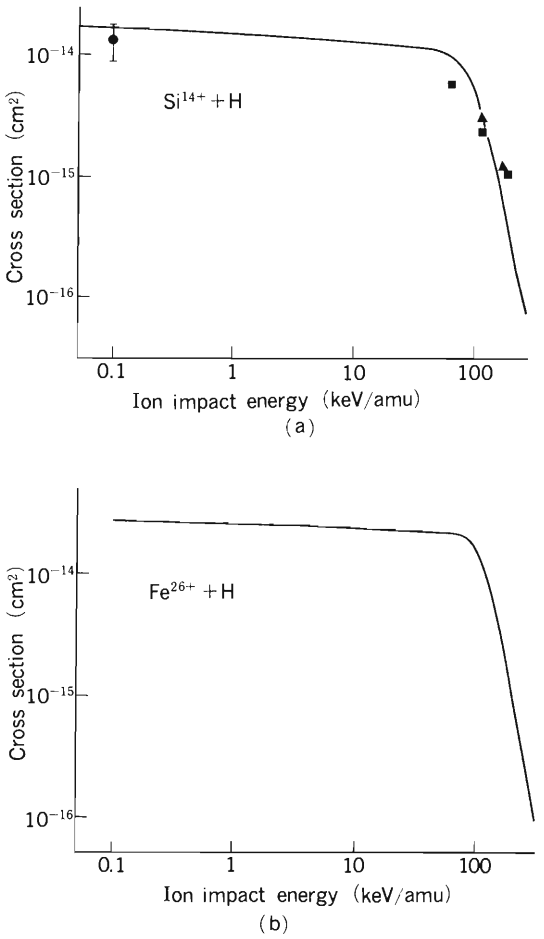

Fig. 1. (a) Total charge transfer cross sections for $Si^{14+}+H$ collisions. Solid line: present theory. Symbols: experimental results for the partially stripped ions: ⊥: Fe^{14+} by Phaneuf *et al.*,[3] ■: Fe^{14+} by Meyer *et al.*,[4] ▲: Mo^{14+} by Meyer *et al.*[4] (b) Total charge transfer cross sections for $Fe^{26+}+H$ collisions. Present theoretical results.

$\Psi - a_0\psi_0 = \sum_q a_q\psi_q$. Then we have the following coupled-channel equations for a_q, which are solved numerically. That is

$$a_q = -i<\psi_0 \mid H - i\partial/\partial t \mid \psi_q>^* a_0 - i\sum_{q'}<\psi_{q'} \mid H - i\partial/\partial t \mid \psi_q>^* a_{q'} \quad (4)$$

Because a_0 is given by Eqn. (3), Eqn. (4) as a whole represents a set of coupled equations for only a_q; Eqn. (4) is partially decoupled naturally according to the symmetry of ψ_q.

Even after the present decoupling, the number of the coupled-channels for the individual subset of equations is still very large if Z is high. The use of a super computer (HITAC S810/20) has been tried in order to facilitate the large scale numerical calculations. Some of the typical results are illustrated in the following. In Fig. 1(a) are shown the total charge transfer cross sections for $Si^{14+}+H$ with the available experimental data for partially stripped ions. The agreement between the theory and experiment at $Z=14$ suggests the validity of the present method for higher-Z ions, because the present method is based on a high-Z approximation. The result for $Fe^{26+}+H$ is illustrated in Fig. 1(b) as an example of the high-Z system. In Fig. 2 the cross sections for charge transfer into the states with specified principal quantum numbers are given for $Si^{14+}+H$ together with other theoretical results.

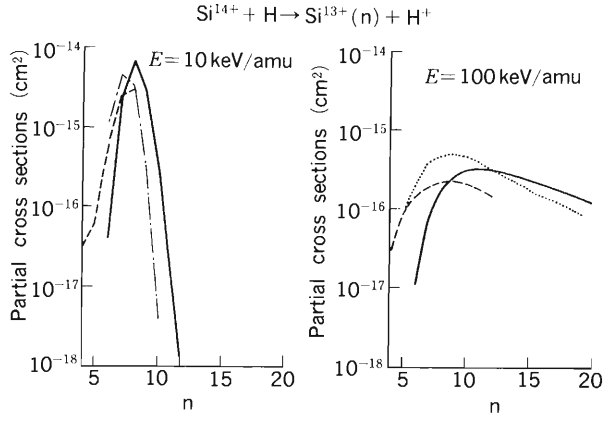

Fig. 2. The principal quantum number n partial cross sections for the charge transfer in $Si^{14+}+H$ collisions. Solid lines: present theory. Broken lines: unitarized distorted wave approximation.[5] Dotted line: classical trajectory Monte Carlo calculation.[6] Dot-dashed line: multi-channel Landau-Zener model calculation with modification in which the effect of the rotational coupling is included.[7]

References

1) L. P. Presnyakov, D. B. Uskov, and R. K. Janev: *Phys. Lett. A*, **84**, 243 (1981).
2) F. Koike: XIII ICPEAC Book of Abstracts, Berlin, p.405 (1983).
3) R. A. Phaneuf, I. Alvarez, F. W. Meyer, and D. H. Crandall: *Phys. Rev. A*, **26**, 1892 (1982).
4) F. W. Meyer, R. A. Phaneuf, H. J. Kim, P. Hvelplund, and P. H. Stelson: *Phys. Rev. A*, **19**, 515 (1979).
5) H. Ryufuku and T. Watanabe: *Phys. Rev. A*, **20**, 1828 (1979).
6) R. E. Olson: *Phys.Rev. A*, **24**, 1726 (1981).
7) R. K. Janev and B. H. Bransden: IAEA Report, INDC (NDS)-135/GA (1982).

RIKEN Accel. Progr. Rep. 19 (1985)

III-2-4. Effect of Minima in Generalized Oscillator Strengths on Integral Cross Sections for Excitation of Atoms

M. Iwai, I. Shimamura, T. Watanabe, and Y. Awaya

The first Born approximation is valid for excitation of atoms by electrons or ions with sufficiently high velocities. The differential cross section in this approximation is expressible as the product of a simple factor and a quantity called the generalized oscillator strength (GOS), which is a generalization of the optical oscillator strength. The GOS is defined as a function of the momentum K transferred from the incident particle to the target atom in the collision. The existence and the general significance of minima in GOS for many atomic and molecular transitions are discussed in the literature.[1)-4)] Effects of these minima on the integral cross sections have also been investigated especially for inner-shell ionization by heavy particles.[3),4)] These analyses have shown frequent appearance of shoulders in the impact energy dependence of the integral ionization cross sections.

In the present report we will show appearance of conspicuous minima, rather than shoulders, in the integral cross sections for some discrete excitation processes due to minima in the corresponding GOS. General conditions for appearance of minima in the integral cross section will be briefly discussed.

The integral cross section for excitation of the target state from $|0>$ to $|n>$ by the projectile with a charge z is given, in the first Born approximation, by[1)]

$$\sigma_{0n}=\left(\frac{2\pi z^2}{E_{0n}}\right)v^{-2}\int_{\ln(K_{\min}^2)}^{\ln(K_{\max}^2)} F_{0n}(K)\,d[\ln(K^2)] \tag{1}$$

where v is the relative velocity and E_{0n} denotes the excitation energy. Here and in the following we use atomic units. $K_{\max}$ and $K_{\min}$ are expressed in terms of the incident wave vector $\boldsymbol{k}_0$ and the scattered one $\boldsymbol{k}_n$ as

$$K_{\max}=k_0+k_n \tag{2}$$

$$K_{\min}=k_0-k_n \tag{3}$$

The generalized oscillator strength $F_{0n}(K)$ is defined by[1)]

$$F_{0n}(K)=(2E_{0n}/K^2)\,|<n|\sum_j \exp(i\boldsymbol{K}\cdot\boldsymbol{r}_j)|0>|^2 \tag{4}$$

with $\boldsymbol{K}=\boldsymbol{k}_0-\boldsymbol{k}_n$, where $\boldsymbol{r}_j$ is the position vector of the jth electron in the target. In Eqn. (4) the average over the magnetic quantum number of the initial state and the summation over that of the final state are implicitly assumed.

As a first example the 2s→3p excitation of Cu^{25+} and Cu^{19+} ions by electron impact, proton impact, and C^{6+} ion impact was studied in the plane-wave Born approximation. Information on this transition in the carbon-copper collisions is useful in analyzing the Cu K X-ray data taken by Awaya *et al.*[5)] for Cu ions incident on C and for C ions incident on Cu.

We calculated the ground-state wave functions of the four-electron target ions in the Hartree-Fock approximation employing Slater-type orbitals. For the excited states we construct the wave functions with proper LS symmetry (^1P in this case) using the virtual orbitals generated by the Hartree-Fock potential of the ground state.

The GOS for the $2s^2{}^1S\rightarrow 2s3p\,{}^1P$ transition in Cu^{25+} is shown in Fig. 1. For a hydrogen-like atom with an effective charge Z_{eff} the GOS for this transition has zero minima at $K=(\sqrt{5}/6)Z_{\text{eff}}$ and $K=(5\sqrt{15}/18)\,Z_{\text{eff}}$.[2)] If we choose a value 26 for Z_{eff} for Cu^{25+} following Slater's rule, the first minimum occurs at $K=9.7$ in excellent agreement with the position of the minimum in the present Hartree-Fock result. The magnitude of

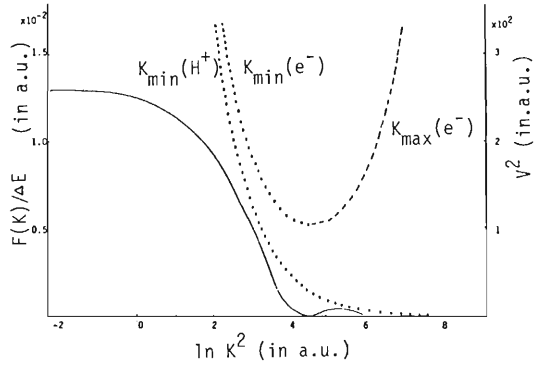

Fig. 1. Generalized oscillator strength devided by the excitation energy for 2s→3p excitation of Cu^{25+}. Plots of $\ln(K_{\min}^2)$ and $\ln(K_{\max}^2)$ against impact velocity v^2 are also included.

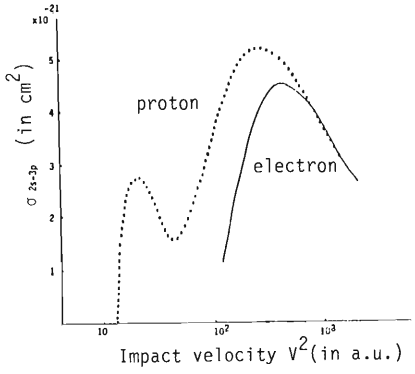

Fig. 2. Integral cross sections for 2s→3p excitation of Cu^{25+} by proton and electron impact.

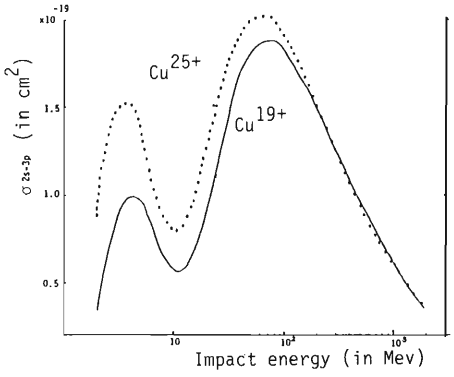

Fig. 3. Integral cross sections for 2s→3p excitation of Cu^{25+} and Cu^{19+} by the C^{6+} ion.

the GOS in the hydrogen-like model also agrees fairly well with the Hartree-Fock result. This indicates that the hydrogen-like model is valid for the present systems owing to the large effective charges that the active electron feels.

Figure 1 also includes plots of $\ln(K_{max}{}^2)$ and $\ln(K_{min}{}^2)$ against v^2 for both electron impact and proton impact. One readily finds from these plots the interval of integration in Eqn. (1) contributing to the integral cross section. For electron impact both K_{min} and K_{max} at the threshold energy are close to the position of the minimum in the GOS. K_{min} decreases (and K_{max} increases) with the increase of v^2. Therefore, the integral cross section increases monotonically, and no minimum occurs (Fig. 2a). For proton impact, however, the situation is totally different. We may actually consider K_{max} to be infinity in this case, and only the position of K_{min} decides the integral cross section. As K_{min} passes a zero of $F_{0n}(K)$ with the increase of v^2, the integral in Eqn. (1) remains nearly constant, and the integral cross section decreases due to the factor $1/v^2$. As v^2 increases further, K_{min} decreases in the region where $F_{0n}(K)$ increases rapidly, and the integral cross section also increases rapidly. This gives rise to the conspicuous minimum in the integral cross section for proton impact as shown in Fig. 2. The K_{min}-to-v^2 and the K_{max}-to-v^2 curves for C^{6+} impact are very similar to those for proton impact. Therefore, a conspicuous minimum occurs also for C^{6+} impact. The integral cross sections for the 2s→3p excitation of Cu^{25+} and Cu^{19+} by the C^{6+} ion are shown in Fig. 3.

Next we consider a systematic method of analyzing the impact-energy dependence of the integral cross section. For simplicity let us focus on heavy-particle impact in which $F_{0n}(K)$ is negligible near $K=K_{max}$ and for $K>K_{max}$. Direct

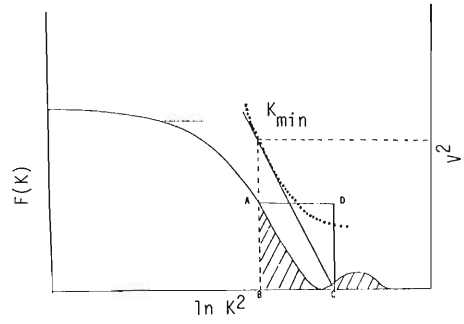

Fig. 4. Graphical analysis of extrema in the integral cross section.

differentiation of Eqn.(1) with respect to v^2 yields

$$\frac{d\sigma_{0n}}{dv^2}=-v^{-2}\left(\sigma_{0n}-\left(\frac{2\pi z^2}{E_{0n}}\right)F_{0n}(K_{min})\times\left|\frac{d[\ln(K_{min}{}^2)]}{d(v^2)}\right|\right) \quad (5)$$

because $F_{0n}(K_{max})\simeq 0$. Equation (5) clearly indicates that σ_{0n} should be decreasing with increasing v^2 when $F_{0n}(K_{min})$ is nearly zero. One finds from Eqn. (5) that extrema of $\sigma_{0n}(v^2)$ occur when the following equality holds:

$$\sigma_{0n}=(2\pi z^2/v^2E_{0n})S' \quad (6)$$

where the quantity S' is defined by

$$S'=F_{0n}(K_{min})\left(v^2\left|\frac{d[\ln(K_{min}{}^2)]}{d(v^2)}\right|\right) \quad (7)$$

and is equal to the area of the rectangle ABCD shown in Fig. 4. Because the integral cross section, σ_{0n}, is the product of $(2\pi z^2/v^2E_{0n})$ and the shaded area (referred to as S) in Fig. 4, Eqn. (6) amounts to an equality $S=S'$. At those v^2 where $S>S'$ ($S<S'$), the right-hand side of Eqn. (5) is negative (positive) and $\sigma_{0n}(v^2)$ is decreasing (increasing). This affords a systematic method of

analyzing the v^2 dependence of σ_{0n} and of investigating the general conditions for the appearance of minima in σ_{0n}.

The positions of minima in the GOS and the magnitude of the GOS are appreciably affected by the wave functions employed; calculations based on more sophisticated wave functions are now in progress.

References

1) M. Inokuti: *Rev. Mod. Phys.*, **43**, 297 (1971); M. Inokuti, Y. Itikawa, and J. E. Turner: *Rev. Mod. Phys.*, **50**, 23 (1978).
2) I. Shimamura: *J. Phys. Soc. Jpn.*, **30**, 824 (1971).
3) M. Matsuzawa, K. Omidvar, and M. Inokuti: *J. Phys. B; Atom. Molec. Phys.*, **9**, 2173 (1976).
4) S. T. Manson and A. Msezane: *J. Phys. B: Atom. Molec. Phys.*, **8**, L5 (1975).
5) Y. Awaya, T. Kambara, M. Kase, H. Shibata, H. Kumagai, T. Mizogawa, Y. Kanai, and K. Shima: p. 70 in this report.

RIKEN Accel. Progr. Rep. 19 (1985)

III-2-5. Theory of Radiative Electron Capture: Relativistic Treatment and Gauge Invariance

K. Hino and T. Watanabe

At present, no theory on the radiative electron captue (REC) process satisfies the following conditions completely: (i) The cross section of REC should be independent of the way to choose the frame of reference, that is, the c.m. frame or the lab. frame: (ii) The charged current of the whole system should be conserved. In other words, the REC scattering matrix must be gauge invariant. The first condition fulfils the relativistic formulation and removes the spurious radiation. Moreover, these two conditions are mutually connected to some extent as is shown below. We use the natural units ($\hbar=c=1$) throughout this report, and we suppose that a particle always has a half-spin unless otherwise stated.

Firstly, some preliminaries for the covariant treatment are introduced. The interaction Lagrangian density of fermions and photons, L_{int}, is given by

$$L_{\text{int}}=j_\mu A_\mu+J_\mu A_\mu \tag{1}$$

where j_μ is the electromagnetic current of a fermion, given by $iZ\bar{\psi}\ \gamma_\mu\psi$, Z the charge of the fermion, and J_μ the external c-number source introduced as a parameter. By the use of Eqn. (1), S-matrix, $<0\mid U(\infty,-\infty)\mid 0>$, is given by

$$<0\mid U(\infty,-\infty)\mid 0> =<0\mid T\ \exp(i\int d^4xL_{\text{int}}(x))\mid 0> \tag{2}$$

and the Schwinger's functional derivative[1] with respect to J_μ is defined as

$$\delta U[J_\mu(y)]/\delta J_\mu(x)=\lim_{\epsilon\to 0}\{U[J_\mu(y+\epsilon\delta^{(4)}(y-x))]-U[J_\mu(y)]\}/\epsilon \tag{3}$$

Equation (3) can lead us to the following convenient relation:

$$-i\cdot\delta T[U,a,b,\cdots]/\delta J_\mu(x)=T[U,A_\mu(x),a,b,\cdots] \tag{4}$$

where a and b stand for field operators.

Corresponding to the (non-relativistic) Weinberg equation,[2] we establish a covariant equation (the relativistic Weinberg equation) for the three-boby covariant propagator K as:

$$K=H+K_0\sum_{N=A,B,C} I_N K_N I^N K \tag{5}$$

where A, B, and C are the channels of a three-body system for a+(b+c), b+(c+a), and, c+(a+b), respectively, and K_N is the three-body propagator where the particle, n, behaves as a spectator, and K_0 the free propagator. Hereafter, a projectile ion, a target nucleus, and an active electron will be labeled with a, b, and c, respectively. H is the inhomogeneous propagator defined as

$$H=K_0(1+\sum_M I_M K_M) \tag{6}$$

and K_0, K_N, and I_N are represented by:

$$K_0=\prod_{n=a,b,c} S'_{F,n} \tag{7}$$

$$K_A=S'_{F,a}G_{bc} \tag{8}$$

$$I_A=i\mathcal{D}_a V_{bc}=i\mathcal{D}_a V_a \tag{9}$$

and so on, where $S'_{F,a}$ indicates the (one-boby) Feynman propagator of fermion, a, and G_{bc} represents the two-body propagator of fermions, b and c, which follows the two-body Bethe-Salpeter (B-S) equation.[3] V_{bc} and V_a stand for the interaction between the particles, b and c. $\mathcal{D}_n(x-x')$ is defined as:

$$\mathcal{D}_n(x-x')=(\gamma^{(n)}\partial_x+m_n)\delta^{(4)}(x-x')+i\Sigma_n^*(x-x') \tag{10}$$

where Σ_n^* is the self-energy of fermion, n, and $\gamma^{(n)}$ is the gamma-matrix of the particle, n. Equation (5) can be symbolically rewritten as:

$$K=(1-F)^{-1}H \tag{11}$$

where F is the kernel of the relativistic Weinberg equation.

Now the three-body REC propagator K_μ is defined by the use of Schwinger's functional derivative method, Eqn. (4), as

$$K_\mu=<0\mid U\mid 0>^{-1}\cdot i\delta[<0\mid U\mid 0>K]/\delta J_\mu \tag{12}$$

The fundamental Eqn. (5) can give us an explicit formal solution of K_μ by using Eqn. (12) as:

$$K_\mu=(1-F)^{-1}(H_\mu+F_\mu K) \tag{13}$$

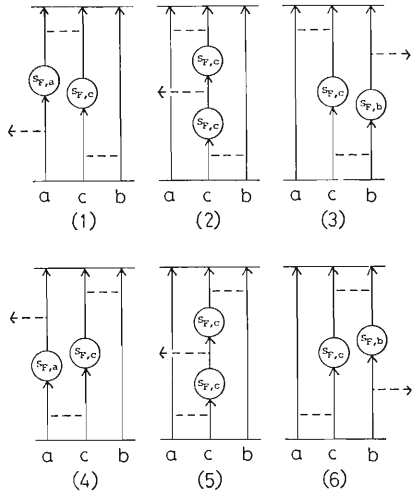

Fig. 1. Feynman diagrams of the relativistic REC process. Longitudinal real lines stand for fermions, broken lines for photons and transversal real lines for three-body B-S amplitudes, respectively.

where

$$P_\mu = <0 \mid U \mid 0>^{-1} \cdot i\delta[<0 \mid U \mid 0>P]/\delta J_\mu \quad (P=H,\ F) \tag{14}$$

The S-matrix of REC can be easily obtained from Eqn. (13) by using the procedure similar to that derived by Nishijima.[4] The final form of REC S-matrix can be written as:

$$S_{\mathrm{fi}} = <\bar{\psi}'_{\mathrm{B},\mu} \mid X^{-1} \hat{\mathcal{H}}_\mu \mid \bar{\psi}_{\mathrm{A}}> \tag{15}$$

where

$$\hat{\mathcal{H}}_\mu = \sum_{\mathrm{N}} [\hat{Y}_\mu I_{\mathrm{N}} K_{\mathrm{N}} I^{\mathrm{N}} + \hat{I}_{\mathrm{N},\mu} K_{\mathrm{N}} I^{\mathrm{N}} + I_{\mathrm{N}} K_{\mathrm{N}} \hat{W}_{\mathrm{N},\mu} I^{\mathrm{N}} + I_{\mathrm{N}} K_{\mathrm{N}} \hat{I}^{\mathrm{N}}_\mu] \tag{16}$$

$$\hat{Y}_\mu = -\sum_{\mathrm{n=a,b,c}} Z_{\mathrm{n}} \Gamma^{(\mathrm{n})}_\mu S'_{\mathrm{F,n}} \tag{17}$$

$$\hat{W}_{\mathrm{N},\mu} = \hat{Y}_\mu + (\hat{I}_{\mathrm{n},\mu} - \sum_{\mathrm{l}} \delta_{\mathrm{nl}} Z_{\mathrm{l}} \Gamma^{(\mathrm{l})}_\mu S'_{\mathrm{F,l}} I_{\mathrm{n}}) G_{\mathrm{n}} \tag{18}$$

$$I_{\mathrm{n},\nu} = i \cdot \delta I_{\mathrm{n}} / \delta J_\nu = \hat{I}_{\mathrm{n},\mu} D'_{\mathrm{F},\mu\nu} \tag{19}$$

$$X = 1 + \sum_{\mathrm{N}} I_{\mathrm{N}} K_{\mathrm{N}} \tag{20}$$

where Z_{n} is the electric charge of the particle, n. $\psi_{\mathrm{A}'}$ the three-body B-S amplitude for the channel A, should be given by the formula corresponding to Eqn. (11): $\psi_{\mathrm{A}} = (1-F)^{-1}\phi_{\mathrm{A}'}$ where ϕ_{A} represents the incident wave. $\bar{\psi}'_{\mathrm{B},\mu}$ is connected with ψ_{B} by the relation that $\bar{\psi}_{\mathrm{B}} = \psi^{+}{}_{\mathrm{B}} \gamma^{(\mathrm{a})}{}_4 \gamma^{(\mathrm{b})}{}_4 \gamma^{(\mathrm{c})}{}_{4'}$ multiplied by the photon wave function with the poralization vector e_μ. And $\Gamma^{(\mathrm{n})}_\mu$ is the vertex function of the n-th particle.

Next, we take the gauge invariance of the REC S-matrix into consideraton. Since the scattering matrix must always keep the gauge invariance, a matrix $G_{\mathrm{fi},\mu}$ defined as $S_{\mathrm{fi}} = e_\mu G_{\mathrm{fi},\mu}$ should satisfy

$$k_\mu G_{\mathrm{fi},\mu} = 0 \tag{21}$$

where k_μ is the energy-momentum vector of the emitted photon. To keep the gauge invariance, we generally need only a set of Feynman diagrams with the same power of coupling constants. The generalized Ward-Takahashi relation for the three-body problem is useful to pick up such diagrams. This powerful relation reads:

$$\begin{aligned}\Box_x \partial^x_\mu T^*[A_\mu(x),\cdots] &= \partial^x_\mu T^*[(i\cdot\delta/\delta A_\mu(x)),\cdots] \\ &+ \sum_j Z_j \sum_{\sigma=1}^{4} T^*[(\psi_{j\sigma}(x)\cdot\delta/\delta\psi_{j\sigma}(x) \\ &- \bar{\psi}_{j\sigma}(x)\cdot\delta/\delta\bar{\psi}_{j\sigma}(x)),\cdots]\end{aligned} \tag{22}$$

where $\psi_{j\sigma}$ indicates the σ-th component for the fermion operator of the j-th particle. By inserting three pairs of fermion operators in the form of $\psi_j\bar{\psi}_j$ (j=a, b, c) into the section denoted by broken lines in Eqn. (22), necessary Feynman diagrams are provided, with which the gauge invariance holds exactly. We obtain four diagrams with the power of coupling constants $Z_{\mathrm{a}}{}^2 Z_{\mathrm{b}} Z_{\mathrm{c}}{}^2$, six with $Z_{\mathrm{a}} Z_{\mathrm{b}} Z_{\mathrm{c}}{}^3$, and four with $Z_{\mathrm{a}} Z_{\mathrm{b}}{}^2 Z_{\mathrm{c}}{}^2$, which amount to fourteen diagrams. We show six of them in Fig. 1, which have dominant contribution and satisfy the restriction, Eqn. (21), approximately.

We will now indicate the relativistic cross section (the photon angular distribution) of the REC process based on only the first three diagrams of Fig. 1. Such a choice is, in fact, incompatible with the gauge invariance. After some complicated trace calculations, the cross section in the c.m. frame can be reduced to:

$$\begin{aligned}\sigma_{\mathrm{fi,CM}}(\Omega_{\mathrm{CM}}) \propto (\mu_{\mathrm{N}}/m_{\mathrm{c}})^2 (Z_{\mathrm{a}}\alpha v^{-1}(1-\beta^2)^{-1/2})^5 \\ \cdot \sin^2\theta_{\mathrm{CM}}/(1-\beta'\cos\theta_{\mathrm{CM}}) \\ \cdot [(Z_{\mathrm{a}}(1-\beta^2)^{1/2}/m_{\mathrm{a}}) - ((Z_{\mathrm{b}}+Z_{\mathrm{c}})/(m_{\mathrm{b}}+m_{\mathrm{c}})) \\ \cdot ((1-\cos\theta_{\mathrm{CM}})/(1+\beta\cos\theta_{\mathrm{CM}}))^2]^2\end{aligned} \tag{23}$$

where

$$\mu_{\mathrm{N}} = m_{\mathrm{a}} m_{\mathrm{b}}/(m_{\mathrm{a}}+m_{\mathrm{b}}) \tag{24}$$

$$\beta = (\mu_{\mathrm{N}}/m_{\mathrm{b}})v \tag{25}$$

$$\beta' = (\mu_{\mathrm{N}}/m_{\mathrm{a}})v \tag{26}$$

v is the relative velocity of the present process and α is the fine-structure constant. The term in the square brackets in Eqn. (23) is of the comparable order in the magnitude of coupling between the photon field and the respective particles, a, b, and c. This is here called the isotope effect. This cross section can be easily reduced to the usual one by taking the non-relativistic limit and by setting both Z_{a} and Z_{b} in the square brackets zero. It is because the usual theories proposed by

setting both Z_a and Z_b in the square brackets zero. It is because the usual theories proposed by the present time take into no consideration the contributions of both the projectile ion and the target nucleus to the radiative interaction. The cross section in the lab. frame is linked up with that in the c.m. frame with the relation that

$$\sigma_{fi,Lab}(\Omega_{Lab})=(1-\beta^2)(1-\beta\cos\theta_{Lab})^{-2} \cdot\sigma_{fi,CM}(\Omega_{CM}) \quad (27)$$

By the use of the Lorentz transformation like this, the differential cross section in the lab. frame is obtained:

$$\sigma_{fi,Lab}(\Omega_{Lab})\propto(\mu_N/m_c)^2(1-\beta^2)^{7/2}(Z_a\alpha/v)^5 \cdot\sin^2\theta_{Lab}/(1-\beta\cos\theta_{Lab})^4 \cdot[(Z_a/m_a)-((Z_b+Z_c)/(m_b+m_c)) \cdot(1-v\cos\theta_{Lab})^2/(1-\beta^2)^{3/2}]^2 \quad (28)$$

Here, we can gain another differential cross section, $\sigma'_{fi,Lab}$, directly in the lab. frame without applying the Lorentz transformation to $\sigma_{fi,CM}$:

$$\sigma'_{fi,Lab}(\Omega_{Lab})\propto(m_c(1-v^2))^{-2}Z_a^2(z_a\alpha/v)^5 \cdot\sin^2\theta_{Lab}/(1-v\cos\theta_{Lab}) \quad (29)$$

These two cross sections in the same frame, $\sigma_{fi,Lab}$ and $\sigma'_{fi,Lab}$, are found different in their form. The physical meaning of $\sigma'_{fi,Lab}$ is explained in terms of the first three Feynman diagrams shown in Fig. 1. As is generally known, the magnitude of coupling between a particle and an external photon is roughly proportional to the velocity of the traveling particle. The projectile ion, a, in the lab. frame propagates with the velocity, v, while the target atom, (b−c), is nearly at rest. Therefore, the coupling magnitude between the projectile and the photon becomes much dominant to that of the target atom. On the other hand, the whole three particles in the c.m. frame move around with a velocity of the order of v. Such situation explaines the cause of the isotope effect in the c.m. frame.

Meanwhile, it is quite necessary for us to consider the gauge invariance explicitly in order to overcome the difficulty that both $\sigma_{fi,Lab}$ and $\sigma'_{fi,Lab}$ are much different from each other. The gauge invariance holds nearly true by adding the last three diagrams to the first ones in Fig. 1. Particularly, the diagram (5) has definite meanings, which, in fact, corresponds to the second term in curl brackets of Eqn. (8) in Ref. 6. Formally, this term was called "spurious radiation" by Shakeshaft and Spruch.[5] From the present point of view, however, this plays quite an important role to maintain the gauge invariance and the spurious radiation has, therefore, the real and essential meanings in the radiative scattering processes as well as in the present radiative electron capture process. As denoted by Briggs and Dettmann[6] by using the non-relativistic and semi-classical method, the diagram (5) gives birth to the consistent cross section even in the lab. frame with that in the c.m. frame. On the contrary, most of the formulations proposed by the present time based on the non-relativistic quantum mechanics do never gives the desirable cross sections holding the gauge features exactly. The physical interpretation, for example, of the diagram (5) is as follows: In the lab. frame, the target electron is firstly ionized to the continuum state with feeling the distortion from the projectile ion, and the coupling magnitude with photon field amounts to be of the order of v, because the intermediate electron is traveling with such order of velocity through the propagator, $S_{F,c}$. The similar discussion will also be held on other particles as well as in other frames.

Both the isotope effect and the relativistic angular distribution of the emitted photon are not guaranteed to be correct as yet until the whole diagrams holding the gauge invariance are included in the scattering matrix. As for the isotope effect, however, we believe its reality, because the mass dependence of X-ray yields was indeed observed in the nucleon-nucleon bremsstrahlung process. The origin of these two effect seems to be the same in spite of the difference in number of particles participating in scattering.

References

1) J. Schwinger: *Proc. Natl. Acad. Sci. U.S.A.*, **37**, 452, 455 (1951).
2) S. Weinberg: *Phys. Rev.*, **113**, 3232 (1964).
3) E. E. Salpeter and H. Bethe: *Phys. Rev.*, **84**, 1232 (1951).
4) K. Nishijima: *Prog. Theor. Phys.*, **10**, 549 (1953).
5) R. Shakeshaft and L. Spruch: *Phys. Rev. Lett.*, **38**, 175 (1977).
6) J. S. Briggs and K. Dettmann: *Phys. Rev. Lett.*, **33**, 1123 (1974).

RIKEN Accel. Progr. Rep. 19 (1985)

III-2-6. Two-Electron Diatomic Molecule: Program Package "MADAM"

H. Sato, E. Ishiguro,* T. Kimura, and T. Takezawa**

Knowledge on the electronic structures of atoms and molecules is necessary to investigate atomic collisions. One of the most elaborate methods for obtaining precise energies and wave functions of two-electron diatomic molecules is the James-Coolidge method.[1] In a previous work,[2] we worked out a computer program to obtain the energies and wave functions in the singlet or the triplet Σ^+ states of two-electron diatomic molecules with any nuclear charge by using this method. This study pursues an extension of the previous one to any state of two-electron diatomic molecules.[3] Reasons to undertake the present study, in spite of a series of excellent work by Kołos, Wolniewicz, and their collaborators, are i) to make the James-Coolidge-type wave functions available at our disposal, ii) to confirm the accuracy of the results obtained by these authors, and iii) to investigate the applicability of the method for a wide range of values of the internuclear distance in various states.

By using elliptical coordinates

$$\lambda_i=(r_{ai}+r_{bi})/R,\ \mu=(r_{ai}-r_{bi})/R,\ \varphi_i\ (i=1,\ 2)$$

and

$$\rho\ =\ 2r_{12}/R$$

the Hamiltonian is expressed as

$$H=T/R^2+(Z_a+Z_b)U^{(1)}/2R+(Z_a-Z_b)U^{(2)}/2R+U^{(3)}/R+Z_aZ_b/R$$

where

$$T=-R^2(\Delta_1+\Delta_2)/2$$

$$U^{(1)}=-4\lambda_1/(\lambda_1^2-\mu_1^2)-4\lambda_2/(\lambda_2^2-\mu_2^2)$$

$$U^{(2)}=4\mu_1/(\lambda_1^2-\mu_1^2)+4\mu_2/(\lambda_2^2-\mu_2^2)$$

$$U^{(3)}=2/\rho$$

and Z_a, Z_b, and R denote the nuclear charges of two nuclei and the internuclear distance. The distance between the electron i and the nucleus A is represented by r_{ai} and the other inter-particle distances are given by similar symbols. We use the atomic units throughout this report.

In order to make applicable to any state and any R, the basis functions of the James-Coolidge type wave function should be generalized to have sufficient flexibility and proper symmetry. In the first place, we introduce the functions

$$\chi(m,n,j,k,p,l_1,l_2\ ;\ \alpha_1,\alpha_2,\beta_1,\beta_2)\equiv\chi$$
$$=(1/2\pi)(2/R)^3\exp[-\alpha_1\lambda_1-\alpha_2\lambda_2-\beta_1\mu_1-\beta_2\mu_2]\lambda_1^{\,m}\lambda_2^{\,n}\mu_1^{\,j}\mu_2^{\,k}\rho^p M_1^{\,|l_1|}\times M_2^{\,|l_2|}\exp[il_1\varphi_1+il_2\varphi_2]$$

where

$$M_i=[(\lambda_i^2-1)(1-\mu_i^2)]^{1/2}\ (i=1,\ 2)$$

Next, we define the functions $\psi(m,n,j,k,p,l_1,l_2\ ;\ \alpha_1,\alpha_2,\beta_1,\beta_2)\equiv\psi$ as

$$\psi=(\chi+\bar{\chi})/2\quad\text{for } \Sigma^+ \text{ state}$$

$$\psi=(\chi-\bar{\chi})/2i\quad\text{for } \Sigma^- \text{ state}$$

$$\psi=\chi\quad\text{for other states}$$

where $\bar{\chi}$ is the complex conjugate of χ.

In a homopolar case, the symmetry adapted basis functions $\psi(m,n,j,k,p,l_1,l_2\ ;\ \alpha_1,\alpha_2,\beta_1,\beta_2)$ are constructed from

$$\psi_A=\psi(m,n,j,k,p,l_1,l_2\ ;\ \alpha_1,\alpha_2,\beta_1,\beta_2)$$

$$\psi_B=\psi(m,n,j,k,p,l_1,l_2\ ;\ \alpha_1,\alpha_2,-\beta_1,-\beta_2)$$

$$\psi_C=\psi(n,m,k,j,p,l_2,l_1\ ;\ \alpha_2,\alpha_1,\beta_2,\beta_1)$$

$$\psi_D=\psi(n,m,k,j,p,l_2,l_1\ ;\ \alpha_2,\alpha_1,-\beta_2,-\beta_1)$$

as

$$\Psi=[(\psi_A+\psi_C)+(-1)^{j+k+l_1+l_2}(\psi_B+\psi_D)]\quad\text{for singlet g state}$$

$$\Psi=[(\psi_A+\psi_C)-(-1)^{j+k+l_1+l_2}(\psi_B+\psi_D)]\quad\text{for singlet u state}$$

$$\Psi=[(\psi_A-\psi_C)+(-1)^{j+k+l_1+l_2}(\psi_B-\psi_D)]\quad\text{for triplet g state}$$

$$\Psi=[(\psi_A-\psi_C)-(-1)^{j+k+l_1+l_2}(\psi_B-\psi_D)]\quad\text{for triplet u state}$$

where normalization factors are omitted for simplicity. In a heteropolar case, in which g-u

* Department of Physics, Faculty of Science, Ochanomizu University.
** Department of Mathematics, College of Science and Technology, Nihon University.

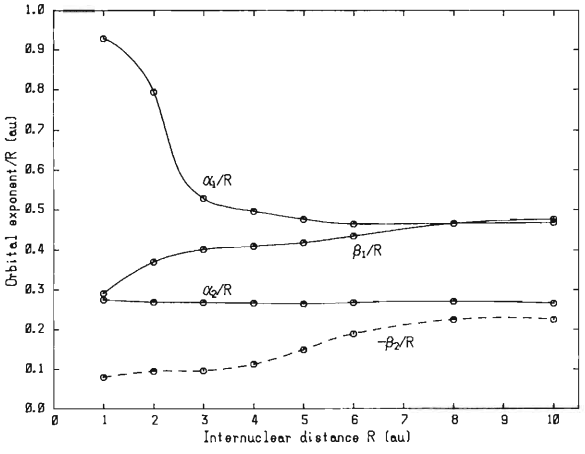

Fig. 1. Orbital exponents for the lowest $^1\Pi_u$ state of H_2.

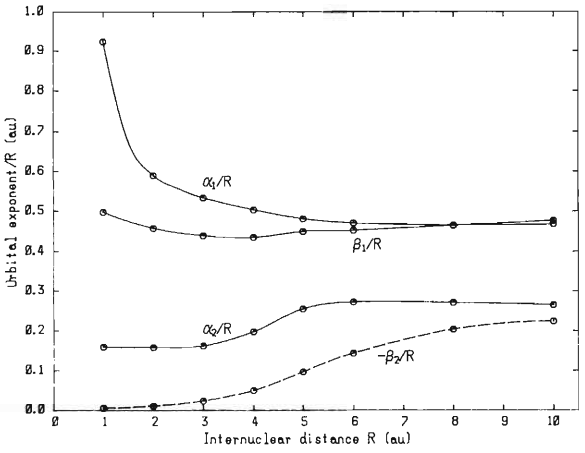

Fig. 2. Orbital exponents for the lowest $^3\Pi_g$ state of H_2.

symmetry is missing, merely the combinations $\psi_A \pm \psi_C$ or $\psi_B \pm \psi_D$ are sufficient. It is to be noted that four parameters α_1, α_2, β_1, and β_2 are introduced in the exponent of Ψ. Moreover, not only ρ but also φ_1 and φ_2 can be involved even in the Σ states and, therefore, the basis functions are more flexible than the original ones adopted by James and Coolidge.

The matrix elements of the Hamiltonian H and the Unity S with respect to the basis function Ψ's can be obtained easily from those with respect to the function χ's. The latter matrix elements can be expressed by the auxiliary function[3]

$$X(M,N,J,K,P,L_1,L_2,\gamma\ ;\ A_1,A_2,B_1,B_2)$$
$$=(1/2\pi)^2\int \exp[-A_1\lambda_1-A_2\lambda_2-B_1\mu_1-B_2\mu_2]$$
$$\times \lambda_1{}^M\lambda_2{}^N\mu_1{}^J\mu_2{}^K\rho^P M_1{}^{L_1}M_2{}^{L_2}\exp[i\gamma(\varphi_1-\varphi_2)]$$
$$\times d\lambda_1 d\lambda_2 d\mu_1 d\mu_2 d\varphi_1 d\varphi_2$$

The function X's can be evaluated using Kotani, Amemiya, and Simose's auxiliary functions.

A package of computer programs named MADAM (Most Accurate DiAtomic Molecular calculation) is constructed by employing the above-mentioned method. MADAM consists of several job steps: calculation of the values of auxiliary functions, construction of the matrix elements, and calculation of the energy and wave function. A lot of machine time is required to optimize the non-linear parameters α_1, α_2, β_1, and β_2 and to find the best set of the basis functions. We determined these parameters for the lowest $^1\Pi_u$ and the $^3\Pi_g$ states of H_2 adopting 64 basis functions ($m,n,j,k,p,l_1,l_2=0,1$, and $l_1+l_2=1$). In Figs. 1 to 3, results are shown. Besides the full

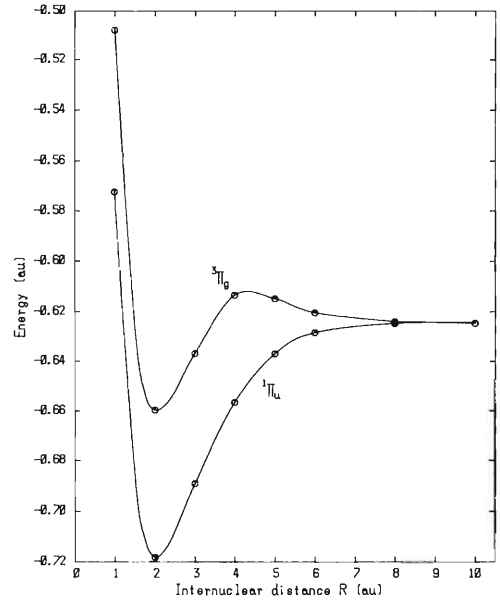

Fig. 3. Potential energy curves of the lowest $^1\Pi_u$ and $^3\Pi_g$ states of H_2.

application of MADAM, we also undertake the calculation of the polarizability of the H_2-like molecules in any state as a natural extension. The details of the application will be published elsewhere.

References

1) H. M. James and A. S. Coolidge: *J. Chem. Phys.*, **1**, 825 (1933).
2) N. Ueda, H. Sato, E. Ishiguro, and T. Takezawa: *Natl. Sci. Rep. Ochanomizu Univ.*, **27**, 33 (1976).
3) H. Sato, E. Ishiguro, T. Kimura, and T. Takezawa: *Natl. Sci. Rep. Ochanomizu Univ.*, **36**, 81 (1985).

RIKEN Accel. Progr. Rep. **19** (1985)

III-2-7. Quantum Mechanical Treatment of Charge-Exchange Processes Using Frame Transformation

I. Shimamura

In ion-atom collisions the ions often capture electrons from the atoms. This process is referred to as an electron-transfer process or a charge-exchange process. Abundant literature exists on applications of the semiclassical impact-parameter formalism to charge-exchange processes. In this formalism the electronic motion is treated quantum mechanically, but the relative motion between the ion and the atom is treated classically. Much less quantum mechanical calculations have been reported so far than semiclassical calculations. This is partly because of the complexity in fully quantum mechanical calculations and partly because of the stronger interest in the medium- to high-energy region than in the low-energy region. The de Broglie wavelength of the relative motion is much shorter than the dimension of the electron clouds of the colliding atoms, unless the collision energy is extremely small. This has been thought to justify the semiclassical treatment except at extremely small collision energies. For collision energies of the order of 10 eV or 1 eV for which the de Broglie wavelength is still short, however, the relative motion may depend strongly on the channel. This is a quantum mechanical effect. It requires a fully quantum mechanical treatment of the collision process at these energies or lower.

Molecular-base expansion is preferable to atomic-base expansion at low energies. The conventional molecular-base perturbed-stationary-state approach, however, has its fundamental difficulties associated with the translational motion of the electrons bound to either of the nuclei that keep moving during the collision.[1] There has been much formal discussion on the effect of the electron translational motion and of the electron translation factor in the wave function.[2] Neglect of this effect would lead to serious errors in the cross sections. Many semiclassical impact-parameter calculations include the electron translation factor. On the other hand all fully quantum mechanical calculations published to date simply disregard the electron translation factor with a very recent exception.[3] This recent work has its own drawback in the sense that the angular-momentum conservation law is violated. The purpose of the present work is to develop a new and practical method of fully quantum mechanical calculations including the electron translation factor.

When the distance R between the ion and the atom is small, the total collision system behaves much like a molecule. The molecular-base expansion is appropriate there. When R is large the ion and the atom maintain their atomic character even at low collision energies. Therefore, the atomic-base expansion is more physical and practical at large R. We may set a boundary between the molecular region and the atomic region at an appropriately chosen value A of R. The molecular-channel wave functions defined for $R<A$ are to be connected smoothly to the atomic-channel wave functions defined for $R>A$ through the frame transformation at $R=A$. It is straightforward to write down coupled equations for channel functions in the atomic region including the electron translation effect, if we use the so-called Jacobi coordinates. These coupled equations are extremely difficult to solve by use of conventional methods. A new numerical method has been devised to solve these equations. In the molecular region the electron translation effect is expected to be small and may be neglected.[4] Then this region may be treated in the conventional molecular-base perturbed-stationary-state approximation.

This approach is a generalization of a semiclassical molecular-base atomic-base matching method of Kimura and Lin[4] for fully quantal calculations.

References

1) D. R. Bates and R. McCarroll: *Proc. Roy. Soc. London, Ser. A*, **245**, 175 (1958).
2) J. B. Delos: *Rev. Mod. Phys.*, **53**, 287 (1981).
3) M. C. van Hemert: *Phys. Rev. A*, **31**, 2227 (1985).
4) M. Kimura and C. D. Lin: *Phys. Rev. A*, **31**, 590 (1985); **32**, 1357 (1985).

RIKEN Accel. Progr. Rep. 19 (1985)

III-2-8. The Rotationally and Vibrationally Resolved Photoionization of H_2 by 736 Å Line

S. Hara

Photoionization of molecules is one of the most fundamental problems in the study of interaction of radiation with matter. In this report, photoionization of H_2 is theoretically investigated.

Intensity distribution of the photoelectron for the rotationally and vibrationally resolved molecular photoionization process is given by

$$I_{J''J'}(\theta) = \sigma_{J''J'}/4\pi[1+\beta_{J''J'}P_2(\cos\theta)]$$

where $\sigma_{J''J'}$ and $\beta_{J''J'}$ are the cross section and the asymmetry parameters, respectively, for the transition from the $(v''=0, J'')$ state to the (v', J') state.

The vibrationally resolved cross section $\sigma_{v'}$ and the asymmetry parameter $\beta_{v'}$ are reduced to[1]

$$\sigma_{v'} = \sum_j \sigma_{0j}$$

$$\beta_{v'} = \left[2.0+\sum_{j\neq 0}\beta_{0j}\frac{\sigma_{0j}}{\sigma_{00}}\right] \Big/ \left[1.0+\sum_{j\neq 0}\frac{\sigma_{0j}}{\sigma_{00}}\right]$$

The measurement of the ratio

$$R_j(\theta) = I_{0j}(\theta)/I_{00}(\theta) = (\sigma_{0j}/\sigma_{00}) \times [1+\beta_{0j}P_2(\cos\theta)] / [1+2.0P_2(\cos\theta)]$$

at $\theta=54.7°$ determines σ_{0j}/σ_{00}. Therefore, an independent measurement of $R_j(\theta)$ at another angle gives β_{0j} and thus $\beta_{v'}$. The ratios σ_{0j}/σ_{00} are obtained for N_2 for $j=2$ and 4 by the deconvolution technique.[2]

When the cross sections for $\Delta J = J'-J'' \geqq 4$ are negligible, σ_{02}/σ_{00} and β_{02} are two essential parameters for $\beta_{v'}$. It was shown that for the photoionization of H_2, the cross sections for $\Delta J \geqq 4$ are small,[3] and that the measurements of the intensity ratio of the S and Q rotational branches at two angles[3),4] determine these two parameters and $\beta_{v'}$.[1]

We have calculated the cross sections σ_{00}, σ_{02} and β_{02} for v' from 0 to 5 for the photoionization of H_2 by 584 Å line.[1] Calculation for the final $H_2^+ + e$ state was carried out, in the two centre spheroidal coordinates, in the static exchange approximation with the adiabatic polarization potential added. Agreement between the calculated results with the values deduced from the experimental data[3),4] is very satisfactory.

Table 1. Cross sections and asymmetry parameters.

v'		σ_{02}/σ_{00}	β_{02}	$\beta_{v'}$
0	a	0.0856	0.2	1.858
	b	0.0850	0.2	1.859
	c	0.0872	0.643	1.891
	d	0.093(2)	0.62(11)	1.882(9)
	e	0.091(3)	0.09(13)	1.841(12)
	f			1.67 (6)
	g	0.2118	0.348	1.711

a, Ref. 7, p wave; b, present, p wave; c, present, p and f waves; d, Ref. 3; e, Ref. 4; f, Ref. 8; g, Ref. 6, p and f waves.

Here we present the results for the photoionization of H_2 by 736 Å line.[5] Table 1 gives the present calculations with the p wave and with the p and f waves of the ejected photoelectron. The results derived from experimental data,[3),4] other theoretical,[6),7] and experimental[8),9] studies are also tablated.

The present results and those of Raoult *et al.*[7] agree with the experiments[3),4] in σ_{02}/σ_{00}. The present results with the p and f waves give large values of β_{02} because of the interference of the p and f waves, and are in good agreement with the experimental results of Ruf *et al.*[3] The vibrationally resolved asymmetry parameters $\beta_{v'}$ do not depend very much on β_{02} since the ratios σ_{02}/σ_{00} are rather small in the present process.

References

1) S. Hara and S. Ogata: *J. Phys. B,* **18**, L59 (1985).
2) Y. Morioka, Y. Hamada, K. Kihara, S. Hara, and M. Nakamura: *J. Phys. B,* **18**, 1369 (1985).
3) M. W. Ruf, T. Bregel, and H. Hotop: *J. Phys. B,* **16**, 1549 (1983).
4) J. E. Pollard, D. J. Trevor, J. E. Reutt, Y. T. Lee, and D. A. Shirley: *Chem. Phys. Lett.,* **88**, 434 (1980).
5) S. Hara: *J. Phys. B,* **18**, 3759 (1985).
6) Y. Itikawa: *Chem. Phys.,* **37**, 401 (1979).
7) M. Raoult, Ch. Jungen, and D. Dill: *J. Chim. Phys.,* **77**, 599 (1980).
8) E. D. Poliakoff, J. E. Dehmer, P. M. Dehmer, and A. C. Parr: *Chem. Phys. Lett.,* **96**, 52 (1983).

RIKEN Accel. Progr. Rep. 19 (1985)

III-2-9. Peak Fitting in Beam-Foil Spectrum

K. Ando, Y. Awaya, S. Kohmoto, H. Kumagai,
T. Tonuma, S. Tsurubuchi, and K. Sato

Spectra observed in beam-foil experiments usually have not high spectral resolution, because of limitation of observation time and/or weakness of light intensities, *etc*. Owing to such insufficient resolution, many lines overlap with each other and the accuracy of wavelength of spectral lines is limited. We tried to make spectral lines fit and deconvolute by assuming a Gaussian profile in order to determine the line positions accurately and separate the overlapped lines.

For the background of measured spectra, light scattering inside a grazing incidence spectrometer is considered to be mainly responsible; the scattered light distributes continuously over the whole spectral region, intensity being strong in the short wavelength region but weakened in the long region. From this viewpoint the background can be expressed by a simple equation of polynomials of low orders, *e.g.*, below 5. For estimation of the background, (1) the whole data are divided into groups each composed of 50 channels and the lowest 5 data were picked out from each group; (2) polynomials were estimated by the least-squares fit with data obtained in (1); (3) the data of (1) were compared with the fitted polynomials at the same wavelengths, and if the difference between data and the fitted value was positive and larger than the standard deviation of fitting, the data were omitted from the next background fitting. This procedure was repeated three times to determine final polynomials. Figure 1 shows three backgrounds, one of which corresponds to polynomials determined in each procedure.

The peak finding procedure of spectral lines was carried out in two steps. First, the half width of spectral lines was found from isolated strong lines with the least-squares fitting of a spectral line profile. Because the half width of a spectral line is the same at any wavelengths for a grazing incidence spectrometer, this estimated half width is applied to every line in the next step. Peak positions of spectral lines were found by the

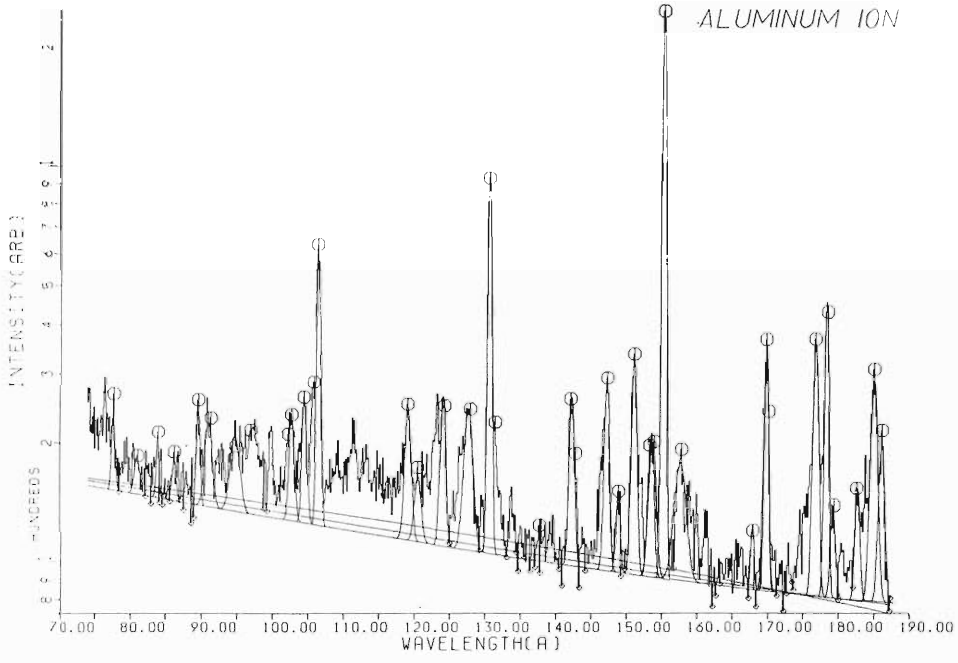

Fig. 1. The spectrum obtained in the beam-foil experiment with estimated backgrounds and first peak fitting. Three backgrounds correspond to the cycles of the estimation procedures. The final background is approximated by a second order polynomials.

Table 1. Results of the peak finding of spectrum data. Values in parentheses in the second and third columns are the standard deviations of fitting peaks positions in Å and of intensities, respectively.

---------- STEP 5 ----------			
JUDGE FOR FITTING: 1.51280		IERROR: 0	
No.	Fitted Peak (Å)	Intensity ERR %	Width in Å
1	173.066 (0.011)	20.285 (6.14) 30	0.550
2	174.591 (0.013)	42.415 (6.82) 16	0.550
3	175.390 (0.016)	63.758 (7.55) 11	0.550
4	176.115 (0.021)	98.660 (9.15) 9	0.550
5	176.773 (0.025)	310.341 (12.13) 3	0.550
6	177.524 (0.019)	98.849 (8.52) 8	0.550
7	178.284 (0.021)	397.129 (12.42) 3	0.550
8	179.302 (0.013)	60.210 (7.02) 11	0.550

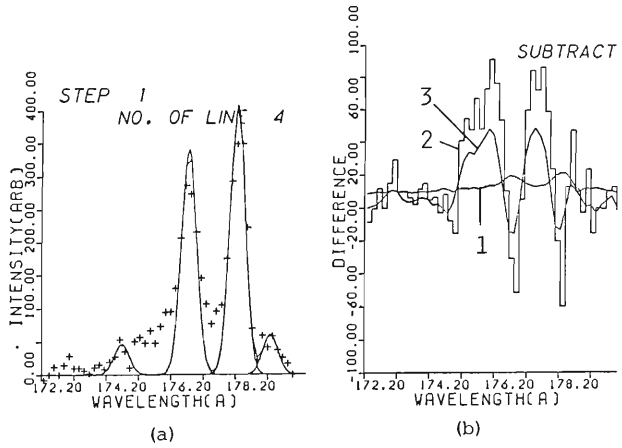

Fig. 2. The first rough estimates by peak fitting applied to a part of a spectrum. (a) shows the data (+) and the fitted spectral lines (solid curve); (b) shows the standard deviation of data (1), the difference between the data and fitted curve (2), and the smoothed difference (3).

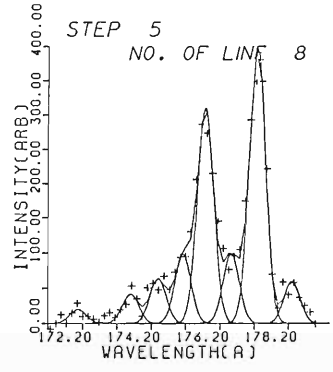

Fig. 3. Final result of peak fitting.

following method. The difference between the data and the fitting curve was calculated and then smoothed, and if the smoothed differences exceeded the standard deviation of data, it was concluded that there exist a line. The position of the maximum smoothed difference was added to the previous fitting and the fitting was repeated. These processes are shown in Fig. 2, where (a) shows the data and the first fitting and (b) the standard deviation, the difference between the data and the fitted curve, and the smoothed difference.

Finally, when the smoothed difference is smaller than the standard deviation, the peak finding process is finished. Figure 3 shows an example of the final result of fitting.

By using the peak finding processes, the accuracy of the position of lines is improved by a factor of 2, that is, ± 0.05 Å. Although the improvement of wavelength accuracy was not necessarily excellent, the overlapping lines were clearly separated by this procedure.

This peak finding program may be successfully applied to general spectra. It should, however, be noticed that in the regions where complex lines overlap this program can not deconvolute lines and, sometimes, the ghost lines appear.

The judgement of fitting was made on graphics of fitting curves. An example of the fitting results for a highly ionized aluminum spectrum in the beam-foil experiment[1] are given in Table 1.

Reference

1) K. Ando, S. Kohmoto, T. Tonuma, H. Kumagai, Y. Awaya, S. Tsurubuchi, and K. Sato: *RIKEN Accel. Progr. Rep.*, **18**, 71 (1984).

RIKEN Accel. Progr. Rep. 19 (1985)

III-2-10. Tilted-Foil Method with Charge-Nonequilibrium Ions

S. Kohmoto, K. Ando, and M. Ishihara

We have verified[1] by an optical method that charge-nonequilibrium ions can be generated by using thin carbon foils of 0.7 μg/cm^2 in thickness for a $^{14}N^{3+}$ ion beam of 28.8 MeV incident energy; some lines of N IV and N V ions were found to survive, which is not the case with thick foil. To see whether or not ions are polarized after passing through thin tilted carbon foil, we measured the polarization of light emitted from the ions about 1.5 cm downstream from a foil tilted at $\pm 45°$.

A calcite Glan-Taylor polarizer was used instead of a Polaroid one to assure the measurement of low-wavelength lines. Figure 1 shows the light-intensity variation I' as a function of phase plate rotation angle β for the N IV 341 nm line. The tilting angles to the beam direction are also given in Fig. 1. The rotation angle β was advanced by 5° for each passed ion currents of 6 μC. The results show that the intensity is gradually lowered on the whole, and the foil seems to be thickened under the bombardment of ions probably because of the insufficient vacuum.

Thus charge state of ions approaches equilibrium, and the number of emitted photons as well as measurement lap time decrease. The results were analyzed by using a function:

$$I'(\beta) = (1/2)\{I + (M\cos 2\beta + C\sin 2\beta)\cos 2(\alpha-\beta) + [(C\cos 2\beta - M\sin 2\beta)\cos\Delta + S\sin\Delta]\sin 2(\alpha-\beta)\} \times \sum_{i=1} N_i \exp(-a_i q)$$

where I, M, C, and S are the Stokes parameters to be determined, Δ is the phase angle of the phase plate which is 130.4° at this wavelength, and the polarizer angle α was fixed to be 0°. The last term is introduced to simulate the thickening effect of the foil phenomenologically, where q is the integrated ion current.

The summation is taken with constraint of $\sum_{i=1} N_i = 1$. A single exponential term, however, is generally sufficient to reproduce the thickenning effect.

From the analysis, we conclude that the ions emit highly linear-polarized light at this incident energy. It was found previously[2] that, in the energy region $E_N < 15$ MeV, the circular polarization has a tendency to diminishing when the incident energy is increased. It does not seem to disappear completely at 28.8 MeV incident energy. Relative Stokes parameters may be dependent on the foil thickness, which is represented by q in the above equation; the present measurements are, however, not necessarily precise to investigate it at this stage.

References

1) S. Kohmoto, K. Ando, M. Ishihara, and T. Nomura: *RIKEN Accel. Progr. Rep.*, **18**, 69 (1984).
2) S. Kohmoto, M. Ishihara, T. Nomura, and Y. Gono: *RIKEN Accel. Progr. Rep.*, **17**, 48 (1983).

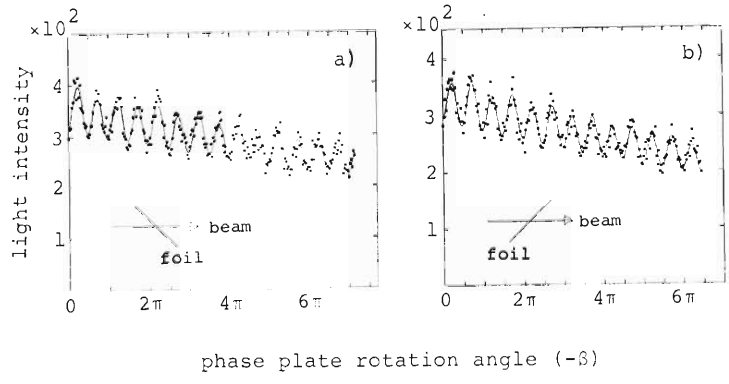

Fig. 1. Light intensity (dots) measured as a function of phase plate rotation angle. Tilting angle is opposite for a) and b). The continuous lines are calculated with the function given in the text. Normalized Stokes parameters used are: a) $M/I = (-13.2 \pm 2.7)\%$, $C/I = (-4.3 \pm 2.7)\%$, $S/I = (+2.7 \pm 3.4)\%$; b) $M/I = (-12.8 \pm 3.1)\%$, $C/I = (-4.6 \pm 3.1)\%$, $S/I = (-2.4 \pm 3.9)\%$.

RIKEN Accel. Progr. Rep. 19 (1985)

III-2-11. Measurement of Lifetimes for Highly-Ionized Aluminium Atoms

S. Kohmoto, K. Ando, Y. Awaya, H. Kumagai,
K. Sato, T. Tonuma, and S. Tsurubuchi

The measurement of beam-foil spectroscopy for Al ions[1] has been carried out making use of RILAC. Spectra were measured at several incident energies in the wavelength region $\lambda < 400$ Å. Line assignment of spectra has been made and details are found in another report.[2] We succeeded to measure some decay curves and present here two of them measured by using of Al^{3+} ion beam at the incident energy E_{Al} of 22.38 MeV. Figure 1 shows the decay curves for a) Al×2s2p $^3P_1$-2p^2 $^3P_2$ 395.36 Å transition and b) Al×2s^2 ^{1}S-2s2p ^{1}P 332.78 Å transition.

The position of the carbon foil, 5 μg/cm^2 in thickness, was shifted along with the beam by 0.05, 0.15, or 0.25 mm for each passed ion currents of 100 μC. A light guide connected to a photomultiplier was mounted downstream from the target assembly in order to detect breakage of the foil. A Perkin Elmer computer in an MSC mode was used to accumulate the photon counts.

These decay curves were analyzed by using the multi-exponential-fitting programme cord DISCRETE,[3] which is based on the eigen-function expansion of the solution of the Fredholm integral equation. This programme decides both the best number of exponentials to be introduced and the transition probabilities. Curve a) is composed of two exponential terms with transition probabilities $A = (2.03 \pm 0.10)$ ns^{-1} and (10.71 ± 0.34) ns^{-1}. Curve b) is reproduced by a single exponential term with $A = (3.11 \pm 0.04)$ ns^{-1}.

We are preparing the decay-curve measurement of the cascade transitions to these levels in order to extract the lifetimes.

References

1) K. Ando, S. Kohmoto, T. Tonuma, H. Kumagai, Y. Awaya, S. Tsurubuchi, and K. Sato: *RIKEN Accel. Progr. Rep.*, **18**, 71 (1984).
2) K. Ando, Y. Awaya, S. Kohmoto, H. Kumagai, T. Tonuma, S. Tsurubuchi, and K. Sato: p. 62 in this report.
3) S. W. Provencher: *J. Chem. Phys.*, **64**, 2772 (1976).

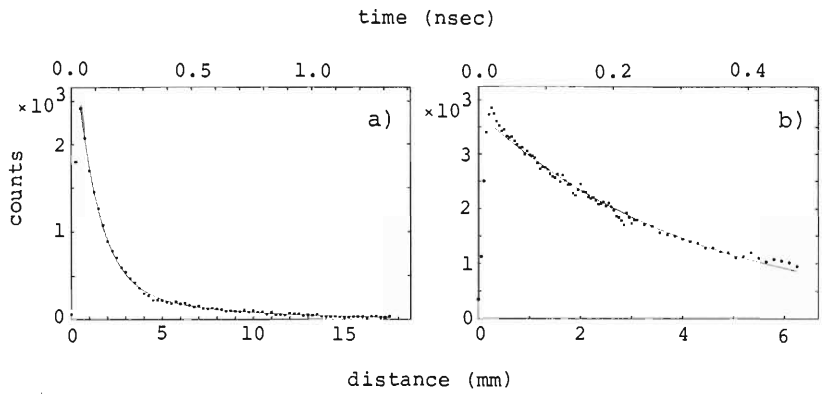

Fig. 1. Measured and calculated decay curves a) for 2s2p $^3P_1$-2p^2 $^3P_2$ 395.36 Å transition and b) for 2s^2 ^{1}S-2s2p ^{1}P 332.78 Å transition.

RIKEN Accel. Progr. Rep. 19 (1985)

III-2-12. Electron Distribution in M- and L-Shells of 33 MeV Ar-Ions in Solid Targets

T. Kambara, Y. Awaya, Y. Kanai, M. Kase,
T. Mizogawa, and H. Shibata

The energy spectra of Kβ X-rays from 33 MeV Ar-ions passing through various solid targets have been measured in order to study the electron distribution in the L- and M- shells of Ar-ions on a K X-ray emission as a function of the target atomic number Z_2. A broad-range crystal spectrometer was used to get an energy resolution high enough to resolve these K X-rays into satellite components which correspond to different hole numbers of the L-shell. Since most of K X-rays are emitted inside the target, we can obtain information about electronic excitation and ionization of the ions in various matters.

The experimental setup and results obtained from Kα X-ray spectra were given in previous reports.[1),2)] The measurement including the Kβ X-rays was started last year, and preliminary results have been reported.[2)] This year the S/N ratio of the X-ray spectra was improved and additional data on Nd and W targets were added.

The intensity of each satellite component KL^n of the Kα and Kβ X-rays was obtained by fitting a sum of Gaussian curves to the observed X-ray spectra. The detection efficiency of the proportional counter of the spectrometer was corrected by using an estimated value of absorption by the gas, but the absorption in the window of the proportional counter was not corrected.

From the satellite intensity distribution of the Kβ X-rays, the average number of the L-shell holes is derived in the same way as that from the Kα X-rays.[1)] The Z_2 dependence of the L-hole number is plotted in Fig. 1 for both Kα and Kβ transitions. The L-shell hole number has the same oscillatory dependence on Z_2 for both cases but that obtained from the Kβ transition is by about 1 larger than that obtained from the Kα transition. The origin of the oscillatory dependence was explained as the Z_2 dependence of electron capture cross section to the Ar L-shell by the level matching effect.[1)]

The intensity ratio of KβL^n to KαL^n X-rays with the same number of L-shell holes is also obtained from the data. The ratio is plotted against Z_2 in Fig. 2 for the L-shell hole number

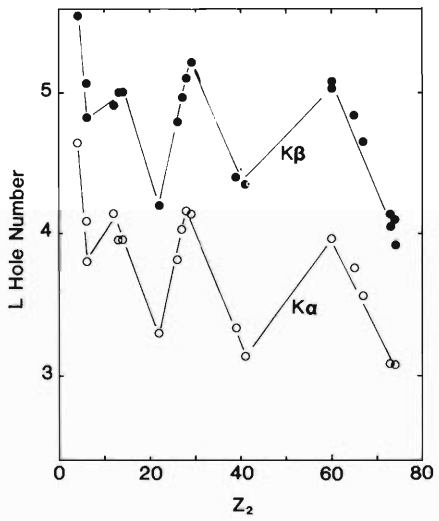

Fig. 1. Target atomic number (Z_2) dependence of the number of L-shell holes of Ar ions obtained from Kα and Kβ X-ray satellite distributions.

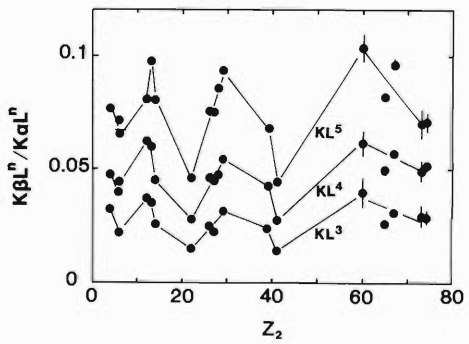

Fig. 2. Target atomic number (Z_2) dependence of the intensity ratio of Ar KβL^n X-ray satellite components for n L-shell holes (n=3,4, and 5).

from 3 to 5. By comparing the intensity ratio with that calculated by Bhalla,[3)] the number of M_{23}-shell electrons (3p electrons) is estimated for these numbers of L-shell holes. The result is shown in Fig. 3 as a function of Z_2. The number of electrons in the M_{23}-shell is smaller than 1 and shows oscillatory dependence on Z_2 which is in phase with that of the L-shell hole shown in Fig. 1.

From the present data, it is concluded that the

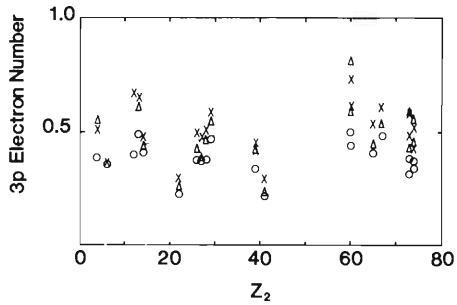

Fig. 3. Target atomic number (Z_2) dependence of the number of M_{23}-shell (3p) electrons at the time of K X-ray emission for different numbers of L-shell holes. Triangles stand for 3 L-shell holes, crosses for 4 holes, and circles for 5 holes.

number of electrons in the L-shell is about 4 and that in the M-shell is smaller than 1. It is also speculated that the number of electron in the M-shell becomes small when the number in the L-shell is large. It is interesting to compare the present data with that of charge state distribution of heavy ions after passage in targets.

References

1) Y. Awaya, T. Kambara, M. Kase, H. Shibata, H. Kumagai, K. Fujima, J. Urakawa, T. Matsuo, and J. Takahashi: *Nucl. Instrum. Methods B*, **10/11**, 53 (1985).
2) T. Kambara, Y. Awaya, M. Kase, H. Shibata, and H. Kumagai: *RIKEN Accel. Progr. Rep.*, **18**, 73 (1984).
3) C. P. Bhalla: *Phys. Rev. A*, **8**, 2877 (1973).

RIKEN Accel. Progr. Rep. 19 (1985)

III-2-13. Target Thickness Dependence of Kα Satellite Intensities of Ar Ions Passing through Thin Carbon Foils

T. Mizogawa, Y. Awaya, T. Kambara, Y. Kanai, M. Kase,
H. Kumagai, M. Mostafa Ismail, and K. Shima

Target-thickness dependence of Ar Kα satellite intensities were measured to study the evolution of L-hole configuration of fast Ar ions in carbon foils. Such a type of measurement gives detailed and direct information about the charge-equilibration process of fast ions in solids and the origin of the strong dependence of experimental K X-ray production "cross section" on the target thickness for extremely thin targets.

Experimental set-up is shown in Fig. 1. A carbon-foil target was bombarded with 50 MeV Ar^{4+} ions from the RIKEN linear accelerator, and resulting Ar K X-ray spectra were measured by using a broad-range crystal spectrometer.[1] A value of integrated Ar^{4+} flux multiplied by the target thickness was determined from the mea-

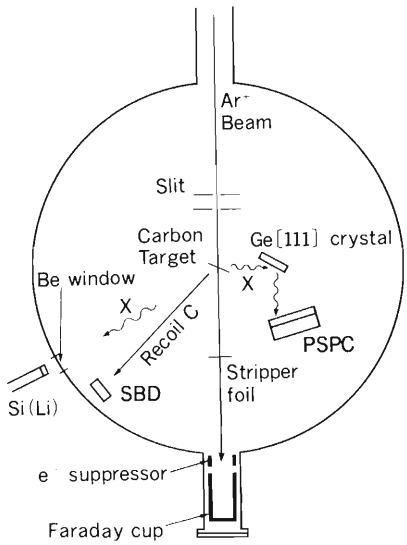

Fig. 1. Experimental set-up. The diameters of slits are 1.5 mm (front) and 2.0 mm. PSPC stands for a position-sensitive proportional counter. The voltage of −1 kV was applied to the electron suppressor.

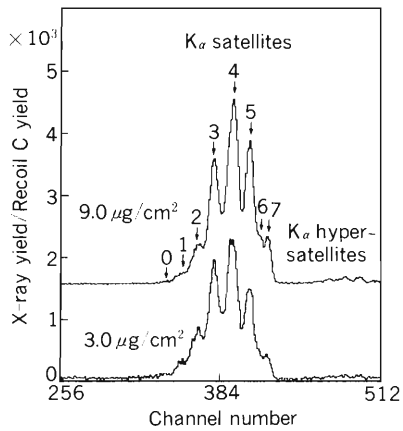

Fig. 2. Ar K X-ray spectra for two different target-thicknesses. Vertical scale is normalized by recoil-carbon yield. For the numbers 0-7, see text.

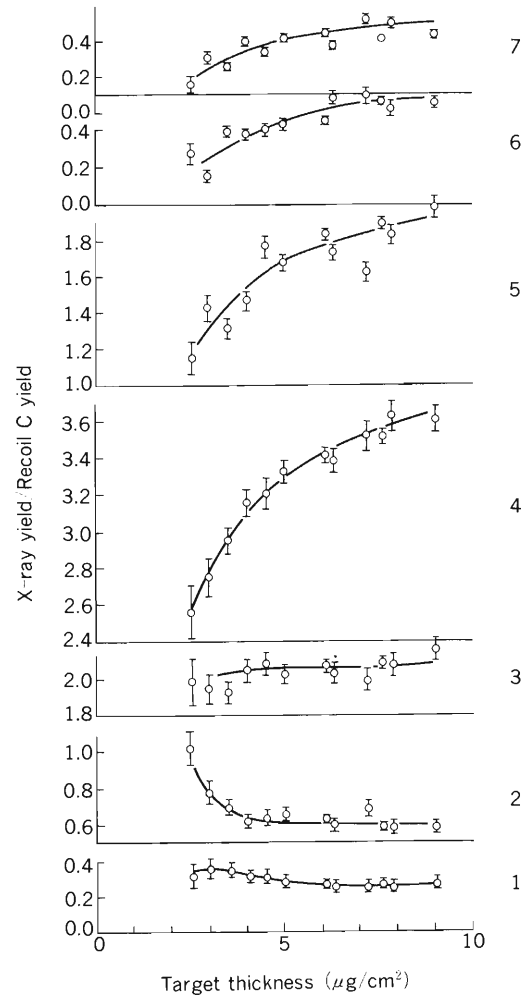

Fig. 3. Target thickness dependence of Kα satellite intensities. Error bars indicate statistical errors only. Solid lines are drawn only for eye-guide.

surement of the yield of recoil carbon using a surface-barrier detector (SBD) placed at 45° to the beam direction. Ions passed through the target foil are stripped again with a 20 $\mu g/cm^2$ carbon foil to be brought into charge equilibrium, and finally collected in a Faraday cup. The integrated Ar^{4+} flux can be determined from the electric current of the Faraday cup by using the well-established data of mean charge.[2] By combining these data with the recoiled-carbon yields, the target thicknesses are directly determined. A Si(Li) detector is also used as a monitor.

Here we report preliminary results. In Fig. 2, the spectra obtained by using the crystal spectrometer are shown for two different target thicknesses. The intensity of each satellite was determined by fitting a sum of 8 Gaussians to the obtained spectra. The results are summarized in Fig. 3, in which the vertical axis shows the intensity divided by the recoiled-carbon yield ("effective X-ray emission cross section" for each satellite). The satellites have not been assigned to electronic transitions yet, and the peaks are labeled 0-7 as shown in Fig. 2. From Fig. 3 it can be seen that the high-energy group of the satellites grows with an increase in target thickness, and the low-energy group tends to decrease. This is considered to be the effect of the increase in K-L excitation and K fluorescence yield due to the development of L-holes during the passage of Ar ions through carbon foils.

Further analysis and experiments are in progress.

References

1) A. Hitachi, H. Kumagai, and Y. Awaya: *Nucl. Instrum. Methods*, **195**, 631 (1982).
2) See for example, R. B. Clark, I. S. Grant, R. King, D. A. Eastham, and T. Joy: *Nucl. Instrum. Methods*, **133**, 17 (1976).

RIKEN Accel. Progr. Rep. 19 (1985)

III-2-14. Cu K X-Rays from Cu Ions on C Target and C Ions on Cu Target

Y. Awaya, T. Kambara, M. Kase, H. Shibata,
H. Kumagai, T. Mizogawa, Y. Kanai, and K. Shima

The ionized state of a target Cu atom excited by C ions and that of Cu projectile ions passing through a C foil target have been studied by high resolution measurements of Cu K X-rays at the same collision velocity. It is expected that the difference of average number of L-holes between Cu ions and Cu target atoms at the emission of K X-rays gives the information about the number of L-holes of Cu ions at a charge equilibrium state in the C foil. The preliminary results obtained with 0.83 MeV/amu projectiles were reported previously.[1] Here, we report the results of further studies carried at various collision energies.

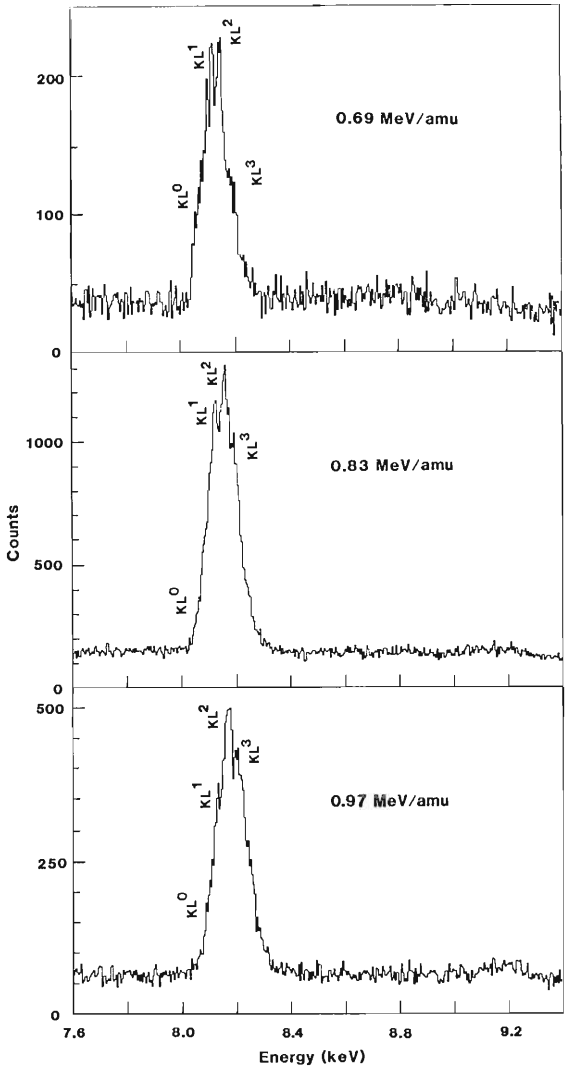

Fig. 1. Spectra of Cu K X-rays obtained from the Cu ions transversing in C target foil. Incident energies of Cu ions are given in the figure.

The experimental set-up was the same as that reported previously.[1] The Cu ions and C ions were accelerated by the linac. The incident energies were 0.69, 0.83, and 0.97 MeV/amu for both the ions and 1.60 MeV for C ions. The thickness of the target Cu foil was 0.22 mg/cm^2 and that of the C foil was 0.08 mg/cm^2. The Cu K X-rays were measured by using a broad-range X-ray crystal spectrometer[2] with a crystal of LiF(220) ($2d=2.848$ Å) placed at 90° with respect to the beam.

The spectra of Cu K X-rays obtained from 0.69, 0.83, and 0.97 MeV/amu Cu ions transversing the C foil and those of Cu target excited by 0.69, 0.83, 0.97, and 1.60 MeV/amu C ions are shown in Figs. 1 and 2. KL^n denotes the configuration of the initial state with single K and n-multiple L-holes for the transition.

The L-shell ionization probability of target Cu atoms accompanied by single K-shell ionization, P_L, was obtained assuming the binomial distribution of L-holes. The effect of rearrangement, which means that the L-hole is filled by an outer-shell electron prior to filling the K-hole, is taken into account for obtaining the relative ionization cross section of simultaneous single K and nL electrons, σ_{KL^n}, from the relative intensity of KL^n lines. The fluorescence yield for KL^n line is also estimated according to Larkin's statistical law[3] assuming that the M-holes are filled before emission of K X-rays because the electrons may easily be fed by the conduction band. The possibility of electron capture from neighbouring Cu atom by the L-hole of a recoiled Cu atom (bearing a K-hole) was estimated to be negligible prior to emission of K X-rays. P_L values thus obtained are shown by open circles in Fig. 3 as a function of $E/\lambda u_L$, where E is the incident energy of projectiles, λ is the mass of projectiles in electron mass unit, and u_L is the binding energy of L electrons. An average number of L-holes is given

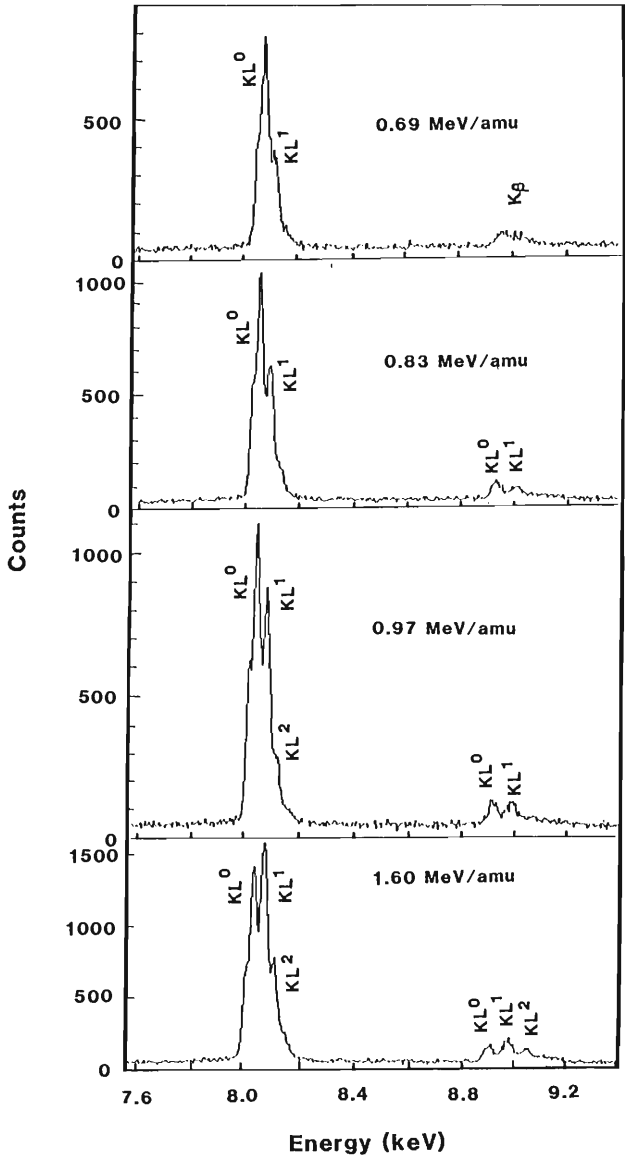

Fig. 2. Spectra of Cu K X-rays obtained from the target Cu foil induced by C-ion bombardment. Incident energies of C ions are given in the figure.

by $<l>\simeq 8\times P_L$. The $<l>$ values without any corrections, where KL^n is assumed to be equal to the relative intensity of KL^n line, are also shown in Fig. 3 by filled circles.

Concerning the Cu ions, the values corresponding to P_L of the target Cu atom are also obtained. The projectile Cu ions are considered to reach an equilibrium state as to L and M electrons after passing through first a few $\mu g/cm^2$ of C foil. The charge of Cu ions in equilibrium state at 0.69, 0.83, and 0.96 MeV/amu is 16.7+, 17.3+, and 18.1+, respectively.[4] There is a possibility that the Cu ions bear some L-holes prior to the collision which induces simultaneous single K and nL ionization.

The density of atoms in the target foil is so high that the successive distant collision with another C atom should be considered for a Cu ion which experienced a close collision to have a K-hole. In such a case the number of L-holes may change during persistence of K-hole due to the processes such as L electron loss, electron capture to L-hole, and L electron excitation. These effects are estimated from the calculated values of the L ionization cross section of Cu ions, the electron capture cross sections to the L-hole of Cu ions from C atoms, the excitation cross section of L electron of Cu ions to outer-shells, the density of C atoms in the foil, the mean life of the K-hole, and the velocity of Cu ions. The first two cross sections are estimated by the binary encounter approximation and Brinkman-Kramers formula. Since neither experimental data nor theoretical calculations for the excitation cross section of L electron to the outer-shell for Cu ions are available, Iwai *et al.*[5] have calculated the excitation cross section of $L_{2,3}$ electron to the M_1 orbit. As the results, it is preliminarily found that the no significant correction is required for the number of L-holes.

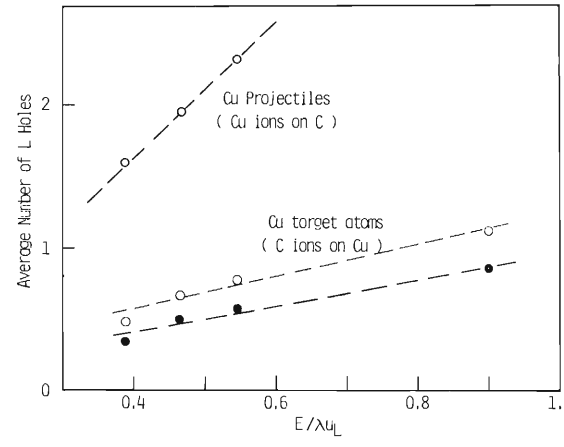

Fig. 3. Average number of L-holes of Cu ions and Cu target atoms. See text for open and filled circles for Cu target.

A constant value of fluorescence yield is assumed for KL^n lines is assumed because the Auger transition rate may be small for Cu ions. The obtained average number of L-holes $<l>$, where $<l>=\Sigma nf_n/\Sigma f_n$ and f_n is the relative intensity of KL^n line, are shown in Fig. 3.

The difference between the average number of L-holes and that of Cu ions and Cu atoms may be correspond to the number of L-holes carried by Cu ions transversing in C foil in the equilibrium state, that is, about one L-hole exists in Cu ions in average in the range of 0.67 to 0.97 MeV/amu.

References

1) Y. Awaya, T. Kambara, M. Kase, H. Shibata, H.

Kumagai, M. Nishida, and K. Shima: *RIKEN Accel. Progr. Rep.*, **18**, 75 (1984).
2) A. Hitachi, H. Kumagai, and Y. Awaya: *Nucl. Instrum. Methods*, **195**, 631 (1982).
3) F. P. Larkins: *J. Phys. B*, **4**, L29 (1971).
4) K. Shima, T. Ishihara, and T. Mikumo: *Nucl. Instrum. Methods*, **200**, 605 (1982).
5) M. Iwai, I. Shimamura, T. Watanabe, and Y. Awaya: p. 52 in this report.

RIKEN Accel. Progr. Rep. 19 (1985)

III-2-15. Measurement of Impact-Parameter Dependent Probabilities and Total Cross Sections for Target K-Shell Ionization by He Ions

R. Schuch, Y. Awaya, T. Kambara, T. Mizogawa,
H. Kumagai, Y. Kanai, K. Shima, and H. Shibata

Impact-parameter (b) dependence of target K-shell ionization probability ($P_K(b)$) in asymmetric collisions was measured up to large b above the Bohr K-shell radius. The energy of projectiles was 1 MeV/amu and the collision velocity was much lower than the Bohr K electron velocity in the targets of Ca, Cr, and Cu. It is expected that the description of initial K-shell states of target atoms changes from united atom (u.a.) description to separated atom (s.a.) one with increasing b and that this is reflected in the experimental results. Much emphasis was put in the accuracy of the value of $P_K(b)$.

The measurements were performed at the heavy-ion linac. A He^+ ion beam of 4.04 MeV was collimated to 1 mm×1 mm with a divergence of 0.02°. Particles scattered by the edge of slits were reduced to a negligible amount by using antiscattering collimators. The target material of Ca, Cr, and Cu was evaporated on a 2.5 $\mu g/cm^2$ C-foil and positioned at 45° relative to the beam axis. The characteristic K X-rays from the target atoms were detected by a 28 mm^2 Si(Li) detector at 90°, in a distance of 16.5 mm relative to the beam. In the forward scattering direction a parallel-plate avalanche counter (PPAC) at 193.5 cm distance from the target covered the laboratory angular region from 0.13° to 1.4°. The anode of the PPAC was divided into 16 rings with an angular resolution of $\Delta\theta/\theta = 0.05$ each. A coincidence circuit between the PPAC and the Si(Li) allowed to measure coincident K X-rays for all scattering angles simultaneously. The coincident events consisting of time, position, and X-ray energy were stored in list mode. The total number of particles per position was also measured and served as normalization for getting absolute K X-ray production probabilities.

For experiments of the total cross section (σ_K) a surface barrier detector with a slit aperture was mounted at 20°. The agreement of the beam axis with the geometrical axis of target chamber was verified independently. Stored X-ray signals and scattered particle spectra from the same runs allowed the determination of total K X-ray production cross sections.

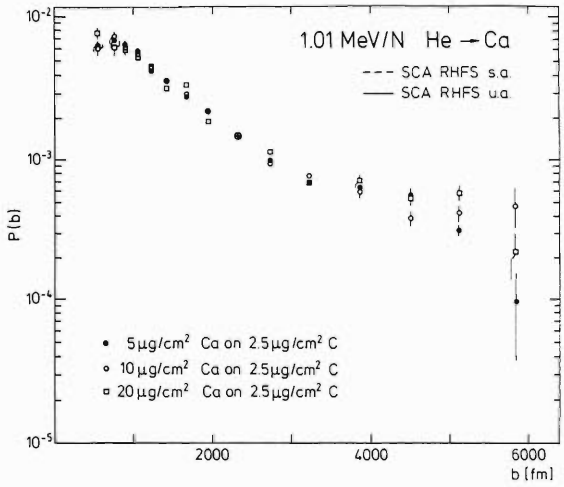

Fig. 1. K vacancy probability of Ca as a function of impact parameter at three different target thicknesses.

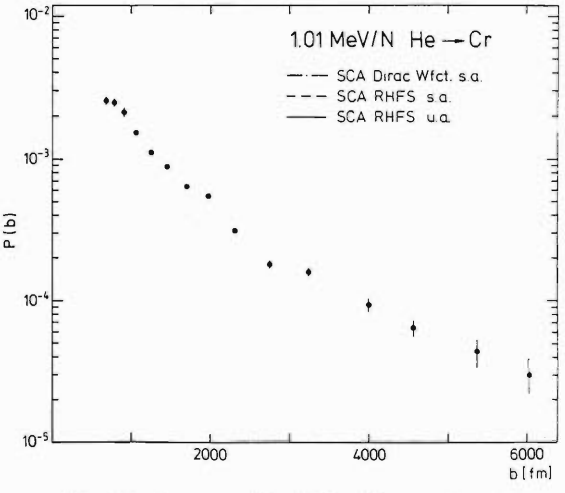

Fig. 2. Same as Fig. 1 for Cr as a target.

The target atom K X-ray production probabilities and total K X-ray ones were corrected with fluorescence yields for neutral atoms in order to obtain the values of $P_K(b)$. Here multiple ionization of the target atoms in collisions with He ions is assumed to be negligible. The error introduced by this assumption in $P_K(b)$ should be

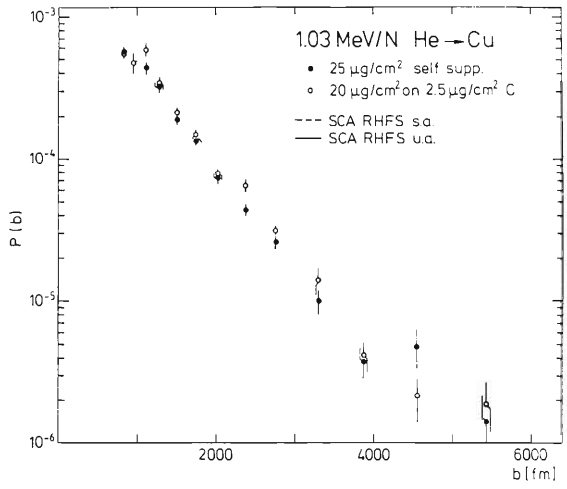

Fig. 3. Same as Fig. 1 for Cu as target.

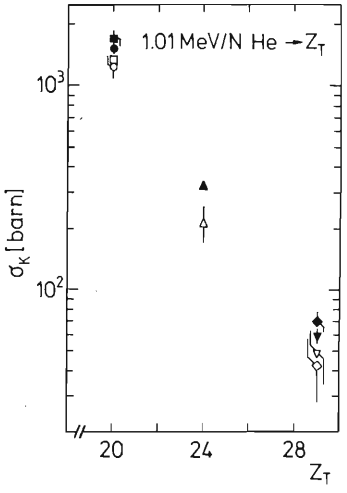

Fig. 4. Total cross sections for K vacancy production (σ_K) as a function of target nuclear charge (Z_T). Open symbols are from integration of $P_K(b)$, full symbols are from a direct measurement (see text).

less than 10%. The impact parameter b was obtained from the scattering angle by using a Bohr screened Coulomb potential.

In Figs. 1, 2, and 3 the values of $P(b)$ are shown for Ca, Cr, and Cu targets in collisions with 1.01 MeV/amu He ions. The error bars given are from statistical errors only. The probabilities of these different target nuclear charges have about the same shape as function of b. They indicate a flat behaviour up to 1,000 fm, show a steep fall off above and then a flat dependence again at $b>$ 3,000 fm. For finding the possible reason for this change in the shape at large b in multiple collisions, the measurements at three different Ca target thicknesses (20, 10, and 5 μg/cm^2) were made. The three sets of $P_K(b)$ agree very well within the error bars, which seems to indicate that multiple collisions are negligible. The contribution of particles scattered from the C backing alone was found to be a small correction.

Figure 4 shows the total cross section for K-shell ionization of the different target species. The target thickness corresponding to the different symbols are: circle and square are 5 and 20 μg/cm^2 Ca on 2.5 μg/cm^2 C, triangle is 15 μg/cm^2 Ca on 2.5 μg/cm^2 C, square and triangle are 25 μg/cm^2 Cu self supporting, and 20 μg/cm^2 Cu on 2.5 μg/cm^2 C.

There are two sets of data: the full symbols represent the direct measurements of σ_K and the open symbols show the results of $\sigma_K = 2\pi \int bP_K(b)db$ performed numerically with the data. The two sets of σ_K agree fairly well within the error bars also for the different target thicknesses. The reason for the σ_K from the integration of $P_K(b)$ being systematically below the direct measurement of σ_K could be an omission of the $P_K(b)$ above the measured b range.

The semi-classical-approximation calculation of $P(b)$ is in progress for the cases of the relativistic Hartree-Fock-Slater K wave function of united atom ($Z=Z_T+2$) and these of target atom ($Z=Z_T$).

RIKEN Accel. Progr. Rep. 19 (1985)

III-2-16. Data Analysis of Recoiled Ar Ions in the High Charge States by Means of a "Compound Atom" Model

A. Ohsaki,* T. Tonuma, H. Shibata, S. H. Be, H. Kumagai, M. Kase, T. Kambara, I. Kohno, and H. Tawara

The partial cross sections for production of slow recoil Ar^{i+} ions in 1.05 MeV/amu Ne^{q+} (q= 2, 7-10) and Ar^{q+} (q=4, 6, 10-14) ion impact have been determined[1] and compared with a "compound atom" model for high-charge state of ions and with a independent electron approximation (IEA) for low-charge state ions.

Recently Meron and Rosner have developed a "compound atom" model,[2] which essentially assumes that, during a close collision, some electrons of both projectile and target atoms, which are not altogether thrown out of the system, create a common structureless electron cloud, which is later redistributed between both atoms. The compound atom is initially composed of N_i electrons in the common cloud and N_f electrons at the final state remain in the cloud after some electrons are ejected. That is, N_i-N_f electrons are ejected before creation of a quasi-stable common cloud. We assume that no further ionization of electrons takes place before separation once the quasi-stable common electron cloud is formed. Then, N_f electrons are divided into N_1 and N_2 electrons, which are the average numbers of electrons captured by the projectiles with the nuclear charge Z_1 and the recoil ions with Z_2, respectively, namely:

$$N_f = N_1 + N_2 \tag{1}$$

According to this model, the probability $P_i^{N_f}$ that out of N_f electrons i electrons escape from the recoil atom is given by

$$P_i^{N_f} = \frac{\binom{N_f}{Z_2(u_c)-i}\binom{Z_1(u_c)+Z_2(u_c)-N_f}{i}}{\binom{Z_1(u_c)+Z_2(u_c)}{Z_2(u_c)}} \tag{2}$$

where $\binom{a}{b}$ denotes the binomial coefficient. $Z_1(u_c)$ and $Z_2(u_c)$ are the effective numbers of electrons of the projectile and the target atoms, respectively, involved in forming a common electron cloud whose velocity is smaller than a critical velocity u_c (Electrons with velocities larger than u_c behave like spectators. For the detailed definition and the notation, see Ref. 2). The sum of $P_i^{N_f}$ over i is unity; in other words, $P_i^{N_f}$ represents the probability that the recoil ions have the charge state i.

The caluculated parameters in this model in collisions of 1.05 MeV/amu Ne^{q+} and Ar^{q+} ions with an Ar target are given in Table 1. The initial number of electrons N_i in the common cloud is given by

$$N_i = Z_1(u_c)+Z_2(u_c)-q \tag{3}$$

where q is the projectile charge-state and the mean charge $<i>$ of the recoil ions is given by $<i>=Z_2(u_c)-N_2$. The fact that $Z_2(u_c)=16.35$ in the present case means that two electrons in the K-shell of Ar atom do not contribute significantly to composing the common electron cloud in the compound atom. In the process going from the initial number of electrons N_i to the final number of electrons N_f in the common

Table 1. Parameters calculated from the compound atom model in collisions of 1.05 MeV/amu Ne^{q+} and Ar^{q+} ion impact with Ar target. N_i and N_f are the initial and the final numbers of electrons in the common electron cloud. N_1 and N_2 are the average numbers of electrons redistributed into the projectile and the recoil ion from N_f. The mean charge of the recoil ions, $<i>$, is given by $<i>=Z_2(u_c)-N_2$. $Z_1(u_c)$ and $Z_2(u_c)$ are the effective numbers of electrons in the projectile and the target atom contributing to forming a common electron cloud. For the detailed description of the parameters, see Ref. 2.

	q	N_i	N_f	N_1	N_2	$<i>$
Ne^{q+} ion impact	2	23.9	16.7	6.2	10.5	5.9
$Z_1(u_c)=9.55$	7	18.9	15.0	5.5	9.5	6.9
$Z_2(u_c)=16.35$	8	17.9	14.5	5.3	9.2	7.2
	9	16.9	14.0	5.2	8.8	7.6
	10	15.9	13.5	5.0	8.5	7.9
Ar^{q+} ion impact	4	28.7	18.6	9.3	9.3	7.1
$Z_1(u_c)=Z_2(u_c)$	6	26.7	18.1	9.1	9.1	7.3
$=16.35$	10	22.7	16.8	8.4	8.4	8.0
	11	21.7	16.5	8.3	8.3	8.1
	12	20.7	16.1	8.1	8.1	8.3
	13	19.7	15.6	7.8	7.8	8.6
	14	18.7	15.1	7.6	7.6	8.8

* Institute for Molecular Science.

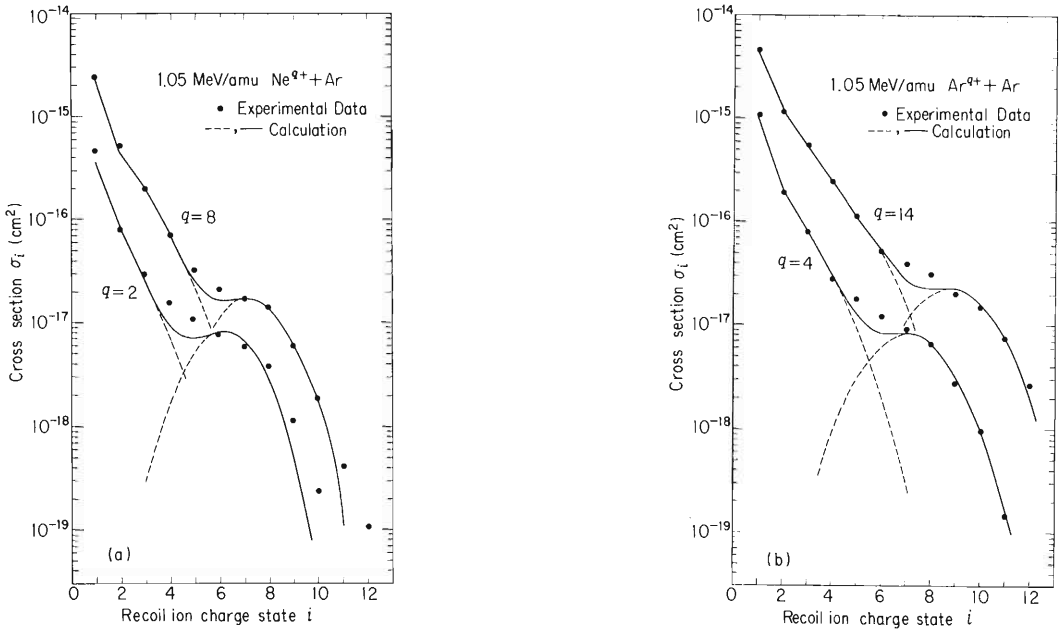

Fig. 1. (a) Partial ionization cross-sections of recoil Ar ions in collisions of 1.05 MeV/amu Ne^{q+} ($q=2$ and 8) ions with Ar atoms as a function of the recoil-ion charge-state i. Filled points give experimental data. Broken lines on the right-hand side represent the charge-state distribution calculated from the compound atom model, where the peak values of the distribution are adjusted on the basis of the experimental data. Broken lines on the left-hand side represent the calculations using the IEA model. The solid lines represent the sums of calculations from IEA and from compound atom model. (b) Partial ionization cross-sections of recoil Ar ions in 1.05 MeV/amu Ar^{q+} ($q=4$ and 14) ions on Ar atoms against the recoil-ion charge-state i. Other explanations are the same as in (a).

cloud, (N_f-N_i) electrons are ejected. The number of electrons ejected in this process decreases with increasing projectile charge state q as indicated in Table 1. The mean charge $<i>$ of recoil Ar ions clearly increase with increasing projectile charge q. The dependence of $<i>$ on the projectile charge-state q is slightly different between Ne^{q+} and Ar^{q+} ion impact, however.

To the data analysis of the low-charge state recoil Ar^{i+} ions, we applied the independent electron approximation (IEA) which assumes binomial statistics to be valid for multiple ionization.[3),4)] (The procedure of data fitting is not described here.)

The charge-state distributions of recoil Ar ions obtained from Eqn. (2) are shown in Fig. 1 (a) and (b), in which the peak values are adjusted to fit the experimental data. The solid lines represent the sums of IEA and compound atom model calculations. Figure 1 shows that the distributions are very similar to Gaussian and the mean charges of the distribution increase with increasing projectile charge-state q. The calculated charge-state distributions for Ar^{q+} ion impact reproduce the experimental data somewhat better than those for Ne^{q+} ion impact. In fact, the deviation in Ne^{q+} ion impact is clearly observed at high-charge states, suggesting that this model is more effective for relatively symmetric collision systems having similar numbers of electrons in both projectile and target atoms. Therefore, it is concluded that, though the charge-state distribution of the recoil ions is underestimated from the compound atom model for low Z projectiles, this model can generally reproduce the experimental data on the charge distribution at high charges.

References

1) T. Tonuma, H. Shibata, S. H. Be, H. Kumagai, M. Kase, T. Kambara, I. Kohno, and H. Tawara: *Atomic Collision Res. in Japan—Progr. Rep.*, No. 11, 84 (1985).
2) M.Meron and B. Rosner: *Phys. Rev. A*, **30**, 132 (1984).
3) J. H. McGuire and L. Weaver: *Phys. Rev. A*, **16**, 41 (1977).
4) P. H. Mokler and H. D. Lissen: Progress in Atomic Spectroscopy, Part C, (ed. by H. F. Berger and H. Kleinpoppen), Plenum Press, New York, p. 321 (1983).

RIKEN Accel. Progr. Rep. 19 (1985)

III-2-17. Highly-Charged Carbon Ions Produced from Carbon-Containing Molecules in Collisions with Energetic Heavy Ions

H. Shibata, T. Tonuma, K. Baba,* S. H. Be, H. Kumagai, M. Kase, T. Kambara, I. Kohno, and H. Tawara

In a previous Progress Report, we presented some results on the observation of multiply-charged, secondary nitrogen ions (N^{i+}) up to $i=7$ from N_2 molecular targets in 1.05 MeV/amu Ar^{4+} and Ar^{12+} ion impact.[1] It has been found in subsequent work that these N^{i+} ions have the initial energies slightly larger than those for single atom targets such as Ar^{i+} and this energy difference increases with increasing the charge (i) of secondary ions. The observed shift in the initial energies of multiply-charged atomic ions, compared with those of molecular target, was in agreement with the calculated values under the assumption that these energies are provided through the Coulomb potential energies between the dissociating ions when multiply-charged molecular ions are dissociated.

Some measurements of total ionization cross sections for hydrocarbon molecules were reported, but very few data of partial ionization cross sections are available, though relative production rates for various ions including singly and at most doubly-charged molecular ions ($C_mH_n^{i+}$) and singly-charged carbon (C^+) ions from some carbon-containing molecules were measured. Up to now, no systematic studies have been made for production of multiply-charged ions. In these ionization processes of molecules, dominant, singly-charged and sometimes relatively weak, doubly-charged parent molecular ions are produced through direct ionization processes, meanwhile most of other observed ions are believed to be produced through dissociative ionization processes of the parent molecular ions. In many cases, the doubly-charged parent molecular ions have short life-times. Therefore, their observed intensities are very low, usually only 1-2 % of those of the singly-charged parent molecular ions, as discussed previously.[2]

In order to understand the production mechanisms of multiply-charged atomic ions from molecular targets, we have used a mass-spectroscopic technique to separate various ions

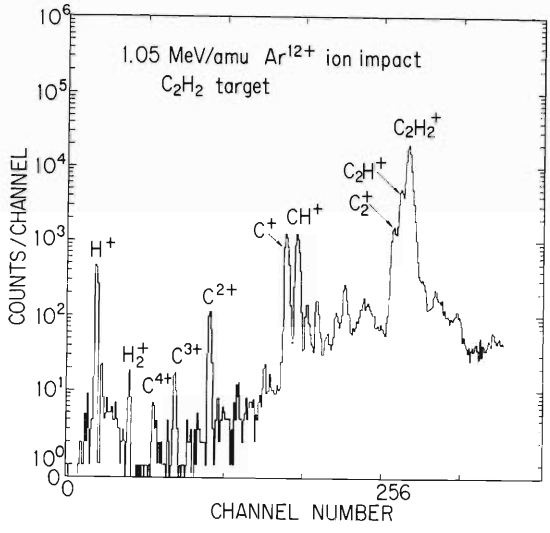

Fig. 1. A typical mass-charge spectrum of ions produced from C_2H_2 molecules in 1.05 MeV/amu Ar^{12+} ion impact.

from CH_4 and C_2H_2 molecules produced by 1.05 MeV/amu Ar^{12+} ion impact obtained from the RIKEN linear accelerator. The produced secondary ions are extracted under the influence of a relatively weak electric field (~40 V/cm), accelerated up to 500 V, and then mass-charge-energy analyzed with a double focusing magnet.[2] A typical mass-charge spectrum of the ions from the C_2H_2 molecular target is shown in Fig. 1, which shows the formation of singly- and multiply-charged carbon ions (C^{i+}) up to $i=5$, in addition to dominant singly-charged parent molecular ions ($C_2H_2^+$) and other molecular ions such as C_2H^+, CH^+, and C_2^+ ions which originate in dissociative ionization. A similar observation for CH_4 targets has also been made. It is found from comparison that production of multiply-charged carbon ions, relative to singly-charged parent molecular ions, is by a factor of about 3, or sometimes one order of magnitude, higher in CH_4 targets than in C_2H_2 targets, even though a C_2H_2 molecule has twice the number of carbon atoms in a CH_4 molecule.

For the elucidation of this difference, compari-

* ULVAC Corporation.

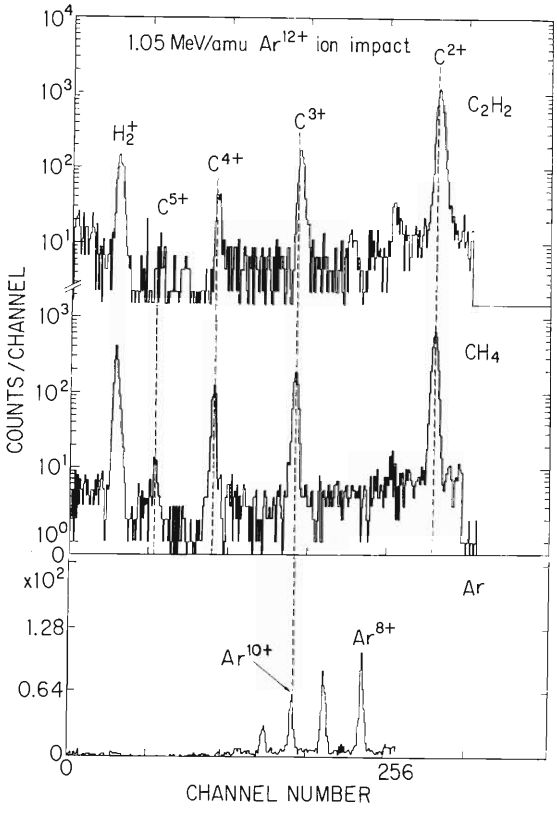

Fig. 2. Comparison of spectra of multiply-charged carbon ions produced from C_2H_2, CH_4, and Ar targets in 1.05 MeV/amu Ar^{12+} ion impact.

son is shown in Fig. 2 of spectra for C^{i+} ions with $i=2$-5 and H_2^+ ions from C_2H_2 and CH_4 molecular targets as well as for Ar^{i+} ions from atomic Ar targets. Though the present analyzing system has no sufficient energy resolution, we can observe slight shifts of the peak positions for these multiply-charged carbon ions from C_2H_2 targets, compared with those from CH_4 targets. It should be noted that the peak position of C^{3+} ions from CH_4 targets coincides with that of Ar^{10+} (both having $m/e=4$). This indicates that the energies of both C^{3+} and Ar^{10+} ions are practically identical within the limit of energy resolution of the present system, though both ions have different origins: Ar^{10+} ions are produced through direct multiple ionization, whereas C^{3+} ions are through dissociative ionization of multiply-charged molecular ions. In the CH_4 targets, the potential energy due to this Coulomb force in multiply-charged molecular ions is parted among the dissociating ions and most of the energy are carried away by four light partner ions (H^+). Then, the energy obtained by carbon ions should be relatively small. By taking into account that carbon in CH_4 molecule stays in the middle of the surrounding hydrogen atoms, the total energy of carbon ions from CH_4 molecules should not be significantly different from the energy obtained in the recoil process, as observed in Fig. 2.

The situation seems to be different in C_2H_2 molecules, where multiply-charged carbon ions are produced through the dissociation of multiply-charged molecular ions having two multiply-charged carbon ions. As discussed in the previous paper,[2] the dissociation processes are relatively slow, compared with the direct ionization processes resulting in the production of multiply-charged molecular ions. Therefore, in C_2H_2 molecules, the dissociation of multiply-charged molecular ions ($C_2H_2^{j+}$) plays a role in the production of multiply-charged carbon ions. In these dissociation processes, $C_2H_2^{j+}$ ions first dissociate into two ions with relatively symmetric charge, both of which obtain relatively large kinetic energies due to Coulomb explosion proportional to j^2, and finally into C^{i+} ions plus H^+ ions. Therefore, the initial kinetic energies due to the Coulomb explosion should be large in C_2H_2 molecules than in CH_4 molecules. This fact can be seen from Fig. 2, where the peak positions of multiply-charged carbon ions in C_2H_2 molecules systematically shift toward the high energy side.

It is concluded from the present work that the production rate of multiply-charged carbon ions seems to be higher in CH_4 molecules than in C_2H_2 and the initial kinetic energies of these carbon ions are generally higher in C_2H_2 molecules than in CH_4 molecules: this can be understood to be due to the Coulomb explosion mechanism. Similar measurements for CO and CO_2 molecular targets are under way.

References

1) H. Tawara, T. Tonuma, S. H. Be, H. Shibata, H. Kumagai, M. Kase, T. Kambara, and I. Kohno: *RIKEN Accel. Progr. Rep.*, **18**, 82 (1984).
2) H. Tawara, T. Tonuma, H. Shibata, M. Kase, T. Kambara, S. H. Be, H. Kumagai, and I. Kohno: to be published in *Phys. Rev. A*, **33**, 1385 (1986).

RIKEN Accel. Progr. Rep. 19 (1985)

III-2-18. Projectile Dependence of Ar-LMM Auger Electrons Ejected from Ar Target by Heavy-Ion Impact (II)

H. Shibata, T. Matsuo, Y. Kanai, Y. Awaya,
T. Kambara, M. Kase, H. Kumagai, and N. Tokoro

We have measured the energy spectra of ejected electrons in heavy ion-Ar collisions in order to obtain detailed information on energy levels of highly ionized atoms and their production mechanism. The spectra of the L_{23}-MM Auger electrons ejected from the Ar target by about 1 MeV/amu He, C, N, Ne, Al, and Ar ion bombardment have been measured at an ejected angle of 135° with respect to the ion-beam direction. The projectile ions were accelerated with the RILAC. The experimental apparatus, conditions, and some results have been reported previously.[1),2)] Examples of the ejected electron spectra obtained are shown in Fig. 1. These spectra are

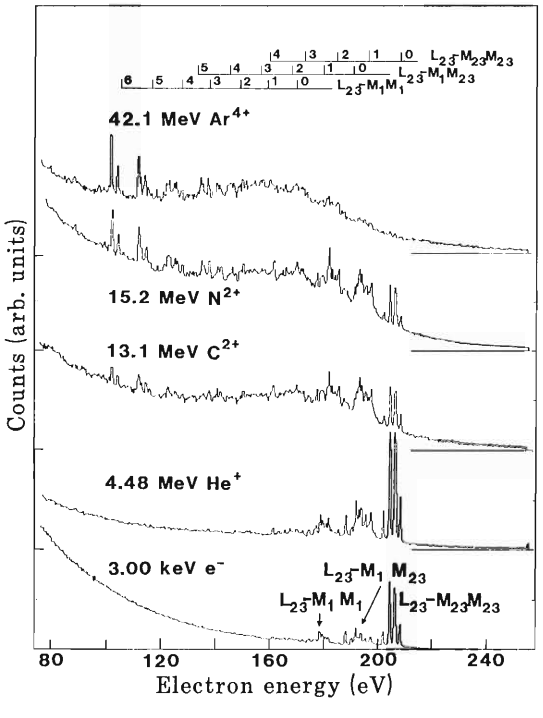

Fig. 1. Energy spectra of electrons ejected from target argon at 135° from the beam direction by about 1 MeV/amu He^+, C^{2+}, N^{2+}, and Ar^{4+} ion impacts and that by 3 keV electron impact. The lines above spectra indicate the calculated energy values for the corresponding transitions denoted on their right hand side. The number on each line shows the number of 3p vacancy in the initial state of Auger transition.

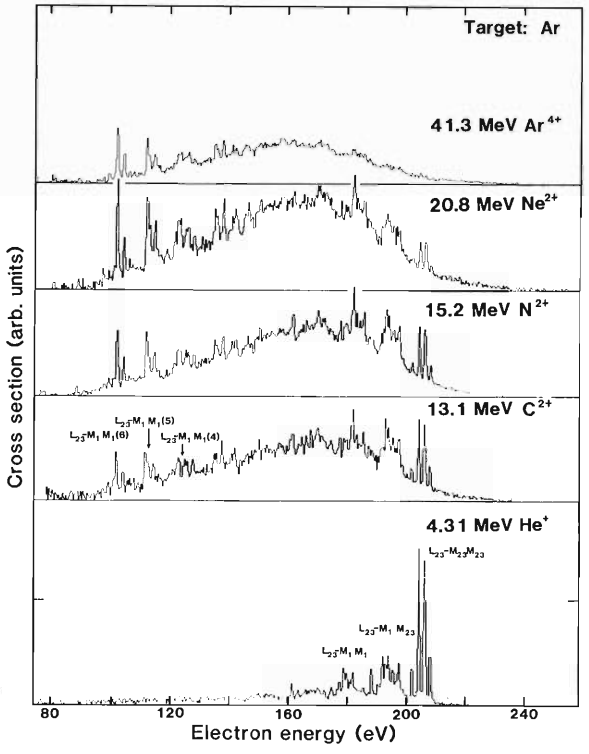

Fig. 2. Ar L-shell Auger spectra produced by about 1 MeV/amu He^+, C^{2+}, N^{2+}, Ne^{2+}, and Ar^{4+} ion impacts. The continuous background estimated by the function Ae^{-BE} is subtracted. The number in the parenthesis for the L-MM notation indicates the number of 3p vacancy in the initial state of Auger transition.

characterized by a continuous background and a complicated Auger structure superimposed on the continuous background resulting from the direct ionization process. The pattern of the continuous background is evaluated assuming an exponential form of Ae^{-BE}, since this form well reproduces the features of the lower and higher energy wings of the measured spectra, where A and B are fitting parameters and E the ejected electron energy. Each spectrum was normalized to the same target pressure and charge of the projectile, and the continuous background was subtracted from each ejected electron spectrum to compare the Auger structure and the yield

obtained with the different projectile. Such a comparison of the Auger spectra is shown in Fig. 2 for about 1 MeV/amu He^{+}, C^{2+}, N^{2+}, Ne^{2+}, and Ar^{4+} ion bombardments.

The following features are seen from Fig. 2.

1) Intensities of normal Auger lines, L_{23}-$M_{23}M_{23}$, L_{23}-M_1M_{23}, and L_{23}-M_1M_1, weaken as the atomic number Z of the projectile increases and become negligible small for Ar^{4+} impact.

2) The cross sections of satellite Auger lines from the charge states of 7+, 6+, and 5+ of Ar enhance as the Z of projectile increases except for Ar^{4+}.

3) The total yield of L-shell Auger electrons increases as the atomic number of projectile of the same charge state increases.

Further analysis is in progress.

References

1) T. Matsuo, H. Shibata, J. Urakawa, A. Yagishita, Y. Awaya, T. Kambara, M. Kase, H. Kumagai, and J. Takahashi: *RIKEN Accel. Progr. Rep.*, **17**, 65 (1983).
2) H. Shibata, T. Matsuo, Y. Awaya, T. Kambara, M. Kase, H. Kumagai, and N. Tokoro: *RIKEN Accel. Progr. Rep.*, **18**, 84 (1984).

RIKEN Accel. Progr. Rep. 19 (1985)

III-2-19. Projectile Dependence of Energy Distribution of Secondary Electrons from Al

A. Koyama, O. Benka, Y. Sasa, and M. Uda

Energy distributions of secondary electrons (SEs) from Al induced by heavy ion impact were measured with a UHV system. The apparatus was described in a previous report.[1] Ions used in the present study were He^+, He^{2+}, N^{2+}, N^{6+}, Ne^{2+}, Ne^{8+}, Ar^{4+}, and Ar^{12+} with the same velocity (1.1 MeV/amu) accelerated by the IPCR linear accelerator. The measuring conditions were almost the same as those for previous one.[2]

Figure 1 (a) shows energy distributions of SEs from Al induced by He^{2+} and Ar^{12+} impact, and Fig. 1 (b) shows the ratio of these two distributions, $R_{He,Ar}(E)=Y_{He^{2+}}(E)/Y_{Ar^{12+}}(E)$, where Y is the yield of SEs per projectile, and E is SE's energy. In the energy region from 20 to 70 eV, the ratios are nearly equal to those of the stopping powers for these two projectiles. That is, the ratios are explained in terms of the stopping power scaling in this energy region of SEs. However, a prominent reduction of $Y_{Ar^{12+}}(E)$ is observed compared with $Y_{He^{2+}}(E)$ in the lower energy region, as seen from the steep increase in $R_{He,Ar}(E)$ in the energy region below 20 eV. It is well known that total yields of SEs induced by light projectiles are propotional to the stopping power for the projectiles. Thus the emission yields of low energy SEs induced by projectiles with high electric charges are considered to decrease compared with the stopping power scal-

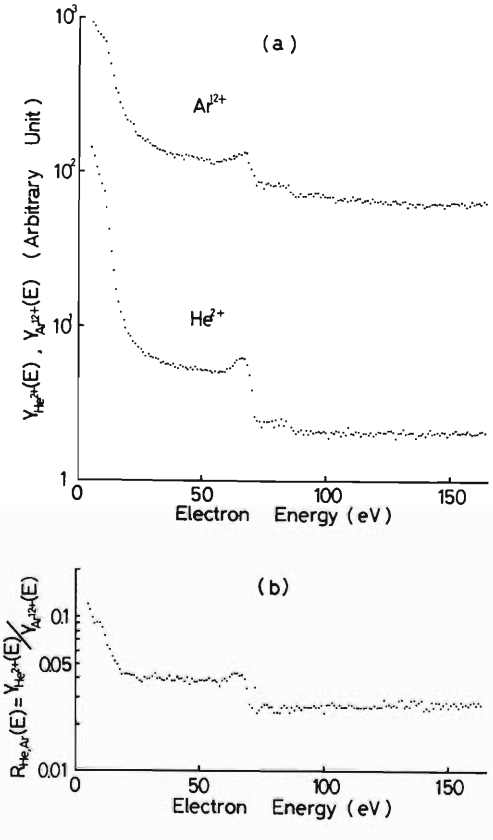

Fig. 1. Energy spectra of SEs induced by the impact of He^{2+} and Ar^{12+} with the same velocity (1.1 MeV/amu): (a) yields of SEs for both projectiles, $Y_{He^{2+}}(E)$ and $Y_{Ar^{12+}}(E)$. (b) ratio of the yields for He^{2+} and Ar^{12+}, $R_{He,Ar}(E)=Y_{He^{2+}}(E)/Y_{Ar^{12+}}(E)$.

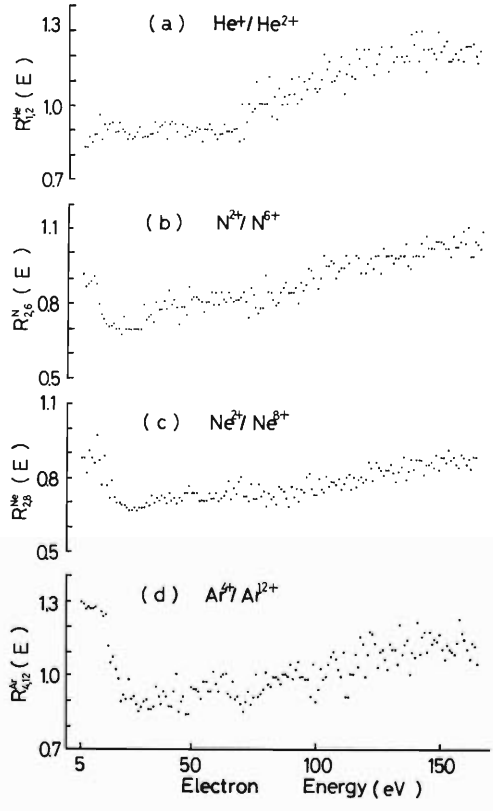

Fig. 2. Ratios of yields for projectiles with the same atomic number, but with different electric charges: (a) for He^+ and He^{2+}, $R^{He}_{1,2}(E)=Y_{He^+}(E)/Y_{He^{2+}}(E)$, (b) for N^{2+} and N^{6+}, $R^{N}_{2,6}(E)=Y_{N^{2+}}(E)/Y_{N^{6+}}(E)$, (c) for Ne^{2+} and Ne^{8+}, $R^{Ne}_{2,8}(E)=Y_{Ne^{2+}}(E)/Y_{Ne^{8+}}(E)$, (d) for Ar^{4+} and Ar^{12+}, $R^{Ar}_{4,12}(E)=Y_{Ar^{4+}}(E)/Y_{Ar^{12+}}(E)$.

ing.

Figure 2 shows the ratios of yields of SEs for projectiles with the same atomic number, but with different electric charges:

(a) for He^+ and He^{2+},
$R^{He}_{1,2}(E) = Y_{He^+}(E)/Y_{He^{2+}}(E)$;

(b) for N^{2+} and N^{6+},
$R^{N}_{2,6}(E) = Y_{N^{2+}}(E)/Y_{N^{6+}}(E)$;

(c) for Ne^{2+} and Ne^{8+},
$R^{Ne}_{2,8}(E) = Y_{Ne^{2+}}(E)/Y_{Ne^{8+}}(E)$;

(d) for Ar^{4+} and Ar^{12+},
$R^{Ar}_{4,12}(E) = Y_{Ar^{4+}}(E)/Y_{Ar^{12+}}(E)$.

The ratios $R^{He}_{1,2}(E)$ is almost constant and equal to 0.9 in the energy region below 70 eV. Above 70 eV, it increases with E and becomes larger than unity above 100 eV. The values larger than unity are due to backscattered loss-electrons stripped from He^+. Ratios between yields for heavier projectiles also show the shapes similar to that of the ratio for He^+ and He^{2+} in the energy region above 20 eV. However clear humps similar to that seen in Fig. 1 (b) appear in the energy region below 20 eV. The height and width of the humps increase from (b) to (d). The appearance of these humps is due to the large magnitude of the reduction in the yields for the projectiles with high electric charges compared with that for those with low electric charges.

From Figs. 1 and 2, it is concluded that the reduction of the emission yield of low energy SEs compared with the stopping power scaling occurs very generally for the impact of fast projectiles with high electric charges. This reduction is considered to be caused by the effect of dense excitation of target electrons.

References

1) A. Koyama, Y. Sasa, Y. Ishibe, A. Shiraishi, T. Shiga, H. Omori, K. Nishi, M. Fuse, and M. Uda: *RIKEN Accel. Progr. Rep.*, **17**, 122 (1983).
2) A. Koyama, Y. Sasa, and M. Uda: *RIKEN Accel. Progr. Rep.*, **18**, 86 (1984).

RIKEN Accel. Progr. Rep. 19 (1985)

III-2-20. Chemical Effects on LVV Auger Spectra of Al and Mg

M. Uda, A. Koyama, O. Benka, and Y. Sasa

Low energy Auger peaks are frequently superimposed on a very high background composed of secondary and backscattered electrons. In order to produce well-resolved and intense Auger lines, an intense electron source is preferably used but it often leads to the decomposition and desorption of the surface layer.[1] Accelerated ions produce much higher ionization cross sections than that of electrons. Measurements of Auger spectra can be performed within a short period of time by the use of fast ions. This technique also provides the advantage of reducing the surface contamination during observation.

In seeking to enhance chemical-bond effects, the low-energy Auger peaks of Al and AlF_3, and Mg and oxygen adsorbed or oxidized Mg were measured, which are characterized by the transitions between valence bands and shallow inner-shells. Electron excited spectra were compared with those excited by fast ions for these chemical compounds.

Fast ions of He^{2+} and Ar^{4+} with the same velocity ($v^2/2=1.14$ MeV/amu) were accelerated by use of the Linac. The beam spot on the target (1 mm in diameter) was defined by a slit, which was located 10 cm in front of the target. The energy analyzed electrons were detected by the Channeltron. The output signals were amplified and accumulated by a multichannel scaler. Each channel was open for the same amount of integrated beam charge on the target. 3 keV electrons were also used for the excitation of secondary and Auger electrons whose spectra were compared with those excited by fast ions. Time necessary to measure each spectrum was restricted within 2 h to prevent surface oxidation and contamination on the target during the measurement because under these conditions a pure Al surface was covered with a monolayer of contaminated carbon after 25 h, corresponding to 0.1 monolayers after 2 h of the experiment.

In Fig. 1 Mg LVV Auger electron spectra are shown for a pure Mg metal and oxidized magnesium which were excited by 3 keV electrons. Here the targets were biased to +4.5 V. Surface oxidation was carried out in 1×10^{-7} Torr O_2 for 500 s (50 L, L; Langmuir) and 1×10^{-6} Torr O_2 for 200 s (200 L), respectively. Peaks 3 and 4 are ascribed to normal Mg $L_{2,3}VV$ transitions and its bulk plasmon losses, respectively.[1)-3)] Peak 2 originated from doubly ionized Mg with two vacancies in the Mg $L_{2,3}$ shells, *i.e.*, a hypersatellite. When oxidation proceeds, peaks 2 and 3 become weak but peak 4 was enhanced as can be seen in Fig. 1. Peak 4 is composed of metal plasmon loss electrons superposed on Mg $L_{2,3}VV$ electrons of MgO,[3)] because the difference of energies for these peaks is only 1 eV. The shift of the Mg $L_{2,3}VV$ main peak to a lower-energy side

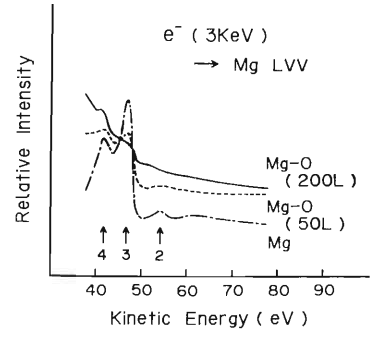

Fig. 1. Mg LVV spectra induced by 3 keV electrons for Mg metal and Mg exposed to pure oxygen for 50 and 200 Langmuirs, respectively. For the peak assignment, see the text.

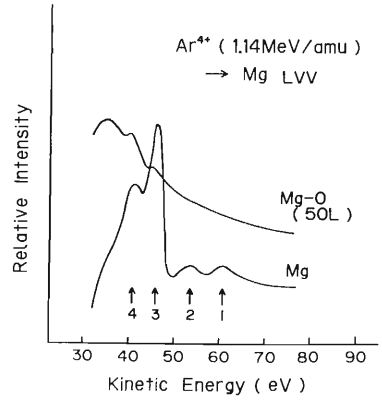

Fig. 2. Ar^{4+} (1.14 MeV/amu) induced Mg LVV spectra for Mg metal and Mg exposed to pure oxygen for 50 Langmuirs.

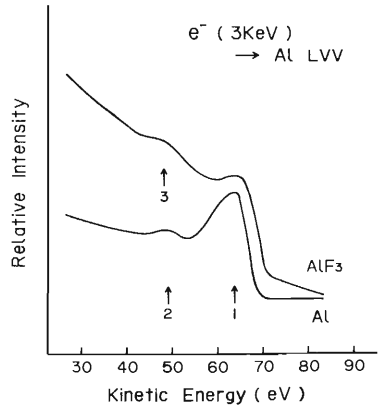

Fig. 3. Al LVV spectra induced by 3 keV electrons for Al and AlF_3. For the peak assignment see the text.

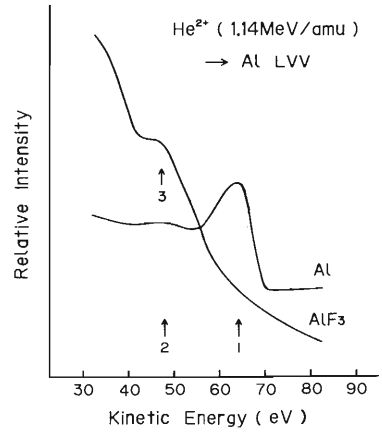

Fig. 4. He^{2+} (1.14 MeV/amu) induced Al LVV spectra for Al and AlF_3.

from that of Mg metal to its oxide is caused by the increase in binding energy of the outermost electrons in Mg when it is oxidized.

Ar^{4+} (1.14 MeV/amu) excited Mg LVV spectra are shown in Fig. 2. A bias potential of +4.5 V was applied to the targets. Peak 1 is assigned to the transition from the initial state with three $L_{2,3}$ vacancies, *i.e.*, a hypersatellite. Peaks 2-4 are common to those in Fig. 1. Peak 1 is more pronounced in Ar^{4+} excitation than in electron excitation. Such a tendency can be explained from the larger ionization cross section for the former than that for the latter. A chemical effect can clearly be seen in the Ar^{4+} excited Auger and secondary electron emission spectra in the kinetic energy region below 40 eV.

Electron excited Al LVV spectra are shown in Fig. 3. A bias voltage of +4.5 V was also applied to the targets. Peaks 1 and 2 are assigned to Al $L_{2,3}VV$ and its bulk plasmon loss. Peak 3 is assumed to be Al $L_{2,3}VV$ emitted from AlF_3, the kinetic energy of which is 2-3 eV lower than that of peak 2. Such a peak assignment was performed by analogy with Auger peaks from Al_2O_3 and MgF_2.[1] Figure 4 shows Al LVV spectra induced by He^{2+} (1.14 MeV/amu) ions. Low energy electrons were returned to the targets by applying +4.5 V. A difference in spectral shape between Al and AlF_3 was much more pronounced in He^{2+} than in electron excited spectra.

The ionization cross sections produced by the fast ions used here are much higher than those produced by electrons. Therefore, surface damage or decomposition, as can be seen in Figs. 1 and 3, during the observation of Auger spectra can be minimized by adopting a shorter measuring time, which also serve to prevent surface contamination. In view of decomposition or desorption, the fast ion excitation is of great advantage over the electron excitation in Auger electron spectroscopy.

References

1) P. H. Citrin, J. E. Rowe, and S. B. Christman: *Phys. Rev. B*, **14**, 2642 (1976).
2) M. Suleman and E. B. Pattinson: *Surf. Sci.*, **35**, 75 (1973).
3) A. P. Jansen, R. C. Shoonmaker, and A. Chambers: *Surf. Sci.*, **47**, 41 (1975).

RIKEN Accel. Progr. Rep. 19 (1985)

III-2-21. Emission Mössbauer Study of ^{151}Gd Adsorbed on YIG

T. Okada, S. Ambe, F. Ambe, and H. Sekizawa

In previous papers,[1),2)] we showed that emission Mössbauer measurement was useful in elucidating the magnetic properties and the chemical states of dilute metal ions adsorbed on magnetic metal-oxide surfaces. The present paper aims to clarify the magnetic and chemical states of dilute trivalent europium ions arising from EC decay of $^{151}Gd^{3+}$ hydrolytically adsorbed on the surfaces of magnetic oxides by means of the same emission Mössbauer technique as we reported.[1)] In the actual work, emission Mössbauer spectroscopy of ^{151}Eu with ^{151}Gd as the source nuclide has been applied to non-carrier-added trivalent gadolinium ion hydrolytically adsorbed on the surfaces of yttrium iron garnet (YIG) (Néel temperature: 545 K). In the measurement, Mössbauer analysis was made on the 21.5 keV γ-rays emitted by ^{151}Eu nuclei in the first excited state (^{151}Eu*, half-life: 9.7 ns) arising from EC decay of ^{151}Gd (half-life: 120 days) (Fig. 1).

The YIG ($Y_3Fe_5O_{12}$) has the garnet type structure. Yttrium or rare earth metal ions occupy the dodecahedral sites of the garnet. The trivalent europium ions are diamagnetic for the ground state with $J=0$. In garnets, however, they are magnetic because of the second order Zeeman contribution of the nondiagonal elements connecting $J=0$ to $J=1$. The magnetization of Eu^{3+} in garnets is proportional to the applied magnetic field and the exchange field arising from the neighbouring magnetic ions. Therefore, the hyperfine magnetic field at Eu^{3+} nuclei in europium iron garnet ($Eu_3Fe_5O_{12}$: EuIG) has a large value of 343 kOe at 296 K. We can obtain information not only on europium ions but also on the magnetic ions around them through the hyperfine magnetic field.

The Eu_2O_3 powder was irradiated to about 3 mC with 16 MeV protons accelerated by the cyclotron. The irradiated Eu_2O_3 (^{151}Gd) was dissolved in conc. HCl. After evaporation, the residue was dissolved in a small amount of distilled water. The solution was put on the top of a column of a cation exchanger washed with 0.4 mol dm^{-3} α-hydroxyisobutylic acid (α-HIBA) solution of pH 3.9. With the α-HIBA solution $^{151}Gd^{3+}$ was eluted at first and collected. The α-HIBA chelating agents in the $^{151}Gd^{3+}$ fraction were removed by means of the cation exchanger resin. Non-carrier-added $^{151}Gd^{3+}$ was obtained in dilute HCl solution free from the chelating agent. The ^{151}Gd ion was adsorbed on YIG powder. Their emission Mössbauer spectra were recorded at 298, 78, and 5 K with a conventional spectrometer in an absorber-drive mode.

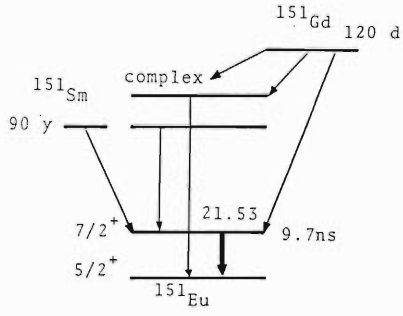

Fig. 1. Decay scheme of ^{151}Eu.

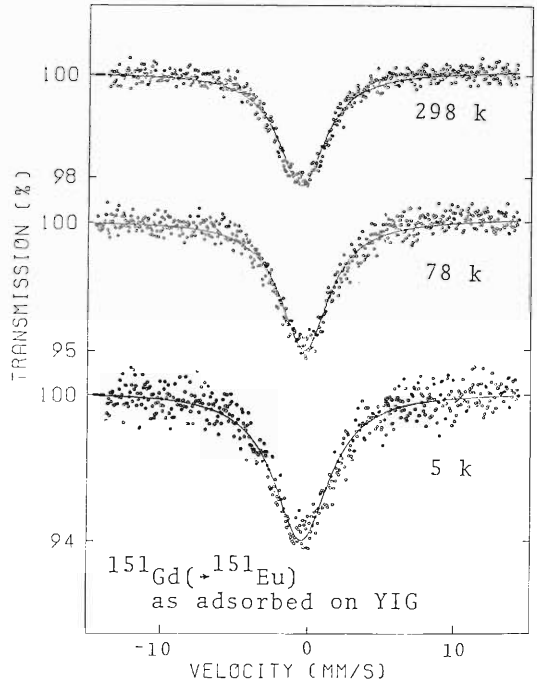

Fig. 2. Emission Mössbauer spectra of ^{151}Gd(→ ^{151}Eu) adsorbed on the surfaces of YIG at 298, 78, and 5 K.

The absorber of enriched $^{151}Eu_2O_3$(15 mg ^{151}Eu/cm^2) was used. The 21.5 keV γ-rays were measured with a Si(Li) detector.

Emission Mössbauer spectra of $^{151}Gd(\rightarrow^{151}Eu)$ adsorbed on YIG are shown in Fig. 2. The spectra were fitted with a Lorentzian line. As can be seen from Fig. 2, the curves calculated by least-squares fitting are in approximate agreement with experimental points within statistical errors. The values of the isomer shift at 298, 78, and 5 K are -0.51, -0.43, and -0.46 mm/s, respectively, relative to Eu_2O_3. The area ratios normalized by the integrated area at 5 K are shown in Fig. 3. The values of the area ratio at 298, 78, and 5 K are 0.3, 0.7, and 1.0, respectively. As seen from Fig. 3, the area ratio of "as adsorbed" specimen at 298 K is nearly the same as the value in europium iron garnet (EuIG). It indicates that the Eu ions arising from ^{151}Gd adsorbed on the surfaces of YIG are strongly bonded to the surrounding anions. It is similar to the situation of Eu ions in EuIG. The width of emission Mössbauer spectra of ^{151}Gd on YIG is independent of temperature and has a constant value of 4.0 mm/s, which is the same as in non-magnetic Eu^{3+} ions, indicating that the Eu^{3+} ions arising from ^{151}Gd adsorbed on YIG are found to be diamagnetic.

We can draw interesting conclusions on the basis of the results obtained from emission Mössbauer measurements on the Eu ions arising from ^{151}Gd hydrolytically adsorbed on the surfaces of YIG as follows:

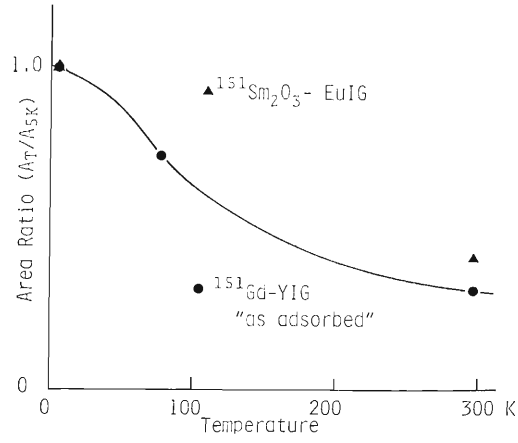

Fig. 3. Temperature dependence of the area ratio of ^{151}Gd emission Mössbauer spectra.

1) Eu ions are trivalent from the isomer shift.

2) Eu^{3+} ions are bonded tightly to oxygen ions as well as in the bulk specimen of EuIG.

3) Eu^{3+} ions are non-magnetic. It means that the Eu^{3+} ions near the surface layers do not occupy the dodecahedral sites but the other positions such as octahedral ones.

References

1) T. Okada, S. Ambe, F. Ambe, and H. Sekizawa: *J. Phys. Chem.*, **86**, 4726 (1982).
2) T. Okada, F. Ambe, S, Ambe, and H. Sekizawa: *RIKEN Accel. Progr. Rep.*, **18**, 90 (1984).

RIKEN Accel. Progr. Rep. 19 (1985)

III-2-22. ^{119}Sb Emission Mössbauer Study on Quenched-in Vacancies in Gold

I. Tanaka, S. Nasu, F. E. Fujita,* F. Ambe,
S. Ambe, and T. Okada

Hyperfine interaction studies utilizing the ^{119}Sb emission Mössbauer effect in gold have been performed in order to understand the nature of quenched-in vacancies and their complexes with solute atoms. Mössbauer spectroscopy is well recognized as a powerful technique to study on the defects-associated states, which are usually introduced by irradiation with energetic particles like electrons, protons, neutrons, and their own ions, by deformation at low temperatures, or by quenching from high temperatures. The present investigation has been focused on understanding the nature of quenched-in vacancies in gold, since only vacancies are introduced by quenching from high temperatures.[1)]

Takamura and his co-workers found that vacancies in gold interact strongly with high-valent solute atoms like Ge, Sn, and Sb from precise investigation using electrical resistivity and positron lifetime measurements.[2)] The vacancy-solute complexes are found to be formed during quenching and on subsequent isochronal annealing. These results suggested that the ^{119}Sb emission Mössbauer study may be the best candidate to detect the vacancy-solute associations in gold.

^{119}Sb atoms, daughters of ^{119m}Te, produced by α-irradiation of a β-tin sheet, were carefully collected by the chemical procedures reported by Ambe.[3)] The ^{119}Sb atoms were electrolytically deposited on pure Au (99.999%) foil (14 μm in thickness). The specimen foil was wrapped in tantalum foil and copper wire and then annealed in purified H_2 gas at 1,123 K for 3.0 ks in order to make a uniform solid solution and avoid the internal oxidation of Sb atoms. ^{119}Sb emission Mössbauer measurements were performed with the combination of ^{119}Sn* source arising from ^{119}Sb in the specimen and a $BaSnO_3$ standard absorber. All the spectra were taken at 77 K.

The spectrum for as-prepared specimen was shown to be a nearly single line and suggested that Sb atoms were almost dissolved into gold matrix. The specimen was annealed for 30 s at 1,073 K and quenched into brine at 253 K. The spectrum obtained just after quenching suggested the existence of the Sb-vacancy pairs, as shown in Fig. 1 (a). Subsequent isochronal annealing was performed; typical spectra observed during the annealing are shown in Fig. 1(b) and (c). Each spectrum shows superposition of three lines: a main line due to Sb dissolved into gold matrix, a defect line whose isomer shift is locat-

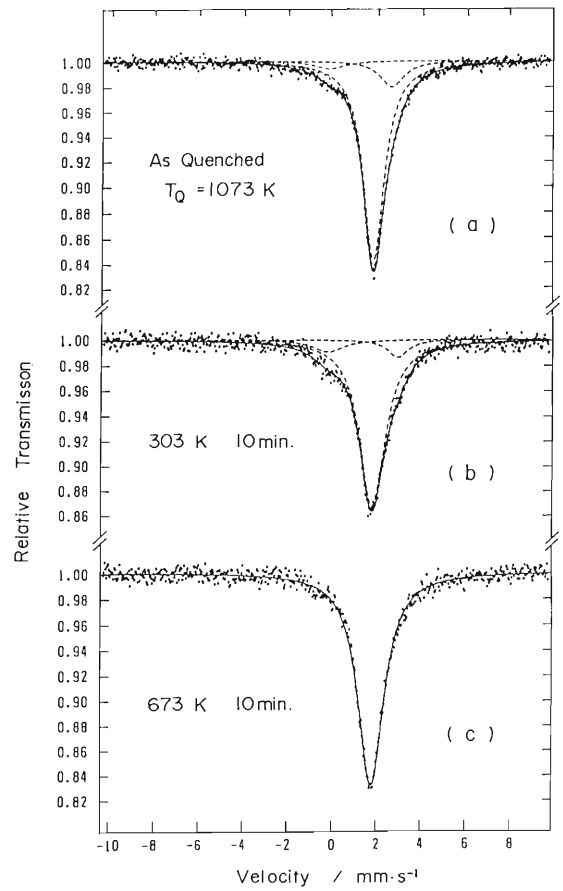

Fig. 1. Typical ^{119}Sb emission Mössbauer spectra obtained immediately after quenching from 1,073 K (a), and on the subsequent isochronal annealing (b) and (c). The solid curves are results of computer fitting to the experimental data and the dotted curves show the resolved partial components.

* Faculty of Engineering Science, Osaka University.

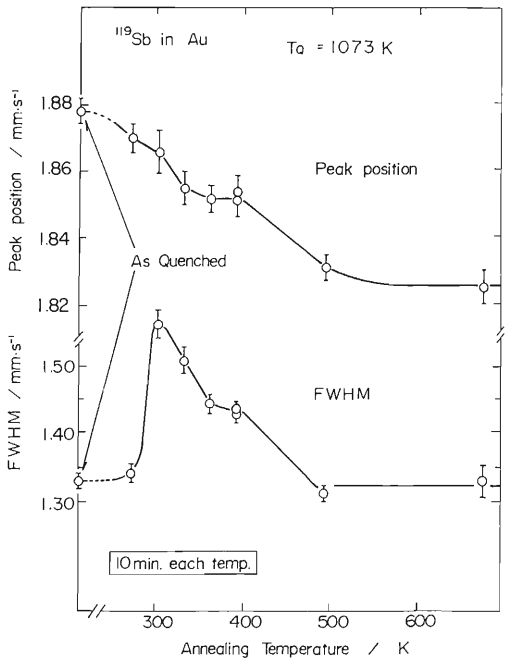

Fig. 2. Dependence of the Mössbauer parameters on the isochronal annealing after quenching from 1,073 K. Points were obtained by least-square-fitting assuming a single Lorentz function as the absorption line.

ed in the larger velocity range, and an oxidized Sb line whose isomer shift is nearly identical to that of the Sn^{4+} state. The intensity of the defect line depends on the isochronal annealing procedure.

Figure 2 shows the Mössbauer parameters obtained from a least-square-fit assuming a single Lorentz function as the absorption line. Rather large changes in these parameters were observed in the temperature range between 300 and 500 K; this should relate with aggregation of Sb-vacancy complexes and annihilation of Sb-vacancy pairs.

About 90% of Sb atoms were found to be internally oxidized in the specimen annealed in H_2 gas at 1,173 K for 3.6 ks without wrapping in tantalum foil and copper wire. This suggests anomalous strong affinity between oxygen and Sb in gold.

References

1) I. Tanaka, S. Nasu, F. E. Fujita, F. Ambe, S. Ambe, and T. Okada: *J. Phys. F,* in press.
2) J. Takamura: Point Defects and Defect Interactions in Metals, (ed. by J. Takamura, M. Doyama, and M. Kiritani), Univ. of Tokyo Press, Tokyo, p. 431 (1982).
3) S. Ambe: *J. Radioanal. Nucl. Chem., Artic.*, **81**, 77 (1984).

RIKEN Accel. Progr. Rep. 19 (1985)

III-2-23. TDPAC of γ-Rays Emitted from $^{111}Cd(\leftarrow{}^{111}In)$ in Fe_3O_4 (II)

K. Asai, T. Okada, and H. Sekizawa

Since Cd ions in magnetic oxides are usually in the form of divalent diamagnetic ions, the hyperfine magnetic fields observed at ^{111}Cd in the oxides originate from the neighboring magnetic ions through the intervening oxygen ions, and thus, they are called the supertransferred hyperfine magnetic fields, H_{STHF}. The magnitude of these fields gives the covalency parameters of the chemical bonds between the magnetic ions and the oxygen ions.[1] These parameters are important in discussing the superexchange mechanism.

In a previous report,[2] we presented some remarks on the detectors geometry in the time differential perturbed angular correlation (TDPAC) measurements of the hyperfine magnetic fields at the nuclei in ferro- or ferrimagnets, and showed experimental results for $^{111}Cd(\leftarrow{}^{111}In)$ in Fe_3O_4. In this report, we discuss these results. Details are given in Ref. 3.

Magnetite, Fe_3O_4, has the inverse spinel structure, in which one Fe^{3+} ion in a chemical formula occupies the A (tetrahedral) site, while remaining nominal Fe^{3+} and Fe^{2+} ions occupy the B (octahedral) sites. This material undergoes a well-known "metal-insulator" phase transition at the Verwey temperature, T_V (=120 K); the conductivity is high above T_V due to the itineration of the 3d electrons of Fe ions on the B sites, whereas it is low below T_V because this itineration ceases.[4),5] It is known that the ^{111}Cd ion arising from ^{111}In ion occupies the A site of Fe_3O_4.[6]

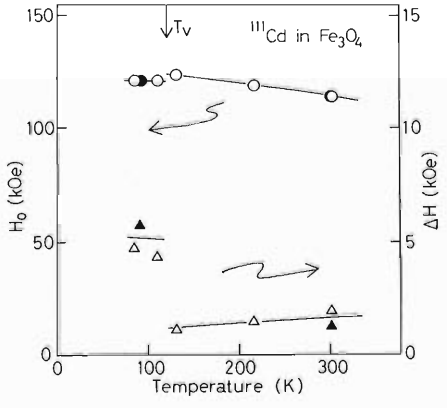

Fig. 1. Temperature dependences of the center value H_0 and the width ΔH of the distribution of H_{STHF}. Symbols ○ and △ denote the values obtained by the "multiple $\pi/4$-method," and ● and ▲ by the "multiple $\pi/2$-method."[2]

Figure 1 shows the center H_0 and the apparent width ΔH of the distribution of H_{STHF} observed at ^{111}Cd in Fe_3O_4 as functions of the temperature. As can be seen, H_0 and ΔH change stepwise at about T_V. It is noted that although the center H_0 changes only slightly, the width ΔH increases appreciably on decreasing the temperature through T_V. The determined values of H_0 and ΔH at low temperatures are +121 kOe and 5 kOe, respectively.

In magnetic oxides with the spinel structure, H_{STHF} at the nucleus on the A site originates dominantly in the magnetic moments of the twelve nearest neighbor ions on the B sites, and can be regarded as the sum of the contributions of individual B sites ions.[6] The B sites in Fe_3O_4 are occupied by the same numbers of the nominal Fe^{2+} and the Fe^{3+} ions on the average. The fact, that the center H_0 of H_{STHF} changes only slightly on passing through T_V, means that the average of the contributions of one Fe^{3+}(B) and one Fe^{2+}(B) to H_{STHF} at $^{111}Cd^{2+}$(A) is not much affected by the itineration of the 3d electrons on these Fe(B) ions. The value of this average is evaluated to be +10 kOe at low temperatures. The positive sign means that the direction of H_{STHF} is parallel to that of the B site magnetization. If we assume that the magnitude of the contribution of each B site ion to H_{STHF} is proportional to the magnitude of its magnetic moment, the proportionality constant χ for $^{111}Cd^{2+}$(A) in Fe_3O_4 amounts to +2.2 kOe/μ_B. Namely, the constant χ represents the contributed H_{STHF} at $^{111}Cd^{2+}$(A) when one of the nearest neighbor B site magnetic ions has a magnetic moment of 1 μ_B. According to a previous NMR study,[6] the value of H_{STHF} at $^{115}In^{3+}$ (A) in $NiFe_2O_4$ is +139 kOe. The derived value of the constant χ for In^{3+}(A) in $NiFe_2O_4$ amounts to +3.3 kOe/μ_B. The constant χ for Cd^{2+}(A) in Fe_3O_4 determined in the present study is 34% smaller than the one for the isoelectronic In^{3+}(A) in $NiFe_2O_4$.

The predominant mechanism of H_{STHF} at the nuclei of the diamagnetic ions whose electronic

orbitals are filled up to $(4d)^{10}$, *i.e.*, Cd^{2+}, In^{3+}, Sn^{4+}, and Sb^{5+}, is the spin transfer from 3d orbitals of the neighboring magnetic ions to 5s orbitals of the diamagnetic ions through the intervening oxygen ions.[6),7)] The smallness of χ for Cd^{2+}(A) in Fe_3O_4 compared with that for In^{3+}(A) in $NiFe_2O_4$ is interpreted as due to the smaller covalence in the Cd^{2+}(A)-O^{2-} bond than in the In^{3+}(A)-O^{2-} bond. In other words, the amount of the transfer of oxygen valence electrons, which are partially polarized by the neighboring B site magnetic ions, is smaller in the former than in the latter. The difference in χ, existing probably between different B site magnetic ions, is ignored in our discussion but will be necessary in a further detailed one.

Then, we discuss the apparent distribution of the magnitude of H_{STHF} at ^{111}Cd in Fe_3O_4. At temperatures above T_V, the point symmetry of the A site is cubic, and all the B site Fe ions are indistinguishable because of the itineration of 3d electrons among them.[4),5)] This is the reason why well-defined H_{STHF} is observed at ^{111}Cd on the A site above T_V. On the other hand, at temperatures below T_V, the crystal symmetry becomes lower, and Fe^{3+} and Fe^{2+} ions are ionically ordered in the B sites.[4),5)] There are two possible causes which induce the apparent distribution of H_{STHF} at ^{111}Cd below T_V. They are (1) fluctuation of the relative populations of Fe^{3+} and Fe^{2+} ions on the neighboring B sites and (2) a small amount of EFG acting on ^{111}Cd along with $H_{\perp}$.

First, we consider the cause (1). The difference in the contribution to H_{STHF} between Fe^{3+}(B) and Fe^{2+}(B) ions is estimated to be 2.2 kOe, if we assume the same values of χ for these ions as described above. Therefore, H_{STHF} is expected to have a distribution with a width of an order of a few kOe if the relative populations of the nearest neighbor Fe^{3+}(B) and Fe^{2+}(B) ions vary from one A site to another. This situation can explain the observed distribution at least qualitatively, but further quantitative estimation is not possible, because the controversy on the ionical order of Fe ions in the B sites has not yet been settled.

Next, we consider the cause (2). If the magnitude of EFG is small, its effect appears in the TDPAC spectrum as an apparent distribution of H_{STHF}.[3)] It is reported that a quadrupole splitting with a magnitude of about 0.05 mm/s is observed in the Mössbauer spectra of ^{57}Fe on the A site of Fe_3O_4 below T_V.[8)] If the same amount of EFG acts on ^{111}Cd, the corresponding apparent width of H_{STHF} is estimated to be 1 kOe. Though this value is much smaller than the observed apparent width, the EFG is a possible cause of the observed distribution because of the following two reasons: i) The nucleus $^{111}Cd(\leftarrow{}^{111}In)$ probably feels an extra EFG due to the after-effects of the preceding EC decay of ^{111}In[9)] because the resistivity is high below T_V; ii) Even if there are no after-effects of the EC decay, the magnitude of the EFG felt at ^{111}Cd is, in general, different from that felt at ^{57}Fe in oxides. For example, the former is five times larger than the latter in α-Fe_2O_3.[9),10)] Quantitative explanation of the observed distribution below T_V remains to be a future problem.

References

1) N. L. Huang, R. Orbach, E. Simánek, J. Owen, and D. R. Taylor: *Phys. Rev.*, **156**, 383 (1967).
2) K. Asai, T. Okada, and H. Sekizawa: *RIKEN Accel. Progr. Rep.*, **18**, 94 (1984).
3) K. Asai, T. Okada, and H. Sekizawa: *J. Phys. Soc. Jpn.*, **54**, 4325 (1985).
4) S. Chikazumi: *AIP Conf. Proc.*, **29**, 382 (1976).
5) S. Iida, K. Mizushima, M. Mizoguchi, A. Ueki, K. Kose, K. Kato, K. Yanai, N. Goto, and Y. Motomura: Proc. 3rd Int. Conf. Ferrites, Kyoto, 1980, Center for Academic Publications Japan, Tokyo, p. 87 (1981).
6) Y. Miyahara and S. Iida: *J. Phys. Soc. Jpn.*, **37**, 1248 (1974).
7) B. J. Evans and L. J. Swartzendruber: *Phys. Rev. B*, **6**, 223 (1972).
8) R. S. Hargrove and W. Kündig: *Solid State Commun.*, **8**, 303 (1970).
9) K. Asai, F. Ambe, S. Ambe, and H. Sekizawa: *J. Phys. Soc. Jpn.*, **53**, 4109 (1984).
10) F. van der Woude: *Phys. Status Solidi*, **17**, 417 (1966).

RIKEN Accel. Progr. Rep. 19 (1985)

III-2-24. Towards Macroscopic Measurement on Radioactive ^{6}He Diffusion in Metals

K. Ishida and K. Nagamine

Diffusion properties of helium in metals have been attracting subjects, since they play important role in the first wall materials of a nuclear fusion reactor. Also they are of fundamental theoretical importance, since helium is the lightest element next to hydrogen and is often the object of theoretical models.[1] Since the solubility of helium is very small, the permeability measurement is not so easy that most of the experiments have been carried out by implantation. In implantation, due to the limit in sensitivity for helium detection, we inevitably need a large amount of helium, which may either cause many-body correlation such as He pair- and He cluster-formation, or produce a lot of defects acting as helium trapping centers. As an alternative and a more sensitive way, we are preparing a new measurement using a radioactive ^{6}He isotope. The experiment will be conducted as described below.

^{6}He decays with a half-life of 0.8 s through emitting β-rays (e^-) having maximum energy of 3.6 MeV. The ^{6}He beam may be available either through nuclear reactions like proton stripping from ^{7}Li or as residual fragments in heavy-ion collisions, and is separated from the other nuclei and transported by using well-designed micro-beam optics with collimators to obtain a small beam spot of less than 100 μm in diameter on a sample. After stopping of the pulsed beam in the sample, β-rays are detected by arrays of multi-wire proportional chambers (MWPC) as shown in Fig. 1; the MWPC is then used to obtain a two-dimensional source-profile at the surface of the sample as a function of time after stopping of ^{6}He. The probability that the particle is found at r at time t starting from r_0, where r and r_0 is the two dimensional projection, is described by using the diffusion constant D as

$$P(r,t) = (1/4\pi Dt)\exp(-(r-r_0)^2/4Dt)$$

Thus, we can obtain the diffusion constant D.

Although there has been no definitive experimental value of D, theoretical estimation of interstitial diffusion constant gives a value of around 10^{-4} cm^2/s,[2] which gives a diffusion length of only around 100 μm during its life. We, therefore, adopted the MWPC system capable of reading out the cathode signal.

In this MWPC system, we can determine the position of the β-ray by finding the center of mass of the pulse heights of the fired cathode signal. For the pulse-height analysis, we use a high-density charge sensitive ADC system of LeCroy Corporation. The system will be triggered with scintilation counter telescopes placed behind the MWPC and open a time gate of ADC.

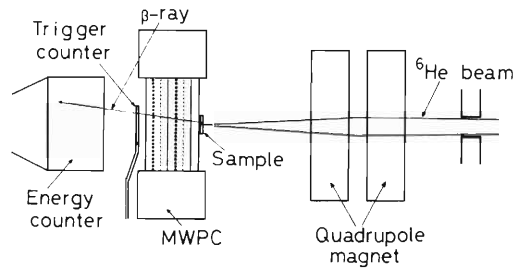

Fig. 1. Counter arrangement to be used in the experiment.

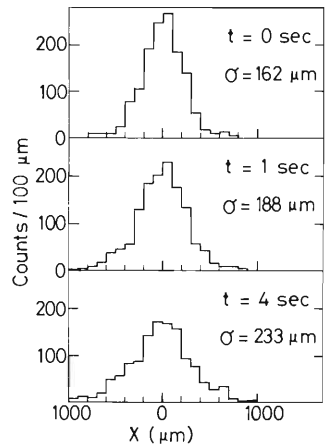

Fig. 2. Simulated distribution of ^{6}He profile at $t=0$, 1, and 4 s measured by tracing back along the β-ray trajectory, where σ is the standard deviation. Diffusion constant was taken to be 10^{-4} cm^2/s. For the beam size, range width, and multiple scattering, see text.

The signal from each wire is amplified, delayed, and supplied to the ADC. The ADC digitizes the charges and then transmits the digital data to the computer, while the time difference between the beam and the decay is given from the TDC reading of the trigger signal.

The position determination by the cathode read-out has intrinsic resolution of below 100 μm. In our case, since the β-rays suffer multiple scatterings in the gas of MWPC, we plan to use a low density gas, for example CH_4 and He, without reducing the operation properties of the counter. In Fig. 2, the simulated data of our experiment are shown, where we assumed the beam spot size of 100 μm, the range width of 20 μm, and the counter resolution of 80 μm, and the multiple scatterings of ^{6}He and β-ray were calculated for the real geometry. The data shows a large dependence on time as a result of He diffusion and that our method is useful as a powerful means of diffusion measurements.

References

1) D. J. Reed: *Radiat. Eff.*, **31**, 129 (1977).
2) B. N. Singh, T. Leffers, W. V. Green, and M. Victoria: *J. Nucl. Mater.*, **125**, 287 (1984).

RIKEN Accel. Progr. Rep. **19** (1985)

III-2-25. Eu-Ion Implantation in CaF_2

K. Aono, M. Iwaki, and S. Namba

Calcium fluoride is a popular fluorite which fluoresces on heating. A study is made on the luminescence during Eu^+-implantation into CaF_2 and its luminescence color depending on Eu^+-doses. In the present work, Eu-depth profiles in Eu^+-implanted CaF_2 have been investigated by means of a He^+ backscattering technique using the TANDETRON.

Calcium fluoride substrates used were (1 1 1) oriented wafers, which were chemically cleaned. The Eu^+-implantation in CaF_2 was performed to doses of 10^{13}–10^{16} Eu^+ cm^{-2} at 100 keV in the random direction at 1×10^{-6} Torr. The target during ion implantation was held at room temperature due to the low dose rate of about 0.2 μA cm^{-2}. Coloring of CaF_2 due to damage by 100 keV Eu^+-ion implantation was not observed in the visible region. The Rutherford backscattering measurement was carried out by using 1.5 MeV He^+ with a fluency of 10 μC to estimate compositions of surface layers of CaF_2. Backscattered particles were detected by using a solid-state detector at a scattering angle of 150°.

The Eu-depth profiles in the random spectra of as-implanted specimen are of a Gaussian-type as shown in Fig. 1. The depth corresponding to the peak in the spectra is about 33.3 nm for the 10^{16} cm^{-2} implanted specimen, 31.2 nm for 10^{15} cm^{-2}, and 27.1 nm for 10^{14} cm^{-2}, which are in good agreement with the predicted range of 33 nm calculated by the LSS theory. The standard deviation calculated from the FWHM of the spectra is about 11.5 nm, which is a little larger than the predicted value of 9 nm.

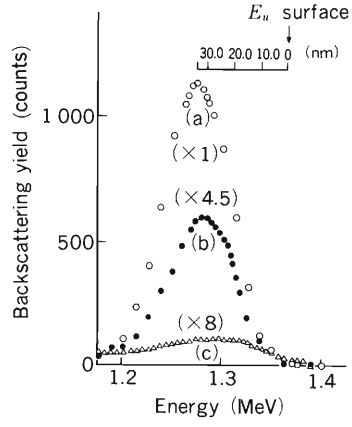

Fig. 1. Random spectra for Eu implanted in CaF_2.
(a) the 10^{16} cm^{-2} Eu-implanted specimen.
(b) the 10^{15} cm^{-2} Eu-implanted specimen.
(c) the 10^{14} cm^{-2} Eu-implanted specimen.

It is concluded that the average predicted range of Eu implanted in CaF_2 is in fairly good agreement with that predicted by the LSS range theory.

RIKEN Accel. Progr. Rep. 19 (1985)

III-2-26. Thermal Extraction of Krypton in Aluminum Using Mass Spectrometer

K. Takaishi,* T. Kikuchi,* K. Furuya,* I. Hashimoto,*
H. Yamaguchi,* E. Yagi, and M. Iwaki

Inert gases injected into metals by ion implantation tend to form bubbles. For Kr implantation, Evans and Mazey have examined the structure of Kr bubbles in Cu, Ni, and Au[1] and observed Kr bubbles formed in a solid phase. The existence of bubbles in the solid phase indicates that the high pressure is involved in bubbles. On the diffusion of Kr Gurevich *et al.*[2] have measured the diffusion coefficients of Kr in Al foils by using ^{85}Kr as a tracer and estimated them to be an order of 10^{-8} to 10^{-7} cm^2/s in a temperature range of 700-800 K. The theoretical investigation on the bubble diffusion of inert gas in solids suggests that the diffusion coefficient depends on the bubble radius.[3] However, the behavior of Kr bubbles in Al has not been clarified. Therefore, in the present study we examine the behavior of Kr bubbles in Al using a thermal extraction-mass spectrometer and an electron microscope equipped with an energy-dispersion X-ray spectrometer.

The specimens were single-crystal Al foils of 99.99% in purity grown by a strain annealing method. The Kr implantation was carried out at an energy of 50 keV and at room temperature with a current density of 0.5 μA/cm^2 up to a dose of 10^{16} Kr/cm^2. In order to avoid the implantation under the channeling conditions the direction of implantation was 8° off the normal to the specimen surface.

The thermal extraction of implanted Kr was performed by heating at a constant rate or by isothermal annealing. The extraction by heating at a constant rate was carried out in the range of 289-1,170 K with a rate of 20 K/min. The isothermal annealing was carried out in the temperature range of 700-900 K for 25 min from 5 min after the furnace temperature was stabilized. The amount of extracted Kr during these heat treatment was determined by a calibration curve obtained by using a small amount of Kr gas of 99.99% in purity.

For the electron microscopic observation, thin films suitable for electron microscopy prepared by conventional electropolishing were implanted by the same method as described above. The implanted thin films were examined by an H-800 electron microscope equipped with an energy-dispersion X-ray spectrometer operated at 100 kV.

It was recognized that Kr in Al foils can be extracted during heating at a constant rate in the range from about 540 to 1,100 K. In order to obtain detailed information, isothermal annealing was carried out at temperature of 713, 748, 772, 781, 793, and 813 K. The typical result at an

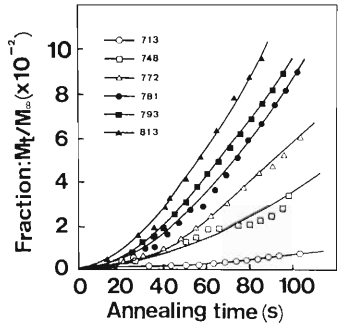

Fig. 1. Early stage of extraction of Kr at various temperatures between 713 and 813 K.

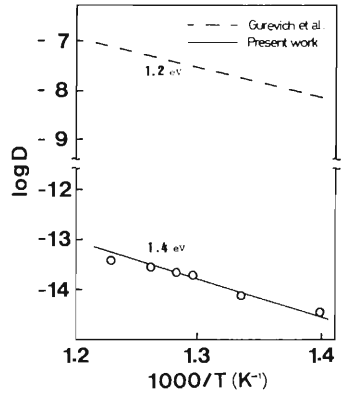

Fig. 2. Plot of log$D$ *vs.* $1/T$.

* Faculty of Science, Science University of Tokyo.

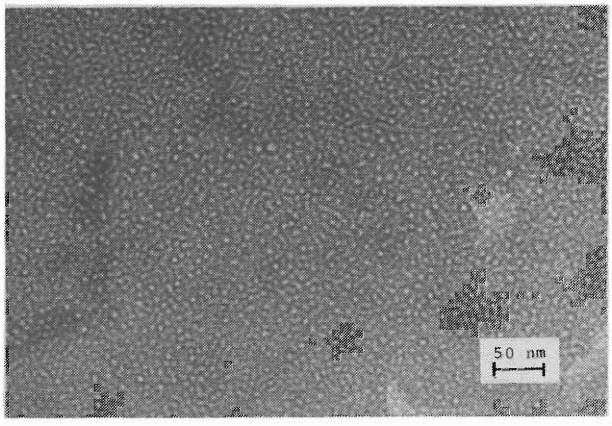

Fig. 3. Kr bubbles in Al implanted to a dose of 10^{16} Kr/cm^2 at an energy of 50 keV. As implanted specimen.

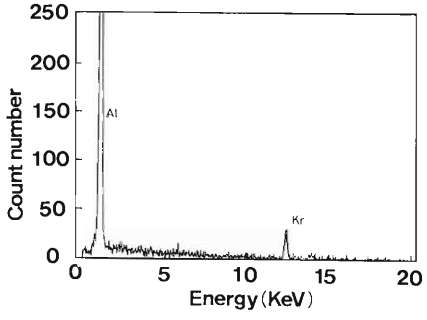

Fig. 4. Energy-dispersion X-ray spectrum in an implanted specimen, where the first and the second peaks are ascribed to Al and Kr, respectively.

early stage of extraction is shown in Fig. 1, where M_t and M_∞ represent the amount of extracted Kr for t s and $t=\infty$, respectively. In this stage the fraction can be expressed by

$$M_t/M_\infty = 1-(8/\pi^2)\exp(-\pi^2 Dt/4L^2) \qquad (1)$$

where D is the diffusion coefficient and L is the depth of implantation. From Eqn. (1), the diffusion coefficient of Kr in Al was estimated to be 10^{-15} to 10^{-14} cm^2/s in the temperature range from 713 to 813 K (Fig. 1). The activation energy for diffusion of Kr was determined and found to be about 1.4 eV as shown in Fig. 2. The diffusion coefficient obtained by the present work is smaller by seven orders of magnitude than that obtained by Gurevich *et al.*[2] using ^{85}Kr as a tracer (Fig. 2). We consider that the difference in the diffusion coefficient is ascribed to the difference in the existing state of Kr in Al: In the experiment of Gurevich *et al.* Kr existed as isolated atoms, while in our specimens Kr existed in bubbles with an average diameter of about 8 nm as shown in Fig. 3. An energy-dispersion X-ray spectrum taken in the selected area containing bubbles is shown in Fig. 4, where the first and the second peaks are ascribed to Al and Kr (around 12.59 keV), respectively. According to a bubble diffusion theory by Kelly,[3] the movement of a bubble can be described as vacancy motion from one position on the bubble surface to another position by diffusion in the surrounding matrix. From this viewpoint, the difference in the diffusion coefficient between Gurevich *et al.*[2] and the present study may be explained in terms of bubble diffusion.

References

1) J. H. Evans and D. J. Mazey: *J. Phys. F*, **15**, L1 (1985).
2) M. E. Gurevich, L. N. Larikov, V. M. Tyshkevich, and V. M. Falchenko: *Ukr. Fiz. Zh.*, **T24**, 658 (1979).
3) R. Kelly: *Phys. Status Solidi*, **21**, 451 (1967).

RIKEN Accel. Progr. Rep. 19 (1985)

III-2-27. Effect of Small Amount of He on Ductility of Various Metals and Alloys

Y. Higashiguchi,* E. Yagi, Y. Suzuki,* and H. Kayano*

The helium embrittlement was investigated on various materials; Nb, Nb-40V, V, V-20Ti, Ti-6.5 Al, and cold worked 316 stainless steel. Among them Nb-40V, V-20Ti, and Ti-6.5Al alloys were prepared by arc-melting and cold-rolled to sheets of 0.3-0.2 mm in thickness, then annealed at 1,473 K, 1,273 K, and 1,123 K for 3 h, respectively, in a vacuum of 1.3×10^{-3} Pa. α-Particles of 36 MeV were injected into the specimens at room temperature by using the cyclotron. An edge-shaped graphite degrader was set in front of the specimens to achieve uniform depth distribution of injected helium. Total helium doses were 7.1×10^{15} and 2.2×10^{16} He/cm^2, which corresponded to the He concentrations of 5-6 appm and 10-20 appm, respectively. The concentrations are listed in Table 1.

Tensile test was carried out for all specimens at 973 K in a vacuum at a strain rate of 8.3×10^{-5} s^{-1}. The stress-strain curves are shown in Fig. 1. Numbering of -1, -2, and -3 in Fig. 1 represents the controlled specimens (uninjected specimen), the specimens injected with low He dose and the specimens injected with high dose, respectively. The He injection increases the yield stress in pure Nb and pure V, but not in Nb and V alloys. In all specimens the ductility decreases with increasing concentration of injected He.

The mechanism of He embrittlement has been considered as follows. He atoms or their small bubbles gathering at grain boundaries during high temperature deformation grow to large bubbles, which lowers the grain boundary energy. Therefore, the fractured surface was observed by a scanning electron microscope (SEM). The results are shown in Fig. 2 for Nb and its alloys as an example. The intergranular fracture pattern was observed in the He-injected Nb-40V but not in the He-injected Nb. A similar result was observed in V-20Ti and V. Microstructures around the fractured area were observed in all specimens by a transmission electron microscope (TEM). No bubbles were visible both in matrix and in grain boundaries in all specimens. Hence the effect of a small amount of He should be considered. The elongations of the controlled specimens (ε_0) and the 2.2×10^{16} He/cm^2 injected specimens (ε_H) were listed in Table 2. The ratio $\varepsilon_H/\varepsilon_0$ and the magnitude of reduction in the elongation per unit He concentration $(1-\varepsilon_H/\varepsilon_0)/C_H$ (C_H: He concentration) were obtained and listed in Table 2. The latter fraction was plotted as a function of the He concentration in Fig. 3. Approximately all points fall on a straight line in the He concentration range covered in the present experiment. In order to obtain a more precise relation it is necessary to investigate the dependence of the fraction in question on the microstructures such as a grain size, a disloca-

Table 1. Concentration of injected helium in each specimen for 7.1×10^{15} and 2.2×10^{16} He/cm^2.

Specimens	He concentration (appm) 7.1×10^{15} He/cm^2	2.2×10^{16} He/cm^2
Nb	6.4	21
V	5.0	16
Nb-40V		19
V-20Ti		16
Ti-6.5Al	6.4	13
SUS316 (20% cw)	5.8	12

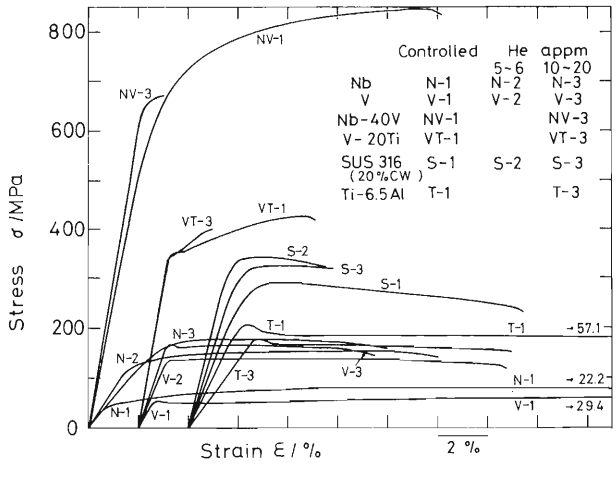

Fig. 1. Stress-strain curves obtained from tensile test at 973 K at a strain rate of 8.3×10^{-5} s^{-1}.

* The Oarai Branch, The Research Institute for Iron, Steel and Other Metals, Tohoku University.

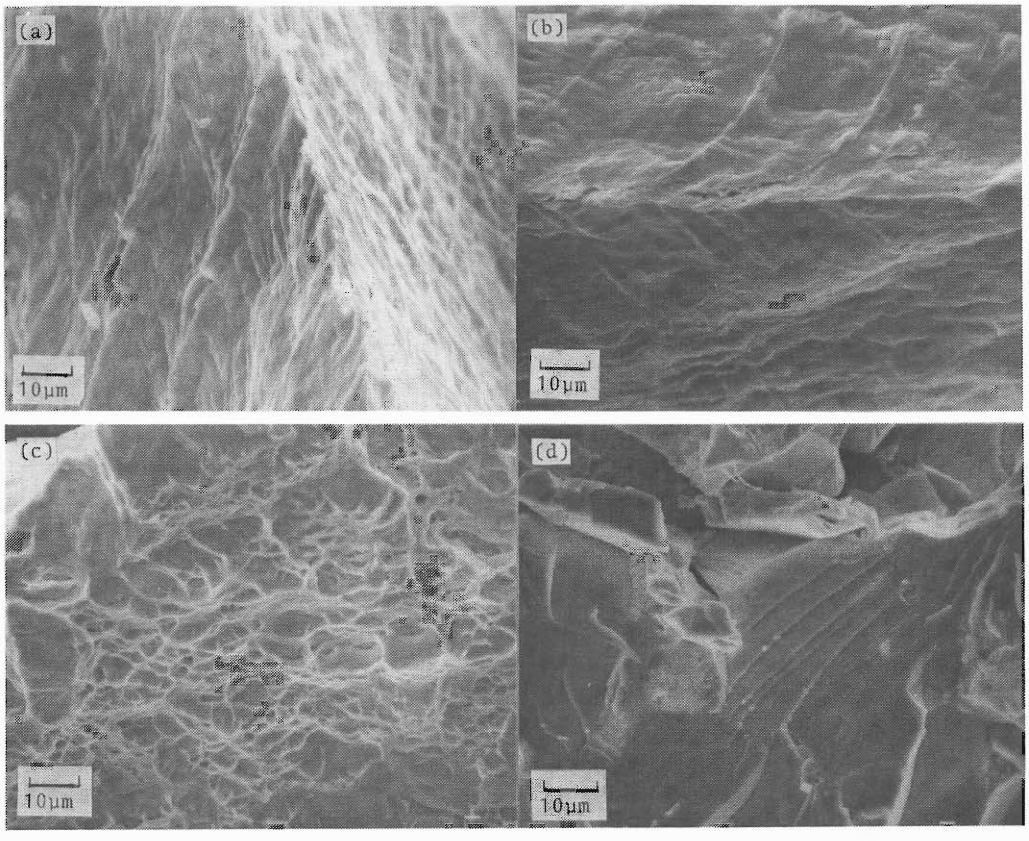

Fig. 2. Scanning electron micrographs of fractured surface of Nb and Nb-40V alloy. (a) Controlled (He-uninjected) Nb, (b) He-injected Nb (21 appm He), (c) Controlled Nb-40V, and (d) He-injected Nb-40V (19 appm He).

Table 2. Reduction of elongation by helium injection.

Specimens	Controlled ε_0%	2.2×10^{16} He/cm^3 ε_H%	$\varepsilon_H/\varepsilon_0$	$(1-\varepsilon_H/\varepsilon_0)/C_H$
Nb	22.5	6.5	0.29	0.0338
Nb-40V	14.2	3.0	0.21	0.0493
V	30.0	9.5	0.31	0.0431
V-20Ti	7.1	2.9	0.41	0.0368
SUS316	13.5	5.8	0.43	0.0475
Ti-6.5Al	57.1	13.0	0.28	0.0553

Tensile tested at 973 K, $\dot{\varepsilon}=8.3\times10^{-5}$ s^{-1}

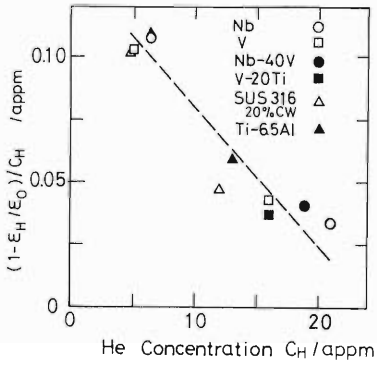

Fig. 3. Magnitude of reduction in elongation per unit He concentration as a function of He concentration.

tion density, and precipitates present before He injection. However, it can be said that a smaller He concentration has a larger effect in reducing the ductility and the magnitude of reduction in the elongation per unit He concentration is nearly the same for all specimens.

RIKEN Accel. Progr. Rep. 19 (1985)

III-2-28. Plasma Surface Interaction—ERD Measurement of Deuterium Retention near Surface of TiC and Graphite Irradiated with Dissociated D Atoms

Y. Sakamoto, Y. Ishibe, K. Okazaki, H. Oyama,
K. Yano, M. Yanokura, and I. Kohno

Titanium carbide and graphite are promising materials for vacuum wall surfaces in contact with plasma because of their heat-resisting properties and relatively low atomic numbers. For example in tokamak devices, they are candidates for limiters and first walls of thermonuclear fusion devices by reason in particular that they are low-atomic number materials. In our previous studies,[1] we have successfully carried out wall conditioning using ECR (Electron Cyclotron Resonance) hydrogen plasma on the basis of chemical sputtering. In this case, neutral hydrogen atoms play an important role because of their chemical activity. The purpose of this study is to investigate the plasma surface interaction between the surfaces of TiC and graphite and deuterium atoms produced in the ECR deuterium plasma in order to clarify the behavior of deuterium atoms in near the surface taking part in the chemical sputtering.

Figure 1 shows a schematic drawing of the ECR deuterium plasma irradiation apparatus. A microwave (2.45 GHz) power of 200 W is launched through a helical antenna with resonance magnetic field of 0.0875 T for production of plasmas. The electron density and electron temperature of a typical plasma were 9.6×10^{9} cm^{-3} and 4.7 eV, respectively, for the gas pressure of 2×10^{-2} Pa. Samples were set 200 mm apart from the center of the plasma column in parallel with the resonance magnetic field so that they could be irradiated with only neutral atom fluxes which are estimated to be about 10^{15} atoms cm^{-2}s^{-1}. TiC samples were prepared by means of CVD (Chemical Vapor Deposition) coating with film thickness of 20 μm on poco graphites, which were also used as graphite samples. These samples contain inevitably many hydrogen atoms as shown in Fig. 3 because they were prepared by the CVD method.

The ERD (Elastic Recoil Detection) by using an Ar^{4+} beam of about 50 MeV was applied to the measurement of the near-surface concentration of deuterium atoms.[2] The arrangement is shown in Fig. 2. An aluminum foil of 20 μm in thickness was inserted just before the detector (SSD 1) in order to eliminate the components like Ar, Ti, and C from recoiled beams.

Figure 3 shows the depth profiles of H and D in the near surfaces of TiC and graphite after 1 h irradiation with dissociated deuterium atoms during rise in the sample temperature. In this case, the deuterium atom fluence is estimated to be about 2×10^{19} atoms cm^{-2}. Incident deuterium

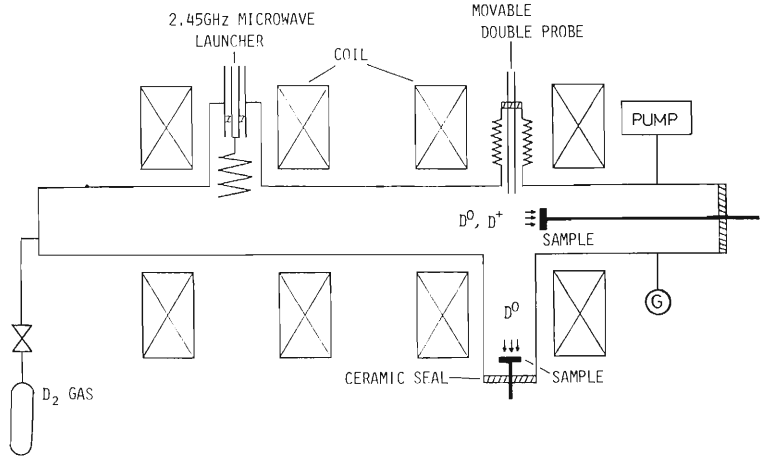

Fig. 1. Schematic arrangement of ECR plasma irradiation apparatus.

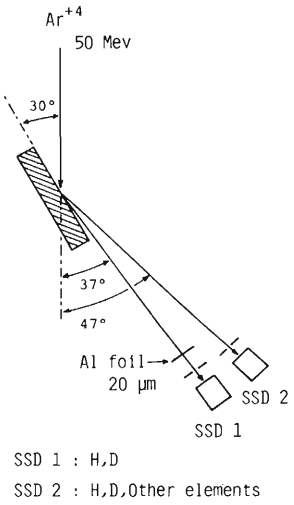

Fig. 2. Diagram of experimental apparatus for profiling H and D.

atoms with energy of about 5 eV are mainly produced by the dissociative excitation process.[3] As seen in Fig. 3, deuterium atoms diffuse from, the surface to inside, ranging over several hundreds of nanometers in TiC as the sample temperature is increased. Deuterium atoms in the graphites are localized at the near surface.

References

1) S. Ishii, K. Okazaki, Y. Sakamoto, and K. Yano: *Jpn. J. Appl. Phys.*, **22**, L403 (1983).
2) K. Yano, Y. Ishibe, H. Oyama,Y. Sakamoto, M. Yanokura, and I. Kohno: Proc. 7th International Symposium on Plasma Chemistry, Vol. 2, p.518 (1985).
3) B. L. Carnahan and E. C. Zipf: *Phys. Rev.*, **16**, 991 (1977).

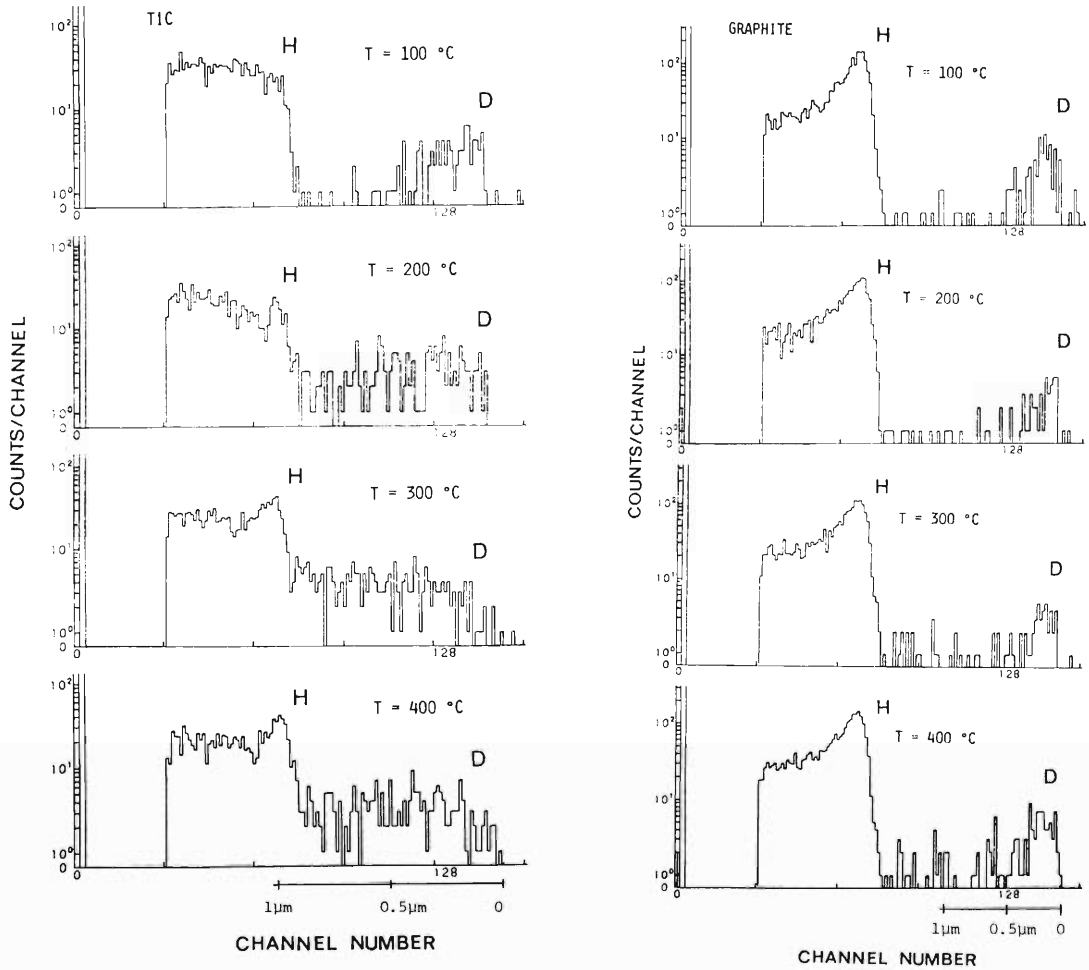

Fig. 3. Depth profiles of H and D in the near surfaces of TiC and graphite irradiated with deuterium atoms during rise in the sample temperature.

RIKEN Accel. Progr. Rep. 19 (1985)

III-2-29. Quantitative Analysis of Hydrogen in Titanium Carbide by ERD

T. Kobayashi, H. Sakairi, M. Yanokura, S. Hayashi,
M. Aratani, M. Iwaki, and S. Oohira

Application of the Elastic Recoil Detection analysis (ERD) to quantitative analysis of hydrogen in solids is in progress. Preliminary results have been reported in the last volume,[1] in which a 2 μm-thick, TiC film plated on an Al substrate was implanted with deuterium with a fluence of 5×10^{16} D/cm^2. The implantation was expected to be a concentration standard for hydrogen analysis. Ar ions of 50.5 MeV were used for ERD to obtain depth profiles of H and D concentrations.

This year studies were performed on

(1) Determination of the TiC film composition (necessary for precise quantitative analysis of H and D) by Rutherford Backscattering Spectrometry (RBS);

(2) Aging effects on H and D concentrations and their profiles; and

(3) Determination of the TiC composition by ERD.

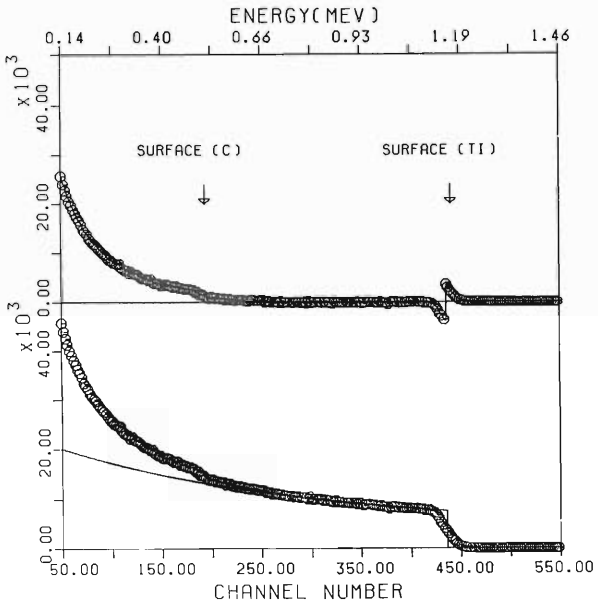

Fig. 1. Lower: RBS spectrum of He ions scattered by a TiC film; a solid line represents a theoretical spectrum for Ti atoms. Upper: a spectrum obtained by subtracting the solid line component from the experimental spectrum, which gives the C contribution.

(1) TiC film used in the ERD study was also analyzed by RBS with 1.5 MeV He^{4+} ions from the RIKEN tandetron. An energy spectrum of He ions backscattered at an angle of 125° was shown by open circles in Fig. 1. The low energy spectrum was divided to two components formed by Ti and C by extrapolating the high energy spectrum (contributed from Ti only) to the low energy region with an approximate expression for energy dependence of backscattering yield $Y(E_1)$,[2]

$$Y(E_1)\simeq\frac{\text{const.}}{(E_0+E_1)^2}$$

where E_0 and E_1 are energies of incident ions and out-going ions, respectively, and energy struggling of ions and a finite energy resolution in the measurement system are neglected.

From an "assumed" concentration ratio of Ti to C, the stopping power of the TiC sample for ^{4}He ions was calculated, the result of which allowed the RBS spectrum to be analyzed and provided a "calculated" concentration ratio of Ti and C. Repeating the above procedure led to a self-consistently determined ratio, Ti/C=1/3.74.

With this ratio, analysis of ERD spectrum obtained on the deuterium-implanted TiC gave a deuterium content of 4.88×10^{16} D/cm^2 which shows a good agreement with the implantation dose, 5×10^{16} D/cm^2. It is also deduced that the content of hydrogen distributed uniformly, which was introduced during the specimen preparation of TiC, is about 4 at.%.

(2) In the ERD study carried out last year, successive experiments provided similar spectra in shape and size, which suggested that the ion irradiation during ERD experiments has no effect of changing, the distribution of hydrogen and deuterium. The sample used last year was again analyzed by ERD this year, about 5 months after the previous ones. Resulting spectrum was shown in Fig. 2 together with the previously obtained spectra: spectrum (a) is the first result obtained 2 weeks after the film preparation; (b), the second one obtained 2 h after the first experiment; and (c), the present one. No changes are observed among the spectra, leading to the con-

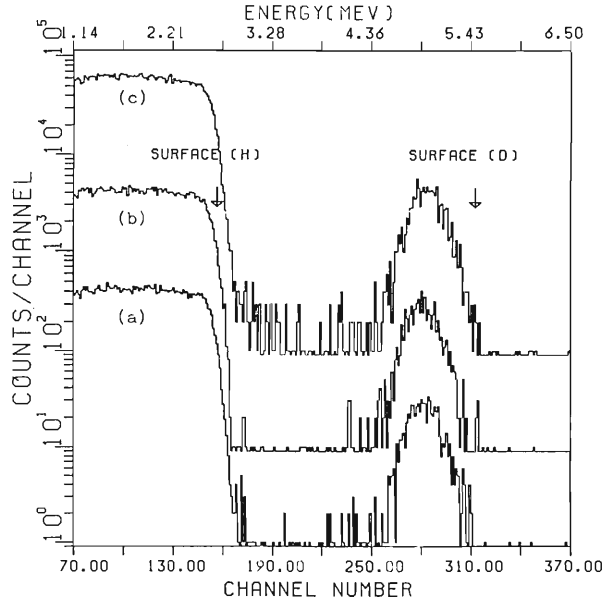

Fig. 2. ERD spectra of H and D recoiled by Ar ions from the TiC film, obtained (a) 2 weeks after the film preparation, (b) 2 h after the first experiment, and (c) in the latest experiments 5 months after the previous one.

clusion that hydrogen and deuterium in titanium carbide are stabilized at room temperature.

(3) The composition of TiC films is expected to be estimated from ERD spectra of recoiled Ti and C ions as from RBS spectra. The use of incident ions lighter than Ti such as Ar, however, makes the spectra for Ti and incident ions overlap and reduces accuracy of the analysis. Such overlap, however, can be removed by employing incident ions heavier than Ti. Thus the ERD was tested with 95.9 MeV Kr ions under almost the same experimental arrangement as in the Ar ERD. Recoiled H, D, C, and Ti ions were detected at an angle of 47°. By another detector only recoiled H and D ions were detected at an angle of 37°, with a 26 μm-thick Al foil absorber in front of the detector.

In Fig. 3, the upper spectrum consists of whole spectra for recoiled Ti, C, D, and H, and the lower spectrum is for D and H. In preliminary

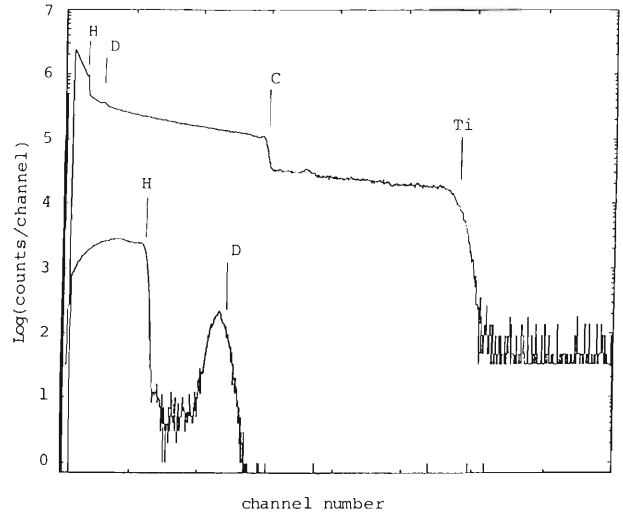

Fig. 3. ERD spectra of a TiC film obtained with Kr ions. Surface positions in the spectra corresponding to each elements are indicated. Upper : detected at an angle of 47°; Lower: detected at an angle of 37°, through an absorber for C and Ti ions. (Two spectra differ in units of the abscissa.)

analysis agreement on the composition of the film seems well between ERD and RBS, and therefore it is expected that ERD is a sufficient tool to determine both the material composition and the hydrogen content.

With heavy ions such as Kr, however, the effect of irradiation on samples must be analyzed in the further study. A particularly interesting problem in future is a relation between hydrogen contents and preparation conditions of TiC films, which can present explanations for the mechanisms of TiC film formation by reactive ion plating.

References

1) T. Kobayashi, S. Hayashi, H. Sakairi, M. Iwaki, M. Aratani, M. Yanokura, and S. Oohira: *RIKEN Accel. Progr. Rep.*, **17**, 103 (1984).
2) L. C. Feldman, J. W. Mayer, and S. T. Picraux: "Materials Analysis by Iron Channeling," Academic Press, New York, p. 220 (1982).

RIKEN Accel. Progr. Rep. 19 (1985)

III-2-30. Lattice Location of H in Ta as Observed by a Channeling Method

E. Yagi, S. Nakamura, T. Kobayashi, F. Kano,
K. Watanabe,* and Y. Fukai*

In previous studies we have determined lattice locations of H in V,[1] Nb,[2] and Ta[3] by the channeling method using a nuclear reaction $^{1}H(^{11}B, \alpha)\alpha\alpha$, and studied the effect of internal strain, which was introduced by precipitation and redissolution of β-phase, on the lattice location of H in V[1] and Nb.[2] It was observed that the hydrogen location in V is more sensitive to the strain than in Nb. The previous experiments on Ta,[3] which was the first experiment for the determination of hydrogen location, was carried out with a ^{11}B beam collimated to have divergence of less than 0.11°. This collimation was worse than that in the experiments on V[1] and Nb.[2] Therefore, such fine structures in the channeling angular profiles as observed for V and Nb were not observed. In the present study, the channeling experiments on H in Ta were repeated with a better collimated beam with divergence less than 0.076° and better statistics than in the previous experiment, and the effect of the internal strain on the location of H was investigated.

The specimen was a single crystal $TaH_{0.07}$ (α-phase). Hydrogen was introduced from gas phase. The channeling angular scan was made for <1 0 0>, <1 1 0>, and {1 0 0} channels at room temperature with 2.08 MeV $^{11}B^{2+}$ beam. The each data point was obtained by accumulating the yield up to the dose of more than 2.7 μC (1.2 μC in the previous experiment). The more detailed description on the experiment was given in the previous papers.[1)-3)]

The fine structures in the profiles of α-particle yields were observed as for V and Nb; a single central peak in the <1 0 0> channel, a central peak superposed with subsidiary peaks located at about $\pm 0.04°$ in the <1 1 0> channel, and a dip superposed with a small central peak in the {1 0 0} channel. These profiles unumbiguously indicate that most of H atoms are located at T (tetrahedral) sites. After this experiment the specimen was cooled to 200 K and kept there for 24 h. Then it was heated to 373 K and kept there for 6.5 h. After furnace-cooling to room temperature, the channeling angular scan was made again for {1 0 0} channel. The result is shown in Fig. 1. Although this heat treatment made the dip of backscattered ^{11}B-yield shallower, the angular profile of α-yield still exhibits a feature characteristic of T-site occupancy. This result leads to the conclusion that the hydrogen location in the α-phase of Ta-H system was not changed by this heat treatment. This result is essentially different from that on H in V; the {1 0 0} α-angular profile was changed markedly by the similar heat treatment.

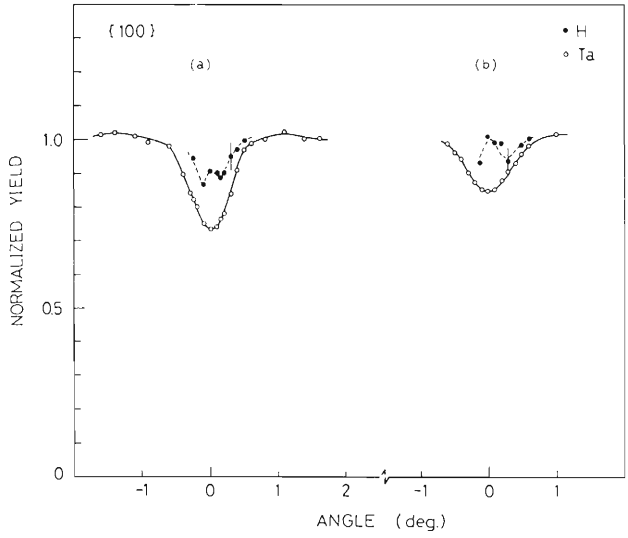

Fig. 1. A change of {1 0 0} angular profiles of α-particle yield (●) and backscattered ^{11}B yield (○) in (a) the virgin α-state and (b) β-redissolved α-state. Full and dashed curves are drawn to guide the eye.

As described in the case of V,[1] most of hydrogen atoms precipitate into the β-phase on cooling and the precipitates are redissolved on reheating, but this process introduces an appreciably large strain into the β-redissolved α-phase. Comparison of the present result with that on H in V indicates that hydrogen location in V was changed even when the {1 0 0} ^{11}B-dip recovered to 75% of its original value by redissolution of the β-phase, while in Ta the hydrogen location was not changed despite much smaller recovery of the {1 0 0} ^{11}B-dip, *i.e.*, only 55%. The observed frac-

* Faculty of Science and Engineering, Chuo University.

tion of such recovery suggests that the heat treatment introduced much larger internal strain in Ta than in V. Therefore the present result indicates that the lattice location of hydrogen is less sensitive to the strain in Ta than in V.

References

1) E. Yagi, T. Kobayashi, S. Nakamura, Y. Fukai, and K. Watanabe: *Phys. Rev. B*, **31**, 1640 (1985).
2) E. Yagi, S. Nakamura, T. Kobayashi, K. Watanabe, and Y. Fukai: *J. Phys. Soc. Jpn.*, **54**, 1855 (1985).
3) E. Yagi, T. Kobayashi, S. Nakamura, Y. Fukai, and K. Watanabe: *J. Phys. Soc. Jpn.*, **52**, 3441 (1983).

RIKEN Accel. Progr. Rep. 19 (1985)

III-2-31. Direct Evidence of Stress-Induced Site Change of H in V Observed by a Channeling Method

E. Yagi, T. Kobayashi, S. Nakamura, F. Kano,
K. Watanabe,* Y. Fukai,* and S. Koike**

Recently, Suzuki *et al.*[1] reported that the diffusivity of H in V is enhanced enormously by applying tensile stress lower than the elastic limit along the <1 1 1> direction, and concluded with the help of their Huang scattering experiments that it is a consequence of stress-induced site change T (tetrahedral site)→ 4T (a group of four T sites). However, their observation of "superdiffusion of 4T hydrogen" has since been questioned by Metzger[2] and Schober and Golczewski,[3] and still remains in dispute. More recently, we have observed that the site of H in V was changed by thermal cycling.[4] In that study, the lattice location of H was determined by the channeling method using a nuclear reaction $^{1}H(^{11}B,\alpha)\alpha\alpha$. In an original specimen of α-$VH_{0.1}$ prepared and measured at 150°C, the lattice location was found to be a T-site. When the specimen was cooled to room temperature and reheated to 150 °C, however, a drastic change in a {1 0 0} channeling angular profile for H was observed ; this indicated the site change from T-sites to displaced-T or 4T configuration. The measurement of the broadening of X-ray (2 0 0) diffraction line showed that the internal stress was introduced by this thermal cycling, apparently because of precipitation and redissolution of the β-phase. Thus we concluded that the observed site change was induced by the internal stress and the observation should be connected to the occurrence of the superdiffusion of H in V. In the present paper we report direct evidence for the stress-induced site change of H in V obtained by performing channeling experiments under well-controlled external stress.

Specimens were cut from a single crystal (99.95% pure vanadium supplied by Aremco Corporation) into a parallelepiped of 2 mm thick, 4 mm wide, and 6 mm long with a wire saw and electro-polished. The largest face was a {1 1 0} plane and the longest edge was parallel to the <1 0 0> direction. The specimen was annealed at about, 1,500°C for 75 h at 10^{-10} Torr, and subsequently doped with hydrogen from gas phase up to a concentration of $VH_{0.010-0.015}$. The channeling experiments were carried out by using a 2.02 MeV $^{11}B^{2+}$ beam in the similar way to that in the previous experiments.[4)-6)] In the present experiment, for the {1 0 0} planar channel configuration, both backscattered ^{11}B and emitted α-particle yields were measured as a function of angle between the incident beam direction and

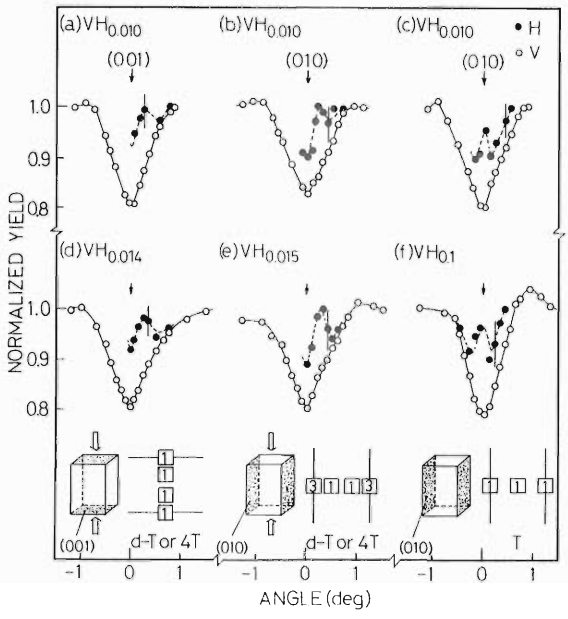

Fig. 1. (0 0 1) and (0 1 0) channeling angular profiles of backscattered ^{11}B and α-particle yields under the [0 0 1] compressive stress $\sigma=7kg/mm^2$ ((a), (b), (d), and (e)) or after releasing the stress (c) in $VH_{0.010}$, $VH_{0.014}$, and $VH_{0.015}$ (room temperature). (0 1 0) angular profiles in $VH_{0.1}$ at 150°C under $\sigma=0$ is shown in (f). The full curves and the dashed curves are drawn to guide the eye. The insets indicate the projections of T-sites and displaced-T or 4T configuration onto the plane perpendicular to the (0 0 1) or (0 1 0) planar channel. The lines represent the projections of atomic planes, and the squares the projected positions of interstitial sites with their relative weights indicated by numbers in squares.

* Faculty of Science and Engineering, Chuo University.
** Faculty of Science, Science University of Tokyo.

a {1 0 0} planar channel.

Under the compressive stress ($\sigma = 7$ kg/mm^2) applied in the [0 0 1] direction, angular scan was made for a (0 0 1) planar channel (perpendicular to the direction of the applied stress) and a (0 1 0) planar channel (parallel to the direction of the applied stress). Angular profiles thus obtained on the specimen of $VH_{0.010}$ are shown in Fig. 1 (a) and (b), and the result obtained after releasing the stress in Fig. 1 (c). Results of additional measurements on other specimens under the conditions corresponding to Fig. 1 (a), (b), and (c) are shown in Fig. 1 (d) for $VH_{0.014}$, 1 (e) for $VH_{0.015}$, and 1 (f) for $VH_{0.1}$, respectively. The angular profile in Fig. 1 (f) is the one obtained on α-$VH_{0.1}$ prepared at 150°C as described in a previous report.[4]

The results shown in Fig. 1 clearly indicate that hydrogen location under the uniaxial compressive stress of 7 kg/mm^2 is distinctly different from that in the stress-free state. The angular profile shown in Fig. 1 (c), which coincides with that in Fig. 1 (f), indicates that hydrogen location recovers to T-sites after releasing the stress. Under $\sigma = 7$ kg/mm^2, the (0 0 1) and (0 1 0) α-angular scans give similar profiles consisting of a wide dip with approximately the same width as that of the ^{11}B-dip and a subsidiary peak located at about 0.25°, the (0 0 1) dip being shallower than the (0 1 0) dip. They are very similar to the α-angular profile obtained after thermal cycling in our previous experiment on H in $VH_{0.1}$.[4] The present result indicates that, under the external stress, a major proportion of H atoms occupies interstitial sites displaced from the normal position of T-sites.

From the consideration on the angular profiles, the only explanation for the H configuration is made in terms of displaced-T or 4T configuration, in which the position of maximum density of H is displaced towards the O-sites (octahedral sites) by 0.44 Å.

Summarizing, we can definitely conclude that the configuration of H in V is extremely sensitive to the presence of stress; the transition T→ displaced-T or 4T can be induced by applying the compressive stress lower than the elastic limit, and the transition can be reversed by releasing the stress. More detailed results are described in Ref. 7.

References

1) T. Suzuki, H. Namazue, S. Koike, and H. Hayakawa: *Phys. Rev. Lett.*, **51**, 798 (1983).
2) T. H. Metzger: *Phys. Rev. Lett.*, **52**, 476 (1984).
3) T. Schober and J. Golczewski: *Phys. Rev. Lett.*, **52**, 478 (1984).
4) E. Yagi, T. Kobayashi, S. Nakamura, Y. Fukai, and K. Watanabe: *Phys. Rev. B*, **31**, 1640 (1985).
5) E. Yagi, T. Kobayashi, S. Nakamura, Y. Fukai, and K. Watanabe: *J. Phys. Soc. Jpn.*, **52**, 3441 (1983).
6) E. Yagi, S. Nakamura, T. Kobayashi, K. Watanabe, and Y. Fukai: *J. Phys. Soc. Jpn.*, **54**, 1855 (1985).
7) E. Yagi, T. Kobayashi, S. Nakamura, F. Kano, K. Watanabe, Y. Fukai, and S. Koike: *Phys. Rev. B*, **33**, 5121 (1986).

RIKEN Accel. Progr. Rep. 19 (1985)

III-3. Radiochemistry and Nuclear Chemistry

1. Production of Radioisotopes and Preparation of Labelled Compounds

T. Nozaki, S. Ambe, M. Iwamoto, E. Gotoh, T. Kitsunai, H. Nakatani, Z. Huang, Y. Minai, I. Arai, M. K. Kubo, M. Suehiro, and F. Yokoi

The following studies were undertaken in this period: (1) synthesis of ^{77}Br-labelled bromoperidol and bromospiperone (Fig. 1) for the study of dopamine receptors in the brain; (2) fabrication of automatic synthesizer for ^{11}C-labelled compounds and their use; (3) production of ^{45}Ti, ^{69}Ge, and ^{48}V and measurement of their uptake by plants, and (4) measurement of the adsorption of ^{29}Al and some other radionuclides by soils. Details of studies (3) and (4) are given separately in this volume.

For comparative study of dopamine-receptor visualizing agents, ^{77}Br-labelled bromoperidol (A) and bromospiperone (B) were synthesized and their behavior in rats and mice was studied. Bromine-77 was produced by the ^{75}As(α, 2n)^{77}Br reaction on a GaAs target, separated as sublimate by RF fusion of the target with copper, and made no-carrier-added aqueous solution.

From this ^{77}Br, A was synthesized by the Sandmeyer reaction as reported previously.[1] For the synthesis of B, the oxidative bromination was examined with H_2O_2 and Chloramine-T as oxidant. All the products were purified by HPLC with an ODS column. The results of the synthesis are shown in Table 1. Chloramine-T was found to be clearly superior to H_2O_2 for the synthesis of B. The comparison of the two bromination methods leads to the following summary. (1) Although the Sandmeyer reaction gives A as a single radioactive product, time-consuming purification processes are needed due to the formation of a lot of non-radioactive by-products. (2) Although B yielded by the oxidative bromination is accompanied with radioactive by-products, it can be purified more easily and rapidly. (3) By the Sandmeyer reaction radiobromine can usually be introduced at any aromatic position whenever the corresponding amine is obtained; but no choice of labelling position is allowed for the oxidative bromination. (4) As for the reaction time, oxidative bromination can be completed much more rapidly than the Sandmeyer reaction and can be used for the labelling with ^{75}Br.

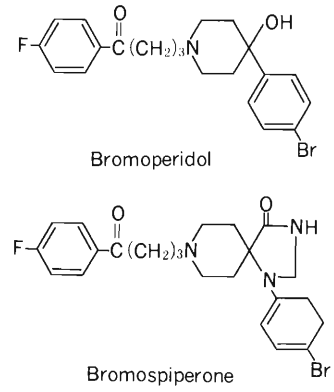

Fig. 1. Bromoperidol and Bromospiperone.

Table 1. Yield and specific activity.

	Bromoperidol	Bromospiperone	
		H_2O_2	Chloramine-T
Synthesis time (min)	15	60	5
Purification time (min)	90	100	80
Yield (%)	16.0	36.0	45.6
Specific activity (Ci/mol)	6×10^3	$>1\times10^6$	$>5\times10^5$

The two ^{77}Br compounds were administered intravenously into rats and mice, and their distribution patterns in the body were followed up to 4 h after the administration by sacrificing the animals. For the ^{77}Br taken up in the brain, fine distribution within this organ was examined by radioautography and the binding state was studied by sucrose gradient ultra-centrifugation of the homogenate and by filter-paper electropho-

resis of the extract. The results lead to the following conclusions. (1) Both A and B show accumulation at the position in the brain where the dopamine receptor is in high concentration. (2) Some parts of the accumulated bromine compounds are bound to the fraction of the cell where the receptor exists. (3) These radioactive compounds in the bound states are replaced by non-radioactive compounds with the same or similar chemical structures and properties. (4) Bromoperidol shows rapider clearance from the blood and higher uptake into the brain. Its considerable portion, however, is bound non-specifically in the brain, resulting in the deterioration of the S/N ratio in imaging. (5) No notable cleavage of C-Br bond was observed for these compounds *in vivo*.

The automatic synthesizer of $^{11}CH_3I$ fabricated previously are working in the National Nakano Chest Hospital. We intend to use it for the synthesis of α-methyl (^{11}C)-fatty acids and their derivatives by malonic ester synthesis. Recently, Dr. Hara, the National Nakano Chest Hospital, developed a suitable synthetic method for pyruvic acid labelled with ^{11}C at the carboxyl position using an enzyme, and demonstrated its extreme usefulness for various kinds of diagnosis and fundamental study concerning metabolism. An automatic synthesizer of this compound is under fabrication in our institute. Details concerning the synthesizer will be reported next year.

Reference

1) M. Suehiro, F. Yokoi, M. K. Kubo, M. Iwamoto, T. Nozaki: Proc. IAEA Conf. Labelled Comp. Radiopharm., p. 311 (1984).

RIKEN Accel. Progr. Rep. 19 (1985)

III-3-2. ^{29}Al Radiotracer Study on Adsorption of Aluminum by Soils

Y. Minai, S. Ambe, and T. Nozaki

In recent a few years, our group has studied cyclotron production of ^{29}Al *via* the ^{26}Mg(α,p)-^{29}Al reaction and its biological use as a tracer. Preliminary results were presented in the recent volumes of this report.[1)-3)] In this period, we studied the adsorption of aluminum from aqueous solution by soils. Also, possible radiochemical impurities in the product were examined and the removal was studied.

Typical Japanese soils from rice fields in Fukui and Tochigi and from forests near these rice fields were used for adsorption study of aluminum. These soils were supplied by Dr. K. Yuita. Each soil sample (5 g) was well mixed with ^{29}Al aqueous solution (50 ml) of pH about 2, 4, or 7. In order to observe adsorption kinetics, a part of mixture was taken at a given interval (maximum mixing time was 20 min) and centrifuged to give supernatant solution. Then the solution was withdrawn and its radioactivity and pH were measured with a Ge(Li) detector and a pH meter, respectively.

Typical results are presented in Fig. 1. In the first few minutes, the adsorption of aluminum proceeded rather quickly. With the mixing time, decrease in activity remaining in the solution and increase in pH were observed for all the soil samples. This implies that adsorption of aluminum hydroxides formed at neutral pH is an important process. For the forest soils from Fukui and Tochigi and for the rice-field soil from Fukui, the activities remaining in the solutions were different while pH values were almost the same pH. For the rice-field soil in Tochigi adsorption kinetics similar to that for the rice-field soil in Fukui was observed, though the pH change was completely different between them. The physical properties including particle size distribution of the soils are different from one another.[4)] Various chemical compositions (*e.g.*, the content of organic carbon) are also different.[4)] These differences in physical and chemical properties may influence the adsorption behavior of aluminum onto soils. Complex formation of aluminum with organic materials dissolved from the soils seems to suppress the adsorption of aluminum from the solution especially for the forest soil from Tochigi.

In Fig. 2 the variations of activity and pH of the HCl solution with addition of disodium ethylenediaminetetraacetic acid (EDTA) are plotted against the contact time. Figure 2 shows that addition of EDTA suppresses the adsorption of ^{29}Al without notable change in the pH. This result suggests that formation of the EDTA complex of ^{29}Al stabilizes aluminum in a solution

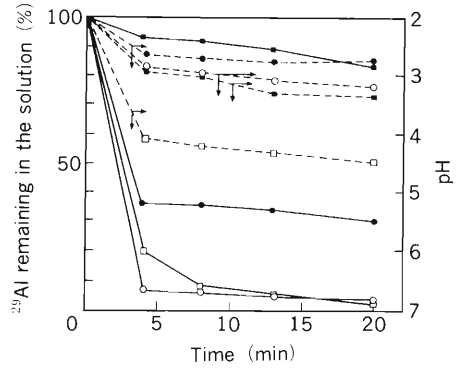

Fig. 1. Variations of the relative activity (solid line) and pH (dotted line) of ^{29}Al-HCl aqueous solution during contact with soils. ●, forest soil from Fukui; ○, rice-field soil from Fukui; ■, forest soil from Tochigi; and □, rice-field soil from Tochigi.

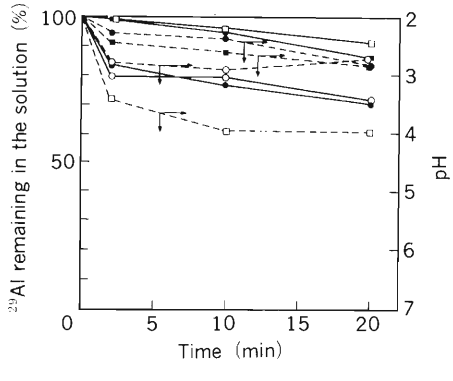

Fig. 2. Variations of the relative activity (solid line) and pH (dotted line) of ^{29}Al-HCl aqueous solution with addition of EDTA during contact with soils. ●, forest soil from Fukui; ○, rice-field soil from Fukui; ■, forest soil from Tochigi; and □, rice-field soil from Tochigi.

phase.

Details on these and previous results[1)-3)] will be published in near future.

References

1) Y. Minai, T. Nozaki, S. Ambe, and M. Iwamoto: *RIKEN Accel. Progr. Rep.*, **16**, 120 (1982).
2) T. Nozaki, S. Ambe, M. Iwamoto, and Y. Minai: *RIKEN Accel. Progr. Rep.*, **17**, 95 (1983).
3) T. Nozaki, S. Ambe, M. Iwamoto, Y. Minai, M. K. Kubo, E. Tsuchida, M. Yuasa, Y. Ogata, H. Nishida, M. Suehiro, and F. Yokoi: *RIKEN Accel. Progr. Rep.*, **18**, 121 (1984).
4) K. Yuita: private communication.

RIKEN Accel. Progr. Rep. 19 (1985)

III-3-3. Preparation of Non-Carrier-Added ^{45}Ti and ^{69}Ge and Their Uptake by Plants

M. K. Kubo, Y. Minai, T. Nozaki, and T. Tominaga*

While titanium and germanium are both present as minor constituents in biological systems, their role and behavior are still unclear. This is partly because adequate radioisotopes for *in vivo* study of such elements in organisms have not been prepared. The aim of the present study is to prepare their radioisotopes (^{45}Ti and ^{69}Ge) and labeled compounds suitable for radiotracer studies and to investigate their uptake by plants.

The excitation functions for the production of ^{45}Ti (3.09 h, β^+ 86%+EC) and ^{69}Ge (39 h, EC 64%+β^+), *i.e.*, ^{45}Sc(p,n)^{45}Ti and ^{69}Ga(p,n)^{69}Ge, were obtained by means of the stacked foil method. The proper incident proton energy for the production of these nuclides was found to be 12 MeV in order to obtain maximum yields, minimizing the generation of radioactive impurities unseparable by radiochemical techniques.

1. ^{45}Ti: The target material (Sc_2O_3 powder wrapped in Al foil) was bombarded with a 12 MeV proton beam from the cyclotron and then dissolved in 12 M HCl. After the extraction of ^{45}Ti into a chloroform solution with oxine, ^{45}Ti was back-extracted into a dilute citric acid solution. Although this solution contained less than 3 ppm Sc, no γ-rays other than those from ^{45}Ti were observed. The radioactivity of the solution was about 2×10^6 Bq/ml.

Young cucumber with root was immersed in this solution, and the uptake of ^{45}Ti was monitored by counting the 0.511 MeV photons from the leaf part by a collimated Ge(Li) detector. ^{45}Ti was found to reach the leaves fairly rapidly. Changing the component of the solution and other factors, the ^{45}Ti uptake process is now being studied systematically. In Fig. 1 the ^{45}Ti accumulation in the leaves for light-on and -off condition was plotted against the amount of water absorbed from the root. The uptake of ^{45}Ti and water was affected by light. ^{45}Ti was not extracted from the leaves by organic solvents or dilute acids, but extracted by an H_2O_2 solution. ^{45}Ti may gradually become strongly bound to cell.

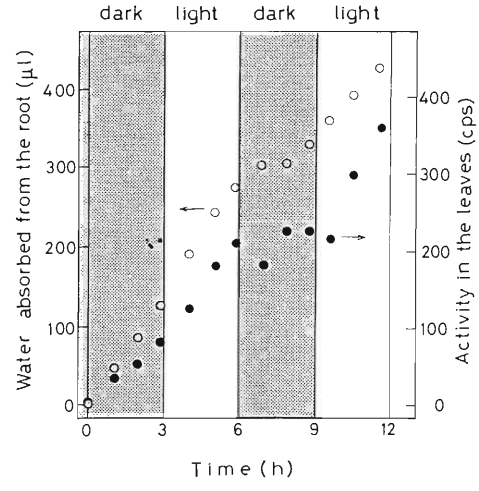

Fig. 1. The change of the activity in the leaves (●) and the amount of water absorbed from the root (○). Light was turned on and off every 3 h. Activity is corrected to the start time of the experiment.

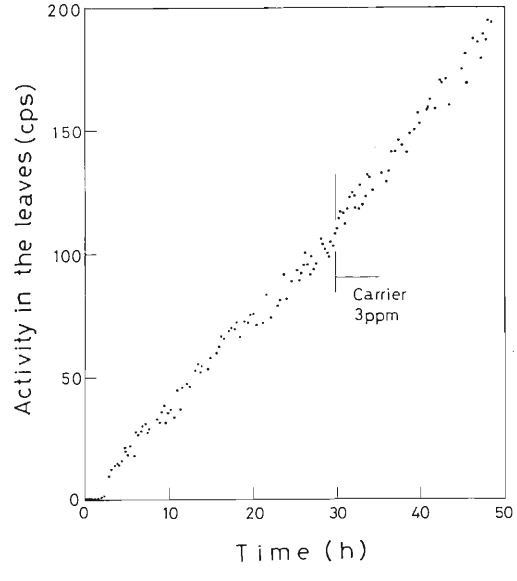

Fig. 2. The absorption of ^{69}Ge by cucumber. Carrier Ge solution was added 30 h after the beginning of the experiment to make up 3 ppm Ge condition. The decay of ^{69}Ge is corrected to the start time of the experiment.

* Faculty of Science, The University of Tokyo.

2. ^{69}Ge: Irradiated Ga_2O_3 powder was dissolved in 12 M HCl and ^{69}Ge was separated by distillation of $^{69}GeCl_4$. $H_2{}^{69}GeO_3$ aqueous solution was obtained finally.

The ^{69}Ge uptake by cucumber from this solution was examined by the method similar to ^{45}Ti. ^{69}Ge was also absorbed from the root and migrated to the leaves rather fast. Addition of carrier did not affect this process (Fig. 2). Unlike ^{45}Ti, ^{69}Ge seemed to be in dissolved state in the leaves, since ^{69}Ge was easily extracted from the leaves by water.

RIKEN Accel. Progr. Rep. 19 (1985)

III-3-4. Charged Particle Activation Analysis

T. Nozaki, Y. Itoh, M. Iwamoto, Y. Ohkubo,
T. Kimura, and H. Fukushima

In this period the following studies were undertaken: (1) reexamination of calibration curves for the IR spectrophotometry of oxygen and carbon in semiconductor silicon; (2) analysis of carbon in gallium arsenide; (3) preliminary study for the use of N-15 as activable tracer of nitrogen in solid state sciences; (4) analysis of carbon in aluminium; (5) surface oxygen analysis under different atmospheric conditions. Also, various samples, about 250 in all, were analyzed for carbon or oxygen in the trust analysis system by the Japan Chemical Analysis Center.[1] Details of studies (2) and (3) are presented individually in this volume.

The IR spectrophotometry is used for routine analysis of oxygen and carbon in semiconductor silicon, though it is of much less sensitivity than charged particle activation analysis. Since semiconductor silicon has become an international trade commodity and since the necessity for the control of its oxygen and carbon concentrations has become widely recognized, it is now urgently needed to obtain highly reliable calibration curves for the two IR determinations and to use them under international consensus. Japan Electronic Industry Development Association thus organized a committee for this purpose and also for the precipitation of IR standard samples with various, excitly known oxygen or carbon concentrations to distribute all over the world. For oxygen, reliable calibration curve was obtained and IR standard samples were prepared and distributed already.[2] National Bureau of Standard, U.S.A., however, proposed to repeat the same procedure as we undertook to get the calibration curve, with American and European laboratories taking not only in the round robin IR measurement but also in the charged particle activation analysis. Thus, samples were prepared and the schedule was set. In Japan both the IR measurement and activation analysis have just been completed.

For carbon, about 70 samples were prepared and submitted to round robin IR measurement by about 20 laboratories including those of foreign organizations. After the IR measurement, each of 24 sample wafers was cut into two pieces and the resultant 48 silicon plates were analyzed by charged particle activation. For this analysis we improved the procedure. Formerly the sample activated by the $^{12}C(^{3}He,\alpha)^{11}C$ reaction was dissolved in a $HF\text{-}HNO_3\text{-}KIO_4$ solution. In this method, however, a small part of the ^{11}C was found to sometimes escape in the form of ^{11}CO without being absorbed by the alkaline solution.[3] Now we dissolve the sample after bombardment, surface etching and, pulverization in a NaOH solution containing carbonate carrier (30 mmol). The solution was heated to dryness and further to dull red in a microwave oven. Then sulfuric acid was added to the resultant mass to generate $^{11}CO_2$, which was converted into Li_2CO_3 precipitate for counting. The annihilation radiation from the filtered precipitate was measured by a well-type NaI scintillator (for C concentrations over 0.5 ppm wt) or a pair of BGO scintillators operated in coincidence (for lower C concentrations). In Fig. 1 is shown the resultant calibration curve, which agrees fairly well with the curve we reported many years ago.[4] This result is as yet rather provisional, because their still exist some uncertainties in the data treatment and also in the activation analysis, in which some corrections due to the difference in the physical and chemical state between the Li_2CO_3 and the activation standard of graphite and to the interference of oxygen *via* the $^{16}O(^{3}He, 2\alpha)^{11}C$ reaction. The final result will be obtained in a few months.

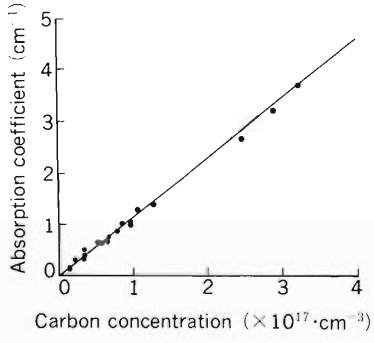

Fig. 1. Calibration curve for IR spectrophotometry of carbon in silicon (Provisional result).

Effects of light element impurities on the property of matrix has attracted a lot of interest in the study and production of semiconductor materials. Recently the necessity of similar analysis has been pointed out by metal industries for some other matrices. Nikkeigiken Co., a producer of aluminium, collaborates with us for the study of carbon in aluminium, for which even the phase diagramme is unknown in extremely low carbon concentration ranges. For the radioactivation of carbon, the $^{12}C(^{3}He,pn)^{11}C$ reaction can not be used, because of the interference of boron *via* the $^{10}B(^{3}He,pn)^{11}C$ reaction. Thus the $^{12}C(d, n)^{13}N$ reaction should be adopted and the ^{13}N(10 min half-life) should be separated quickly. We first studied the separation of the ^{13}N, and set up the following separation procedure: (1) dissolve the sample after bombardment and surface etching in conc. hydrochloric acid containing NH_3 as carrier, (2) add granular NaOH to the solution, and distill $^{13}NH_3$, and (3) catch the distillate by a sodium tetraphenylboron solution, and then collect ammonium tetraphenylboron precipitrate. Various aluminium samples suitable for the measurement of some physical constants and of the behavior of carbon in aluminium have been collected and are going to be analyzed.

The surface oxygen analysis has been continued using a new bombardment apparatus,[5] and a summary of the results will be published soon.

References

1) T. Nozaki, Y. Itoh, M. Iwamoto, H. Shinyashiki, K. Nomura, T. Kimura, and H. Fukushima: *RIKEN Accel. Progr. Rep.*, **17**, 96 (1983).
2) T. Iizuka, S. Takasu, M. Tajima, T. Arai, T. Nozaki, N. Inoue, and M. Watanabe: *J. Electrochem. Soc.*, **132**, 1707 (1985).
3) T. Nozaki, Y. Yatsurugi, and N. Akiyama: *J. Radioanal. Chem.*, **4**, 87 (1970).
4) Y. Endo, Y. Yatsurugi, N. Akiyama, and T. Nozaki: *Anal. Chem.*, **44**, 2258 (1972).
5) T. Nozaki and M. Iwamoto: *IPCR Cyclotron Progr. Rep.*, **11**, 116 (1977).

RIKEN Accel. Progr. Rep. 19 (1985)

III-3-5. Utilization of N-15 as Activable Tracer

T. Nozaki and Y. Itoh

The solubility and diffusion constant have remained obscure for nitrogen in most solid substances. Nitrogen is abundant in nature, and the determination of its trace in a solid bulk is often interfered with nitrogen on the surface and from the environment. Natural abundance of nitrogen-15 is 0.365%. We intend to use N-15 as activable tracer for the measurement of the above two physical constants first in semiconductor silicon. The following three nuclear reactions are regarded as promising for the activation: (1) $^{15}N+p\rightarrow{}^{12}C+\alpha+\gamma$ (4.4 MeV): (2) $^{15}N+d\rightarrow{}^{16}O+n$ (or p and β^-)$+\gamma$ (6.13, 7.11 MeV), and (3) $^{15}N(\alpha, n)^{18}F$. Reactions 1 and 2 are the reverse reactions used for the depth profiling of H and high sensitivity determination of D, respectively.[1]

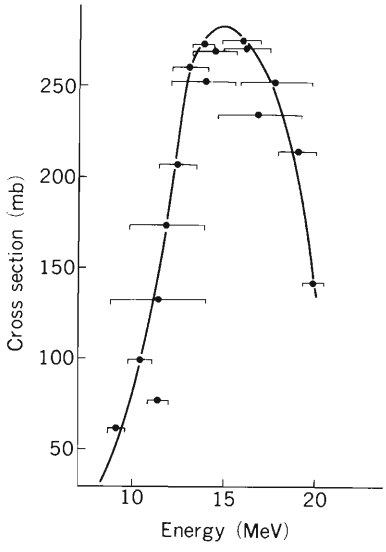

Fig. 1. Excitation function for the $^{15}N(\alpha,n)^{18}F$ reaction (indicated by the smoothening of the histograms).

We measured the excitation function and thick target yield for Reaction 3. Stacked targets of $30.2\pm0.5\%$ enriched $Na^{15}NO_2$ on aluminium foils were prepared by the precipitation method and used for the excitation function measurement. The thick target yield was measured with the $Na^{15}NO_2$ disk prepared by pressing. The results are shown in Figs. 1 and 2. The thick target yield for the $^{16}O(^3He, p)^{18}F$ is also shown in Fig. 3.[2] We have already developed a very suitable method for separating ^{18}F from any matrices, and now can determine as low as 1 ppb of oxygen.[3] From Fig. 2, it is thus clear that down to 1 ppb of ^{15}N can be determined. We formerly developed also a method of activating O with equal probability along the depth by rotating a set of aluminium absorbers in the incident ^3He path.[4] A similar method can be used in the activation of ^{15}N. The α-particle energy for this activation, however, should be limited to 23 MeV for samples containing O, which for higher energies gives ^{18}F by the

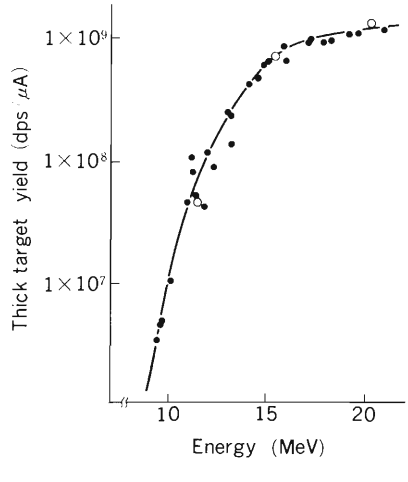

Fig. 2. Thick target yield for the $^{15}N(\alpha, n)^{18}F$ reaction. ●: Observed. ○: Calculated from the excitation function.

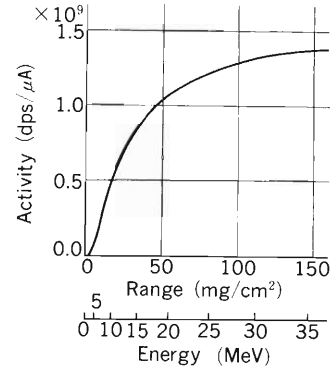

Fig. 3. Thick target yield for the $^{16}O(^3He,n)^{18}F$ reaction.

$^{16}O(\alpha, pn)^{18}F$ reaction.

We intend to measure the solubility and diffusion constant of N first in semiconductor silicon at various temperatures. Shallow parts ($\lesssim 50$ μm from the surface) of the sample will be analyzed by Reactions 1 and/or 2, and Reaction 3 will be used for deep portions. We are keenly interested in examining closely whether any enhanced solubility and diffusion be observed in the sample portion near the surface as compared with deeper portions.

References

1) S. Hayashi, H. Nagai, M. Aratani, T. Nozaki, M. Yanokura, I. Kohno, O. Kuboi, and Y. Yatsurugi: *RIKEN Accel. Progr. Rep.*, **18**, 134 (1984).
2) T. Nozaki, M. Iwamoto, and T. Ido: *Int. J. Appl. Radiat. Isotopes*, **25**, 393 (1974).
3) T. Nozaki: *J. Radioanal. Chem.*, **72**, 527 (1982).
4) Y. Itoh and T. Nozaki: *J. Radioanal. Chem.*, **70**, 329 (1982).

RIKEN Accel. Progr. Rep. 19 (1985)

III-3-6. Simultaneous Charged Particle Activation Analysis of Carbon and Boron in Gallium Arsenide

T. Nozaki, Y. Itoh, Y. Ohkubo, T. Kimura, and H. Fukushima

Carbon in semiconductor GaAs is thought to be an electrically active impurity, and its exact determination is urgently needed in the research and production of this material. In this determination, an absolute carbon content in the bulk matrix should be known free from surface carbon and external contamination. Various methods,[1)-5)] have been used for this purpose, but some problems still exist in the sensitivity, reliability or exactitude. For most of the methods, a calibration curve or a reference sample is needed in order to obtain an absolute carbon concentration.

Charged particle activation analysis is an exception; graphite can be an ideal reference material. The $^{12}C(^{3}He,\alpha)^{11}C$ reaction is mostly used for the activation of carbon in various matrices, but boron interferes with this analysis by giving ^{11}C *via* the $^{10}B(^{3}He,pn)^{11}C$ reaction. Most of present gallium arsenide semiconductors are produced by the liquid encapsulated Czochralski (LEC) method and contain a much higher concentration of boron than carbon. Hence, the $^{12}C(d,n)^{13}N$ reaction should be adopted for activation and the ^{13}N rapidly separated and measured (^{13}N: 9.96 m, β^+, no γ). It is clear that carbon and boron can be determined simultaneously when individual separation of the ^{13}N and ^{11}C formed by $^{10}B(d,n)^{11}C$ and $^{11}B(d,2n)^{11}C$ is possible. Photon activation analysis by the $^{12}C(\gamma,n)^{11}C$ reaction can be interfered with a much higher concentration of boron through the proton-generating reactions [$^{69}Ga(\gamma,p)^{68}Zn$, $^{71}Ga(\gamma,p)^{70}Zn$, and $^{75}As(\gamma,p)^{74}Ge$] and the succeeding $^{11}B(p,n)^{11}C$ reaction. A simple calculation leads to a result that for LEC GaAs the ^{11}C activity induced by this secondary reaction could be comparable to that by the $^{12}C(\gamma,n)^{11}C$ reaction.

We made efforts to find out a simple procedure for separating ^{13}N and ^{11}C in GaAs based on dry fusion.[6),7)] By the recoil implantation of ^{13}N and ^{11}C into GaAs plates in the reactions $^{16}O(p,\alpha)^{13}N$ and $^{14}N(p,\alpha)^{11}C$ induced in O_2 and N_2 near the plates, we were able to prepare suitable samples for this study and then to prove that in our procedure given below the ^{13}N and ^{11}C were separated in individual columns with satisfactory purity.

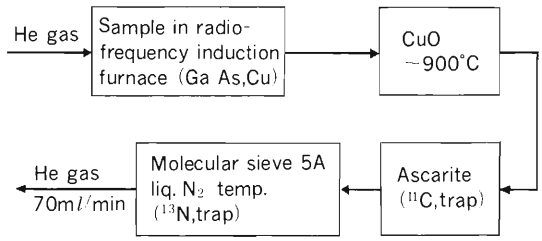

Fig. 1. Schematic diagram of separation procedures.

A GaAs plate (2×1.5 cm^2 in area, 0.5-2 mm in thickness) was bombarded for 10 min with a deuteron beam (10 MeV, 1.5 μA). After removing surface contamination of the bombarded plate, as shown in Fig. 1, the sample was fused by radiofrequency heating together with copper grains in a helium stream passing through columns of CuO heated to 900°C, Ascarite, and Molecular Sieve 5A cooled with liquid nitrogen. The radioactivity of ^{13}N trapped in the molecular sieve was measured by coincidence counting of annihilation radiations with a pair of bismuth germanium oxide scintillators. The ^{11}C in Ascarite was counted by a well-type NaI detector. It took about 20 min to initiate counting after bombardment. A graphite plate and B_2O_3 powder were used as activation standards for carbon and boron, respectively.

The detection limit in this method is estimated to be 2×10^{14} atoms cm^{-3} for both carbon and boron. Carbon concentrations between 8×10^{14} and 3×10^{16} atoms cm^{-3} have been found, depending on the sample history. For boron, LEC crystals have been found to contain 1×10^{15} to 8×10^{17} atoms cm^{-3}. The absorptivity of carbon in GaAs has not been clear in IR spectrophotometry. Our results have given carbon concentrations a few times smaller than the values given by FTIR measurement calibrated indirectly from the electrical conductivity.[3)]

Studies are in progress to obtain a more reliable calibration curve for IR spectrophotometry and to obtain results meaningful in semiconduc-

tor science and technology.

References

1) Y. Homma and Y. Ishii: *J. Vac. Sci. Technol. A*, **3**, 356 (1985).
2) Y. Homma, Y. Ishii, T. Kobayashi, and J. Osaka: *J. Appl. Phys.*, **57**, 2931 (1985).
3) M. R. Brozel, J. B. Clegg, and R. C. Newman: *J. Phys. D: Appl. Phys.*, **11**, 1331 (1978).
4) G. B. Stringfellow, K. Koschel, F. Briones, J. Gladstone, and G. Patterson: *Appl. Phys. Lett.*, **39**, 581 (1981).
5) M. Valladon, G. Blondiaux, C. Koemmerer, J. Hallais, G. Poiblaud, A. Huber, and J. L. Debrun: *J. Radioanal. Chem.*, **58**, 165 (1980).
6) A. Marschal, I. Gosset, and C. Engelmann: *J. Radioanal. Chem.*, **8**, 243 (1971).
7) J. M. A. Lenihan, S. J. Thomson, and V. P. Guinn: Advanced in Activation Analysis, Academic Press, London and New York, Vol. 2, p. 47 (1972).

RIKEN Accel. Progr. Rep. 19 (1985)

III-3-7. Application of PIXE to Medical Science (III)

K. Maeda, H. Kusuyama, Y. Sasa, Y. Yokode, and M. Uda

Elemental analysis of biological samples is of prime importance from the diagnostic and therapeutic viewpoints. We have continued a study on the application of the particle induced X-ray emission (PIXE) analysis to medical science. In previous reports,[1),2)] we described the analysis of some human tissue samples using 5 MeV protons accelerated by the cyclotron as projectiles. From the end of the last year, He^+ ions with energy up to 8 MeV have been available from the linac and greatly improved sensitivities for detection of elements having medium atomic numbers.

The samples analyzed were (1) malignant tumors, benign tumors, and normal tissues around tumors taken from patients suffering from diseases in thyroid, kidney, bladder, and testis, and (2) urinary calculi taken from patients of stone diseases. Freeze-dried tissue samples were sectioned with a microtome to about 10 μm thick slices and then backed with 1 μm thick polypropylene or 4 μm thick Mylar film. Calculus samples were mechanically broken in appropriate form for scanning analysis and served as targets without pre-treatments.

Representative spectra induced by 8 MeV He^+ ions are shown in Fig. 1. The samples are tumor and normal tissues in a thyroid gland. L X-ray peaks of iodine, which could not be distinguished

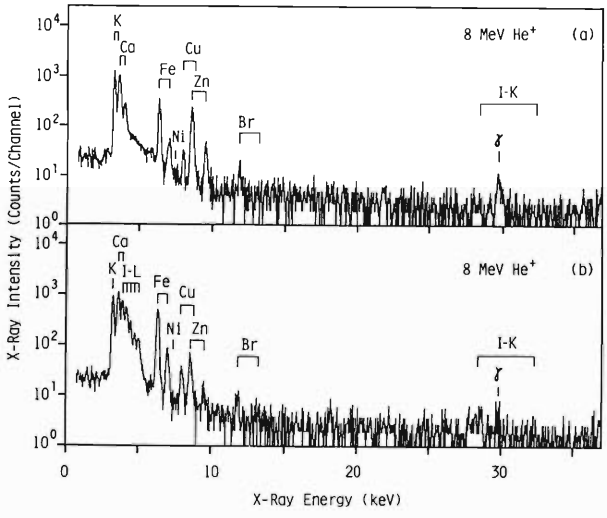

Fig. 1. PIXE spectra of (a) tumor and (b) normal tissues in a thyroid gland taken from a patient of colloid adenoma. A 1 mm thick polyethylene film was used as an X-ray absorber. γ-Rays at 29.6 keV are due to ^{40}K produced by the $^{37}Cl(\alpha,n\gamma)$ reaction.

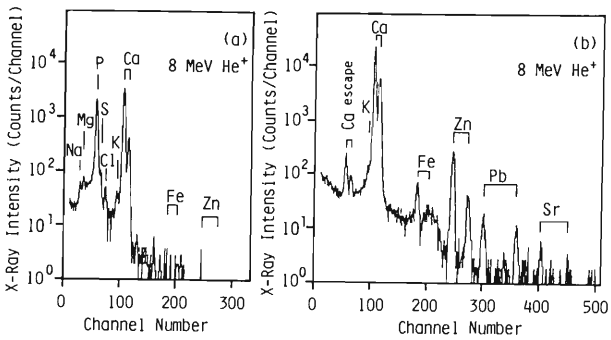

Fig. 2. PIXE spectra of a ureter stone. (a) A 1 μm thick polypropylene and (b) a 1 mm thick polyethylene films were used as X-ray absorbers.

in the 5 MeV H^+ induced spectra[1)] because low energy characteristic X-rays were superimposed on a high background due to continuous X-rays, are clearly observed in the spectrum obtained from normal tissue. Peak to background ratios for K X-rays of Fe, Ni, Cu, and Zn are also much higher in 8 MeV He^+ impact than in 5 MeV H^+ impact. Previously, we found deficiency of iodine in diseased thyroid tissues[1)] and enrichment of iron in renal cancers.[2)] The PIXE analysis of the tissue samples with 8 MeV He^+ impact supports such findings.

Analysis of calculus composition is an interesting subject of the PIXE because the precise mechanism of stone formation is still unknown in spite of frequent occurrence of bilary and urinary stone diseases. We have analyzed several human bladder and ureter stones. Na, Mg, P, and Ca as major elements and K, Fe, Zn, and Sr as minor elements were detected in all the stones analyzed here. The Mg content of the bladder stones was very high as compared to that of the ureter stones. Pb was found, in relatively high concentration, in a ureter stone taken from a female patient who had been working in an automobile service station for many years. The PIXE spectra obtained from this stone are shown in Fig. 2.

References

1) M. Uda, K. Maeda, Y. Yokode, and Y. Sasa: *RIKEN Accel. Progr. Rep.*, **17**, 134 (1983).
2) K. Maeda, H. Kusuyama, Y. Yokode, Y. Sasa, S. El. Nasr, M. Kobayashi, and M. Uda: *RIKEN Accel. Progr. Rep.*, **18**, 128 (1984).

RIKEN Accel. Progr. Rep. **19** (1985)

III-3-8. Geochemical Application of PIXE (I)

H. Yabuki, A. Okada, S. Yabuki, K. Maeda,
Y. Sasa, and M. Uda

Since 1960's, an electron microprobe has been widely used for non-destructive determination of major elements (more than *ca.* 1,000 ppm) in microscopic objects. Recently, however, the importance of the information about elements present in each constituent in geological samples in concentrations below their detection limits has been emphasized. The particle-induced X-ray emission (PIXE) spectroscopy is expected to meet the request for *in situ* quantitative analysis of trace elements with high precision.

We have initiated the application of PIXE to geological and cosmological samples. Here we report the preliminary results of qualitative analyses by PIXE using the linac

The experimental setup used has been described by Maeda *et al.*[1),2)] As target objects, we used polished thin sections, 30 μm or thicker, prepared for conventional geological use. The targets were bombarded with He^+ ions accelerated by the linac to 2.0 MeV/amu and emmited X-rays were detected with a Si(Li) detector. The size of ion beams focused on the targets was larger than 0.5×0.5 mm^2. Appropriate absorbers were selected and inserted between the sample and the detector to obtain better statistics in a high energy X-ray region.

The samples under study and the elements detected by this method are listed in Table 1. Figures 1 (a) and (b) show the representative PIXE spectra obtained from apatite and fergusonite, respectively. Major elements as well as minor or trace ones, especially a series of rare-earth elements, were successively detected in various minerals. Cobalt (~0.5 wt %) was not identified in iron meteorite because of the presence of adjacent high peaks of iron and nickel.

References

1) K. Maeda and M. Uda: *Reports I.P.C.R.*, **58**, 96 (1982) (in Japanese).
2) K. Maeda, Y. Sasa, and M. Uda: *RIKEN Accel. Progr. Rep.*, **17**, 123 (1983).

Table 1. Results of qualitative analysis of various minerals and an iron meteorite (Odessa) by PIXE spectroscopy.

Sample name (Locality)	Formula or major elements	Detected elements
Fergusonite (Japan)	$(Y,Er,Ce,Fe)(Nb,Ta,Ti)O_4$	P,Cl,Ca,Ti,Fe,Zn,Se, Y,Zr,Nb,Cd,Ce,Nd,Gd, Er,Yb,Ta,Bi,Th,U
Samarskite (Japan)	$(Y,Er,Ce,U,Ca,Fe,Pb,Th)(Nb,Ta,Ti,Sm)_2O_6$	Cl,Ca,Sc,Ti,Mn,Fe,Nb, Ta,Au,Pb,U
Monazite (Japan)	$(Ce,La,Nd)PO_4$	Na,Al,Si,P,Rh,Ag,Te, Cs,La,Ce,Nd,Gd(?),Er(?), Tm(?),Th
Gadolinite (Norway)	$Be_2FeY_2O_2(SiO_4)_2$	Al,Si,Cl,Ti,Y,Nb,Cd,Te, Nd,Gd,Dy,Er,Yb,Ta,Ar, Th,U
Columbite (Japan)	$(Fe,Mn)(Nb,Ta)_2O_6$	Si,Ti,Mn,Fe,Ge,Nb,Ta
Beryl (Korea)	$Be_3Al_2Si_6O_{18}$	Al,Si,K,Fe,Zn,Cs,La
Biotite (Japan)	$H_2K(Mg,Fe)_3Al(SiO_4)_3$	Al,Si,K,Ca,Ti,Mn,Fe, Zn,U(?)
Apatite (Japan)	$3Ca_3(PO_4)_2 \cdot CaF_2$	P,Ca,Mn,Fe,Sr,Y,Ce, Nd,Sm
Apatite (Mexico)	$3Ca_3(PO_4)_2 \cdot CaF_2$	P,Ca,Fe,As,Y,La,Ce,Nd, Sm,Gd
Iron meteorite (U. S. A.)	Fe,Ni,Co	Cr,Fe,Ni,La,Sm

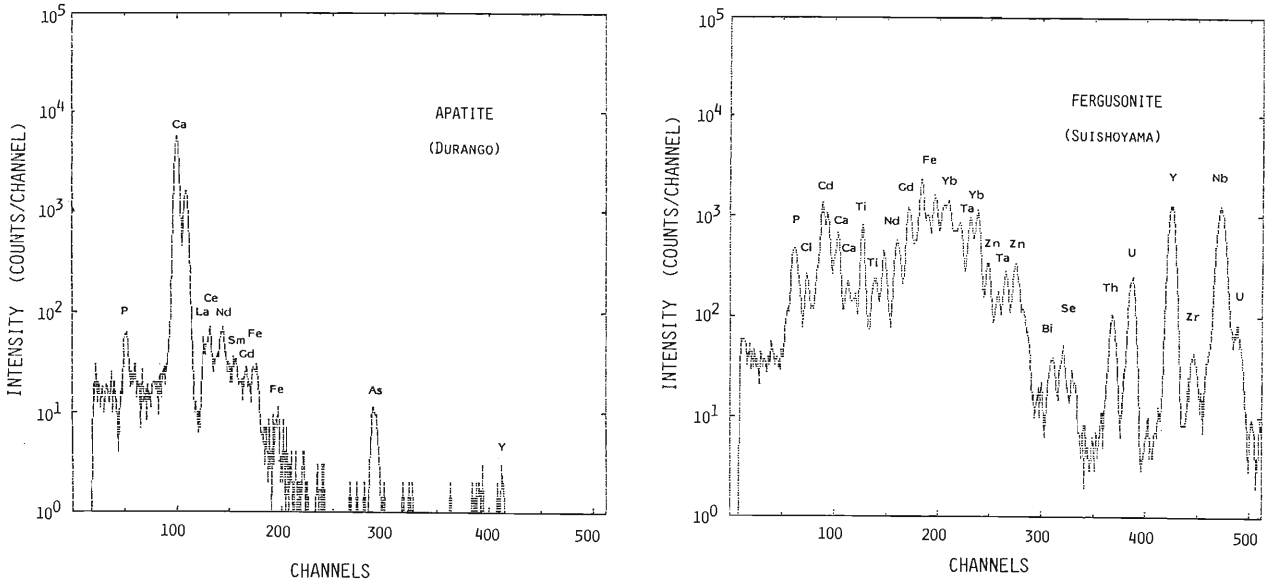

(a) (b)

Fig. 1. PIXE spectra obtained from (a) apatite (Durango, Mexico) and (b) fergusonite (Suishoyama, Japan) irradiated with 8.1 MeV He^+. 27 mg/cm^2 polyethylene film was used as an absorber.

RIKEN Accel. Progr. Rep. 19 (1985)

III-3-9. Hydrogen Analysis in Thin Surface Layer of Amorphous Silicon by the Rutherford Forward Scattering Method

K. Saito,* H. Yamaguchi,* H. Nagai, M. Yanokura,
M. Aratani, S. Hayashi, Q. Qiu, and T. Nozaki

Hydrogen is one of the main impurities for some semiconductor materials such as amorphous silicon (a-Si: H) films and insulation films. Since the properties of these materials are seriously affected by hydrogen content, precise analysis of hydrogen has been requested in the semiconductor production process.

Generally, well-known methods such as Infrared Spectrometry (IR), Secondary Ion Mass Spectrometry (SIMS), or Mass Analysis have been used in routine analysis. However, for the precise quantification of hydrogen, well characterized standard samples are required in these methods. In the present study, the Rutherford Forward Scattering (RFS) method[1] was applied to the analysis of a-Si: H films by using the linac. In this method, no standard samples are required.

1. Accuracy of Hydrogen-depth Analysis by the RFS Method

Accuracy of hydrogen-depth analysis was checked from the depth profile of hydrogen implanted into single crystal of silicon substrate determined with the energy of 35 keV and the dose of 5×10^{16} ions/cm^2. Measurements were performed on the samples for three times and Gaussian type profiles, as expected from the LSS** theory, were obtained as shown in Fig. 1.

The depth at the peak of profiles agreed with the value calculated by using LSS theory and the total hydrogen content obtained from the integration of the profile agreed with implantation dose within the error of 10%. A small peak found at the surface was attributed to absorbed hydrogen. The height of this peak varied due to reabsorption of recoiled hydrogen.

2. Quantification of Hydrogen in a-Si:H Films

The contents of hydrogen in a-Si: H films were determined by the RFS method and the obtained values were used for calibration for IR or SIMS analysis. Samples examined were hydrogenated a-Si: H films grown by a plasma CVD method on silicon substrates under different conditions.

Results of hydrogen analysis obtained by the RFS method are shown in Fig. 2 which represents concentration-depth profiles of the samples with different concentrations and different film thicknesses.

The IR and SIMS analyses were performed for the same samples. Absorbance of the Si-H bond at 4.8 μm was measured by IR analysis and the

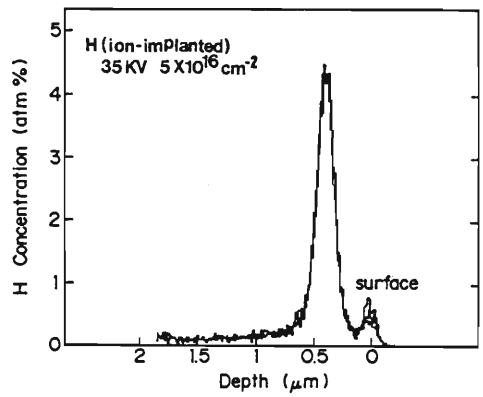

Fig. 1. Depth profiles of hydrogen in hydrogen implanted standard sample measured by the RFS method.

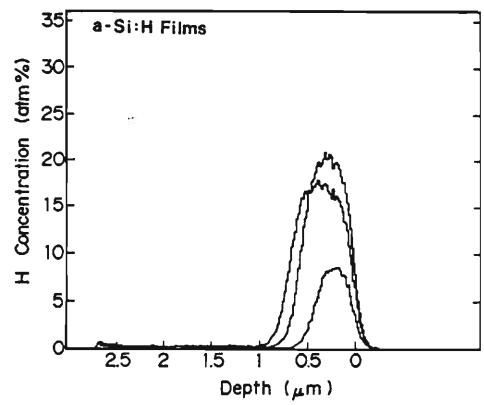

Fig. 2. Depth profiles of hydrogen in the amorphous silicon sample measured by the RFS method.

* R&D Center, Toshiba Corp.

** LSS: Profiles of implanted atoms were theoretically estimated originally by J. Lindhard, M. Scharff, and H. E. Schiott in 1963. Detailed data calculated with computer were listed in 'Projected range statistics,' J. Gibbons, W. Johnson, and S. Myroies, 1975.

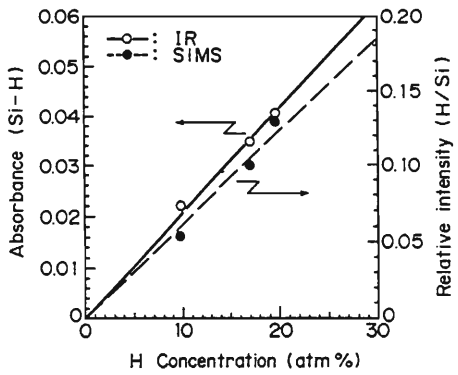

Fig. 3. Correlation of hydrogen contents determined by the RFS method to the values obtained by IR and SIMS methods.

ion intensity ratio H^+/Si^+ was measured by SIMS. The relation between these values and contents of hydrogen determined by the RFS method is shown in Fig. 3. Fairly good linear relationships were obtained.

From these results, the RFS method was found to be useful as a standard method for hydrogen calibration in IR or SIMS analysis.

Reference

1) H. Nagai, M. Aratani, S. Hayashi, T. Nozaki, M. Yanokura, I. Kohno, O. Kuboi, and Y. Yatsurugi: *RIKEN Accel. Progr. Rep.*, **17**, 102 (1983).

RIKEN Accel. Progr. Rep. 19 (1985)

III-3-10. Detection Limit of Hydrogen in Elastic Recoil Detection Analysis

H. Nagai, M. Aratani, S. Hayashi,* Q. Qiu, T. Nozaki,
M. Yanokura, I. Kohno, O. Kuboi, Y. Yatsurugi, and A. Hayashi

Elastic recoil detection analysis has been used successfully in the analysis of hydrogen on and near the surface of a solid of relatively high hydrogen content.[1] We intended, next, to apply this method to samples of low hydrogen contents such as quartz. However, various results obtained by us suggested that the surface hydrogen would interfere with the bulk hydrogen analysis.[2]

To examine this interference and to determine the detection limit, we measured bulk and surface hydrogen for the following samples by the procedure reported previously:[3] (1) a silicon wafer, (2) silicon wafers oxidized with H_2O at 830°C to 12 and 34 nm in thickness, and (3) silicon wafers oxidized by chemical vapor deposition to 13 and 20 nm in thickness. Argon ions were used as the incident particles. The beam current was 30 to 50 nA, and the counting was continued for 30 to 90 min.

Typical energy spectra of low hydrogen samples are shown in Fig. 1. The individual spectrum consists of two parts: a large peak and a continuum covering the entire channels below the peak. The peak is clearly due to the surface hydrogen recoiled by a single scattering, and the continuum is supposed to result from the surface hydrogen after multiple scattering and bulk hydrogen after single scattering. The apparent bulk-hydrogen content obtained from the height and/or area of the continuum is thus thought to be correlated with the surface-hydrogen amount. The results of the measurement on five kinds of samples of low bulk-hydrogen contents are shown in Fig. 2. It is clear that the apparent bulk-hydrogen content is proportional to the surface-hydrogen amount. On average, 10^{16} atoms/cm^2 surface hydrogen gives a count rate identical with that given by 2.6×10^{18} atoms/cm^3 bulk hydrogen in the bulk hydrogen region of the spectrum. We thus conclude that the detection limit for bulk hydrogen in a thick quartz sample is 1 to 2×10^{18} atoms/cm^3 (about 1 wt. ppm), when its surface-hydrogen amount is about 5×10^{15} atoms/cm^2 which is the average value in the present experiment.

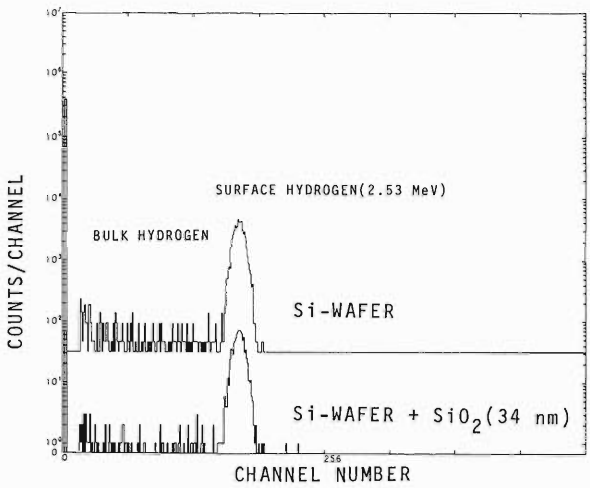

Fig. 1. The energy spectra of hydrogen atoms recoiled by 49.73 MeV Ar-ions in the Si-wafer and surface oxidized samples. The spectra were divided into two region. Large peaks in the higher energy region are due to recoiled surface hydrogen, and continua in lower energy region are due to recoiled bulk hydrogen.

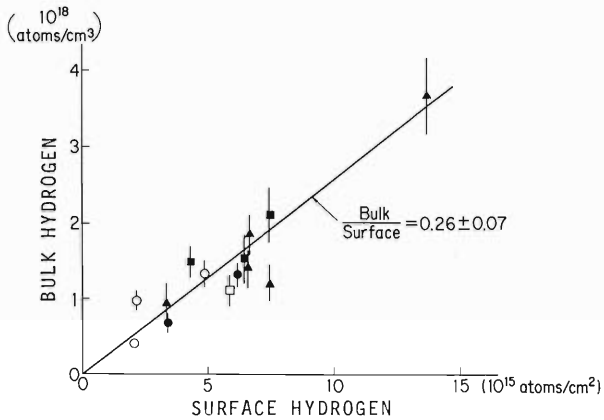

Fig. 2. Apparent bulk-hydrogen contents *vs.* surface-hydrogen amounts. Sample: ▲=silicon wafer ; ○,□=SiO_2 films prepared by oxidation of silicon wafers with H_2O at 800°C (12 nm and 34 nm); ●,■=SiO_2 films prepared by oxidation of silicon wafer by CVD (13 nm and 20 nm).

* Shimadzu Corporation.

References

1) Y. Yatsurugi, O. Kuboi, M. Hashimoto, H. Nagai, M.

Aratani, M. Yanokura, I. Kohno, and T. Nozaki: *Appl. Phys. Lett.*, **44**, 246 (1984).
2) H. Nagai, M. Aratani, S. Hayashi, M. Yanokura, I. Kohno, T. Nozaki, Y. Yatsurugi, and O. Kuboi: *RIKEN Accel. Progr. Rep.*, **18**, 130 (1984).
3) H. Nagai, M. Aratani, S. Hayashi, M. Yanokura, I. Kohno, T. Nozaki, Y. Yatsurugi, and O. Kuboi: *RIKEN Accel. Progr. Rep.*, **17**, 102 (1983).

RIKEN Accel. Progr. Rep. 19 (1985)

III-3-11. Heavy-Ion Rutherford Backscattering Analysis Applied to the Electronic Materials

K. Ikeda, N. Ito, M. Yanokura, Q. Qiu,
M. Aratani, and T. Nozaki

In the fabrication of a Schottky-barrier diode, the conditions for the deposition of metal layers affect the electrical characteristics. We applied heavy-ion Rutherford backscattering[1),2)] (RBS) to the study of the behavior of each layered metal at heat treatment in the production of the diode, making use of its nondestructiveness, good depth resolution for heavy metals, and insensitiveness to light elements. In this report, the estimation is given for the behavior of metal layer systems used frequently in Schottky-barrier diode and the change is qualitatively explained in heat treatment of them at various temperatures.

The structure of the present samples before heat treatment is shown in Fig. 1. Molybdenum, platinum, and aluminum were successively deposited on a silicon wafer by sublimation. The sample was then heated at various temperatures in nitrogen atmosphere. The temperature was set successively higher following the series from Sample A to Sample E. After heat treatment the aluminum layer was removed from the samples in order to observe detailed behavior of Mo and Pt layers.

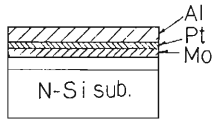

Fig. 1. Samples used in the present study.

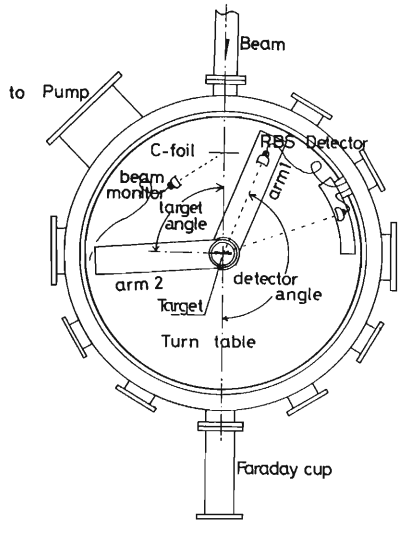

Fig. 2. Experimental arrangement.

The arrangement for the RBS measurement is shown in Fig. 2. The incident ion was $^{14}N^{2+}$ with 19 MeV in energy and several nA in beam current. The incident angle and the detector angle were 90° and 157°, respectively, and the beam spot was 1.5×1.5 mm². The measurement was continued for 10-30 min.

The backscattering spectra of Mo-Pt-Al systems are shown in Fig. 3. The solid lines A, B, C, and D are for heat treated samples and the dotted line is for an as-deposited sample. Spectra of Al-etched samples are shown in Fig. 4. The metal system is seen to mix in the heat treatment, as is evidenced from the facts that (1) platinum reacts with aluminum at low temperatures to give a stoichiometric compound[3),4)] (about 1 : 1), which does not change by temperature elevation; (2) platinum spreads up to the surface of aluminum layer; and (3) a small part of molybdenum

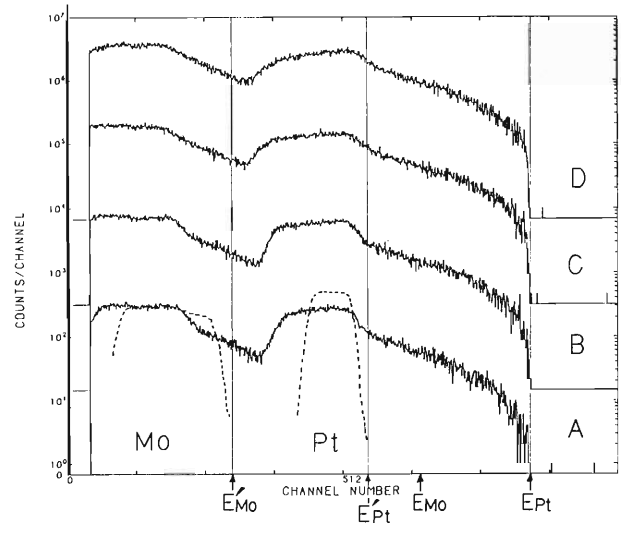

Fig. 3. RBS spectra of Mo-Pt-Al system on Si substrate. Treatment temperature, A<B<C<D; doted line, evaporated sample; E_{P_t} and E_{M_o}, maximum energy of Pt and Mo; E'_{P_t} and E'_{M_o}, maximum energy of evaporated sample.

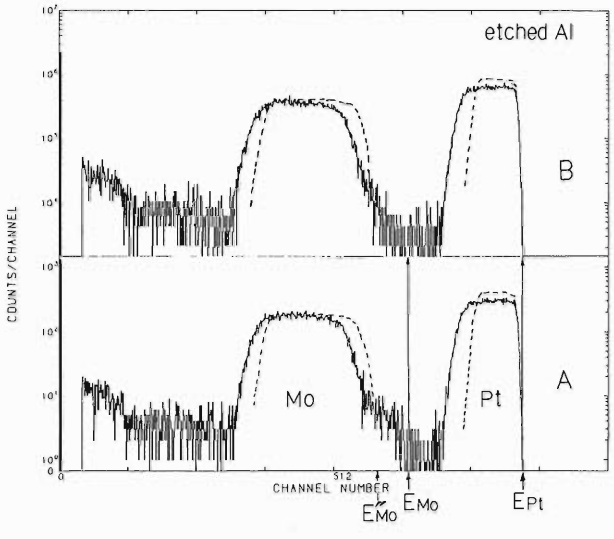

Fig. 4. RBS spectra of Mo-Pt-Al system (Al etched). E'_{M_o}, maximum energy of as evaporated sample (Al etched).

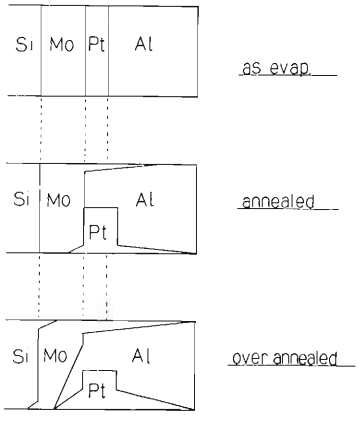

Fig. 5. Modified diagram of Mo-Pt-Al system.

diffuses into the platinum layer and also reacts with silicon to form silicide. In higher-temperature heat treatment, this system gave considerably different features. In the spectrum of aluminum-etched sample, only molybdenum peak was observed. This result suggests that a considerable portion of Al diffused into the Mo layer to make most of Mo be etched off with Al and that the Mo peak thus was derived from the Mo-Si layer. When the sample of the Pt-Mo system with no Al layer was heated, much less

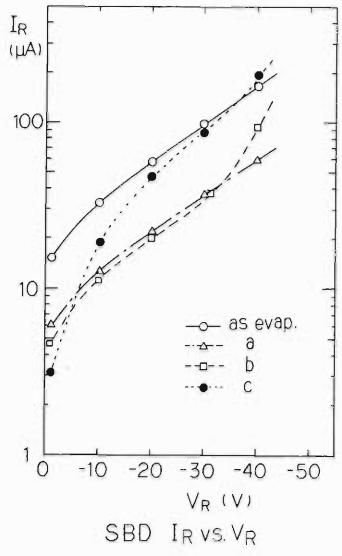

Fig. 6. V-I characteristics of Schottky-barrier diode. Treatment temperature: a<b<c.

change was observed in the RBS spectrum. From this result, the Al layer is considered to promote the inter-layer reaction.

The movement of each element in each heat treatment is shown in Fig. 5. The change in electrical characteristics (reverse biased V-I curve) of Schottky-barrier diode caused by heat treatment is shown in Fig. 6. These results indicate that lower temperature is preferred for the heat treatment in the production of the electric device, also, heavy-ion RBS has proved to be highly effective for the study of heat-treatment behavior of layered metals.

References

1) M. Yanokura, M. Aratani, H. Nagai, S. Hayashi, I. Kohno, T. Nozaki, O. Kuboi, and Y. Yatsurugi: Proc. 8th Symp. on Ion Sources and Ion-Assisted Technol., p. 425 (1984).
2) K. Ikeda, N. Ito, T. Aimi, S. Hayashi, M. Yanokura, I. Kohno, H. Nagai, M. Aratani, and T. Nozaki: *RIKEN Accel. Progr. Rep.*, **18**, 101 (1984).
3) Landolt-Börnstein, Neue Serie, Band III, "Structural Data and Intermetallic Phases," Springer-Verlag, Berlin, Heidelberg, New York, p. 268 (1971).
4) V. R. Huch und W. Klein: *Z. Anorg. Allg. Chem.*, **329**, 123 (1964).

RIKEN Accel. Progr. Rep. 19 (1985)

III-3-12. Elastic Recoil Analysis of Hydrogen for the Study of the Formation of Radiation-Resistant Oxide Film on Silicon

K. Yamamoto, M. Aratani, M. Yanokura, Q. Qiu,
H. Nagai, I. Kohno, and T. Nozaki

Recent developments in semiconductor integrated circuits, especially Si-MOS•LSI, depend on various progresses in fundamental techniques including improved preparation of high-quality oxide films on substrate silicon. The characteristics of the devices are generally influenced by physical and chemical states of the oxide film, such as its composition, defects and impurities in it, and mechanical stress and electric voltage applied on it. Hydrogen in the oxide film has been qualitatively confirmed to have some influence on the diffusion of other elements and on some electrical properties. It is also known that low-temperature processes should be used in the oxide film formation in order to obtain radiation-resistant devices.

Precise determination of impurities in the film, especially of light elements, has thus become essential for future development of the electric elements. However, since no method of analysis was applicable to hydrogen in solids with enough sensitivity and accuracy, no reliable knowledge has been obtained concerning the concentration and distribution of hydrogen in the oxide film and, consequently, no technique has been developed for the control of them.

We paid attention to recent advances[1),2)] in the heavy-ion Rutherford forward recoil measurement applied to the determination and depth-profiling of hydrogen in amorphous silicon[3),4)] and silica,[5)] and tried to apply the method to the analysis of thermal oxide film. This sample was

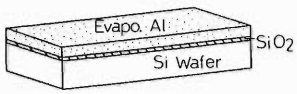

Fig. 1. Structure of the sample for characterization of hydrogen on SiO_2/Si interface.

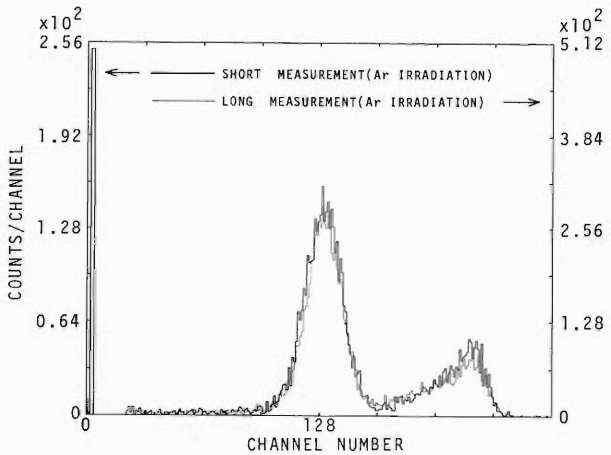

Fig. 2. Stability of hydrogen distribution for prolonged measurement time.

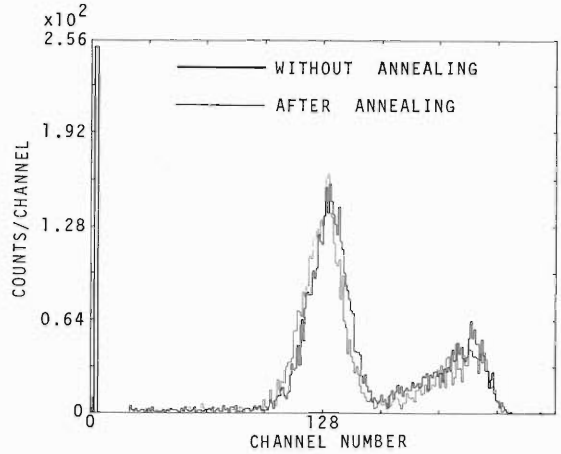

Fig. 3. Spectra for thermal oxide film with and without annealing at 1,000°C for 60 min in nitrogen.

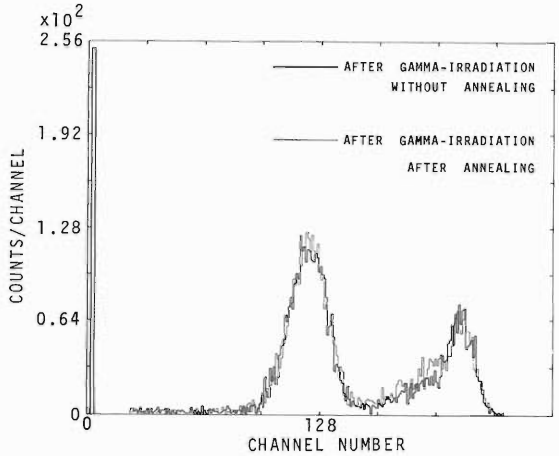

Fig. 4. Spectra for thermal oxide film with and without annealing under the same conditions as in Fig. 3 after irradiation with 1×10^6 rad (Si) gamma-rays.

of still lower hydrogen concentration and smaller thickness than usual silica samples. Samples were prepared in Toshiba Corporation, R&D Center, with special care for keeping surface adsorbed hydrogen as low as possible in order to distinguish the position of interface from the bulk of substrate and film in the spectrum. For this purpose, oxide surface of the sample was covered with evaporated aluminum films of about 1 μm in thicknesses. The structure of the sample is illustrated in Fig. 1. In Fig. 2, two spectra of the same sample are superposed for comparison with those measured at different times; integrated $^{40}Ar^{4+}$ ion fluence as expressed by recoil Si ion counts was 8.5×10^4 and 2.05×10^5 for them. This result shows that slight elevation of temperature of the sample due to prolonged measurement time has no influence on hydrogen distribution. Figure 3 illustrates spectra obtained with thermal oxide film of 1,600 Å in thickness produced by hydrogen combustion method with and without annealing at 1,000°C for 60 min in nitrogen. Heat treatment at 1,000°C for 60 min shows a slight decrease in hydrogen concentration in the sample. In Fig. 4 are given spectra obtained with the same samples in the same manner as that in Fig. 3 but after irradiation with 1×10^6 rad (Si) gamma-rays under +5 V applied voltage. The position of hydrogen peak is seen to shift to lower energy than before irradiation. This shift corresponds to a higher concentration of hydrogen on the interface than in the oxide.

Following model can be assumed from these results.

[Step 1] Generation of eletron-hole pair by gamma-ray irradiation:

$$\text{gamma-ray} \rightarrow e^- h^+$$

[Step 2] Dissociation of Si-H bond by the hole:

$$\equiv Si\text{-}H + h^+ \rightarrow \equiv Si^- + H^+$$

[Step 3] Drift of the H^+ according to applied electric field to cause the dissociation of Si-H and Si-OH bonds on its path:

$$\equiv Si\text{-}H + H^+ \rightarrow \equiv Si^+ + H_2$$
$$\equiv Si\text{-}OH + H^+ \rightarrow \equiv Si^+ + H_2O$$

These reactions in the oxide film, with which the existence of hydrogen is concerned, lead to the formation of positive and negative charges in the film and some surface electric state at SiO_2/Si interface. The preparation process of radiation-resistant oxide film is thus supposed to correspond to the condition under which low hydrogen-content film is formed. The study will be continued to elucidate detailed mechanisms.

References

1) H. Nagai, M. Aratani, T. Nozaki, M. Yanokura, and I. Kohno: Proc. 6th Symp. on Ion Sources and Ion-Assisted Technol., p. 221 (1982).
2) H. Nagai, M. Aratani, T. Nozaki, M. Yanokura, I. Kohno, O. Kuboi, and Y. Yatsurugi: *RIKEN Accel. Progr. Rep.*, **16**, 125 (1982).
3) Y. Yatsurugi, O. Kuboi, M. Hashimoto, H. Nagai, M. Aratani, M. Yanokura, I. Kohno, and T. Nozaki: *Appl. Phys. Lett.*, **44**, 246 (1984).
4) O. Kuboi, M. Hashimoto, Y. Yatsurugi, H. Nagai, M. Aratani, M. Yanokura, S. Hayashi, I. Kohno, and T. Nozaki: *Appl. Phys. Lett.*, **45**, 543 (1984).
5) M. Aratani, H. Nagai, M. Yanokura, O. Kuboi, S. Hayashi, I. Kohno, and T. Nozaki: 7th Int. Conf. Ion Beam Analysis, Berlin (FRG), 7-12, July (1985).

RIKEN Accel. Progr. Rep. 19 (1985)

III-3-13. Utilization of the D(^{3}He,p)^{4}He Reaction in Quantitative Analyses with High Sensitivity of Deuterium in Solids

Q. Qiu, T. Kobayashi, M. Yanokura, M. Imai,
Y. Yatsurugi, and T. Nozaki

Up to now, many methods have been recommended for detection of hydrogen in solids. In all of these methods, the sensitive portion is limited to a surface layer of about several hundred nm thickness. For quantitative analysis of hydrogen, a high sensitivity is often required. The interference of environmental contamination is also a serious problem. We have chosen deuterium as an activable tracer in the study of hydrogen is solids, and utilized the D(^{3}He,p)^{4}He reaction for detection.

The cross section of the D(^{3}He,p)^{4}He reaction at a laboratory angle of 86° shows a peak value of 70 mb/sr at an incident ^{3}He energy of 645 keV; its resonance width is about 350 keV.[1] The energy of emitted protons of about 13 MeV does not strongly depend on the emission direction. The deuterium concentration in solids is obtained by counting these 13 MeV protons.

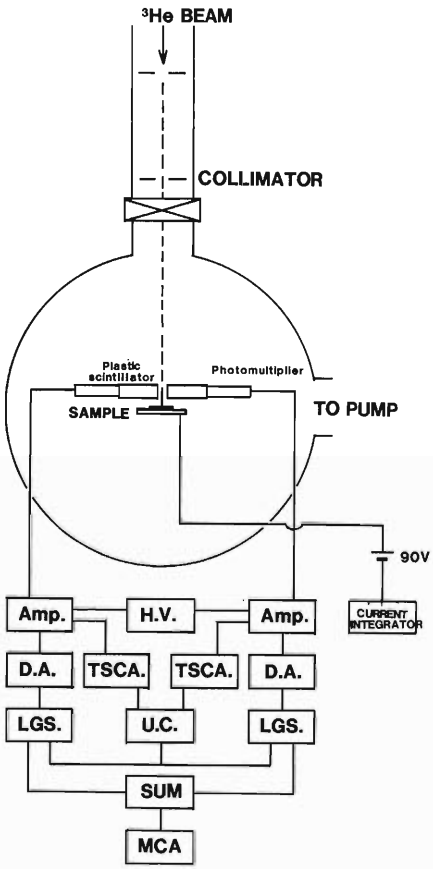

Fig. 1. Schematic diagram of the experimental setup.

The experimental setup is shown in Fig. 1. A beam of $^3He^+$ ions was supplied from the TANDETRON (maximum terminal voltage: 1 MV). The incident beam energy was 900 keV, which corresponds to the depth of about 1.3 μm in silicon wafer. The beam current was about 10 nA, and the beam spot had a diameter of 3 mm. We detected 13 MeV protons using an annular plastic scintillator (NE102A, 73 mm×10 mm), which had a wide solid angle of about 0.8π. The ^{4}He particles emitted by the reaction and scattered ^{3}He particles were stopped with a 10 μm aluminium foil on the plastic scintillator. Two photomultipliers were coupled to the plastic scintillator and operated in coincidence for the suppression of background counts.

Figure 2 shows three typical spectra for protons in the D(^{3}He,p)^{4}He reaction. They were obtained separately from A: a D-containing amorphous silicon film (4,860 Å); B: a sample of single crystal silicon saturated with D at the melting point; and C: background. The samples

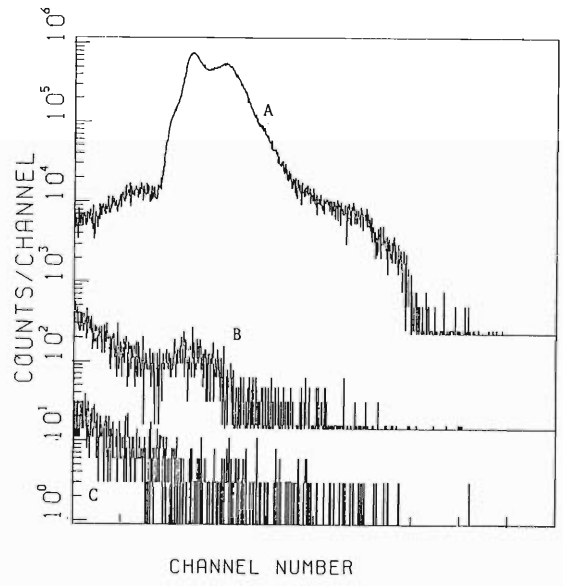

Fig. 2. Spectra of protons in D(^{3}He,p)^{4}He reaction.

were supplied by Komatsu Electronic Metals Co., Ltd. The background in the signal region amounts to about 0.07 cps, which determines a detection limit of this method to be about 2×10^{16} atoms/cm^3.

Because the resonance width is very wide, the depth profile can not be obtained, unlike the $H(^{15}N,\alpha\gamma)^{12}C$ reaction. By a fine etching technique, however, depth information of deuterium in solids can be obtained with a step size of several micrometers. We are investigating the solubility of deuterium in single crystal silicon using this method.

Reference

1) J. W. Mayer and E. Riminin: Ion Beam Handbook for Material Analysis, Academic Press Inc., New York (1977).

RIKEN Accel. Progr. Rep. 19 (1985)

III-3-14. Comparative Mössbauer and TDPAC Studies on the After-Effects of the EC Decays of ^{119}Sb and ^{111}In in α-Fe_2O_3

F. Ambe, K. Asai, S. Ambe, T. Okada, and H. Sekizawa

Mössbauer spectroscopy and TDPAC (time differential perturbed angular correlation) of γ-rays have many characteristics in common as hyperfine spectroscopies, but they have many differences too. Comparison of Mössbauer emission spectra of (^{119}Sb→)^{119}Sn and TDPAC of (^{111}In→)^{111}Cd is especially interesting, because the EC decays of the source nuclides can produce isoelectronic $^{119}Sn^{4+}$ and $^{111}Cd^{2+}$ ions in solids. Mössbauer emission measurements on (^{119}Sb →)^{119}Sn in insulators provide valuable information on the chemical states of ^{119}Sn down to liquid nitrogen temperature.[1),2)] On the contrary, the after-effects associated with the EC decay of ^{111}In are usually so large in non-conductive materials that the TDPAC spectra are attenuated strongly at room temperature providing little information on the atomic environment of ^{111}Cd.[3)] To clarify the origin of the apparently large difference in the after-effects of the EC decays, we compared the Mössbauer emission spectra of (^{119}Sb→)^{119}Sn and TDPAC of (^{111}In→)^{111}Cd in the same matrix, the corundum-type antiferromagnetic oxide, α-Fe_2O_3.[4)]

The source nuclide ^{119}Sb was separated repeatedly from ^{119m}Te, which had been produced by α-irradiation of tin with the cyclotron,[5)] while ^{111}In was obtained commercially. The samples were prepared by hydrolytic adsorption of no-carrier-added $^{119}Sb^{5+}$ and $^{111}In^{3+}$ on α-Fe_2O_3 particles followed by calcination in air at 800°C for 1 h and at 1,000°C for 2 h, respectively. Their Mössbauer emission spectra and TDPAC spectra were recorded at various temperatures with conventional experimental setup. The absorber used for the Mössbauer emission measurement was $BaSnO_3$ (0.9 mg ^{119}Sn/cm^2) kept at room temperature.

Typical Mössbauer emission spectra of (^{119}Sb →)^{119}Sn in α-Fe_2O_3 are shown in Fig. 1. Each spectrum consists dominantly of magnetic sextet of Sn^{4+}, with asymmetry ascribable to the electric quadrupolar interaction, over the temperature range studied. The curves in Fig. 1 were obtained by least-squares fitting of the experimental points with six Lorentzian lines of the same width. As seen in Fig. 1, the results of the fitting are satisfactory down to 7 K, though a minute contribution of Sn^{4+} in lower magnetic fields as well as that of Sn^{2+} cannot be ruled out. The isomer shift is slightly positive against $BaSnO_3$ kept at room temperature (0.2 mm/s at 7

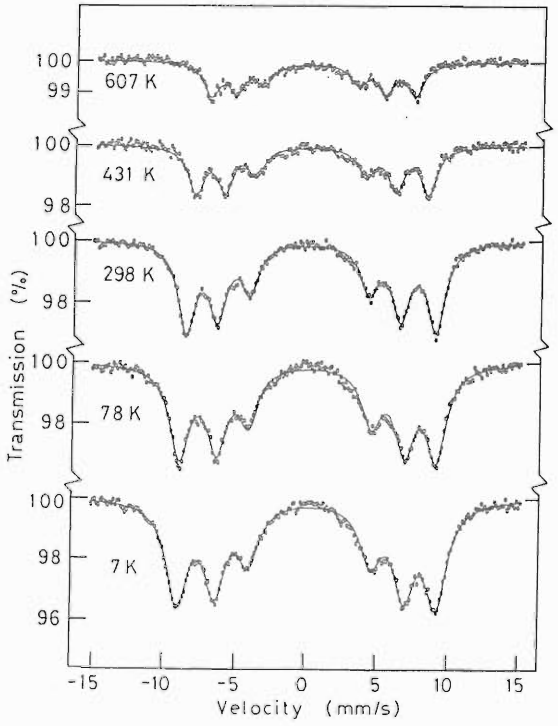

Fig. 1. Mössbauer emission spectra of (^{119}Sb→)^{119}Sn in α-Fe_2O_3. Each curve is the result of fitting with six Lorentzian lines of the same width.

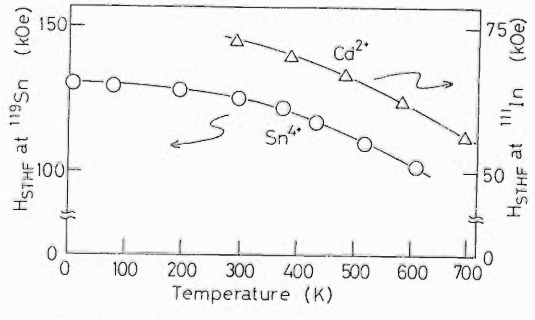

Fig. 2. Hyperfine magnetic fields at ^{119}Sn and ^{111}Cd nuclei in α-Fe_2O_3 derived from the Mössbauer and the TDPAC spectra.

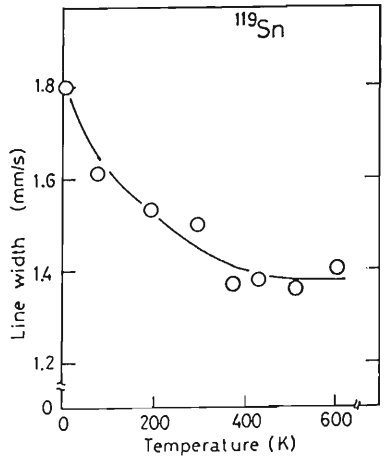

Fig. 3. Line width of the Mössbauer emission spectra of (^{119}Sb→)^{119}Sn in α-Fe_2O_3.

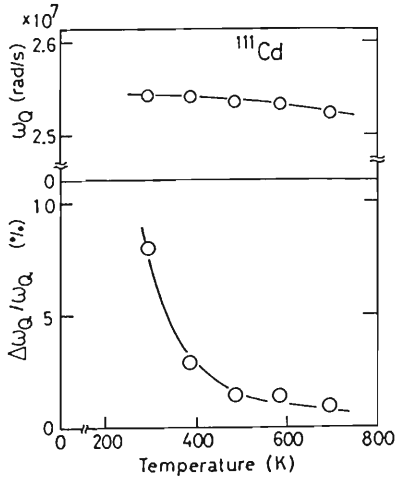

Fig. 4. Center and width of the distribution of ω_Q giving the best fit for the TDPAC spectra of (^{111}In →)^{111}Cd in α-Fe_2O_3.

K and 0.1 mm/s at 607 K). The value of e^2qQ estimated from the asymmetry of the spectra is -0.5 ± 0.2 mm/s. The hyperfine magnetic fields at the ^{119}Sn nuclei are given in Fig. 2. The mean full-widths at half-maximum of the lines are shown in Fig. 3.

The TDPAC coefficient $A_{22}\cdot G_{22}(t)$ of (^{111}In→) ^{111}Cd in α-Fe_2O_3 at 693 K and above is reproduced well by an analysis with a unique set of ω_L and ω_Q, while assumption of a distribution of ω_Q is necessary to obtain satisfactory results in the analysis at lower temperatures.[6] The values of ω_Q and the relative width $\Delta\omega_Q/\omega_Q$ giving the best fit are shown in Fig. 4. The hyperfine magnetic fields derived from ω_L are given in Fig. 2.

It can be concluded on the basis of the observations described above that the EC decay of ^{111}In gives rise to a distribution of e^2qQ at the ^{111}Cd nuclei and results in decrease in the anisotropy of the TDPAC spectra at low temperatures. On the other hand, the shift of each Mössbauer line $\varepsilon(=e^2qQ(3\cos^2\theta-1)/8)$, due to the quadrupolar interaction, is only of the order of one tenth or less of the line width($\varepsilon\fallingdotseq0.06$ mm/s above the Morin temperature (260 K) and -0.12 mm/s below it; (line-width)$\gtrsim$1.4 mm/s). Therefore, a distribution of e^2qQ around the intrinsic value, due to the EC decay of ^{119}Sb, brings about only broadening of the lines in the Mössbauer spectra. The increase in line-width at low temperatures seen in Fig. 3 is attributed, at least partly, to the increase in the width of distribution of e^2qQ.

In the present case of α-Fe_2O_3 matrix, apparently much pronounced after-effects of the ^{111}In $\underset{\cdot}{\text{EC}}$ ^{111}Cd decay observed in the TDPAC spectra as compared with those of the ^{119}Sb $\underset{\rightarrow}{\text{EC}}$ ^{119}Sn in the Mössbauer spectra are thus attributed mainly to the fact that the EC decays bring about a relative distribution in e^2qQ much larger than in hyperfine magnetic field. The distribution in e^2qQ affects the TDPAC spectra much strongly than the Mössbauer spectra, because $|Q|$ of the intermediate level of ^{111}Cd nucleus ($Q=0.77$b) is much larger than that of the first excited level of ^{119}Sn ($Q=-0.065$b).

Temperature dependence of the observed hyperfine magnetic fields at ^{119}Sn and ^{111}Cd (Fig. 2) is proportional to the reported one at ^{57}Fe in α-Fe_2O_3[7] within experimental uncertainties.

References

1) F. Ambe, S. Ambe, H. Shoji, and N. Saito: *J. Chem. Phys.*, **60**, 3773 (1974).
2) T. Okada, S. Ambe, F. Ambe, and H. Sekizawa: *J. Phys. Chem.*, **86**, 4726 (1982).
3) P. Lehmann and J. Miller: *J. Phys. Radium*, **17**, 526 (1956).
4) F. Ambe, K. Asai, S. Ambe, T. Okada, and H. Sekizawa: *Hyp. Int.*, **29**, 1197 (1986).
5) S. Ambe: *J. Radioanal. Nucl. Chem. Artic.*, **81**, 77 (1984).
6) K. Asai, F. Ambe, S. Ambe, and H. Sekizawa: *J. Phys. Soc. Jpn.*, **53**, 4109 (1984).
7) F. van der Woude: *Phys. Status Solidi*, **17**, 417 (1966).

RIKEN Accel. Progr. Rep. **19** (1985)

III-3-15. Time Differential Perturbed Angular Correlation Study on (^{111}In→)^{111}Cd in In_2O_3

F. Ambe, K. Asai, S. Ambe, and H. Sekizawa

Time-differential perturbed angular correlation (TDPAC) of γ-rays is a useful hyperfine technique utilizing unstable nuclei and has many similarities to Mössbauer spectroscopy. However, application of the former to solid-state physics and chemistry is still much more limited than that of the latter. For the most popular TDPAC source nuclide ^{111}In decaying to ^{111}Cd, after-effects of the Auger process accompanying the EC decay are usually very large in non-conductive compounds. Consequently, the anisotropy in TDPAC spectra is attenuated strongly at room temperature and provides little information on the chemical state of ^{111}Cd.[1),2)] It has been shown recently that time spectra free from the after-effects can be obtained on (^{111}In →)^{111}Cd even in insulators from measurement at higher temperatures.[3)-5)]

In literature, there are conflicting reports on the temperature dependence of TDPAC spectra of ($^{111}In^{3+}$→)^{111}Cd in In_2O_3. In 1964, Salomon reported that the time spectrum at room temperature exhibited no periodic behavior because of the heavy after-effects, but the one at 280°C was interpretable assuming an electric quadrupolar interaction frequency with 10% of spread due to the diminished after-effects.[6)] Later, Uhrmacher and Bolse observed TDPAC spectra of $^{111}In_2O_3$ down to 14 K, which are reproduced well with two sets of electric quadrupolar components in accordance with the two different lattice sites of In^{3+} in the oxide.[7)] To clarify the large discrepancy observed in the earlier work, we measured TDPAC of ($^{111}In^{3+}$→)^{111}Cd in carefully prepared $^{111}In_2O_3$ samples and made a detailed analysis on the time spectra obtained.

Indium metal (99.9999%) was dissolved in concentrated HCl. After addition of ^{111}In, indium hydroxide was precipitated from the solution by neutralization with ammonia. The $^{111}In_2O_3$ samples were prepared by dehydrating the hydroxide at 1,100°C for 1 h in air. The TDPAC spectra of 171-245 keV γ-γ cascade emitted from (^{111}In→)^{111}Cd in the In_2O_3 samples were measured at various temperatures with a conventional fast-slow coincidence setup using two NaI(Tl) detectors.

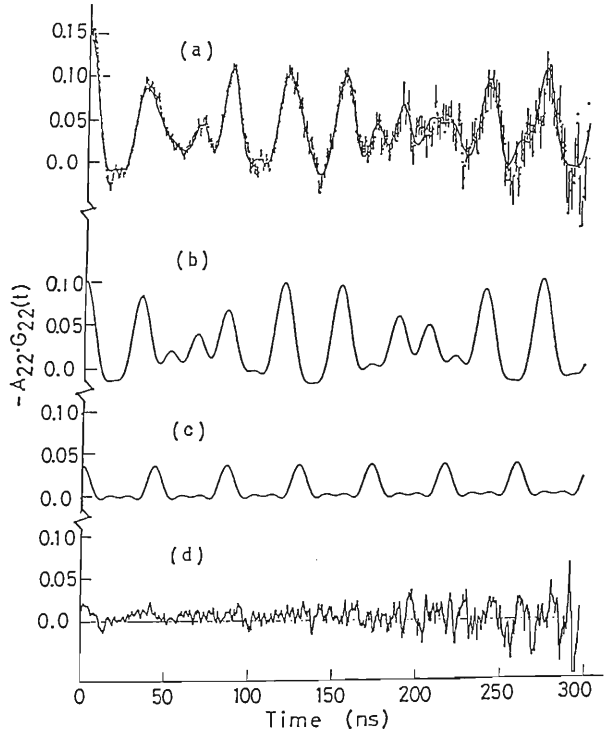

Fig. 1. The TDPAC spectrum of (^{111}In→)^{111}Cd in In_2O_3 at 400°C. (a), experimental points and the result of analysis with a sum of two sets of electric quadrupolar components; (b) and (c), calculated curves corresponding to each of the two sets; (d), difference between the experimental points and the sum curve.

The TDPAC spectrum obtained at 400°C is shown in Fig. 1 (a). As the curve in Fig. 1 (a) shows, the spectrum is analyzable as the sum of two sets of electric quadrupolar components ((b) and (c)), not suffering from after-effects of the EC decay. Figure 1 (d) shows the difference between the experimental points and the sum curve. No exponential attenuation of the anisotropy reported by Uhrmacher and Bolse[7)] is observed in our spectrum. At room temperature, a spectrum with little structure was observed as a result of smearing out by the after-effects. This observation is in agreement with that reported by Salomon[6)] and not with that by Uhrmacher and Bolse.[7)]

References

1) P. Lehmann and J. Miller: *J. Phys. Radium*, **17**, 526 (1956).
2) H. Haas and D. A. Shirley: *J. Chem. Phys.*, **58**, 3339 (1973).
3) P. W. Martin, S. R. Dong, and J. G. Hooley: *J. Chem. Phys.*, **80**, 1677 (1984).
4) K. Asai, F. Ambe, S. Ambe, and H. Sekizawa: *J. Phys. Soc. Jpn.*, **53**, 4109 (1984).
5) F. Ambe, K. Asai, S. Ambe, T. Okada, and H. Sekizawa: *Hyp. Int.*, **29**, 1197 (1986).
6) M. Salomon: *Nucl. Phys.*, **54**, 171 (1964).
7) M. Uhrmacher and W. Bolse: *Hyp. Int.*, **15/16**, 445 (1983).

RIKEN Accel. Progr. Rep. 19 (1985)

III-4. Radiation Chemistry and Radiation Biology

1. Cellular Lethal Effect of α-Particles on Four Different Cell Lines

H. Majima, K. Eguchi, I. Kaneko, K. Nakano, and S. Okada

It is observed *in vitro* and *in vivo* that high LET (linear energy transfer) radiation enhances cellular lethality.[1),2)] Cells are known to have various radiosensitivities to X-rays (low LET beam). The question is whether there is any relationship between cellular sensitivity to low LET radiation and that to high LET radiation.

In the present study, the biological effect of α-particles accelerated with the cyclotron was studied with four different mammalian cell lines: CHO (Chinese hamster ovary cells), V-79 (Chinese hamster lung cells), HMV-I (a human melanoma cell line), and A-7 (a human glialblastoma cell line). Survival curves of each cell line were obtained, and the RBEs were calculated from the ratios of doses that produce an identical biological effect for X-rays and α-particles.

The four cell lines were cultured at 37°C as monolayers in plastic flasks (LUX company limited, U.S.A.) containing McCoy's Medium 5a (GIBCO, U.S.A.), in air plus 5% CO_2. The medium was supplemented with 10% calf serum and 5% fetal calf serum. The cells were irradiated with α-particles (LET-38 keV/μm) or X-rays (200 kVp, 20 mA, H.V.L.=20.6 mm Al), and then incubated for colony formation. The surviving fractions were obtained with corrections of the plating efficiency and the cell multiplicity.

The values of RBE were listed in Table 1. Every cell line tested showed RBE of higher than 1, which are in the range of RBE reported for radiation similar LET.

Table 1. RBE values of α-particles for four cell lines.

Cell	10% dose[a] (Gy)		RBE[c]	1% dose[b] (Gy)		RBE[d]
	X	α		X	α	
CHO	4.3	1.9	2.3	7.3	3.8	1.9
V-79	6.5	2.4	2.7	10.5	4.8	2.2
HMV-I	5.5	1.7	3.2	9.7	3.3	2.9
A-7	5.5	1.9	2.9	8.4	3.5	2.4

[a] Dose required to obtain 10% survival fraction.
[b] Dose required to obtain 1% survival fraction.
[c] RBE at 10% survival fraction (10% dose X/10% dose α).
[d] RBE at 1% survival fraction (1% dose X/1% dose α).

Among these four cell lines, the most resistant cell line to X-rays was V-79, and the most sensitive line was CHO. The RBE for V-79 was higher (2.7, ratio at 10% dose) than that for CHO (2.3). And the highest RBEs were found for HMV-I (3.2) and A-7 (2.9), of which radiosensitivities to X-rays were in middle range among those four cell lines. These results show little relationship between radiosensitivity and RBE.

References

1) G.W. Barendsen: *Curr. Top. Radiat. Res. Q.*, **4**, 293 (1968).
2) T. Ohno, T. Nishimura, K. Nakano, and I. Kaneko: *Int. J. Radiat. Biol.*, **45**, 21 (1984).

RIKEN Accel. Progr. Rep. 19 (1985)

III-4-2. Oxygen Effects on Inactivation of the Human Melanoma Cells by Accelerated α-Particles

K. Eguchi, I. Kaneko, T. Kosaka, T. Takahashi, and K. Nakano

Reduction of the oxygen enhancement ratio (OER) on cell inactivation is one of the major features of high LET radiations in comparison with low linear energy transfer (LET) radiations. Heavy ion beams effectively kill even hypoxic cells,[1] which are probably present in solid tumors and lead to failure in the radiation cancer therapy. Therefore, such a report[1] prompted us to examine the oxygen enhancement ratio of accelerated ions in inactivation of highly radioresistant cells and for any cell damage specific to accelerated ions. A special apparatus used for irradiation under hypoxic conditions with ions accelerated on the RIKEN cyclotron was devised in cooperation with the RIKEN technology division (Figs. 1 and 2). By using this apparatus highly radioresistant human melanoma cells (HMV-I) were irradiated with α-particles under aerobic or hypoxic conditions, and OER and OGF (oxygen gain factor) were calculated. Dosimetry was carried out in cooperation with Dr. A. Maruhashi, Univ. of Tsukuba.

1) Chambers for hypoxic irradiation

An apparatus made of stainless steel and

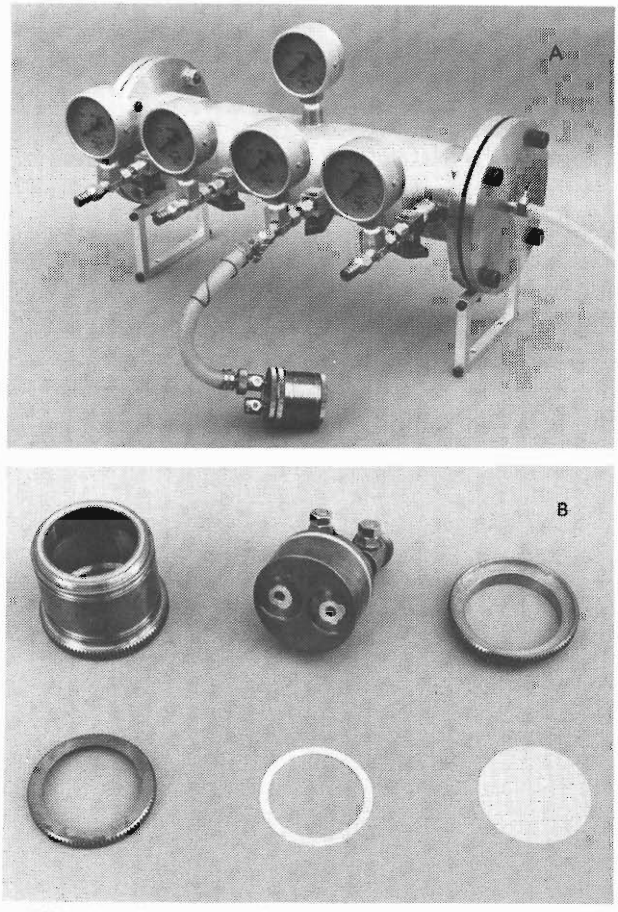

Fig. 1. Apparatus for gas exchange. A: Hypoxic chamber is connected to a gas regulator; B: Hypoxic irradiation chamber.

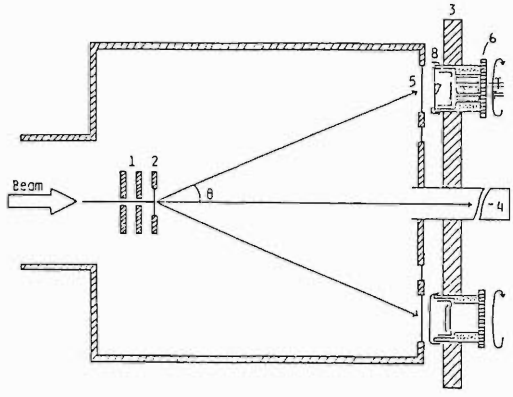

Fig. 2. Apparatus for α-particle irradiation. A horizontal beam passing through the slit (1) is scattered through gold foil (2). A hypoxic chamber (6) with biological sample (7) is fixed in sample wheel (3). Scattered beam is led to open air through a aluminum window (5) and then irradiated sample (7) through a window (8). Irradiation dose is monitored with a Farady cup (4).

Table 1. Oxygen effect on inactivation of human melanoma HMV-I cells by α-particle.

	LET (keV/μm)	RBE[a]	OER[b]	OGF
^{60}Co-γ-ray	0.3	—	2.1	—
α-Particle				
Mylar 6 μm	38.7	1.4	—	—
Al 16 μm	41.5	1.6	(1.2)	(1.8)
50 μm	43.5	2.0	1.4	1.5
100 μm	57.7	2.6	1.5	1.4

[a] RBE values at 1% survival level.
[b] OER values at 1% survival level.

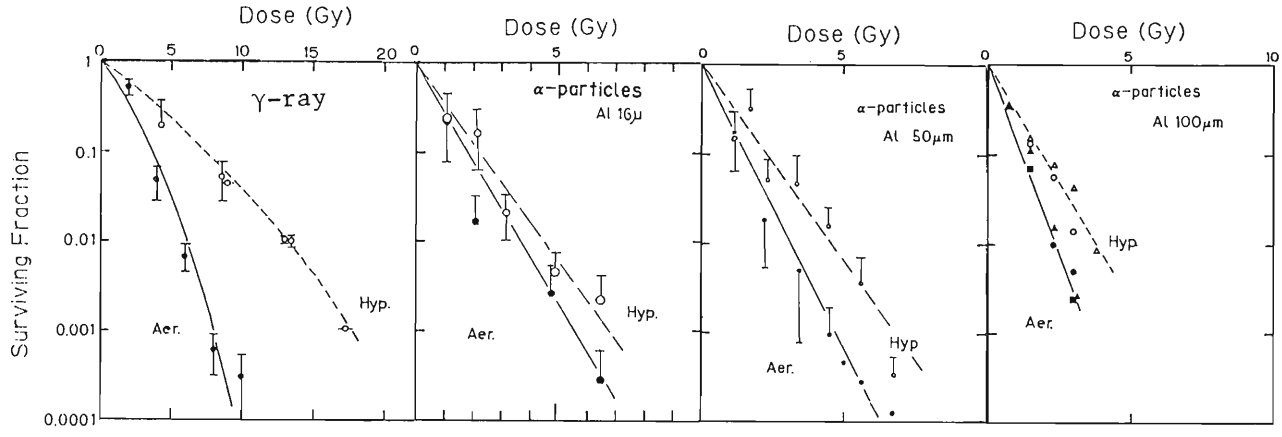

Fig. 3. Dose-survival curves for HMV- I cells irradiated with α-particles under aerobic and hypoxic conditions.

Teflon was used in order to protect the cells environment from the toxicity and to be sterilized for prevention of biological contamination. The apparatus enables us to exchange the atmosphere on the samples simultaneously for 4 chambers (Fig. 1). After replacement of air by nitrogen gas, the irradiation chambers are sealed, removed from the apparatus, and then set in front of a 25 μm thick aluminum window (Fig. 2). Twenty two MeV α-particles were led to open air through the window. Each chamber was rotated during irradiation to assure uniform irradiation. The window of hypoxic chamber (8 in Fig. 2) is made of aluminum and is exchangeable.

2) Effect of α-particles with different LET's on HMV-I

LET of α-particles in the sample is varied by changing the thickness of the aluminum window of the hypoxic irradiation chamber. The relative biological effectiveness (RBE) for cell inactivation increased with increasing LET as listed in Table 1.

3) Oxygen effect on cell inactivation

Cell survival curves under aerobic or hypoxic conditions are shown in Fig. 3. Each experiment was repeated twice. The curves in Fig. 3 were fitted to a linear-quadratic relationship by a linear regression analysis. The OER and the OGF of α-particles to γ-rays are listed in Table 1. The OER of α-particles was about 1.5, which is less than that of γ-rays (2.1). The OER value for 41.5 keV/μm α-particles was the lowest in the curves in the present study; however, this result may not be accurate because aluminum of 16 μm thickness is too thin and easily broken in the procedure of exchanging gas. When 100 μm thick window was used, largest correlation coefficient was obtained among hypoxic survival curves. An aluminum window of 100 μm thickness was found to be most useful for this purpose.

Reference

1) E. A. Blakely, C. A. Tobias, T. C. H. Yang, K. C. Smith, and J. T. Lyman: *Radiat. Res.*, **80**, 122 (1979).

RIKEN Accel. Progr. Rep. 19 (1985)

III-4-3. Microdosimetric Considerations of the Effect of Heavy Ions on Microorganisms

T. Takahashi, F. Yatagai, K. Izumo, S. Konno, and T. Katayama

In a recent paper,[1] inactivation cross sections of *B. subtilis* spores for heavy ions were analyzed by assuming that the area of the sensitive element or the target is nearly equal to the spore core area, in contrast to Katz's theory in its original form. In the present paper, the authors try to obtain an analytical expression for inactivation cross sections for the spores, vegetative cells of *E. coli* $B_{s\text{-}1}$ and B/r as a function of LET, since such an attempt may be useful as a step toward a clear insight into the heavy-ion action on microorganisms.

According to Butts and Katz,[2] the density of energy delivery (erg/cm^3) as a function of distance from the trajectory of an ion is given by a simple formula $D_{KZ}=CZ^{*2}(1-X/X_m)^{-\alpha}/(2\pi\alpha\beta^2\times X^2)$. Here, X is the distance from a trajectory, C is a constant ($C=0.85$ keV/μm for water), α is taken to be unity in Ref. 2, β is the velocity of ion relative to that of light, X_m is the maximum range of δ-electrons, and the effective charge Z^* is given by $Z^*=Z\ [1-\exp(-125\beta Z^{-2/3})]$, where Ze is the nuclear charge of the projectile. The formula D_{KZ} has been proved to be useful for interpretation of biological effects as well as for that of LET dependence of scintillation and track widths in emulsions. According to Ahlen,[3] however, the "prompt primary dose" (D_p) which includes dose due to distant collisions may be added to Butts and Katz's dose because the distant-collision dose might be effective to biological systems. For H_2O, *e. g.*, one would expect that ~20% of the distant collision dose involves inner shells for which deexcitation leads to Auger emission. Ahlen pointed out that the prompt-dose profile should differ from delayed electronic dose by about 20% and the prompt dose will be distributed throughout a cylinder of radius 15 Å. In the present paper, D_p added to Butts and Katz's dose was denoted by D_{KA} (Katz-Ahlen dose). Chatterjee and Schaefer[4] established an expression (D_{CS}) for the core dose and the penumbral dose. D_{CS} is normalized to the stopping power. Takahashi, *et al.*[1] attempted to analyze the inactivation cross section of *B. subtilis* spores by using D_{KZ}, D_{KA}, and D_{CS}.

The energy dependence of the inactivation cross section of *B. subtilis* spores for heavy ions (carbon through neon) was found to be only slight as shown in Fig. 1. The 37% dose for gamma-rays was 63.5 krad. To interpret these results and He ion data, analysis has been carried out along lines similar to Katz's theory,[5] but parameters were chosen so that they have an experimental basis. For dose evaluation, a cylindrical target with nearly the same radius a as the spore core is assumed and mean dose $\bar{D}(r)$ is calculated. Here, r is the distance between the center of a target and the path of an ion. It is also possible to calculate the mean dose for a spherical target (Fig. 1). The inactivation cross section S for nitrogen or carbon ions is fairly well explained if we assume that S is expressed as

$$2\pi\left(\int_0^a P_{in}\,r\,dr+\int_a^\infty P_\delta\,r\,dr\right)$$

where P_{in} is larger than P_δ. Here, $P_{in}=1-\exp(\bar{D}(r)/E_{in})$ is the probability of inactivation when the ion impinges upon and goes through the spore core ($r<a$) and $P_\delta=1-\exp(\bar{D}(r)/E_\delta)$ is the probability of inactivation when the ion passes by the spore core and the trajectories of

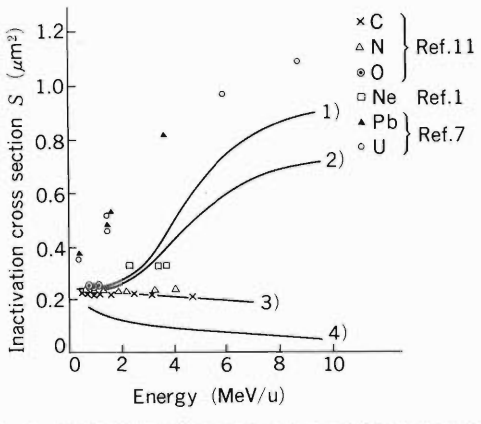

Fig. 1. Experimental and theoretical inactivation cross sections. 1-4: Theoretical curves calculated by using D_{CS} for a spherical target whose cross-sectional area is assumed to be 0.25 μm^2. 1, U ion, $E_\delta=45$ krad, $E_{in}=10$-63.5 krad; 2, U ion, $E_\delta=E_{in}=63.5$ krad; 3, N ion, $E_\delta=45$ krad, $E_{in}=12$ krad; 4, N ion, $E_\delta=E_{in}=63.5$ krad. Calculation for the cylindrical target gave nearly the same result as shown in Fig. 7 of Ref. 1.

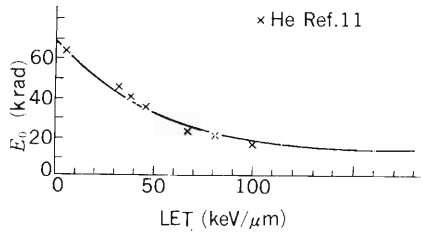

Fig. 2. Relation between E_0 and LET. Solid line shows that the relation is represented approximately by Eqn. (1).

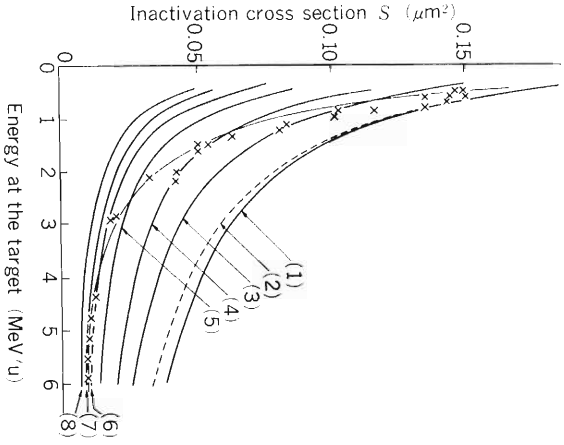

Fig. 3. Inactivation cross sections S of *Bacillus subtilis* as a function of He ion energy. ×, Experimental; 1-8, Theoretical curves for $\pi a^2=0.22$ μm² calculated by D_{CS} (cylindrical model). 1, $E_0=10$ krad; 2, $E_\delta=63.5$ krad, $E_{in}=10$ krad; 3, $E_0=15$ krad; 4, $E_0=20$ krad; 5, $E_0=30$ krad; 6, $E_0=40$ krad; 7, $E_0=50$ krad; 8, $E_0=63.5$ krad. The thin solid line shows the calculated inactivation cross section under the assumption that E_0 is a function of LET and is given by Eqn. (1).

its δ-electrons come into the spore core ($r>a$). This implies that radiosensitivity of the spore for the core of heavy ion, $1/E_{in}$ is higher than that of δ-electrons $1/E_\delta$ (Fig. 1). For He ions, without separating P_{in} and P_δ, inactivation cross sections are assumed to be expressed as

$$2\pi\int_0^\infty Prdr,$$

where $P=1-\exp(\bar{D}(r)/E_0)$ and E_0 is a dose at which there is an average of one hit per target. From Fig. 3, it is clearly seen that E_0 is not a constant but it decreases from about 45 krad to 10 krad as ion energy decreases. Since E_0 (krad) is a function of LET (which is expressed by $\mathcal{L}$ keV/μm), it can be expressed approximately by a single curve if the following expression

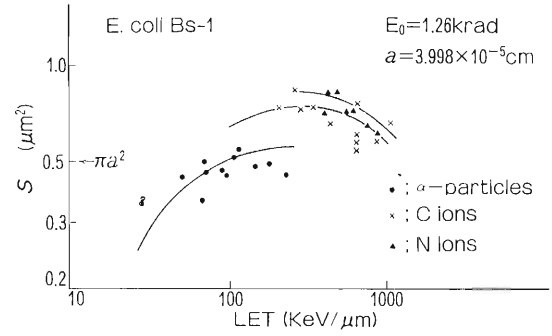

Fig. 4. Inactivation cross section S *vs.* LET for *E. coli* B_{s-1}. Solid lines show the calculated result for a cylindrical target by using D_{KA}. The cross sectional area πa^2 of the target was determined by least squares analysis. E_0 value was assumed to be the same as the 37% dose for gamma-rays.

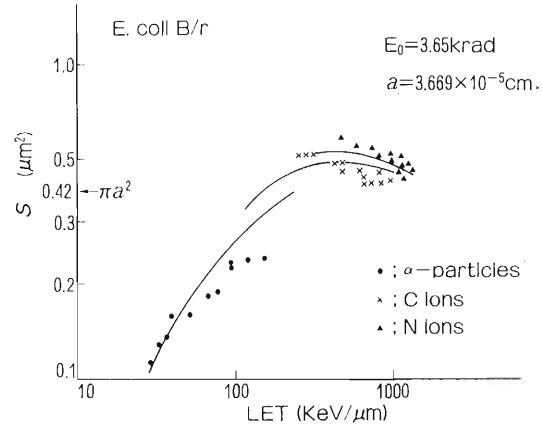

Fig. 5. S *vs.* LET for *E. coli* B/r. Solid lines are calculated for a cylindrical target by using D_{KA}.

$$E_0(\mathcal{L})=59\exp(-0.02\mathcal{L})+10 \qquad (1)$$

is assumed as shown in Figs. 2 and 3 (thin solid line). The general trend seems explicable from Horneck's experiment[6] which showed decrease in repairability with increasing LET, but as to the functional form, no explanation is possible at the present time. The difference between experimental inactivation cross sections measured by Facius, *et al.*[7] and calculated results for U ions (Fig. 1) may be attributable to the thermal spike or shock wave.[7)-9)] Higher radiosensitivity ($1/E_\delta$) for δ-electrons, which would give higher cross sections, should be ruled out from the reasons described in Ref. 1, where discussions were made based on Howard-Flanders' figure on the fraction of energy dissipation per unit interval of keV/μm.[10] The RBE peak appears at about 150 keV/μm which corresponds to about 0.8 MeV/u He ions (Fig. 9 of Ref. 1).

For *E. coli* B_{s-1} and B/r, the procedure was

found to be useful but no change in E_0 value was necessary to interpret inactivation cross sections for He ions. Even for C and N ions, it was possible to interpret inactivation cross sections by assuming $E_{in}=E_\delta=E_0$ (Figs. 4 and 5). It was demonstrated that for *E. coli*, RBE monotonously decreases as LET increases and the peak of RBE does not appear for both strains.[11] The E_0 value for *E. coli* B/r is 3.65 krad whereas that for $B_{s\text{-}1}$ is 1.26 krad as shown in Figs. 4 and 5. The difference in E_0 value may be ascribed to the higher repair capability in *E. coli* B/r, which is independent of LET, than that in spore.

References

1) T. Takahashi, F. Yatagai, and S. Kitayama: *Adv. Space Res.*, **3** (8), 95 (1983); T. Takahashi and F. Yatagai: *RIKEN Accel. Progr. Rep.*, **16**, 139 (1982).
2) J. J. Butts and R. Katz: *Radiat. Res.*, **30**, 855 (1967).
3) S. P. Ahlen: *Rev. Mod. Phys.*, **52**, 121 (1980).
4) A. Chatterjee and H. J. Schaefer: *Radiat. Environ. Biophys.*, **13**, 215 (1976).
5) R. Katz: 9th Int. Conf. Solid State Track Detectors (1976); R. Katz, B. Ackerson, M. Homoyoonfer, and S. C. Sharma: *Radiat. Res.*, **47**, 402 (1971).
6) G. Horneck: 1st Int. Conf. Cell and Molecular Biology in Space, Toledo (1978).
7) R. Facius, M. Schäfer, and H. Bücker: *Adv. Space Res.*, **3** (8), 85 (1983); M. Schäfer, R. Facius, K. Baltschukat, and H. Bücker: 7th Symp. Microdosimetry (1980).
8) T. Takahashi, F. Yatagai, and A. Matsuyama: *Sci. Papers I.P.C.R.*, **74**, 51 (1980).
9) T. Takahashi, F. Yatagai, T. Katayama, A. Yunoki, Y. H. Kang, D. S. Kim, I. Kaneko, and S. Okada: *RIKEN Accel. Progr. Rep.*, **18**, 147 (1984).
10) P. Howard-Flanders: *Adv. Biol. Phys.*, **6**, 553 (1958).
11) F. Yatagai, T. Takahashi, and A. Matsuyama: *J. Radiat. Res.*, **16**, 99 (1975).

RIKEN Accel. Progr. Rep. 19 (1985)

III-4-4. High-Density Excitation by Heavy-Ions : Formations of Dimer and Clusters of Helium-Excimers in Condensed Phase

K. Kimura, M. Kataoka, K. Hara, and T. Iida

We are interested in the high-density electronic excitation induced by heavy-ion impingement and also in dE/dx dependence of excitation along the path of heavy-ions. This report describes that new emission bands found in N-ion impinged dense helium gas and liquid are attributed to emissions from clusters composed of helium-excimers. Recently, one of the present authors has reported that N-ion impinged dense helium gas (~400 Torr at 5.2 K) presents new triplet emission bands centered at 4,587 Å and they are assignable to vibronic bands of the dimer of helium-excimers.[1] One of constituent excimers of the excimer-dimer has been shown to be the lowest triplet metastable excimer a^3 (lifetime is ~1 ms) and the other is b^3, c^3, or d^3, where the alphabetical notation of the excimers is according to Herzberg. It has also been shown that overall reactions for the high-density excitation by N-ions are exhibited by

$$He^* + 2He, \quad He_2^+ + e\cdots \rightarrow He_2^* \qquad (1)$$

where $He_2^* = a, b, c, d, \cdots, A, B, C, D, \cdots$

$$a^3 + a^3 \rightarrow d^3,\ c^3,\ C^1,\ D^1,\ A^1 + 2He \qquad (2)$$

$$d^3 + He_{2,l}^* \rightarrow He_{2,m}^* + He_{2,n}^* \text{ or } He_{2,k}^* + h\nu \qquad (3)$$

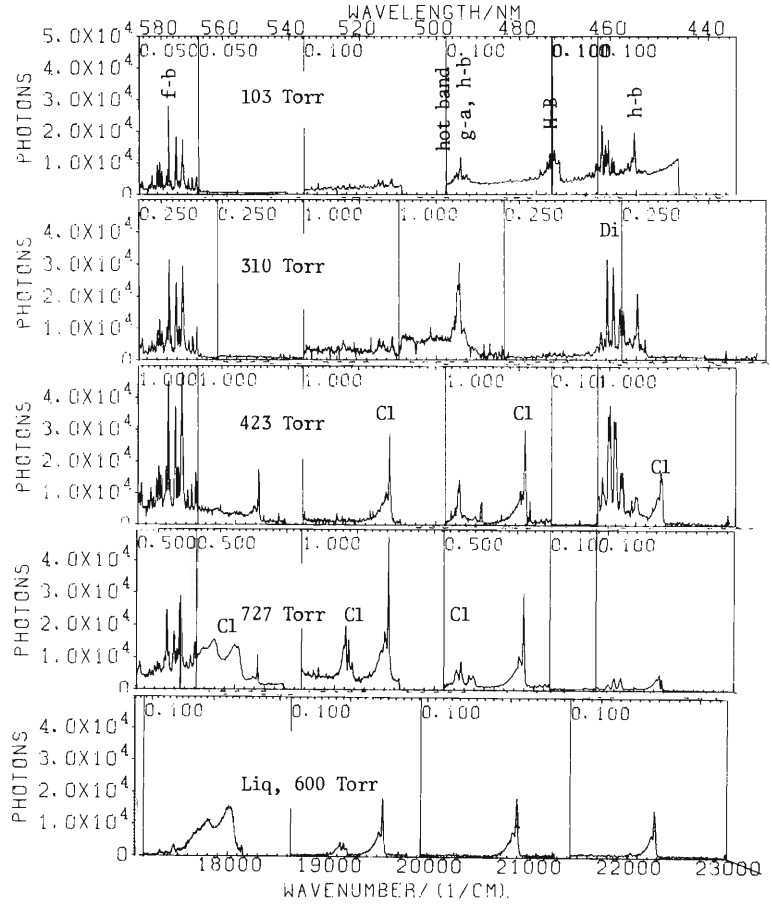

Fig. 1. Pressure dependence of emission spectra of N-ion impinged dense helium gas at 5.5 K and liquid at 3.9 K. Real spectral intensity can be obtained by deviding that read on the spectrum by a scale factor which is given just in the upper area of each band. Notation such as f→b denotes the excimer-emission and those of Di and Cl denote the excimer-dimer and excimer-cluster emissions.

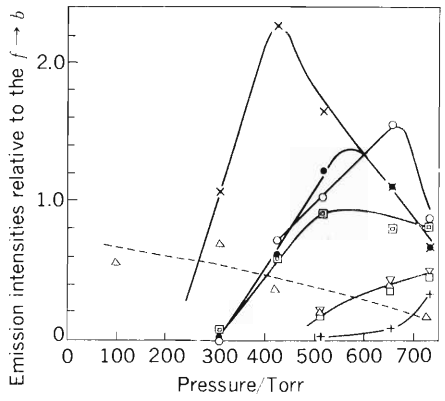

Fig. 2. Pressure dependence of emission-intensities relative to that for the f→b emission. △, h→b; ×, Di-emission; ○, ●, ⊡, ▽, □, and + stand for the Cl-emissions at 4,493, 4,785, 5,117, 5,619, 5,554, and 5,234 Å; measurement was carried out at 5.5 K.

$$a^3 + He_{2,i}^* \rightarrow He_{2,j}^* + He_{2,k}^* \text{ or } He_{2,m}^* + h\nu \quad (4)$$

or in a general form,

$$He_{2,k}^* + He_{2,l}^* \rightarrow He_{2,m}^* + He_{2,n}^* \text{ or } He_{2,i}^* + h\nu \quad (5)$$

$$a^3 + c^3, b^3, d^3 \rightarrow \text{excimer-dimer (Di)} \quad (6)$$

Of the above reactions, reactions (2)-(6) are very characteristic. Namely, reactions between excimers lead to the conversion of the excimers into other excimers, the dimer-formation, and the photoemission, but do not lead to quenching processes; this is quite different from the usual density-effect for excited large molecules whose collisions lead to quenching.

For liquid helium, whose density is 20 times larger than that of the gas sample used here or in which energy dissipation increases in a similar manner, the emission spectrum was found to present new bands quite different from the gas spectra in the wavelength region from 4,000 to 6,800 Å. Now, neither excimer-emissions nor the Di-emission (emission from Di) can not be observed. All broad bands observed at 5,600, 5,220, 5,110, 4,980, 4,780, and 4,480 Å can be attributed to new ones which have not been found so far by the methods using electron impingement. In a last progress report, we have tentatively proposed that these new bands are due to emissions from the clusters composed of the helium-excimers. The present report presents important experimental result which supports the previous tentative assignment.

Spectra given in Fig. 1 show the variation of the emission spectra with increasing gas pressure at 5.5 K up to liquid state at 3.9 K. This pressure dependence corresponds to shortening in an average atomic-distance from ~10 Å to ~3 Å or to an increase in energy dissipation from ~0.2 eV/Å to ~20 eV/Å. At 103 Torr, only excimer-emissions are observed in Fig. 1, but neither Di- nor Cl-emission are yet recognized. As the pressure increases up to ~200 Torr, the Di-emission appears and at 423 Torr, both Di- and Cl-emission are observed, while the excimer-emissions are suppressed. With further increase

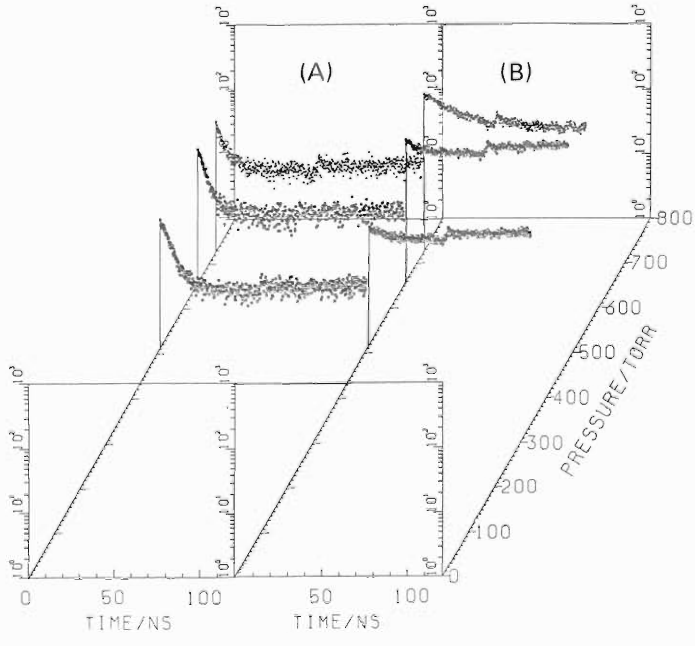

Fig. 3. Decay curves of the Cl-emissions at 5,105 (A) and 5,557 (B) Å at several gas pressures at 5.5 K.

in pressure, the Di-emission are suppressed, while the Cl-emission increases. In this pressure-range, the excimer-emissions can not be recognized except for the intense one for the f→b transition and those due to the transitions between higher Rydberg states which appear in the wavelength region larger than 6,000 Å.[1] In the liquid phase, both excimer- and Di-emissions are completely suppressed in the wavelength region where the Cl-emission appear. The pressure dependence of the emission intensities is shown in Fig. 2, where the emission intensities are plotted relatively to that for the f→b excimer-emission. The f state can be regarded as the best standard for the density-effect, since its lifetime is short (~4 ns) and free from second order reaction 2. Figure 2 shows obvious density dependence of the Di- and Cl-formation, suggesting that following reactions become important with density,

$$Di + He_2^* \rightarrow (He_2^*)_3 \quad (7)$$

$$(He_2^*)_3 + He_2^* \rightarrow (He_2^*)_4 \quad (8)$$

and further clustering where He_2^* is considered to be lower lying excimers, b^3, c^3, or d^3 as shown later. The result that the broad band near 5,600 Å appears at pressure higher than 500 Torr in contrast with other Cl-emissions beginning to appear near 300 Torr suggests that this band may be due to the cluster composed of a larger number of excimers. This may be supported by the result that the emission intensities without those at 5,557 and 5,234 Å begin to decrease from ~500 Torr.

Next, two typical decay data are presented in Fig. 3, in which (A) and (B) show pressure-dependent decay curves of the emission bands at 5,557 and 5,105 Å, respectively. A common result derived from the two emission bands is that the decay-curve can be separated into the fast and the very slow components. The former component increases with pressure, although the one for 5,105 Å decays much faster than that for 5,557 Å. The latter component, which has so long decay time that their changes cannot be recognized in this time-range, increases with pressure. This component makes principal contribution to the total emission intensity compared with the fast component. The slow decay component may be explained by taking into account of the regeneration (2), since Cl-states impossibly has such long spontaneous lifetimes, because of their allowed transitions. Namely, the long decay times of the Cl-emissions should be decided by bimolecular regeneration-reactions which can produce c^3, d^3, and perhaps b^3 as long as the a^3 exist; the concentration of the a^3 is considered always to be the highest of all excimers under the present experimental conditions.[1] This explanation is the same as that done in Ref. 1 for the very long decay time of the Di-emission. The fast decay components and their increase with pressure can be explained as due to a large initial concentration of the excimers. The faster decay for the 5,105 Å band than that for 5,557 Å may be easily understood from the stepwise clustering shown in reactions (7) and (8). The decay curves for the other Cl-emission, those at 4,493, 4,785, 5,234, and 5,619 Å, are classified as follows. Those at 5,234 and 5,619 Å bands have the similar decay to that at 5,557 Å, while those at 4,493 and 4,785 Å are similar to that at 5,105 Å. This classification agrees well with that for the pressure dependence shown in Fig. 2.

Reference

1) K. Kimura: *J. Chem. Phys.*, 84, 2002, 2010 (1986).

RIKEN Accel. Progr. Rep. 19 (1985)

III-5. Instrumentation

1. Test of EBIS for Electron-Ion Merging Beam Experiment

S. Ohtani, Y. Awaya, Y. Itoh, T. Kambara, Y. Kanai, T. Koizumi,
T. Mizogawa, K. Okuno, H. Shibata, S. Takagi, and S. Tsurubuchi

We are starting an ion-injected EBIS (Electron Beam Ion Source) experiment using the linac. The purpose is to study collisional processes of electrons and heavy ions by a merged electron-ion beam method using a heavy ion beam. The EBIS apparatus used is called "proto-NICE,"[1] which has been developed at Institute of Plasma Physics, Nagoya University.

In the present stage, the proto-NICE has been rebuilt in the experiment area of the linac and the test operation of an electron gun and extraction of the produced ions are being carried out. Figure 1 shows a schematic view of the proto-NICE. The electron gun is of a Frost type[2] with about 2 micro-perveance and operated under the conditions of the Brillouin flow. The typical current density of the electron beam is estimated to be more than 10 A/cm^2. At present, more than 95% of the electron beam emitted from the cathode (about 100 mA) can reach the electron collector electrode. Fourteen drift tubes with an internal diameter of 6 mm, whose potentials are variable independently, are used to provide good conditions for EBIS operation. The produced ions are extracted and their charge states are analyzed by using a sector magnet. An example of the charge state distribution of the ions

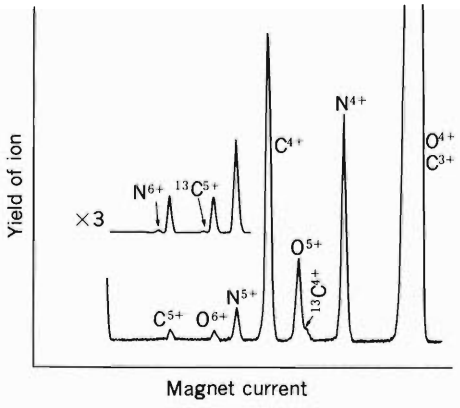

Fig. 2. Typical spectrum of the charge-state distribution of ions extracted from the proto-NICE analyzed by a magnet. The ions are from residual gas with H, C, N, O, and $^{13}CO_2$ gas supplied from the outside. The measurement was carried out under the conditions that the electron beam intensity was 76 mA at 1.9 keV and the background pressure was about 2.6×10^{-8} Torr.

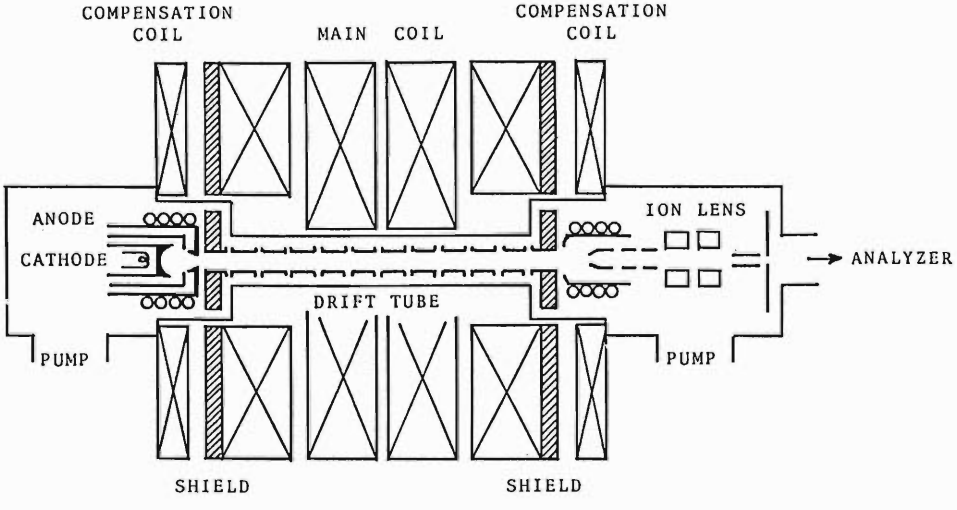

Fig. 1. Schematic view of the proto-NICE. The distance between the cathode and the ion lens is about 60 cm.

extracted from the proto-NICE is shown in Fig. 2. In this case 99% enriched $^{13}CO_2$ gas was supplied from the outside to separate produced naked carbon ions from background H_2^+ ions. The N and O ions in Fig. 2 are from the $^{13}CO_2$ gas and the residual gas, mainly CO_2, H_2O, and N_2. Typical intensities, at present, of the extracted Li-like ions of C^{3+} and O^{5+} are about 10^6 cps, and that of naked carbon ions, $^{13}C^{6+}$, was about 50 cps. We also observed about 250 cps of naked nitrogen ions $^{15}N^{7+}$ by supplying enriched $^{15}N_2$ gas.

References

1) H. Imamura, Y. Kaneko, T. Imai, S. Ohtani, K. Okuno, N. Kobayashi, S. Tsurubuchi, M. Kimura, and H. Tawara: *Nucl. Instrum. Methods*, **188**, 233 (1981).
2) R. Frost: *Proc. IRE*, **56**, 1800 (1962).

RIKEN Accel. Progr. Rep. 19 (1985)

III-5-2. Test of a Position-Sensitive Parallel Plate Electrostatic Spectrograph

Y. Kanai, Y. Itoh, T. Koizumi, H. Shibata, T. Matsuo,
H. Kumagai, T. Kambara, M. Kase, T. Mizogawa, and Y. Awaya

Analysis of charged particles can be carried out magnetically or electrostatically. For low energy electrons ($E<10$ keV), electrostatic analyzers are available. A parallel plate electrostatic analyzer has a structure simpler than that of other electrostatic analyzers and may be constructed accurately. We have constructed a position-sensitive parallel plate electrostatic spectrograph using a position-sensitive electron detector, described in a previous report,[1] in which a tandem microchannel plate (MCP: Hamamatsu Photonics F1552-03×2) and a Si position-sensitive detector (PSD: Hamamatsu Photonics S1352) are used in order to measure the electrons ejected in heavy-ions atom collisions.

A schematic drawing of the spectrograph is shown in Fig. 1. The spectrograph is composed of three parts: (1) a triple aperture lens; (2) a 45° type electrostatic parallel plate analyzer; and (3) a position-sensitive electron detector. The advantage of using the position-sensitive electron detector is that it allows us to obtain broad-range energy spectra of electrons at a time. The potential V_0 of Analyzer plate 2 determines the energy E_0 of the electron detected at the center of MCP: $E_0=eV_0$ in the ideal case. The potential difference V_d between Analyzer plates 1 and 2 determines the width E_w of the electron energy spectra obtained at a time: $E_w=0.45\ eV_d$ in the present case.

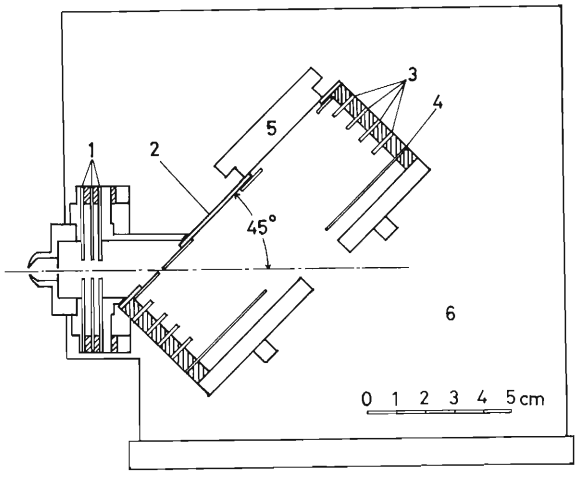

Fig. 1. Schematic drawing of the Spectrograph. 1, Triple aperture lens; 2, Analyzer plate 1; 3, Guard rings; 4, Analyzer plate 2; 5, Position-sensitive electron analyzer (MCP, PSD); 6, Holder.

Typical results obtained with the 1.5 keV electron impact Ar L-MM Auger electrons are shown in Fig. 2, in which the values of V_0 and V_d of each spectrum are given. We can obtain spectra with relatively high resolution as V_d is decreased. The spectra in Fig. 2 (b) corresponds to the highest energy group of the peaks shown in Fig. 2 (a). The L_3-$M_{2,3}M_{2,3}(^3P)$ and the L_2-$M_{2,3}M_{2,3}(^1D)$ peaks are clearly separated from each other in Fig. 2 (b).

We have also carried out preliminary measure-

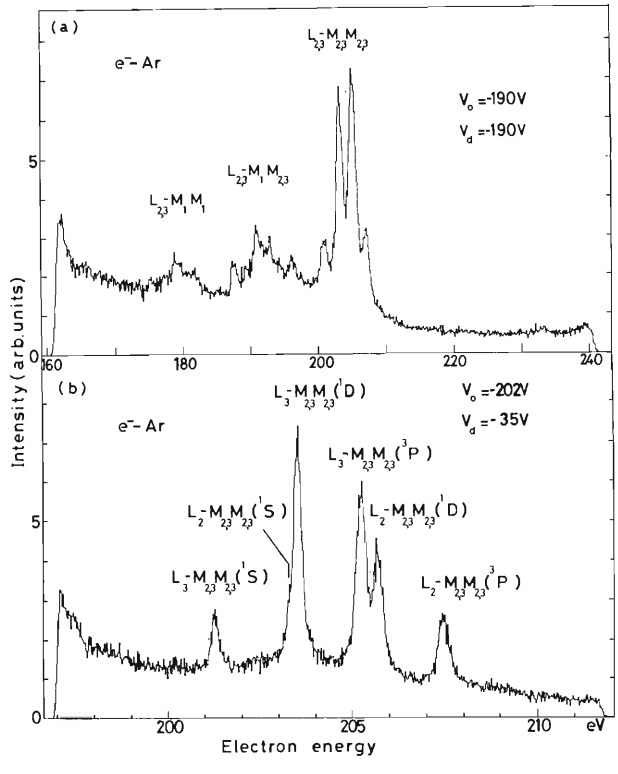

Fig. 2. Typical results of electron impact Ar L-MM Auger electrons.

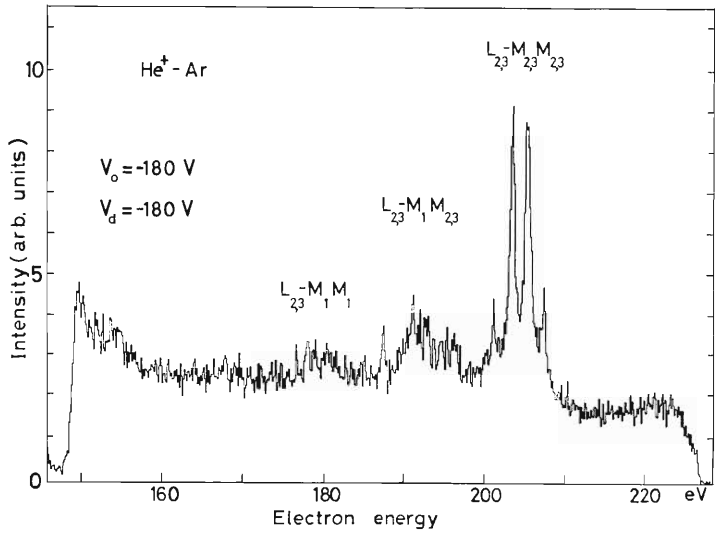

Fig. 3. Preliminary results of Ar L-MM Auger electrons in He^+-Ar collisions.

ment of the Ar L-MM Auger electrons in He^+-Ar collisions. The results are shown in Fig. 3. The background level is higher than that in the electron impact case. A part of the background is due to the dark counts of MCP of about 0.9 counts per second. The high background level is an obstacle to measurement of the electrons ejected in heavy-ions atom collisions; an effort of reducing the background is in progress.

Reference

1) H. Kumagai, Y. Itoh, T. Koizumi, H. Shibata, and Y. Awaya: *RIKEN Accel. Progr. Rep.*, **18**, 162 (1984).

RIKEN Accel. Progr. Rep. 19 (1985)

III-5-3. Parallel Plate Avalanche Counters

H. Kumagai, T. Kubo, M. Ishihara, M. Fuse, and E. Gotoh

The parallel plate avalanche counter (PPAC)[1] has an excellent timing property, high counting rate capability, and superior registance against radiation damage. Previously we constructed a prototype model of the one-dimensional position-sensitive PPAC and studied its fundamental characteristics.[2] Based on the techniques established through this work, we have newly constructed two PPACs of different types. In this report we present the result of investigation on the timing characteristics, the position resolution, and the detection efficiency for these detectors as well as for the previous one, using particle beams obtained from a radioactive source, the Cyclotron, and the RIKEN heavy-ion linear accelerator (RILAC).

1) A one-dimensional position-sensitive PPAC with a grid

Structure of this counter and the associated gas-feed system and electronic circuits are described in Ref. 2. Briefly, the chamber of the counter contains two pairs of electrodes: one (with a grid) for position detection and the other for provision of a stop signal for timing measurements. The counter, which was filled with isobutylene gas (10 Torr) and applied voltage 800 V, was exposed to a uniform-intensity beam of α-particles from a ^{241}Am source. Pulse-hight distribution of the grid signal is shown in Fig. 1. Figure 2 shows the obtained position spectrum, in which each peak seen corresponds to the position of the respective grid wire strung at 2 mm intervals. Figure 3 shows the result for the timing characteristics, which was obtained by using a finely collimated α-beam from ^{241}Am and with an applied voltage of 850 V. A full-width-at-half-maximum (FWHM) of 0.82 ns observed for the peaks implies that a time resolution intrinsic to each pair of electrodes is 0.58 ns.

2) A position sensitive PPAC with a multi-strip cathode

We have constructed a one dimensional position sensitive PPAC whose cathode consists of a hundred strips of conductors (46×0.9 mm^2) with 0.1 mm inter-strip spacing. These strips are formed on a printed circuit board (100×46 mm^2), and all contiguous strips are connected to each other by chip resisters of 100 Ω. An anode, made of a 60 μg/cm^2 thick Au layer evaporated on 1.5 μm thick Mylar foil, has a sensitive area of 100×20 mm^2. The cathode and the anode are aligned parallel to each other with a 3 mm gap. Figure 4 shows the result of measurement of the position

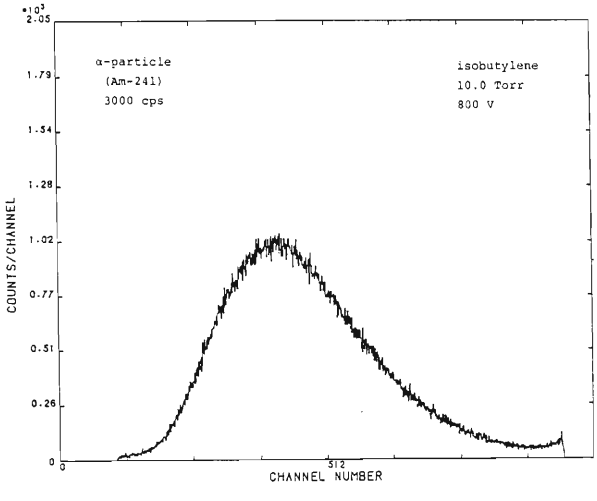

Fig. 1. Pulse-height distribution of signals from the grid of a one-dimensional position-sensitive PPAC exposed to a uniform-intensity beam of α-particles from a ^{241}Am source.

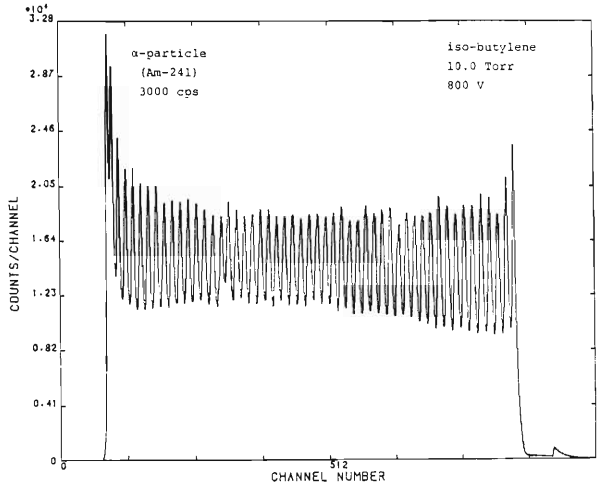

Fig. 2. Position spectrum obtained by using the same setup as that in Fig. 1.

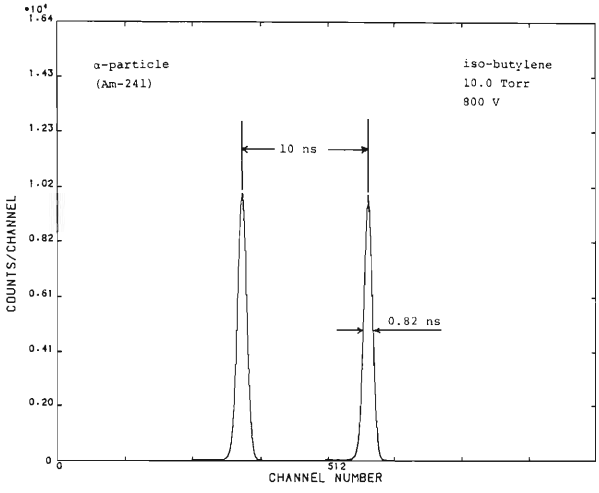

Fig. 3. Timing characteristics of the one-dimensional position sensitive PPAC.

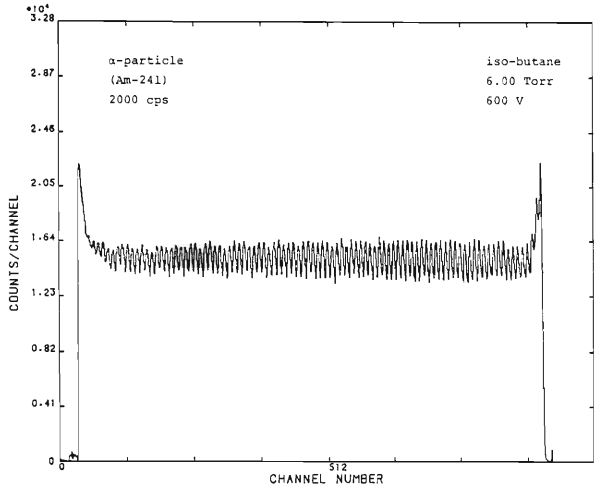

Fig. 4. Position spectrum obtained with a position-sensitive PPAC with a multi-strip cathode. Conditions for the incident particles used are same as those given in Fig. 1.

detection characteristics, obtained by the same incident beam as that was used for determination of the spectrum of Fig. 2, with filled iso-butane gas (6.0 Torr), and an applied voltage of 600 V. The interval between adjacent peaks of the spectrum shown in Fig. 4 correspond to 1 mm spacing between the cathode strips. This PPAC will be used by an atomic physics research group with a magnetic analyzer for measurement of charge distributions of scattered particles in atomic collisions.

3) Disc-type PPACs

In order to investigate the timing characteristics and the counting-rate capability using beams obtained from the Cyclotron or RILAC, we have constructed two PPACs of a small-size with disc-shaped electrodes: one (PPAC-30) with both

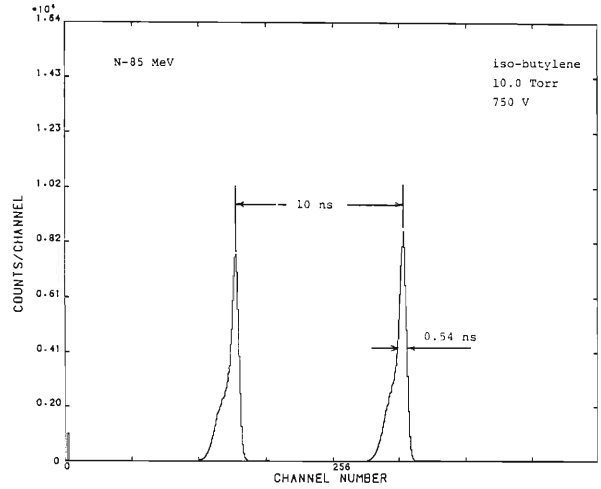

Fig. 5. Timing characteristics of the disc-type PPACs of a small size, obtained for the incident particles of ^{14}N at 85 MeV.

electrodes 30 mm in diameter and with a 3 mm gap and the other (PPAC-6) with both electrodes 6 mm in diameter and with a 3 mm gap. The two counters are placed in parallel 6 mm apart from each other. The time resolution was measured by using an 85 MeV ^{14}N beam from the Cyclotron. The result is shown in Fig. 5. A FWHM of the peak of 0.54 ns was observed, which corresponded to the time resolution intrinsic to each counter of 0.38 ns.

The counter response to high counting rates was investigated by using a 6.8 MeV α-particle beam accelerated with the RILAC. Experimental arrangement is shown in Fig. 6. The α-particles traversed through 2 mg/cm^2 thick Au foil (a beam spot size of about 5×5 mm^2), entered PPAC-6 and PPAC-30 placed at 0°, and finally were collected in a Faraday cup, at which the beam current was measured with a current meter. The beam intensity was also monitored by detecting scattered particles from the Au foil using a SSD placed at 20°. Signals from the two PPACs and the SSD, together with the output of the beam current meter converted into a pulse signal by means of a voltage-to-frequency converter unit, were fed to an on-line data acquisition system.[3] The system was operated in an 8-parameter multi-channel scaling (MCS) mode with an advance signal of 0.1 s, thus enabling us to record data every 0.1 s. The result of investigation on the counting rate capability is shown in Fig. 7, where the counting rates in the detectors are plotted as function of beam current (both axes are in logarithmic scale). Only three data points were plotted for PPAC-6, since further measurement has not been made for this counter due to damage of the electrodes induced by the

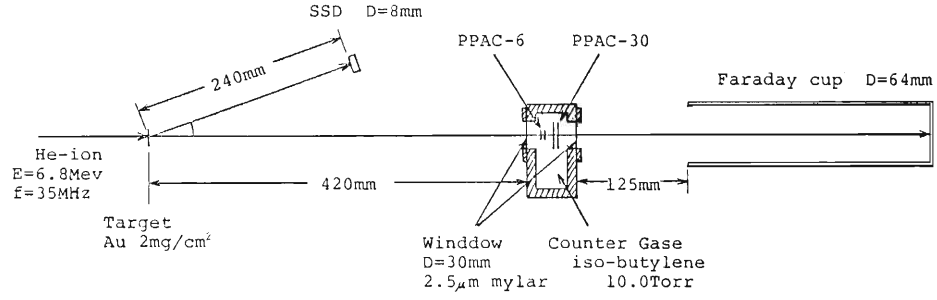

Fig. 6. Experimental arrangement used in the investigation of the counting rate characteristics using α-particle beam from the RILAC.

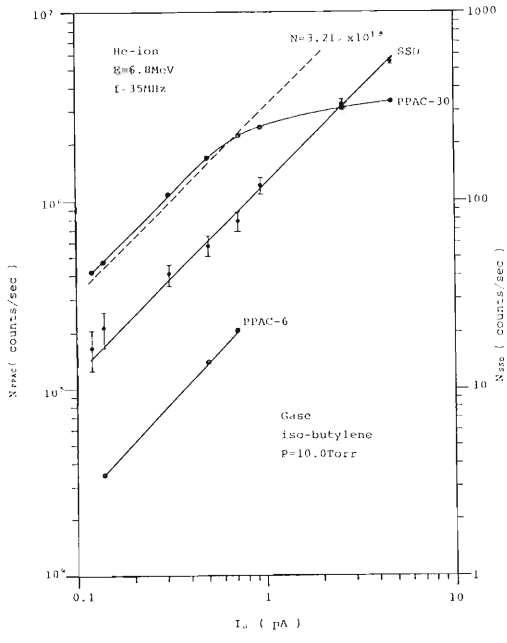

Fig. 7. Result for the counting rate characteristics of the disc-type PPACs. Counting rates in PPAC-30, PPAC-6, and SSD (beam monitor) are plotted as function of beam current. Broken line represents the number of particles per unit time deduced from the beam current.

glow discharge. The curve for the PPAC-30 increases linearly in the region of low counting rates but begins to deviate from linearity at a counting rate of about 2×10^6 cps, exhibiting a tendency towards saturation at higher counting rates. Though the position distribution of the beam intensity was not uniform, it can be concluded that the saturation begins to take place at a local density of incident particles of 7×10^5 cps/cm^2 at the central region of the sensitive area, based on the observed curve for the counter (PPAC-6) of a smaller-size. The broken line in Fig. 7 represents the number of incident particles deduced from measured beam current. Observed 10% deviation from the PPAC-30 curve in the low intensity region can be attributed to misalignment of the Faraday cup and the uncertainty ($\pm6\%$) in the beam current meter used.

References

1) H. Stelzer: *Nucl. Instrum. Methods*, **133**, 409 (1976).
2) H. Kumagai, S. H. Be, M. Ishihara, Y. Ikegami, M. Fuse, and E. Gotoh: *RIKEN Accel. Progr. Rep.*, **18**, 164 (1984).
3) H. Kumagai, S. Sasagase, and T. Wada: *Reports I. P. C. R.* (in Japanese), **62**, 114 (1986).

RIKEN Accel. Progr. Rep. 19 (1985)

III-5-4. Performance of a BaF_2 Scintillator as a Charged Particle Detector

T. Murakami, J. Kasagi, H. Tachibanaki, K. Yoshida, and T. Kubo

We have tested the performance of a BaF_2 scintillator as a charged particle detector, since the BaF_2 was found to have many attractive features as described in Ref. 1. So far, we have investigated the possibility of the particle identification by a pulse-shape-discrimination technique and measured the response of the scintillator to protons, deuterons, and α-particles.[2] No information on the response to heavy particles is available. In the present study we have measured the response to ^{16}O and ^{40}Ar particles.

The scintillator response was measured with elastically scattered ^{16}O and ^{40}Ar ions obtained from RILAC. A thin gold foil was bombarded by ^{16}O beams with energies ranging from 9.5 MeV to 22 MeV and by ^{40}Ar beams from 23 MeV to 54 MeV. The BaF_2 crystal used was rectangular one with dimensions of $2\times4\times1$ cm^3. In order to detect the fast component efficiently, the photomultiplier with a quartz window (Hamamatsu, R329-Q) was employed. The crystal was wrapped with a conical mirror and attached to the photomultiplier by using silicone grease. The detector was set at 30° with respect to the beam direction. Dynode pulses were fed into a preamplifier (ORTEC113) and an amplifier (ORTEC572), then digitized by a NIM ADC.

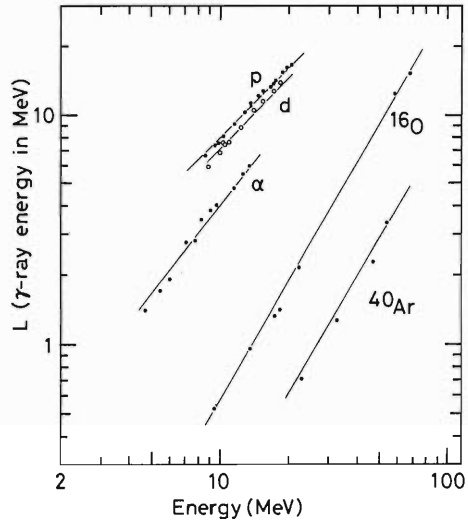

Fig. 1. Light output (L) of a BaF_2 scintillator for various particles in units of γ-ray energy determined by ^{60}Co and ^{137}Cs.

Table 1. Relative values of L for a BaF_2 and a plastic scintillators.

	Proton	α	^{16}O
BaF_2	100	59	13
Plastic	100	27	3.9

Figure 1 shows the light output, L, for various particles as a function of particle energy. The units for L represented by the γ-ray energy were determined by the output for ^{60}Co and ^{137}Cs.

Several features are observed in Fig. 1. First, L for protons is almost linear with particle energy. Furthermore, the amount of L for all particles is roughly described by the relation $L\sim E^n$. The case of $n=1$ corresponds to the data for protons. The value of n becomes larger for heavier particles and it reaches about 1.5 for the case of ^{40}Ar.

Second, the amount of L at the same particle energy is largest for protons and it decreases for heavier particles, that is a common feature of scintillation detectors. However, the BaF_2 scintillator emits larger output for heavier particles than other kinds of scintillators. Relative values of L for protons, α-particles, and ^{16}O particles of 20 MeV are tabulated in Table 1, where the value of L for protons is normalized to 100. Also shown are the ratios for plastic scintillators cited from Ref. 3. The ratios of L to detect heavier particles are 2 or 3 times larger for the BaF_2 scintillator than for the plastic scintillator.

As a result we conclude that the BaF_2 scintillator is suited for charged-particle detection.

References

1) T. Murakami, J. Kasagi, T. Inamura, and M. Ishihara: *RIKEN Accel. Progr. Rep.*, **18**, 160 (1984).
2) T. Murakami, J. Kasagi, Y. Nagashima, T. Nakagawa, W. Galster, W. Yokota, and S. M. Lee: *UTTAC*, **50**, 31 (1985).
3) F.D. Becchetti, C. E. Thorn, and M. J. Levine: *Nucl. Instrum. Methods*, **138**, 93 (1976).

RIKEN Accel. Progr. Rep. 19 (1985)

III-5-5. Response of BaF_2(Powder)-Plastic and BaF_2 Scintillators to Protons

S. Kubota, T. Motobayashi, J. Ruan (Gen),* T. Shimizu,**
I. Kohno, and M. Ishihara

We have developed a BaF_2-plastic mixture (scintillator) which has a response as fast as that of BaF_2 crystal, wavelength of 410+30(−20) nm, and good mechanical properties. The response curves of this scintillator and BaF_2 were obtained for proton beams of <15 MeV.

The barium-fluoride plastic scintillator (BPS) consists of BaF_2 powder (70 wt %) and methylmethacrylate (30%). Luminescence from powder BaF_2 is converted by ~1% buthyl-PBD (2-(4-*t*-butylphenyl)-5-4-(4-biphenyl)-1,3,4-oxadiazole) and 0.02% BDB (4,4-bis-(2,5-dimethylstyryl)-diphenyl). The reflective index for resin (methylmethacrylate) is matched to that of BaF_2.

In this experiment, 15 MeV proton beams from the cyclotron were elastically scattered from a Au target and extracted from a vacuum chamber through a 15 μm Mylar window. Passage through Al absorbers allowed us to vary the ion energy entering the scintillator. Proton energy was measured with a silicon semiconductor detector calibrated with 5.16 MeV (^{239}Pu), 5.49 MeV (^{241}Am), and 5.80 MeV (^{244}Cm) α-particles.

The light outputs from BPS and BaF_2 (Horiba, Kyoto, 20 mm dia.×10 mm) were measured with either an R329 (borosilicate glass window) or an R1668 (fused silica window) photomultiplier. An aluminium foil was used as a light reflector. Figure 1 shows energy spectra obtained with BPS (R329) and BaF_2 (R1668) for scattered protons without an absorber. As shown in Fig. 1, 4.4 MeV γ-rays were also detected. These γ-rays were induced by proton bombardment at a carbon plate used as a beam stopper. The FWHM energy resolutions for 15.4 MeV protons were 12.1%, 9.8%, and 16% for BPS (R329), BaF_2

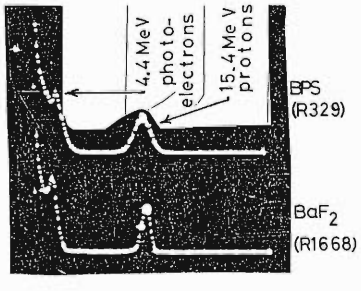

Fig. 1. Energy spectra of 15.4 MeV protons measured with BPS (R329) and BaF_2 (R1668).

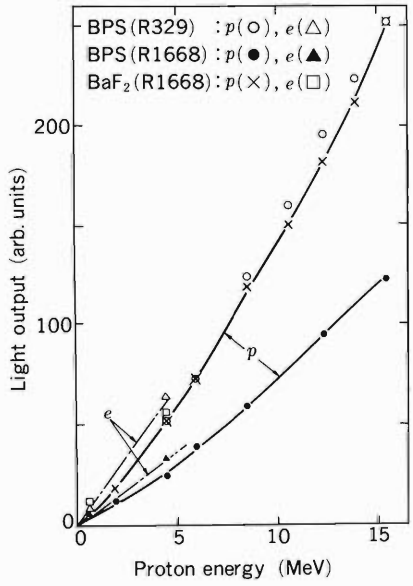

Fig. 2. Light response curves for protons and 4.4 and 0.661 MeV photoelectrons.

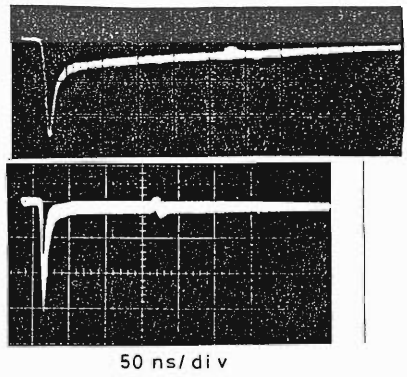

Fig. 3. Oscilloscope traces for the scintillation pulses from BPS for 15 MeV proton beam excitation (upper trace) and relativistic electron beam excitation (lower trace).

* Rikkyo University.
** Kyowa Gas Chemical Ind. Co., Ltd.

(R1668), and BPS (R1668), respectively. Figure 2 shows response curves of BPS (R329), BaF_2 (R1668), and BPS (R1668). The relative pulse height for BPS (R329) is normalized at 15.4 MeV to that for BaF_2 (R1668). Data points for 4.4 and 0.661 MeV electrons are also shown. The response curves for BPS and BaF_2 crystals are clearly convex over the entire energy region studied. The light outputs of both scintillators for 4.4 MeV protons are 80% of those for electrons of the same energy.

Figure 3 shows oscilloscope traces for the scintillation pulses from BPS excited by 15 MeV proton beam (upper trace) and by relativistic electrons (lower trace). The slow component fraction of 600 ns for proton beam excitation is greater than that for electron excitation. This large difference will be used for n-γ-pulse shape discrimination.

The new BaF_2-plastic scintillator we have developed will be extended in size and will be applied to many fields.

RIKEN Accel. Progr. Rep. 19 (1985)

III-5-6. RIKEN BGOACS and Château de Cristal

Y. Gono, M. Fukuda, T. Kohno, M. Sugawara, H. Kamitsubo, F. A. Beck,* T. Byrski,* G. Costa,* C. Gehringer,* B. Haas,* J.C. Merdinger,* B. Nourredine,* S. Rouabah,* and J. P. Vivien*

Six sets of anti-compton shields (ACS) made of bismuth germanate (BGO) crystals were constructed in 1984.[1] Four of them were sent to CRN (Centre de Recherches Nucléaires), Strasbourg, in August, 1985, and used with Château de Cristal[2] for the in-beam γ-ray spectroscopy studies. The Château de Cristal is a $4\pi\gamma$-ray detector system consisting of 74 hexagonal BaF_2 counters. A picture of BGOACS and Château de Cristal set in the beam line of MP tandem at CRN Strasbourg is shown in Fig. 1. This combined system was almost ready for experiments in November, 1985, and has been used for some test experiments.

Since the Château de Cristal is a national project in France, many groups proposed experiments. The RIKEN group proposed a joint experiment with Orsay and Strasbourg group (Ch. Briancon, G. Bastin, F. Hannachi, M. G. Porquet, C. Schuck, J. P. Thibaud, and N. Schulz) on Th isotopes. A test experiment has been successfully made on ^{222}Th using the ^{208}Pb(^{18}O, 4n)^{222}Th reaction in November, 1985.

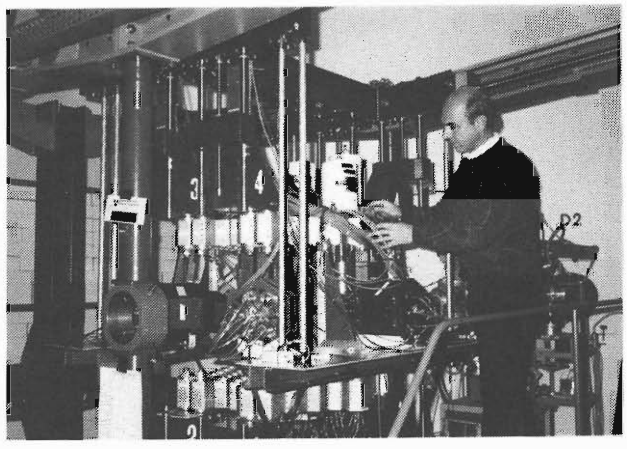

Fig.1. RIKEN BGOACS with Château de Cristal set in CRN Strasbourg.

References

1) M. Fukuda, Y. Gono, Y. Ishikawa, M. Sugawara, T. Inamura, M. Ishihara, T. Nomura, I. Kohno, H. Kamitsubo, J. Kasagi, and T. Murakami: *RIKEN Accel. Progr. Rep.*, **18**, 152 (1984).
2) F. A. Beck: Proc. Int. Conf. on Instrumentation for Heavy Ion Nuclear Research, Oct. 22-25, p. 129 (1984).

* Centre de Recherches Nucléaires Strasbourg.

RIKEN Accel. Progr. Rep. 19 (1985)

III-5-7. Radioactive Beam Production at GANIL

R. Bimbot,* P. Aguer,** G. Bastin,** R. Anne,*** H. Delagrange,***
Y. Schutz,*** Y. Gono, K. Hatanaka, and H. Kamitsubo

A radioactive beam production experiment was performed at GANIL (Grand Accélérateur National d'Ions Lords) in 1985 using LISE[1] (Ligne d'Ions Super-Epluches). The primary beam of ^{18}O ($E=65$ MeV/A) was provided by GANIL. Production rates of ^{16}C ($T_{1/2}=0.75$ s), ^{17}N ($T_{1/2}=4.17$ s) and other elements were measured. Targets used were Be (569, 1,036 mg/cm^2), AL (622, 1,138 mg/cm^2) and Ni (748, 1,351 mg/cm^2). Reaction products were transported by LISE and identified with a ΔE(500 μm$\times$300 mm^2)$-E$(5,000 μm$\times$300 mm^2) counter telescope of Si detectors. Time-of-flight information was recorded at the same time. Since the targets were very thick, the energy spread of the reaction products was large. Consequently various kinds of reaction products were brought to the detector position by one momentum setting of the magnets. Those reaction products were separated from each other by using an energy degrador of Al (150 mg/cm^2) placed between two dipole magnets. The differences in energy loss among various ions by the degrador were large enough in the present experiment to separate the reaction products. The ions of ^{16}C and ^{17}N were obtained rather purely up to about 10^6 and 10^7 pps, respectively, with the primary beam intensity of 10^{12} pps. The target dependence of the yields was almost constant if this quantity was calculated per one target atom. This leads to a conclusion that the targets of lighter elements give larger yields of the radioactive beam when target thicknesses are adjusted to give the same energy losses for the reaction products. An example of the yield curves for carbon isotopes is shown in Fig. 1.

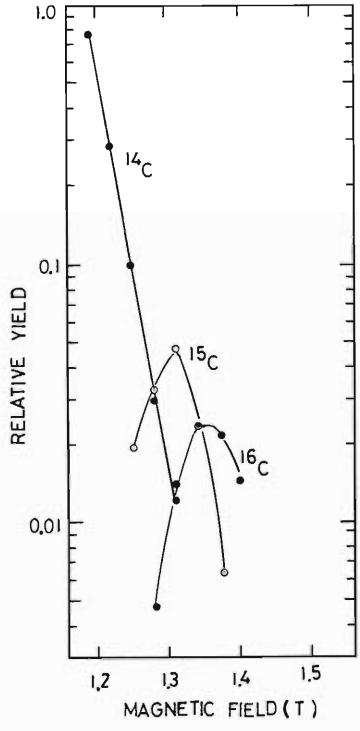

Fig. 1. Relative yields of $^{14,15,16}C$ ions from the Be+^{18}O reaction at 65 MeV/A. Horizontal axis is the magnetic field strength of the second dipole magnet.

Reference

1) M. Langevin and R. Anne: Proc. Int. Conf. on Heavy Ion Nuclear Research, Oct. 22-25, p. 191 (1984).

* Institut Physique Nucléaire Orsay.
** CSNSM Orsay.
*** GANIL.

RIKEN Accel. Progr. Rep. 19 (1985)

III-5-8. Monte Carlo Calculations of Detector Response to High Energy Photons

H. Tachibanaki, T. Murakami, and J. Kasagi

A detector for high energy γ-rays up to 50 MeV is presently being constructed. Large NaI crystals and recently BGO scintillators are widely used as high energy photon detectors.[1),2)] However we have decided to employ a BaF_2 scintillator because it is superior to NaI or BGO on the following points: BaF_2 has 30% larger efficiency than NaI. It has a good timing resolution which is essential to discriminate the events of γ-ray from those of neutrons. Cost is much lower than BGO. A number of segments can be easily assembled to one detector.

We have written a computer program to calculate detector response functions for high energy γ-rays. Although a lot of simulation programs have been reported, they deal with the detectors of NaI or Ge.[3)] Our program provides the response functions for various detector material including BaF_2, BGO, and NaI. The aims of this program are as follows.

1) It is used to obtain an optimum design with regard to response functions, detector volume and cost.

2) The response functions for γ-rays of various energies are necessary to unfold an experimental spectrum when it is compared with the calculated one. Since it is difficult to prepare the experimental response functions for wide energy range, the calculated ones will be employed after the program verification.

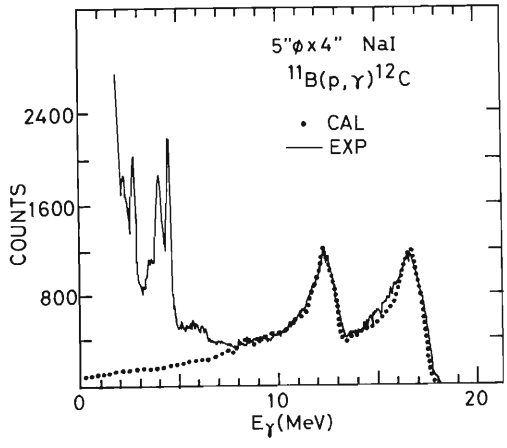

Fig. 1. Calculated (dots) and measured (solid lines) response of 5"ϕ×4" NaI to the γ-rays of 17 and 12.5 MeV.

The Monte Carlo program simulates the interaction between γ-rays (electrons and positrons) and detector material. The physical processes considered in the program are as follows: (1) Compton effect, (2) photoelectric effect, (3) pair production, (4) bremsstrahlung production, (5) positron annihilation, and (6) continuous energy loss of electrons or positrons. Energy and/or angular distributions of γ-rays and electrons are treated as correctly as possible. The obtained response is folded with a distribution function to simulate the effect of finite resolution of the actual instrument. This distribution function is given by the Gaussian distribution whose width depends on the γ-ray energy.

The computation was proceeded by FACOM at the RIKEN Computer Center. An example of the calculated results is shown in Fig. 1. In this calculation, γ-rays of 17 and 12.5 MeV are assumed to be injected on the 5"ϕ×4"NaI crystal without collimation. The intrinsic resolution of 600 keV at 17 MeV is used. In the figure also shown is the experimental spectrum obtained from the $^{11}B(p,\gamma)$ reaction at $E_p=1$ MeV, which produces the 17 MeV and 12.5 MeV γ-rays. The calculated results are normalized to the 17 MeV peak of the experimental one. In general, response functions for high energy γ-rays are characterized by huge low-energy tails and the calculation reproduces these tails very well. CPU time of 40 s is required to calculate the detector response for about 20,000 events of γ-rays.

The calculation for other material are now in progress and the design of a high energy γ-ray detector is being discussed.

References

1) A. M. Sandorfi and M. T. Collins: *Nucl. Instrum. Methods*, **222**, 479 (1984).
2) D. J. Wagenaar, N. R. Roberson, H. R. Weller, and D. R . Tilley: *Nucl. Instrum. Methods, A*, **234**, 109 (1985).
3) D. W. O. Rogers: *Nucl. Instrum. Methods*, **199**, 531 (1982).

RIKEN Accel. Progr. Rep. 19 (1985)

III-5-9. A Test Apparatus for Resonance Ionization Spectroscopy of Atomic Nuclides

T. Inamura, K. Morita, K. Ando, H. Katsuragawa,
T. Minowa, and M. Shimazu

A resonance ionization technique is one of the most powerful methods of spectroscopy of elements in trace amounts. Its high selectivity and sensitivity for all of the elements (except He and Ne) in the periodic table have well been recognized in the last decade.[1] To make a full use of this excellent laser technique, however, it is still needed to develop an innovative device for each experimental purpose.

Here we briefly describe a test apparatus with which we will study how to improve the sensitivity up to its ultimatum, *i.e.*, a single-atom detection in about 10^{19} atoms. In Fig. 1 is presented a photograph of the apparatus. Figure 2 shows the schematic presentation of the experiment using the apparatus.

Test species are put on a tantalum tray (1) and then vaporized by heating with an electric heater or with laser beams. The vaporized species are ionized by a resonance ionization method with other lasers. Ions and electrons thus produced in the resonance cell (2) are detected with ceratrons (3) placed face to face: They are measured in coincidences to improve the signal-to-noise ratio. A pair of mirrors (4) is placed in parallel between the detectors to increase efficiency of ionization: The laser beams will be reflected five to ten times between the mirrors.

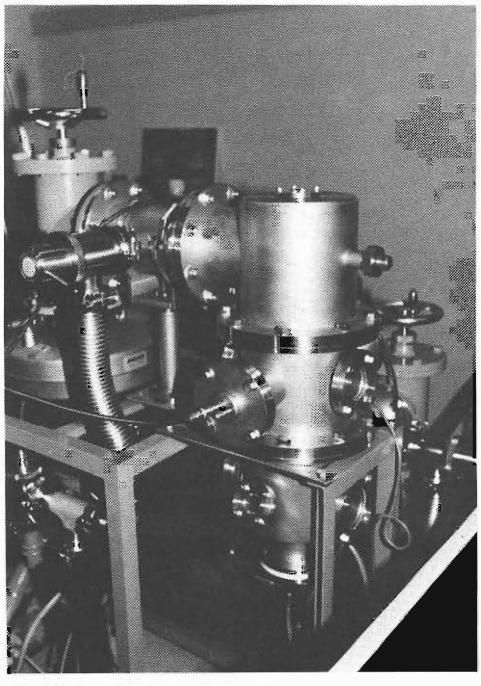

Fig. 1. Photograph of a test apparatus for resonance ionization spectroscopy. Lasers come into the resonance cell through a window on the right of the middle part of the chamber; an electric heater is in the bottom; infrared lasers will be introduced through a small window of the bottom (at the front) or through a window on the top when test species are vaporized by lasers.

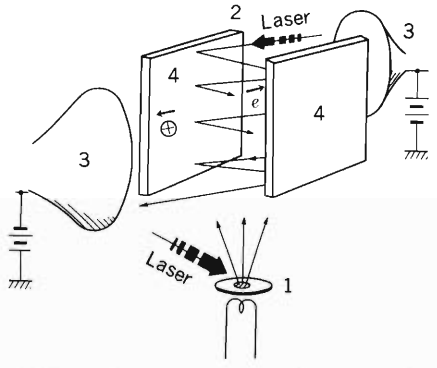

Fig. 2. Schematic presentation of our experiment. (1) tantalum tray; (2) resonance cell; (3) ceratrons; and (4) mirrors.

First we try spectroscopy of stable isotopes to test our method, and we proceed to spectroscopy of radioactive isotopes. In the end we aim to measure hyperfine structure to determine spins and moments of nuclei far from the stability line and also to measure isotope shifts to deduce the change in charge radius of these nuclei as a function of the number of neutrons.

This test apparatus will also be used for the study of the way to boost the efficiency of the ion-guided isotope separator on-line (IGISOL).[2]

References

1) G. S. Hurst: Resonance Ionization Spectroscopy 1984, (ed. by G. S. Hurst and M. G. Payne), The Institute of Physics, Bristol and Boston, p.7 (1984).
2) K. Morita, T. Inamura, T. Nomura, J. Tanaka, H. Miyatake, K. Sueki, M. Fujioka, T. Shinozuka, M. Yoshii, H. Hama, K. Taguchi, H. Kudo, Y. Hatsukawa, K. Furuno: p.158 in this report.

RIKEN Accel. Progr. Rep. **19** (1985)

III-5-10. Development of the Ion Guide Isotope Separator On-Line for Heavy Ion Induced Reaction

K. Morita, T. Inamura, T. Nomura, J. Tanaka, H. Miyatake, K. Sueki, M. Fujioka, T. Shinozuka,* M. Yoshii,* H. Hama,* K. Taguchi,* H. Kudo, Y. Hatsukawa, and K. Furuno**

An Ion Guide Isotope Separator On-Line (IGISOL) system has been constructing at Cave 1 of INS SF-cyclotron.

An Isotope Separator On-Line (ISOL) technique has been a powerful way for the study of short lived exotic nuclides. The essential part of the ISOL is an ion source; the features of the ISOL can be mostly decided by its ion source. The IGISOL was developed at Uväskylä University[1] and Tohoku University as a new method of the ISOL. The purpose of our development is to apply the IGISOL to the study of exotic nuclides produced by higher-energy heavy ion-induced reactions.

The difference between the IGISOL and the ordinary type ISOL is that the former system requires no ionizer. For the IGISOL, energetic recoiled isotopes produced by nuclear reactions are stopped in the helium gas. During thermalization in the gas, the ionic charge of the recoiled isotopes decreases *via* charge exchange processes, and finally become 1+ because of the high ionization potential of helium atoms. The 1+ ions are then transported to the low-pressure region by gas jet, and accelerated by an electrostatic field, and separeted with masses by a magnetic field. Because the IGISOL has no ionizer, there are advantages as: the system can be operated at room temperature and the extraction efficiency of ions is not affected strongly by the nature of isotopes.

Figure 1 shows the ion-guide stage of the isotope separator we developed. The ion guide vacuum chamber is evacuated with a mechanical booster pump having a high pumping speed of 4,200 m^3/h. This vacuum chamber is isolated with thin stainless-steel foil (10 μm) from a cyclotron beam duct, and floating on the high voltage of the mass separator. The target chamber is 5.5 cm long and has a volume of 11 cm^3. The diameter of the exit hole of the target chamber is 1.5 mm. The diameter of the skimmer is 1.5 mm.

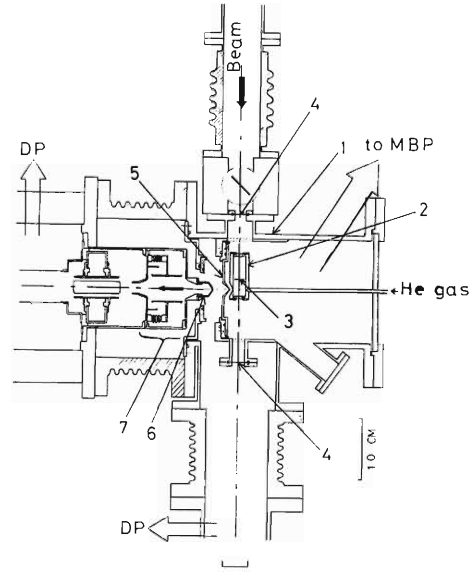

Fig. 1. Ion-guide stage of the ISOL. 1, Vacuum chamber; 2, Target chamber; 3, Target; 4, Window (10 μm SUS); 5, Skimmer; 6, Extraction electrode; 7, Einzel lens.

The extraction efficiency of ions and the transportation efficiency were checked by using the $^{27}Al(\alpha, 2p)^{29}Al$ and $^{27}Al(\alpha, 2pn)^{28}Al$ reactions. Incident energy of α-beam was 35 MeV, and recoil energy per nucleon of ^{29}Al and ^{28}Al was 146 keV/u. The pressure of the target chamber was 50 mbar. The extraction efficiency was about 3 % to the stopped ions. The transportation efficiency was 30%. Further test experiment is now in progress.

Reference

1) J. Äystö, J. Ärje, V. Koponen, P. Taskinen, H. Hyvönen, A. Hautojärvi, and K. Vierinen: *Phys. Lett. B*, **138**, 369 (1984).

* Cyclotron and RI Center, Tohoku University.
** Tandem Accelerator Center, University of Tsukuba.

RIKEN Accel. Progr. Rep. 19 (1985)

III-5-11. Proposal for Applying Piezoelectric Actuators to Mössbauer Drive System

N. Sakai, F. Ambe, and K. Asai

In-beam Mössbauer spectroscopy using γ-rays from Coulomb-excited nuclei often requires to cool both a source and an absorber at liquid N_2 temperature, because these Mössbauer γ-rays have relatively high energy of tens of kilo-electron volts, and the resulting recoil-free fraction of them are very small at room temperature. Therefore, a usual electromechanical drive system, which is practically held at room temperature, must solve a problem of how to keep the Doppler-modulated absorber at low temperature and in a high vacuum of the accelerator. Although a piezoelectric drive system can resolve the problem, the system has two shortcomings: the obtainable maximum velocity is of the order of 100 μm/s, and the useful frequency of this device is around 100 kHz, depending on its shape. Then, hitherto, the application of this device to the Mössbauer drive system has been restricted to some particular nuclei.

A piezoelectric *actuator* can overcome the shortcomings of the usual piezoelectric device mentioned above. The actuator consists in principle of a piezoelectric thin plate sandwiched by metallic electrodes, and one of the electrodes is made of a metallic thin plate. It vibrates in the transverse direction when an a.c. voltage is applied between them. A proposed drive system using two piezoelectric actuators is shown in Fig. 1. An absorber holder is connected to two actuators which vibrate in phase with the same amplitude. The vertical motion of the holder can be achieved with this device. It will be necessary to connect the absorber holder and the actuators with V-shaped metallic plates, as shown in Fig. 1, to compensate a slight change in the horizontal length of the actuators during their vibration. The measured displacement at the top of a free actuator (10 mm×30 mm×0.7 mm) is about 1 mm at the frequency of 30 Hz, which corresponds to 188 mm/s. This velocity is sufficient to measure a Mössbauer spectrum with any Mössbauer nucleus. The actuator itself can be used at liquid N_2 temperature.

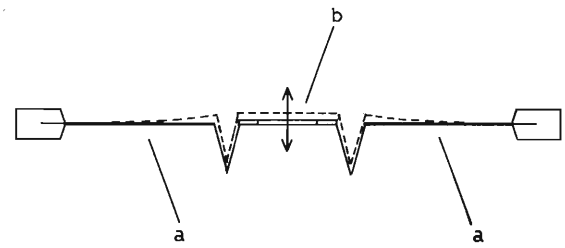

Fig. 1. Piezoelectric-actuator device for Mössbauer drive system.
a, piezoelectric actuator; b, absorber holder.

A disadvantage of the actuator drive system will be its inferior reproducibility of the velocity. Since the mass of the actuator is very small, the change in mass of the absorber will affect strongly the vibrating amplitude of the actuator. Nevertheless, it is possible to increase the mass of the actuator by enlarging its size and strengthening its power. Moreover, it is easy to make a velocity monitor to detect the velocity of the absorber: for example, by using a small permanent magnet on the absorber holder together with a pick-up coil.

RIKEN Accel. Progr. Rep. 19 (1985)

III-5-12. CAMAC Data Acquisition System with an Auxiliary Crate Controller

T. Ichihara, T. Inamura, K. Asahi, and M. Ishihara

A data acquisition system for the experiments at the GANIL (under Japan-France collaboration program) and for the test and development of the new data-acquisition system at the RIKEN Ring Cyclotron facility is now under construction. The system is divided into two parts:

(1) A CES 2180 CAMAC Auxiliary Crate Controller (ACC) system

(2) A Micro VAX-II system of a minimum configuration.

The configuration is shown in Fig. 1.

The CES 2180 ACC is the fastest ACC commercially available. It is a single-board CAMAC module built around a Digital Equipment latest 16/32-bit microprocessor, J-11.

This ACC provides following hardwares:

- 16/32-bit, 267 ns-cycle Digital Equipment J-11 microprocessor
- Auxiliary Crate Controller logic
- mixed EPROM/static RAM configuration
- DEC compatible RS-232C interface
- interval timer
- front-panel Q22 bus for system extensions including coprocessors, memory extensions, and stand-alone system with disk driver and operating system.

The most important feature is that any software written for the PDP-11 can be executed in the CES 2180 ACC as far as it can be loaded inside the 2180 ACC's memory (128 kB).

The CAMAC access time (peak value) is about 2.3 μs/16 bit-Read (890 kb/s) and 1.9 μs/16 bit-Write (1.1 Mb/s). A dual floppy-disk driver (RX-50) with the RQDX2 Interface is connected to the ACC for software development as a stand-alone system. The operating system (OS) which we have chosen for 2,180 ACC is RT-11, a real time single task OS. The interrupt response time of RT-11 OS is the fastest (zero OS overhead) among the OS's for a PDP-11 family (*e.g.*, RSX-11 M). In future, all software development will be carried out on the host processor (Micro VAX-II).

Generally the ACC is used for event-by-event

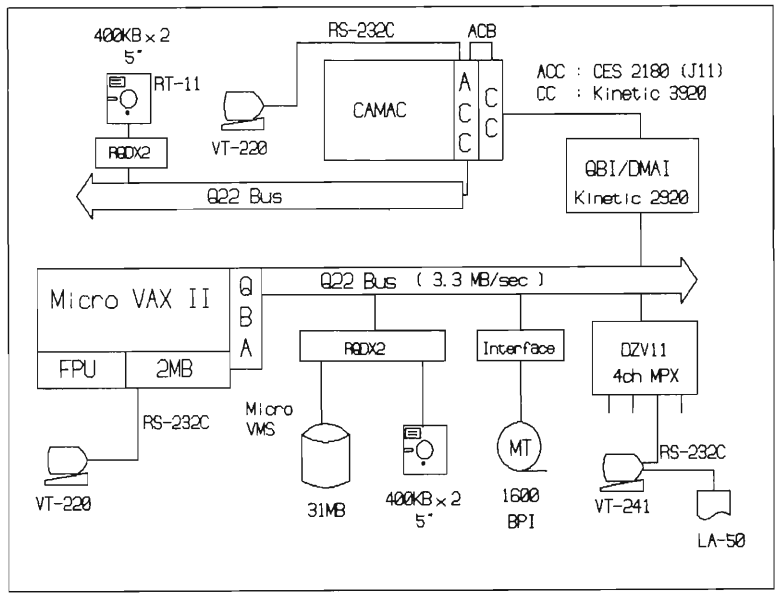

Fig. 1. A block diagram of the Micro VAX-II and CES 2180 ACC (J-11) data acquisition system for the GANIL experiments and for test and development of RIKEN Ring Cyclotron data acquisition system.

data acquisition initiated by the interrupt (event signal from the experimental logic) and for the data-buffering. When the buffer is full, it changes the current buffer (double buffering) and tells to the host processor that the buffer is full through look-at-me (LAM) interrupt.

The host processor is a Micro VAX-II, a newest member of a VAX family. The CPU has a capacity of about 85-90% and the price is about 10-20% of the VAX-11/780. The CPU consists of a one-chip ZMOS microprocessor (40 MHz clock) 78032 and a one-chip floating point coprocessor 78132 . The interrupt response time of the Micro VAX-II is about 30μs in the device driver level (OS level) and is about 400μs in the asynchronous system trap (AST) level (user process level including the overhead of the OS).

The operating system (OS) is a Micro VMS, which supports both the real-time multi-task environment and time sharing system (TSS) environment at the same time.

The interface between the Micro VAX-II and a CAMAC crate is a Kinetic 3920-2920Z2B dedicated crate controller (DCC), which is capable of direct memory access (DMA) in block-made CAMAC operation.

We have already developed device-driver software for the Kinetic DCC in the Micro VMS environment and the data transfer rate in a DMA mode is about 400 kB/s. The maximum I/O bandwidth of the Q22 bus is 3.3 Mb/s, whereas the internal memory bandwidth is 10 Mb/s, which indicates that the CPU Micro VAX 78032 can run at full speed without being affected by simultaneous Q-bus DMA I/O transfer to private memory.

After receiving the interrupt (LAM) from the 2180 ACC, the host processor starts the data transfer from the buffer of the ACC to the buffer of the Micro VAX-II in a Q-stop block mode (DMA mode), and then analyzes the event-by-event data, creates the on-line multi-parameter histogram, and displays it on a semigraphic color terminal (VT-241).

Examination of the basic function of the CES 2180 ACC and the Micro VAX-II has been completed and no serious trouble has been encountered. The specific feature of this data acquisition system is that all the central processors used are one-chip micro processors, J-11 and VAX-78032 CPU's.

We intend to extend this system, in the near future, including high speed magnetic tapes (6250 BPI), bit-map high-resolution high-speed color graphic display, high-resolution color hardcopy, large amount memory and disk, optical disk driver if available, CAMAC serial highway driver (SHD), *etc.* toward the final form. As for the front-end of the data acquisition system at RIKEN Ring Cyclotron facility, a VME-based CAMAC system[1] is also under consideration.

Reference

1) *IEEE Trans. Nucl. Sci.*, **NS-32**, No.4 (1985).

RIKEN Accel. Progr. Rep. **19** (1985)

IV. NUCLEAR DATA

1. Status Report of the Nuclear Data Group

A. Hashizume, Y. Tendow, Y. Ohkubo, and T. Nozaki

In this period main efforts have been directed to the operation of the programs related to the EXFOR systems and compilation of new EXFOR files of the nuclear reaction cross sections concerning the productions of ^{11}C, ^{13}N, ^{15}O, ^{18}F, ^{28}Mg, ^{52}Fe, ^{67}Ge, ^{74}As, ^{77}Br, ^{82}Br, ^{77}Kr, ^{81}Rb, ^{82m}Rb, ^{111}In, ^{123}Xe, ^{127}Xe, ^{123}I, ^{124}I, ^{125}I, nuclei.[1),2)] We have also compiled the reaction cross sections of various combinations of incident particles and target nuclei described in the same reports. In this respect, it was decided in the consultants meeting held in October in Paris to make good contact with the charged-particle center in Moscow (CaJad) to avoid duplications.

(1) We have continued to implement the program systems offered from IAEA. These programs are written by PLI language which is the first case for a FACOM 380M at RIKEN. Among the program systems, the EXFOR System consisting of four program groups, that is, Check Entry Run, Extract from Master Run, Prepare Edited Exfor Listing Run, and Prepaire Author Proof Listing Run has been implemented. Check New Entry Run checks errors and gives diagnosis of the new files. Extract from Master Run makes the lists of entries and subentries. Prepaire Edited Exfor Listing Run makes the edited listings which are more legible than the original file format. In general, data given in the EXFOR format should be confirmed by the original authors. Prepair Author Proof Listing Run gives the list of data confirmed by the authors. For Dictionary System, the program GENDICT which makes a VSAM file from the Dictionary file has been operated. This Dictionary file is renewed every three month. The VSAM file is referred by the Check New Entry Run program.

(2) The compilation of data to make a new file in the EXFOR format has become a routine work. The data represented by graphs in reports were read by using a graph reader. A graph reader TEKTRONIX 4051 was replaced by a TEKTRONIX 4052. By using this system, the amounts of data became about 1.5 MB, in which total reaction cross sections, differential cross sections, polarizations, and theoretical curves such as DWBA analysis are included. The third and forth EXFOR files (R003, R004) were transmitted to Nuclear Data Section in IAEA. The number of subentries amounted to 274. The third file consists of corrections of the first and second files. From the third file, the error check was made by the Check New Entry Run program mentioned above.

(3) The references of I-131 concerning reaction cross sections, differential cross sections, individual yields and product yields were compared with the Recent References compiled by Brookhaven National Laboratory Data Center (BNL), and the coverage of references was checked. This revision has been begun with contact with BNL. The complete reference files as well as recent Evaluated Nuclear Structure Data File (ENSDF) were obtained from BNL. Programs to compile the recent reference file and ENSDF have been made.

(4) For the mass chain evaluations of nuclear structure data, we have finished the evaluation of the $A=120$ chain and, after inspection of other Japanese groups, the file was sent to BNL for publication.

References

1) "Report on the 7th IAEA Consultants Meeting" of Nuclear Reaction Data Centers, INDC (NDS-154) (1984).
2) A. Hashizume, Y. Tendow, and T. Nozaki: *RIKEN Accel. Progr. Rep.*, **17**, 74 (1984).

RIKEN Accel. Progr. Rep. 19 (1985)

IV-2. On Nuclear Data for Production of ^{123}I

A. Hashizume and Y. Tendow

Owing to the suitable nuclear decay properties, ^{123}I is considered one of the best radionuclides for *in vivo* diagnostic nuclear-medical studies using single-photon emission computed tomography. Although more than twenty kinds of reactions have been proposed for the production of ^{123}I, selection should be made from several essential view points, that is, the price of enriched isotope for a target, ease of recovery and recovery percentage of the isotope after irradiation, beam requirements whether the kind of incident beam and its energy are easily available, the production yield rate, the chemical separation yield, and impurities of other radioactive iodine isotopes for the final product.

$^{124}Te(p, 2n)$ reaction. This reaction has been used most extensively in the routine production of ^{123}I. Its excitation function is shown in Fig. 1. By using a 99.87% isotopically enriched isotope, each point was determined with uncertainties of between 4% and 12% except for the lowest energy point. The cross sections were also measured with a 91.86% enriched isotope as a target. As a whole, the cross sections were obtained at precision of about 10%, but the production rates as a function of energy reported by different authors differ more than about a factor of two.

There are many reports concerning practical product yields of ^{123}I as illustrated in Fig. 2, which shows that the reported product yields are scattered in a wide range. A part of the reasons may be attributed to the loss of ^{123}I during irradiation. If the precaution is not sufficient, the product yield will be a function of beam intensity due to loss of iodine during the irradiation.

$^{127}I(p, 5n)^{123}Xe$ reaction. The excitation functions have been reported by four different authors. The functions are shown in Fig. 3, in which the values reported by Syme *et al.* are most elaborated taking into account the various errors included in the measurement. Each author took the precautions for the loss of the target or reaction products during irradiation. One of the reason for differences between these absolute cross sections may be attributed to the value of beam current integration. Paans and Wilkins have measured the beam current directly; Dick and Syme used the monitor reaction such as $^{27}Al(p, 3pn)^{24}Na$ and $^{12}C(p, pn)^{11}C$. It seems that the results of Dick and Syme are comparatively

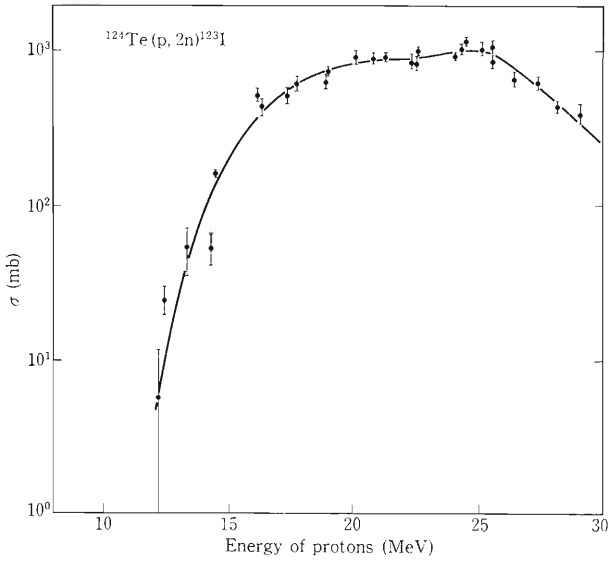

Fig. 1. Excitation function of $^{123}Te(p, 2n)^{123}I$ on 99.87% and 91.86% isotopic enrichment of ^{124}Te (K. Kondo *et al.*: *Int. J. Appl. Radiat. Isot.*, **28**, 395 (1977)).

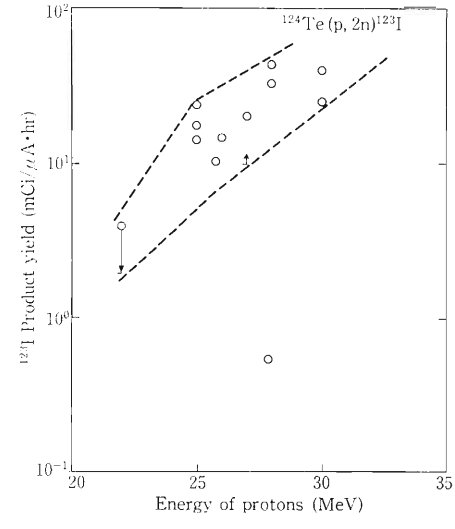

Fig. 2. Practical yields of ^{123}I in the $^{124}Te(p, 2n)^{123}I$ reaction.

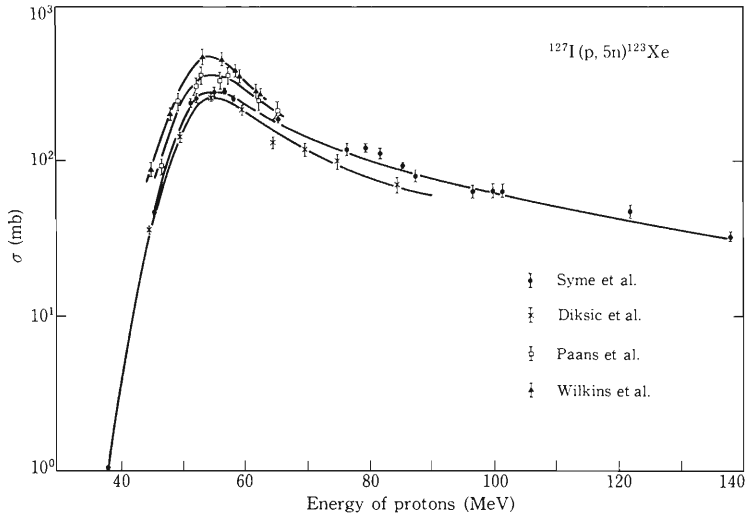

Fig. 3. Comparison of excitation functions of the ^{127}I(p, 5n)^{123}I reaction (Syme *et al.*: *Int. J. Appl. Radiat. Isot.*, **29** (1978); Diksic *et al.*: *J. Inorg. Nucl. Chem.*, **39**, 1299 (1977); Paans *et al.*: *Int. J. Appl. Radiat. Isot.*, **27**, 465 (1976); Wilkins *et al.*: *Int. J. Appl. Radiat. Isot.*, **26**, 279 (1975)).

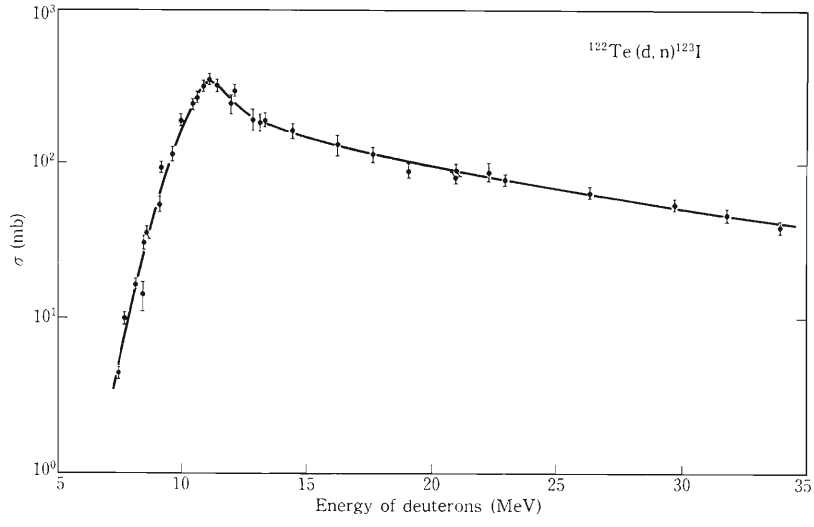

Fig. 4. Excitation function of ^{122}Te(d, n)^{123}I reaction (Zaidi *et al.*: *Int. J. Appl. Radiat. Isot.*, **34**, 1425 (1983)).

good.

Deutron induced reactions. The ^{122}Te(d, n)^{123}Xe and ^{127}Te(d, 6n)^{123}Xe reactions have been reported. Zaidi insisted that the ^{122}Te(d, n) reaction can produce ^{123}I with better purity than that using the ^{124}Te(p, n) reaction. The cross sections are plotted in Fig. 4. There is only one measurement concerning the absolute value for this reaction.

Alpha induced reactions. The ^{121}Sb(α, 2n), ^{123}Sb(α, 4n) and also ^{122}Te(α, 3n)^{123}Xe reactions are the scope of interest. The cross sections for ^{121}Sb(α, 2n)^{123}I have been measured from the interest to compare them with a theory. Absolute cross sections in the energy range from threshold to 27 MeV have been measured and compared with a statistical theory in which the competition of γ-decay was taken into account.

The product yield rate of ^{123}Sb(α, 4n) has been measured in the incident energy range between 50 and 75 MeV.

The ^{122}Te(α, 3n) reaction is a method to produce ^{123}Xe with minimum impurities such as ^{124}I, ^{125}I and others; however its cross section is not found in our survey.

Other reactions. Among other reactions explained above, ^{3}He induced reactions with ^{122,123}Te as targets have a high ^{123}Xe yield compared with alpha particle induced reactions. However there are no reports on the absolute cross sections.

It is known that the spallation reaction induced by high energy protons have relatively

high yield of ^{123}I. The cumulative cross sections for ^{123}Xe decrease slowly with increasing incident proton energy. Typical cumulative cross section values are 40 and 29 mb at 342 and 660 MeV, respectively.

About impurity. The long-lived ^{124}I(4.2 d), ^{125}I(60.2 d) *etc.*increase the absorbed dose of a patient when his thyroid is administrated by ^{123}I. In addition, the tomography is obscured by contaminated gamma-rays. Because of these reasons, the existence of impurity in ^{123}I is the most critical factor to determine the producing reaction. By using 96.2% isotopically enriched ^{124}Te as a target in the (p, 2n) reaction, the impurity of ^{124}I and ^{121}I in ^{123}I were found to be 0.05 and 0.5%, respectively. These values are comparable with those in the ^{122}Te(d, n) reaction using a 95.4% enriched Te target. The impurities caused in ^{123}I by the latter method were reported to be 0.09, 0.04, 0.86, and 0.09% for ^{124}I, ^{126}I, ^{130}I, and ^{131}I, respectively. There is a paper which reports that no impurity was found except 1% of ^{131}I by using the ^{127}I(d, 6n) reaction ; in this case there is no need of using enriched isotope. In conclusion, ^{122}Te(d, n)^{123}Xe and ^{124}Te(p, 2n)^{123}I are most promising reactions providing ^{123}I containing minimum impurity.

RIKEN Accel. Progr. Rep. 19 (1985)

V. ACCELERATOR DEVELOPMENT

1. Present Status of RIKEN Ring Cyclotron Project

H. Kamitsubo

Although the construction of RIKEN Ring Cyclotron is a little behind the schedule, it has reached the final stage. Four sector magnets together with trim coils were assembled in the cyclotron vault in 1984 and their power supplies were also set up in the basement of the cyclotron vault. Injection and extraction elements were fabricated and carried in, too. Vacuum chambers, RF resonators and their power amplifier system are in the works. Two computers and several sets of CAMAC modules were carried in and are in operation to develop the computer programs for control of the cyclotron. The building including experimental rooms, a beam transport area, and rooms for power supplies are under construction and will be completed in May, 1986. Radiation-monitoring and the safety systems of the facilities are also being fabricated in the factory.

Measurements of field distributions as well as excitation characteristics of sector magnets were performed. Even at a fixed excitation current, the field strength of a large scale electromagnet changes very slowly before it reaches the final value. A time constant of this variation is very large and, for the present sector magnets, it takes more than 1 h to settle the field at the final value within an accuracy of 10^{-4}. The current setting procedure of the magnets was investigated to get the final value of the field within a time as short as possible.

Distributions of the base field produced by the sector magnet were measured for the south sector magnet (S-sector magnet) at excitation currents of 300, 520, 640, 710, 800, 940, and 1,050 A. Field perturbations induced by injection elements were investigated at the same excitation currents as mentioned above by setting up each element at the position and measuring the field distributions over four sector magnets.

Field distributions produced by trim coils were measured along the center line of the S-sector magnet at the same values of the main coil currents as above by exciting each trim coil at the maximum current of its power supply and then at two thirds and one third of the maximum current. From these data it was confirmed that isochronous fields can be produced for all the ions in the designed energy region. These measurements were finished in December, 1985.

Two of four magnet chambers, which are vacuum chambers in the pole gaps of the sector magnets, were completed. Cleaning up of the inner surfaces was repeated by spraying neutral detergent (NEOS K), solvent (fluorohydrocarbon), acid (NEOS CM305FP), counteragent (NEOS CM308), and demineralized water. Then air leakage through the welding parts of the chamber was carefully checked. The other two will be completed soon and all of them will be installed one by one in early 1986.

All cryopumps, turbomolecular pumps and other vacuum components have been carried in and ready for assembling. Valley chambers and the RF resonators are in the works and will be completed by the end of March, 1986. Surface cleaning and leakage test are to be done at the factory.

Static RF characteristics such as resonance frequency, Q-value, shunt impedance, and dee voltage distribution are also to be measured for the RF resonators at the factory. Low level amplifiers and power amplifiers have been almost completed at the factory and cold tests were performed to measure the static characteristics of the amplifier system.

Final design of a beam transport lines between the RILAC and RIKEN Ring Cyclotron and between RIKEN Ring Cyclotron and experimental rooms has been finished and ordered to the companies. Several pulse magnets will be installed to realize time sharing of a beam between the linac experimental site and RIKEN Ring Cyclotron and also between two experimental sites in the down stream of RIKEN Ring Cyclotron. Beam pipes, magnet chambers and chambers for beam diagnostic devices will be made of alminum. We expect that an acceleration test

will start at RIKEN Ring Cyclotron in October, 1986.

Design of the experimental facilities which will be built in the experimental halls has been performed in collaboration with universities and other research institutions. The budget for these facilities and the remaining part (phase 3) of the building as well as another injector, an AVF cyclotron, will be allocated in 1987 through 1988. Design study of the AVF cyclotron is also in progress.

RIKEN Accel. Progr. Rep. 19 (1985)

V-2. Present Status of RF Resonator for RIKEN Ring Cyclotron

K. Ogiwara, T. Fujisawa, S. Kohara, Y. Oikawa, and I. Takeshita

The radio-frequency (RF) system of RIKEN Ring Cyclotron ($K=540$) is required to work in a frequency range of 20 to 45 MHz and to generate the maximum acceleration voltage of 250 kV. We developed a new type variable-frequency resonator[1] called a movable box type, to avoid difficulties arising in a usual coaxial resonator equipped with a movable short end; one difficulty is due to a large total height of the resonator and the other is to sliding contactors enduring high current density on the inner conductor.[2] This resonator is a compact half-wave length coaxial type (2.1 m (H)×3.5 m (W)×1.6 m (D))(See Fig.1).

The delta-shaped dee whose radial length is 2.7 m is supported in a median plane by vertical stems from the both sides. The resonant frequency is varied with a pair of boxes surrounding the stems. Both inductance and capacitance of the resonator are varied by moving the boxes so that travelling distances of movable parts and the total height of the resonator can be saved remarkably compared with a usual movable shorting plate type, which varies only inductance. The problem in sliding contactors disappears in the new type resonator because the movable boxes are contact only with outer walls where current density is low. Now, a pair of the resonators are being constructed by Sumitomo Heavy Industries Co., Ltd., and will be installed at RIKEN in 1986.

Figure 1 shows the actual resonator under construction. The vacuum chamber is divided into two compartments by a wall having many holes for evacuation. The main part is the RF resonator, and the other is a space for the fine tuner and coupler positioning mechanism and a vacuum system. The stem, dee, and outer wall are made of copper-clad stainless steel which has many cooling channels engraved on the surface of the stainless steel under the copper overlay. Figure 2 shows the cross sectional view of the clad. A cryo-panel for evacuation is installed inside the stem. The movable box and the fine tuner are constructed with stainless steel frames and copper sheet covers. The movable box is supported by three rods which accomodate the piping for cooling water and pneumatic pressure.

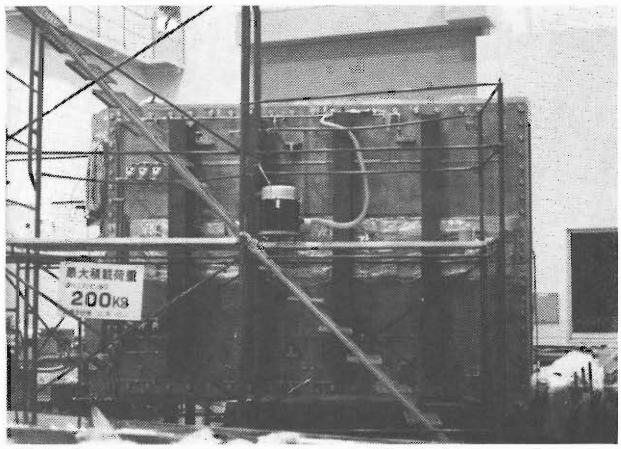

a) Chamber of RF resonator.

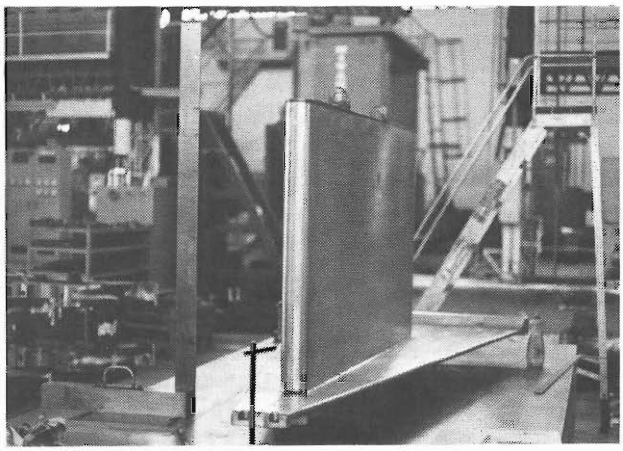

b) Upper half of the dee and stem.

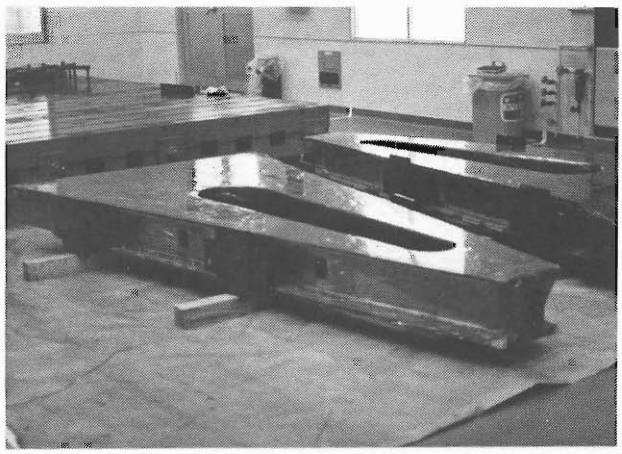

c) Movable boxes.

Fig. 1. Picture of the movable box type resonator.

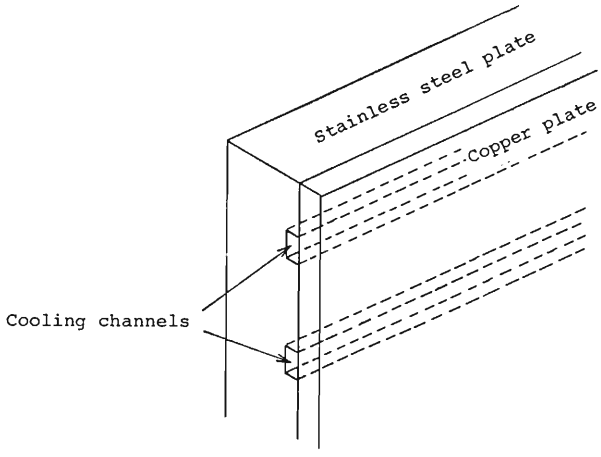

Fig. 2. Cross sectional view of the copper-clad stainless steel having water cooling channel.

Sliding contact fingers made of silver rods are pressed to the outer conductor by pneumatic pressure. The main cryo-pump and turbo-molecular pump are mounted on the outer wall of the compartment for the mechanism. All the systems are installed on a platform car and can be moved about 2 m from the valley space between the magnets leaving the side walls to make the resonator accessible for maintenance.

References

1) T. Fujisawa, K. Ogiwara, S. Tohara, Y. Oikawa, I. Yokoyama, I. Takeshita, Y. Chiba, and Y. Kumata: *Sci. Papers I.P.C.R.*, **79**, 12 (1985); K. Ogiwara, T. Fujisawa, Y. Oikawa, and S. Kohara: *RIKEN Accel. Progr. Rep.*, **18**, 172 (1984).
2) K. Ogiwara, M. Hara, and T. Fujisawa: *Rep. I.P.C.R.*, **57**, 222 (1981).

RIKEN Accel. Progr. Rep. 19 (1985)

V-3. Present Status of RF Power Amplifier for RIKEN Ring Cyclotron

T. Fujisawa, S. Kohara, K. Ogiwara, I. Yokoyama,
M. Nagase, and Y. Chiba

The basic parameters of the RF system of RIKEN Ring Cyclotron ($K=540$) are summarized in Table 1. The design of the RF system[1] has been completed and main parts of the amplifier system are being constructed at a factory. All of the system are to be installed at RIKEN in the middle of 1986.

Figure 1 shows a block diagram of the amplifier system. An RF reference signal is fed from the injectors in normal operation and a local synthesized signal generator is prepared for maintenance. The signal is split and fed to two amplifier systems and a beam buncher system. The amplitude and phase of the signal are adjusted by the amplitude and phase modulators, respectively. The signal is modulated by the pulse modulator until multipactorings in the resonator are broken through. The RF power is amplified by the three stages amplifier system and is fed into the resonator through a 50 Ω coaxial feeder line (~1.8 m length) which is coupled with the resonator in good impedance matching by means of a variable capacitive coupler. The pre-amplifier is of a wide-band solid-state type. The driver and the final amplifiers are of tuned tetrode amplifiers. The input circuit of the driver is a pair of all-pass networks.[1),2)] Tuning and impedance matching for the resonator are carried out automatically by detecting the incident and reflected wave on the feeder line. Acceleration voltage and phase of each resonator are also adjusted automatically by comparing the signals picked up from the resonator with the reference signals. Setting and logging of all parameters are performed with the computer control system.

Table 1. Basic parameters of the RF system.

Number of resonators	2
RF frequency	20~45 MHz
Harmonic number	5, 9, 10, 11
RF peak voltage	250 kV
Frequency stability	10^{-8}
Voltage stability	10^{-4}
Phase stability	$<1^{\circ}$
Mean injection radius	89.3 cm
Mean extraction radius	356 cm
Dee angle	23.5°
Output power of each RF amplifier	300 kW

Figure 2 shows a photograph of the final amplifier under construction. The power tube, RS2042SK, is used as grounded grid configuration.[1] The plate tuning element is an adjustable $\lambda/4$ coaxial stub whose stroke is 1.2 m. The center conductor of the stub is a copper pipe of 18

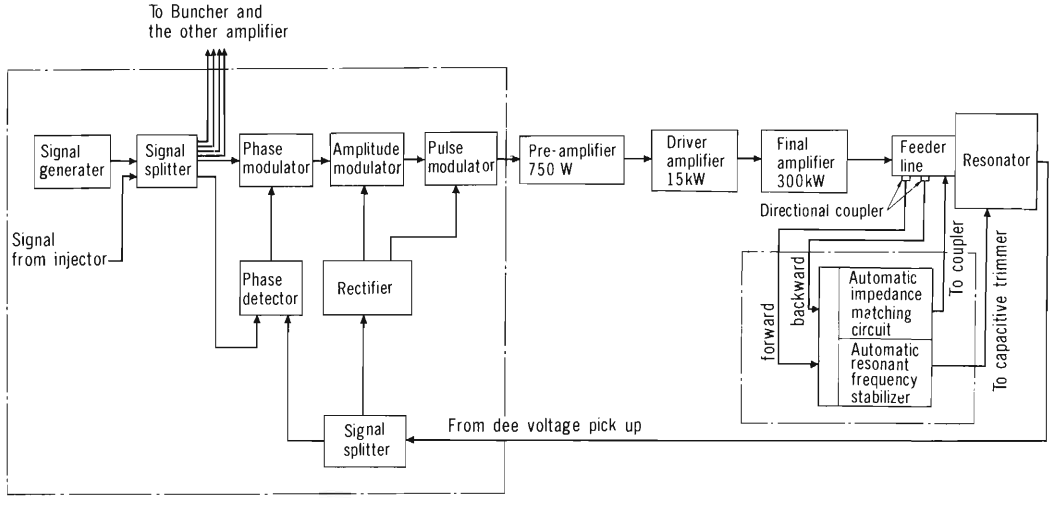

Fig. 1. Block diagram of the amplifier system.

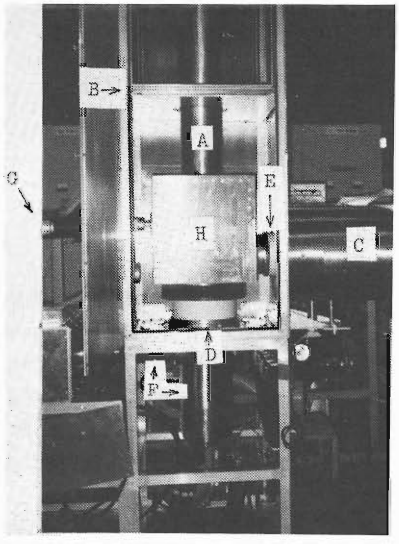

Fig. 2. Photograph of the final amplifiers. A: Inner conductor of the plate stub, B: Movable shorting plate of the plate stub, C: Feeder line, D: RS2042SK tetrode, E: Impedance matching capacitor, F: Cathode tuning circuit, G: 50 kW dummy load. H: Box surrounding the plate blocking capacitor. The screen and control grid bypass capacitors are mounted on the base plate below the tetrode. The driver amplifier is in the aluminum box at lower left side.

cm in diameter in which cooling water pipes and a DC power line for the tube pass through. The plate DC blocker is a cylindrical capacitor (2,350 pF) whose insulator is made of Kapton film (125 μm$\times$16 turns). The screen (0.09 μF) and control grid (0.115 μF) bypass capacitors are parallel plate disc capacitors, whose insulators are made of 50 μm copper-clad Kapton films. A vacuum variable capacitor for load resistance matching is mounted on the output port of the amplifier. The cathode circuit consists of a variable tuning capacitor (20 to 600 pF) and a fixed $\lambda/4$ coaxial stub, through which the filament current is supplied from a power source at ground potential.

Two plate power supplies, which are located in a building about 100 m far from the cyclotron vault, are provided for the two final tubes, respectively. The output voltage can be set at 10, 12, and 14 kV by changing the taps on the primary windings of the transformer and the maximum current is 40 A. The voltage ripple at the rated load is better than 2% in peak to peak. The voltage ratio of the full load to the non-load is better than 95%. The power supply is protected by an over current relay, an overvoltage relay, and an undervoltage relay at the DC side, and by an over current relay, a ground relay, and a phase unbalance relay at the AC side. The rube is protected by an ignitron crowber circuit. Within 30 ms after the ignitron is fired, the primary 6.6 kV line is opened by a vacuum circuit breaker to protect the power supply.

References

1) T. Fujisawa, K. Ogiwara, S. Kohara, Y. Oikawa, I. Yokoyama, I. Takeshita, Y. Chiba, and Y. Kumata: *Sci. Papers I.P.C.R.*, **79**, 12 (1985); K. Ogiwara, K. Fujisawa, Y. Oikawa, and S. Kohara: *RIKEN Accel. Progr. Rep.*, **18**, 172 (1984); T. Fujisawa, K. Ogiwara, S. Kohara, and Y. Kumata: *RIKEN Accel. Progr. Rep.*, **18**, 174 (1984).
2) S. W. Mosko, J. D. Raylander, and G. K. Schulze: *IEEE Trans. Nucl. Sci.*, **NS-24**, No.3, June, 1786 (1977).

RIKEN Accel. Progr. Rep. 19 (1985)

V-4. Progress in Sector Magnets for RIKEN Ring Cyclotron

S. Motonaga

Final measurement of the magnetic field of the sector magnets was finished in December, 1985.[1] Detailed analysis of the field data is now in progress. Installation of acceleration vacuum chambers in the magnet part will start in January, 1986.

1) Power supplies

Description of the power supplies for main and trim coils has been presented elsewhere.[2] Tests of all power supplies were carried out during a period from August, 1984, to February, 1985, to obtain strict current stability. Current stabilities of 2×10^{-6} and 1×10^{-5} for 8 h were achieved for the main coil and trim coil power supplies, respectively.[3] Their power efficiencies are listed in Table 1.

The power supplies are controlled by a computer through CAMAC modules. All power supplies were operated by a computer control system throughout the magnetic field measurement performed during a period of February to December, 1985. Overall performance of the system was very well.

2) Field measurement

Field measurement was started in February, 1985.

At first, the optimum procedures were investigated to ensure fast setting and good reproducibility of the magnetic field and the best procedure of the field setting was established. Reproducibility of the field was obtained to be better than 5×10^{-4} and required time to obtain a

Table 1. Current specification, electric power, and power efficiency for various types of main coil and trim-coil power supplies. All power supplies having a total of 67 output terminals are housed in 11 cubicles. Total input power of the power supplies is 1,183kW. Total required power is estimated to be about 1,329 kW, if the power factor of the power supplies is assumed to 0.89. Power efficiencies of almost all the trim coil power supplies are poor because of their high current and low voltage.

Type	Input power (kW)	Output power (kW)	Current (A)	Voltage (V)	Number of output terminals	Power efficiency (Output power / Input power)
Main coil						
M1	414	355	1,050	352	1	0.86
M2	182	133	1,050	126	5	0.73
Trim coil						
TA1245	94	50	330, 410 520, 550	16, 19 35, 34	4	0.53
TA3	37	26	490	53	1	0.70
TB12	27	6.5	410, 220	12, 7	10	0.24
TB3	55	33	530	62	9	0.6
TB45	56	30	540, 580	34.5 19	10	0.54
TC12	33	10	450, 500 500	9, 4.8 5.2	3	0.30
*TD12	109	22	245, 390	5, 45.5	12	0.20
*TD3-1	80	21	540	6, 6.2 6.6, 6.5 6.5, 6.5	6	0.26
*TD3-2	96	22	545	6.2, 6.3 6.8, 6.7 6.6, 6.7	6	0.23

* Polarity of these power supplise can be changed.

stable field was about 3 h.[3]

For a period of April-July, 1985, measurement of base field distributions and a field of each trim coil was performed for one sector magnet to estimate trim coil currents necessary for forming an isochronous field. The measurement was carried out for seven field levels of 6, 10, 12, 13, 14, 15, and 15.5 kG.

From September to December, after installation of the magnetic elements for injection and extraction, the magnetic fields inside them were measured for three base fields of 10, 14, and 15.5 kG. Each element was excited at its level corresponding to the base field.[4] In this period a field effect caused by the magnetic elements was measured. It was found that this effect can be compensated by adjusting of the trim coil currents of four sector magnets.

A final subject of the measurement was the formation of isochronous field for selected ions by use of the above field data. Calculation of optimum trim coil currents was performed for 210 MeV proton, 70 MeV/u C^{6+}, 28 MeV/u Ar^{13+}, and 22 MeV/u Xe^{14+}. From this calculation, it was found that the maximum powers of the trim coils power supplies are lower than those required for the formation of the isochronous field in the nose region, then it was decided that iron shims should be placed in the nose region of the sector magnets. Magnetic fields produced with the help of these iron shims will be remeasured after installation of the vacuum chambers for the sector magnet parts.

References

1) A. Goto, H. Takebe, S. Motonaga, K. Hatanaka, Y. Yano, T. Wada, N. Nakanishi, and M. Hara: p. 178 in this report.
2) H. Takebe, S. Motonaga, T. Wada, I. Takeshita, and H. Kamitsubo: Proc. 5th Symp. on Accelerator Science and Technology, KEK, p. 197 (1984); S. Motonaga, H. Takebe, T. Wada, A. Goto, I. Takeshita, J. Fujita, H. Kamitsubo, J. Abe, H. Saito, and T. Mita: *RIKEN Accel. Progr. Rep.*, **18**, 170 (1984).
3) H. Takebe, S. Motonaga, and T. Wada : p. 174 in this report.
4) Y. Yano, A. Goto, K. Hatanaka, H. Takebe, and S. Motonaga: p. 180 in this report.

RIKEN Accel. Progr. Rep. 19 (1985)

V-5. Power Supply of the Sector Magnets

H. Takebe, S. Motonaga, and T. Wada

The sector magnets of RIKEN Ring Cyclotron were assembled in the cyclotron vault in April, 1984, and the power supplies (PS's) for main and trim coils were brought in July. The maximum currents of the PS's and the connecting coils are listed in Table 1. From July to December, PS's were finally adjusted and the stability, ripple, and so on were examined. Table 2 lists the achieved stability of the PS's of the main and trim coils. The stabilities and ripples are sufficiently smaller than the guaranteed values.

From January to December in 1985, the PS's were operated to measure the characteristics and field distributions of the sector magnets. During this period, total operating time was about 3,400 h, and only one transistor was broken, tens of fuses and tens of lamps (tungsten type) were cut down (the total number of the transistors is about 7,000 and oven control and interfaces circuits were being turned on for about 8,000 h).

The power supplies of the main and trim coils are controlled by a control computer: a Mitsu-

Table 2. Current stability of the power supply.

Name	Guarantee (×10E-4 /8 h)	Measured (×10E-4 /8 h)	Measured (×10E-4 /24 h)
M1	0.1	0.075 (1,050A) 0.02 (300A)	0.1 (1,050A)
M2	0.1	0.05 (1,050A) 0.02 (500A)	0.07 (1,050A)
M2, 1-4	3.8	0.1	Following values are in a maximum current.
TA1245	1.0	0.1	
TA3	1.0	0.1	
TB12	1.0	0.15-0.2	
TB12, 1-8	2.0	0.2-0.3	
TB3	1.0	0.1	
TB3, 1-8	2.0	0.1-0.15	
TB45	1.0	0.2-0.15	
TB45, 1-8	2.0	0.1-0.2	
TC12	1.0	0.1-0.35	
TD12	1.0	0.1-0.15	
TD3-1	1.0	0.1-0.25	
TD3-2	1.0	0.1-0.25	

Table 1. Maximum current and connecting coils.

Name	Current	Coil#	Name	Current	Coil#	Name	Current	Coil#
M1	1059.0A	Main 1	-2	50.5A	W18-19	-3	404.0A	E#6
M2-0	1065.0A	Main 2	-3	50.5A	N10-11	-4	404.0A	N#28
-1	−101.0A	W-sector	-4	50.5A	N18-19	-5	404.0A	W#26
-2	−101.0A	N-sector	-5	50.5A	E10-11	-6	404.0A	W#27
-3	−101.0A	E-sector	-6	50.5A	E18-19	-7	404.0A	W#6
-4	−101.0A	S-sector	-7	50.5A	S10-11	-8	404.0A	N#6
TA1245			-8	50.5A	S18-19	-9	404.0A	E#28
-1	333.3A	#8	TB45-0	554.9A	#14-15	-10	404.0A	S#26
-2	414.0A	#9	-1	40.4A	W	-11	404.0A	S#27
-3	535.0A	#12-13	-2	40.4A	N	-12	404.0A	S#6
-4	565.8A	#23-24	-3	40.4A	E	TD3-1		
TA3	493.6A	#16-17, #20-21	-4	40.4A	S	-1	555.5A	W#4
TB12-0	232.3A	#7	TB45-1	596.4A	#22	-2	555.5A	W#5
-1	55.5A	W	-1	50.5A	W	-3	555.5A	N#26
-2	55.5A	N	-2	50.5A	N	-4	555.5A	N#27
-3	55.5A	E	-3	50.5A	E	-5	555.5A	N#4
-4	55.5A	S	-4	50.5A	S	-6	555.5A	N#5
TB12-1	424.2A	#25	TC12			TD3-2		
-1	50.5A	W	-1	455.1A	#3-N-E	-1	555.5A	S#4
-2	50.5A	N	-2	505.4A	#3-W	-2	555.5A	S#5
-3	50.5A	E	-3	505.3A	#3-S	-3	555.5A	E#26
-4	50.5A	S	TD12			-4	555.5A	E#27
TB3	535.4A	#10-11, #18-19	-1	252.5A	W#28	-5	555.5A	E#4
-1	50.5A	W10-11	-2	252.5A	S#28	-6	555.5A	E#5

Table 3 (a). Pin assignment of the output port from the DIM.

Pin #	Port DO /DT	Data #	Contents	hi=0 (Open)	low=1 (Close)
1		GND			
2		GND			
3	DO-0	0	DAC data (LSB)	0	1
4	DO-0	1	DAC data	0	1
5	DO-0	2	DAC data	0	1
6	DO-0	3	DAC data	0	1
7	DO-0	4	DAC data	0	1
8	DO-0	5	DAC data	0	1
9	DO-0	6	DAC data	0	1
10	DO-0	7	DAC data	0	1
11		GND			
12		GND			
13	DO-1	0	DAC data	0	1
14	DO-1	1	DAC data	0	1
15	DO-1	2	DAC data	0	1
16	DO-1	3	DAC data	0	1
17	DO-1	4	DAC data	0	1
18	DO-1	5	DAC data	0	1
19	DO-1	6	DAC data	0	1
20	DO-1	7	DAC data (MSB)	0	1
21		GND			
22		GND			
23	DO-2	0	Address 0	0	1
24	DO-2	1	Address 1	0	1
25	DO-2	2	Address 2	0	1
26	DO-2	3	Address 3	0	1
27	—	5	NC		
28	—	4	NC		
29	—	6	Polarity+	0	1
30	—	7	Polarity−	0	1
31		GND			
32		GND			
33	DO-3	0	Strobe	0	
34	—	1	On command	0	1
35	—	2	OFF/reset	0	1
36	—	3	NC		
37		4	NC		
38		5	NC		
39		6	NC		
40		7	NC		
41		GND			
42		GND			
43		GND			
44		GND			
45~50					

Table 3 (b). Pin assignment of the input port to the DIM.

Pin #	Port DO /DI	Data #	Contents	hi=0 (Open)	low=1 (Close)	
1		GND				
2		GND				
3	DI-0	0	Water flow	Ok	Not	
4	—	1	Water temp.	Ok	Over	
5	—	2	Door	Ok	Not	
6	—	3	Mag inter lock	Ok	Not	
7	—	4	Off fault	Ok	Fault	
8	—	5	Over curr	Ok	Over	
9	—	6	Fuse	Ok	Cut	
10	—	7	Transister	Ok	Break down	
11		GND				
12		GND				
13	DI-1	0	Local/remote	Remotes	Local	
14	—	1	Oven	On	Off	
15	—	2	Main CB	On	Off	
16	—	3	Off/ready	Ready	Not off ready	
17	—	4	NC			
18	—	5	NC			
19	—	6	NC			
20	—	7	NC			
21		GND				
22		GND				M1: Sun coller status
23	DI-2	0	Polarity 1	—	+	Polarity
24	—	1	Polarity 2	—	+	Water level Ok
25	—	2	Polarity 3	—	+	Temp Ok
26	—	3	Polarity 4	—	+	Cool Water Ok
27	—	4	Polarity 5	—	+	Pump Ok
28	—	5	Polarity 6	—	+	Cool Pump Ok
29	—	6	Polarity 7	—	+	Heater On
30	—	7	Polarity 8	—	+	Chiller On
31		GND				
32		GND				
33	DI-3	0	Polarity 9	—	+	
34	—	1	Polarity 10	—	+	
35	—	2	Polarity 11	—	+	
36	—	3	Polarity 12	—	+	
37	—	4	NC			
38	—	5	NC			
39	—	6	NC			
40	—	7	NC			
41		GND				
42		GND				
43		GND				
44		GND				
45~50						

bishi 32 bit minicomputer, M350/60-500 (M60), through a CAMAC interface and CIM-DIM modules.[1)]

Table 3 shows the pin assignment of a connector between the DIM input/output ports and the PS. These lines are isolated by using photocouplers of 12V negative logic.[2)] The output signals to the PS from the DIM port consist of 16 bit currrent data, 4 bit DAC adress data, 2 bit polarity data, 1 bit strobe signal, 1 bit ON command, and 1 bit OFF command. The DIM input signals consist of 12 bit interlock and status signals, and 12 bit (max.) polarity data from the PS.

Table 4, shows the structure of the programs for the PS control sequence. At the 1st level, 2 byte read/write routines (CIM-DIM handler: DIMI, DIMO) for the DIM input/output port were developed by using CAMAC handlers supplied from Mitsubisi Electronic Company. At the 2nd stage, PS control subroutines, for example, PS on, PS off, polarity change, current set, current step set, and status read, are developed.

A flow chart of this current step set program is shown in Fig. 1. When the PS name, the DAC number, and objective current data are given

from the main program as arguments, this routine obtains a conversion factor for 16 bits DAC data, the current step, and the other parameters from the main memory (Global Common Area) of the data-base table. After checking the PS status and the last current (from the memory and the ADC current monitor of the DIM), the current is changed with a certain step (2A-3A) to the aimed current. In each 10 steps, actual current, obtained by the ADC current monitor of the DIM, is compared with each set current. If the difference between them exceeds a given value, this program displays an error message and stop this current set sequence. Actual speed of this current step set is about 10 steps/s.

This current step set routine is written in FORTRAN language of the M60 computer at this time. At the next time, multiple task of the current step set is needed for a fast setting and for bypass control type PS's (M2, TB12, TB3, and TB45), then a micro program of the DIM will be developed.

Table 4. Sector magnets control programs.

Structure	Programs
User application program	AUTOTM, MAP, SCLTRM, PSVIPO
PS-Controle program	PS-ON, CYCLA, PS-END, PS-SVY
PS-Interface subroutines	PS-ON, PS-OFF, STATUS, CURRENT-SET, POLARITY-CHENGE, ADC-READ, STROBE, CURRENT-STEP-SET
CIM, DIM handler subroutines	CIMINT, DIMINT, DIMO, DIMI, DIMTST
CAMAC handler subroutines	CFSA, CDREG
CIM micro programs	
DIM micro programs	

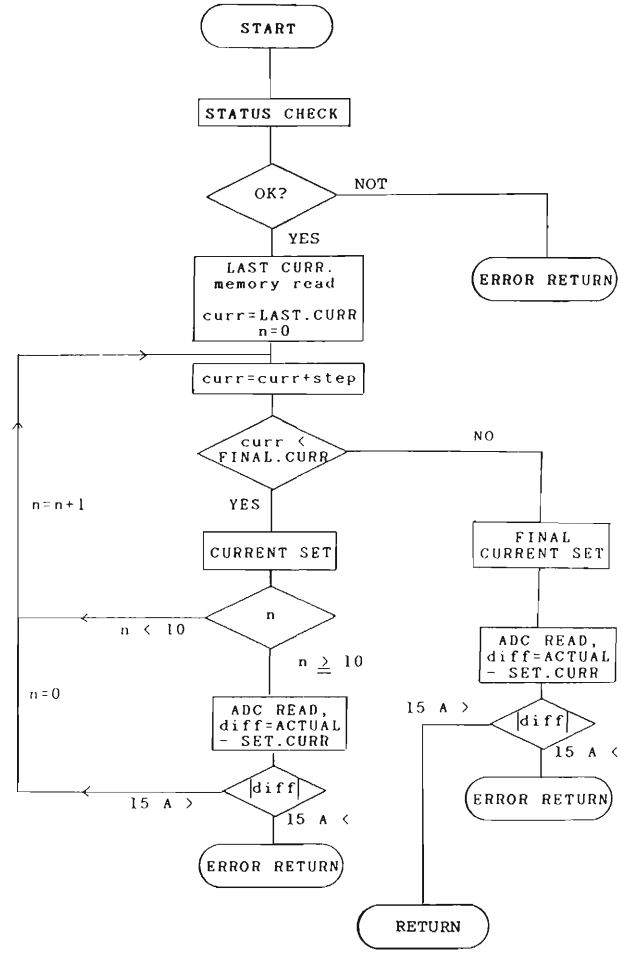

Fig. 1. Flow chart of the current step set program.

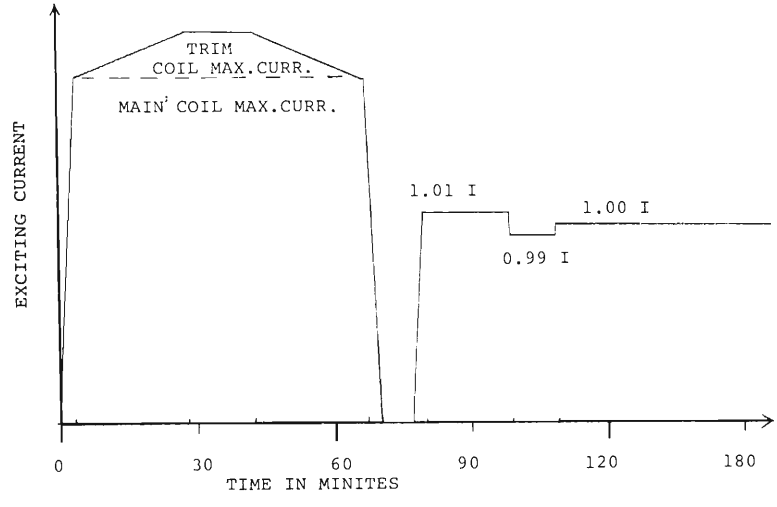

Fig. 2. Time chart of the excitation for the sector magnets main coil and trim coils (CYCLING).

In magnetic field measurements of the sector magnets, following excitation method (CYCLING) was taken (see Fig. 2) in order to obtain a good reproducibility of the field distribution and to get a fast stability.

1. All PS's are operated at maximum current.
2. Wait 20 min.
3. All PS's are turn off.
4. Wait 7 min.
5. Current×1.01 of main coil is excited.
6. Wait 20 min.
7. Current×0.99 of main coil is excited.
8. Wait 10 min.
9. Current×1.00 of main coil is excited.
10. Wait 50 min.

Total setup time of the sector magnet excitation is about 2.5 h. For a lower magnetic field (< 13 kG) this setting method is very important.

References

1) T. Wada, J. Fujita, K. Shimizu, I. Yokoyama, T. Kambara, and H. Kamitsubo: *RIKEN Accel. Progr. Rep.*, **18**, 185 (1984).
2) H. Takebe, S. Motonaga, T. Wada, I. Takeshita, and H. Kamitsubo: Proc. 5th Symp. Accelerator And Technology, p. 197 (1984); S. Motonaga, H. Takebe, T. Wada, A. Goto, I. Takeshita, J. Fujita, H. Kamitsubo, J. Abe, H. Saito, and T. Mita: *RIKEN Accel. Progr. Rep.*, **18**, 170 (1984).

RIKEN Accel. Progr. Rep. 19 (1985)

V-6. Magnetic Field Measurement for RIKEN Ring Cyclotron

A. Goto, H. Takebe, S. Motonaga, K. Hatanaka,
Y. Yano, T. Wada, N. Nakanishi, and M. Hara

Measurement of the magnetic field of the sector magnet was performed during the past year from January to December. The measuring system was almost the same as one that had been used in a preliminary measurement performed at the factory three years ago,[1] except for the following: the guide rail for the Hall assembly was extended to make it possible to measure the field over the whole range of 360°, a DEC LSI-11 micro computer was replaced by a super minicomputer (M60: M350-60/500) for control of the measuring system, and all the power supplies were controlled by the computer through the CAMAC modules named CIM and DIM. Working conditions of the system were very well throughout the measurement.

At first, the field setting procedure was studied to obtain reproducible and fast stabilizing field distribution. Various modes of setting procedures were examined and it was found that the best procedure is first to excite the magnet by use of all the main and trim coil power supplies up to the maximum field level and then to deexcite it before reaching the final level. The former process is essential to obtain reproducible distribution and the latter is necessary to stabilize the distribution as quickly as possible. Reproducibility of the field distribution was found to be better than 5×10^{-4}. Consuming time to reach a stable field level was about 1.5 h for higher excitations and 3 h for the lowest.

Trim coil fields were measured along the sector center line at an interval of 10 mm for seven levels of main coil currents (300, 520, 640, 710, 800, 940, and 1,050 A). These main coil currents correspond to the base fields of 6, 10, 12, 13, 14, 15, and 15.5 kG, respectively. The measurement was performed only for one sector magnet (S-sector magnet). Three levels of currents were chosen for each trim coil to obtain a non-linearity of the effectiveness of the trim coil field. For the first cycle, every coil was excited coil by coil by one-third of the maximum current of its power supply and the field distribution was measured at each step. In the same way, for the second cycle two-thirds of its maximum current was fed to each coil and, for the last cycle, its maximum current. It is noted that the current once fed to a coil never be switched off again throughout the above procedure. This is because we found, in a preliminary measurement, that the data taken in such a way that the current was switched off after each step of measurement gave a poor prediction for an isochronous field distribution. The measurement at each step was started 10 to 15 min after excitation of a trim coil. In the course of these measurements, differences in field distribution among four sector magnets were measured in two cases in which trim coils were not excited at all (base field) and they were kept at the maximum excitation. The maximum of these differences was 60 G for both cases.

To estimate the required isochronous field distribution along the sector center line, we have used the method of GANIL,[2] in which equilibrium orbits are calculated and the ratios between the average radius and average field strength along the orbits and those at the sector center line (K_b and K_r values) are deduced. Map data of the field distribution are then indispensable for that purpose. Measurement of the field map was carried out under two situations. One is the situation in which no injection and extraction elements are present around the sector magnets (unperturbed field) and the other the situation in which they* are present (perturbed field) . Unperturbed fields were measured for the S-sector magnet only at the same field strengths as those for the trim field measurement. The azimuthal range of the map was 90°(from valley to valley) with intervals of 0.25°, 0.5°, 1°, and 2° according to the sharpness of the azimuthal distribution. The radial interval was 20 mm over the whole region. The number of the mesh points was 15,765. It took about 4.5 h for each measure-

* In this case no extraction elements were set because otherwise the map data could not be taken owing to their disturbances to the measuring apparatus. However, it can be said that there is no problem because perturbations caused by these elements were found to be small from another measurement.

ment. Not only the base field distribution but also the field distributions when the trim coils were excited were measured for each main coil current. The latter measurement is necessary because in our case the field rise of an isochronous field is rather high for some kinds of ions and, therefore, the azimuthal distribution is expected to change. Every trim coil was excited at a half maximum and the maximum of its power supply. Thus a total of 21 map data were taken for unperturbed field distributions. Perturbed fields were measured for four sector magnets. The radial interval was taken to be 35 mm in order to reduce the measuring time. The time taken for each measurement was 2.5 h. Each injection element was excited corresponding to the main coil current during the measurement, but the trim coils were not excited at all.

By use of the above data, an isochronous field distribution along the center line of each sector magnet can be calculated and currents of the main and trim coils necessary to produce it can be obtained. The procedure to obtain K_b and K_r values for each sector magnet for perturbed fields is as follows: at first, equilibrium orbits in the unperturbed field are calculated. Then, average field strengths along these orbits are calculated for perturbed fields. K_b values for perturbed fields are thus obtained. (K_r values are the same as those for unperturbed fields.) These K_b and K_r values are calculated for each sector magnet for a number of combinations: seven cases of main coil currents of 300, 520, 640, 710, 800, 940, and 1,050A times three cases of all the trim coil currents with zero, their half maximum, and maximum. Main and trim coil currents required to achieve an isochronous field are obtained using this data base. In order to check the validity of the above method, the field distributions calculated by using this method for the argon ion (28 MHz), which is expected to be the first ion accelerated, were realized and measured for four sector magnets. It was confirmed from the computer simulation that the ion can be accelerated in this field very well and the method is reliable.

From a series of measurements mentioned above, we found that the powers of the trim coil power supplies for the injection region are not enough. The currents required for these power supplies were found to exceed their maximum currents designed. Therefore, it was decided that iron shims be placed beneath the trim coils. Their thicknesses are 1, 0.5, and 0.2 mm for the regions covered by trim coils No. 1-3, No. 4, and about half of the coil No. 5, respectively.

Effects of the stainless steel membranes of vacuum chambers could not be measured at this time. As of January 1986, installation of the vaccum chambers is being carried out, and so after that these effects as well as the effects of iron shims will be measured using another measuring apparatus. We believe that, except for these terms, the data obtained during the past year's measurement form an almost complete set of data to produce isochronous field distributions.

References

1) H. Takebe, I. Takeshita, J. Fujita, T. Wada, I. Yokoyama, N. Nakanishi, S. Motonaga, and T. Sato: *Sci. Papers I.P.C.R.*, **77**, 20 (1983).
2) M. Barre, D. Bibet, A. Chabert, A. Dael, C. Eveillard, P. Lapostolle, J.F. Libin, M. Ohayon, and J. Sauret: 9th Int. Conf. on Cyclotrons and their Applications, p. 371 (1981).

RIKEN Accel. Progr. Rep. 19 (1985)

V-7. Beam Injection and Extraction System of RIKEN Ring Cyclotron

Y. Yano, A. Goto, K. Hatanaka, H. Takebe, and S. Motonaga

RIKEN Ring Cyclotron has two types of injectors: the RILAC and the K65 AVF cyclotron. A beam accelerated by one of these injectors is led to RIKEN Ring Cyclotron through an injection beam transport line, which is positioned 4 m above the median plane of RIKEN Ring Cyclotron. In the north-west valley of this Cyclotron, a beam is levelled down to the median plane at a slope of 45 degrees by a "canted injection system." It consists of a couple of 45 degree bending magnets, a couple of quadrupole doublets and a quadrupole singlet. These quadrupole magnets and the drift spaces between them are screened from the leakage magnetic flux from the sector magnets. This system makes achromatic beam transport in vertical direction possible.

Figure 1 shows a layout of the beam injection and extraction system and Table 1 lists its characteristics. In the central region of the Cyclotron, a beam is put onto the median plane by BM2, one of the vertical bending magnets mentioned above, and is led radially to the first acceleration orbit by following elements: a bending magnet, BM1, a couple of magnetic inflection channels, MIC2 and MIC1, and an electrostatic inflection channel, EIC.

The beam accelerated up to the outermost radius is peeled off by an electrostatic deflection channel, EDC, and is extracted out of the Cyclotron through a couple of magnetic deflection channels, MDC1 and MDC2. A couple of bending magnets, EBM1 and EBM2, lead the extracted beam to the beam handling system.

The above four bending magnets are of a modified window frame type. They are placed in the atmosphere and fixed in position. On the beam-entrance side of BM2, a magnetic field clump is mounted which has a symmetric shape with respect to the median plane of the Cyclotron. This field clump absorbs the leakage mag-

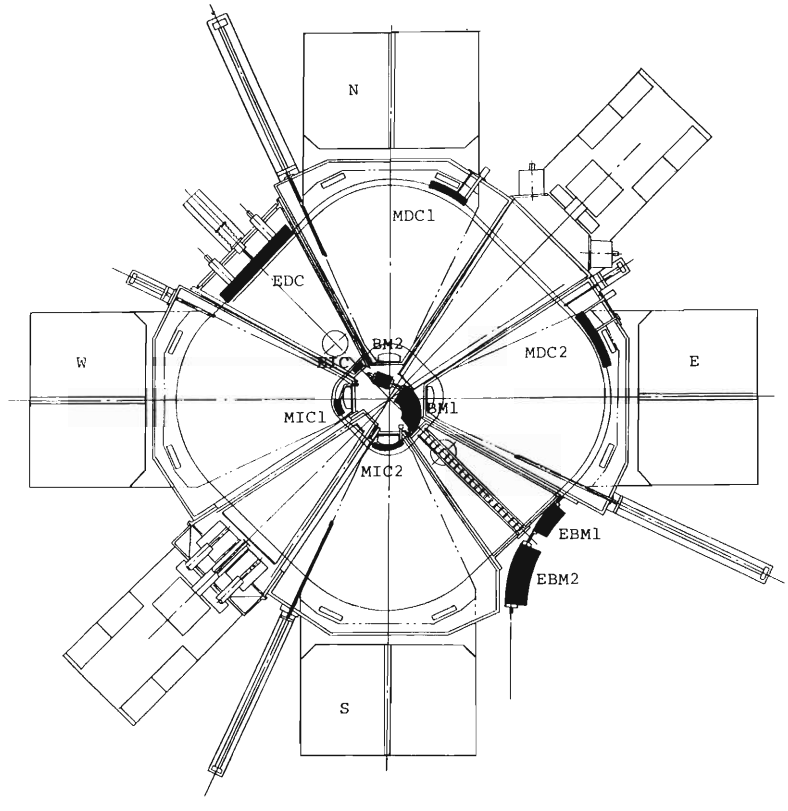

Fig. 1. Layout of the beam injection and extraction system.

Table 1. Characteristics of the beam injection and extraction system.

Element	Radius of curvature	Bend angle	Maximum field	Gap width	Entrance/exit face angle
BM2	46.0 cm	45.0 deg.	1.66 T	42.0 mm	45.0/0.0 deg.
BM1	45.7	102.75	1.67	42.0	15.0/−13.5
MIC2	41.5	78.69	1.87		
MIC1	49.8	39.7	1.59		
EIC	364.5	3.62	50.0k V/cm	18.0	
EDC	straight	1.08	50.0	18.0	
MDC1	212.6	17.79	1.62 T		
MDC2	229.9	24.66	1.51		
EBM1	229.5	15.0	1.51	42.0	
EBM2	215.0	30.2	1.61	42.0	15.0/15.0

netic flux from BM2, which is harmful to the accelerated beam because it sweeps out the beam vertically. Eight turns of twenty-four turn coils of BM1 are divided into two portions: a beam entrance and an exit sides. Different magnetic field strengths can be set in each portion with two power supplies. This enables BM1 to have a function of steering the beam radially both in its position and direction.

The magnetic channels are inserted between pole gaps of the sector magnets and also fixed in position. MIC1 and MIC2 consist of floating iron shims and coils, while MDC1 and MDC2 consist of coils only. The configurations of the iron shims and coils or the coils were designed so that uniform magnetic fields of a sextupole component better than $1\times10^{-3}/cm^2$ can be produced inside the channels. Every magnetic channel except MIC2 is equipped with the other coils wound by the side of the above coils. Such coils are called "compensation coils" and are used to reduce the magnetic field perturbations brought about by the magnetic channels in the sector fields outside them. These compensation coils and the coils for adjusting the beam trajectory are connected in series. MIC2 has no compensation coils because of the lack of space. The iron shims and coils are mounted on a stainless-steel frame; these are contained with a vacuum tight case of 3 mm thick stainless steel plates. The beam passage is provided by a stainless-steel pipe of 24 mmϕ in aperture. The inside of this vacuum-tight case is filled with epoxy resin.

The electrostatic channels are of a conventional type. Their radial positions at beam entrance and exit can be remotely adjusted by ± 10 mm each. The maximum DC voltage of 100 kV is applied to the 18 mm wide gap between the anode and the cathode.

From September to December, 1985, we carried out comprehensive magnetic field measurements, installing the beam injection and extraction elements except the electrostatic channels and the magnetic shield for the canted injection line at each due position. The magnetic field maps inside the elements as well as those in the sector magnets were measured at seven sector field levels from 7 kG up to 15.5 kG. The magnetic field distributions inside the elements were obtained nearly as expected. On the basis of these data, small modifications will be made for each element to improve the distributions. The magnetic field perturbations in the sector magnets could be corrected by the trim coils. The detailed analysis of the data is under way.

RIKEN Accel. Progr. Rep. 19 (1985)

V-8. Beam Transfer Line from RILAC to RIKEN Ring Cyclotron

K. Hatanaka, T. Inamura, Y. Yano, A. Goto,
M. Kase, K. Ozawa,* and H. Kamitsubo

The desigh of the beam transfer line from the heavy-ion linac (RILAC) to RIKEN Ring Cyclotron was completed in 1984 and the elements of the line are now under construction.

The system consists of 8 dipole magnets, 14 quadrupole doublets, 13 quadrupole singlets, and many kinds of beam diagnostic devices. Parameters for the dipole magnets are summarized in Table 1. The end profiles and the cross sectional shapes of the pole of the dipole magnets were determined from the numerical calculation of a magnetic field with the computer program TRIM.[1] The pole of the quadrupole magnet is 170 mm long and the diameter of the inscribed circle of the pole is 70 mm. The quadrupole magnet has complete four-fold symmetry in order to eliminate the octupole component in the magnetic field. The pole width is 70 mm, possessing a hyperbolic shape. In order to obtain the wide flat region of the effective length, which is estimated to be 200 mm, the optimum end-cut shape was determined by referring the experimental results obtained at KEK and INS.[2] The coil is wound of copper hollow-conductor having a cross section of 6×6 mm^2 with a hole of 4 mm in diameter and the number of windings is 30 turns per pole. Each coil permits the excitation current up to 260 A. The total length of the line is about 64 m and the vacuum pipe is made of aluminum alloy. The system is required to be held at pressure lower than 2×10^{-7} Torr. The aluminum vacuum system will enable us to achieve the required performance with a small number of evacuating pumps.

Table 2. Designed values of electrical characteristics of DAL0.

Resistance		
Coil	2.8 mΩ	
Cable	0.2 mΩ	
Inductance		
Coil	72 μH	
Cable	3 μH	
Power loss		
Coil	3.5 kW	AC mode
Cable	8.7 kW	AC mode
Coil	8.0 kW	DC mode
Cable	16.0 kW	DC mode
Rise time	2.5 ms$<t<$5 ms	
Fall time	2.5 ms$<t<$5 ms	

Table 1. Parameters of the dipole magnets in the transfer line.

Name of magnet	DAL0	DML1	DML2	DMJ3 & DMJ4	DMS5	DMS6	DMS7
Deflection angle (deg.)	5.73	20.0	20.73	90.0	40.0	40.0	45.0
Curvature radius (m)	3.0	1.0	1.0	0.8	0.6	0.6	0.46
Maximum field (T)	0.27	0.8	0.8	1.0	1.31	1.4	1.71
Pole gap (mm)	60	60	60	60	60	60	42
Size of hollow-conductor (mm)	□9-φ6	□6-φ4	□6-φ4	□9-φ6	□9-φ6	□9-φ6	□9-φ6
Total number of windings	8	80	256	132	168	168	140
Maximum excitation current (A)	1,700	600	200	450	450	450	500
Maximum voltage (V)	4.9	60	66	83	54	63	47

* College of Humanities and Science, Nihon University.

One of the characteristic features of the beam line is beam sharing between RIKEN Ring Cyclotron and the RILAC experimental hall.[3] For this purpose, the first dipole magnet in the line (DAL0) is excited by pulsed current. The DC excitation of this magnet is also possible. Electrical parameters for the magnet are listed in Table 2.

References

1) J.S. Colonias and J.H. Porst: Magnet Design Applications of the Magnetostatic Problem Called TRIM, UCRL-16382 (1965).
2) M. Kumada, H. Someya, I. Sakai, and H. Sasaki: Proc. 2nd Symp. on Accelerator Science & Technology, p. 73 (1978).
3) K. Hatanaka, T. Inamura, Y. Yano, K. Yamaguchi, and H. Kamitsubo: *RIKEN Accel. Progr. Rep.*, **18**, 181 (1984).

RIKEN Accel. Progr. Rep. 19 (1985)

V-9. Model Study of the Beam Buncher

A. Goto, T. Fujisawa, I. Takeshita, and K. Ogiwara

A life size model of the beam buncher was constructed according to the design given in a previous progress report,[1] and its electrical characteristics were measured. Figure 1 shows a photograph of the model; a schematic drawing is shown in Fig. 2. Measurements were performed for various combinations of positions of the capacitive frequency tuner (d) and the shorting plate (s). The definitions of values d and s are given in Fig. 2. Figure 3(a) gives resonant frequencies, Q values, and shunt impedances against s for $d=84$ mm (max) and Fig. 3(b) is the same as Fig. 3(a) except for $d=10$ mm, together with the resonant frequencies for $d=5$ mm. The shunt impedance was deduced from measurements of the drift tube voltage and the rf excitation power. The drift tube voltage was measured

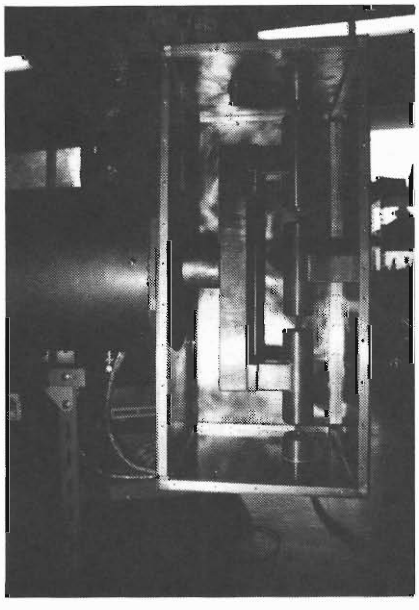

Fig. 1. Photograph of the model buncher.

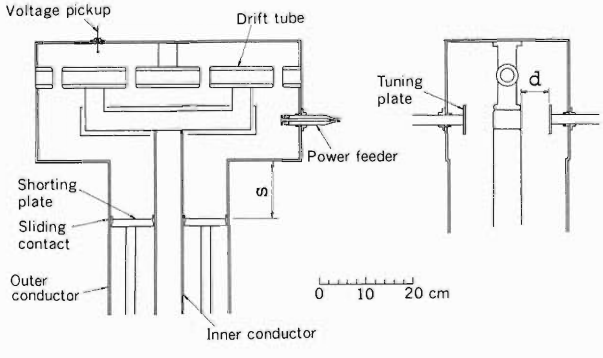

Fig. 2. Schematic drawing of the model buncher.

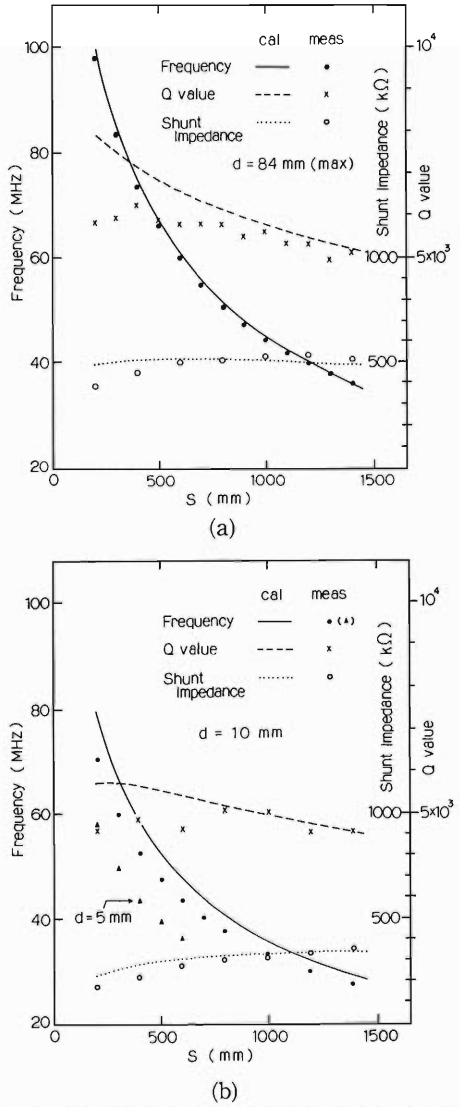

Fig. 3. (a) Measurements of resonant frequencies, Q values, and shunt impedances against the position of the movable shorting plate for $d=84$ mm (max). The calculations using the transmission line approximation are also shown for comparison. (b) The same as Fig. 3(a) except for $d=10$ mm. The measurements of resonant frequencies are also shown for $d=5$ mm.

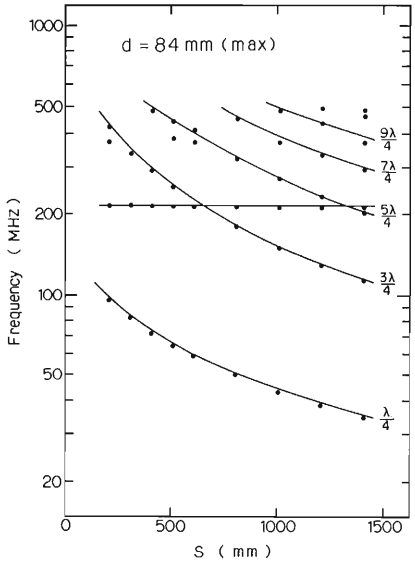

Fig. 4. Higher modes of resonance when the tuner is at the position of the side wall. A parasitic resonance can also be seen at about 210 MHz. Solid lines are the calculations using the transmission line approximation.

with a calibrated voltage pick-up. The excitation power was obtained by measuring input rf current, voltage, and their phase on the feeder. The calculations based on the transmission line approximation shown in these figures are in good agreement with the measurements, though the agreement in resonant frequencies is slightly poor when d is small. Measurements of resonances of higher modes and parasitic modes up to 500 MHz were performed, and the results are shown in Fig. 4, together with the calculations. It was found that, besides the resonances of higher modes, there is a rather strong parasitic resonance in the vicinity of 210 MHz. This is the resonance of a 1/2 λ wave standing on the support of drift tubes and having a node at its center. In fact, its resonant frequency is almost constant independently of the position of the shorting plate. Electric field distributions were also measured along the axis of the drift tubes by a perturbation method. The shape and amplitude of the distribution were almost the same for all the four gaps. The rf power is fed into the resonator through a 50 Ω coaxial feeder line coupled with the resonator by a tunable capacitive coupler. The measurement confirmed that the impedance matching could be achieved as expected by using this coupler.

It was found from the above measurements that the model works well in accordance with the desigh, and we have fixed the specifications for the beam buncher. The length of the coaxial part (s) was decided to be 60 cm and maximum power of a power amplifier to be 750 W. The beam buncher system is scheduled to be completed by the end of July, 1986.

Reference

1) A. Goto, T. Fujisawa, and I. Takeshita: *RIKEN Accel. Progr. Rep.*, **18**, 184 (1984).

RIKEN Accel. Progr. Rep. 19 (1985)

V-10. Control System of RIKEN Ring Cyclotron

T. Wada, J. Fujita, K. Shimizu, I. Yokoyama,
T. Kambara, and H. Kamitsubo

RIKEN Ring Cyclotron[1] is controlled by means of three mini-computers, which are linked with one another through an optical fiber loop.[2] A CAMAC serial crate network and a GP-IB are used for the control of accelerator devices. The computers are of the same type, a 32-bit industrial computer MELCOM 350-60/500 of Mitsubishi Electric Corp.

Computer #1 controls the ring cyclotron through the CAMAC bit serial loop. Computer # 2 is used to store the base of the whole control system into disk files. Computer #3 controls the heavy ion linac (RILAC) through a GP-IB using optical fiber links.[3]

Table 1. Configuration of computer #3.

Memory	3 MB
Fixed disk	202 MB
Magnetic tape	1 (1,600/800 bpi)
Line printer	1 (390 lpm)
Plotter	1 (10 pens)
20″graphic display	1 (7 color)
Hard copy	1
20″character display	1 (7 color)
Rotary encoder	4
Plasma display	1
Toutch panel and CRT	1
GP-IB	2 (400 kB/s)
CAMAC SHD	1 (5 MB/s)

Computer #2 was already installed in August, 1984, and has been used for programs, data base development,[4] and field measurements of the four sector magnets;[5] The computer was installed temporarily in RIKEN Ring Cyclotron vault. Despite of operation in unconditioned atmosphere, no hardware errors took place during 13 months.

Computer #3 and the GP-IB interface was installed in October, 1985, in the control room of the RILAC. Table 1 lists the configurations of the memory and peripheral devices. The RILAC has been controlled by a HP-1000 computer through a GP-IB. This network will be reconnected to the new MELCOM computer. Some newly developed beam diagnostic devices will be controlled through a CAMAC serial loop using CIM and DIM modules.[6] The program conversion is now in progress.

Computer #1 and an operator console will be installed in May, 1986, and then the three computers will be linked with one another by optical

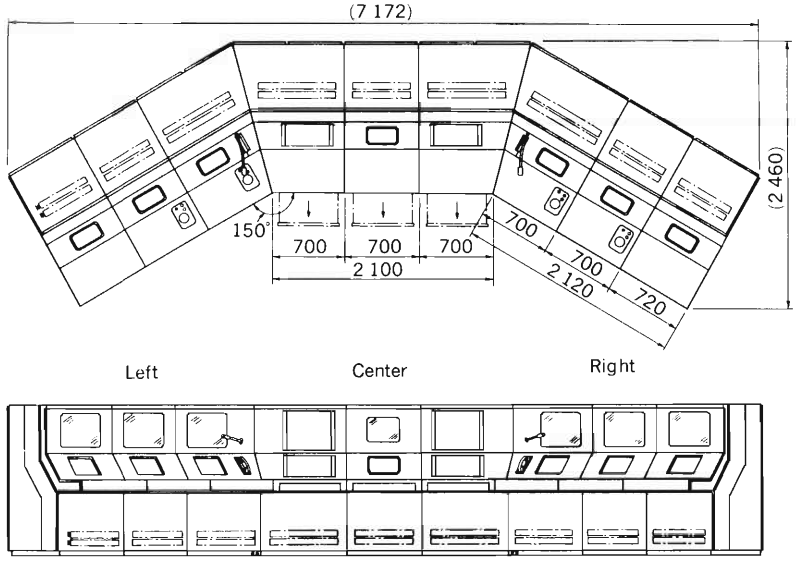

Fig. 1. Top and front views of operator console.

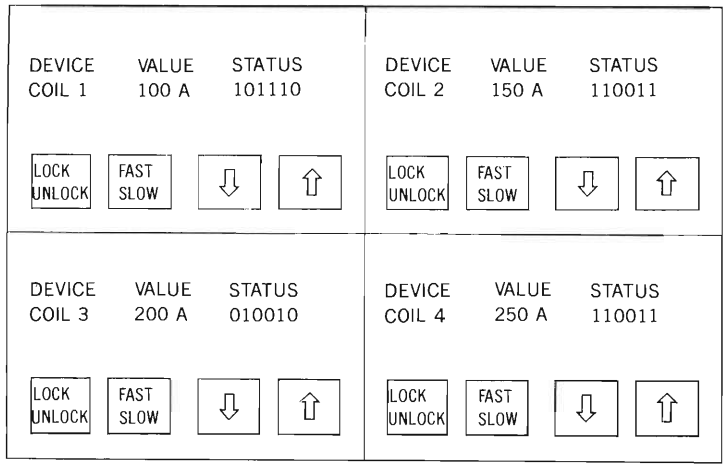

Fig. 2. An example of display on the touch pannel display.

fiber cables and RS 232C serial lines. The serial lines are used to transfer data using an UUCP function of UNIX system. Figure 1 shows the operator console which consists of three parts (center, left, and right parts). The left and the right parts are made equivalent to each other for the convenience of accelerator diagnostics. At least two operators can access the accelerator system independently using the left and the right parts.

In the first design of the operator console, rotary encoders and push buttons were to be used for the manual control of each device. This has, however, difficulty in changing the number of encoders and buttons, and the encoder system was replaced with a touch pannel system. Figure 2 shows an example of displays on the touch pannel CRT. The number or functions of 'buttons' can be easily changed depending on controlled devices. The touch pannel is a model 1024 of Japan Binary Corp., and the CRT is a DEC model VT241.

For the operator console of RILAC, a rotary encoder system is used because of its compatibility to a HP-1000 computer system. A plasma display and four rotary encoders of 100 pulses per turn are arranged on a pannel.

References

1) S. Motonaga: Proc. 1985 Particle Accelerator Conf., Vancouver, Canada, p. 2712 (1985).
2) T. Wada, J. Fujita, K. Shimizu, I. Yokoyama, T. Kambara, and H. Kamitsubo: Proc. 1985 Particle Accelerator Conf., Vancouver, Canada, p. 2095 (1985).
3) T. Kambara and M. Odera: Proc. 5th Symp. on Accelerator Science and Technololgy, Tsukuba, p. 364 (1984).
4) T. Wada, J. Fujita, K. Shimizu, I. Yokoyama, T. Kambara, and H. Kamitsubo: *RIKEN Accel. Progr. Rep.*, **18**, 185 (1984).
5) A. Goto, H. Takebe, S. Motonaga, K. Hatanaka, Y. Yano, T. Wada, N. Nakanishi, and M. Hara: p. 178 in this report.
6) K. Shimizu, T. Wada, J. Fujita, and I, Yokoyama: Proc. 10th Int. Conf. on Cyclotron and their Applications, East Lansing, Michigan, USA, p. 392 (April 1984).

RIKEN Accel. Progr. Rep. 19 (1985)

V-11. Sequential Control Using an Intelligent Interface Module

K. Shimizu, M. Nagase, H. Takebe, and S. Motonaga

Current regulators are used for exciting the magnet coils of RIKEN Ring Cyclotron. Each regulator has a control element, an error voltage amplifier, a standard registor and a 16 bit D-A converter (DAC) for accepting a digital reference. It is required that each output of these regulators increases linearly with time. However, since the time constant of the magnet coils is very long, it takes at least twenty minutes in increasing all the regulator outputs to predetermined final values. Although such a long time sequential control can be done with a host computer, it is not always effective in the usage of the host computer. Two types of intelligent interface modules (CIM and DIM)[1] are used in our control system.[2] In particular, the DIM can perform various kinds of controls independently of a control computer by only firmwaring respective programs into its ROM. Therefore, a program which enables the DIM to perform the sequential control was developed. Protocol on the program will be explained below.

Parameters are sent to the DIM firstly to start the sequential control. These parameters consist of the following items.

1. Number of DACS: number of the controlled regulators.
2. Resetting Interval: repetition time on varing a reference as a jump function based on a linear function.
3. DAC Number: this means a regulator number.
4. Initial Value: initial output current of each regulator.
5. Final Value: final output current of each regulator.
6. Reference Step Value: increment of each reference.
7. Allowable Deviation: upper limit of the difference between each reference and an output current borne by it.

Figure 1 shows the format of the parameters. A CIM/DIM system provides various instructions. A block information transfer instruction is used for sending the parameters to the DIM. After sending the instruction, the sequential control is performed if an instruction for starting it

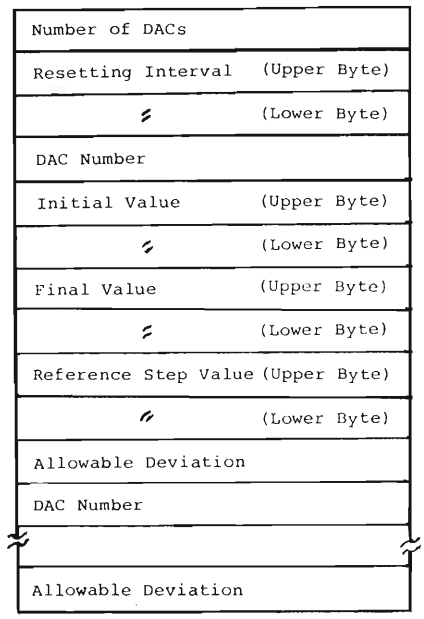

Fig. 1. Format of parameters.

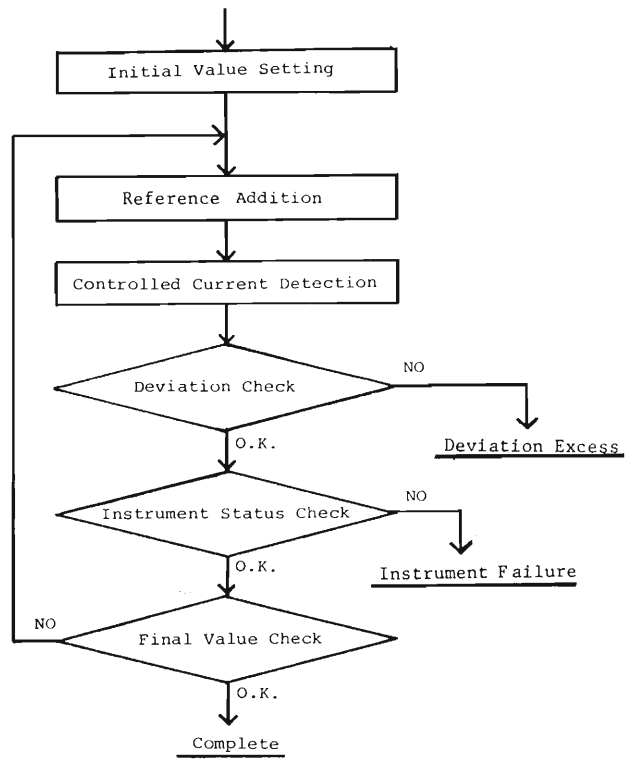

Fig. 2. Operation flow diagram.

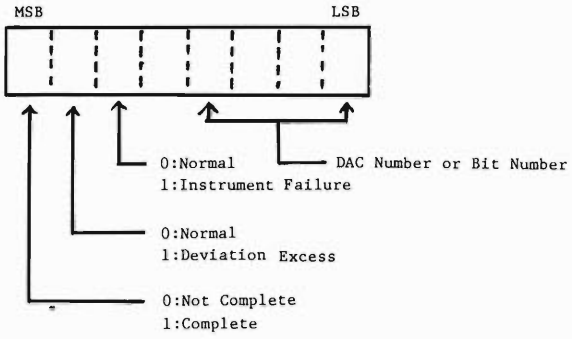

Fig. 3. Format of the message coming from DIM.

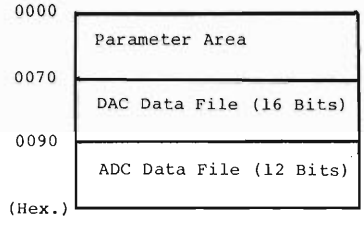

Fig. 4. Memory map.

is sent to the DIM.

Figure 2 shows the operation flow diagram of the sequential control. The DIM gives each initial reference to each regulator as the Initial Value Setting step sequentially. Then, the following operation is repeated at the resetting interval until all the regulator outputs reach respective final values. In the reference addition step, the DIM adds each reference step value to the previous reference and gives the result to each regulator as the following reference sequentially.

The DIM detects the output current of each regulator through its 12 bit A-D converter and checks the difference between the detected current and a reference bearing the output current in the controlled current detection and deviation check steps sequentially. Then, DIM checks whether instrument status is normal or not and whether all the output currents reached the final values or not.

When the difference exceeds each allowable deviation in the deviation check or the instrument status is not normal in the instrument status check, the DIM stops performing the sequential control and sends a signal to the control computer through a CIM connected to it.

When all the output currents reached the final values, the DIM also sends the signal to the control computer. After the recognization of the signal, if a message is fetched from the DIM with an instruction, the cause of the generation of the signal (Deviation Excess, Instrument Failure, Complete) is found out from the message.

The format of the message is shown in Fig.3. In the format, the most significant bit represents whether the sequential control is complete or not. Deviation excess is defined on the second upper bit. An instrument failure is defined on the third upper bit. The lower four bits are used for representing a DAC number related to the deviation excess or a bit number related to the instrument failure in the status information.

Figure 4 shows a memory map used for the sequential control. The parameters from the control computer are stored in the parameter area, where the most significant bit in each byte assigned to the DAC number is set if each regulator output reached its final value. The reference and output current of each regulator are rewritten into the DAC Data File (16 bits) and ADC Data File (12 bits) at every the resetting interval, respectively. As the contents of the memory can be read out with another block information transfer instruction, each situation of the sequential control can be found out. It will be understood from the explanation mentioned above that the control computer can execute other tasks during the DIM performs the sequential control.

The DIM can reduce the load of the control computer because it can be used not only for interfacing between the control computer and instruments but also for controlling thus instruments sequentially. Furthermore, the DIM can respond to request from the control computer even during it performs the sequential control. Such a function of the DIM is superior to that of a general purpose sequential controller. The function makes the control system more flexible and powerful.

References

1) K. Shimizu: *Nucl. Instrum. Methods Phys. Res. A*, **236**, 109 (1985).
2) K. Shimizu, J. Fujita, T. Wada, and I. Yokoyama: *RIKEN Accel. Progr. Rep.*, **17**, 141 (1983).

RIKEN Accel. Progr. Rep. 19 (1985)

V-12. Practical Use of an Intelligent CAMAC GP-IB Controller

J. Fujita

An outline of an intelligent CAMAC GP-IB controller module was described in a previous report.[1] The present report describes the module used practically in RIKEN Ring Cyclotron magnetic field measurement.

A present configuration of the magnetic field measurement system is shown in Fig. 1, where an M60/500 Mitsubishi computer[2] and an LSI-11 microcomputer systems[3] are depicted simply and other instruments not related directly to the GP-IB route are not shown. The LSI-11 is used for controlling GP-IB devices and linking both systems via handshake between two CAMAC 16 bits I/O registers. Since only two bytes are transferred by one access to the 16 bits I/O register and block transfer is not carried out in this system, it takes about $6.8\times(N/2)$ ms for M60 to receive data of N bytes and, conversely, $5.1\times(N/2)$ ms to deliver them to the LSI-11.

Replacement of the LSI-11 system with the GP-IB controller module will make configuration of the measurement system very simple, as shown in Fig. 2, and will shorten data handling time as mentioned below. The module has capability of CAMAC block transfer with a 24 bits full word mode. The block transfer rate of a CAMAC serial loop in the M60 system is 20 kB/s. Data receiving and delivering times in the same case as before are about $9.6+0.15\times(N/3)$ ms and $10.4+0.15\times(N/3)$ ms, respectively. Therefore, the data transfer time in this system is reduced to 1/3 of that in the former system for $N=12$ bytes, and 1/20 for $N=120$ bytes.

In order to make use of the GP-IB module easy, a library file, /usr/rlib/gpm.tl, on UNIX and an object module file, SYS001/ROF;GPMINI, on

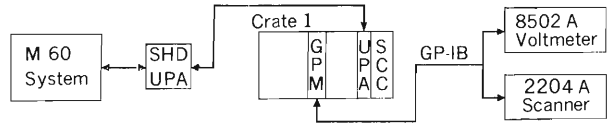

Fig. 2. Replaced system with an intelligent GP-IB module. GPM; an intelligent GP-IB module.

M60 are constructed. These files consist of four subroutines, GPMINI, GPMSND, GPDRCV, and GPMWRK.

GPMINI must be issued once at the beginning of a main program. It defines CAMAC addresses with regard to the module and sets it to an initial state.

GPMSND transforms a given character string of an EBCDIC code in M60 to an ASCII one, rearranges the string locations of 32 bits full word in M60 to CAMAC 24 bits word, and sends the resulting ASCII string to the module.

GPDRCV makes acknowledgement of preceding GPMSND and, at the same time, if data from GP-IB devices are stored in the module, receives them. It must be used somewhere to complete one cycle of state transition in the module after GPMSND is called.

GPMWRK is a serial combination of GPMSND and GPDRCV, and executes sending message and receiving data continuously.

At present actual programs for measuring the magnetic field are being developed.

References

1) J. Fujita: *RIKEN Accel. Progr. Rep.*, **18**, 187 (1984).
2) T. Wada, J. Fujita, K. Shimizu, I. Kambara, and H. Kamitsubo: *RIKEN Accel. Progr. Rep.*, **18**, 185 (1984).
3) J. Fujita, T. Wada, and H. Takebe: *RIKEN Accel. Progr. Rep.*, **15**, 177 (1982).

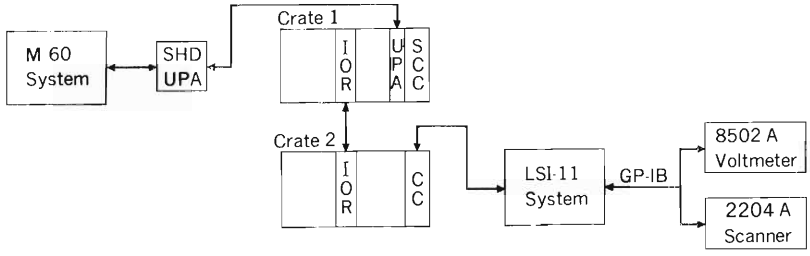

Fig. 1. Present magnetic field measurement system. SHD, Serial Highway Driver; UPA, U-Port Adapter; SCC, Serial Crate Controller; IOR, 16 bits I/O Register module; CC, JLSI-10 Crate Controller.

RIKEN Accel. Progr. Rep. 19 (1985)

V-13. Cryopumps for RIKEN Ring Cyclotron Vacuum Chamber

N. Ohsako,* K. Morimoto,* T. Kikuchi,* K. Ikegami,
S. Nakajima, Y. Oikawa, and S. H. Be

For evacuation of RIKEN Ring Cyclotron vacuum chamber, we have developed two types of cryopumps and constructed ten cryopumps of $1\times10^4 l/s$ for nitrogen (ANELVA model CAP-200) and four panel type cryopumps of $5\times10^3 l/s$ (ANELVA model CAP-610). These are designed to have large adsorptive capacity for hydrogen because the regeneration interval of these pumps is limited by adsorptive capacity.

A cross sectional view of CAP-200 cryopump is shown in Fig. 1. The pump housing of 500 mm in diameter surrounds the cryopanels which are cooled to cryogenic temperature by means of a G-M refrigerator (Sumitomo Heavy Industry Co. model SRD-208). A quantity of charcoal stuck on the inner surface of the second stage cryopanels of each cryopump is ~300 g. A refrigeration capacity of the SRD-208 cryogenerator is 8 watt at 20 K on the second stage and 70 watt at 77 K on the first stage. The CAP-610 has a geometry like a waterwheel as shown in Fig. 2 and is directly inserted in the stem of the resonator. A quantity of charcoal stuck on the inner surface of the second stage cryopanels is ~270 g. A refrigerator (SRD-208) is also employed in this cryopump.

The performance tests for these pumps were carried out on a test chamber. After evacuating the test chamber to 10 Pa by a mechanical pump, the cryopump was turned on. The temperature of the second stage cryopanels was reduced below 20 K within 150 min for CAP-200 and within 220 min for CAP-610. Furthermore the pressure became below 1×10^{-4} Pa at the end of cooldown time, and after 13 h below 1×10^{-7} Pa without baking.

Figure 3 shows results of pumping speed measurements. Pumping speeds at various pressures were determined from equilibrium pressure measured at various flow rates of inlet N_2 or H_2 gas. The average pumping speed of CAP-200 is $\sim1\times10^4$ l/s for nitrogen and $\sim2\times10^4$ l/s for hydrogen, and that of CAP-610 is $\sim6.3\times10^3$ l/s for nitrogen and $\sim8.3\times10^3$ l/s for hydrogen. They are in good agreement with calculations.

Finally we investigated an adsorptive capacity for hydrogen of these cryopumps keeping a flow rate (~18 Pa l/s) of gases constant. Figure 4 shows that the equilibrium pressure increases, *i.e.*, the pumping speed decreases, with an increase in a total amount of hydrogen adsorbed

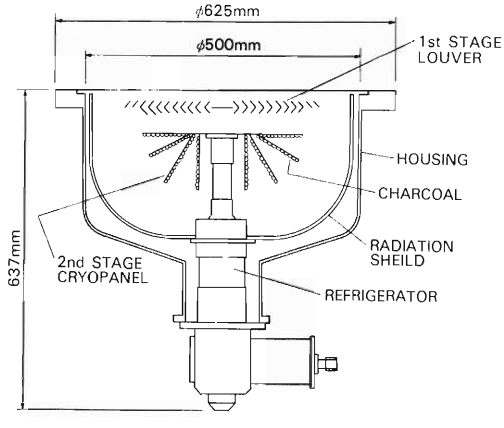

Fig. 1. Cross sectional view of CAP-200 cryopump.

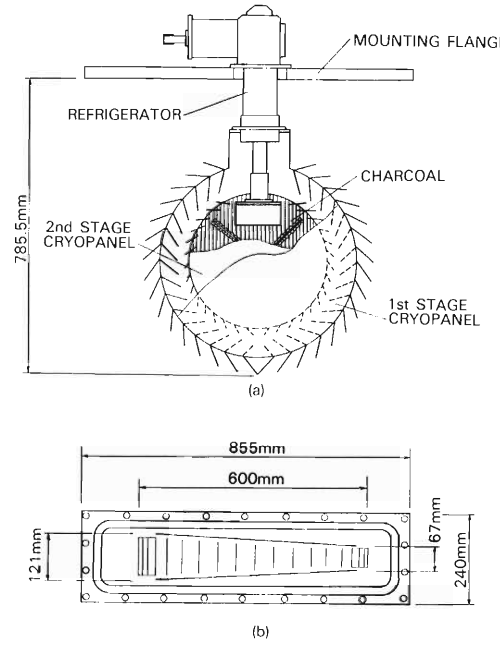

Fig. 2. Cross sectional view of CAP-610 cryopump. (a) a front view, (b) a bottom view.

* ANELVA Corporation.

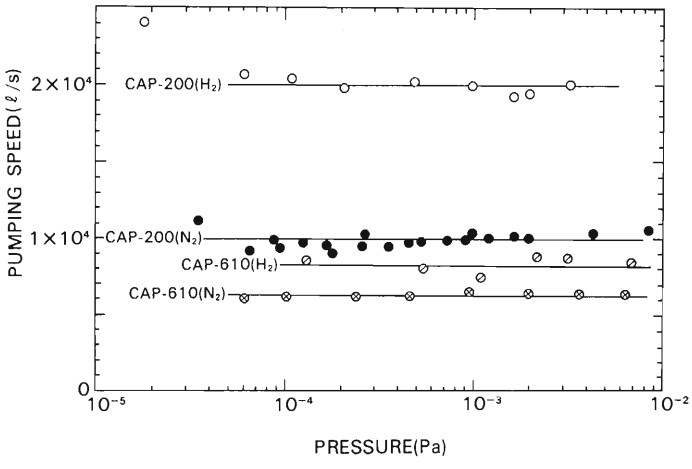

Fig. 3. Results of pumping speed measurement for cryopumps.

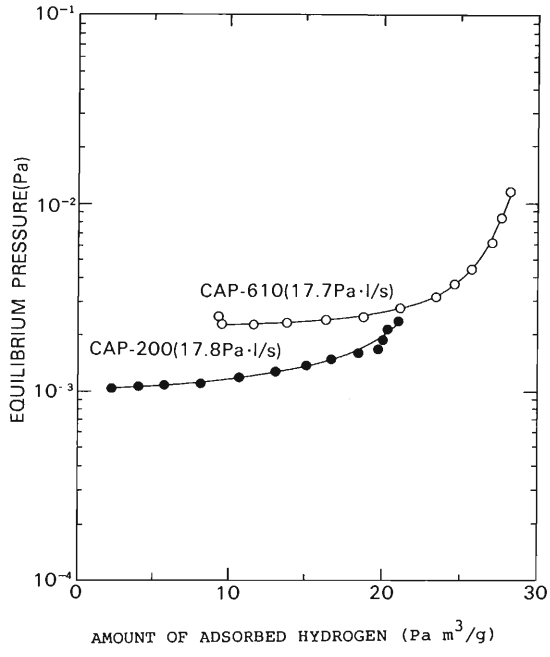

Fig. 4. Variation of an equilibrium pressure with a total amount of adsorved hydrogen.

on charcoal. From Fig. 4 we can see that the adsorptive capacity for hydrogen without seriously decreasing the pumping speed (until the speed becomes one half of the initial value) is $\sim 6\times10^{3}$ Pa m^3 for CAP-200 and $\sim 6.5\times10^{3}$ Pa m^3 for CAP-610. The adsorptive capacity, however, depends on the equilibrium pressure and decreases with a decrease in pressure.[1] Since partial hydrogen pressure in the vacuum chamber of the ring cyclotron will be of the order of 1×10^{-6} Pa, the adsorptive capacities of these pumps may be estimated to be one half or one third[2] of the values measured above.

References

1) "le Vide les Couches Minces" supplement "Vide et Cryogenie," ed. by Société Française du Vide, p. 17 (1984).
2) "Basics of Cryopumping," Air Products and Chemicals Inc. (1980).

RIKEN Accel. Progr. Rep. 19 (1985)

V-14. Outgassing Rates of Materials Used in the Vacuum Chamber for RIKEN Ring Cyclotron

K. Ikegami, Y. Ishibe, and S. H. Be

The vacuum chamber of RIKEN Ring Cyclotron uses various materials such as stainless-steel (SUS), alumina, and viton O-ring. For evaluation of the gas load due to outgassing from these materials and the corresponding pumping requirements, measurements of the outgassing rates are indispensable. The apparatus for measuring the outgassing rates is shown in Fig. 1. The test chamber, which is made of SUS and has an inner surface area of 1,800 cm^2, was evacuated through an orifice of 11 mm in diameter open to a high-vacuum chamber placed under the test chamber. The orifice is capable of conducting N_2 at 10 l/s or H_2O at 12 l/s. The high-vacuum chamber was evacuated directly with a turbomolecular pump of 300 l/s and a backing rotary pump of 250 l/min. An ionization gauge in the test chamber was used for measuring an increase in the pressure by outgassing and a variable leak valve for gas inlet. A quadrupole mass analyzer connected to the high-vacuum chamber was used for observing residual gases and the components of released gases. The outgassing rates were determined from a surface areas of the respective materials and the pressure differences between two chambers, by using the orifice conductance of 12 l/s for H_2O because the gases was composed mainly of water vapor.

Figure 2 shows the outgassing rates for various materials, which decrease with time after the start of pumping. The rate for SUS-304L polished mechanically by a glass beads blast (G.B.B.) is of the order of $\sim 10^{-7}$ Pa m^3/s m^2 at 150 h after pumping and this value is lowered by a factor of

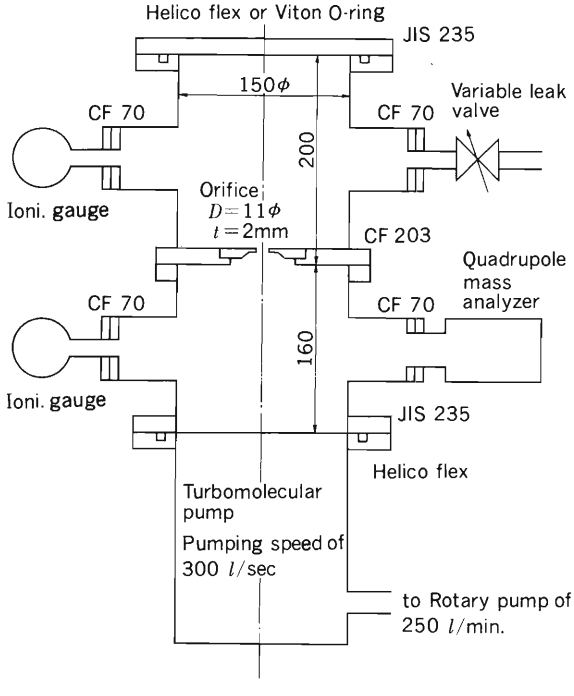

Fig. 1. Schematic diagram of the apparatus for measuring outgassing rates.

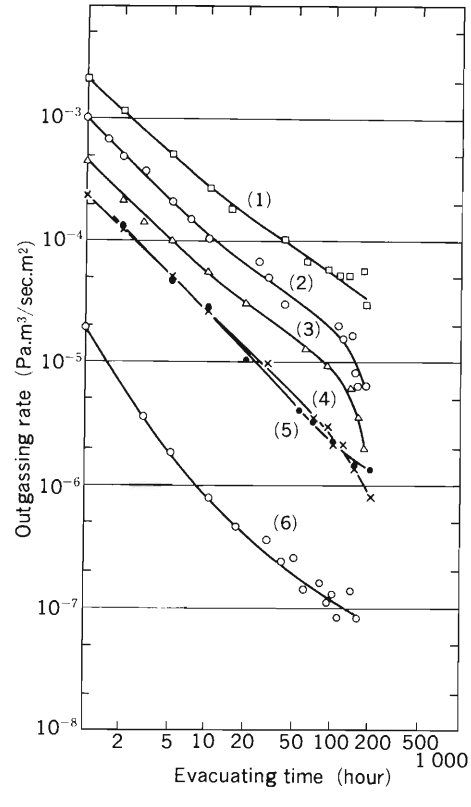

Fig. 2. Outgassing rate for various materials *vs.* time. (1) Unbaked viton O-ring. (2) Viton O-ring immediately after baking in vacuum. (3) Thin alumina layer deposited with SiO_2. (4) Thin alumina layer flash-coated on a copper plate. (5) Solder applied to a thin copper plate. (6) Stainless-steel (304L) polished mechanically by G.B.B.

5 compared to that for untreated SUS-304L, which is not shown here. The SUS-304L is to be used for RIKEN Ring Cyclotron chamber. The outgassing rates from a solder of Sn-Ag alloy and a thin alumina layer flash-coated on a copper plate were also measured. The solder is to be used in welding a water cooling pipe to an inner part of the dee in the resonator; its outgassing is $\sim 10^{-6}$ Pa m^3/s m^2 after 100 h. The thin alumina layer is used as an insulator for trim coils in the sub-vacuum chambers of four sector magnets and for coils of magnetic channels; its outgassing rate is $\sim 4 \times 10^{-6}$ Pa m^3/s m^2 at 150 h after the start of pumping. The outgassing rate from a thin alumina layer deposited with SiO_2 is $\sim 10^{-5}$ Pa m^3/s m^2, which is over 2 times greater than that from an alumina layer only. From these results, we chose the alumina layar as a suitable insulator.

We also measured the outgassing rates for viton O-rings (Dainichi Densen, 320-75) pre-baked for 24 h at 120°C in a vacuum. Since detailed results of the prebaking and degassing will be described by Y. Ishibe *et al.*,[1] a part of the results is shown in Fig. 2 in comparison with other materials. The O-rings were placed into a standard rectangular groove on the top flange of the test chamber and assumed that only a part of the surface, a half of a total surface area, is exposed to a vacuum. The outgassing rate involving permeation from the O-ring immediately after baking was $\sim 2 \times 10^{-5}$ Pa m^3/s m^2 at 100 h after the start of pumping. This value is lower than one third of that for an unbaked O-ring.

These experimental results show that the outgassing rates of materials depend strongly on the state of the surface such as polished or unpolished, and baked or unbaked.

Reference

1) Y. Ishibe, K. Ikegami, and S. H. Be: p. 195 in this report.

RIKEN Accel. Progr. Rep. 19 (1985)

V-15. Evaluation of an Outgassing Rate from Pretreated Elastomers

Y. Ishibe, K. Ikegami, and S. H. Be

An operating pressure requried for the vacuum chamber of RIKEN Ring Cyclotron is of the order of 10^{-6} Pa, which is determined from an evacuating capacity of vacuum pumps and an outgassing rate from surfaces of materials used in the vacuum system including vacuum seals. The materials include stainless steel, copper, aluminum, ceramics, viton O-ring, *etc.* and outgassing rates from these respective materials depend on a pump down time; the rates decrease with time. In the present case, the overall outgassing rate estimated from published data 10-50 h after the start of pumping is $\sim 4\times10^{-4}$ Pa m^3/s, and that from viton O-rings used as parts of vacuum seals is approximately $1\sim2\times10^{-4}$ Pa m^3/s, corresponding to about one or two thirds of the overall outgassing rate. Since O-rings are also permeable to gases, we plan to use double O-rings, the space between which is evacuated with a separate pump to prevent permeation of atmospheric gas.

In order to reduce the outgassing rate, we have carried out preliminary experiments with prebaked elastomers. Two procedures were examined for degassing: baking in air in the temperature range from 120 to 200°C and baking at ~1 Pa at 150°C.

Weight-recovery rates $((w_t-w_0)/w)$ of elastomers are shown as a function of time after baking in air in Fig.1. Here w is the initial weight of an O-ring, w_0 is the weight immediately after degassing, and w_t is the weight at given time. Figure 1 indicates that the weight recovery rates for two elastomers increase with time; These elastomers increase their weights continuously over 400 h, when the weights level off. The recovery rate of the viton O-ring, however, is consider-

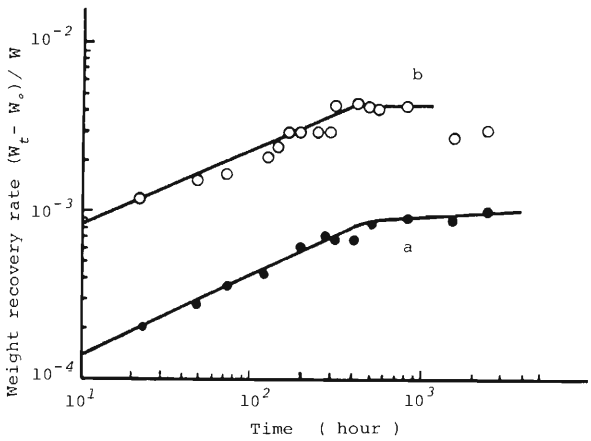

Fig. 1. Weight-recovery rates of elastomers baked in air as a function of time. a, fluoroelastomer (viton) baked for 10 h at 200°C; b, nitrile rubber (NBR) baked for 20 h at 120°C.

Table 1. Weight-loss rate after baking in air and at ~1 Pa.

Rate	Material		
	NBR	Silicone	Viton
$\left(\frac{w-w_0}{w}\right)$ in atmosphere	1.2×10^{-2} (120°C 20 h)	1×10^{-2} (120°C 20 h)	2.5×10^{-3} (210°C 10 h)
$\left(\frac{w-w_0}{w}\right)$ in vacuum	4.4×10^{-2} (150°C one day)	4.6×10^{-2} (150°C one day)	8.3×10^{-4} (150°C one day)

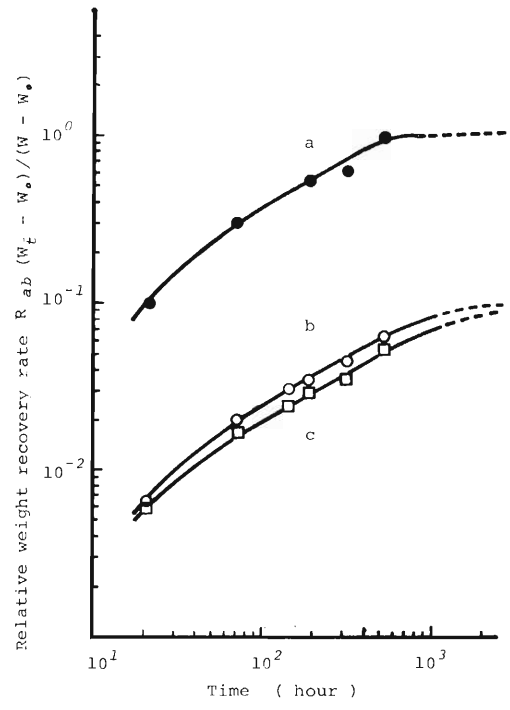

Fig. 2. Relative weight-recovery rate R_{ab} of elastomers baked at ~1 Pa as a function of time. a, viton; b, NBR; c, silicone.

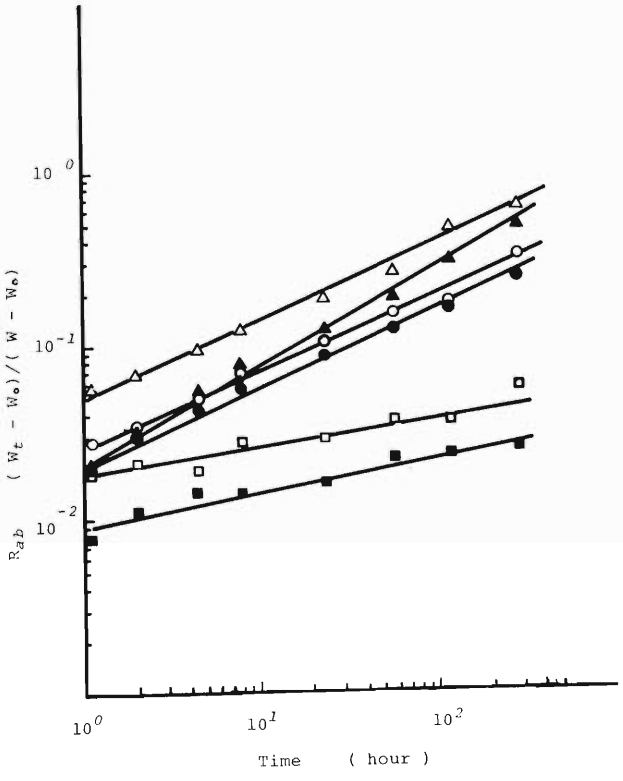

Fig. 3. Time-dependent relative weight-recovery rate of viton O-ring under different stored conditions after baking. Baking conditions: □○△, one day at 150°C at ~1 Pa; ■●▲, one day at 150°C in air. Stored conditions: □■, with silicagel; ○●, in air; △▲, in saturated water vapor.

ably lower than that of the NBR O-ring. The weight loss rates for various elastomers pretreated in air and at reduced pressure are given in Table 1. The weight loss rates cannot directly compared with each other because the pretreatment was carried out under different degassing conditions. However, the weight loss rate of viton O-ring is about one order of magnitude smaller than those for other elastomers.

Time-dependent relative weight recovery rates calculated from $R_{ab}=(w_t-w_0)/(w-w_0)$ for elastomers baked at ~1 Pa are shown in Fig. 2, which shows that R_{ab} for the viton O-ring reaches 1, namely its weight becomes the same as the initial weight. This means that gases are reabsorbed to the same level as that before degassing. On the other hand, R_{ab}'s for silicone and NBR O-ring level off at $R_{ab}=0.1$. A reason for this difference is not clear; we think that the weight loss for the viton O-rings is due mostly to the desorption of

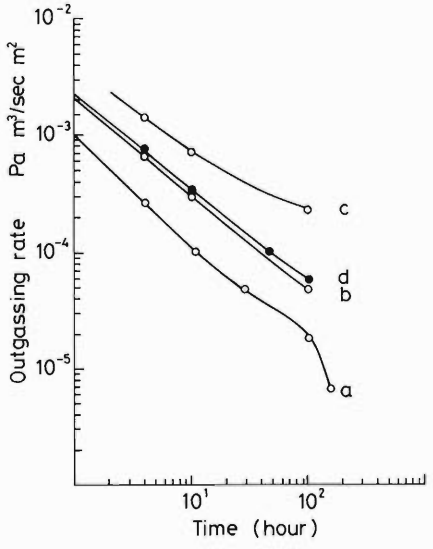

Fig. 4. Outgassing rate from viton O-ring after baking in vacuum; a, just after degassing by baking; b, after exposure to 100 % humidity at R.T. for 5 h; c, after 240 h at 100 % humidity; d, original elastomer without degassing.

gases, and that for silicone and NBR O-rings is due to the removal of a plasticizer together with absorbed gases.

The relative weight-recovery rates at different relative humidities in air were also investigated; the results are shown in Fig. 3, which suggests that the humidity of the ambient atmosphere in which elastomers are stored plays an important role in reabsorption of gases.

Finally, we measured the outgassing rate from viton O-rings after baking, and the results are shown in Fig. 4. The details for measuring the outgassing rates will be reported by Ikegami *et al.* in this report.[1] As shown in Fig. 4, the outgassing rate increases with an increase in exposure time in air, and depends strongly on the storing conditions. We also found that the outgassing rate from the viton O-ring just after baking decrease by about one order of magnitude faster than that from the O-ring without baking.

In conclusion, the pre-treatment of degassing by baking is useful to decrease the outgassing rate of elastomers.

Reference

1) K. Ikegami, Y. Ishibe, and S. H. Be: p. 193 in this report.

RIKEN Accel. Progr. Rep. 19 (1985)

V-16. AVF-Cyclotron as an Injector

N. Nakanishi and T. Kageyama

RIKEN Ring Cyclotron is planed to have two injectors. One is a variable frequency linac RILAC, which was completed in 1980, and the other is an AVF cyclotron which will be constructed in the near future. This report describes fundamental parameters for the AVF cyclotron.

In designing the new cyclotron, we took the following points into consideration: 1) the AVF cyclotron must be matched precisely to the post accelerator, RIKEN Ring Cyclotron, in view of beam optics; 2) the cyclotron must be adaptable to external ion sources; 3) the cyclotron will be used mainly as an injector; 4) the most portions of the cyclotron will be made by orthodox techniques, because of a few man power and an insufficient budget.

Matching conditions between two cyclotrons include the constancy of a longitudinal distance between beam pulses, a beam velocity, and a particle regidity. From these conditions we can obtain expressions, $N_a \cdot R_a/H_a = N_s \cdot R_s/H_s$, $f_a \cdot R_a = f_s \cdot R_s$, and $q_a \cdot B_a \cdot R_a = q_s \cdot B_s \cdot R_s$, where R_a and R_s are mean extraction radius of the AVF cyclotron and mean injection radius of the ring cyclotron, H_a and H_s, f_a and f_s, q_a and q_s, and B_a and B_s are harmonic numbers, orbital frequencies, charge states, and mean magnetic flux densities in respective cyclotrons. Using above

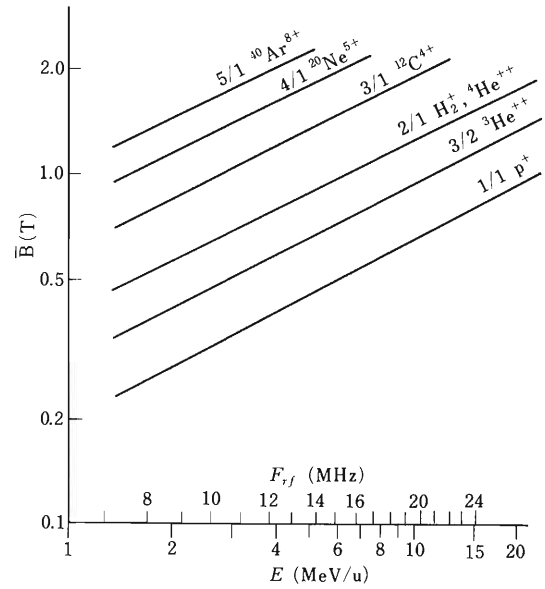

Fig. 1. Relation among energy per nucleon, magnetic field, and RF frequency. The number on each line is the mass to charge ratio.

Table 1. Selected parameter groups for AVF cyclotrons. $\eta = \sin(H \cdot \text{dee angle}/2)$

Type	K (MeV)	R_a(m)	R_s(m)	H_a	H_s	N_a	N_s	$1/N_s$	Dee angle	η_a	η_s
A	110	0.893	0.893	3	6	1	2	0.5	60°	1.0	0.94
B	70	0.714	0.893	2	5	1	2	0.5	90°	1.0	0.85
C	70	0.714	0.893	4	5	1	1	1.0	45°	1.0	0.85

Table 2. Beam energies obtainable at the AVF cyclotron.

A/q	Typical nuclei	E (MeV/u)	B_{ext}(T)	f_0(MHz)
1	p^+	13.3-8.8	0.74-0.60	11.25-9.18
3/2	$^3He^{2+}$	13.3-3.9	1.10-0.60	11.25-6.12
2	d^+, α^{2+}	13.3-2.6	1.47-0.65	11.25-5.00
3	$^{12}C^{4+}$	7.9-2.6	1.70-0.98	8.67-5.00
4	$^{20}Ne^{5+}$	4.4-2.6	1.70-1.31	6.50-5.00
5	$^{40}Ar^{8+}$	2.8-2.6	1.70-1.63	5.20-5.00

Table 3. Design characteristics of the AVF cyclotron.

K-value	70
No. of sectors	4
Extraction radius	0.174 m
Max. mean magnetic field	1.7 T
Max. magnetmotive force	4×10^5 AT
No. of harmonic coils	4
No. of dees	2
No. of cavities	2
Dee angle	90°
RF range	10-22.5 MHz
Dee voltage	50kV
Harmonic No.	2
Ion source	Internal and External
Pressure	5×10^{-7} Torr

Table 4. Maximum beam energies obtainable at RIKEN Ring Cyclotron.

Typical nuclei	E_{in} (MeV)	E_{ext} (MeV)	B (T)	f_0 (MHz)	ν_{zext}
p^+	10.0	210	0.87-11.06	7.7	0.51
$^3He^{2+}$	9.3	193	1.26-1.52	7.5	0.57
d^+, α^{2+}, $^{12}C^{6+}$	7.0	134	1.45-1.66	6.5	0.67
$^{20}Ne^{9+}$	5.9	109	1.47-1.66	6.0	0.73
$^{40}Ar^{15+}$	4.4	78	1.53-1.67	5.1	0.75

relations and imposing other restrictions, we selected three possible types of AVF cyclotron. These parameters are tabulated in Table 1. From examination of beam energies, cyclotron sizes, dee angles, acceleration efficiencies, and others, we finally decided to employ the type B. Beam energies obtainable for typical nuclei are listed in Table 2, and the relation among beam energy, magnetic field strength, and orbital frequency is shown in Fig. 1. Design characteristics of the AVF cyclotron are shown in Table 3. Maximum beam energies obtainable at RIKEN Ring Cyclotron are also given in Table 4 along with used magnetic strengths, radio-frequencies, and axial betatron frequencies.

Although an internal ion source will also be used, the cyclotron must be designed to be adaptable to external ion sources such an ECR ion source, and polarized ion sources. To this end extensive studies should be carried out for an axial injection system, a reflection system, and dee structure in a central region as well as a basic design study of the AVF cyclotron. Such studies are in progress.

RIKEN Accel. Progr. Rep. 19 (1985)

V-17. Sixth Harmonic Acceleration in the Baby Cyclotron

T. Karasawa

In the Baby Cyclotron, protons are accelerated with a second harmonic mode and deuterons with a fourth harmonic mode. We have studied capability of the sixth harmonic-mode acceleration in the central region by the use of numerical orbit calculation.

The procedure of the calculation is the same as that used by Nieuwland and Hazewindus.[1] We employ a left-handed rectangular coordinate system, with the origin at the center of the cyclotron; the z axis is the direction of the magnetic field and $x=0$ is a center line of the dee. The horizontal geometry of the central region (ion source, puller, 30 degree dee and dummy dee) is shown in Fig. 1. The aperture of the puller is 5 mm and that of the dee and the dummy dee is 10 mm. The magnetic field distribution is shown in Fig. 2.

Figure 3 shows an example of the orbits calculated for four rays leaving the ion source with different starting phases: −27 degree, −36 degree, −45 degree, and −54 degree at a RF phase, where 0 degree corresponds to the peak RF voltage. The accelerating parameters of the ions are as follows. The ion-source position is $(x, y)=(-8, 9.5)$ in mm and the dee voltage is 24 kV at $B=1.5$ Tesla for $^{15}N^{5+}$ ion. When suitable condition is applied, we could accelerate a well-centered beam with a sixth harmonic mode in the central region. The difference of electrode shape

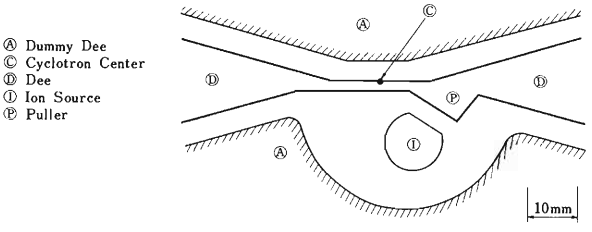

Fig. 1. Horizontal geometry of the central region.

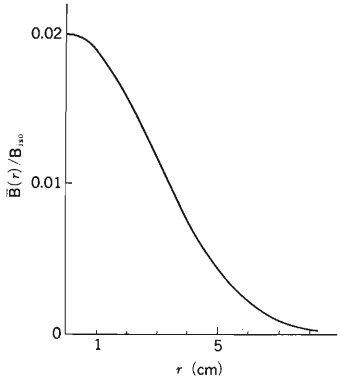

Fig. 2. Relative magnetic field distribution.

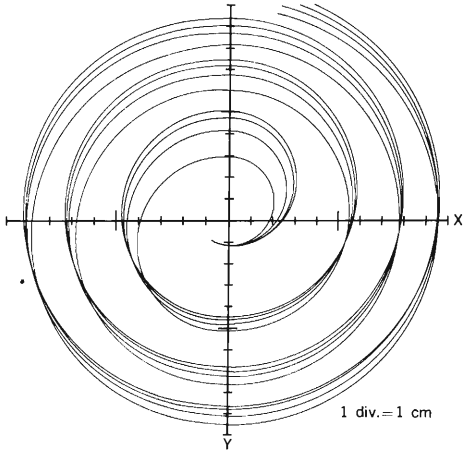

(A)

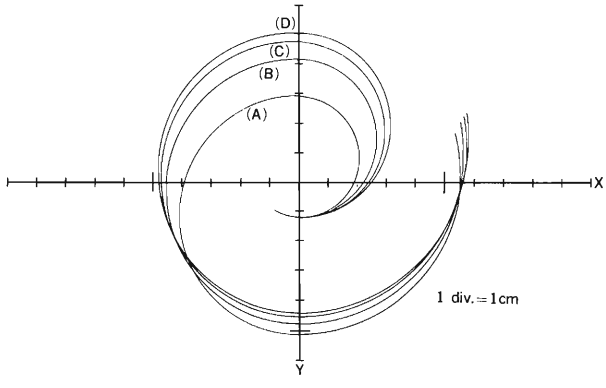

(A), (B), (C), (D): starting phase; see Table 1.

(B)

Fig. 3. (A) Calculated horizontal orbit. (B) Calculated horizontal orbit (enlarged).

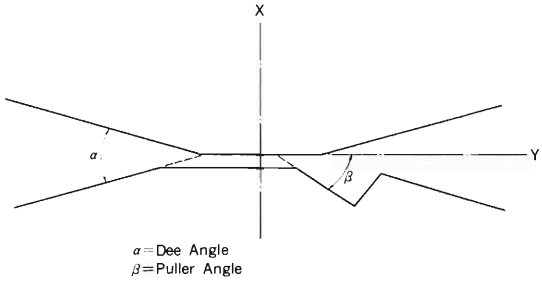

Fig. 4. Definition of the dee angle and the puller angle.

Table 1. Orbit center and RF phase after three revolution.

Symbol	Starting phase (degree)	Orbit center (x, y) mm	mm	RF phase (degree)
(A)	−27	1.2,	2	95
(B)	−36	−0.4,	−2	113
(C)	−45	−0.8,	−5	116
(D)	−54	−0.8,	−8	111

between sixth and the fourth harmonic mode is as follows. The dee angle is narrowed from 35 to 30 degree and puller angle is narrowed from 42 to 33 degree. These angles are shown in Fig. 4.

The orbit center and the RF phase at crossing the y axis (center line of the dee) after three revolutions are tabulated in Table 1.

Vertical motions are calculated simultaneously with horizontal motion with an initial condition that $z(0)=1$ and $dz(0)=0$, where z is the vertial displacement; the results are shown in Fig. 5.

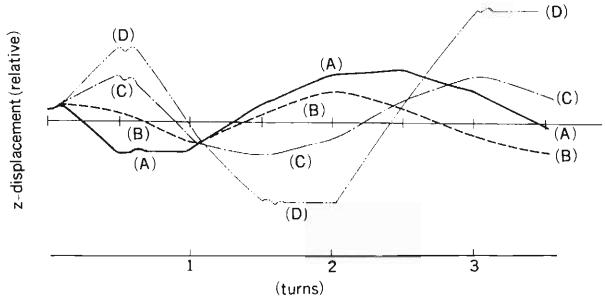

(A),(B),(C),(D) : starting phase; see Table 1.

Fig. 5. Calculated vertical orbit.

The vertical focusing in the sixth harmonic mode is, for most phases, stronger than in the fourth harmonic mode; however, it also shows stronger phase dependence. It is necessary to shift the RF phase towards the declining phase of the cosine; this means that a specific range of the starting phase should be selected.

These results will be applied to acceleration of N ions in the Baby Cyclotron. Until we put the sixth harmonic acceleration mode into practice, following problems should be solved. Both sixth and fourth mode acceleration are realized by use of the same puller, dee, and dummy dee except for ion source position and relative magnetic field distribution.

Reference

1) J.M. van Nieuwland and N. Hazewindus: *Philips Res. Rep.*, **29**, 528 (1974).

RIKEN Accel. Progr. Rep. 19 (1985)

V-18. Proposal of Synchrotron Radiation Source

M. Hara, T. Wada, and H. Kamitsubo

The synchrotron radiation source provides intense, polarized, and continuously-tunable radiation in a wide range of wavelength. The photon beam is used in a variety of fields such as physics, chemistry, biology, engineering, medicine, and agriculture. Synchrotron radiation (SR) is becoming an important tool in many branches of science, especially in interdisciplinary fields. In Japan, the Photon Factory at KEK[1] is only facilities that can provide hard X-ray as SR, and it has made a remarkable success. Recently, insertion devices such as wigglers or undulators have rapidly been developed and radiations from these insertion devices are becoming more important than that from a bending magmet. In the future, more demands are expected on the radiation with higher energies and higher intensity. Now, we should have a plan to construct new SR facilities.

There are three reasons favorable to construct SR facilities in RIKEN. Firstly, RIKEN has a tradition as a pioneer in the field of accelerator in Japan. We have made four cyclotrons and one heavy-ion linac.[2] Now we are constructing a ring cyclotron[3] that is a first class heavy-ion cyclotron in the world. We have enough potential and excellent staff to construct SR facilities. Secondly, in RIKEN, basic and application research in physics (nuclear, material and applied), chemistry, pharmacology, biology, agriculture, medicine, and fundamental technology are treated. Active cooperation is expected in the design and use of SR. Thirdly, all the accelerator facilities in RIKEN are opened to researchers of private companies, universities, and research institutes in the world.

(1) An Outline of the Facility

Proposed general facilities are composed of a 6 GeV main storage ring, a booster synchrotron, a 1.5 GeV storage ring, a 1.5 GeV injector linac, a positron production linac and high energy electron beam utilization facilities including a pulse stretcher ring and spectrometers.

1) 6 GeV main ring

Energy of the main ring is determined so that photons in a wavelength range from submillimeter to 0.1 A can be used from radiation with a bending magnet. The wavelength of 0.1 A comes from the K-absorption edge of uranium. The specification of the 6 GeV ring is:

Energy 6 GeV
Current 200 mA
Circumference about 1,000 m

In order to get stable photon beams without serious ion-trapping instability, positrons can be stored and a full energy injection system should be adopted. Many long free spaces are provided and cares are taken to the flexibility of a lattice.

2) 1.5 GeV ring

The small ring for XUV is:

Energy 1.5 GeV
Current 300 mA
Circumference about 150 m

Not only electrons but also positrons can be stored, and lines for wigglers, undulators, and free electron lasers are also provided.

Both rings are to be designed to get photon

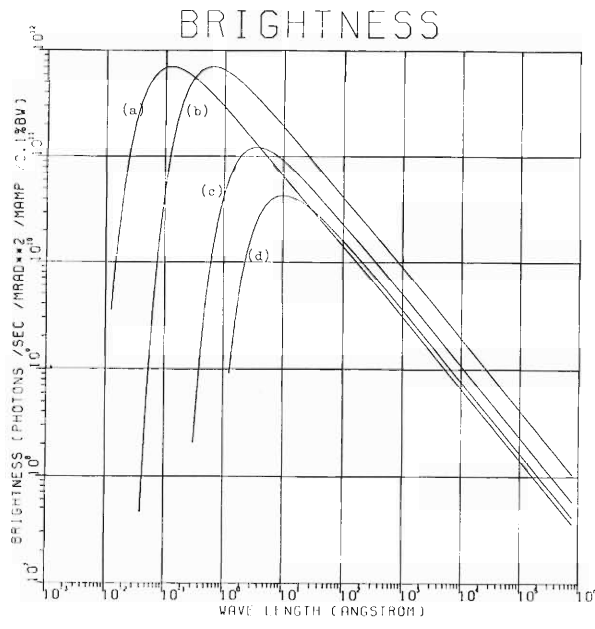

Fig. 1. Spectral brightness of synchrotron radiation. (a) 6 GeV ring, $B_0=5.0$ T, wiggler; (b) 6 GeV ring, $B_0=1.0$ T, dipole magnet; (c) 2.5 GeV ring, $B_0=1.0$ T, dipole magnet (Photon Factory at KEK); (d) 1.5 GeV ring, $B_0=1.0$ T dipole magnet.

beams with high brilliance and high stability. The spectral range and brightness of the sources are given in Fig. 1. Not only ordinal radiation courses but also undulator courses for a free electron laser (FEL) are inserted. High energy monochromatic and polarized γ-ray using inverse Compton scattering of laser light with high energy stored electrons (positrons) is used.

3) Booster synchrotron

The booster synchrotron is used to full energy injection to the 6 GeV ring.

4) 1.5 GeV linac

This is an injector to the 1.5 GeV SR ring and also to the booster synchrotron. This injector has two preinjectors: one is 5 MeV electron linac and the other is 250 MeV positron linac. The beam is used also for nuclear physics. The specification of this linac is:

Energy	(no load)	2.0 GeV
	(100 mA)	1.5 GeV
Current		100 mA
Pulse width		0.2-1.0 μs
$\Delta E/E$		about 1%
repetition rate		50 Hz

5) Positron production linac

This is composed of two parts. One is an electron linac to produce positrons and the other is to accelerate positron beams. Their characteristics are:

	e^-linac	e^+linac
Energy	300 MeV	250 MeV
Peak current	5 A	5 mA
Pulse width	3-20 ns	3-20 ns
Repetition rate	50 Hz	50 Hz
Frequency	3 GHz	3 GHz

6) Injector utilization facility

Efficient use of injectors are also considered. A positron beam is used to be transported to the positron utilization laboratory. A low energy intense positron beam is useful in materials science, especially to diagnostics and characterization of materials. A high energy electron beam is also used for nuclear physics with a pulse stretcher, spectrometers, for pulsed neutron source, or for meson production.

References

1) H. Huke, N. Kajiura, Y. Kamiya, N. Kanaya, T. Katsura, M. Kihara, H. Kitamura, H. Kobayakawa, M. Kobayashi, T. Koide, C.O. Pak, S. Sato, S. Shibata, T. Yamakawa, and Y. Yamazaki: *IEEE Trans. Nucl. Sci.*, **NS-30**, 3130 (1983).
2) M. Odera, Y. Chiba, T. Tonuma, Y. Miyazawa, T. Inoue, T. Kambara, M. Kase, T. Kubo, and F. Yoshida: *Nucl. Instrum. Methods*, **227**, 187 (1984).
3) S. Motonaga: *IEEE Trans. Nucl. Sci.*, **NS-32**, 2712 (1985).

RIKEN Accel. Progr. Rep. 19 (1985)

V-19. Characteristics of Radiofrequency Field in an Alvarez-Type Resonator Having Chain-Like Electrodes with Varying Cell Length

M. Odera and M. Hemmi

Characteristics of the electromagnetic field in a chain electrode resonator having constant cell length have been reported previously.[1] In order to investigate an effect of uneven cell lengths on the RF field, a model having a varying cell length satisfying a synchronous acceleration condition was constructed in June 1985. Figure 1 shows a photograph of its electrode array redesigned from that of the former model to facilitate change in cell geometries. A cell length of 60 mm at injection and a mean acceleration gradient of 1 MV/m along the accelerator axis were assumed. This cell length at injection corresponds to the velocity of injected ions of 6 % of the light velocity or energy of 1.7 MeV/n for acceleration frequency of 300 MHz. A charge to mass ratio of 1/2 was assumed to give a notable change in cell length by acceleration. The last cell length was 66.29 mm.

Measured gap voltage decreases with acceleration as shown in Fig. 2. The distributions shown

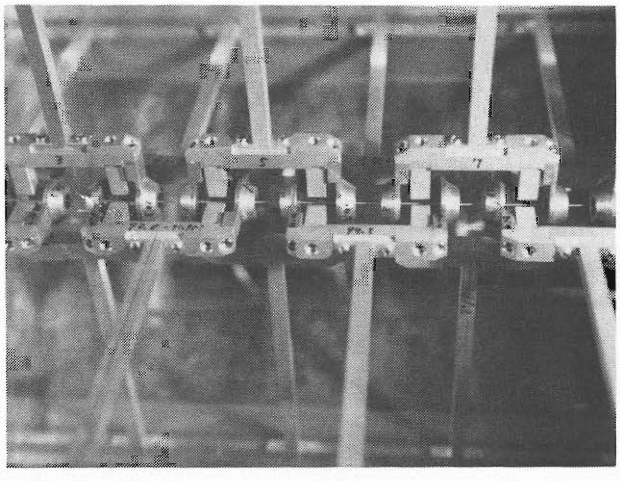

Fig. 1. Electrode array of the new acceleration model.

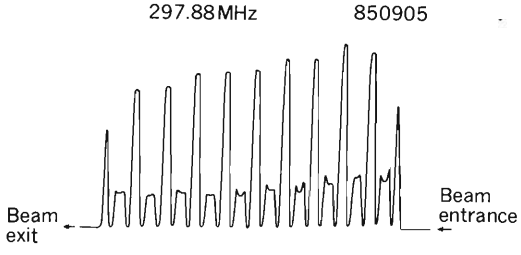

Fig. 2. Distribution of acceleration voltage in the gaps of the acceleration model. It is really a distribution of voltage squared. Distributions in the other figures are also squared one. Note that peak voltage decreases towards exit end.

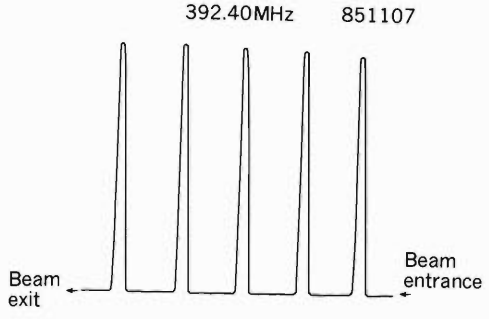

Fig. 3. Distribution of gap voltage when all horizontal components are removed. It increases towards exit end and shows characteristics of an Alvarez resonator.

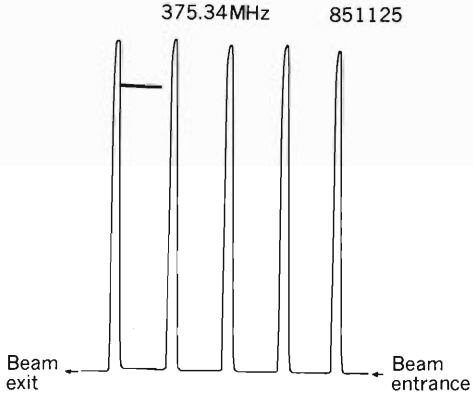

Fig. 4. Gap voltage distribution when T-shaped horizontal stems are fixed only on the right-hand side (viewed toward downstream) of the resonator. Neither semi-circular forcusing electrodes nor transversal plates with acceleration aperture are attached to the horizontal stems. Peak voltage increases towards exit end and still shows Alvarez tendency.

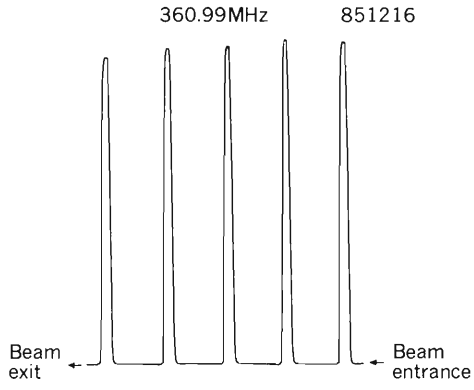

Fig. 5. Gap voltage distribution when the horizontal stems are fixed on the both sides of the resonator. No focusing electrodes nor transversal plates are attached to the horizontal stems. Distribution shows a slight decrease, contrary to the Alvarez-type tendency shown in Fig. 4

in Fig. 2 and in the other figures are those of the bead pulling measurements and represent square of voltage distributions. The decreasing gap voltage is contrary to that for an usual Alvarez structure, where the gap voltage increases with cell length when a ratio of gap to cell length and transversal dimensions of the cavity were kept constant. Similar voltage decreasing tendency was also observed in a model study of the RILAC.[2] The comparison suggests that field characteristics inside the chain structure resemble that of a single element resonator rather than a system composed of a number of weakly coupled resonators having the same resonant frequency, such as an Alvarez structure. In spite of the seeming similarity, the chain resonator does not show characteristics of the coupled resonator system of the Alvarez cavities.

Initially, the gap distances of the acceleration model were different for each cell to keep a ratio of gap to cell, g/L, constant as is usual for Alvarez linacs. The distances were readjusted for all gaps to be the same so that the resonant frequency of each cell should decrease with increase in the cell length more rapidly than that in the case of the constant g/L ratio. This modification still gave no increasing distribution towards downstream which should be expected for a coupled resonator system.

On the other hand, it is well known that the field distribution in the Alvarez cavities can be tuned by introducing elements which increase coupling between neighboring cells. A multi-stem structure of Giordano[3] and a post-coupler structure of Swenson[4] are such structures and used

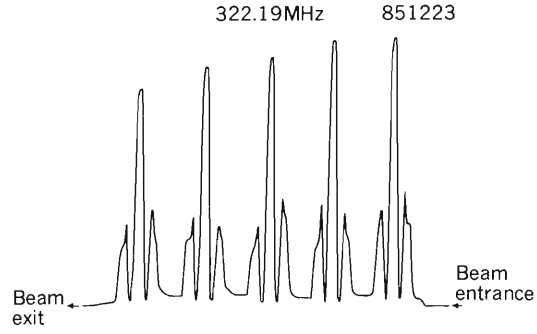

Fig. 6. Gap voltage distribution when all the focusing electrodes are set in their proper positon but transversal plates are not set for the horizontal member.

widely in the modern Alvarez linacs. By choosing suitable parameter values, the distance of a nearest undesirable resonant frequency from a frequency of a wanted mode can be made large and the field distribution becomes relatively insensitive to geometry errors. The resonator is said "stabilized" in such case. In our chain structure where the horizontal and the vertical members are interlaced, coupling strength may be too strong to leave each cell to have "eigen" frequency. Notion of the coupled resonator system may not be applicable to the chain structure.

In order to test this supposition, the original schedule of test acceleration of electrons was postponed to study this problem of field distribution further.

Firstly, the horizontal electrode assembly was removed so that the structure configuration becomes that of Alvarez's. For the sake of simplicity of assemblage and alignment of the resonator after each alteration of geometry, the distances were kept the same for all the gaps hereafter. Figure 3 shows measured gap voltage distribution which increases with an increase in cell length. With vertical members only, field characteristics resumes those of the Alvarez as expected. As seen from Fig. 3, there is no electric field inside square frame made of aluminum bars having a 10×10 mm cross section. The frame perfectly shields ions traveling inside the frame from the RF field, in spite of its structure open on both sides of the frame. For this configuration, deformation of the TM 010 field distribution near the central axis by the frame is different from that by the cylindrical drift tube and may have introduced some difference in the coupling strength of the cells from that in the Alvarez. But it does not seem large enough to make distribution different at least.

Next, only the right-hand side of the horizontal

stems, viewed toward downstream, was attached. Focusing electrodes were removed to leave only weak coupling between neighboring cells of the vertical member *via* horizontal stems.

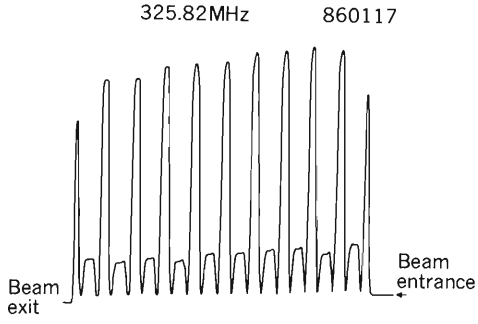

Fig. 7. Gap voltage distribution when all the focusing electrodes are removed from the vertical as well as horizontal stems. Transversal plates and acceleration electrodes are in each positions. Peak voltage behavior is similar to that of Fig. 2.

Figure 4 gives gap voltage distribution thus obtained. There is no substantial difference from the distribution shown in Fig. 3 where the horizontal stems are missing.

Then, left-hand side horizontal stems without the focusing electrodes were also added. The gap field showed a decreasing tendency with increase in cell length as shown in Fig. 5. The presence of the horizontal stems on both sides changed resonator behavior from that of Alvarez-type to the single element resonator type. Probably, tuning of the coupling strength in fine steps should have been tried to find out point of transition between increasing and decreasing distributions. However, the model is not provided with such tuning mechanism at present.

Furthermore, the semi-circular poles for focusing were attached to the horizontal stems to increase coupling strength between cells. Figure 6 shows a distribution for this case. Sag of the distribution becomes more pronounced and the

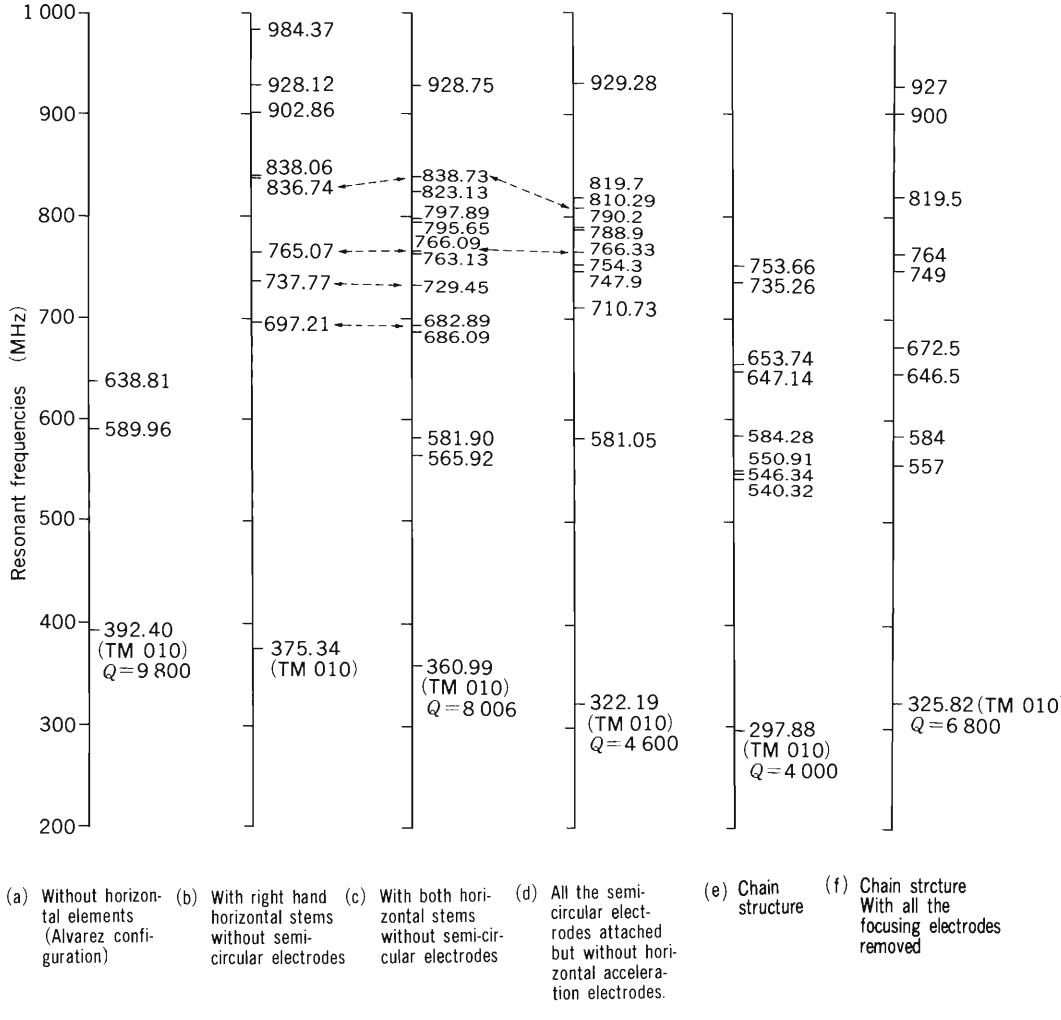

Fig. 8. Shift of resonant frequencies by loading of electrodes of the resonator in various ways. Dotted lines connect frequencies which show similar gap voltage patterns.

resonant frequency much decreases by increase in capacitive load.

Figure 7 shows a gap voltage distribution for the chain structure with all the focusing electrodes removed from vertical as well as horizontal stems. Transversal plates which hold acceleration electrodes are in each position. The number of acceleration gaps is the same as that of Fig. 2 and an overall tendency of the voltage distribution is similar, though resonant frequency is much higher.

Figure 8 shows the change in resonant frequency with changes in the electrode configurations. Q-values as well as frequencies decrease with an increase in coupling between neighboring cells. Though comparison was not made thoroughly, frequencies which were found to have the same voltage distribution pattern were connected by dotted lines. Further study of the characteristics of RF field in the chain structure is in preparation.

References

1) M. Odera and M. Hemmi: *Sci. Papers I.P.C.R.*, **79**, 51 (1985); M. Odera, M. Hemmi, and A. Goto: *IEEE*, **NS-32**, 3222 (1985).
2) M. Odera, Y. Chiba, M. Hemmi, Y. Miyazawa, T. Tonuma, T. Inoue, T. Kambara, M. Kase, M. Yanokura, T. Kubo, E. Ikezawa, T. Chiba, A. Shimamura, and F. Yoshida: *Sci. Papers I.P.C.R.*, **79**, 34 (1985).
3) S. Giordano: *BNL*, **AGCSD-7** (1966); S. Giordano and J.P. Hannwacker: *IEEE*, **NS-14**, 290 (1967).
4) D. A. Swenson, E. A. Knapp, J. M. Potter, and E. J. Schneider: Proc. 6th Conf. on High Energy Accelerators, Cambridge, p. 167 (1967).

RIKEN Accel. Progr. Rep. 19 (1985)

V-20. Development of an Electrostatic Quadrupole Lens Having Beam Steering Capability

M. Hemmi

At present, an effort is being paid to increase intensity of beam accelerated by the RILAC. Ion source improvement[1] and modification of the beam handling elements between the ion source and the entrance to the accelerating column of the injector are being made for that purpose. An electrostatic quadrupole doublet lens (ESQ) was fabricated and recently set at the exit of the ion source chamber to investigate its performance and reliability. Preliminary results of investigation were given in this report.[2] The device works very well and the beam intensity was increased by a factor of 2-5 for Ar^{2+} ions extracted at 7 kV on the ion source test bench. Then the device was

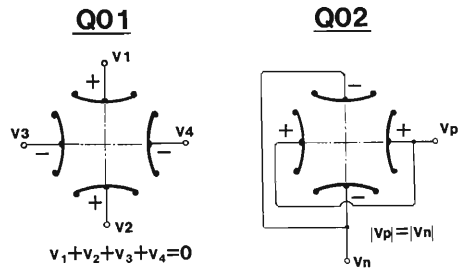

Fig. 1. Asignment of polarity and adjustment of voltage difference between paired electrodes of the electrostatic lens (ESQ).

Table 1. Specifications of the ESQ/EST device.

Total length: 200 mm (190-207 with bellows)
Size of vacuum flange: NW-63
Aperture (A): 63.5 mm (2.5″)
Curvature of electrode surface: 80 mm R (1.25 A)
Length of the electrodes (L): 35 mm
Electrode potential (V_Q): 0-5 kV
Voltage gradient (G): 0-1.57 kV/cm
$G \times L$: 0-5 kV
Pot. difference for steering (V_{st}): 0±1 kV
Distance between electrodes: 56 mm
Power supply
Voltage: 0-6 kV (6-channel)
Stability: 10^{-4}
Dimension: EIA-19″, 2U (88 mm)

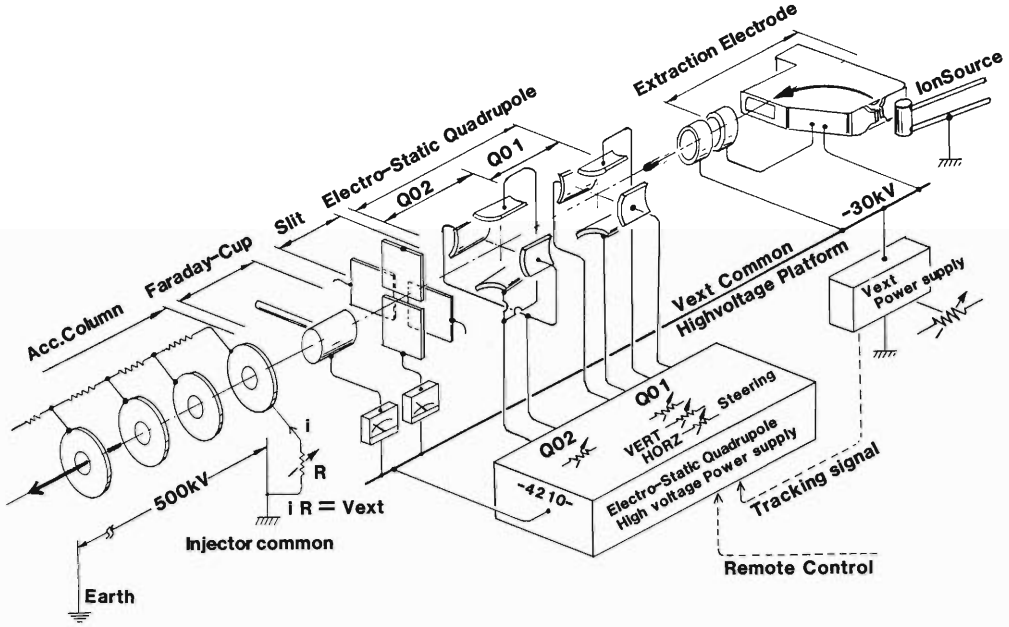

Fig. 2. Layout of the beam handling equipments including the ESQ/EST device in the ion source housing on the high voltage terminal.

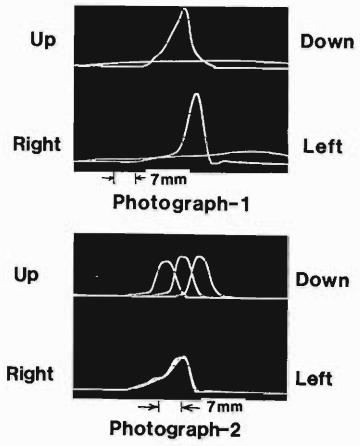

Fig. 3. Effects of the ESQ/EST device. Photograph-1; Flat profile is for beam without voltage on the ESQ electrodes and peak is for the case when voltage is on. Photograph-2; Beams deflected by use of uneven voltage on the electrodes as EST function. Little deterioration of the beam profile is observed within the voltage difference used.

installed in the ion source housing on the high voltage terminal. The intensity of $^{40}Ar^{4+}$, for example, was increased by a factor of 3 on the target.

The ESQ features a double role of a focusing lens and a beam steering element (EST). The capability shows a better overall performance over the usual ESQ alone device considering space it occupies and cost, though the capability may not be optimal compared with a larger system composed of separate ESQ and EST.

Compatibility of the two functions was studied experimentally. Polarity asignment and magnitude adjustment of voltage applied to each electrode of the ESQ/EST device are shown in Fig. 1.

Q_{01} plays a role of EST by given voltage difference between paired electrodes, as $V_1 \neq V_2$, $V_3 \neq V_4$ while maintaining $V_1 + V_2 = \text{const}$, $V_3 + V_4 = \text{const}$, and $V_1 + V_2 + V_3 + V_4 = 0$ to preserve approximate quadrupole characteristics. The voltage allotment is made by using an arithmetic circuit based on operational amplifiers. Table 1 gives geometrical and electrical parameters of the ESQ/EST assembly. Its layout among the beam transport equipments between the ion source and the accelerating column is shown in Fig. 2.

The first photograph of Fig. 3 shows beam profiles measured at the position corresponding to the entrance of the accelerating column on the ion source testing stand. An almost flat profile is for beam without applied voltage on ESQ and another showing a peak with focusing field. A beam intensity measured by a Faraday-cup at the position was found increased by a factor of 2 -5 by use of the ESQ. The second photograph gives an example of the ESQ functioning as EST. As seen from the photograph, no significant deterioration of the focusing effect was generated by use of uneven voltage within 10% for the ESQ electrodes in order to steer the beam.

Structure and outer appearance of the ESQ/EST device are shown schematically in Fig. 4. The beam trajectory controlled by this device

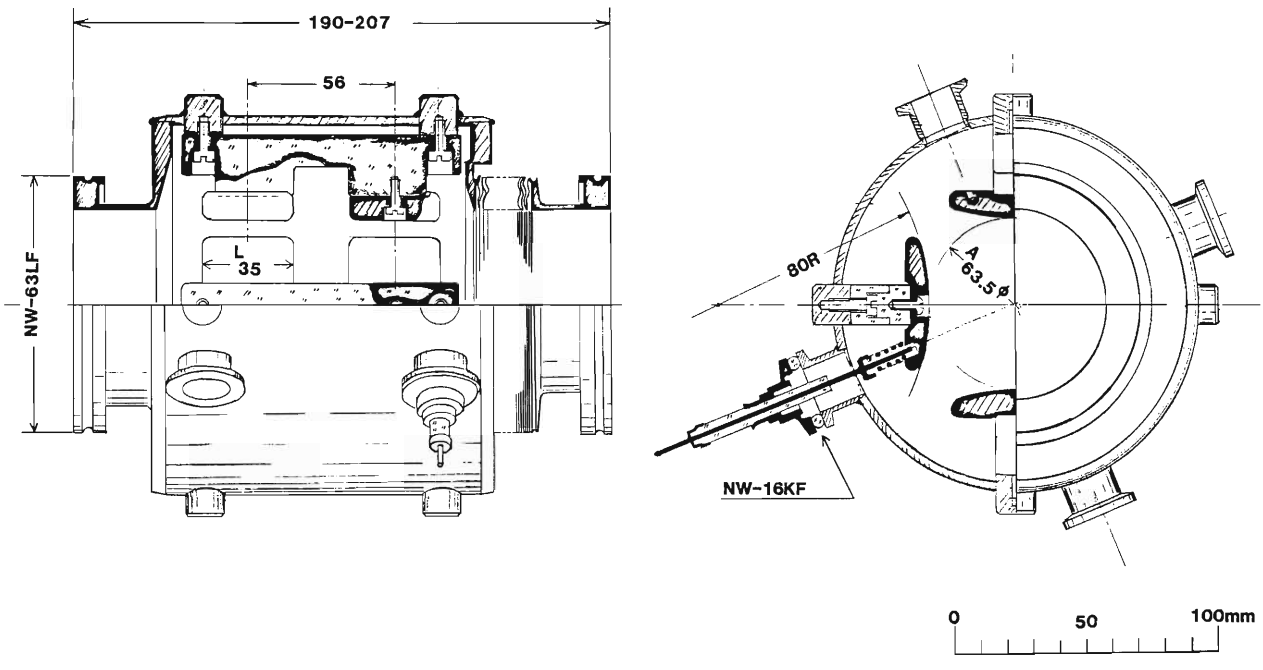

Fig. 4. Construction of the ESQ/EST device.

can made constant of the ion species by choosing voltage on the electrodes always proportional to the beam extraction voltage of the ion source as predicted from the theory of electrostatic lens. Therefore, installation of the lens system adds no surplus load to linac operators by keeping the proportionality principle. A tracking circuit to fulfil this condition is under preparation. It is expected that, after completion of the circuit, functioning of the ESQ/EST device becomes fully automatic and the beam keeping under computer control can be easier.

References

1) Y. Miyazawa, M. Hemmi, T. Chiba, and M. Kase: p. 212 in this report.
2) Y. Miyazawa, M. Hemmi, T. Chiba, and M. Kase: Fig. 1, p. 212 in this report.

RIKEN Accel. Progr. Rep. 19 (1985)

V-21. Non-Destructive Measurement of Beam Intensity

M. Kase and E. Ikezawa

During operation of an accelerator, especially a multi-stage accelerator, it is often necessary for operators to obtain the information about beam intensities at several positions along a beam line. For this purpose, Faraday cups equipped with an electric or magnetic suppressor for secondary electron emissions have been installed on each acceleration stage of the linac. However, the beam destructive measurement with these probes needs several-step operation, *i.e.* selection of the probe, actuating and setting it on the beam, reading beam currents on it, and, finally, removing it from the beam line. Sometimes operators have to repeat these procedure several times. It takes much time and shortens the life of welded bellows used as a vacuum seal of the probe. And, in the course of experiments carried out at the end of the beam line, such destructive measurements should interrupt them. Therefore the non-destructive measurement of beam intensity is desired for a multi-stage accelerator having a long beam line like the RIKEN linac-RIKEN Ring Cyclotron facilities.

Among several methods applicable to the non-destructive beam-intensity measurement, we have chosen a method using the ionization process of a beam with residual gas inside a beam pipe, because its measurement principle is very simple and needs no special electronics. It can be also said that this method is suitable for a heavy-ion accelerator because of the large ionization cross sections of heavy ions.

We made a prototype of the non-destructive-type beam-intensity monitor, installed it in the RILAC beam line, and carried out some preliminary tests. Schematic drawings of the monitor are shown in Fig. 1. It consists of a pair of parallel plate electrodes, between which the beam passes through. One electrode (B) is biased at a positive voltage, and the other (A) is connected, *via* a vacuum feed through, to a high-impedance input of electrometer and kept at the ground potential. The electrons and ions produced between the two electrodes in the ionization process with the residual gas are collected efficiently in the relatively low electric field, since they have generally very small momentum and their density is so low that no appreciable recombination processes take place. In practice, the electric current I_i obtained from electrode (A) changes very slowly for the bias voltages over +100 V.

The signal I_i given by

$$I_i = KI_b\sigma_i pLA, \tag{1}$$

where K is the constant (3.5×10^{16}[Torr^{-1} cm^{-3}]), I_b the beam current in particle amperes, σ_i the cross section of ionization of ions in the beams with residual gases, p the vacuum pressure and L the collision length, that is nearly equal to the length of the electrode, l. A factor of A is the enhancement factor for the electron emissions by slow ion bombardment on surface of the elec-

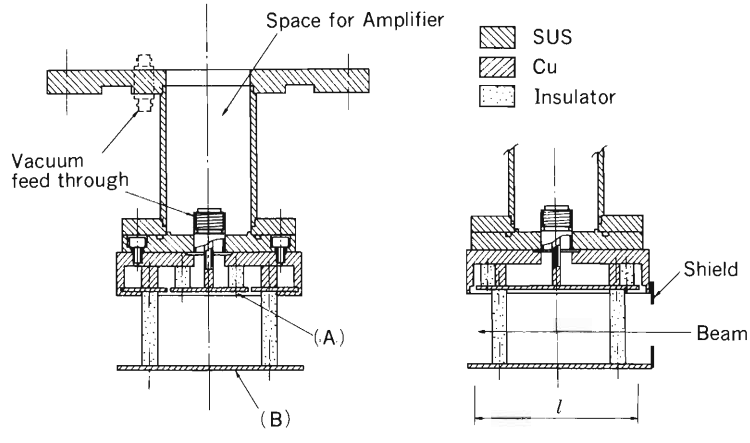

Fig. 1. Schematic drawings of the non-destructive-type beam-intensity monitor.

Table 1. Sensitivity coefficients of the intensity monitor for Ar^{4+} beam.

Acceleration stage	Beam energy [MeV/u]	S [$Torr^{-1}$]
Injector	0.04	2.3×10^{2}
Cavity 1	0.20	2.2×10^{2}
2	0.56	2.1×10^{2}
3	0.83	1.2×10^{2}
4	1.1	8.5×10^{1}

trode (A).

It is difficult to estimate the ionization cross section σ_i accurately, which depends on the accelerator conditions, such as ion species, beam energy, and the gas contents inside the beam pipe. Furthermore, the accurate estimations of L and A are not easy. Therefore a calibration is made using a Faraday cup and a vacuum gauge which are installed near to the monitor. Once I_b and p are obtained simultaneously with these instruments, the sensitivity coefficient, S ($=K\sigma_i LA$), is given from Eqn.(1). Then, the beam intensity I_b can be obtained from a relation of $I_b=I_i/Sp$ using the measured I_i and p values.

The values for S obtained experimentally using the RILAC Ar^{4+} beam are listed in Table 1. The coefficient S becomes smaller and smaller as the beam energy increases. In general, σ_i has a large value for the RILAC injection energy (20-110 keV/u) and becomes small as the beam energy increases.

In a long duration, the gas contents may change to some extent, causing the variation in S. However, if an ionization pressure gauge is used as a vacuum gauge, this effect is partly cancelled out, because the ionization cross sections of 100 eV electron and 100keV/u ions vary in a similar way. It is better, however, to repeat the calibration periodically

This measurement is very sensitive to the effect of a stray beam which hits directly upon the electrode surface. It causes a large error in the measurement. A shield plate that prevents such stray beam from hitting on the electrode must be set in front of a sensitive region.

The beam, during traversing through the prove, is bent somewhat by the electric field. This effect is important when the beam energy is low, *i.e.* in the injection beam line of the RILAC. For example, when the injection voltage is set at 400 kV, the bending angle is as small as 0.3 mrad. The effect can be well compensated by a steering magnet.

The small change at the bias voltage over 100 V is probably due to the change in the factor A. It is expected that the factor A is increased by proper selection of the material of the electrode surface and its structure. If A is large, the signal handling becomes easy.

RIKEN Accel. Progr. Rep. 19 (1985)

V-22. RILAC Ion Source

Y. Miyazawa, M. Hemmi, T. Chiba, and M. Kase

Beam intensities of Ne, Ar, Kr, and Xe ions obtained from the PIG ion sources of the linac have been measured for two types of anode bores. The purpose is to improve the PIG sources in supplying more highly-charged heavy ions for the linac. Figure 1 shows a schematic plane view of the ion source facilities installed on a high voltage platform. The test facilities used for these measurements were also improved this summer.

As illustrated in Fig. 1 an electrostatic quadrupole doublet (e.s.q.d.) was installed instead of an einzel lens to focus beams at the Faraday cup; beam intensities at the Faraday cup were increased up to three times that obtained without the e.s.q.d.

The source anode is made of copper, which is cooled with water, and has an bore of 8 mm in diameter. The anode slit of 1 mm in width and 20 mm in height, through which ions are extracted, is made of molybdenum and protrudes 1 mm into the arc bore. The puller electrode, at negative potential (30 kV max.), consists of two replaceable molybdenum blades located 2.5 mm from the anode slit and spaced 2 mm apart. The beam is bent at an angle of 120°in the source magnet as shown in Fig. 1 and the currents for various charge state are collected by a Faraday cup with an entrance diamater of 28 mm.

The spectra of beams of Ne, Ar, Kr, and Xe have been measured for the PIG sources with anode bores of 8 and 10 mm by changing the extraction voltage. The magnetic field was 3-5 kG and the extraction voltage was varied from 0 to 25 kV. Figure 2 shows the charge state spectra for Ne, Ar, Kr, and Xe ions from the source with an anode bore of 10 mm. The arc discharge is in DC operation. The maximum source output currents is limited by the drain current of 30 mA of the extraction power supply. A large part of the drain current is induced when low charge state ions drawn from the ion source hit the extractor surface. Gas flow in the ion source is subsequently reduced to the minimum value required to maintain stable arc discharge and to maximize the high charge states of ions. Figure 3 shows the charge distributions for the both types of anode bores. From these measurement, it can be said that the beam intensity increases with increasing anode bore-diameter. For large anode bores, the stable arc discharge have been obtained in low magnetic field with low gas flow ratings.

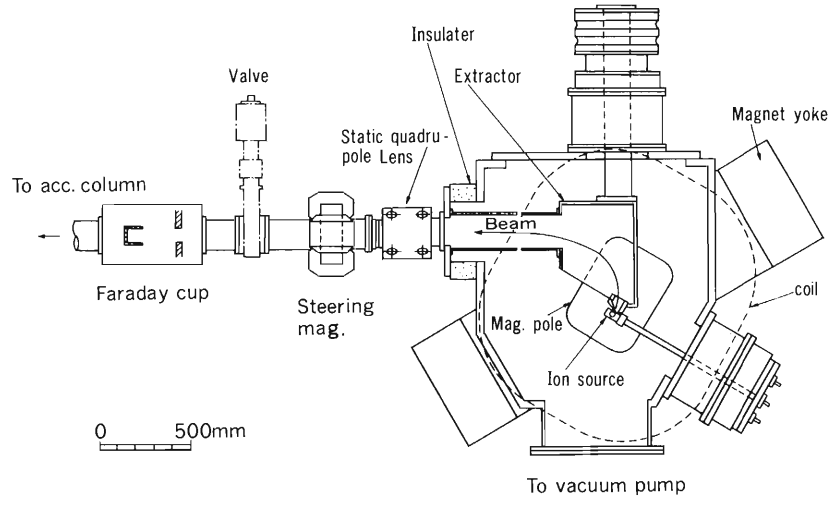

Fig. 1. Sectional view of linac ion source, showing the beam transport system.

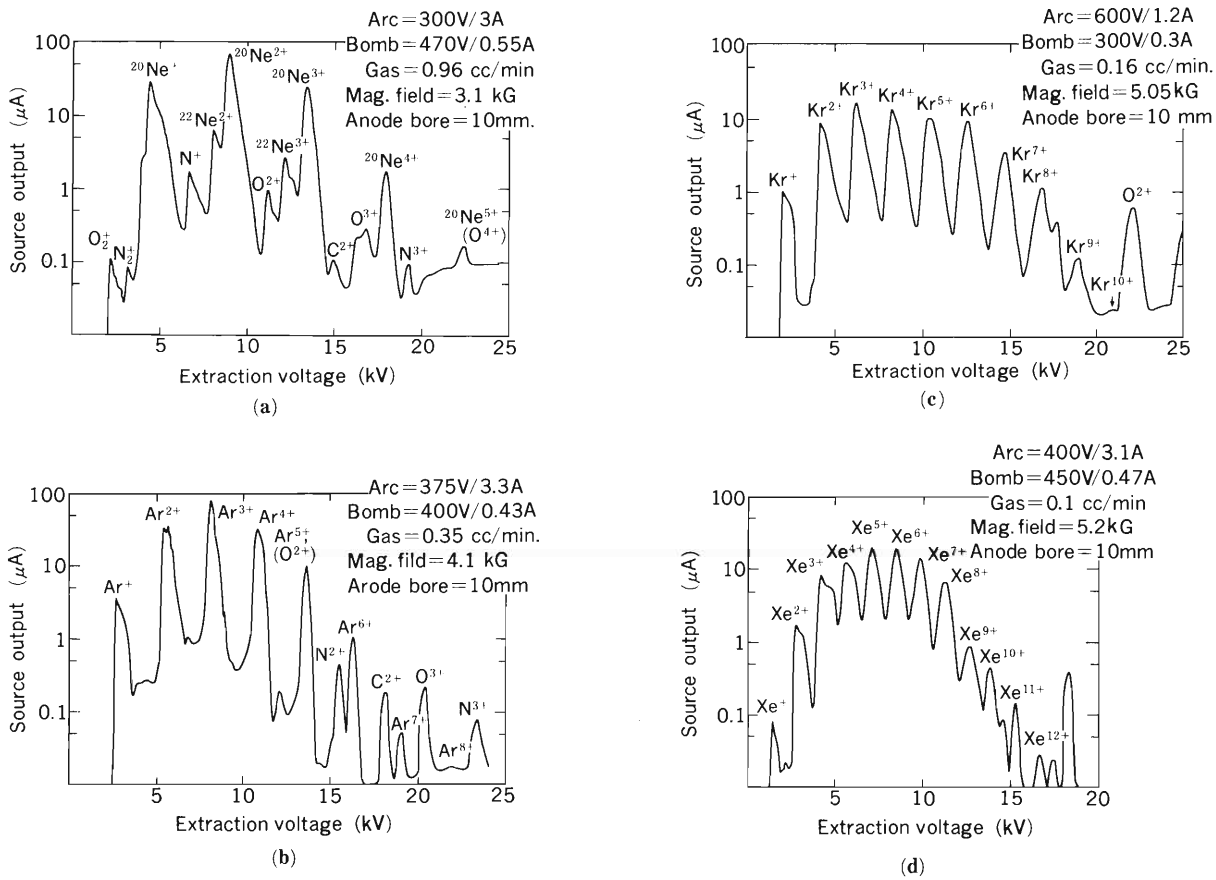

Fig. 2. Charge state spectra for Ne, Ar, Kr, and Xe ions obtained with an anode bore of 10 mm in DC arc operation. (a) Charge state spectrum in neon gas discharge, (b) Charge state spectrum in argon gas discharge, (c) Charge state spectrum in kripton gas discharge, (d) Charge state spectrum in xenon gas discharge.

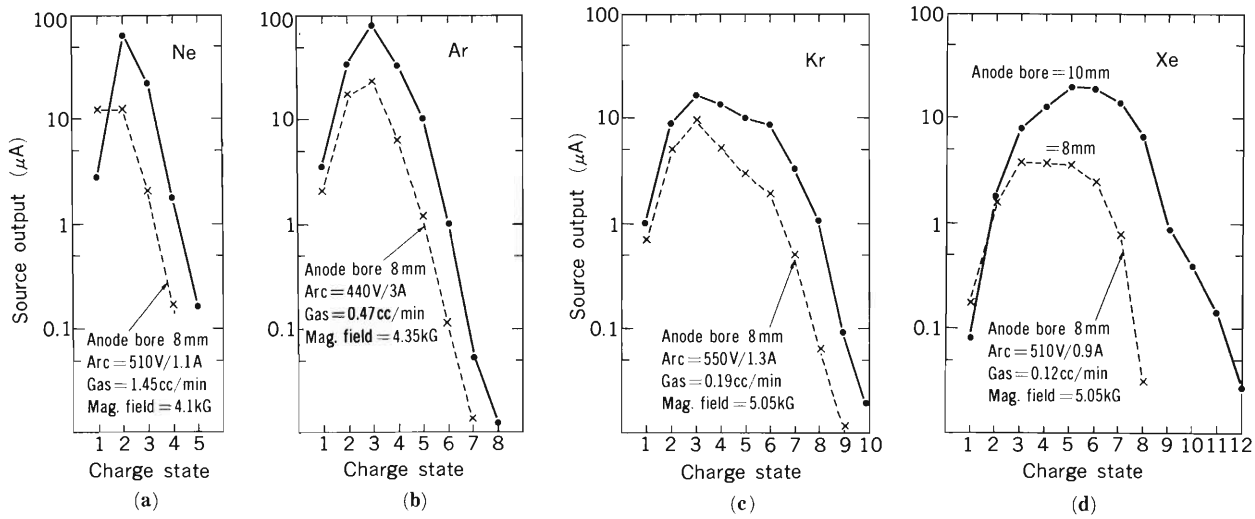

Fig. 3. Charge state distributions for Ne, Ar, Kr, and Xe ions in a DC operation of arc discharge. Solid line represents that for an anode bore of 10 mm and dotted line for 8 mm. Arc condition for solid line is given in Fig. 2.

RIKEN Accel. Progr. Rep. 19 (1985)

V-23. Test of the RIKEN ECR2

M. Yanokura, S. Ishii, and Y. Sakamoto

Construction of the RIKEN ECR 2 ion source shown in Fig. 1 was completed in June, 1985, and preliminary tests have been started. The ECR2, designed to operate at a frequency of 2.45 GHz, consists of two stages, and is similar to MINIMAFIOS[1] with respect to size. The first stage, which supplies plasma to the second stage to facilitate maintenance of ECR plasma and further charge stripping of the ions in a high vacuum-stage, was initially operated in an over-dense mode[2]. A coaxial antenna was used to inject microwave into the first stage located in an axial magnetic field of less than 0.5 kG. The plasma was controlled by adjusting the microwave power-level and by gas pressure variable over the range of 10^{-3}-10^{-4} Torr. The microwave power injected into the first stage was obtained from the main supply for the second stage by use of a power divider. The second stage is separated from the first one by a small piece of tubing of a small diameter for effective differential pumping. Pressure in the second stage was maintained at 10^{-5}-10^{-4} Torr during source operation. Since this pressure range, however, is not sufficiently low for efficient production of highly charged ions, the first stage and the differential pumping section were modified to improve the second stage vacuum.

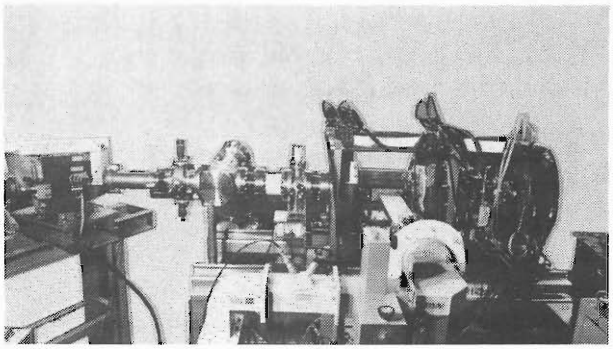

Fig. 1. Photograph of the RIKEN ECR2.

In the second stage, electrons confined in a minimum-B field were heated by resonant absorption of the microwave injected radially. The minimum-B structure was produced by superposition of an axial mirror field and a radial hexapole field. Three conventional water-cooled solenoids were used to establish the axial magnetic field. The hexapole field was produced by an assembly of $SmCo_5$ permanent magnets positioned on the cylindrical vacuum wall of the

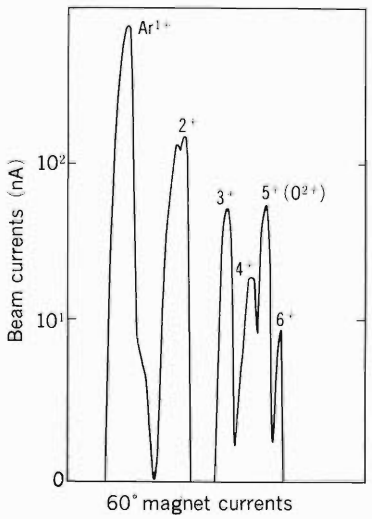

Fig. 2. Charge distribution of the extraced Ar beam. Input microwave power is about 200 W and vacuum pressure of the second stage is 1.2×10^{-4} Torr. Extraction high voltage is 7 kV.

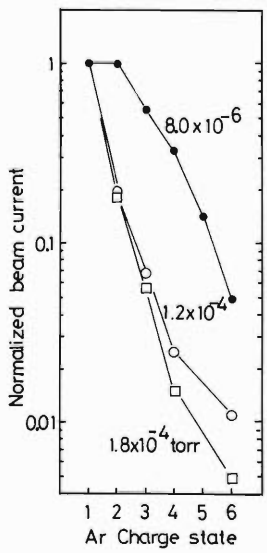

Fig. 3. Vacuum pressure dependence of charge distribution for extracted Ar beam.

second stage. The permanent magnet assembly was cooled with water circulated around the same vacuum wall.

The source is divided into three sections, each of which is supported separately with precision tracks. The three solenoid coils are supported with the same tracks and freely movable to change the axial mirror ratio of the second stage. Ion extraction was conducted by using the three-element extraction electrode which includes an einzel lens. The position of the extraction electrode can be varied by means of a welded bellow mechanism. The extraction gap can also be varied with shims. The entrance slit assembly of the charge analysing system was located about 50 cm downstream from the source anode; the object-image distance for the 60° magnet was 106 cm. Two Faraday cups were used to measure beam currents: one, which is located in the straight section downstream of the magnet, is for total extracted currents measurement; the other behind the exit slits is for charge selected beam currents measurement.

The first result of operation of the ECR2 was not satisfactory; only few nA of Ar^{6+} was obtained as shown in Fig. 2. There are two main reasons for the unsatisfactory result. One is unfavorable pressure in the second stage. In operation, the pressure was around 10^{-5} Torr in which the recombination cross section becomes very large. Even if high charge state ions were formed, they would be degraded rapidly to low charge-state ions. The other reason is poor impedance matching between the plasma and the microwave antenna in the first stage. A large part of the injected microwave was reflected at the plasma surface. After improvement of the first stage and the differential pumping section, pressure of the second stage became around 10^{-6} Torr. Charge distribution of the extracted beams shifts to the high charge state as shown in Fig. 3. We are now planning to change geometry of the coaxial antenna, to minimize the reflection of injected microwave power.

References

1) R. Geller, B. Jacquot, and M. Pontonnier: *Rev. Sci. Instrum.*, **56**, 1505 (1985).
2) S. Ishii: *Sci. Papers I.P.C.R.*, **74**, 27 (1979).

RIKEN Accel. Progr. Rep. **19** (1985)

V-24. Characteristics of a Hot Plasma for Highly Charged Ion Source

S. Ishii, M. Yanokura, and Y. Sakamoto

Highly charged ions are produced in plasma by collision of hot electrons with atoms. To find optimum conditions for producing such ions we have set up a hexapole-mirror device eligible for plasma diagnostics. The device has been described previously in this report.[1),2)] Before extracting and analyzing ion beams, we examined plasma parameters of the hot plasma.

Both mirror and hexapole magnetic field strengths of the present device can be varied by changing driving currents. It is well known that the minimum-B fields such as a hexapole field are effective in stabilizing plasmas. To make sure the function of this device we produced dense plasma in the same way as described in Ref. 3 and injected it pulsedly to the hexapole-mirror field. Figure 1 shows floating potentials of a Langmuir probe and its ion saturation currents (a) without and (b) with the hexapole field. The stabilization effect is clearly demonstrated.

The plasma is round in cross section at the magnetic mirror where it is generated and is deformed as flowing down along the field lines of force. To take a sight of this behavior we measured radial density profiles by using two probes. Figure 2 shows an example of the measured radial density profiles together with a sketch of the cross-sectional view of the plasma and hexapole conductors. The experimental curves elucidate the asymmetrical shape of the plasma cross section.

Hot plasmas were generated by 2.45 GHz microwave, the resonance zone of which was located between the axial magnetic mirrors. Available power of this microwave was 4 kW. The density measurement was conducted by using a 35 GHz microwave interferometer and a probe located at the plasma edge ($r=43$ mm). The interferometric measurement provides only line densities without knowing radial profiles, while the probe measurement giving the profiles is possible only at low powers. Figure 3 shows dependences of the electron density of the edge plasma and the line density on argon gas pressure. Electron temperature determined by the probe measurement ranges from 5 to 10 eV.

Figure 4 shows the arrangement for hard

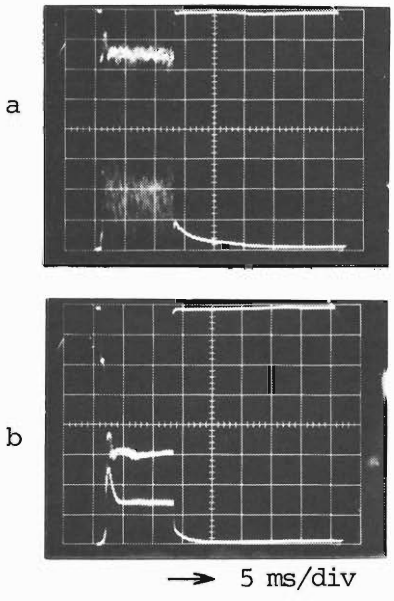

Fig. 1. Time variations of floating potentials (upper traces) and ion saturation currents (lower traces) of Langmuir probes without (a) and with (b) the hexapole field. The ordinates are in arbitrary scale. Experimental condition: microwave power (9GHz) = 2 kW, argon pressure = 4×10^{-4} Pa.

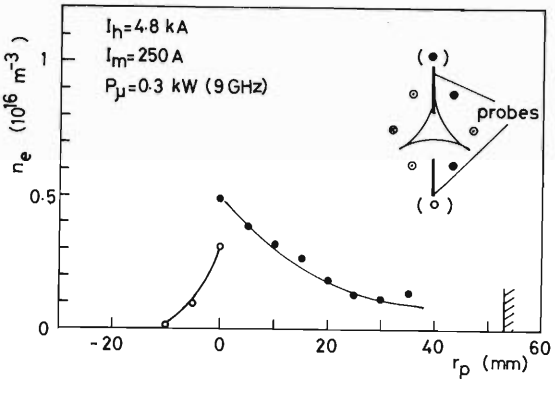

Fig. 2. An example of radial density profiles obtained with the Langmuir probes. The inserted sketch depicts the cross-sectional view of the plasma and location of the probes. Directions of the hexapole currents are indicated by enclosed dots and crosses around the plasma. Dark and light points in the experimental plots were obtained with the upper and lower probes, respectively.

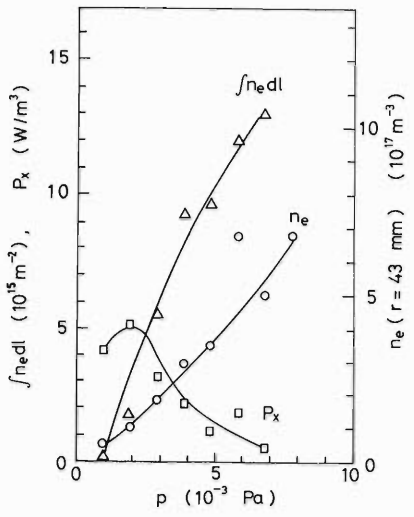

Fig. 3. Pressure dependence of electron density n_e, line density $\int n_e dl$, and hard X-ray power P_x of the hot plasma. Microwave power (2.45 GHz)=2 kW.

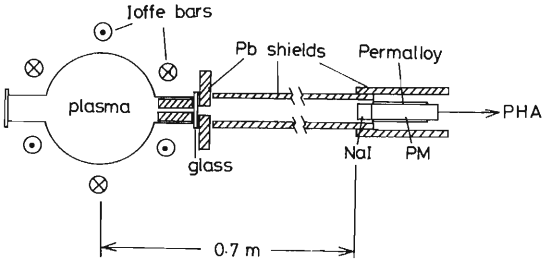

Fig. 4. Scheme of X-ray measurement. PM: photomultiplier, PHA: pulse height analyzer.

X-ray measurement. The view solid angle of the NaI scintillator is finely collimated by using a lead orifice so that the wall of the vacuum vessel is out of scope. An example of the X-ray spectra

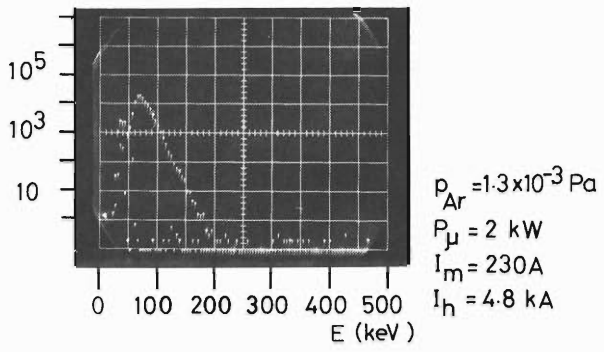

Fig. 5. Hard X-ray spectrum of the hot plasma. The ordinates indicate photon counts per second.

is shown in Fig. 5, which suggests that there exists a minority of electrons whose energy ranges up to 200 keV. The energy scale was calibrated with reference to a barium radioisotope Ba^{133}. As the soft X-ray range should be cut off by absorption of the view port and the detector housing of this arrangement, we tentatively took integrated radiation power over the hard X-ray range as a measure of power loading of the hot plasma. This quantity is shown in Fig. 3 as a function of argon gas pressure. Electron energy necessary for highly charged ions covers the soft X-ray range. A measuring equipment for the soft X-ray is urgently required to qualify the present plasma as a highly charged ion source.

References

1) S. Ishii, Y. Sakamoto, and M. Yanokura: *RIKEN Accel. Progr. Rep.*, **17**, 177 (1983).
2) S. Ishii, H. Amemiya, Y. Sakamoto, and M. Yanokura: *RIKEN Accel. Progr. Rep.*, **18**, 205 (1984).
3) S. Ishii: *Sci. Papers I.P.C.R.*, **74**, 27 (1980).

RIKEN Accel. Progr. Rep. 19 (1985)

VI. RADIATION MONITORING

1. Calculation for the Neutron Shielding Design of RIKEN Ring Cyclotron Facility

T. Shikata, N. Nakanishi, S. Fujita, and T. Kosako*

By using the neutron-photon multigroup cross section library DLC-87/HILO for neutron energies from thermal to 400 MeV and photon energies from 10 keV to 14 MeV, recalculation of shielding for RIKEN Ring Cyclotron was performed. Calculation was carried out using the one-dimensional discrete ordinate code ANISN with S_{16} for the slab scheme and that with S_8 for the spherical scheme, respectively. In both cases P_3 expansion was used. Fluence-to-dose equivalent conversion factors for neutrons recommended by ICRP Publ.21 were used. Neutron spectra used for our calculation are those generated by reactions of (1) 200 MeV protons with a thick aluminum target[1] and (2) 135 MeV/A carbon ions with a thick iron target. For the lack of data, we have approximated the spectrum obtained with a reaction of 100 MeV/A ^{12}C on ^{56}Fe target[2] by extrapolation above 35 MeV. These neutron energy spectra correspond to the ion beams of 6×10^{12} pps are abbreviated hereafter as (p+Al) and (C+Fe), respectively.

The obtained results can be classified into two kinds of charts, which are useful for determination of the concrete-wall thickness of the building and local iron or heavy concrete shield. Using

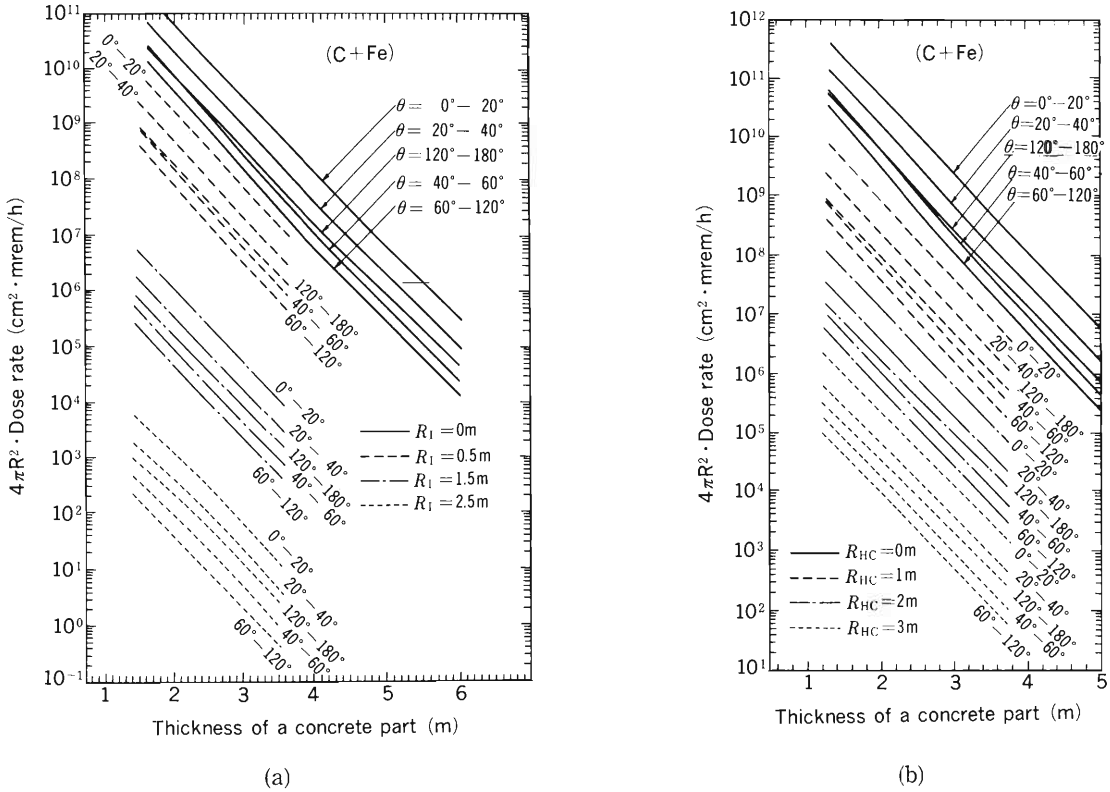

Fig. 1. Neutron dose rate multiplied by squared source distance as a function of thickness of a concrete part. (a), Concrete-iron case; (b), Concrete-heavy concrete case.

* Research Center for Nuclear Science and Technology, The University of Tokyo.

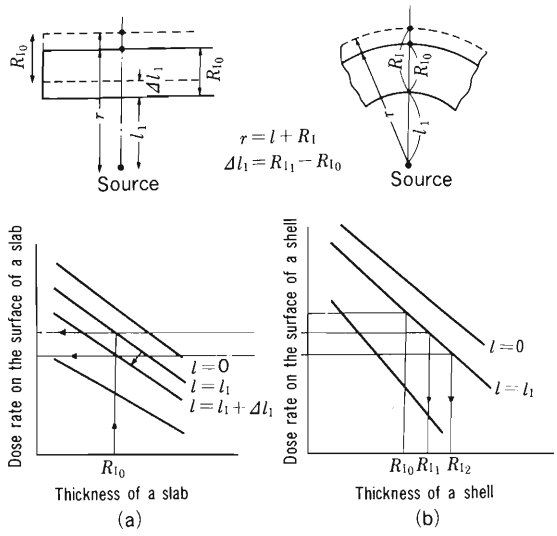

Fig. 2. Neutron dose rate on the surface of a local shield as a function of thickness. (a), Slab shield (source S is not enclosed); (b), Spherical shell (source S is enclosed) .

one chart we can chose an arbitrary combination between thickness of concrete wall of the building and that of local iron or heavy concrete shield (R_{CN_0} and R_{l_0}, respectively) at a given dose rate. The results calculated for (C+Fe) are shown in Fig. 1, which were obtained from the transport calculation of source neutrons through a double layer slab composed of a concrete and an iron or a heavy concrete with normal incidence. The other chart can be utilized for a spherical shield enclosing a point neutron source, when the thickness of the spherical shield R_{l_0} will be inadequate because of reflection of backward emitted neutrons. The necessary thickness can be determined by searching the thickness of a spherical shell so that dose rates at both surfaces of a spherical shell and a slab of thickness R_{l_0}, which are situated at the same distance from the source, become the same. For this purpose, it is necessary to obtain the relation between the dose rate at the surface of a local shield and the

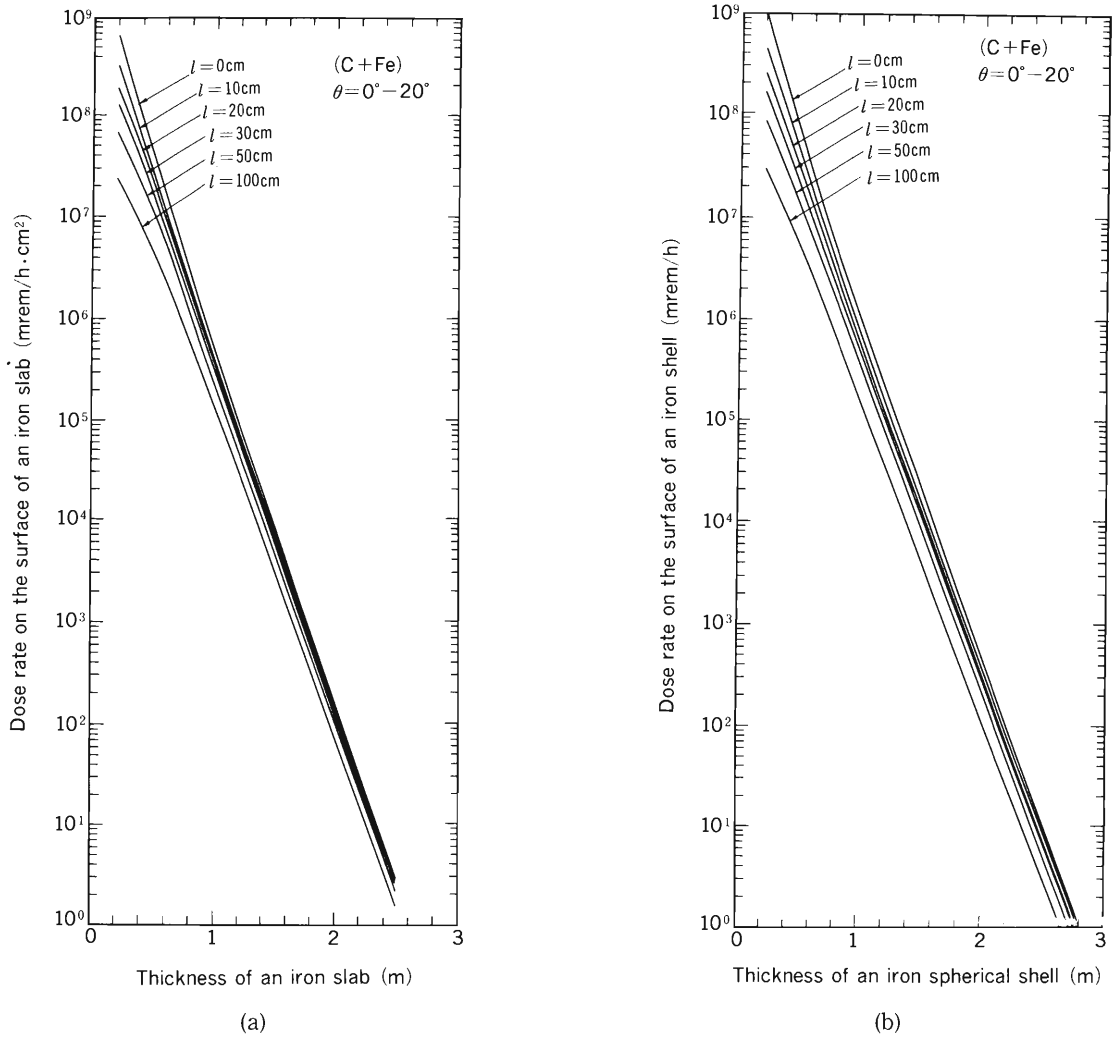

Fig. 3. Neutron dose rate on the surface of an iron local shield as a function of thickness. θ stands for an emission angle of neutrons with respect to the beam direction. (a), Slab case corresponding to Fig. 2 (a); (b), Shell case corresponding to Fig. 2 (b).

thickness, by taking a distance from the source to the shield l as parameter, for both the slab and the spherical shell. One can understand how to determine the necessary thickness of a spherical shell R_{l_n}(n will be about 2) from a schematic figure shown in Fig. 2 by the iteration method. This increment of thickness $R_{l_n}-R_{l_0}$ increases as the parameter l decreases. A pair of the calculated relations corresponding to Fig. 2 is shown in Fig. 3 as an example.

Thus the thickness of concrete walls of the building and corresponding local shield will be designed easily from the charts shown in Figs. 1 and 3.

References

1) H. A. Smith: IUCF Int. Rep., No. 74-6, Radiation Shielding Note 1 (1974).
2) J. Drouet and A. Leleux: D. CEN-S/SPR/SRI/78-342 GRA-066JD/AI 5 mai (1978).

RIKEN Accel. Progr. Rep. 19 (1985)

VI-2. Routine Monitoring of RIKEN Accelerators

I. Sakamoto, S. Fujita, M. Yanokura, T. Kobayashi,
O. Kurihara, and I. Kohno

The present report describes the results of routine radiation monitoring carried out for the cyclotron, RILAC, and TANDETRON from April, 1984, to March, 1985. Aspects of the leakage radiation from the cyclotron are described in a succeeding report.

1) Residual radiation of the cyclotron

In August, 1984, the cyclotron had been operated for about 22 h with 20 MeV deuterons and with a target beam current of 10 μA. The dose rates due to residual activities of the machine were measured 25 days after shutdown. The result is shown in Table 1.

The external exposure doses of two workers during replacement of the septum were 20 and 50 mrem.

Table 1. Dose rates of residual activities.

Location	Dose rate (mR/h)
ca. 50 cm apart from septum (before replacement of septum)	100
ca. 30 cm apart from septum holder (after replacement of septum)	100

2) Surface and air contamination in the cyclotron building

The surface contamination has been kept below 10^{-5} μCi/cm^2 on the floors of the cyclotron vault and the experimental areas, and below 10^{-6} μCi/cm^2 on the floors of the underground passage, hot laboratory, and chemical laboratories. The radioactive nuclides found by γ-ray spectrometry were ^{65}Zn, ^{185}Os, ^{183}Re, and ^{184}Re in the cyclotron vault and ^{67}Ga, ^{75}Se, ^{77}Br, and ^{137}Cs in the hot laboratory and chemical laboratories. The contamination was wiped off twice a year, and immediately after this decontamination, the activities on the floor of the most of above places were reduced to below 10^{-7} μCi/cm^2.

When the radioactive substances were handled in the hot laboratory and chemical laboratories, the air in the draft chamber was activated. The air in the draft chamber was exhausted; the radioactivity in the exit was below 10^{-13} μCi/cm^3.

3) Drainage

The radioactivities in drain water from the cyclotron and the linac building were found to be

Table 2. Annual exposure doses received by RIKEN accelerator workers from April, 1984 to March, 1985.

Workers	Number of persons				Collective dose (man-mrem)
	Dose undetectable	10-100 (mrem)	> 100 (mrem)	Total	
Cyclotron operation and maintenance group	0	7	1	8	890
Linac operation and maintenance group	8	2		10	50
Nuclear physicists	4	5		9	100
Accelerator physicists	10	3		13	80
Physicists in other fields	18	4		22	80
Nuclear chemists	1	4	2	7	610
Radiation chemists	1			1	
Biological chemists	7			7	
TANDETRON workers	11			11	
Health physicists	6			6	
Total	66	25	3	94	1,810

Average annual dose per person: 19.2 mrem.
Maximum individual annual dose: 390 mrem.

of the order of 10^{-8}–10^{-5} μCi/cm^3. The total activities in aqueous effluents was about 920 μCi, in which the main radioactive nuclide was tritium, the radioactivity was about 670 μCi, and the other nuclides found by γ-ray spectrometry were ^{57}Co, ^{67}Ga, ^{75}Se, ^{77}Br, ^{137}Cs, and ^{183}Re.

4) Radiation monitoring of RILAC and TANDETRON

Leakage radiation during operation of the RILAC was measured in the circumference of the linac building every month. No leakage of γ-rays and neutrons from the linac building was detected. No contamination of the surface and air due to residual activities was found in the control area in the linac building.

X-ray monitoring was carried out for the TANDETRON when helium ions were accelerated. When a titanium target was bombarded with 1 MeV He^+ ions at 15 nA, the maximum irradiation dose rates measured around TANDETRON was 0.02 mR/h. No leakage X-rays was detected around the target chamber and outside the TANDETRON room.

5) Personnel monitoring

The external exposure doses to personnel were measured by using γ-ray and neutron film badges. The doses received during the present period by accelerator workers are shown in Table 2. The collective γ-ray dose to all workers was 1,810 man-mrem, while the collective dose owing to thermal and fast neutron exposures were too small to be detected. The collective dose to the workers was about 190% of the value in the preceding period.

In this period the average annual dose per person was 19.2 mrem, and the maximum individual annual dose was 390 mrem.

RIKEN Accel. Progr. Rep. **19** (1985)

VI-3. Leakage-Radiation Measurement in the Underground Passage of the Cyclotron Building

I. Sakamoto, S. Fujita, and I . Kohno

Leakage doses measured from April, 1984, to March, 1985, with γ-ray and neutron film badges placed at two positions on the underground passage (points A and B in Fig. 1) are shown in Table 1. In this period, the beam time allotted to deuteron acceleration was 125 h (72 h in May, 9 h in June, 14 h in July, 22 h in August, and 8 h in December). Fast neutrons were generated at the end of the beam course No. 2 by bombarding a thick beryllium target with 20 MeV deuterons in August; the average beam current was 10 μA. The doses of γ-rays, thermal neutrons, and fast neutrons were 800 mrem, 250 mrem, and 1,440 mrem, respectively.

Table 1. Leakage-radiation dose (in mrem) in the underground passage of the cyclotron building from April, 1984 to March, 1985.

Radiation	Position*					
	A					B
	August	December		Other months	Total	
	Deuteron	Deuteron	Other ions			
γ-Rays (mrem)	800	40	120	3,060	4,020	80
Thermal neutrons (mrem)	250	10	30	750	1,040	20
Fast neutrons (mrem)	1,440	50	30	700	2,220	50
Total (mrem)	2,490	100	180	4,510	7,280	150

* indicated in Fig. 1.

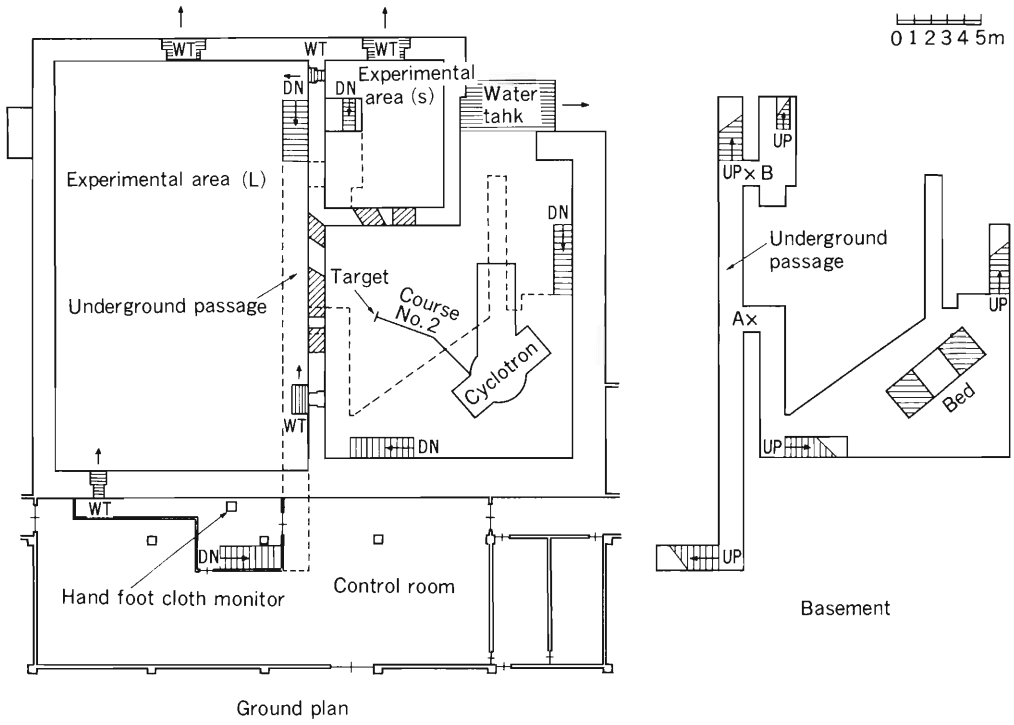

Fig. 1. Measurement positions of neutron and γ-ray doses in the cyclotron building.

VII. LIST OF PUBLICATIONS

1. Accelerator development and accelerator physics
   1) S. Motonaga: "Present Status of RIKEN Ring Cyclotron," *IEEE Trans. Nucl. Sci.*, **32**, 2712 (1985).
   2) M. Odera, M. Hemmi, and A. Goto: "Field Characteristics of an Alvarez-Type Linac Structure Having Chain-Like Electrode Array," *IEEE Trans. Nucl. Sci.*, **32**, 3222 (1985).
   3) T. S. Park, W. S. Lee, and S. H. Be: "Design of Accelerator for Negative Ion Beams by Computer Simulation," *J. Appl. Phys.*, **58**, 1701 (1985).
   4) Y. Sakamoto: "Discharge Cleaning and Surface Conditioning," *Kakuyugo Kenkyu* (in Japanese), **53**, 7 (1985).
   5) H. Oyama, S. Ishii, and Y. Sakamoto: "Technical Development for ECR Discharge Cleaning," *Kakuyugo Kenkyu* (in Japanese), **54**, 79 (1985).
   6) K. Shimizu: "New General Purpose Interfacing Modules for an Accelerator Control System," *Nucl. Instrum. Methods A*, **236**, 109 (1985).
   7) T. Fujisawa, K. Ogiwara, S. Kohara, Y. Oikawa, I. Yokoyama, I. Takeshita, Y. Chiba, and Y. Kumata: "Design of Radio Frequency System for the RIKEN Separated Sector Cyclotron," *Sci. Papers I. P. C. R.*, **79**, 12 (1985).
   8) M. Odera, Y. Chiba, M. Hemmi, Y. Miyazawa, T. Tonuma, T. Inoue, T. Kambara, M. Kase, M. Yanokura, T. Kubo, E. Ikezawa, T. Chiba, A. Shimamura, and F. Yoshida: "RILAC, Frequency Tunable Linac for Acceleration of Heavy-Ions," *Sci. Papers I. P. C. R.*, **79**, 34 (1985).
   9) M. Kase, T. Kambara, and M. Odera: "RILAC Beam-Energy Tuning Method (I)," *Sci. Papers I. P. C. R.*, **79**, 45 (1985).
   10) M. Odera and M. Hemmi: "Proposal of a New Alvarez-Type Linac Structure with Chain-Like Electrodes," *Sci. Papers I. P. C. R.*, **79**, 51 (1985).
   11) Y. Sakamoto, H. Oyama, and S. Kakinuma: "ECR Discharge Cleaning Device with Permanent Magnet," *Shinku* (in Japanese), **5**, 385 (1985).
   12) K. Nagamine: "Large Superconducting Solenoid and Its Cooling System for Muon Channel," *Teion Kougaku* (in Japanese), **20**, 187 (1985).
   13) S. Motonaga: "Separated Sector Cyclotron Project at RIKEN," Proc. 9th Symp. on Ion Sources and Ion-Assisted Technology, Tokyo, p. 163 (1985).

2. Nuclear physics and nuclear instrumentation
   1) K. Nagamine: "Muon Catalyzed Nuclear Fusion," *Butsuri* (in Japanese), **40**, 787 (1985).
   2) T. Doke, A. Hitachi, J. Kikuchi, K. Masuda, S. Tamada, A. Mozumder, E. Shibamura, and T. Takahashi: "Estimation of the Fraction of Electrons Escaping from Recombination in the Ionization of Liquid Argon with Relativistic Electrons and Heavy Ions," *Chem. Phys. Lett.*, **115**, 164 (1985).
   3) T. Hashimoto, Y. Aoyagi, H. Kudo, and T. Sotobayashi: "Range Calculation of Alpha-Recoil Atoms in Some Minerals Using LSS-Theory," *J. Radioanal. Nucl. Chem. A*, **90**, 415 (1985).
   4) J. Kasagi, T. Murakami, and T. Inamura: "Use of Charge Integration ADC's with Pulse Shape Discriminators for Neutron-Gamma Discrimination," *Nucl. Instrum. Methods A*, **236**, 426 (1985).
   5) S. Kato, N. Matsuoka, T. Noro, T. Saito, H. Sakai, M. Nakamura, M. Yosoi, T. Ichihara, K. Hatanaka, and H. Ogawa: "Analyzing Power Measurements for d-^{12}C Elastic Scattering between 35–70 MeV," *Nucl. Instrum. Methods A*, **238**, 453 (1985).
   6) T. Murakami, J. Kasagi, H. Harada, and T. Inamura: "Performance of a Neutron Multiplicity Filter Composed of Six Liquid Scintillation Detectors," *Nucl. Instrum. Methods A*, **241**, 172 (1985).
   7) K. Nisimura, H. Shimizu, K. Imai, T. Ichihara, N. Matsuoka, K. Hatanaka, H. Sakai, T. Saito, K. Hosono, M. Kondo, and A. Okihana: "Elastic Scattering of 56 MeV Polarized Deuterons on ^{4}He," *Nucl. Phys. A*, **432**, 378 (1985).
   8) M. Ohshima, E. Minehara, M. Ishii, T. Inamura, and A. Hashizume: "Multiple Coulomb Excitation of ^{167}Er," *Nucl. Phys. A*, **436**, 513 (1985).
   9) M. Sugawara, Y. Gono, Y. Ishikawa, M. Fukuda, and I. Fujiwara: "In-Beam γ-Ray

Study of ^{212}Po," *Nucl. Phys. A*, **443**, 461 (1985).
10) A. Goto, H. Kamitsubo, N. Matsuoka, and H. Sakaguchi: "Prior-Form DWBA Analysis of (^{3}He, pd) Elastic Breakup at 90 MeV," *Nucl. Phys. A*, **444**, 248 (1985).
11) Y. Nojiri, K. Asahi, K. Matsuta, T. Takeyama, and T. Minamisono: "Nuclear Spin Polarization by the Tilted Foil Technique," Nuclear Spectroscopy and Nuclear Interactions, World Scientific Publ. Co., Singapore, p. 25 (1984).
12) H. Sakamoto, M. Nakamura, H. Sakaguchi, H. Ogawa, S. Kobayashi, S. Kato, N. Matsuoka, K. Hatanaka, and T. Noro: "Polarization Transfer in the Deuteron Break-up Reaction at 56 MeV," *Phys. Lett. B*, **115**, 227 (1985).
13) K. Ieki, M. Ishihara, T. Inamura, S. Kohmoto, H. Utsunomiya, K. Sueki, and H. Kudo: "Spin Polarization of Residual Nuclei in (^{14}N, α) Reactions at 115 MeV," *Phys. Lett. B*, **150**, 83 (1985).
14) N. Yoshida and A. Arima: "Aligned Bands in Ge Isotopes in the Interacting Boson Model," *Phys. Lett. B*, **164**, 231 (1985).
15) J. Kasagi, B. Remington, A. Galonsky, F. Haas, J. J. Kolata, L. Satkoviac, M. Xapsos, R. Racca, and F.W. Prosser: "Neutron Spectra and Level Density Parameters from the ^{16}O+^{12}C Fusion Reactions," *Phys. Rev. C*, **31**, 858 (1985).
16) G. Caskey, A. Galonsky, B. Remington, M. B. Tsang, C. K. Gelbke, A. Kiss, F. Deak, Z. Seres, J. J. Kolata, J. Hinnefeld, and J. Kasagi: "Asymmetric Neutron Emission in ^{14}N+^{165}Ho Reaction at 35 MeV/Nucleon," *Phys. Rev. C*, **31**, 1597 (1985).
17) S. Kato, K. Okada, M. Kondo, K. Hosono, T. Saito, N. Matsuoka, K. Hatanaka, T. Noro, S. Nagamachi, H. Shimizu, K. Ogino, Y. Kadota, S. Matsuki, and M. Wakai: "Inelastic Scattring of 65 MeV Protons from ^{12}C, ^{24}Mg, ^{28}Si, and ^{32}S," *Phys. Rev. C*, **31**, 1616 (1985).
18) T. Inamura, A. C. Kahler, D. R. Zolnowski, U. Garg, T. T. Sugihara, and M. Wakai: "Gamma-Ray Multiplicity Distribution Associated with Massive Transfer," *Phys. Rev. C*, **32**, 1539 (1985).
19) K. Morita, S. Kubono, M. H. Tanaka, H. Utsunomiya, M. Sugitani, S. Kato, J. Schimizu, T. Tachikawa, and N. Takahashi: "Possible Quasimolecular Bands in ^{32}S," *Phys. Rev. Lett.*, **55** , 185 (1985).
20) V. Barci, H. El-Samman, A. Gizon, J. Gizon, T. Bengtsson, and Y. Gono: "Possible Shape-Change Observed at High Spin in ^{123}Cs," *Z. Phys. A*, **321**, 353 (1985).

3. Atomic and solid-state physics
1) M. Uda, A. Koyama, K. Maeda, and Y. Sasa: "Valence Electron Rearrangement Prior to X-Ray or Auger Emission," Proc. Int. Conf. on X-Ray and Inner-Shell Processes in Atoms, Molecules and Solids (ed. by A. Meisel and J. Finster), Leipzig, p. 307 (1984).
2) T. Watanabe: "Atomic Physics Using High Energy Heavy Ions," Proc. RIKEN Symposium on Nuclear Physics Research in Impact Energy Range of 10-100 MeV/u, Wako, SSC-PI, p. 38 (1984).
3) M. Kase, T. Akioka, H. Mamyouda, J. Kikuchi, and T. Doke: "Fano Factor in Pure Argon," *Nucl. Instrum Methods A*, **227**, 311 (1984).
4) A. C. Roy and T. Watanabe: "Doubly Differential Cross Sections for Electron-Impact Ionization of Helium," Atomic Collision Res. in Japan-Prog. Rep., No. 11, p. 3 (1985).
5) A. Ohsaki, T. Watanabe, K. Nakanishi, and K. Iguchi: "Classical Trajectory Monte Carlo Calculation for Collision Processes of e^++(e^-p) and μ^++(μ^-p)," Atomic Collision Res. in Japan-Prog. Rep., No. 11, p. 9 (1985).
6) Q. Ma, X. Zhang, Z. Liu, Y. Liu, and T. Watanabe: "Quantum Mechanical Study for the Process of μ^++(μ^-)→($\mu^+\mu^-$)+p," Atomic Collision Res. in Japan-Prog. Rep., No. 11, p. 13 (1985).
7) K. Hino, N. Toshima, I. Shimamura, and T. Watanabe: "Theory of Radiative Electron Capture I: Nonrelativistic Treatment of Theoretical Paradox," Atomic Collision Res. in Japan-Prog. Rep., No. 11, p. 53 (1985).
8) K. Hino and T. Watanabe: "Theory of Radiative Electron Capture II: Relativistic (Semi-Covariant) Treatment," Atomic Collision Res. in Japan-Prog. Rep., No. 11, p. 57 (1985).
9) K. Fujima, T. Watanabe, and Y. Awaya: "K-Hole Production Probability by the Rotational Coupling in Ar-Ti, Co, and Zn Systems," Atomic Collision Res. in Japan-Prog. Rep., No. 11, p. 65 (1985).
10) H. Tawara, T. Tonuma, S. H. Be, H. Shibata, H. Kumagai, M. Kase, T. Kambara, and I. Kohno: "Highly-Ionized

Atomic Ions Produced in Energetic Heavy Ion Impact on Molecular Targets," Atomic Collision Res. in Japan-Prog. Rep., No. 11, p. 78 (1985).
11) S. H. Be, T. Tonuma, H. Kumagai, H. Shibata, M. Kase, T. Kambara, I. Kohno, and H. Tawara: "Multiple Ionization of Rare-Gases by 1.05 MeV/amu Heavy Ion Impact," Atomic Collision Res. in Japan-Prog. Rep., No. 11, p. 81 (1985).
12) T. Tonuma, H. Shibata, S. H. Be, H. Kumagai, M. Kase, T. Kambara, I. Kohno, and H. Tawara: "Production of Highly Charged Slow Ar Ions Recoiled in 1.05 MeV/amu Ne^{q+}(q=2, 7-10) and Ar^{q+}(q=4, 6, 10-14) Ion Bombardment," Atomic Collision Res. in Japan-Prog. Rep., No. 11, p. 84 (1985).
13) H. Shibata, Y. Awaya, T. Kambara, M. Kase, H. Kumagai, T. Matsuo, and N. Tokoro: "Ar L-MM Auger Electron Spectra in Heavy-Ion-Ar Collisions," Atomic Collision Res. in Japan-Prog. Rep., No. 11, p. 90 (1985).
14) T. Kambara, Y. Awaya, M. Kase, H. Kumagai, and H. Shibata: "Target Atomic Number Dependence of Kα and Kβ X Rays from 33 MeV Ar Ions in Solid Targets," Atomic Collision Res. in Japan-Prog. Rep., No. 11, p. 93 (1985).
15) Y. Awaya, T. Kambara, M. Kase, H. Shibata, H. Kumagai, T. Mizogawa, Y. Kanai, and K. Shima: "High Resolution Measurement of Cu K X Rays from Collision Systems of Cu Ions on C Target and C Ions on Cu Target," Atomic Collision Res. in Japan-Prog. Rep., No. 11, p. 96 (1985).
16) S. Karashima, T. Watanabe, T. Kato, and H. Tawara: "Stopping Power Theories for Charged Particles in Inertial Confinement Fusion Plasmas (Emphasis on Hot and Dense Matters)," IPPJ-AM-42, Inst. Plasma Phys., Nagoya Univ. (1985).
17) T. Watanabe and K. Hino: Theory of Ion-Atom Collisions at High Energy I: Non-Radiative and Radiative Electron Capture," Rep. 1st Joint Seminar on Atomic Phys., Solid State Phys., and Material Science in the Energy Region of Tandem Accelerators, JAERI-M 85-125, p. 3 (1985).
18) S. Karashima and T. Watanabe: "Theory of Ion-Atom Collisions at High Energy II: Charge Stripping Cross Sections," Rep. 1st Joint Seminar on Atomic Phys., Solid State Phys., and Material Science in the Energy Region of Tandem Accelerators, JAERI-M 85-125, p. 22 (1985).
19) T. Matsuo, H. Shibata, J. Urakawa, A. Yagishita, Y. Awaya, T. Kambara, M. Kase, and H. Kumagai: "Auger Electrons in Ar^{4+}+Ar Collisions," Rep. 1st Joint Seminar on Atomic Phys., Solid State Phys., and Material Science in the Energy Region of Tandem Accelerators, JAERI-M 85-125, p. 85 (1985).
20) H. Tawara, T. Tonuma, S. H. Be, H. Shibata, M. Kase, T. Kambara, H. Kumagai, and I. Kohno: "Production of Multiply Charged Ions in Energetic Heavy Ion+Molecular Target Collisions," Rep. 1st Joint Seminar on Atomic Phys., Solid State Phys., and Material Science in the Energy Region of Tandem Accelerators, JAERI-M, 85-125, p. 100 (1985).
21) E. Yagi, A. Koyama, S. Nakamura, H. Sakairi, and R. R. Hasiguti: "Defect-Trapping by Sn Atoms Implanted in Al," *Jpn. J. Appl. Phys.*, **24**, 137 (1985).
22) S. H. Be, and K. Yano: "Cluster Beam Production by a Slit-Throat Nozzle," *Jpn. J. Appl. Phys.*, **24**, 589 (1985).
23) H. Aizawa, K. Wakiya, H. Suzuki, F. Koike, and F. Sasaki: "Autoionising States of K^+ and K Excited by Slow K^+ Impact on He," *J. Phys. B: At. Mol. Phys.*, **18**, 289 (1985).
24) J. Mizuno, T. Ishihara, and T. Watanabe: "Energy Exchange between Two Outgoing Electrons in the Post-Collision Interaction Process," *J. Phys. B: At. Mol. Phys.*, **18**, 1241 (1985).
25) Y. Morioka, Y. Hanada, K. Kihara, S. Hara, and M. Nakamura: "Rotational Intensity Distribution of the N_2 Photoelectron Spectrum," *J. Phys. B: At. Mol. Phys.*, **18**, 1369 (1985).
26) S. Hara: "Theoretical Study of Photoionisation of H_2," *J. Phys. B: At. Mol. Phys.*, **18**, 3759 (1985).
27) S. Hara and S. Ogata: "Photoionisation of the H_2 Molecule," *J. Phys. B: At. Mol. Phys.*, **18**, L59 (1985).
28) T. Watanabe: "Comment on the Relation between the Cross Section for Electron Stripping from a Helium-like Ion in Collision with Atomic Hydrogen and the K-Shell Ionisation Cross Section for Proton Impact," *J. Phys. B: At. Mol. Phys.*, **18**, L111 (1985).
29) N. Sakai and H. Sekizawa: "A New Technique of Mössbauer Spectroscopy without Using Doppler Modulation," *J. Phys. Soc.*

Jpn., **54**, 474 (1985).
30) E. Yagi, S. Nakamura, T. Kobayashi, K. Watanabe, and Y. Fukai: "Lattice Location of Hydrogen in α-Phase in Nb-H System as Observed by Channeling Method," *J. Phys. Soc. Jpn.*, **54**, 1855 (1985).
31) K. Asai, T. Okada, and H. Sekizawa: "TDPAC of γ-Rays Emitted from ^{111}Cd ($\leftarrow^{111}$In) in Fe_3O_4," *J. Phys. Soc. Jpn.*, **54**, 4321 (1985).
32) S. Karashima and T. Watanabe: "Charge Equilibrium of Fast Heavy Ions Traversing through Gaseous Media," *Laser and Particle Beams*, **2**, 477 (1985).
33) S. Karashima, T. Watanabe, Y. Awaya, and Y. Liu: "Electron Stripping Cross Section from Multiply Charged Ions by Neutral Atoms," *Nucl. Instrum. Methods, A*, **240**, 505 (1985).
34) S. M. Shafroth, Y. Awaya, M. Kase, T. Kambara, H. Kumagai, M. Nishida, H. Shibata, and H. Tawara: "Angular Distribution of REC for Ar^{4+} on C at 1 MeV/amu," *Nucl. Instrum. Methods A*, **240**, 546 (1985).
35) T. Tonuma, S. H. Be, H. Kumagai, H. Shibata, M. Kase, T. Kambara, I. Kohno, and H. Tawara: "Ionization of He, Ne, and Ar Atoms by 1.05 MeV/amu C^{q+}(q=2-6) and Ar^{q+} (q=4-14) Ion Impact," *Nucl. Instrum. Methods, B*, **9**, 429 (1985).
36) Y. Awaya, T. Kambara, M. Kase, H. Shibata, H. Kumagai, K. Fujima, J. Urakawa, T. Matsuo, and J. Takahashi: "Target Atomic Number Dependence of Simultaneous K-Shell and L-Shell Ionization of Projectile Heavy Ions," *Nucl. Instrum. Methods, B*, **10** & **11**, 53 (1985).
37) K. Maeda, M. Uda, and Y. Hayasi: "Oxygen Kα Emission Spectrum Free from Multiple-Vacancy Satellites," *Phys. Lett., A*, **112**, 431 (1985).
38) M. C. van Hemert, E. F. van Dishoeck, J. A. van der Hart, and F. Koike: "Quantum Mechanical and Impact-Parameter Treatment of He^{2+}-H Collisions," *Phys. Rev. A*, **31**, 2227 (1985).
39) A. Ohsaki, T. Watanabe, K. Nakanishi, and K. Iguchi: "Classical Trajectory Monte Carlo Calculation for Collision Processes of $e^+ + (e^- p)$ and $\mu^+ + (\mu^- p)$," *Phys. Rev. A*, **32**, 2640 (1985).
40) Q. Ma, X. Zhang, Z. Liu, Y. Liu, and T. Watanabe: "First-Order Distorted-Wave Born Cross Sections for $\mu^+ + (\mu^- p) \rightarrow (\mu^+ \mu^-) + p$," *Phys. Rev. A*, **32**, 2645 (1985).
41) A. C. Roy and T. Watanabe: "Doubly Differential Cross Sections for Electron-Impact Ionization of Helium," *Phys. Rev. A*, **32**, 3090 (1985).
42) K. Fujima, T. Watanabe, and H. Adachi: "Analysis of the Electronic Properties of Extremely Condensed Matter by the Discrete-Variational X Method: Application to Cold Neon Plasma," *Phys. Rev. A*, **32**, 3585 (1985).
43) E. Yagi, T. Kobayashi, S. Nakamura, Y. Fukai, and K. Watanabe: "Stress-Induced Site Change of H in V Observed by Channeling Experiments," *Phys. Rev. B*, **31**, 1640 (1985).
44) K. Ishida, K. Nagamine, T. Matsuzaki, Y. Kuno, K. Nishiyama, T. Yamazaki, E. Torikai, H. Shirakawa, and J. H. Brewer: "Diffusion Properties of Muon Produced Soliton In *trans*-Polyacetylene," *Phys. Rev. Lett.*, **55**, 2009 (1985).
45) T. Watanabe: "Electron Capture Processes of Multicharged Ions from H and He (Theory)," Proc. First Asia-Pacific Physics Conference, Singapore 1983, Vol. 1, Eds. A. Arima, C. K. Chew, T. Ninomiya, P. P. Ong, K. K. Phua, and K. L. Tan, World Scientific Publishing Co. Pte. Ltd., p. 644 (1985).
46) K. Okazaki, A. Minoh, S. Ishii, Y. Ishibe, H. Oyama, Y. Sakamoto, and K. Yano: "LIFS Measurement of Sputtering Particle Density by Plasma Irradiation to a Metal Sample," *Shinku* (in Japanese), **5**, 388 (1985).

4. Radiochemistry, radiation chemistry and radiation biology

1) Y. Itoh, T. Nozaki, T. Masui, and T. Abe: "Calibration Curve for Infrared Spectrophotometry of Nitrogen in Silicon," *Appl. Phys. Lett.*, **47**, 488 (1985).
2) N. Sakai, F. Sakai, and H. Sekizawa: "Mössbauer Study of ^{60}Co γ-Ray Irradiated $Fe_xMg_{1-x}(NH_4)_2(SO_4)_2 \cdot 6H_2O$," *Bull. Chem. Soc. Jpn.*, **58**, 574 (1985).
3) K. Kimura: "Large Yield of Photoemission near Maximum Stopping Power in the Track of N-ion Impinged Helium Gas; Possibility of Cluster Formation of Excimers in Liquid Helium," *Hoshasen (Ion. Radiat.)*(in Japanese), **11**, 94 (1985).
4) T. Takahashi, K. Eguchi, T. Katayama and I. Kaneko: "Recent Topics on Biological Heavy-Ion Action and the Track Structure," *Hoshasen (Ion. Radiat.)* (in

Japanese), **11**, 122 (1985).
5) M. Yanokura: "Heavy-Ion RBS," *Isot. News*, No. 373, p. 6 (1985).
6) Y. Itoh and T. Nozaki: "Solubility and Diffusion Coefficient of Oxygen in Silicon," *Jpn. J. Appl. Phys.*, **24**, 279 (1985).
7) T. Nozaki, Y. Itoh, Y. Ohkubo, T. Kimura, and H. Fukushima: "Simultaneous Charged Particle Activation Analysis of Carbon and Boron in Gallium Arsenide," *Jpn. J. Appl. Phys.*, **24**, 801 (1985).
8) Y. Sugita, H. Kawata, S. Nakamichi, T. Okabe, T. Watanabe, S. Yoshikawa, Y. Itoh, and T. Nozaki: "Measurement of the Out-Diffusion Profile of Oxygen in Silicon," *Jpn. J. Appl. Phys.*, **24**, 1302 (1985).
9) M. Nakamura, Y. Mochizuki, K. Usami, Y. Itoh, and T. Nozaki: "Infrared, Raman, and X-Ray Diffraction Studies of Silicon Oxide Films Formed from SiH_4 and N_2O Chemical Vapor Deposition," *J. Electrochem. Soc.: Solid-State Sci. Technol.*, **132**, 482 (1985).
10) M. Nakamura, Y. Mochizuki, K. Usami, Y. Itoh, and T. Nozaki: "Infrared Absorption Spectra and Compositions of Evaporated Silicon Oxides (SiO_x)," *Solid State Commun.*, **50**, 1079 (1984).

(Papers Presented at Meetings)

1. Accelerator development and accelerator physics

1) T. Fujisawa, K. Ogiwara, S. Kohara, Y. Oikawa, Y. Chiba, and Y. Kumata: "Design of Radio Frequency System for the RIKEN Separated Sector Cyclotron," RCNP-Symp. Accelerator Engineering for the RCNP Project, Osaka, Feb. (1985).
2) M. Yanokura: "Report of RIKEN ECR2," RCNP I. S. Workshop, Osaka, Mar. (1985).
3) A. Goto, T. Fujisawa and I. Takeshita: "Design of Beam Buncher in the RIKEN Ring Cyclotron Injection Beam Transport Line," 40th Ann. Meeting Phys. Soc. Jpn., Kyoto, Apr. (1985).
4) T. Fujisawa, K. Ogiwara, S. Kohara, Y. Oikawa, and Y. Chiba: "Design of High Power Amplifier of the RIKEN SSC," 40th Ann. Meeting Phys. Soc. Jpn., Kyoto, Apr. (1985).
5) N. Nakanishi, T. Shikata, S. Fujita, and T. Kosako: "Calculation on Design of Beam Dump in RIKEN SSC," 40th Ann. Meeting Phys. Soc. Jpn., Kyoto, Apr. (1985).
6) S. Motonaga: "Present Status of RIKEN Ring Cyclotron," 1985 Particle Accelerator Conf., Vancouver, Canada, May (1985).
7) T. Fujisawa, K. Ogiwara, S. Kohara, Y. Oikawa, I. Yokoyama, I. Takeshita, Y. Chiba, and Y. Kumata: "Design of Radio Frequency System for the RIKEN Separated Sector Cyclotron," 1985 Particle Accelerator Conf., Vancouver, Canada, May (1985).
8) S. Motonaga: "Separated Sector Cyclotron Project at Riken," Proc. 9th Symp. on Ion Sources and Ion-assisted Technology, Tokyo, June, p. 163 (1985).
9) S. Ishii: "Development of an Efficient Highly Charged Ion Source," 9th Symp. on Ion Sources and Ion-Assisted Technology, Tokyo, June (1985).
10) T. Shikata, N. Nakanishi, and S. Fujita, and T. Kosako: "Calculation for the Neutron Shielding Design of the RIKEN SSC," 1985 Fall Meeting Phys. Soc. Jpn., Kofu, Oct. (1985).
11) A. Goto, H. Takebe, S. Motonaga, K. Hatanaka, Y. Yano, T. Wada, N. Nakanishi, M. Hara, and S. H. Be: "Magnetic Field Measurement for the RIKEN Ring Cyclotron," 1985 Fall Meeting Phys. Soc. Jpn., Kofu, Oct. (1985).
12) M. Yanokura: "RIKEN ECR2 (2)," 1985 Fall-Meeting Phys. Soc. Jpn., Kofu, Oct. (1985).

2. Nuclear physics and nuclear instrumentation

1) M. Sugawara, G. Iwasaki, Y. Gono, M. Fukuda, Y. Ishikawa, T. Kohno, M. Adachi, H. Taketani, and P. Aguer: "In-Beam Electron and Alpha-Particle Measurements Utilising Super Conducting Solenoid," 40th Ann. Meeting Phys. Soc. Jpn., Kyoto, Mar. (1985).
2) Y. Gono, M. Fukuda, Y. Ishikawa, and M. Sugawara: "BGO Anti-Compton Spectrometer and Monte Carlo Simulation," 40th Ann. Meeting Phys. Soc. Jpn., Kyoto, Mar. (1985).
3) T. Motobayashi, H. Sakai, N. Matsuoka, T. Saito, K. Hosono, A. Okihana, M. Ishihara, A. Sakaguchi, and S. Shimoura: "(d, ^{2}He) Reaction with Polarized Deuteron," 40th Ann. Meeting Phys. Soc. Jpn., Kyoto, Apr. (1985).
4) T. Murakami and J. Kasagi: "Charged Particle Detection with a BaF_2 Scintillator," 40th Ann. Meeting Phys. Soc. Jpn.,

Kyoto, Apr. (1985).
5) H. Harada, T. Murakami, H. Tachibanaki, K. Yoshida, J. Kasagi, and T. Inamura: "Excited Levels of ^{110}Sn Produced by ^{98}Mo(^{16}O, 4nγ)^{110}Sn(II)," 40th Ann. Meeting Phys. Soc. Jpn., Kyoto, Apr. (1985).
6) T. Murakami, H. Harada, H. Tachibanaki, K. Yoshida, J. Kasagi, and T. Inamura: "Excited Levels of ^{112}Sn Produced by ^{100}Mo(^{16}O, 4nγ)^{112}Sn," 40th Ann. Meeting Phys. Soc. Jpn., Kyoto, Apr. (1985).
7) T. Inamura: "Present Status of RIKEN Ring Cyclotron and Nuclear Data Acquisition System," Workshop on Fast Data Acquisition System Based on CAMAC, Wako, June (1985).
8) H. Harada, T. Murakami, H. Tachibanaki, K. Yoshida, J. Kasagi, and T. Inamura: "Negative-Parity High Spin States in ^{110}Sn and ^{112}Sn," Symp. on Highly Excited and Higher Spin States in Atomic Nuclei, Kyoto, July (1985).
9) T. Murakami, J. Kasagi, H. Harada, H. Tachibanaki, K. Yoshida, T. Kubo, and T. Inamura: "High Spin States in ^{112}Sn," Symp. on Highly Excited and Higher Spin States in Atomic Nuclei, Kyoto, July (1985).
10) K. Asahi, M. Ishihara, T. Shimoda, T. Fukuda, N. Takahashi, K. Katori, S. Shimoura, N. Ikeda, C. Konno, K. Hanakawa, T. Itabashi, Y. Nojiri, and T. Minamisono: "Beta Decay of Polarized Nucleus ^{15}C Produced in Heavy-Ion Reaction," 6th Int. Symp. on Polarization Phenomena in Nuclear Physics, Osaka, Aug. (1985).
11) H. Ohsumi, M. Ishihara, S. Kohmoto, K. Asahi, K. Sugimoto, T. Tanabe, T. Hattori, H. Hamagaki, and K. Haga: "Nuclear Spin Polarization of ^{27}Al Produced by Tilted-Foil Method and Determination of the Polarization by Coulomb Excitation," 6th Int. Symp. on Polarization Phenomena in Nuclear Physics, Osaka, Aug. (1985).
12) T. Kubo and H. Ohnuma: "Deuteron D-State Effects on the Vector Analyzing Power and Polarization in (d, p) Reactions," 6th Int. Symp. on Polarization Phenomena in Nuclear Physics, Osaka, Aug. (1985).
13) S. Yamaji, H. Hofmann, and R. Samhammer: "Self-Consistent Transport Coefficients for Damped Large Scale Collective Motion," Conf. on Fission Held at RCNP, Osaka, Sept. (1985).
14) T. Ichihara, T. Inamura, and M. Ishihara: "RIKEN Ring Cyclotron Nuclear Data Acquisition System Based on CAMAC," 1985 Fall Meeting Phys. Soc. Jpn., Kofu, Oct. (1985).
15) H. Ohsumi, M. Ishihara, S. Kohmoto, K. Asahi, K. Sugimoto, T. Tanabe, H. Hamagaki, T. Hattori, and K. Haga: "Spin Polarization of ^{27}Al by Tilted-Foil Method Detected by Means of Coulomb Excitation," 1985 Fall Meeting Phys. Soc. Jpn., Kofu, Oct. (1985).
16) T. Ichihara, T. Inamura, and M. Ishihara: "Preparation for the CAMAC-based Data Aquisition System at the RIKEN Ring Cyclotron Facility," 1985 Fall Meeting Phys. Soc. Jpn., Kofu, Oct. (1985).
17) T. Ichihara, H. Sakaguchi, M. Nakamura, M. Yosoi, M. Ieiri, Y. Takeuchi, H. Togawa, T. Tsutsumi, and S. Kobayashi: "Inelastic Scattering of Polarized Protons Exciting the γ-Vibrational Band in Deformed Nuclei at 65 MeV," 1985 Fall Meeting Phys. Soc. Jpn., Kofu, Oct. (1985).
18) T. Motobayashi, H. Sakai, N. Matsuoka, T. Saito, K. Hosono, A. Okihana, M. Ishihara, A. Sakaguchi, and S. Shimoura: "Spin Flip States Studied by the ^{90}Zr(d, ^{2}He) Reaction," 1985 Fall Meeting Phys. Soc. Jpn., Kofu, Oct. (1985).
19) N. Yoshida and A. Arima: "High-Spin States in Ge Using the IBM," 1985 Fall Meeting Phys. Soc. Jpn., Kofu, Oct. (1985).
20) R. Bambot, S. Della-Negra, R. Anne, H. Delagrange, Y. Schutz, P. Aguer, G. Bastin, Y. Gono, and K. Hatanaka: "Radio-Active Beam Production at GANIL," 1985 Fall Meeting of the Phys. Soc. Jpn., Kofu, Oct. (1985).
21) A. Yunoki, A. Hitachi, K. Masuda, S. Suzuki, T. Doke, J. Kikuchi, and T. Takahashi: "Electric Field Effect on the Scintillation of Liquid Argon Induced by α-Particles," 1985 Fall Meeting Phys. Soc. Jpn., Chiba, Oct. (1985).
22) S. Suzuki, A. Yunoki, A. Hitachi, T. Doke, K. Masuda, and T. Takahashi: "Photoionization in Liquid Argon Admixtured by Small Amount of TEA and TMA," 1985 Fall Meeting Phys. Soc. Jpn., Chiba, Oct. (1985).
23) M. Magara, K. Sueki, H. Kudo, Y. Hamajima, Y. Hatsukawa, H. Yoshikawa, H. Nakahara, and I. Kohno: "Study of Es Isotopes Produced by ^{238}U+^{14}N Reaction," 29th Symp. on Radiochemistry, Funabashi,

Oct. (1985).

24) T. Shimizu, S. Kubota, T. Motonaga, J. Ruan (Gen), F. Shiraishi, and Y. Takami: "A New Barium-Fluoride Plastic Scintillator," IEEE Nuclear Science Symposium, San Francisco, Oct. (1985).

3. Atomic and solid-state physics

1) T. Matsuo, H. Shibata, J. Urakawa, A. Yagishita, Y. Awaya, T. Kambara, M. Kase, and H. Kumagai: "Auger Electrons in Ar^{4+}+Ar Collision," 1st Joint Seminar on Atomic Physics, Solid State Physics and Material Science in the Energy Region of Tandem Accelerators, Tokai, Jan. (1985).
2) E. Yagi: "Diffusion of Positive Muons in Iron," 1st Joint Seminar on Atomic Physics, Solid State Physics and Material Science in the Energy Region of Tandem Accelerators, Tokai, Jan. (1985).
3) Y. Awaya: "Experiments of Atomic Collisions at RIKEN," 6th Symp. on Atomic Collisions by Using Accelerators, Wako, Feb. (1985).
4) E. Yagi: "Determination of Lattice Locations of Hydrogen in Solids by Channeling Method," Riken Symp. Characterization of Semiconductor Materials and Hydrogen Analysis by Using Accelerators, Wako, Feb. (1985).
5) T. Kambara, Y. Awaya, M. Kase, H. Kumagai, H. Shibata, and T. Tonuma: "Target Isotope Dependence of REC X-Ray Yields," 40th Ann. Meeting Phys. Soc. Jpn., Kyoto, Mar. (1985).
6) H. Tawara, H. Shibata, T. Tonuma, S. H. Be, M. Kase, T. Kambara, H. Kumagai, and I. Kohno: "Production of Multicharged Secondary Ions in Collisions of Energetic Heavy Ions with Molecular Targets," 40th Ann. Meeting Phys. Soc. Jpn., Kyoto, Apr. (1985).
7) S. H. Be, T. Tonuma, H. Kumagai, H. Shibata, M. Kase, T. Kambara, I. Kohno, and H. Tawara: "Total Cross Sections for Ionization of Rare-Gas Atoms by Heavy Ion Collisions," 40th Ann. Meeting Phys. Soc. Jpn., Kyoto, Apr. (1985).
8) Y. Awaya, T. Kambara, M. Kase, H. Shibata, H. Kumagai, and K. Fujima: "K X-Rays of 33 MeV Ar Ions Passing through Solid Targets (I)," 40th Ann. Meeting Phys. Soc. Jpn., Kyoto, Apr. (1985).
9) T. Kambara, Y. Awaya, M. Kase, H. Shibata, and H. Kumagai: "K X-Rays of 33 MeV Ar Ions Passing through Solid Targets (II)," 40th Ann. Meeting Phys. Soc. Jpn., Kyoto, Apr. (1985).
10) K. Fujima, T. Watanabe, and Y. Awaya: "K X-Rays of 33 MeV Ar Ions Passing through Solid Targets (III). The Calculation for Ar K Ionization Cross Section Due to Rotational Couplings," 40th Ann. Meeting Phys. Soc. Jpn., Kyoto, Apr. (1985).
11) H. Shibata, T. Matsuo, Y. Awaya, T. Kambara, M. Kase, H. Kumagai, and N. Tokoro: "Projectile Dependence of Ar L-MM Auger Electron Spectra," 40th Ann. Meeting Phys. Soc. Jpn., Kyoto, Apr. (1985).
12) Y. Awaya: "Atomic Process Time and Nuclear Reaction Time," 40th Ann. Meeting Phys. Soc. Jpn., Kyoto, Apr. (1985).
13) H. Sato, N. Shimakura, and T. Watanabe: "Charge Transfer Processes between a Multicharged Ion and He in Low Energy Regions," 40th Ann. Meeting Phys. Soc. Jpn., Kyoto, Apr. (1985).
14) T. Watanabe: "Similarity of Process between Electron Stripping and Inner-Shell Ionization," 40th Ann. Meeting Phys. Soc. Jpn., Kyoto, Apr. (1985).
15) Q. Ma, X. Zhan, Z. Liu, Y. Liu, and T. Watanabe: "Born Approximation Calculation for $\mu^+ + (\mu^- p) \rightarrow (\mu^+ \mu^-) + p$ II," 40th Ann. Meeting Phys. Soc. Jpn., Kyoto, Apr. (1985).
16) K. Hino, I. Shimamura, and T. Watanabe: "Relativistic Theory on Radiative Electron Capture I," 40th Ann. Meeting Phys. Soc. Jpn., Kyoto, Apr. (1985).
17) S. Karashima, H. Kawagoshi, and T. Watanabe: "Electron Stripping Cross Sections of Incident Highly Charged Ions II," 40th Ann. Meeting Phys. Soc. Jpn., Kyoto, Apr. (1985).
18) K. Ishida, K. Nagamine, Y. Kuno, T. Matsuzaki, H. Shirakawa, and J. H. Brewer: "Muon Spin Resonance Studies on Polyacetylene II," 40th Ann. Meeting Phys. Soc. Jpn., Kyoto, Apr. (1985).
19) A. Koyama, O. Benka, Y. Sasa, and M. Uda: "Energy Distribution of Secondary Electrons Induced by He^+ and He^{2+}," 40th Ann. Meeting Phys. Soc. Jpn., Kyoto, Apr. (1985).
20) A. Koyama, Y. Sasa, and M. Uda: "Secondary Electrons Emitted from Al under Bombardment with He^+ and He^{++}," 40th Ann. Meeting Phys. Soc. Jpn., Kyoto,

Apr. (1985).
21) E. Yagi: "Comment on the Quantum Diffusion of Light Particles in Metals," 40th Ann. Meeting Phys. Soc. Jpn., Kyoto, Apr. (1985).
22) K. Asai, T. Okada, and H. Sekizawa: "A Study of Ferrites with the Spinel Structure by Means of TDPAC of γ-Rays Emitted from ^{111}Cd($\leftarrow^{111}$In)," 40th Ann. Meeting Phys. Soc. Jpn., Kyoto, Apr. (1985).
23) K. Kimura: "Unusual Emission Spectra from Heavy-Ion Impinged Liquid Helium (III)," 40th Ann. Meeting Phys. Soc. Jpn., Kyoto, Apr. (1985).
24) K. Asai, T. Okada, F. Ambe, S. Ambe, and H. Sekizawa: "TDPAC of γ-Rays Emitted from ^{111}Cd($\leftarrow^{111}$In) in Magnetic Oxides," XX Winter School on Physics, Cracow, Apr. (1985).
25) Y. Yokode, F. Koizumi, T. Furusaka, S. Kawamura, A. Kida, and H. Tomita: "Elemental Analysis of Tissues Using Ion Induced X-Ray Spectroscopy," 9th Meeting Soc. Head and Neck Tumor Jpn., Tokyo, Apr. (1985).
26) K. Fujima and T. Watanabe: "Atomic Models in Hot and Dense Plasmas," Senimar on Atomic Models in High Density Plasmas, Nagoya, June (1985).
27) H. Shibata, S.H. Be, T. Tonuma, H. Kumagai, M. Kase, T. Kambara, I. Kohno, and H. Tawara: "Ionization of Rare Gas Atoms in 1.05 MeV/amu Fully Stripped Ion Impact," 14th Int. Conf. on the Physics of Electronic and Atomic Collisions, Stanford University, Palo Alto, U.S.A., July (1985).
28) H. Tawara, T. Tonuma, S.H. Be, H. Shibata, H. Kumagai, M. Kase, T. Kambara, and I. Kohno: "Production of Multiply Charged Ions from Molecular Targets in Heavy Ion Impact," 14th Int. Conf. on the Physics of Electronic and Atomic Collisions, Stanford University, Palo Alto, U.S.A., July (1985).
29) S. Hara and H. Sato: "The Lowest $^1\Sigma_u^+$ Autoionizing State of H_2," 14th Int. Conf. on the Physics of Electronic and Atomic Collisions, Stanford University, Palo Alto, U.S.A., July (1985).
30) S. Hara: "The Rotationally and Vibrationally Resolved Photoionization of H_2 by 736A line," 14th Int. Conf. on the Physics of Electronic and Atomic Collisions, Stanford University, Palo Alto, U.S.A., July (1985).
31) T. Kambara, Y. Awaya, M. Kase, H. Shibata, and H. Kumagai: "High Resolution Measurement of Kα and Kβ X Rays from 33 MeV Ar Ions in Solid Targets," 14th Int. Conf. on the Physics of Electronic and Atomic Collisions, Stanford University, Palo Alto, U.S.A., July (1985).
32) I. Shimamura and A.C. Roy: "Transitions of Molecules between High-Angular-Momentum States," 14th Int. Conf. on the Physics of Electronic and Atomic Collisions, Stanford University, Palo Alto, U.S.A., July (1985).
33) I. Shimamura: "Rotational Excitation of Molecules by Slow Electrons," 14th Int. Conf. on the Physics of Electronic and Atomic Collisions, Stanford University, Palo Alto, U.S.A., July (1985).
34) T. Nakanishi, T. Watanabe, A. Ohsaki, and K. Iguchi: "Classical Trajectory Monte Carlo Calculation for $\mu^+ + (\mu^- p) \rightarrow (\mu^+ \mu^-) + p$ and $e^+ + (e^- p) \rightarrow (e^+ e^-) + p$," 14th Int. Conf. on the Physics of Electronic and Atomic Collisions, Stanford University, Palo Alto, U.S.A., July (1985).
35) Y. Awaya, T. Kambara, M. Kase, H. Kumagai, S. Shibata, T. Mizogawa, and K. Shima: "High Resolution Measurements of Cu K X Rays from Collision Systems of Cu Ions on C Target and C Ions on Cu Target," 14th Int. Conf. on the Physics of Electronic and Atomic Collisions, Stanford University, Palo Alto, U.S.A., July (1985).
36) H. Shibata, T. Matsuo, Y. Awaya, T. Kambara, M. Kase, H. Kumagai, and N. Tokoro: "Projectile Dependence of L-MM Auger Electrons Ejected from Ar Target by Heavy Ion Impact," 14th Int. Conf. on the Physics of Electronic and Atomic Collisions, Stanford University, Palo Alto, U.S.A., July (1985).
37) K. Hino, I. Shimamura, and T. Watanabe: "Relativistic Treatment of Radiative Electron Capture," 14th Int. Conf. on the Physics of Electronic and Atomic Collisions, Stanford University, Palo Alto, U.S.A., July (1985).
38) Q. Ma, X. Zhang, Z. Liu, Y. Liu, and T. Watanabe: "Quantum Mechanical Study for the Processes of $\mu^+ + (\mu^- p) \rightarrow (\mu^+ \mu^-) + p$," 14th Int. Conf. on the Physics of Electronic and Atomic Collisions, Stanford University, Palo Alto, U.S.A., July (1985).
39) S. Karashima, T. Watanabe, and Y. Liu:

"Electron Stripping Cross Section from Multicharged Ions by H and He," 14th Int. Conf. on the Physics of Electronic and Atomic Collisions, Stanford University, Palo Alto, U.S.A., July (1985).

40) S. Kakinuma, H. Oyama, and Y. Sakamoto: "Study of Resuscitation Mechanism and Deoxidation Process for Titanium-Titanium Oxide System by Synergism of Both Hydrogen Ions and Neutral Atoms and Molecules," Proc. 7th Int. Symp. on Plasma Chemistry, Eindhoven, The Netherlands, July, p. 430 (1985).

41) K. Yano Y. Ishibe, H. Oyama, Y. Sakamoto, M. Yanokura, and I. Kohno: "Deuterium Retention and Depth Profile in Near Surface of TiC and C Irradiated with Dissociated Deuterium Atoms in an ECR Plasma," Proc. 7th Int. Symp. on Plasma Chemistry, Eindhoven, The Netherlands, July, p. 518 (1985).

42) T. Watanabe: "Photoexcitation, Photoionization and Photo-Chemical Processes of Atoms and Molecules," Advanced Summer School of Phys. Soc. Jpn. on Synchrotron Radiation, Tokyo and Osaka, July (1985).

43) Y. Awaya: "High Resolution Measurements of X-Rays from Heavy Ions Passing through Thin Foils," 10th Meeting Soc. for Atomic Collision Research, Chofu, July (1985).

44) T. Watanabe: "Muon and Positron Scattering Problem by CTMC, FBA and DWBA," Japan-UK Seminar on Theory of Atomic Collisions, Susono, Aug. (1985).

45) T. Watanabe: "Theory of Radiative Electron Capture (REC)," Japan-UK Seminar on Theory of Atomic Collisions, Susono, Aug. (1985).

46) T. Watanabe: "Electron Stripping Process of a Fast Ion by Collision with a Neutral Atom," Japan-UK Seminar on the Theory of Atomic Collisions, Susono, Aug. (1985).

47) T. Watanabe: "Models for State Resolved Charge Transfer Process," Japan-UK Seminar on the Theory of Atomic Collisions, Susono, Aug. (1985).

48) I. Shimamura: "Quantum Mechanical Treatment of Charge Exchange Processes Using Frame Transformation," Japan-UK Seminar on the Theory of Atomic Collisions, Susono, Aug. (1985).

49) I. Shimamura: "Rotational Excitation of Molecules by Electron Impact," Japan-UK Seminar on the Theory of Atomic Collisions, Susono, Aug. (1985).

50) K. Fujima: "Statistical Theory of Multiple Charge Transfer," Japan-UK Seminar on Theory of Atomic Collisions, Susono, Aug. (1985).

51) T. Kambara, Y. Awaya, M. Kase, H. Kumagai, H. Shibata, T. Mizogawa, and K. Shima: "Cu K X Rays from Cu-C and C-Cu Collision Systems," 9th Int. Seminar on Ion-Atom Collisions, Flagstaff, U.S.A., Aug. (1985).

52) Y. Awaya: "Experiments on the Target Isotope Dependence of REC X-Ray Yields," 9th Int. Seminar on Ion-Atom Collisions, Flagstaff, U.S.A., Aug. (1985).

53) T. Watanabe: "Charge Changing Processes in Ion-Atom Collisions," China-Japan Joint Meeting on Atomic and Molecular Physics, Chengdu, China, Aug. (1985).

54) T. Watanabe: "Research Activity on Atomic Physics in the Institute of Physical and Chemical Research (RIKEN)," China-Japan Joint Meeting on Atomic and Molecular Physics, Chengdu, China, Aug. (1985).

55) K. Fujima and T. Watanabe: "Electronic Properties of Hot Dense Plasma," Int. Symp. on Atomic Processes in Fusion Plasma, Santa Cruz, U.S.A., Aug. (1985).

56) A. Koyama, O. Benka, Y. Sasa, and M. Uda: "Energy Spectra of Secondary Electrons from Al Induced by High Speed He^{++} and Ar^{12+} Impact," 11th Int. Conf. on Atomic Collisions in Solids, Washington, D.C., U.S.A., Aug. (1985).

57) M. Uda, A. Koyama, Y. Sasa, and O. Benka: "Chemical Effects on Auger Spectra Induced by Fast Ions," 11th Int. Conf. on Atomic Collisions in Solids, Washington, D.C., U.S.A., Aug. (1985).

58) O. Nomura, K. Kon, Y. Kogure, and K. Kimura: "Electronic States of Excited Helium Molecules," Symp. on Molecular and Electronic Structures, Tokyo, Sept. (1985).

59) Y. Awaya: "Studies on Charge Distribution of Heavy Ions after Passing through the Foil," 1st Symp. on Interaction of Ion Beam with Solids, Kyoto, Sept. (1985).

60) I. Shimamura: "Theory of Electron Transfer in Ion-Atom Collisions," Japan-UK Joint Symp. on Molecular Quantum Chemistry, Okazaki, Sept. (1985).

61) K. Takaishi, T. Kikuchi, K. Furuya, I. Hashimoto, H. Yamaguchi, E. Yagi, and M. Iwaki: "Thermal Extraction of Krypton in Aluminum Using Mass Spec-

trometer," 24th Colloq. Spectroscopium Internationale, Garmisch-Partenkirchen, Sept. (1985).
62) E. Yagi: "Lattice Location Study on Hydrogen in Metals by Channeling Method," Symp. Problems of Solid State Physics and Mater. Sci. on Metal-Hydrogen System, Hakone, Sept. (1985).
63) N. Sakai and H. Sekizawa: "Observation of Mössbauer Spectrum without Utilizing Doppler Motion," ICAME'85, Leuven, Sept. (1985).
64) A. Koyama, O. Benka, Y. Sasa, and M. Uda: "Energy Distributions of Secondary Electrons from Al Induced by Heavy Projectiles," 1985 Fall Meeting Phys. Soc. Jpn., Chiba, Oct. (1985).
65) M. Uda, A. Koyama, Y. Sasa, and O. Benka: "Chemical Effects on Auger Spectra Induced by Fast Ions (II)," 1985 Fall Meeting Phys. Soc. Jpn., Chiba, Oct. (1985).
66) O. Benka and M. Uda: "A Molecular Orbital Model for the Effect on F K-X-Ray Spectra," 1985 Fall Meeting Phys. Soc. Jpn., Chiba, Oct. (1985).
67) I. Tanaka, S. Nasu, E. Fujita, F. Ambe, S. Ambe, and T. Okada: "Mössbauer Effect of ^{119}Sb in Au," 1985 Fall Meeting Phys. Soc. Jpn., Chiba, Oct. (1985).
68) T. Tonuma, A. Ohsaki, H. Shibata, M. Kase, T. Kambara, H. Kumagai, S.H. Be, I. Kohno, and H. Tawara: "Analysis Using Compound Atom Model of Secondary Ions Produced in 1.05 MeV amu^{-1} Ar^{q+} + Ar Collisions," 1985 Fall Meeting Phys. Soc. Jpn., Chiba, Oct. (1985).
69) A. Koyama, M. Uda, Y. Sasa, and O. Benka: "Secondary Electron Energy Spectra Emitted from Al Induced by Heavy Ion Impacts," 1985 Fall Meeting Phys. Soc. Jpn., Chiba, Oct. (1985).
70) E. Yagi, T. Kobayashi, S. Nakamura, F. Kano, K. Watanabe, and Y. Fukai: "Hydrogen State in Vanadium under Uniaxial Stress," 1985 Fall Meeting Phys. Soc. Jpn., Chiba, Oct. (1985).
71) K. Asai, T. Okada, F. Ambe, S. Ambe, and H. Sekizawa: "A Study of the Hyperfine Magnetic Fields at ^{111}Cd($\leftarrow{}^{111}$In) in Magnetic Oxides by means of γ-γ Perturbed Angular Correlation," 1985 Fall Meeting Phys. Soc. Jpn., Chiba, Oct. (1985).
72) K. Kimura, M. Kataoka, K. Hara, and T. Iida: "Unusual Emission Spectra from Heavy-Ion Impinged Liquid Helium (IV)," 1985 Fall Meeting Phys. Soc. Jpn., Chiba, Oct. (1985).
73) K. Kimura: "Possibility of Dimerization and Clustering of Helium-Excimers Produced by Heavy-Ion Impingement," 1985 Fall Meeting Phys. Soc. Jpn., Chiba, Oct. (1985).
74) T. Watanabe: "Positron Collision from Atoms and Molecules," 1985 Fall Meeting Phys. Soc. Jpn., Chiba, Oct. (1985).
75) A.C. Roy and T. Watanabe: "The Calculation for Double Differential Cross Section of Helium Ionization Process by Electron Impact," 1985 Fall Meeting Phys. Soc. Jpn., Chiba, Oct. (1985).
76) S. Karashima and T. Watanabe: "Electron Stripping Cross Section of Incident Multicharged Ions III," 1985 Fall Meeting Phys. Soc. Jpn., Chiba, Oct. (1985).
77) I. Kohno, M. Yanokura, S. Motonaga, H. Kamitsubo, M. Yatsuhashi, T. Suematsu, and H. Kobayashi: "Effects of the Fast Neutron Irradiation on Cable Materials," IEEE 1985 Nuclear Science Symposium, San Francisco, U.S.A., Oct. (1985).
78) Y. Sakamoto and N. Noda: "Nuclear Fusion Devices and the Carbonization of the Wall Surface," Riken Symp. Modification of Solid Surfaces with Plasma, Wako, Nov. (1985).
79) Y. Ishibe and K. Okazaki: "Carbonization Experiment in RIKEN ECR-2 Device," Riken Symp. Modification of Solid Surfaces with Plasma, Wako, Nov. (1985).
80) S. Amemiya and K. Yano: "Characterization of Carbon Films, with Plasma," Riken Symp. Modification of Solid Surfaces with Plasma, Wako, Nov. (1985).
81) I. Shimamura: "R-Matrix Method and Atomic Collisions," Symp. on Atomic Physics, Nagoya, Nov. (1985).
82) Y. Awaya: "Experiments by Using High Energy Multiply Charged Ions," Symp. on Atomic Physics, Nagoya, Nov. (1985).
83) Y. Ishibe, H. Oyama, K. Okazaki, K. Yano, Y. Sakamoto, N. Noda, and Y. Hori: "Carbon Coating with ECR Plasmas," Proc. 26th Vacuum Symp., Tokyo, Nov., p. 116 (1985).
84) M. Uda: "PIXE Analysis for Medical Science," 3rd Seminar on Science and Technology—Small Accelerators and Their Application, Interchange Association Japan, Tokyo, Nov. (1985).

4. Radiochemistry, radiation chemistry and radiation biology

1) Y. Ito, Y. Tabata, and K. Kimura: "Electron Scavenger Effects on the Fluorescence Induced by Single High-LET Particle," 7th Int. Conf. on Positron Annihilation, New Delhi, India, Jan. (1985).
2) T. Takahashi: "Effect of Heavy Ions on Microorganisms," RIKEN Symp. on Studies by Using RIKEN Accelerators-1984, Wako, Mar. (1985).
3) T. Takahashi, F. Yatagai, T. Katayama, and K. Masuda: "Analysis of Lethal Effect Induced by Heavy-Ion Bombardment," 32nd Spring Meeting Jpn. Soc. Appl. Phys. and Related Societies, Tokyo, Mar. (1985).
4) K. Asai, F. Ambe, S. Ambe, T. Okada, and H. Sekizawa: "TDPAC Studies on ^{111}Cd(← ^{111}In) in α-Fe_2O_3 at High Temperature," 50th National Meeting Chem. Soc. Jpn. (Spring), Tokyo, Apr. (1985).
5) S. Ambe, F. Ambe, and T. Okada: "Adsorption Kinetics of Carrier-Free ^{119}Sb(V) onto α-Fe_2O_3," 50th National Meeting Chem. Soc. Jpn. (Spring), Tokyo, Apr. (1985).
6) M. Aratani, H. Nagai, M. Yanokura, O. Kuboi, S. Hayashi, I. Kohno, and T. Nozaki: "Forward Scattering Analysis by Heavy-Ion Beam Applied to the Study of Hydrogen in Amorphous Silicon and Silica," 7th Int. Conf. on Ion Beam Analysis, Berlin, FRG, July (1985).
7) F. Ambe, K. Asai, S. Ambe, T. Okada, and H. Sekizawa: "Comparative Mössbauer and TDPAC Studies on the After-Effects of the EC Decays of ^{119}Sb and ^{111}In in α-Fe_2O_3," Int. Conf. Applied Mössbauer Effect, Leuven, Sept. (1985).
8) F. Ambe, S. Ambe, T. Okada, and H. Sekizawa: "*In situ* Mössbauer Emission Spectroscopy of $^{57}Co^{2+}(\rightarrow{}^{57}Fe^{3+})$ and $^{119}Sb^{5+}(\rightarrow{}^{119}Sn^{4+})$ at the α-Fe_2O_3-Aqueous Solution Interfaces," Int. Conf. Applied Mössbauer Effect, Leuven, Sept. (1985).
9) T. Takahashi, K. Eguchi, A. Hashizume, and T. Inada: "Data Requirements in Heavy Ion Radiotherapy—Considerations on Available Physical Quantities—," IAEA Advisory Group Meeting on Nuclear and Atomic Data for Radiotherapy and Radiobiology, Rijswijk, The Netherlands, Sept. (1985).
10) F. Ambe, S. Ambe, T. Okada, and H. Sekizawa: "*In situ* Mössbauer Studies of α-Fe_2O_3/Aqueous Solution Interfaces with Adsorbed $^{57}Co^{2+}$ and $^{119}Sb^{5+}$ Ions," 1985 ACS Ann. Meeting, Chicago, Sept. (1985).
11) M. Yanokura, Q. Qiu, M. Aratani, H. Nagai, I. Kohno, and T. Nozaki: "Utilization of Linear Accelerator for the Study of the Formation of Radiation-Resistive Oxide Film on Silicon," 29th Symp. on Radiochemistry, Funabashi, Oct. (1985).
12) T. Ohtsuki, Y. Hatsukawa, T. Miura, K. Sueki, H. Nakahara, and I. Kohno: "Proton Induced Fission of ^{237}Np," 29th Symp. Radiochemistry, Funabashi, Oct. (1985).
13) N. Ito, K. Ikeda, M. Yanokura, S. Hayashi, Q. Qiu, H. Nagai, M. Aratani, I. Kohno, and T. Nozaki: "Heavy-Ion Probe Rutherford Backscattering Applied to the Fabrication Process of Schottky-Barrier Diode," 29th Symp. on Radiochemistry, Funabashi, Oct. (1985).
14) Y. Hamajima, K. Sueki, M. Magara, H. Nakahara, and I. Kohno: "Mass Division on Low Energy Nuclear Fission of ^{238}U," 29th Symp. on Radiochemistry, Funabashi, Oct. (1985).
15) K. Asai, F. Ambe, S. Ambe, T. Okada, and H. Sekizawa: "TDPAC and Emission Mössbauer Studies on the After-Effects of the EC Decays of ^{111}In and ^{119}Sb in α-Fe_2O_3," 29th Symp. on Radiochemistry, Funabashi, Oct. (1985).
16) F. Ambe, K. Asai, S. Ambe, and H. Sekizawa: "Time Differential Perturbed Angular Correlation Study on (^{111}In →) ^{111}Cd in In_2O_3," 29th Symp. on Radiochemistry, Funabashi, Oct. (1985).
17) T. Nozaki, Y. Itoh, Y. Ohkubo, T. Kimura, and H. Fukushima: "Simultaneous Charged Particle Activation Analysis of Carbon and Boron in Gallium Arsenide," 29th Symp. on Radiochemistry, Funabashi, Oct. (1985).
18) Y. Minai, S. Ambe, and T. Nozaki: "Preparation and Application of ^{29}Al Produced by the ^{26}Mg(α,p)^{29}Al Reaction," 29th Symp. on Radiochemistry, Funabashi, Oct. (1985).
19) T. Nozaki, Y. Itoh, Y. Ohkubo, T. Kimura, H. Fukushima, and Y. Kadota: "Determination of Carbon in Galium Arsenide with Reaction of ^{12}C(d, n)^{13}N," 46th Fall Meeting Jpn. Soc. Appl. Phys., Kyoto, Oct. (1985).
20) K. Eguchi, I. Kaneko, T. Kosaka, K. Nakano, and Sushiana: "Non-Repairable DNA Lesions in HMV-I Cells Irradiated with N-Ion Beams," Ann. Meeting Jpn. Soc. Radiation Research, Nara, Oct. (1985).

21) K. Kimura, T. Azuma, Y. Aoki, T. Kuriyama, K. Akasu, Y. Itoh, and Y. Tabata: "Roles of Helium-Excimer-Clusters in Heavy-Ion Impinged Condensed Helium," 28th Conf. on Radiation Chemistry, Sapporo, Nov. (1985).
22) K. Kimura: "Formation of the Dimer and Cluster of Helium-Excimers in the Heavy-Ion Irradiated Dense Helium at 3.9-5.2 K," 28th Conf. on Radiation Chemistry, Sapporo, Nov. (1985).
23) Y. Ito, T. Azuma, Y. Aoki, Y. Katsumura, Y. Tabata, and K. Kimura: "A Study of the Spur and Track Using a Technique of the Single-Particle Hitting and Single-Photon Counting," 28th Conf. on Radiation Chemistry, Sapporo, Nov. (1985).
24) M. Yanokura, Q. Qiu, K. Ikeda, N. Ito, M. Aratani, and T. Nozaki: "Heavy-Ion Rutherford Backscattering Analysis Applied to the Electronic materials," 4th Symp. on Ion Beam Technology, Hosei University, Tokyo, Dec. (1985).

VIII. LIST OF OUTSIDE USERS AND THEIR THEMES

(Jan.-Dec. 1985)

1)	T. Kimura and H. Hukushima "Radiochemical Analysis of ^{16}O, ^{14}N and ^{12}C in Si Crystal and GaAs"	Japan Chemical Analysis Center
2)	H. Nakahara "Production of ^{97}Ru"	Faculty of Science, Tokyo Metropolitan Univ.
3)	S. Orito and S. Nakamura "Test of Sensibility of CR39 Track Detector for High Energy Proton"	Faculty of Science, Univ. Tokyo
4)	H. Homareda "Production of ^{43}K"	Faculty of Medicine, Kyorin Univ.
5)	Y. Moriguchi "Radiation Damage of Cover Glass for a Solar Cell"	R & D Div., Asahi Glass Co., Ltd.
6)	T. Hayashi "Radiation Damage of Cover Glass for a Solar Cell"	Institute of Space and Astronautical Science
7)	K. Yamamoto "Study of Single Event Upset in Microprocessors by Bombarding ^{14}N and ^{40}Ar Particles"	Semiconductor R & D Lab. Toshiba Co., Ltd.
8)	S. Yoshida and M. Goto "Study of Effect by Bombarding High Energy Proton on a GaAs Solar Cell"	LSI R & D Lab. Kamakura Works Mitsubishi Electric Co., Ltd.
9)	K. Omura and T. Abe "Calibration of Space Environment Monitor Carried on a Satellite with Variable Particles"	Kamakura Works Mitsubishi Electric Co., Ltd.

IX. LIST OF SEMINARS

(Jan.-Dec. 1985)

1) S. K. Nanda, Univ. Minnesota-LAMPF (USA), 25 February
"Observation of Ml-Excitations in Intermediate Energy Proton Scattering"

2) A. Shimizu, RCNP (Osaka), 13 March
"Vacuum Characteristics of Alminium RF-Cavity and Design of Evacuating System for Accelerators"

3) F. A. Beck, CRN (France), 16 March
"Château de Crystal"

4) R. Schuch, Max Planck Institut (West Germany), 19 March
"On the Plan of the Cooler Ring at Heidelberg"

5) W. von Oertzen, Hahn-Meitner-Institut (Berlin), 26 March
"Transfer Reactions with Intermediate Energy Heavy Ions"

6) I. Tanihata, INS (Tokyo), 27 March
"Experiments with Beam of Unstable Nuclei"

7) S. Iwasaki, Univ. of Chiba (Chiba), 8 May
"Structure of $K=1^+$ Band in Deformed Nuclei"

8) J. Ärje, Jyuäsky lä Univ. (Finland), 28 May
"IGISOL; Now and in Future"

9) S. Takeda, ISIR (Osaka), 31 May
"Novel Accelerators"

10) T. Katayama, INS (Tokyo), 7 June
"Beam Cooling"

11) M. Oshima, JAERI (Ibaraki), 25 June
"Shape Change at High Spin States in Deformed Nuclei"

12) H. Shimizu, Tokyo Inst. Technol.(Tokyo), 2 July
"Nucleon-Nucleon Scattering and Dibaryon"

13) M. Olivier, Saclay (France), 5 July
"SATURNE II—A Heavy Ions and Polarized Particles Synchrotron for Intermediate Energy Physics"

14) M. Sugita, Univ. of Tokyo (Tokyo), 9 July
"Shape Change Transition in the Region of $Z=40$"

15) Y. Sakuragi, INS (Tokyo), 15 July
"Non-Central Force between Two Nuclei and Polarized Heavy Ion Scattering"

16) R. Wada, GSI (West Germany), 19 July
"Production Mechanism of Light and Medium Heavy Fragments at 48 and 84 MeV/N"

17) K. Yazaki, Univ. of Tokyo (Tokyo), 24 July
"Nuclear Shell Model or Quark Shell Model?"

18) K. Yoshida, INS (Tokyo), 25 July
"GeV Electron Accelerators"

19) T. Numao, TRIUMF (Canada), 2 August
"Experiments at TRIUMF"

20) P. Egelhof, Maintz Univ. (West Germany), 22 August
"High Precision Spectroscopy on Light Nuclei Using Aligned Beams and Muonic Atoms"

21) C. Gagliardi, Texas A & M Univ. (USA), 3 September
"(n,p) Scattering at Intermediate Energies"

22) K. Seth, North Western Univ. (USA), 4 September
"Perspectives in Intermediate Energy Proton and Pion Physics"

23) B. Mayer, Saclay(France), 5 September
"Experiments Using Intermediate Protons and Antiprotons"

24) D. Fick, Marburg Univ. (West Germany), 6 September
"Polarized Li Ion Source and Applications

to Nuclear and Surface Physics"

25) J. Raynal, Saclay (France), 6 September
"Coupled-Channel Description of Inelastic Scattering with a Dirac Equation"

26) H. Sagawa, Univ. of Tokyo (Tokyo), 17 September
"Vibration and Vaporization of Thermal Nuclei"

27) B. Müller, Frankfurt Univ. (West Germany), 24 September
"Collective Pion Radiation from Nuclear Collision"

28) J. Kasagi, Tokyo Inst. Technol. (Tokyo), 1 October
"Neutron-Fragment Coincidence Measurement in $^{14}N+^{165}Ho$ and Ni Reactions"

29) A. Iwamoto, JAERI (Ibaraki), 22 October
"Particle Emissions from Preequilibrium States in Heavy Ion Collisions"

30) H. Toki, Tokyo Metropolitan Univ. (Tokyo), 29 October
"Pion Absorption in Nuclei"

31) H. Tanaka, Hokkaido Univ. (Hokkaido), 6 November
"Multiple Scattering and α-particle"

32) N. Takigawa, Tohoku Univ. (Miyagi), 14 November
"Heavy Ion Fusion Reactions below the Coulomb Barrier"

33) K. Kaneko, INS (Tokyo), 15 November
"Present Status of Measurement of Vacuum in the Region of $10^{-2}\sim10^{-12}$ Torr"

34) J. Aysto, Jyuäsky lä Univ. (Finland), 22 September
"Trends in the Study of Light Proton Rich Nuclei"

35) K. Sugawara-Tanabe, Univ. of Tokyo (Tokyo), 26 September
"Thermal High Spin Giant Dipole Resonance"

36) T. Kajino, Tokyo Metropolitan Univ. (Tokyo), 6 December
"Pionic Fusion and Cluster Correlation in Nuclei"

37) D.W.L. Sprung, McMaster Univ. (Canada), 10 December
"Some Aspects of Hatree-Fock Calculations of Nuclear Structure"

38) Y. Koike, RCNP (Osaka), 12 December
"Application of Three-Body Faddeev Equation to Nuclear Scattering"

X. LIST OF PERSONNEL

Members of the Board

AWAYA Yohko 粟屋容子
HASHIZUME Akira 橋爪 朗
KAMITSUBO Hiromichi 上坪宏道
KIRA Akira 吉良 爽
KURIHARA Osamu 栗原 修
NOZAKI Tadashi 野崎 正
SAKAIRI Hideo 坂入英雄
SEKIZAWA Hisashi 関沢 尚
WATANABE Tsutomu 渡部 力*
CHIBA Yoshiaki 千葉好明
ISHIHARA Masayasu 石原正泰
KANEKO Ichiro 金子一郎
KOHNO Isao 河野 功
NAGAMINE Kanetada 永嶺謙忠
OKADA Shigefumi 岡田重文
SAKAMOTO Yuichi 坂本雄一
UDA Masayuki 宇田応之

* chairman

Cyclotron Operation and Maintenance Group

FUJITA Shin 藤田 新
KAGEYAMA Tadashi 影山 正
KOHNO Isao 河野 功
TAKEBE Hideki 武部英樹
IKEGAMI Kumio 池上九三男
KOHARA Shigeo 小原重夫
OGIWARA Kiyoshi 荻原 清

Linac Operation and Maintenance Group

CHIBA Yoshiaki 千葉好明
IKEZAWA Eiji 池沢英二
KAMBARA Tadashi 神原 正
KUBO Toshiyuki 久保敏幸
YANOKURA Minoru 矢野倉 実
HEMMI Masatake 逸見政武
INOUE Toshihiko 井上敏彦
KASE Masayuki 加瀬昌之
MIYAZAWA Yoshitoshi 宮沢佳敏

Scientific and Engineering Personnel

Cyclotron Laboratory

BE Suck Hee 裵 碩喜
FUJITA Jiro 藤田二郎
HARA Masahiro 原 雅弘
INAMURA Takashi 稲村 卓
KARASAWA Takashi 唐沢 孝
MORITA Kohsuke 森田浩介
NAGASE Makoto 長瀬 誠
NAKANISHI Noriyoshi 中西紀喜
SAKAMOTO Ichiro 坂本一郎
FUJISAWA Takashi 藤沢高志
GOTO Akira 後藤 彰
HATANAKA Kichiji 畑中吉治
KAMITSUBO Hiromichi 上坪宏道
KOHNO Isao 河野 功
MOTONAGA Shoshichi 元永昭七
NAKAJIMA Shunji 中島諄二
OIKAWA Yoshifumi 老川嘉郁
SHIKATA Takashi 四方隆史

SHIMIZU Kazuo 清水和男
WADA Takeshi 和田 雄
YANO Yasushige 矢野安重
YOSHINAGA Naotaka 吉永尚孝
TAKESHITA Isao 竹下勇夫
YAMAJI Shuhei 山路修平
YOKOYAMA Ichiro 横山一郎

(Visitors)
DOKE Tadayoshi 道家忠義* (Sci. and Eng. Res. Lab., Waseda Univ.)
FUJIOKA Manabu 藤岡 学 (Cyclotron and Radioisotope Center, Tohoku Univ.)
FUKUMOTO Sadayoshi 福本貞義 (KEK)
FURUNO Kohei 古野興平 (Inst. Phys., Univ. Tsukuba)
GOU Minyan 郭 敏燕 (Inst. Mod. Phys., Academia Sinica, China)
HIRAKI Akio 平木昭夫 (Fac. Eng., Osaka Univ.)
IEKI Kazuo 家城和夫 (Dept. Phys., Tokyo Inst. Technol.)
INOUE Makoto 井上 信 (RCNP, Osaka Univ.)
ISOYA Akira 磯矢 彰 (School Sci., Tokai Univ.)
KAMIMURA Masayasu 上村正泰 (Dept. Phys., Kyushu Univ.)
KASAGI Jirota 笠木治郎太 (Dept. Phys., Tokyo Inst. Technol.)
KATORI Kenji 鹿取謙二 (Dept. Phys., Osaka Univ.)
KATSURAGAWA Hidetsugu 桂川秀嗣 (Dept. Phys., Toho Univ.)
KIKUCHI Fumio 菊地文男 (Dept. Math., College of General Education, Univ. Tokyo)
KONDO Michiya 近藤道也 (RCNP, Osaka Univ.)
KUDO Hisaaki 工藤久昭 (Dept. Chem., Niigata Univ.)
MINOWA Tatsuya 箕輪達哉 (Dept. Phys., Toho Univ.)
MIURA Iwao 三浦 岩 (RCNP, Osaka Univ.)
MIYATAKE Hiroari 宮武宇也 (Inst. Nucl. Study, Univ. Tokyo)
MURAKAMI Takeshi 村上 健 (Dept. Phys., Tokyo Inst. Technol.)
NAGAKAWA Johsei 永川城正 (Nat. Res. Inst. for Metals)
NAGAMIYA Shoji 永宮正治 (Dept. Phys., Univ. Tokyo)
NAKAHARA Hiromichi 中原弘道 (Dept. Chem., Tokyo Metropolitan Univ.)
NOMURA Toru 野村 亨* (Inst. Nucl. Study, Univ. Tokyo)
ODERA Masatoshi 小寺正俊* (Sci. and Eng. Res. Lab., Waseda Univ.)
SATO Kenichi 佐藤憲一 (Division Phys., Tohoku College of Pharmacy)
SHIRAISHI Haruki 白石春樹 (Nat. Res. Inst. for Metals)
SHIMAZU Mitsuyoshi 島津備愛 (Dept. Phys., Toho Univ.)
SUEKI Keisuke 末木啓介 (Inst. Nucl. Study, Univ. Tokyo)
TAKEKOSHI Hidekuni 竹腰秀邦 (Inst. Chem. Res., Kyoto Univ.)
TAKEMASA Tadashi 武政尹士 (Dept. Phys., Saga Univ.)
TANAKA Jinichi 田中仁市 (Inst. Nucl. Study, Univ. Tokyo)
TORIZUKA Kanji 鳥塚莞爾 (Fac. Med., Kyoto Univ.)
YAMAMOTO Norikazu 山本徳和 (Nat. Res. Inst. for Metals)
YONG Shangyun 楊 尚運 (Inst. Mod. Phys., Academia Sinice, China)
YOSHIDA Nobuaki 吉田宣章 (Dept. Phys., Univ. Tokyo)
YOSHIDA Shiro 吉田思郎 (Dept. Phys., Tohoku Univ.)

* Visiting Professor

(Students)
HARADA Hideo 原田秀郎 (Dept. Phys., Tokyo Inst. Technol.)
HATSUKAWA Yuichi 初川雄一 (Dept. Chem., Tokyo Metropolitan Univ.)
OZAWA Keiko 小沢恵子 (College Hum. and Sci., Nihon Univ.)
SHIDA Kenji 志田剛二 (Fac. Sci. and Eng., Chuo Univ.)
TACHIBANAKI Hiroshi 橘木 寛 (Dept. Phys., Tokyo Inst. Technol.)
WAKASUGI Eiichi 若杉栄一 (Fac. Sci. and Eng., Chuo Univ.)
YOSHIDA Koichi 吉田光一 (Dept. Phys., Tokyo Inst. Technol.)

Linac Laboratory

CHIBA Toshiya 千葉利哉
GONO Yasuyuki 郷農靖之
INOUE Toshihiko 井上敏彦
KASE Masayuki 加瀬昌之
KUMAGAI Hidekazu 熊谷秀和
MIZOGAWA Tatsumi 溝川辰己
YANOKURA Minoru 矢野倉 実
CHIBA Yoshiaki 千葉好明
HEMMI Masatake 逸見政武
KAMBARA Tadashi 神原 正
KUBO Toshiyuki 久保敏幸
MIYAZAWA Yoshitoshi 宮沢佳敏
TONUMA Tadao 戸沼正雄

(Visitors)
FUJIWARA Ichiro 藤原一郎 (Inst. Atomic Energy, Kyoto Univ.)
ITO Noriaki 伊藤憲昭 (Dept. Crystalline Materials, Nagoya Univ.)
SUGAWARA Masahiko 菅原昌彦 (Fund. Sci., Chiba Inst. Technol.)

(Student)
FUKUDA Mitsunori 福田光順 (Fac. Sci., Tokyo Inst. Technol.)

Radiation Laboratory

ASAHI Koichiro 旭 耕一郎
ICHIHARA Takashi 市原 卓
IZUMO Koichi 出雲光一
KONNO Satoshi 金野 智
TAKAHASHI Tan 高橋 旦
HASHIZUME Akira 橋爪 朗
ISHIHARA Masayasu 石原正泰
KOHNO Toshiyuki 河野俊之
OKANO Masaharu 岡野真治
TENDOW Yoshihiko 天道芳彦

(Visitors)
DOKE Tadayoshi 道家忠義 (Sci. and Eng. Res. Lab., Waseda Univ.)
FUJIOKA Manabu 藤岡 学 (Dept. Phys., Tohoku Univ.)
HASEGAWA Takeo 長谷川武夫 (Inst. Nucl. Study, Univ. Tokyo)
HITACHI Akira 月出 章 (Sci. & Eng. Res. Lab., Waseda Univ.)
IIO Masahiro 飯尾正広 (Fac. Med., Univ. Tokyo)
KANG Yung-Ho 姜 栄浩 (Dept. Natural Sci., Kyung-Pook Univ.)
KOBAYASHI Hisanobu 小林久信 (Fac. Eng., Saitama Univ.)
KUBOTA Shinzou 窪田信三 (Fac. Sci., Rikkyo Univ.)
LEE Sang Mu 李 相茂 (Univ. Tsukuba)
MASUDA Kimiaki 増田公明 (School Sci. Eng., Waseda Univ.)

MOTOBAYASHI Toru 本林 透 (Fac. Sci., Rikkyo Univ.)
MURAMATSU Hisakazu 村松久和 (Nat. Lab. High Energy Phys.)
NAGAHARA Teruaki 永原照明 (Inst. Atomic Energy, Rikkyo Univ.)
OHSUMI Hideaki 大隅秀晃 (Fac. Sci., Osaka Univ.)
OHTSUKA Hideko 大塚秀子
OHTSUKA Rikuro 大塚陸郎 (Nagoya Inst. Technol.)
ONAI Yoshio 尾内能夫 (Dept. Phys., Cancer Inst.)
SHIBAMURA Eido 柴村英道 (Saitama College of Health)

(Students)
MIURA Taichi 三浦太一 (Dept. Chem., Tokyo Metropolitan Univ.)
SUZUKI Satoshi 鈴木 聡 (School Sci. Eng., Waseda Univ.)
YANAGA Makoto 矢永誠人 (Dept. Chem., Tokyo Metropolitan Univ.)
YUNOKI Akira 柚木 彰 (School Sci. Eng., Waseda Univ.)

Atomic Processes Laboratory

ANDO Kozo 安藤剛三
AWAYA Yohko 粟屋容子
HITACHI Akira 月出 章
IWAI Masahiro 岩井正博
KANAI Yasuyuki 金井保之
KOHMOTO Susumu 河本 進
NISHIDA Masami 西田雅美
SHIMAMURA Isao 島村 勲
WATANABE Tsutomu 渡部 力

(Visitors)
FUJIMA Kazumi 藤間一美 (Dept. Phys., Chuo Univ.)
HARA Shunsuke 原 俊介 (Dept. Phys., Univ. Tsukuba)
ISHII Keishi 石井慶之 (Dept. Eng. Sci., Kyoto Univ.)
ISMAIL M. Mostafa (Dept. Phys., Cairo Univ.)
ITOH Yoh 伊藤 陽 (Fac. Sci., Josai Univ.)
KARASHIMA Shosuke 唐島照介 (Dept. Electr. Eng., Tokyo Univ. Sci.)
KOBAYASHI Nobuo 小林信夫 (Dept. Phys., Tokyo Metropolitan Univ.)
KOIKE Fumihiro 小池文博 (School Med., Kitasato Univ.)
KOIZUMI Tetsuo 小泉哲夫 (Dept. Phys., Rikkyo Univ.)
KOYAMA Naoto 小山直人 (Dept. Eng. Phys., Univ. Electrocommunications)
LIN Chii-Dong 林 啓東 (Dept. Phys., Kansas State Univ.)
MATSUMOTO Atsushi 松本 淳 (Inst. Plasma Phys., Nagoya Univ.)
MATSUO Takashi 松尾 崇 (Dept. Pathology, Tokyo Med. and Dent. Univ.)
MATSUZAWA Michio 松澤通生 (Dept. Eng. Phys., Univ. Electrocommunications)
MCDOWELL M. R. Coulter (Dept. Math., Royal Holloway & Bedford New College)
OHTANI Shunsuke 大谷俊介 (Inst. Plasma Phys., Nagoya Univ.)
OKUNO Kazuhiko 奥野和彦 (Dept. Phys., Tokyo Metropolitan Univ.)
SATO Hiroshi 佐藤浩史 (Dept. Phys., Ochanomizu Univ.)
SATO Kuninori 佐藤国憲 (Inst. Plasma Phys., Nagoya Univ.)
SCHUCH Reinhold (Dept. Phys., Heidelberg Univ.)
SHIBATA Hiromi 柴田裕実 (Research Center for Nucl. Sci. & Technol., Univ. Tokyo)
SHIMA Kunihiro 島 邦博 (Inst. Appl. Phys., Univ. Tsukuba)
SHIMAKURA Noriyuki 島倉紀之 (General Educ. Dept., Niigata Univ.)

TAKAGI Shoji 高木祥示 (Dept Phys., Toho Univ.)
TAWARA Hiroyuki 俵 博之 (Inst Plasma Phys., Nagoya Univ.)
TOKORO Nobuhiro 所 伸宏 (Res. Lab. Nucl. Reactors, Tokyo Inst. Technol.)
TOSHIMA Nobuyuki 戸嶋信幸 (Inst. Appl. Phys., Univ. Tsukuba)
TSURUBUCHI Seiji 鶴淵誠二 (Fac. Technol., Tokyo Univ. Agric. Technol.)
URAKAWA Junji 浦川順治 (Nat. Lab. High Energy Phys.)

(Students)
HINO Kenichi 日野健一 (Dept. Appl. Phys., Univ. Tokyo)
NAKANISHI Kiyotaka 中西清隆 (Dept. Chem., Waseda Univ.)

Metal Physics Laboratory
ISHIDA Katsuhiko 石田勝彦
KOYAMA Akio 小山昭雄
NAGAMINE Kanetada 永嶺謙忠
SHIOTANI Nobuhiro 塩谷亘弘
YAGI Eiichi 八木栄一

(Students)
KANO Fumitoshi 鹿野文寿 (School Sci. Eng., Waseda Univ.)
NAKAMURA Shiho 中村志保 (School Sci. Eng., Waseda Univ.)

Magnetic Materials Laboratory
ASAI Kichizo 浅井吉蔵
OKADA Takuya 岡田卓也
SAKAI Nobuhiko 坂井信彦
SEKIZAWA Hisashi 関沢 尚

Plasma Physics Laboratory
ISHIBE Yukio 石部行雄
ISHII Shigeyuki 石井成行
OKAZAKI Kiyohiko 岡崎清比古
OYAMA Hitoshi 大山 等
SAKAMOTO Yuichi 坂本雄一
YANO Katsuki 矢野勝喜

Semiconductors Laboratory
(Visitor)
AONO Keiko 青野桂子 (College of Liberal Arts, Kitasato Univ.)

Solid-State Chemistry Laboratory
KOBAYASHI Masayoshi 小林雅義
MAEDA Kuniko 前田邦子
SASA Yoshihiko 佐々嘉彦
UDA Masayuki 宇田応之

(Visitors)
BENKA Oswald (Johannes Kepler-Univ. Linz, Austria)
KUSUYAMA Hiroyuki 楠山弘之 (Cancer Institute Hospital Tokyo)
YOKODE Yutaka 横出 裕 (School Med., Nihon Univ.)

Radiochemistry Laboratory

AMBE Fumitoshi 安部文敏
AMBE Shizuko 安部静子
ARATANI Michi 荒谷美智
HAYASHI Shigeki 林 茂樹*
ITOH Yoshiko 伊東芳子
IWAMOTO Masako 岩本正子
NOZAKI Tadashi 野崎 正
OHKUBO Yoshitaka 大久保嘉高

*through March 31, 1985

(Visitors)

AIMI Toshihiko 相見俊彦 (NEC Corporation)
FUKUSHIMA Hiroto 福嶋浩人 (Japan Chemical Analysis Center)
HASHIMOTO Tetsuo 橋本哲夫 (Fac. Sci., Niigata Univ.)
HUANG Ziwei 黄 子蔚 (Inst. Biology, Pedology and Psamology Res., China)
IKEDA Kazuko 池田和子 (NEC Corporation)
IMAI Masato 今井正人 (Komatsu Electronic Metals Co., Ltd.)
ITOH Nobuyuki 伊藤信之 (NEC Corporation)
KIMURA Toshimasa 木村敏正 (Japan Chemical Analysis Center)
KUBOI Osamu 久保井 収 (Komatsu Electronic Metal Co., Ltd.)
MINAI Yoshitaka 薬袋佳孝 (Fac. Sci., Univ. Tokyo)
NAGAI Hisao 永井尚生 (College Hum. and Sci., Nihon Univ.)
NASU Saburo 那須三郎 (Fac. Eng. Sci., Osaka Univ.)
OOHIRA Shigeo 大平重男 (Nikkei Techno Res. Co., Ltd.)
SUEHIRO Makiko 末広牧子 (Tokyo Metropolitan Geriatric Hospital)
YATSURUGI Yoshifumi 八劔吉文 (Komatsu Electronic Metals Co., Ltd.)
YOKOI Fuji 横井風児 (Mental and Muscular Disorders, National Center for Nervous)
HAYASHI Akira 林 瑛 (NSG Yamaguchi Corporation Ltd.)
YAMAMOTO Kazuhiko 山本和彦 (Toshiba Corporation, R & D Center)

(Students)

ARAI Iwao 新井五輪夫 (Fac. Pharm., Sci. Univ. Tokyo)
KUBO Kenya 久保謙哉 (Fac. Sci., Univ. Tokyo)
TANAKA Isao 田中 功 (Fac. Eng. Sci., Osaka Univ.)
QUI Qi 邱 斉 (Nucl. React. Res. Lab., Tokyo Inst. Technol.)

Radiation Chemistry Laboratory

KIMURA Kazuie 木村一宇

(Visitor)

ITO Yasuo 伊藤泰男 (Res. Center Nucl. Sci. and Technol., Univ. Tokyo)

(Students)

HARA Korehisa 原 是久 (Dept. Phys., Chuo Univ.)
IIDA Tsuyoshi 飯田 剛 (Dept. Phys., Chuo Univ.)
KATAOKA Masayoshi 片岡将克 (Dept. Phys., Chuo Univ.)

Radiobiology Laboratory

EGUCHI Kiyomi 江口清美
KANEKO Ichiro 金子一郎
NAKANO Kazushiro 中野和城
OKADA Shigefumi 岡田重文

(Visitors)
KOSAKA Toshiyuki 小坂俊之 (College Agric. Vet. Med., Nihon Univ.)
MAJIMA Hideyuki 馬嶋秀行 (Fac. Med., Univ. Tokyo)
OKADA Gensaku 岡田源作 (Tokyo-Toritsu-Itabashi-Kango-Senmon-Gakko)

Safety Control Affairs Office

KAGAYA Satoru 加賀屋 悟
KATOU Takeo 加藤武雄
KURIHARA Osamu 栗原 修
MATSUZAWA Yasuhide 松沢安秀
MIYAGAWA Makoto 宮川真言
SAKAMOTO Ichiro 坂本一郎
SHINOHARA Shigemi 篠原茂己
TAKI Kenro 滝 剣朗
USUBA Isao 薄葉 勲

Beam Analysis Center

IWAKI Masaya 岩木正哉
KOBAYASHI Takane 小林 峰
SAKAIRI Hideo 坂入英雄

(Visitor)
OOHIRA Shigeo 大平重男 (Nikkei Techno-Research Co.)

AUTHOR INDEX

RIKEN Accelerator Progress Report

理化学研究所加速器年次報告　第19巻（1985）

印　刷　昭和61年（1986）8月5日
発　行　昭和61年（1986）8月10日
発行者　理化学研究所
代表者　宮　島　龍　興
〒351-01　埼玉県和光市広沢2番1号
電話（0484）62－1111
編集者　理化学研究所加速器運営委員会
製　作　財団法人　学会誌刊行センター
〒113　東京都文京区弥生2丁目4番16号
印刷所　勝　美　印　刷　株　式　会　社
〒112　東京都文京区小石川1丁目3番7号

定価 5,000円

理化学研究所

埼玉県　和光市　広沢